The Platreef magma event at the world-class Turfspruit Ni-Cu-PGE deposit: implications for mineralisation processes and the Bushveld Complex stratigraphy

Hannah. G. Stephenson

Submitted in fulfilment of the requirements for the degree PhD

December 2018

DECLARATION

This work has not been submitted in substance for any other degree or award at this or any other university or place of learning, nor is being submitted concurrently in candidature for any degree or other award.

Signed ……..… (candidate)

Date ……..……..……..……..

STATEMENT 1

This thesis is being submitted in partial fulfilment of the requirements for the degree of PhD.

Signed ……..……(candidate)

Date ……..……

STATEMENT 2

This thesis is the result of my own independent work/investigation, except where otherwise stated, and the thesis has not been edited by a third party beyond what is permitted by Cardiff University's Policy on the Use of Third Party Editors by Research Degree Students. Other sources are acknowledged by explicit references. The views expressed are my own.

Signed……..……(candidate)

Date ……..……..

STATEMENT 3

I hereby give consent for my thesis, if accepted, to be available online in the University's Open Access repository and for inter-library loan, and for the title and summary to be made available to outside organisations.

Signed……..……..(candidate)

Date ……

STATEMENT 4

I hereby give consent for my thesis, if accepted, to be available online in the University's Open Access repository and for inter-library loans **after expiry of a bar on access previously approved by the Academic Standards & Quality Committee.**

Signed……..……..(candidate)

Date ……..……...

Acknowledgements

First and foremost I would like to thank the mining company Ivanplats Pty Ltd., for their generous sponsorship and ongoing support throughout this PhD. In particular, my thanks go to; Danie Grobler (Principal Geologist), Alexandra Crossingham (database manager), Albie Brits (structural geologist) and Tim Dunnett (exploration geologist).

My thanks go to my supervisor Iain McDonald for his guidance, analytical and motivational support; I have really enjoyed looking at South African rocks and this wouldn't have happened without you. Academic support was also provided by Hannah Hughes who can always be relied upon for fruitful scientific discussions, I have enjoyed talking Bushveld with you! Hannah Hughes is also thanked for the collection of samples of the Pietersburg Greenstone Belt for use in this study accompanied by Bianca Kennedy and Tshilisanani (Simon) Nethononda.

The sulphur isotope work wouldn't have been possible without funding by a NERC NIG grant; the following contributors are thanked for their support and technical input to this successful grant application Adrian Boyce, Hannah Hughes and Iain McDonald. I would also like to thank the staff at SUERC, in particular Alison McDonald for supervision and training on both the conventional and laser sulphur lines and for running a small selection of prepared samples through the mass spectrometer on my behalf.

The majority of the analytical work was facilitated by technical staff at Cardiff University. Lindsey Axe is thanked for setting up the optical microscope ready for petrographic studies. Anthony Oldroyd for preparing all polished thin sections and assisting with numerous lab equipment set up and resolving of issues that occurred during the course of the analytical work. Christopher Brosson is thanked for helping to set-up the reduction column and for sharing bottles of chromous chloride when I ran out of my own supply. Finally, Duncan Muir for assistance setting up and running the scanning electron microscope and Iain McDonald the mass spectrometers and laser ablation system.

Last, but by no means least, this project wouldn't have been completed without the support of my friends and family. I feel really lucky to have studied for my PhD at the same time as Bianca Kennedy, Andrew Martin and Emma Bennett who have always been willing to listen, give advice and share knowledge. Mum and Dad thank you for being there whenever you were needed, for repeatedly telling me to "just get on with it" and for looking after Eva when I needed to long days in the office/lab. Josh – your support, love, encouragement and our dreams of a future together have made the long days writing up in dark November/December a lot easier!

Abstract

The Platreef Ni-Cu-PGE deposit as identified on the farm Turfspruit, northern limb of the Bushveld Complex, extends westwards and down-dip from the surface exposure. The orebody transitions with increasing depth from highly contaminated 'Platreef-style' mineralisation to a dominant magmatic stratigraphy hosting 'Merensky-style' mineralisation associated with persistent chromitites in the Flatreef and Deep Platreef. Four drill holes sampling each sector of the orebody have been examined to determine; the origin of the stratigraphy, the controls on the Ni-Cu-PGE mineralisation and the relationship of the Platreef to the wider Bushveld Complex.

Orthomagmatic processes, operating at depth in a staging chamber, are proposed to be dominant in generating the high PGE tenors in sulphides (> 600 ppm) and a magmatic platinum-group mineral (PGM) assemblage consisting of; Pt/Pd sulphides, Pt-Fe alloys, Pt-tellurides and laurite. This is supported by magmatic $\delta^{34}S$ values (av. +2 ‰) determined in sulphides in unaltered pyroxenites. Two stages of crustal contamination affected the development of the Platreef orebody on Turfspruit: (1) early-stage contamination homogenised in the parental magma at depth in a staging chamber; (2) in situ contamination through interaction with the footwall sediments of the Duitschland Formation (DF). The lithostratigraphy of the DF varies between the carbonate-dominated Upper DF and the shale-dominated Lower DF; which, results in mineralogical and geochemical heterogeneity across the deposit. This variability is especially evident in the $\delta^{34}S$ values with contaminated $\delta^{34}S$ signatures identified throughout the shallow Platreef (up to +19.6‰) and a systematic increase to heavy isotopic values (> +10 ‰) with depth is recorded in the Deep Platreef; in contrast, sulphides in the Flatreef give mainly magmatic $\delta^{34}S$ values. The presence of elevated $\delta^{34}S$ values in the Deep Platreef corresponds with a progressive decoupling of PGE grade from sulphides and the introduction of arsenide and antimonide PGMs.

The stratigraphic position of the Platreef, directly below the Main Zone, has led previous workers to conclude that it correlates with the Upper Critical Zone. This work, however, suggests that the relationship is more complex. The magmatic lineage of the Platreef across Turfspruit represents a 'hybrid' composition with contrasting Cr/MgO and Ce/Sm ratios, which consistently plot within the Critical and Main Zone ranges, respectively. Furthermore, there is no systematic increase in the Pt/Pd ratio with depth; this represents a key test of models proposing their lateral continuity. The northern limb is proposed as a discrete system, part of a larger network of sills and magma chambers, operating independently but connected at depth to the wider Bushveld Complex.

Table of Contents

List of Appendices

All appendices on CD provided.

Appendix A for Chapter 5

Appendix B for Chapter 6 (Electronic Appendix B)

Appendix C for Chapter 7 (Electronic Appendix C)

Appendix D for Chapter 8 (Electronic Appendix D.1, D.2, D.3, D.4, D.5)

Appendix E for Chapter 9

Appendix F for Chapter 10 (Electronic Appendix F)

List of Figures

CHAPTER 1

CHAPTER 2

CHAPTER 3

CHAPTER 7

List of Tables

Common Abbreviations

BIC – Bushveld Igneous Complex

BSE – backscattered electron

HREE – heavy rare earth elements

ICP-MS – inductively coupled plasma mass spectrometry

ICP-OES – inductively coupled plasma optical emission spectroscopy

LREE – light rare earth elements

REE – rare earth elements

PGE – platinum-group elements

PGM – platinum-group minerals

PPL – plane polarised light

RLS – Rustenburg layered suite

SEM – scanning electron microscope

TML – Thabazimbi Murchison Lineament

UCZ – Upper Critical Zone

XP – crossed polars

Chapter 1

Introduction

1.0 The Platinum Group Elements

The platinum-group elements (PGEs) are a series of six metallic elements: platinum (Pt), palladium (Pd), rhodium (Rh), iridium (Ir), osmium (Os) and ruthenium (Ru). They are found together, along with Fe, Co and Ni, in Group VIII of the d-block transition metals in the Periodic Table (see Figure 1.1 below). They form a geochemically coherent group and consequently behave similarly in natural systems; hence why they are commonly found in close association with each other in mineral deposits.

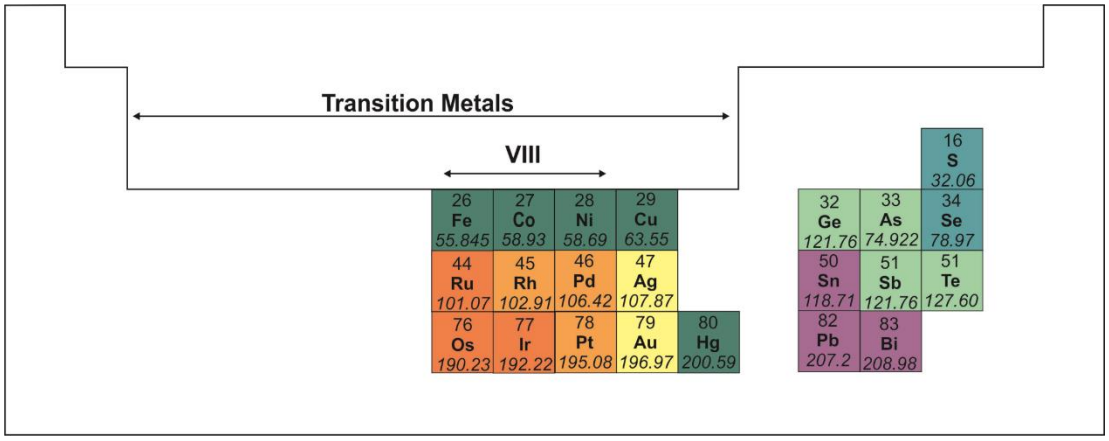

Figure 1.1: Periodic Table highlighting the position of the Group VIII transition metals; other elements included are frequently found in association with the Group VIII metals.

In contrast, the physical properties of PGEs vary significantly, albeit systematically with increasing atomic number, allowing their application in numerous industrial sectors. A summary of the main physical characteristics of the noble metals (PGEs and Au) are presented below in Table 1.1. The lanthanide contraction is responsible for the apparent similarities in the atomic radius, melting point and mechanical properties of vertically adjacent PGE in the Periodic Table (see Figure 1.1). The PGEs are unreactive in dilute acids and alkalis but are dissolved slowly in concentrated acid; this resistance to corrosion makes them suitable for several cosmetic and medical uses. Arguably, the most important structural feature of the Group VIII metals is that they have partially filled d-electron orbitals; it is this electron configuration that results in their effective catalytic properties. Pt and Pd exhibit the best catalytic properties, which form the basis of their important application in two main sectors: emission control systems on automobiles and process catalysts for chemical industries (Gunn et al., 2009).

Table 1.1: The main physical properties of the PGEs and Au. Source: [1]Gunn et al., 2009. [2]Royal Society of Chemists, 2015.

Physical Property	Ru	Rh	Pd	Os	Ir	Pt	Au
Atomic Number	44	45	46	76	77	78	79
Atomic Weight	101.07	102.94	108.42	190.23	192.22	195.08	196.97
Atomic Radius (cm^{-8})[1]	1.336	1.342	1.373	1.350	1.355	1.385	1.44
Density (g/cm^3)[1]	12.45	12.41	12.02	22.61	22.65	21.45	19.3
Melting Point (°C)[1]	2310	1960	1554	3050	2443	1769	1064
Boiling Point (°C)[1]	3900	3727	3140	5027	4130	3827	2836[2]
Electrical Resistivity (μΩcm at 0°C)[1]	6.8	4.33	9.93	8.12	4.71	9.85	2.15
Hardness (Mohs)[1]	6.5	5.5	4.75	7	6.5	4 - 4.5	2.5 - 3
Most Abundant Isotope[2]	^{102}Ru	^{103}Rh	^{106}Pd	^{192}Os	^{193}Ir	^{195}Pt	^{197}Au
Oxidation State: Common[2]	+3	+3	+2	+4	+3	+2	+1, +3
Oxidation State: Highest[2]	+8	+6	+4	+8	+6	+6	+5

1.1 PGEs on Earth

PGEs are rare in the silicate Earth; their concentration represents only ≈ 1 % of their concentration in chondrites, as demonstrated in Table 1.2. Consequently, there are very few places in the Earth's upper crust where we have found sufficient PGE to make an economically mineable deposit (> 1 ppm). Typical crustal abundances of the PGE are a few parts per billion (ppb) or less; the highest concentrations are measured in mafic and ultramafic igneous rocks e.g. komatiites (see Table 1.2). To achieve ore grades a mechanism is required that concentrates these elements by a factor of 10,000 times that of typical crustal rock values (Zientek & Loferski, 2010).

Table 1.2: The average PGE and associated highly siderophile elements in a range of Earth reservoirs and rocks compared to chondritic values. Source: 1 - Lodders, 2003; 2 - McDonough & Sun, 1995; 3 - McDonough, 1998; 4 - Rudnick & Gao, 2004; 5 - Salters & Stracke, 2004; 6 - Maier et al., 2012.

Element		Cl-Chondrite	Silicate (Primitive) Earth	Earth's Core	Upper Continental Crust	Depleted Mantle	Komatiite
ppm							
Ni		10,640	1,960	5.2 (wt%)	47	1960	-
Cu		127	30	125	28	30	-
ppb							
IPGEs	**Os**	486	3.4	2800	0.03	3.0	-
	Ir	470	3.2	2600	0.02	2.9	1.6
	Ru	692	5.0	4000	0.3	5.7	4.5
PPGEs	**Rh**	141	0.9	740	-	1.0	1.1
	Pt	1004	7.1	5700	0.5	6.2	8.6
	Pd	588	3.9	3100	0.5	5.2	8.2
Au		146	1.0	500	1.5	1.0	-
Re		37	0.3	230	0.2	0.2	-
References		*1*	*2*	*3*	*4*	*5*	*6*

Geochemical data of PGE and Au concentrations analysed in natural samples is typically presented normalised to their abundance in chondrite or in the Earth's mantle and plotted in order of increasing melting point as shown in Figure 1.2 (Naldrett & Duke, 1980 and Mathez & Peach, 1989). The resulting PGE patterns may be different for different geological environments and degrees of partial melting. For example, in Figure 1.2 the komatiitic rocks of Kambalda and Langmuir have relatively flat patterns whereas steep fractionated PGE patterns characterise the sulphide ores of mafic/ultramafic rocks e.g. the J-M reef at Stillwater and the Merensky Reef of the Bushveld Complex (Mathez & Peach, 1989).

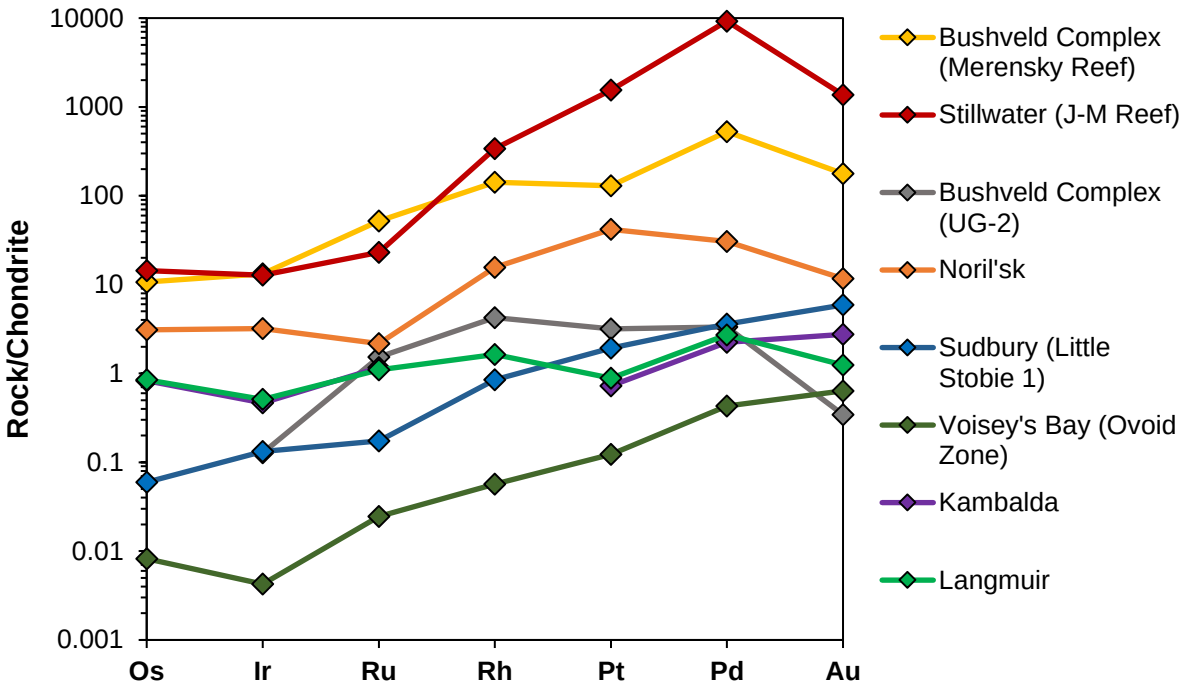

Figure 1.2: A chondrite-normalised PGE + Au plot for a variety of igneous rocks and magmatic sulphides deposits. “Merensky Reef” a mineralised pyroxenite layer within the Bushveld Complex (Barnes & Naldrett, 1985); “J-M Reef” a chromite layer of the Stillwater Complex, Montana (Barnes et al., 1985); “UG-2” a chromite layer of the Bushveld Complex (McClaren & DeVilliers, 1982); “Noril’sk” a Ni-Cu-PGE deposit associated with flood basalts (Barnes & Naldrett, 1985); “Sudbury” magmatic sulphide from the Little Strobie #1 Mine of the Sudbury intrusion (Naldrett et al., 1979); ”Voisey’s Bay” a Ni-Cu (PGE) sulphide deposit hosted in a troctolite-anorthosite complex in Labrador, Canada (Naldrett et al., 2000); “Kambalda” a komatiite hosting Ni-Cu (PGE) mineralisation in Australia (Naldrett & Duke, 1980); “Langmuir” sulphide from the Langmuir komatiite, Canada (Naldrett et al., 1979).

The Earth’s mantle represents the main accessible repository of the planets PGE budget; this discounts the PGE locked in the Earth’s core that are presumably inaccessible due to magmatic processes. It is unsurprising, therefore, that the known PGE deposits are found in association with large magmatic systems. In particular, those of mafic and ultramafic compositions, which require high degrees of partial melting of a mantle source. PGE mineralisation found in this geological setting is typically generated through orthomagmatic processes, meaning that the intrusive magmas are the source of the metals, fluids and energy required in ore genesis. The global distribution of the known significant occurrences of Ni-Cu-PGE are shown in Figure 1.3.

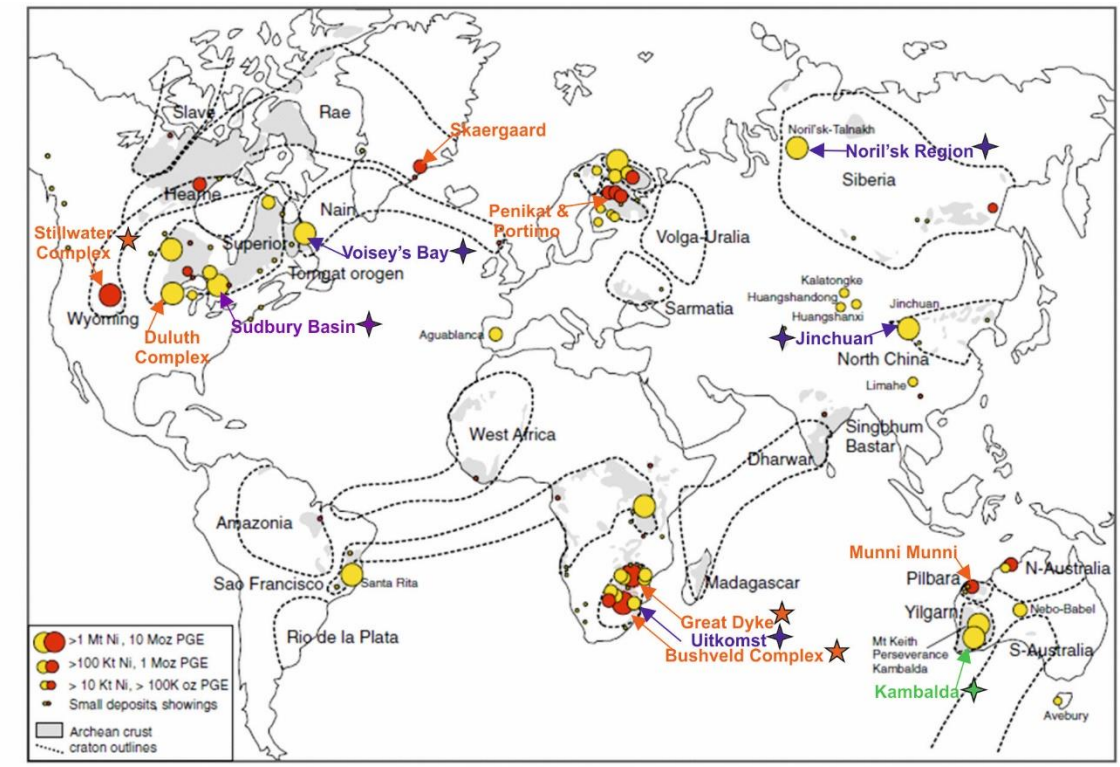

Figure 1.3: The global distribution of Ni-Cu-PGE magmatic sulphide deposits. Highlighted are key deposits that are colour coded according to their geological setting with: orange = layered intrusions; blue = conduit systems; green = komatiite; purple = meteorite impact-melt sheet. Note: 4-legged stars denote deposits mined for their Ni content and 5-legged stars denote those mined for their PGE contents. Modified after Maier & Groves (2011).

Global-scale studies on the distribution of Ni-Cu-PGE sulphide deposits in both space and time (*e.g.* Groves *et al.,* 1987; Tredoux *et al.,* 1989; Begg *et al.,* 2010; and Maier & Groves, 2011) have revealed an apparent close spatial and temporal association with Archean cratons (see Figure 1.3). Within these ancient cratons the deposits are typically found in proximity to rifted margins, intraplate rifts or large igneous provinces (LIPs) (Naldrett, 1999, 2004; Lightfoot, 2007; Begg *et al.,* 2010). These geological settings facilitate the formation of these deposits by effectively generating and channelling mantle-derived melt through the crust resulting in their emplacement at shallow levels (Barnes & Lightfoot, 2005). In addition, LIPs show evidence for large degrees of partial melting, required for both the formation of compositionally primitive magmas and to elevate the concentration trace elements in these magmas to economic levels.

The temporal link to the Archean may be an artificial result that has arisen because of both the favourable preservation potential of 'buoyant' stable cratons and an exploration model bias. Erosion over billions of years has the potential to strip away the volcanic edifices and expose the once subterranean magma chambers on

surface; this may be assisted by uplift and deformation during plate tectonic processes. The Noril'sk-Talnakh (late Permian to Triassic Period) and Skaergaard (Tertiary Period) attest to more recent (post-Paleoproterozoic) Ni-Cu-PGE sulphide ore deposit formation and both of these deposits have been linked to plume magmatism (Lightfoot et al., 1993; Brooks et al., 1999). Alternatively, this Archean preference may represent a true reflection of favourable tectonics, possibly plume-dominated, and a higher geothermal gradient present on Archean Earth. The restricted temporal occurrence of high MgO (>18 wt%) komatiitic basalts hosting Ni-Cu (PGE) enrichment (e.g. Kambalda) to the Paleoproteozoic or older time periods probably attests to a hotter mantle temperatures facilitating higher degrees of partial melting enabling the concentration and enrichment in Ni-Cu-PGE (Naldrett, 2010).

1.2 PGE in Modern Society

The unique physiochemical properties of the platinum group elements (PGE), as described in section 1.1 (see Table 1.1), have made them indispensable in many modern life applications. In recognition of this they are listed as one of twenty 'critical' raw materials identified by the European Commission (European Commission, 2017). These 'critical' raw materials are defined as being of fundamental importance to the European economy and are required in order to maintain and improve quality of life in the region (European Commission, 2017). Their high economic importance to the European Union (EU), is coupled with a high risk associated to their supply from a limited number of countries and they plot in the 'critical' field, as shown in Figure 1.4.

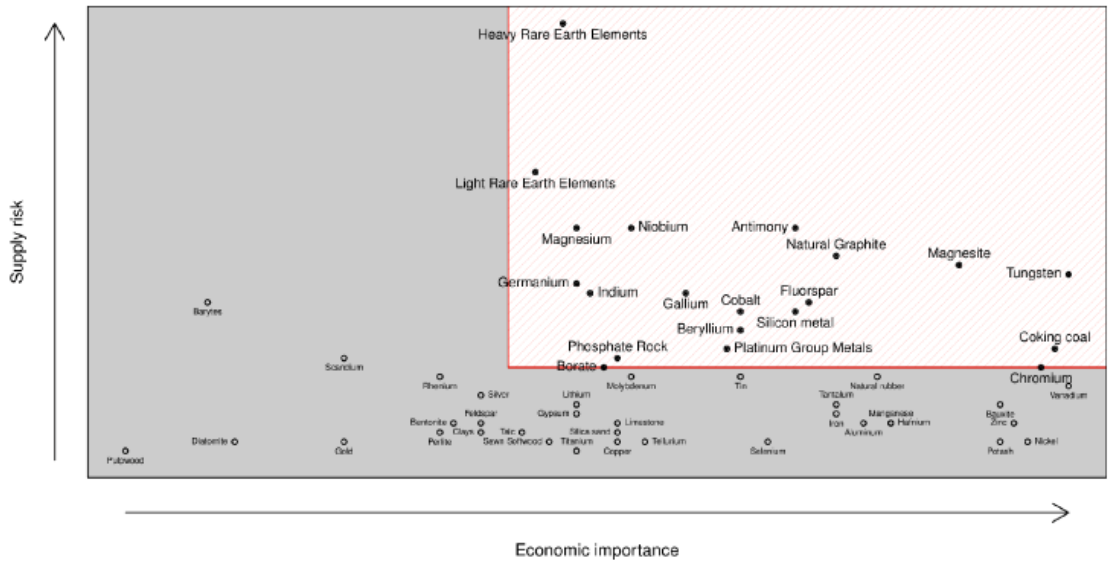

Figure 1.4: A plot of the supply risk vs economic importance of raw materials for the EU; the 20 critical raw metals as outlined by the EU are highlighted in the hatched red box. Source: European Commission, 2014.

Several reviews on the industrial and societal application of the PGE can be found in the following publications: the British Geological Survey Commodity Summary (Gunn et al., 2009); Gunn (2014), the United States Geological Survey 2015 Minerals Yearbook, the European Commission published “Study on the review of the list of critical raw materials” (2017) and in the Johnson Matthey PGM market report (2018a).

Economically, the most important PGEs are Pt, Pd and Rh; consequently, mines exploiting PGE often report their resources as a combination of these using the abbreviation 3PGE. The PGE are sold on international metals exchanges; their market price is primarily influenced by market forces of supply and demand although other geopolitical, economic, social and technological (PEST) factors can have short/long term influences. The market price of these elements over a 15-year period is shown in Figure 1.5 below. The 3PGE all have similar patterns over this time period, however there are significant differences in the spot price between the elements with Rh typically fetching the highest prices and Pd the lowest. The price of the 3PGE rose until 2008 when the global financial crash caused the value to plummet. Historically Pt was typically worth double the value of Pd however, recently (as shown in Figure 1.5) the Pd price is at a record high and above that of Pt. This shift in commodity prices has fundamentally altered the price dynamic for many PGE deposits; Pd-rich deposits used to be less favoured by exploration and mining companies compared to Pt-dominated deposits.

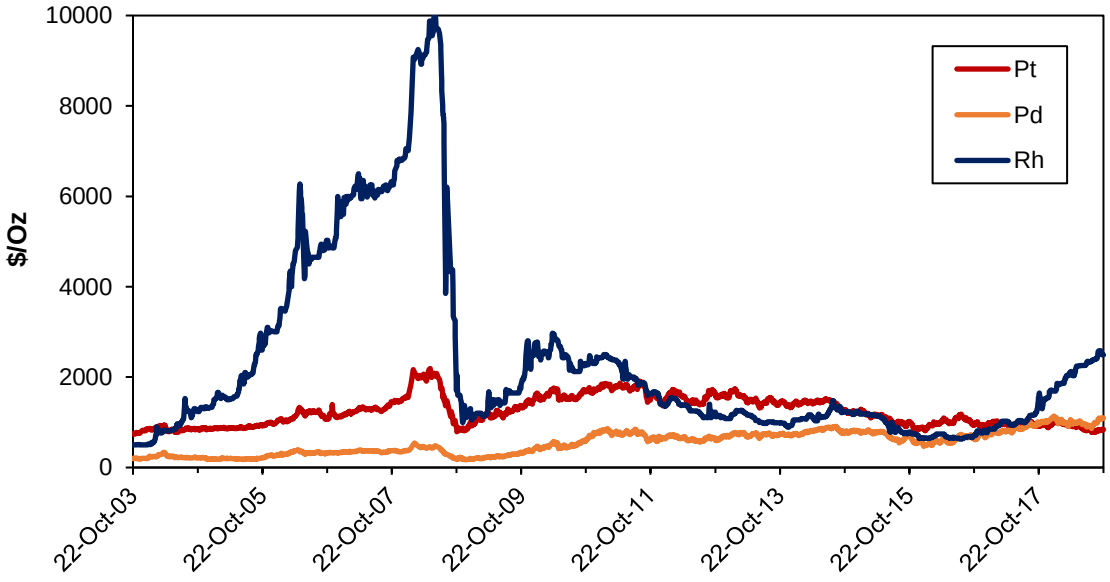

Figure 1.5: A 15-year price chart of the precious metals: Au, Ag and Pt. Source: Johnson Mathey 2018b.

Countries supplying 3PGE to the global market are shown in Figure 1.6; importantly, only four countries contribute significantly to the global demand. South Africa dominates the supply of both platinum and rhodium 73% and 82 %, respectively (see Figure 1.6 A and 1.6E). Russia is the leading producer of palladium, 41 % with South Africa making a significant contribution at 39 % (see Figure 1.6C). This dependence on two producer countries for 80% of global 3PGE is regarded as a supply risk because it leaves the supply vulnerable to any social, political, economic or environmental issues in those countries. The need for diversification of supply was highlighted in 2014 when the EU and the United States of America imposed economic sanctions on Russia and there was prolonged strike action in South Africa. Consequently, 2014 recorded the third consecutive deficit year in global platinum supply at -885,000 ounces (see Figure 1.7, Johnson Matthey, 2015).

The automotive industry represents the largest users of platinum (41%), palladium (78%) and rhodium (84%), as demonstrated above in Figure 1.6, where they are used in catalytic converters. Catalytic convertors act to remove pollutants namely; carbon monoxide, unburned hydrocarbons and nitrogen (II) oxide from automobile exhausts. The convertor is placed between the engine and the outlet of the exhaust pipe; it consists of a metal casing in which there are two metals, for example Pd and Rh, dispersed finely on the surface of a ceramic support with a honeycomb texture. The rise of this market can be attributed to the growth of "clean air" legislation (USA 1975) aimed at reducing air pollution in order to protect public health. The catalytic properties of the PGEs are also exploited in the chemical industry, which uses Pt and Pt-Rh alloys to manufacture speciality silicones and to make nitric oxide (the raw material for fertilisers), nitric acid and explosives (Zientek & Loferski, 2010).

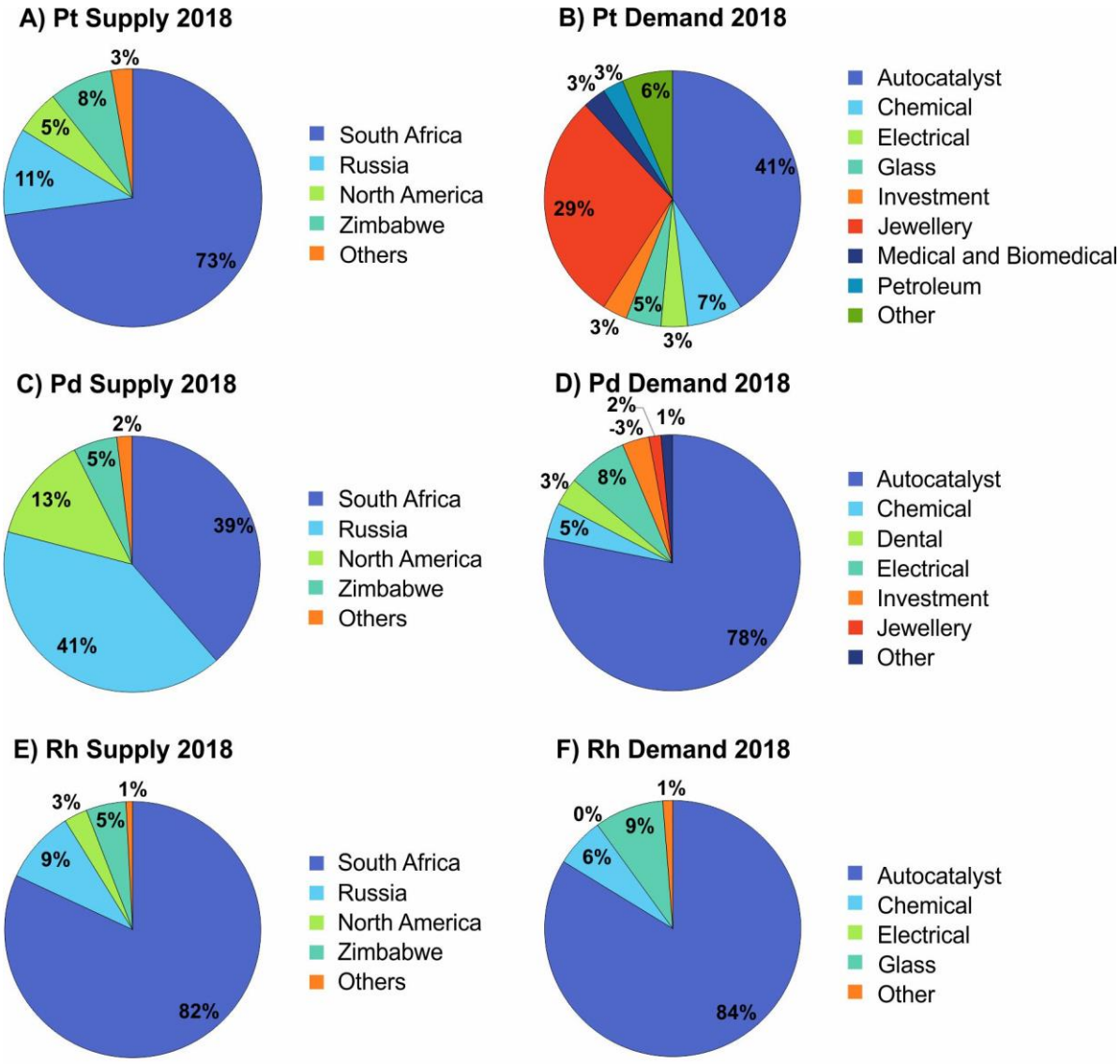

Figure 1.6: The global supply and demand for Pt, Pd and Rh (3PGE). Data from Johnson Mathey, 2018a.

A secondary supply of Pt, Pd and Rh is obtained through the recycling of jewellery, electronic equipment and catalytic convertors. As shown in Figure 1.7, recycling rates are increasing year on year and it is beginning to provide a significant proportion of the total world supply. Recycling helps to close the gap between mine production and consumption; although net deficits are still being recorded (see Pd 2018 in Figure 1.7). Recycling volumes are sensitive to the PGE prices with a corresponding increase in recycling with higher prices for the mined metals.

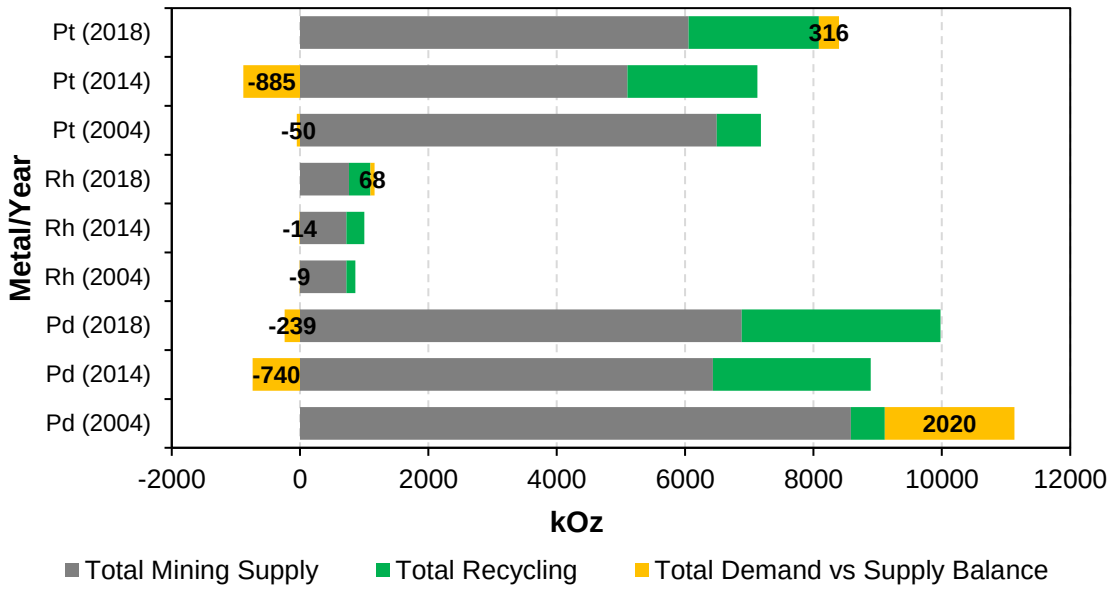

Figure 1.7: The overall supply of Pt, Pd and Rh derived from both mining and recycling activities plotted with the net balance of total supply vs gross demand (values shown on figure). The changes in the relative proportion of these and the net balance are over a 14-year period from 2004 to 2018.

The future demand for primary produced PGE is uncertain; the automotive industry is likely to experience fundamental change over the coming decades. Recently, technological advances and the global political environmental agenda has led to countries including the UK, India, France and Norway to announce a ban on the sale of non-electric cars by 2040. Emission-free electric cars require a different array of elements in the Li-ION batteries they are powered by including Li, Ni, Co, Al and Mn. This will have a significant impact on the demand for PGE as their principal market, once created in order to reduce air pollution by the implementation of environmental policy is being degraded by the same means. The effect of this legislation may be offset by hydrogen fuel cell technology which uses PGE as catalysts; in addition, heavy goods vehicles are exempt from the car sale ban and shipping will likely still use diesel.

1.3 PGE Mining in South Africa

In the previous section (1.2) the significance of the PGEs to modern society and the importance of the PGE mining industry in South Africa to meeting the demand are highlighted. The majority of PGE production from South Africa is centred on one geological feature, the Bushveld Igneous Complex (BIC). The world-class PGE resource of the BIC was first described in 1924 by Dr Hans Merensky when following up on the discovery of an alluvial deposit of platinum in Lydenburg, Mpumalanga Province, South Africa. Dr Hans Merensky, a geological prospector, traced this

platinum occurrence back to its source in the BIC. Since its discovery in the 1920s the BIC has been continuously mined for its PGE content.

Historically, the majority of production has come from the eastern and western limbs where layers known as 'reefs', namely the Merensky Reef and Upper Group 2 (UG2) chromitite, are present. They carry economic grades, > 2 g/t, of PGE associated with sulphides and/or chromites in intervals typically less than one-metre thick. These narrow widths of mineralisation are mined selectively using labour intensive methods with increasing depths of extraction e.g. > 2 km below surface at the Zondereinde mine, owned by Northam Platinum. In recent years, the traditional platinum mining industry in South Africa has been struggling to maintain profit margins due to increasing depths of extraction causing rising costs of production; this has been exacerbated by fluctuating platinum prices (see Figure 1.5) and labour unrest in underground mines. In contrast, the mineralisation of the Platreef, which represents the third largest PGE deposit in the World (Ihlenfeld & Keays, 2011), located on the relatively under-developed northern limb offers an alternative style of platinum mining. Correspondingly, the focus of both the mining and academia are shifting from the historically important eastern and western limbs to the northern limb (Kinnaird & McDonald, 2018).

Characteristics of the Platreef, including the greater width (10 – 400 m) of the mineralised interval with greater base metal credits than available from the Merensky or UG2 ores, make it amenable to bulk and automated extraction methods. Current mining of the Platreef is undertaken solely by Anglo American Platinum on the adjacent farms (from south to north) Sandsloot (236 KR), Zwartfontein (818 LR) and Overysel (815 LR), which are collectively known as the Mogalakwena mine complex (see Figure 1.8A below). This represents the largest PGE producing mine in the World with a series of five open pits covering a strike length of >10 km, exploiting a westerly dipping pyroxenite ore body with an average grade of 3.3 g/t (3PGE + Au; Muzondo, 2015). Consequently, most exploration on the northern limb has focused on finding similar deposits along strike. The relatively steep dips of the ore body at surface combined with the overall lower PGE grades were thought to preclude economic extraction at depth. However, exploratory drilling through the Main Zone rocks to intersect the down dip (westwards) mineralisation of the Platreef led to the discovery of the Flatreef deposit located 8 km SE of Sandsloot on the farm Turfspruit (241 KR) owned by Ivanplats Pty Ltd (see Figure 1.8A below).

1.3.1 The Turfspruit Discovery

A local geological map of Farm Turfspruit (241 KR) is provided in Figure 1.8A; the majority of the licence area is covered on surface by Main Zone gabbronorites with Upper Zone ferrogabbros present in the southwest portion. The outcrop of the Platreef lies on the eastern edge of the licence area and forms a relatively thin mafic orebody dipping steeply (≈ 45°) beneath the overlying Main Zone. The immediate footwall to the mineralised Platreef rocks on Turfspruit are sediments of the Duitschland Formation (DF, see Figure 1.8A) part of the Chuniespoort Group a division of the Transvaal Supergroup. The DF represents a ≈1 km thick package of interbedded dolomite, stromatolite, marls, mudstones and shales that are commonly subdivided into upper and lower units based on the dominance of carbonate vs. siliceous material, respectively.

The Flatreef deposit, so called because of its sub-horizontal geometry (see Figure 1.8C), represents a layered and cyclical magmatic stratigraphic package hosting PGE mineralisation at depths of between 700 to 1000 m below surface and ≈ 1.5 to 2 km west of the surface exposure. Ivanplats have a NI 43:101 compliant Indicated Mineral resource of 42 Moz 4E (Pt + Pd + Rh + Au; 2 g/t cut-off grade) and have begun the construction of an underground mine (Ivanhoe Mines Ltd, 2016). The flat-lying structure of the deposit, as shown schematically in Figure 1.8C differs from the steep dips as observed at surface. This has been interpreted by Ivanplats geologists (based on drilling data) to result from faulting and folding of the floor rocks, which took place prior to the intrusive event (Brits, 2018). This is supported by surface observations from the Sandsloot open-pit where the Malmani Formation of the Transvaal Supergroup preserves evidence of open folding (Armitage, 2011; McDonald & Holwell, 2011; and Kinnaird & McDonald, 2018).

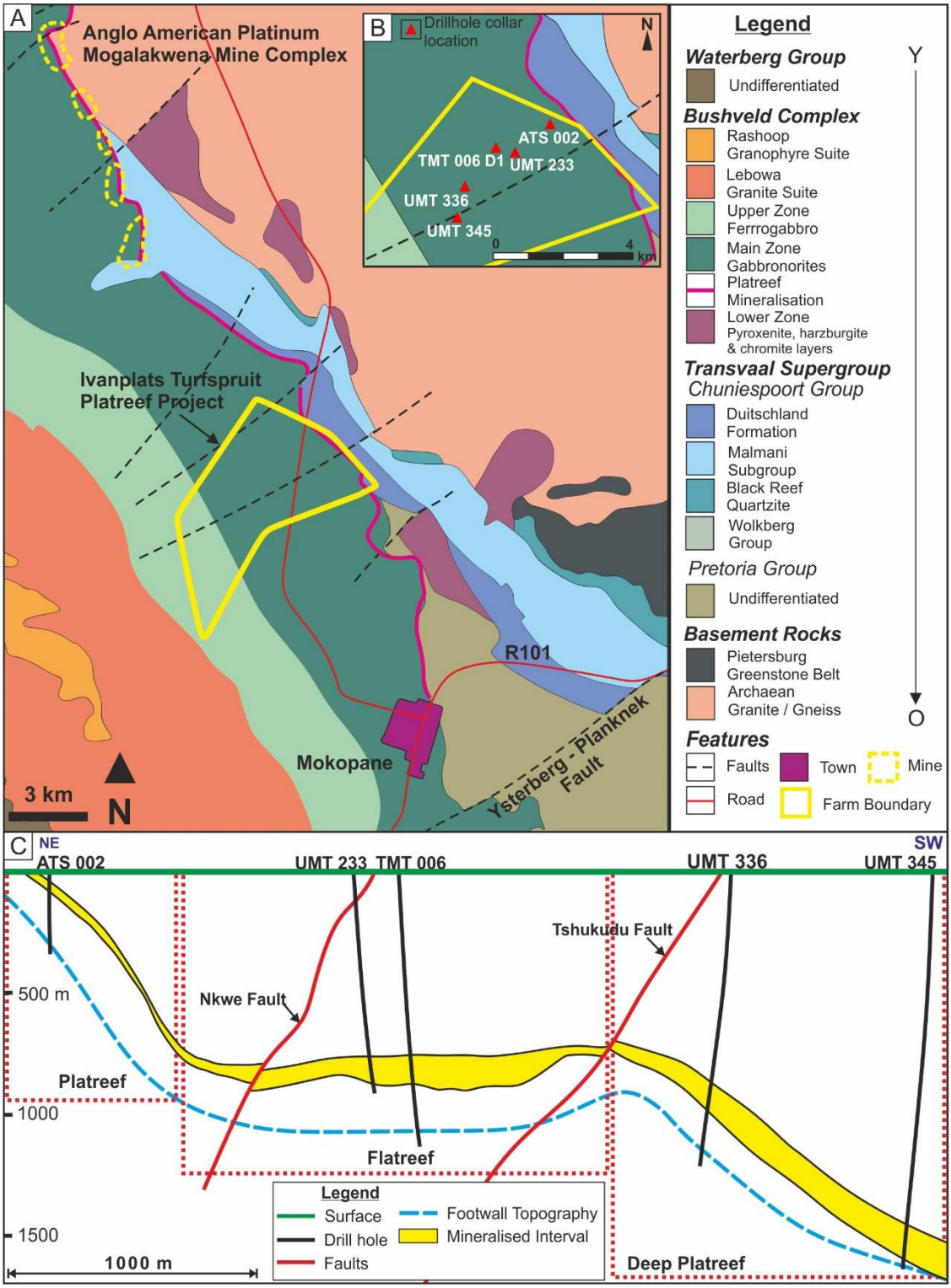

Figure 1.8: An overview of the Turfspruit deposit location and structure. (A) Regional geological map of the Platreef north of the Ysterberg-Planknek Fault. (B) A zoomed in plan view of the drill hole collar positions of drill holes used in this study in relation to the Turfspruit licence boundary. (C) Schematic cross-section showing the 3D profile of the orebody on Turfspruit and the location of the drill holes used in this study.

The orebody can be divided into three domains based on its geometry and the presence of similar stratigraphic and mineralisation characteristics these are the

Platreef, Flatreef and Deep Platreef; these names will be used throughout this study. The Flatreef and Deep Platreef preserve a thick sequence of relatively undisturbed magmatic layering with thin marker horizons including chromite stringers that can be traced between drill holes enabling the development of a stratigraphic framework for the project (Grobler & Neilsen, 2012; Neilsen & Grobler, 2012; Grobler & Dunnett, 2016; Grobler et al., 2018). This contrasts to the shallow Platreef, which is typically highly disturbed with a notable absence of well-developed and laterally continuous layering, which traditionally gave rise to many of the complications encountered when attempting to fit the Platreef into the stratigraphic framework of the main Bushveld Complex. Since the earliest investigations by Wagner (1929), a stratigraphic correlation and inferred petrogenetic link between the northern limb with the eastern and western limbs of the Bushveld Complex (and by extension the Merensky Reef with the Platreef) has been speculated on and argued over.

There have been a number of academic studies on the near-surface Platreef at Turfspruit and there is a current high level of interest in the Flatreef. The near-surface Platreef on Turfspruit has been studied by a few authors including metamorphic studies on country rock interlayers by Sluzhenikin et al., (2015), and mineralogical and geochemical studies on both the near-surface mineralisation by Hutchinson & Kinnaird (2005) and Hutchinson & McDonald (2008). Kinnaird (2005) studied the geochemistry of the Platreef rocks at Turfspruit and she identified distinct trends in the ratios of major elements (e.g. SiO_2/Al_2O_3, CaO/Al_2O_3 and $Al_2O_3/(FeO+MgO)$) suggesting emplacement as a series of pyroxenite sills. The effect of crustal contamination on the Platreef sulphide mineralisation at Turfspruit has been investigated by Sharman-Harris et al., (2005) and Sharman et al., (2013). Moving down-dip the Normal Flatreef has recently been studied in a combined Re-Os and S-isotope by Yudovskaya et al., (2017a) and a detailed study on the PGE mineralisation by Yudovskaya et al., (2017b). The stratigraphy and mineralisation of the Flatreef and Deep Platreef are the focus of a paper by Grober et al., (2018) and the results of this detailed study should complement the deposit overview outlined in this paper.

1.4 Project Overview

This PhD project is funded and supported by Ivanplats Pty Ltd, from hereon in referred to as Ivanplats, a Canadian junior mine development and exploration company. Ivanplats own the mining licences for the contiguous farms: Turfspruit, Macalaskop and Rietfontein and have begun mine development on the former. The current project has arisen from previous collaboration between Cardiff University and Ivanplats in the

form of Master projects for Cardiff MEarthSci students (Smart, 2013; Nodder, 2015; Marquis, 2015; and Kvadsheim, 2017).

In the scientific literature on the Bushveld Complex there is a lot of debate around the genetic relationship between Platreef and the Upper Critical Zone (UCZ) hosting the stratiform mineralisation of the eastern and western limbs. Significant crustal contamination of the near-surface Platreef is often used to explain the geochemical differences between the northern limb and the rest of the Bushvled Complex. The discovery of an apparent magmatic, cyclically layered igneous stratigraphic sequence with traceable mineralised horizons present down-dip of the surface 'Platreef-style' mineralisation opens up a new opportunity to test the stratigraphic and petrogenetic relationship of the northern limb to the western and eastern limbs. The collection of a robust and complementary petrographic, geochemical, and mineral chemistry database forms an essential part of this project; developing on previous studies that focussed on the Platreef as briefly outlined above. The Flatreef and Deep Platreef deposit potentially represents the best example identified to date of the cyclic UCZ stratigraphy of the eastern and western limbs enabling correlation between these limbs and accordingly between the Platreef and the Merensky Reef.

1.4.1 Aims and Objectives

A plan-view of the location of the drill hole collars for the four drill holes used in this study are shown in Figure 1.8B. The drill holes cover a surface distance of 4 km and are located progressively westwards away from the surface exposure of the Platreef; this means that they intersect the orebody at increasing depths moving in this direction (see Figure 1.8C; for more detailed cross sections see Appendix A). The distance between the drill holes means that the km-scale variability of both the mineralogy and geochemistry of the deposit can be explored in detail for the first time. Furthermore, the two drill holes studied for the Flatreef and Deep Platreef intersect 'thick' (TMT_006_D2 and UMT_345) and 'thin' (UMT_233) mineralisation styles, respectively. This enables a comparison to be made to see what is controlling the varying thicknesses of mineralisation in these domains. There are five principal objectives as follows:

1. To asses the variability in the stratigraphy and mineralised intervals moving from the Platreef, Flatreef and Deep Platreef.
2. Establish the geochemical characteristics of the Platreef, Flatreef and Deep Platreef to constrain any correlation between drill holes and with the Upper Critical Zone of the eastern and western limbs.

3. To undertake a baseline geochemical study (including Cr, Ni, Cu, PGE and Au) of the Duitschland Formation to establish the different inputs from these units and how to recognise them in contaminated Platreef magmas.
4. Improved understanding of how Platreef magma (or magmas) intruded and interacted with the pre-existing country rocks.

1.4.2 Thesis Outline

This thesis reports the results of a multi-disciplinary study on drill holes collected across the Turfspruit project area intersecting the orebody as it changes with depth from the Platreef, Flatreef and Deep Platreef (see Figure 1.8). The thesis has been divided into chapters as outlined below:

Chapter 2 Orthomagmatic Ni-Cu-PGE Deposits – a review on our current understanding of the physical and chemical processes that result in the formation of economic concentrations of base metals and PGE in orthomagmatic deposits.

Chapter 3 Overview of the Bushveld Complex – an overview of the available literature on the Bushveld Complex covering the key features such as its age, structure, the stratigraphy of the igneous layering, parental magma compositions and petrogenetic models. This provides an introduction to the regional geological setting of the project area.

Chapter 4 Methodology – an overview of the analytical methods including whole-rock geochemistry, in situ mineralogy and sulphur isotope geochemistry that have been used in this study. In addition, details are provided on a new analytical technique developed as part of this study at Cardiff University using the scanning electron microscope to perform automated searches for platinum-group minerals.

Chapter 5 Core Logging Results and the Turfspruit Stratigraphy – presents detailed descriptions on the lithologies and contact relationships observed during geological logging of drill core; the existing stratigraphic framework as developed by Ivanplats is outlined and a new one as developed in the current study is presented.

Chapter 6 Country Rock Geochemistry – the results of a whole-rock geochemical study on the footwall rocks of the Duitschland Formation as sampled at a location distal to contact aureole. Results of a preliminary investigation of the geochemical composition of the Archean basement rocks of the Pietersburg Greenstone Belt are presented.

Chapter 7 Whole Rock Geochemistry: Core Samples – the major and trace element data are presented for each drill hole studied. Major element ratios and trace element ratios are used to constrain the magmatic lineage and contamination signature by comparing with similar studies conducted on Bushveld rocks from elsewhere.

Chapter 8 Mineralogy and Mineral Chemistry – detailed descriptions on the silicate and sulphide mineralogy as observed in thin sections of selected samples from across the Turfspruit deposit. In addition, the results of a quantitative in situ mineral chemistry study on the major minerals orthopyroxene, plagioclase, clinopyroxene and olivine are presented.

Chapter 9 Sulphur Isotope Geochemistry – the S isotope signature across the Turfspruit deposit is investigated to constrain the role of crustal contamination in the formation of the sulphides and how this signature varies moving from the near-surface to the deep extensions of the orebody.

Chapter 10 PGE Hosts: Base Metal Sulphides and Platinum Group Minerals – this study focuses on samples from the Deep Platreef the distribution of the PGE between base metal sulphides and as discrete PGMs between the different stratigraphic units is investigated.

Chapter 11 Discussion and Conclusions – the results are summarised into five discussion topics: (1) the role of magmatic processes; (2) the role of contamination; (3) the role of hydrothermal fluids; (4) correlations across the Bushveld Complex and; (5) an emplacement model for the orebody on Turfspruit.

Chapter 2

Fundamentals of Orthomagmatic Ni-Cu-PGE Deposits

2.0 Petrogenetic Models for Magmatic Sulphide Deposits

Orthomagmatic sulphide deposits are commonly divided into two groups depending on whether the most valuable commodity mined is the base metal or PGE content (e.g. Ni-Cu (PGE) deposits and PGE (Ni-Cu) deposits). The ratios of PGE to base metals, expressed as (Pt+Pd)/(Ni+Cu), can provide a useful tool in discriminating between deposit types. Base metal-rich ores have low ratios around < 0.5 increasing to 5 if related to flood basalts (Naldrett, 2011). PGE-rich ores have high ratios frequently between 10 to 30 and rarely > 100 (Naldrett, 2011). These mineralisation styles are often described as being either S-rich (> 10 vol% sulphide minerals) or S-poor (0.5 to 5 vol%; Naldrett, 2011), respectively. Further categorisation of magmatic sulphide deposits has been undertaken using numerous criterion including: morphology (e.g. stratiform, stratabound, discordant), mineralogical associations (e.g. chromite, sulphides), geological setting (e.g. layered intrusion vs. komatiites) and tectonic regime (e.g. intraplate rift vs. back-arc basin). For more details see reviews by Naldrett (2004, 2011).

A combination of several fundamental physical and chemical processes are required to occur sequentially in order to form economic, magmatic sulphide deposits from mafic to ultramafic magmas (e.g. Lesher, 1989; Keays, 1995; Naldrett, 1999, 2004 and 2011; Li et al., 2001). These are described in detail in the following sections.

2.1 PGE Behaviour in Silicate Magma

The behaviour of PGE in a silicate magma is dependent on both their internal physiochemical properties (as outlined in Chapter 1) and the external geochemical and physical conditions of their environment. In a crystallising magma, the PGE are retained only in certain mineral phases such as sulphides, chromites and metal alloys. The degree to which the PGE are concentrated into these phases is governed by their partitioning coefficients. The fractionation of trace elements between two phases in equilibrium can be quantified using Nernst partition coefficients. For example, in a system where a sulphide liquid is separating from a silicate melt the partition coefficient (K_D) for the PGE (*i*) is calculated by:

$$K_{Di}^{(sulphide/silicate)} = \frac{wt\ \%\ i^{(sulphide)}}{wt\ \%\ i^{(silicate)}} \qquad \textbf{Equation 2.1}$$

The calculated $K_{Di}^{(sulphide/silicate)}$ values (also known as D values) for the PGE using a variety of experimental, empirical and theoretical methods available in the current literature are presented in Table 2.1.

Table 2.1: Summary of the partition coefficients of base metal, PGE and associated highly siderophile elements between sulphide liquid and silicate magma. Note: source of values referenced in the table.

	Element	K_D	Method	References
Base Metals	Ni	500	Experimental (*In situ*)	Mungall & Brenan, 2014
		500 - 900	MORB	Peach et al., 1990
	Cu	1470	Experimental (*In situ*)	Mungall & Brenan, 2014
		1383	MORB	Peach et al., 1990
IPGE	Os	740,000	Experimental (*In situ*)	Mungall & Brenan, 2014
		2200 - 2500	Experimental	Fleet et al., 1999
	Ir	458,000	Experimental	Mungall & Brenan, 2014
		12,000 – 16,000	MORB	Peach et al., 1990
		460,000	UG2	Campbell & Barnes, 1984
		1800 - 3500	Experimental	Fleet et al., 1999
	Ru	415,000	Experimental (*In situ*)	Mungall & Brenan, 2014
		2400 – 2800	Experimental	Fleet et al., 1999
PPGE	Rh	205,000	Experimental (*In situ*)	Mungall & Brenan, 2014
	Pt	317,000	Experimental (*In situ*)	Mungall & Brenan, 2014
		>2400	MORB	Peach et al., 1990
		490,000	UG2	Campbell & Barnes, 1984
		120,000	UG2	Campbell et al., 1983
		6450	Merensky Reef	Campbell et al., 1983
		1400-3900	Experimental	Fleet et al., 1999
	Pd	190,000	Experimental (*In situ*)	Mungall & Brenan, 2014
		35,000	MORB	Peach et al., 1990
		310,000	UG2	Campbell et al., 1983
		6375	Merensky Reef	Campbell et al., 1983
		2900-3400	Experimental	Fleet et al., 1999
HSE	Au	1000-10,000	Experimental (*In situ*)	Mungall & Brenan, 2014
		15,000-19,000	MORB	Peach et al., 1990
		600-900	Experimental	Fleet et al., 1999
	Re	400-800	Experimental (*In situ*)	Mungall & Brenan, 2014

The very high $D_i^{sulphide-silicate}$ values of the PGE, between 10^3 to 10^5 (see Table 2.1), suggest strongly chalcophile behaviour. Notably, the D values for Cu and Ni are several orders of magnitude lower than those for PGE at 10^3 and 10^2, respectively (see Table 2.1). In particular, Ni shows lithophile tendencies and can be incorporated into olivine. The metal concentration of sulphide liquids depends on the mass of

silicate magma they can process for metals expressed as the ratio of sulphide liquid:silicate magma known as the R factor, discussed below in section 2.2.4 (Campbell & Naldrett, 1989; Kerr & Leitch, 2005).

The PGE also demonstrate extreme siderophile tendencies; according to Goldschmidt's geochemical classification the PGEs (and Au/Re) are grouped as highly siderophile elements (HSE) in the periodic table. The overall siderophile tendency decreases amongst the PGE as follows Os>Ir>Pt>Ru>Rh>>Pd, with D values ($D_{PGE}^{metal-silicate}$) varying on the order of 10^5 to 10^8 (Fleet and Stone, 1991; O'Neill *et al.,* 1995; Tredoux *et al.,* 1995). The D values in this metal-silicate system are up to three orders of magnitude greater than that of a sulphide-silicate system. This dual siderophile/chalcophile behaviour of the PGE has raised questions and much contention over which is dominant in controlling their concentration in magmatic systems.

The frequently observed mineralogical association of PGE with magmatic base metal sulphides, has strongly influenced the development of deposit models. The chalcophile model relies on an immiscible sulphide liquid collecting and accumulating PGE from the silicate magma e.g. Barnes et al., (1985), Arndt et al., (2005), Maier (2005), Naldrett *et al.,* (2008) and Naldrett (2011). However, sulphide-rich layers are not the only ones in layered intrusions that show enrichment in PGE; for example chromite layers frequently contain enhanced concentrations of Os, Ir, Ru (the IPGEs) and Rh (Barnes *et al.,* 1985). As the chalcophile model is the most popular model in the literature it shall be discussed in detail in section 2.2 below; and some alternative ideas are presented at the end in sub-section 2.2.6.

2.2 The Chalcophile Model

The chalcophile model can be broken down into five principal stages based on the work of Campbell & Naldrett (1979), Arndt et al., (2005), Maier (2005), Naldrett et al., (2009) and Naldrett (2004, 2011): (1) production of a PGE fertile magma; (2) transport to the upper crust as a sulphur undersaturated melt; (3) sulphide saturation achieved forming an immiscible sulphide liquid; (4) sulphide liquid interacts with a significant amount of silicate magma to increase PGE tenor (5) sulphides are physically concentrated into an restricted area. An overview of the main processes operating at each stage are covered in the following sections (2.2.1 to 2.2.5).

2.2.1 Production of a PGE fertile parental magma

The PGE abundance in the mantle is discussed in Chapter 1 (section 1.1). PGE in the upper mantle and sub-continental lithospheric mantle (SCLM) are hosted in base

metal sulphides (BMS) including pyrrhotite, pentlandite and chalcopyrite; present as accessory phases (Lorand et al., 2013). The concentration of PGE in these sulphides (ppm level) is ≈ three orders of magnitude greater than those in the bulk rock silicate mantle (Lorand et al., 2013; Lorand & Luguet, 2016; O'Driscoll & González-Jiménez, 2016). As a consequence, the behaviour of the BMS during mantle melting exerts a significant control over whether the PGE are retained in the mantle or are mobilised into the melt. BMS are one of the first phases to melt; therefore, increasing the melt fraction (F) increases the S wt% in the melt until all BMS are dissolved. Modelling of batch equilibrium melt processes operating in the mantle has calculated that between 15 to 25% partial melting are required to dissolve all the BMS contained within the mantle source region (see Figure 2.1).

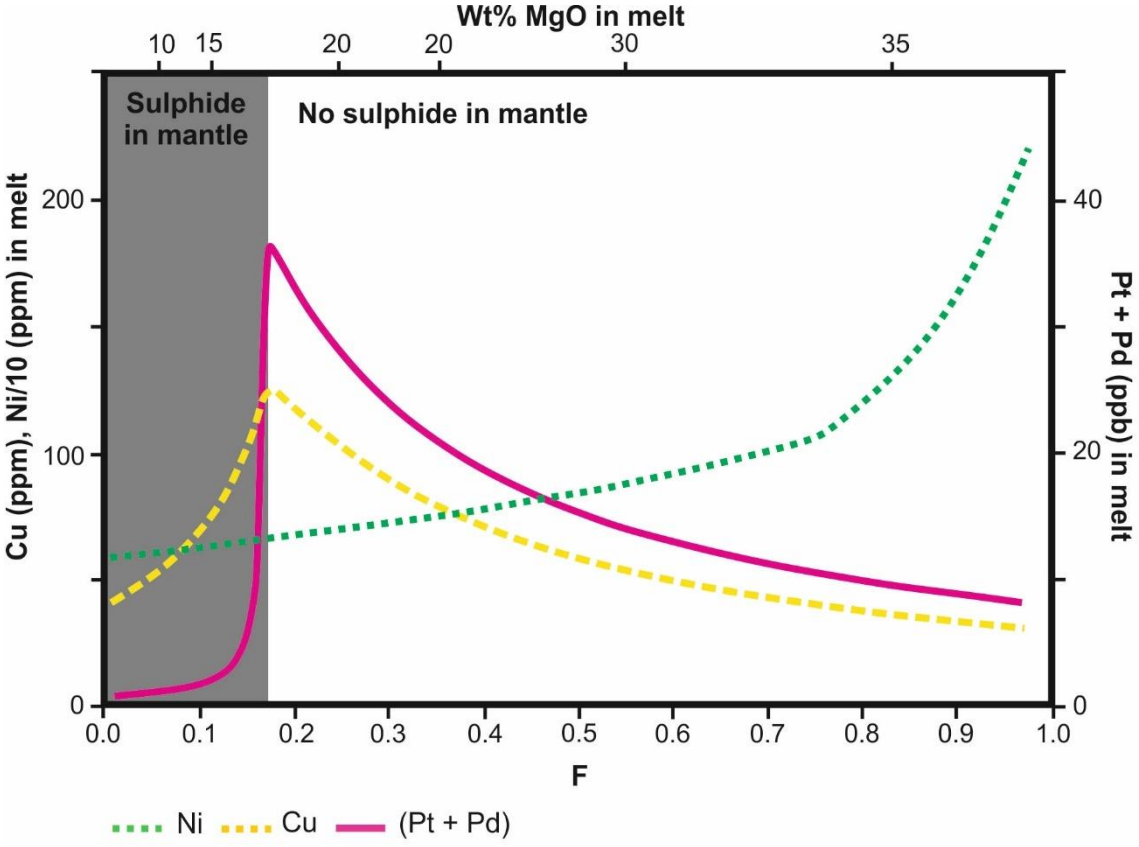

Figure 2.1: The effect of the degree of partial melting (F) of the mantle on the metal contents (Ni & Cu, Pt & Pd) of the resultant partial melt. Note: the value of F is dependent on the assumed initial S concentration of the peridotite and the depth of melting. Modified from Naldrett, 2010.

Once the mantle source region is exhausted of S the concentration in the magma becomes diluted, as does the corresponding PGE content, with increased melting; as shown in the gently downward slope of Pt + Pd from a spike at between 0.1 to 0.2 F in Figure 2.1. Therefore, the PGE content of a mantle-derived melt is principally

controlled by the degree of partial melting; <10% and the PGE are left in residual mantle sulphides whereas, >20% the PGE grade becomes diluted.

2.2.2 Magma ascent to the Upper Crust

To be exploited as an ore deposit the mantle-derived magma must be emplaced at shallow levels in the Earth's upper crust at depths amenable to economic extraction (i.e. < 3 km below surface); this is age-dependent extensive erosion and tectonism can expose formerly deep-seated layered intrusions in older rocks. This requires a favourable tectonic regime enabling the mafic/ultramafic magma to ascend into the upper crust in a state of S undersaturation. Experiments by Mavrogenes & O'Neill (1999) on sulphur solubility in basaltic systems at magmatic temperatures showed that the conditions of magma upwelling i.e. decreasing pressure increases S solubility (improving the magmas S carrying capacity). It is therefore, unlikely that a mafic/ultramafic magma will achieve S saturation in the crust unless there is some other process involved.

2.2.3 Sulphur Saturation

A silicate magma at sulphur saturation can no longer hold sulphur in solution and it exsolves to form an immiscible sulphide melt. The sulphur content at sulphide saturation (SCSS) varies depending on the melt composition and external factors controlling S solubility including temperature and pressure (Shima & Naldrett, 1975; Mavrogenes & O'Neill, 1999). Several processes can trigger sulphur saturation in an undersaturated magma including:

1. **Fractional crystallisation -** promotes sulphur saturation by: (A) forming silicate and oxide minerals (that sulphur is not incorporated into) thereby increasing the S content of the magma (see Figure 2.2); or (B) crystallising olivine, chromite and magnetite minerals that are Fe-rich, thereby decreasing the amount of Fe^{+2} in the magma to which S is bonded (Shima & Naldrett, 1975; Li et al., 2001).

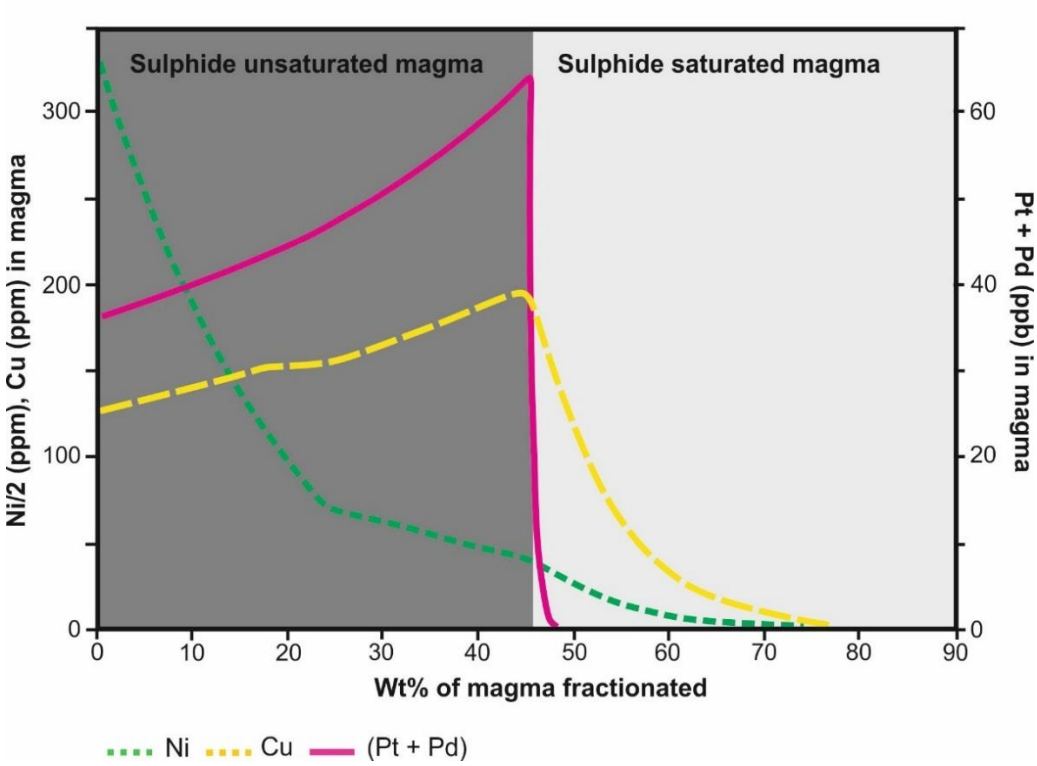

Figure 2.2: The effect of the degree of fractional crystallisation on the S solubility of the magma and consequently metal contents (Ni & Cu, Pt & Pd). Modified from Naldrett, 2010.

2. **Crustal contamination** can affect S solubility in a number of ways depending on the composition of the assimilated material:
    A. The addition of crustal S to the magma through the interaction with S-bearing country rocks e.g. anhydrite or pyritic shales; this increases the S content of the silicate melt resulting in S saturation. The chemical transfer of external sulphur to the magma occurs via processes of partial melting, bulk assimilation or devolatisation (Lesher & Burnham, 2001). Evidence for the incorporation of crustal-derived sulphur into magmatic sulphides is preserved in non-mantle S isotope values (for details see section 2.5.2, Ripley & Li, 2003; Ripley & Li, 2013) and high S/Se ratios (Queffurus & Barnes, 2015).
    B. The assimilation of siliceous partial melts of the country rocks lowers the S solubility of the magma (Irvine, 1975; Maier, 2005 and Naldrett, 2011).
    C. An increase in fO_2 resulting from contamination of oxygen-bearing country rocks (e.g. dolomites and limestones) can trigger chromite/magnetite precipitation and/or lower the FeO content and therefore affect the sulphur carrying capacity of the magma (Naldrett, 2011).

3. **Magma mixing** of two compositionally different sulphur-undersaturated magmas may in principal cause S saturation (e.g. Hoatson, 1998; Naldrett & von Gruenewaldt, 1989; Li et al., 2001).

It is important to note that the dominant process in triggering S saturation is an area of debate and varies between deposit types. The relative influence of each of these processes will differ depending on a variety of factors including: emplacement mechanism, tectonic setting, magma dynamics and geochemistry of the country rock between each deposit, to name but a few variables. For example, differentiation and fractionation processes are probably most influential in closed-magmatic systems such as the Skaergaard intrusion (McBirney, 1996) whereas magma mixing will have a profound affect in open-magmatic systems e.g. the Bushveld Complex (Irvine, 1973). Furthermore, the assimilation of country rock S is considered critical to ore genesis of many Ni and Cu-rich deposits such as the Duluth Complex (Ripley & Li, 2003) supported by S isotope data.

2.2.4 Sulphide Upgrading

To achieve the PGE tenors measured in sulphides for ore deposits (100's ppm) the immiscible sulphide liquid must upgrade its PGE content; this requires high R factors (silicate:sulphide ratio) enabling the sulphide melt to equilibrate with a large volume of magma. Campbell & Naldrett (1979) provided a mathematical formulation to the R-factor which shows that the grade of a sulphide liquid (C_l) results from the initial concentration of metal in the silicate magma (C_o), the partition coefficient (D_i), and the R-factor as shown in Equation 2.2 below:

$$C_l = [C_o D_i (R + 1)]/(R + D_i) \quad \textbf{Equation 2.2}$$

Estimations of R-factor values for magmatic sulphide deposits vary depending on whether the deposit is dominated by Ni-Cu (PGE) at 10^3 compared to PGE (Ni-Cu) at > 10^5 (see Figure 2.3). The largest R factors are needed to explain the high PGE tenors of sulphides in stratiform reef type deposits in layered intrusions e.g. Pt and Pd tenors in sulphides from the J-M reef ≈5000 ppm and between 250 to 600 ppm in the Merensky Reef (Naldrett, 2011). Gravitational settling of sulphide globules through a km-thick magma column scavenging PGE from the silicate melt as they descend is frequently proposed as the process enabling these high R values. The physical interaction of the sulphide globule with the silicate magma during lateral of vertical magma flow may be enhanced by turbulent mixing in the plume of injecting magma.

The interaction of sulphide liquids with high volumes of magma is perhaps easier to envisage considering a conduit-style setting. Magma conduits, acting as feeder zones channelling magma from depth to the surface, are known to host Ni-Cu (PGE) mineralisation in structural traps. In this setting early-formed sulphides trapped are subjected to repeated injection of new magma; this open-system multi-stage upgrading model was proposed by Naldrett et al., (1995) for the Noril'sk deposit. This model was further modified by Kerr & Leitch (2005) to the "multistage-dissolution upgrading" model. This model considers that later sulphur undersaturated magmas will redissolve some of the pre-existing sulphide liquids increasing the metal concentration in the residual sulphides. Quantitative modelling of this process by Kerr & Leitch (2005) have shown that this is an effective method for producing high PGE tenor sulphides and can reduce the mass of silicate magma required to be processed for their metal content by as much as two orders of magnitude (see Figure 2.3).

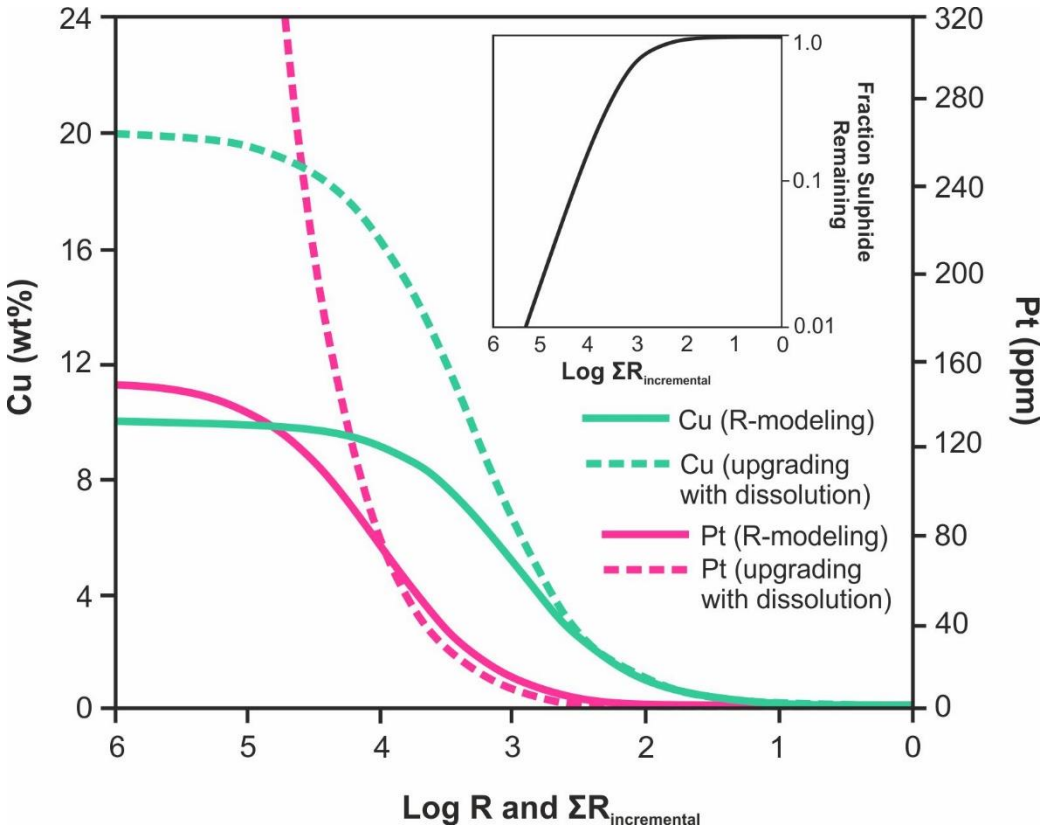

Figure 2.3: Comparing the effect of simple R factor modelling (Campbell & Naldrett, 1979) to that of the multistage-dissolution upgrading model, $\Sigma R_{incremental}$ (Kerr & Leitch, 2005) on the Cu and Pt concentrations in sulphides. The inset box shows the effect of the $\Sigma R_{incremental}$ model on the amount of sulphide remaining.

2.2.5 Physical Concentration of Sulphides in the Crust

The deposition of sulphide minerals at either predictable horizons (e.g. stratiform) or in concentrated pockets of sufficient size to be amenable for extraction is an essential

requirement to forming an orebody. This means that processes affecting the sulphide liquid after its exsolution including transport, coalescence and collection are fundamental in ore genesis; an overview of our current understanding of the physical and chemical processes resulting in the deposition of sulphides is provided in Barnes et al., (2016).

A typical magma column consists of a liquid upper portion, a solidified lower part and an intervening 'crystal mush' (a poorly consolidated pile of crystals; see Figure 2.4A). Once formed, sulphide droplets sink through the silicate magma due to the appreciable density contrast between the two coexisting liquids. Sulphide liquid has an approximate density of 4.5 g cm^{-3} (Mungall & Su, 2005) whereas mafic magmas range between 2.7-3.0 g/cm^3 (Naldrett, 2011). In crystal-poor magmas, sulphide droplets maintain their spherical shape and descend freely at a rate dependent on: sulphide-silicate density contrasts, acceleration due to gravity, the radius of the sulphide droplet and the silicate magma viscosity (Chung & Mungall, 2009).

Higher crystal fractions result in increased crystal-crystal interactions creating a solidified silicate framework through which the sulphide droplets must navigate or become stranded. The downward percolation of sulphide droplets can be inhibited by factors including: the degree of crystallisation of the silicate magma (affecting viscosity; Chung & Mungall, 2009), changes in lithology (Godel *et al.,* 2006), the cumulate minerals grain size (affecting the intergranular porosity; Godel *et al.,* 2006, Chung & Mungall, 2009), compaction of the cumulate pile and the presence of impermeable barriers (e.g. the presence of a chilled contact, Chung & Mungall, 2009). The movement of a liquid in a solid matrix is governed by surface energies of crystal-crystal and crystal-melt interfaces. This can be quantified by measuring the dihedral angles, θ, between the sulphides and silicates. Studies on magmatic rocks by Rose & Brenan (2001) and Brenan & Rose (2002) have shown that when dihedral angles between crystals and liquid measure <60° (see Figure 2.4E) the surface is wetted enabling sulphide melt migration in the cumulate pile (Mungall & Su, 2005; Godel *et al.,* 2006). In contrast, where dihedral angles are >60° (see Figure 2.4G) no wetting is possible restricting the migration of a sulphide melt (Mungall & Su, 2005; Godel *et al.,* 2006).

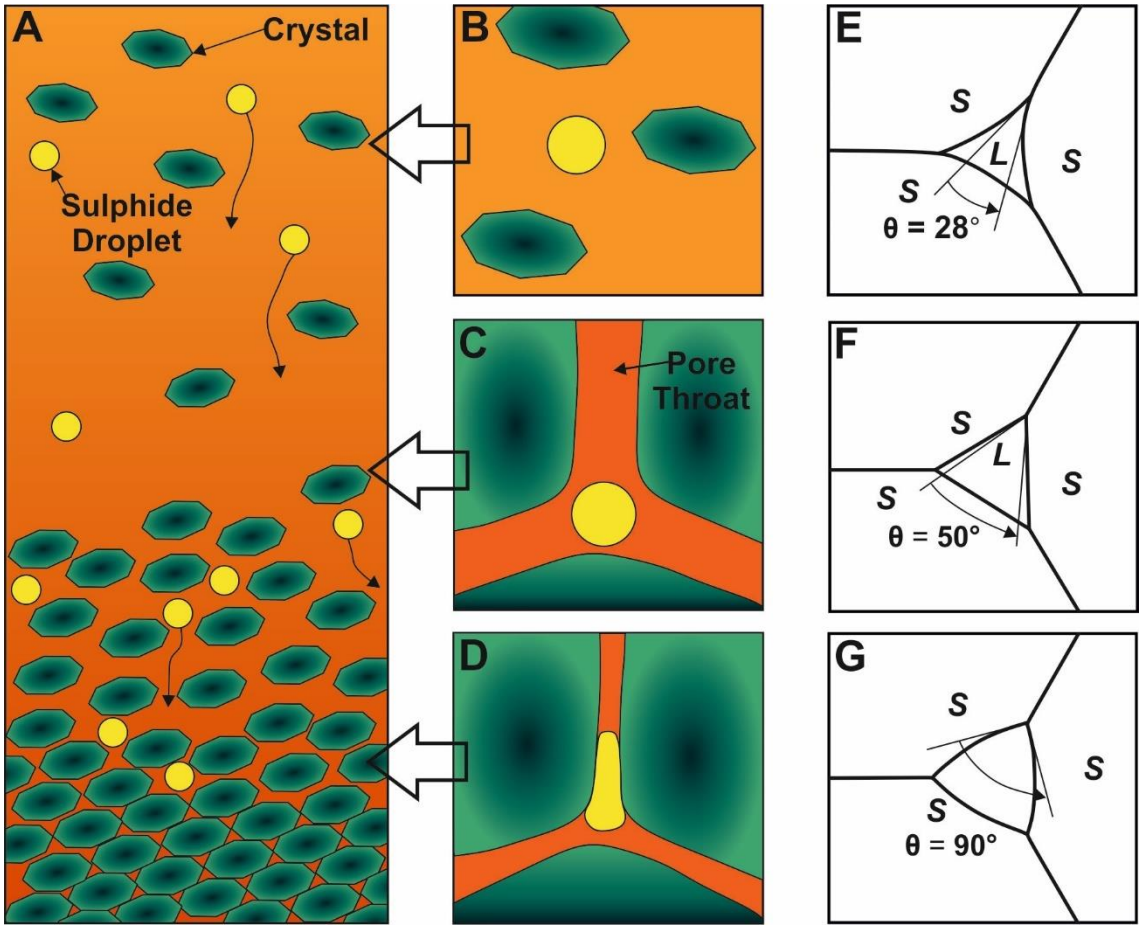

Figure 2.4: Schematic magma column showing sulphide settling at the magma-cumulate interface. (A) Stratification of a crystallising magma column. (B) Sulphide droplet in crystal-poor magma. (C) Sulphide in intergranular pore space in poorly packed crystals. (D) Sulphide deforming through a narrow pore throat in the crystal mush. (E-G) Variations in the dihedral angle in partially molten rocks.

2.2.6 Alternative Models

There are a few authors who believe that the purely chalcophile nature of the PGE is overstated (e.g. Tredoux *et al.,* 1995; Ballhaus & Sylvester, 2000) and that alterative processes can have a 'first-order' control on mineralisation.

The physical state of PGE within silicate magmas is not well understood i.e. are they dissolved in the silicate melt or present as atomic 'clusters' of PGE and semi-metals ± S (Tredoux et al., 1995). Evidence for the early formation of magmatic PGE nuggets was first visualised by Ballhaus & Sylvester (2000) in an in-situ laser ablation inductively coupled plasma mass-spectrometry (LA-ICP-MS) study on sulphides where they identified PGE micro-inclusions. Ballhaus & Sylvester (2000) suggested that their presence indicates PGE oversaturation prior to sulphur saturation in the magma. These small PGE nuggets can be mechanically collected by chromites and sulphides, as favoured by Tredoux et al., (1995) and Ballhaus & Sylvester (1999, 2000).

Volatile elements, present either as an independent vapour or dissolved in the melt, may contribute significantly to the petrogenesis of PGE-rich horizons. The role of fluids as a primary means of PGE enrichment is a contentious subject but models have been suggested for the formation of both the Merensky Reef (Boudreau & McCallum, 1992; Mathez, 1995 and Mathez et al., 1997) and J-M Reef (Boudreau & Meurer, 1999). The source of aqueous fluids transporting the PGE may be magmatic, metamorphic, hydrothermal or meteoric. A mixture of experimental and petrological observations are cited in the literature as evidence for fluid activity.

Experiments by Hanley et al., (2005) revealed that NaCl brines (at controlled pressure, oxygen fugacity and temperature 600-800 °C) can dissolve very high concentrations of Pt (1000 to 3000 ppm). These results demonstrate that certain PGE (Pd + Pt) are volatile and may be transported in oxidised Cl-rich aqueous fluids as chloride complexes e.g. $PtCl_4^{2-}$ and $PdCl^{2-}$. The dissolved PGE load carried in these fluids is deposited when the physiochemical conditions change e.g. at a redox boundary. A type locality for these processes operating unequivocally in nature is the Waterberg hydrothermal Pt deposit located 15 km west of Mookgophong in northern South Africa (McDonald & Tredoux, 2005; Holwell et al., 2017). This deposit sits on the Welgevonden-Planknek Fault network and the mineralisation hosted in structurally controlled quartz-Pt veins. The source of the Pt is proposed to be mafic/ultramafic Bushveld Complex rocks (McDonald & Tredoux, 2005; Holwell et al., 2017).

Petrological evidence for the role of volatiles in the formation of a PGE deposit include: the close association with pegmatitic rocks e.g. the Merensky pegmatoid; the presence/close association with magmatic, volatile-bearing minerals e.g. Cl-apatite in the Stillwater Complex (Boudreau et al., 1986), REE enrichment in pyroxenes from the Merensky Reef (Mathez, 1995) and the identification of both fluid and hydrous melt inclusions in silicates and oxides from mineralised intervals (McFall et al., 2018).

2.3 Ore Mineralogy and PGE Partitioning

Pyrrhotite, pentlandite and chalcopyrite (in varying proportions, ± pyrite) are the dominant primary magmatic base metal sulphides (BMS) found in most PGE deposits. These BMS minerals form during cooling of an originally homogenous sulphide liquid. The fractional crystallisation history of the sulphide has been determined both experimentally and through direct measurement to have an influence on the distribution of the PGE which are heterogeneously dispersed between the BMS phases. The PGE partitioning behaviour is controlled by their partition coefficients

between these BMS phases and may be affected by the presence of a semi-metal melt.

Our understanding of how PGE are contained in BMS has improved significantly with advances in in situ nanoscale analytical techniques. In particular, the development of laser ablation inductively coupled plasma mass spectrometry (LA-ICP-MS). LA-ICP-MS studies on magmatic sulphides deposits including: (1) the Platreef by Holwell & McDonald (2007), Hutchinson & McDonald (2008), Holwell & McDonald, (2010), Yudovskaya et al., (2017b) and Junge et al., (2018); (2) Merensky Reef by Godel et al., (2007), Ballhaus & Sylvester (2000) and Osbahr et al., (2013); (3) the J-M Reef by Godel & Barnes, 2008 and (4) the Main Sulphide Zone Great Dyke Oberthur et al., (1997). These separate studies on different deposits have revealed the following patterns in common in the PGE partitioning behaviour observed: (1) pyrrhotite and pentlandite contain the bulk of the IPGE (Os, Ir, Ru) and Re; (2) Co and in certain examples Rh, are largely hosted in pentlandite; (3) Pd is primarily hosted in pentlandite and Pd minerals; (3) Pt and Au are not present in BMS and form discrete minerals.

Laboratory experiments in the Fe-Ni-S and Fe-Cu-S system by Fleet & Stone (1991), Barnes et al., (1997), Fleet et al. (1999), Mungall et al., (2005) and Liu & Brenan (2015) exploring the partitioning behaviour of the PGEs during crystallisation of a sulphide liquid have shown that their distribution is primarily temperature dependent. The calculated partitioning coefficients for PGE, in addition to selected metals and semi-metals, between the Fe-rich (red line) and Cu-rich (yellow line) sulphide phases as recorded in Liu & Brenan (2015) are shown in Figure 2.5.

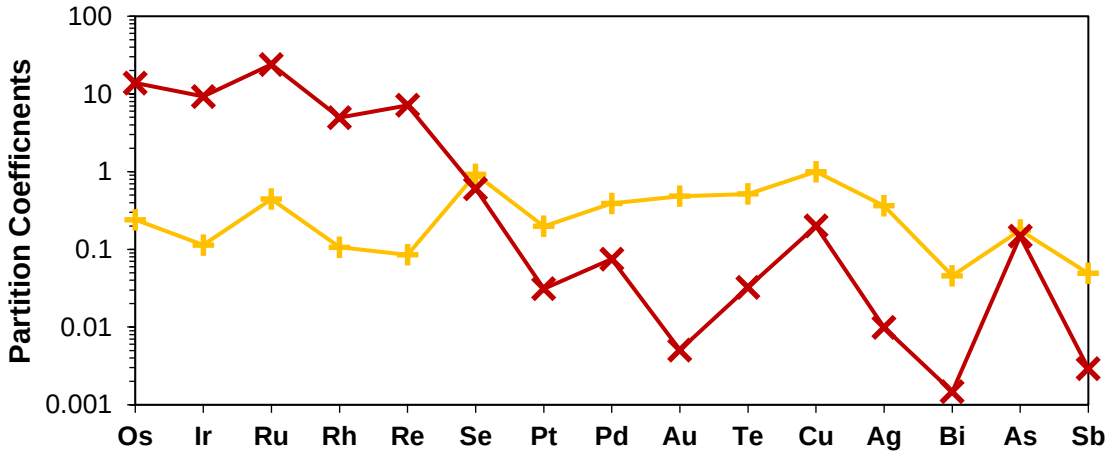

Figure 2.5: The partitioning of precious and semi-metals into MSS (red) and ISS (yellow) based on LA-ICP-MS data. Source: Liu & Brenan (2015).

A schematic representation, combining the results of both experimental work and analyses on natural samples, of the crystallisation and PGE partitioning history of a magmatic sulphide droplet as cooling progresses is presented in Figure 2.6. At magmatic temperatures, 1200 °C, typical of basaltic systems the immisicible sulphide liquid is present as a homogenous globule (see Figure 2.6A). Fractionation of the sulphide liquid begins as the magma cools. At 1000 °C crystallisation of monosulphide solid solution (MSS), compositionally equivalent to Ni-rich pyrrhotite, leaves a Cu-rich residual sulphide liquid (see Figure 2.6B). At this stage the IPGE (+ Rh, + Re) partition into the MSS with D values ranging from ≈20 to ≈5 (see Figure 2.5, Liu & Brenan, 2015). Pt, Pd and Au (+ chalcogens) are incompatible, with D values ranging from ≈0.1 to ≈1 x 10^{-3} and enter the residual sulphide liquid (Fleet et al., 1993; Barnes et al., 1997; Mungall et al., 2005; Liu & Brenan, 2005). Further cooling to 900 °C results in the crystallisation of the Cu-rich liquid as intermediate solid solution (ISS, see Figure 2.6C). Experimental data collected by Peregoedova et al., (2004) showed that Pt, Pd and Au are also incompatible in ISS and consequently they become incorporated into semi-metal rich melts (see Figure 2.6C).

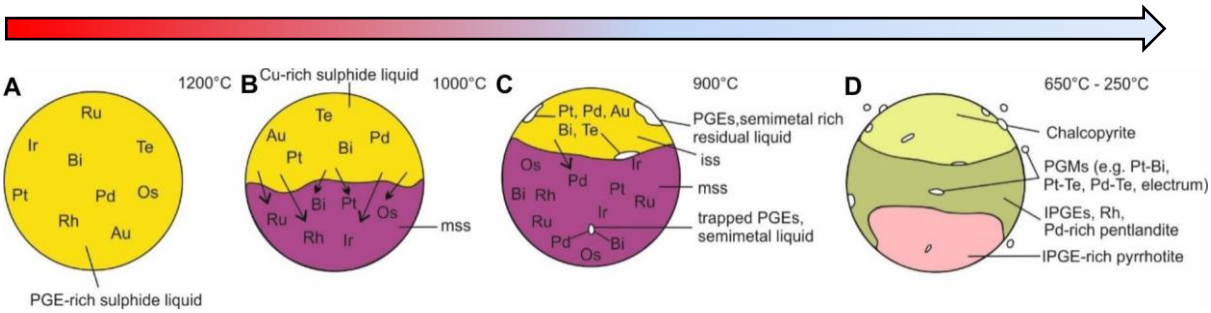

Figure 2.6: Schematic representation of the fractionating pattern of PGE in a cooling immiscible sulphide droplet in a S-rich system. Modified after Holwell & McDonald, 2010.

Subsolidus remodification at temperatures of <650°C (see Figure 2.6) results in pyrrhotite and pentlandite ± pyrite exsolving from MSS and chalcopyrite ± cubanite ± pyrite exsolving from ISS. Pyrrhotite and pentlandite retain the IPGE in solid solution inherited from MSS; although some modification is evidenced with Rh and Pd strongly favouring pentlandite over coexisting pyrrhotite (Naldrett, 1989; Barnes & Ripley, 2016). The incompatibility of all PGE with ISS means that the resultant chalcopyrite holds negligible PGE in solid solution. Chalcopyrite has been measured as containing concentrations of Zn, Cd and Ag (Barnes et al., 2008).

The last phases to form are discrete platinum group minerals (PGMs); dominated by Pt and Pd phases that combine with P-block semimetals including As, Sb, Te and Bi. These semimetals may be present within the magmatic system from source (Lorand

et al., 2013), although it has been proposed that additional semimetals can be incorporated into the magma at a later stage via local contamination processes e.g. the assimilation of Sb- and/or As-bearing sediments has been suggested a potential source for the Pt and Pd arsenides and antimonides dominating the PGM assemblage in the Turfspruit area of the Platreef (Northern Limb, Bushveld; Hutchinson & McDonald, 2008).

Au typically combines with Ag to form the alloy electrum (Helmy et al., 2007). The late stage of their crystallisation means that PGM are often found on grain boundaries (either between sulphide phases or on the outside edge of sulphide in contact with coexisting oxides/silicates) although they are also frequently found as inclusions in sulphides. If the original immiscible sulphide melt is deficient in semimetals Pt and Pd can enter solid solution in sulphides not excluding the subsolidus crystallisation products of MSS (Helmy et al., 2007; Holwell & McDonald, 2010).

An additional step, not shown in Figure 2.6, is proposed here that involves later stage secondary replacement of base metal sulphides by hydrothermal fluids resulting in the decoupling of PGM from the sulphide. The importance of secondary, hydrothermal alteration and resulting S loss and redistribution of chalcophile elements is highlighted in a study by Li et al., (2004) on the Merensky Reef and UG2 chromitite mineralisation. This study found that the Pt and Pd PGM are retained in proximity to the previous sulphide whereas the corresponding Ni and S are absent. This has implications both for PGE recovery and for the evaluation of PGE perspectivity based on base metal ratios. A more recent study by Holwell et al., (2017) demonstrates that low-temperature (≈ 200°C) hydrothermal alteration can also significantly affect the trace element composition of sulphides. In Holwell et al., (2017) sulphides from the Grasvally Norite-Pyroxenite-Anorthosite (GNPA) member on the northern limb of the Bushveld complex have undergone a continuum of mineralogical transitions with progressive alteration; from an original magmatic pyrrhotite-pentlandite-chalcopyrite assemblage to the altered pyrite-millerite-chalcopyrite (PMC) assemblage. The initial stages of alteration increase the Cu, Ni and PGE tenors of the remaining sulphides before ultimately the breakdown of pentlandite liberates Pd (and potentially Pt) from the sulphide at the final stage of the alteration.

2.4 Geological Setting

Magmatic Ni-Cu-PGE sulphide deposits are hosted in a variety of geological settings. The majority of Ni-Cu (PGE) ores are present as irregular ore bodies in conduit systems (e.g Uitkomst and Voisey's Bay) and at the base of komatiitic lava flows (e.g. Kambalda). One notable exception to this is the Ni-Cu (PGE) mineralisation of the Sudbury Igneous Complex, which represents a meteorite impact-triggered crustal melt. PGE-dominated deposits are found within and on the margins of mafic/ultramafic intrusions (e.g. Bushveld Complex and Stillwater Complex). In the following sections we will describe three geologic settings which host the majority of the World's PGE resource: (1) stratiform reefs in layered mafic/ultramafic intrusion; (2) contact-style deposits found on the edge of large intrusions and; (3) Ni-Cu (PGE) sulphide deposits related to the magma chamber plumping systems.

2.4.1 Layered Mafic/Ultramafic Intrusions

Layered mafic/ultramafic intrusions hosting PGE mineralisation range in scale from 10 to 100's of km's in size e.g. the 11 km wide and 2.5 km thick Skaergaard intrusion (Holness *et al.,* 2017) compared to the 65,000 km^2 and 8 km thick Bushveld Complex. These intrusions represent solidified closed and open-system magma chambers, respectively i.e. they either formed from the crystallisation of one parental magma or experienced multiple phases of magmatism during their crystallisation. The largest layered igneous intrusions including the Bushveld Complex, the Stillwater Complex, and the Great Dyke show evidence for open-system behaviour.

A single layered igneous intrusion, particularly larger ones, may contain a variety of styles of PGE-mineralisation that have formed in numerous ways and at different times in its crystallisation history (see Figure 2.7).

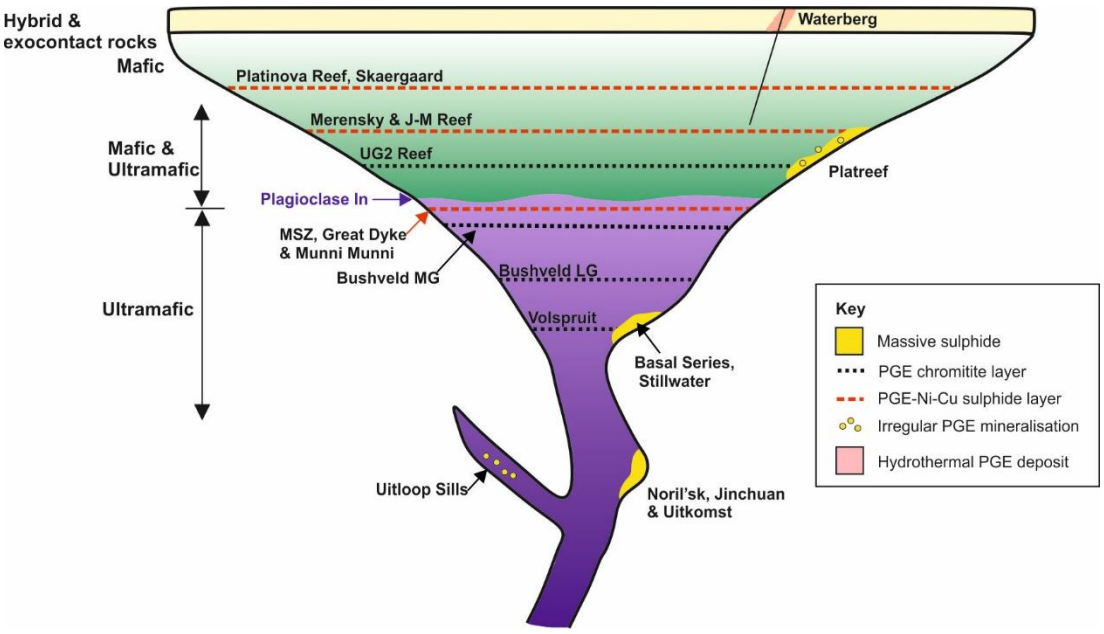

Figure 2.7: A schematic diagram showing the location of known PGE deposits within an ultramafic/mafic layered intrusion and in their feeder conduits. Modified after Maier (2005) and Naldrett (2010).

Mineralised layered intrusions are strongly differentiated resulting in a broad compositional change with height, as shown schematically in Figure 2.7 and with examples in Figure 2.8. In open systems, the parental magmas feeding the intrusion have been found to evolve over time and are typically characterised by an early MgO, Cr- and SiO_2 rich (U-type) magma followed by a later Al_2O_3-rich tholeiitic magma (Naldrett, 2011). On the intrusion scale magmatic sulphide PGE reefs are frequently developed near the boundary between these two magma types, which represent a transition from ultramafic to mafic compositions, as illustrated using stratigraphic logs of mineralised intrusions in Figure 2.8.

In order to predict the occurrence of mineralised horizons layered intrusions are often treated like a sedimentary sequence with layers grouped into stratigraphic units demonstrating similar compositional or textural characteristics (hence the term stratiform). Systematic mineral compositional changes with stratigraphic height typically reflect patterns that are consistent with the expected crystallization path of a mafic magma (i.e. Bowens reaction series). Perturbations from a steady-state crystallisation sequence may be common with fractionation discontinuities, intervals of homogenous mineral compositions and abrupt reversals in the mineral crystallization sequence evidenced, particularly in open systems. Lithogeochemical tools have been applied to intrusions in order to assess their PGE-bearing potential

and to predict the level of mineralised stratigraphic intervals. For example, Maier et al., (1996) identified Cu/Pd ratios to be useful for identifying sulphide depletion; the difference in D values for Cu and Pd means that a sulphide event at high R factors will deplete Pd more effectively than Cu and drive the Cu/Pd ratio to very high values in rocks that form immediately after a mineralisation event.

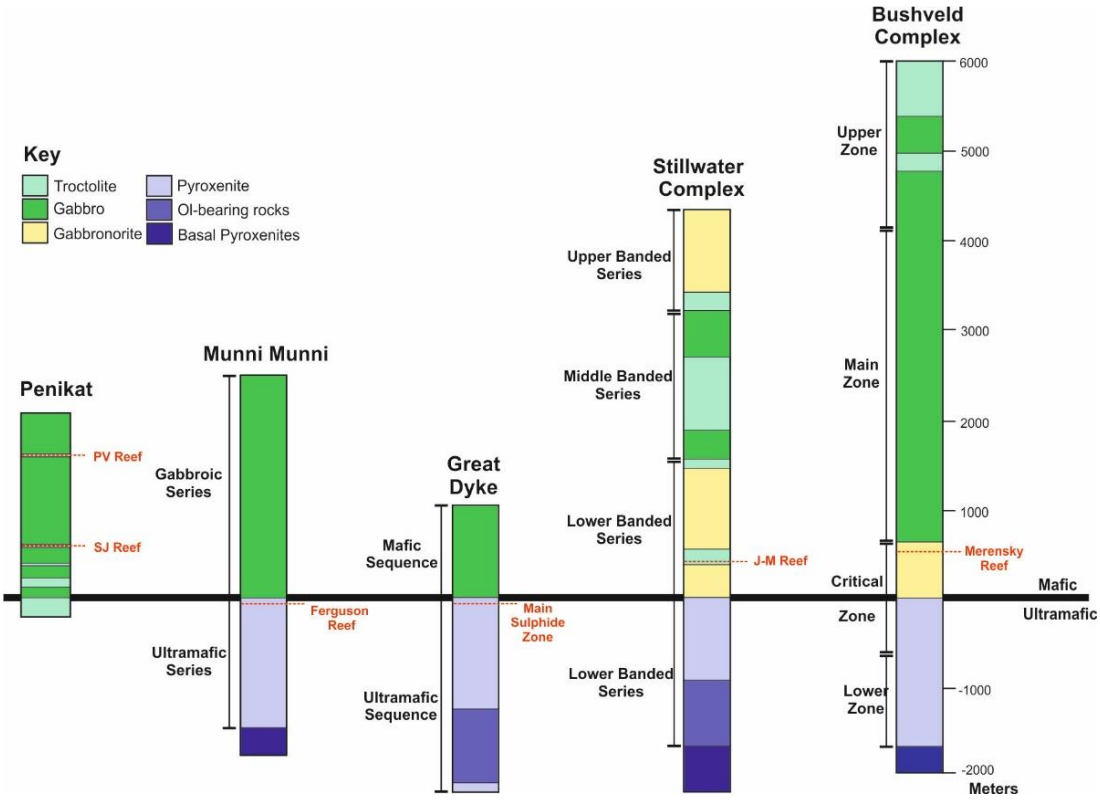

Figure 2.8: Generalised stratigraphic columns showing the height of PGE reefs within the igneous layering for a variety of intrusions. Modified after Zientek, 2012.

The formation of a PGE deposits within a layered intrusion requires an interplay of both chemical (e.g. elemental concentrations of PGE and partition coefficients) and physical processes (e.g. relating to the method of magma emplacement). An overview of the different settings of PGE mineralisation within layered intrusions, as stratiform reefs (2.4.1.1) and on the margins as contact-style deposits (2.4.1.2), are covered below.

2.4.1.1 Stratiform PGE Reefs

Stratiform deposits contain the richest PGE grades over narrow intervals (e.g. J-M reef contains 18 ppm Pt + Pd over 1 to 3 m; Naldrett, 2011) and the mineralisation is hosted within silicate or chromitite layers with associated base metal sulphides (BMS) (Eales & Cawthorn, 1996; Naldrett, 2011). In this context they are referred to as ‘reefs’ by mining geologists and this term has permeated into the scientific literature.

Examples of this type of deposit type are shown in Figures 2.7 and 2.8 and include: the Merensky Reef, UG2 chromitite, the J-M Reef and the Main Sulphide Zone. A variety of ore-forming processes have been proposed as being the dominant mechanism for producing this deposit type, schematic representations of the most popular hypotheses are shown in Figure 2.9 (A-H).

One of the earliest proposed models for the formation of stratiform PGE reefs is the magma mixing model (see Figure 2.9A) by Campbell et al., (1983) and Naldrett et al., (1987). Sulphur saturation is achieved through the mixing of two sulphur undersaturated magmas following fresh magma injection as a plume into depleted resident magma (Naldrett et al., 2012). High R factors are achieved through gravitational settling (for details see section 2.2.4). This model is supported by geochemical (e.g. Cu/Pd ratios; Maier, 2005) and isotopic (e.g. Sr-isotopes; Kruger, 1994) evidence that confirm the injection of new magma at mineralised intervals. In addition to the observed occurrence of PGE reefs at stratigraphic intervals coinciding with major lithologic and petrologic changes in the layered igneous intrusion (see Figure 2.7).

Lateral mixing (see Figure 2.9B) was developed by Scoon & Teigler (1994), and later adopted by Naldrett et al., (2011). This model suggests chromite crystallisation occurred on the floor of the chamber with dense new magma injected as a basal layer on the cumulate/magma boundary layer. This turbulent high-density flow results in high R factors achieved through lateral movement compared to vertical movement of models shown in Figure 2.9A and 2.9C.

The interaction between fresh magma injecting as a fountain and the roof rocks (Figure 2.9C) of the magma chamber was suggested by Kinnaird (2005) for the formation of the Merensky Reef. The primitive magma assimilates roof rock material which, depending on composition, triggers sulphur/chromite saturation as outlined in section 2.2.3. The processes are similar to those forming ‘contact-style’ deposits located on the margins of the intrusion. The collapsing sides of the fountain carry the sulphide globules and/or chromite grains to the top of the cumulate pile and during descent these minerals interact with the resident magma generating high R factors.

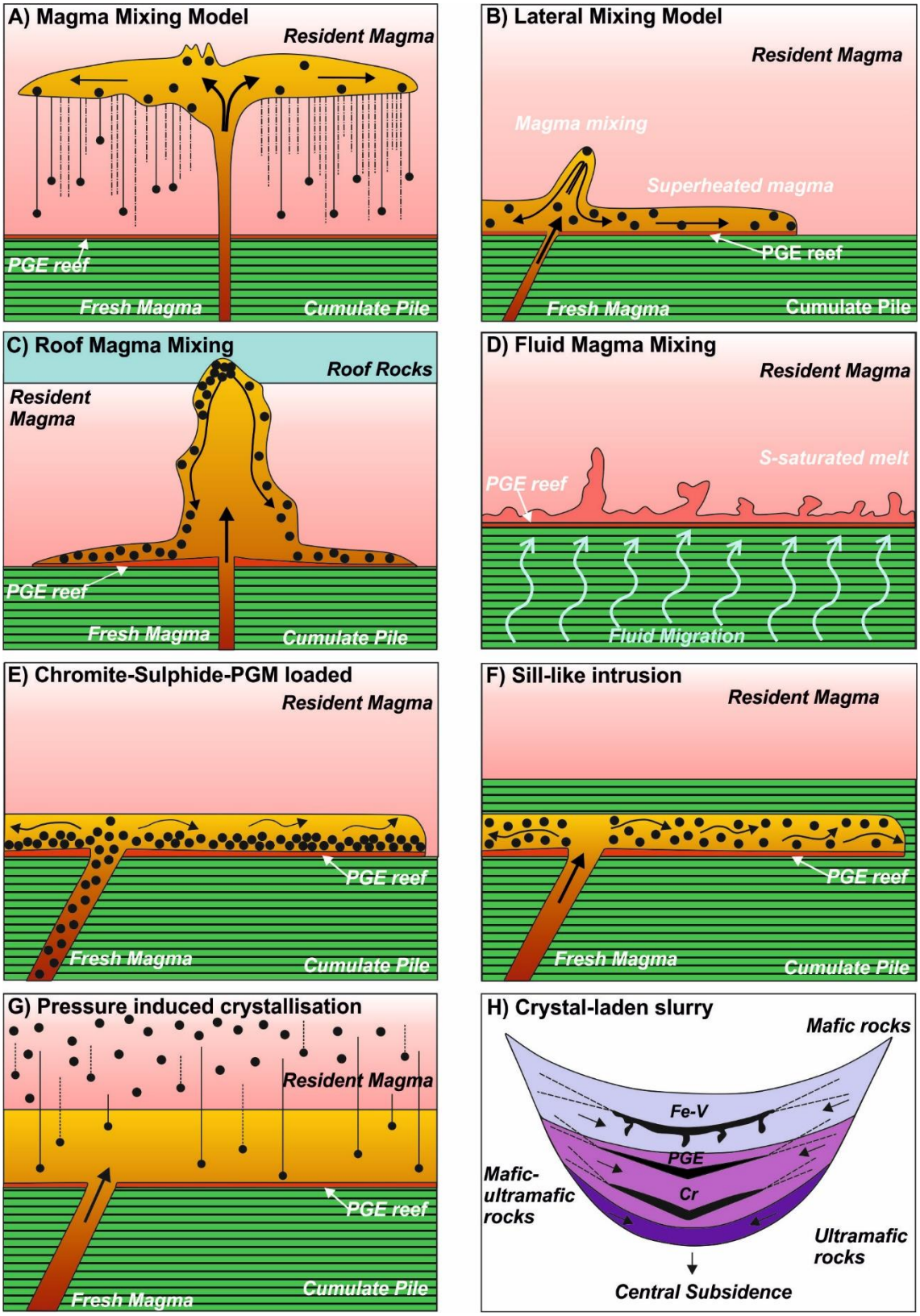

Figure 2.9: Various petrogenetic models for the formation of stratiform reef PGE and chromite mineralisation within layered intrusions. Modified after Latypov et al., 2016. For details see text.

An overview of the fluid involvement in PGE concentration is provided in section 2.2.6 and a representation is shown in Figure 2.9D. The volatile fluxing model involves the release of volatiles from a cooling, compacting, semi-consolidated crystal pile. This volatile front ascends dissolving S, Ni, Cu, Pd and to a lesser extent Pt as it goes before depositing at a chemical front (e.g. Boudreau & McCallum, 1992; Mathez, 1995 and Mathez et al., 1997). This chemical front represents the top of the cumulate pile where the S saturated fluids meet fluid-undersaturated magma resulting in the precipitation of the transported sulphide and associated metals.

The injection of a sulphide and/or chromite saturated magma (see Figure 2.9E) was suggested for the formation of the Merensky Reef by Hutchinson et al., (2015), of monomineralic chromitite layers by Voordouw et al., (2009) and in the formation of the Platreef in McDonald & Holwell (2011). In this model sulphides enriched in PGE PGE are formed in a staging chamber with significant PGE grade achieved in processes outlined in section 2.2.4.

Out-of-sequence emplacement of primitive magma as sills into the existing cumulate pile (see Figure 2.9F) has been suggested by Mitchell & Scoon (2007), Kruger (2010) and Mungall et al., (2016). The most recent study by Mungall et al., (2016) is based on the results of detailed U-Pb dating of zircon and baddeleyite on Upper Critical Zone (UCZ) rocks of the Bushveld Complex. The emplacement ages indicate that new ultramafic UCZ magma emplaced as sills into pre-existing mafic rocks of the Main Zone. This raises questions over the formation of a magma chamber; it is often assumed that all layered intrusions represent a simple stratigraphic sequence with oldest rocks at base and youngest at top. The interpretation of this geochronological data has been questioned (e.g. Latypov et al., 2017) as it contradicts well-documented field relationships including Main Zone potholes (Mitchell & Scoon, 2004) at Winnaarshoek and chilled margins observed in outcrops in the Zwartfontein and recorded in Holwell & Jordaan (2006) that the Main Zone crystallised after the UCZ. Latypov et al., (2017) present alternative interpretations of the zircon crystallisation dates such as: (1) the zircons may be inherited from earlier melt in a staging chamber and; (2) the zircon may have a long crystallisation period within intercumulus melt.

Pressure induced crystallisation (see Figure 2.9G) of chromite- and PGE-bearing stratiform horizons has been advocated by Cawthorn (2005; 2011). This hypothesis is strongly influenced by the regional-scale lateral continuity of these mineralised layers; requiring a petrogenetic process capable of operating simultaneous

throughout the entire magma chamber. An increase in pressure promotes sulphur solubility (Mavrogenes & O'Neill, 1999) and influences the stability of both chromite (Cameron, 1982) and pyroxene (Cawthorn, 2003). There are two proposed mechanisms capable of causing sudden fluctuations in pressure in the magma chamber: (1) injection of new large volume of magma and; (2) syn-emplacement tectonic/seismic activity resulting from crustal loading (Naslund & McBirney 1996). This model is difficult to test as it leaves no direct evidence in the magmatic system. Furthermore, there is a growing appreciation of the regional variability of the 'stratiform' mineralised horizons and this hypothesis is not generally considered seriously as a in situ petrogenetic process.

The mechanical deposition of crystals as gravity-driven slurries was proposed in a landmark paper by Maier et al., (2013; see Figure 2.9H). The driving force behind these slurries is central subsidence of the magma chamber due to crustal loading resulting in the slumping of unconsolidated cumulates towards the central depression. During transport hydrodynamic sorting creates the observed separate layers of chromite, PGE sulphide bearing pyroxenites and magnetite.

Traditionally, these models could be split into two schools of thought termed the 'Uppers' and the 'Downers' (Naldrett et al., 2009). The 'Uppers' maintain that the source of the metals is from the footwall cumulates whereas the 'Downers' consider that the metals were derived from a new magma pulse entering the magma chamber and concentrated downwards. The latest developments in the literature suggest that they can also be divided based on whether the mineralisation processes occur via in situ chemical and physical interactions in the magma column vs transported as pre-formed phases either from depth in a staging chamber or from the side walls of the intrusion as slurries. Importantly, in contrast to most Ni-Cu (PGE) deposits there is minimal inferred influence of assimilated external crustal material in ore formation. This is supported by S isotope studies on S poor stratiform reefs within layered mafic-ultramafic intrusions, e.g. both the Merensky Reef of the Bushveld Complex and the J-M reef of the Stillwater Complex have restricted ranges of $\delta^{34}S$ values around zero (± 2 ‰) indicating minimal or no contribution from the country rocks to the magmas S budget (Liebenberg, 1968; Penniston-Dorland et al., 2008).

2.4.1.2 Marginal or Contact-Style

Marginal or contact-style deposits are found at the base and side walls of mafic/ultramafic intrusions and the sulphide-hosted PGE mineralisation may extend into the surrounding country rock. Examples of this style of mineralisation include the

Basal Series (Stillwater Complex) and the Platreef (northern limb, Bushveld Complex the latter two examples are shown in Figure 2.7). In contrast to 'reef-type' deposits, this mineralisation style is characterised by a greater thickness (ranging from 10's to 100's metres), the ores are massive to disseminated, generally discordant and enriched in base metal sulphides (>5 vol%). Currently, the only mined example of this deposit type is the Platreef, exposed on the northern limb of the Bushveld Complex (White, 1994); although there is debate around whether this represent a true contact deposit in the classic sense (McDonald & Holwell, 2011).

2.4.2 Dynamic Magma Conduit

The most significant Ni-Cu (PGE) deposits are found in magmatic conduit structures which once formed the plumping system for intrusions e.g. Noril'sk (Naldrett, 1987), Voisey's Bay (Hiebert et al., 2013), the Uitkomst Complex (Gauert, 2001) and Jinchaun (Duan et al., 2016). Magma conduits represent an ideal environment for a sulphide liquid to upgrade its metal tenor via interaction with significant fluxes of undepleted magma (Barnes et al., 2016). These structures may take the form of dykes (e.g. Voisey's Bay), sills (e.g. Noril'sk) or staging chambers (e.g. Uitkomst) which supplied incoming volumes of fresh magma from depth to surface. Once an immiscible sulphide melt segregates from the host magma their depositional site is controlled by morphological features of the conduits which may act as fluid dynamic traps e.g. changes in the width, orientation and any structural discontinuities such as embayments and/or fractures in the wall rocks. For example the Ovoid Deposit (Voisey's Bay) is located at a dilation point in the conduit dyke (Hiebert et al., 2013).

The orebodies are characterised by sulphide concentrations that are greater than could have dissolved from the magma body based on the present volume of rock (Barnes et al., 2016). To account for this excess in sulphide and chalcophile elements a fundamental ore-forming process is the triggering of sulphur saturation through the assimilation of crustal S (for more information see section 2.2.3). The assimilation of crustal S is envisaged to have been crucial in the formation of the Noril'sk (Li et al., 2003; Malitch et al., 2014), the Uitkomst Complex (Gauert, 2001; Li et al., 2002; Sarkar et al., 2008) and Voisey's Bay (Ripley et al., 1999; Hiebert et al., 2013). This is supported by independent non-magmatic S isotope values.

The application of S isotopes has been established as a very effective means of identifying crustal input into a magma; largely because there is significant variation between the range of $\delta^{34}S$ values observed between igneous and sedimentary rock types. A narrow range of $\delta^{34}S$ values are expected for igneous rocks, 0 ± 2 ‰, centred

on mantle values. The magmatic values can be modified based on the oxidation state of the magma increasing the range to -4 to +4 ‰ (Ohmoto & Rye, 1979). Crustal rocks that have been involved in the sedimentary cycle and subjected to biogenic processes can have a wide range in values typically within +/- 50 ‰. It is important to note that in order to impart a non-magmatic S isotopic signature to a mafic magma the surrounding country rocks must contain S-bearing mineral phases. The identification of S-bearing country rock sediments has been used as an exploration tool for Ni-Cu-PGE deposits (Barnes et al., 2016). In sedimentary rocks S may be found as pyrite in shales or as sulphate minerals in evaporates e.g. anhydrite and gypsum. During the assimilation of shales S is added to the magma by conversion of pyrite to pyrrhotite in a diffusive process (Naldrett, 1966 and Ripley, 1991). Sulphate can be incorporated but the S must be reduced to sulphide (Naldrett, 2004 and Jugo & Lesher, 2005).

The mass-dependent $\delta^{34}S$ values are determined by measuring the most abundant isotopes of sulphur, ^{32}S and ^{34}S. The isotopic abundance variation is then calculated using the abundance ratio of $^{34}S/^{32}S$ and expressed relative to the standard VCDT (Vienna Canyon Diablo Troilite) using the following equation:

$$\delta\,^{34}S\ (‰) = \left\{\frac{(^{34}S/^{32}S)\ sample}{(^{34}S/^{32}S)\ standard}\right\} - 1 \quad \textbf{Equation 2.3}$$

The resulting values are related to a standard “δ” notation and expressed in parts per thousand (per mil). Any recorded large mass differences between the two principal isotopes of sulphur can be used to understand the depositional histories of sulphide minerals. When interpreting $\delta^{34}S$ values it is important to appreciate that this ratio, $^{34}S/^{32}S$, may be altered by magmatic (Ripley & Li, 2003) and hydrothermal processes (Penniston-Dorland *et al.,* 2008). For example, sulphide minerals precipitated in response to crustal contamination and deposited in a dynamic environments will be subjected to high fluxes of magma which will have the effect of shifting their S isotope values towards the mantle range due to the high R-factor (Lesher, 2017). In addition, it has been noted that Proterozoic and Archean sedimentary rocks contain a limited range of $\delta^{34}S$ values that may be indistinguishable from magmatic sulphides (Ripley & Li, 2003; Lesher, 2017).

Recently, multiple sulphur isotope studies, which measure both mass-dependent ($\delta^{34}S$) and mass independent ($\Delta^{33}S$) S isotopes, have been applied to magmatic systems that have intruded Archean (> 2.5 Ga) rocks. Mass-independent fractionation (MIF) of S is thought to have occurred due to photochemical reactions of SO^2 gas in the Earth’s oxygen-deficient Archaean atmosphere resulting in large magnitude shifts

in $\Delta^{33}S$ away from 0 (Farquhar *et al.,* 2001). Studies on the Archean sulphur cycle have found that nonzero $\Delta^{33}S$ values only result from surface processes (Farquhar & Wing, 2003). Therefore, if nonzero $\Delta^{33}S$ values are found in magmatic sulphides it can only be sourced from the assimilation or contamination of crustal material. $\Delta^{33}S$ is calculated Equation 2.4 from Farquhar et al., (2000):

$$\Delta^{33}S = \delta^{33}S - 1000\,x\,[(1+\delta^{34}S/1000)^{0.515} - 1$$ **Equation 2.4**

$\Delta^{33}S$ values are considered chemically conservative and will remain unaltered at the high temperatures found in magmatic and metamorphic systems (Penniston-Dorland *et al.,* 2008). A combination of the two isotopic systems can be used to unravel any secondary processes fractionating the mass dependent $\delta^{34}S$ values, but not affecting the $\Delta^{33}S$ (Penniston-Dorland et al., 2008).

Chapter 3

Overview of the Bushveld Complex

3.0 Regional Geological Setting

The Palaeoproterozoic Bushveld Igneous Complex (BIC) is located in the Limpopo Province in northern South Africa (see inset Figure 3.1). It is unusually well preserved despite its great age being relatively undeformed by subsequent tectonic activity or regional metamorphism; although it has undergone extensive erosion (Eales & Cawthorn, 1996). The BIC represents a continental large igneous province (LIP) comprising an early extrusive felsic volcanic phase, as preserved in the Rooiberg Group, followed by three main intrusive suites: the mafic/ultramafic Rustenburg Layered Suite (RLS), the Lebowa Granite Suite and the Rashoop Granophyre Suite (see Figure 3.1; South African Committee for Stratigraphy, 1980). In the scientific literature, the term Bushveld Complex is frequently used only in reference to the layered mafic/ultramafic suite of the RLS; this distinction is applied in this study.

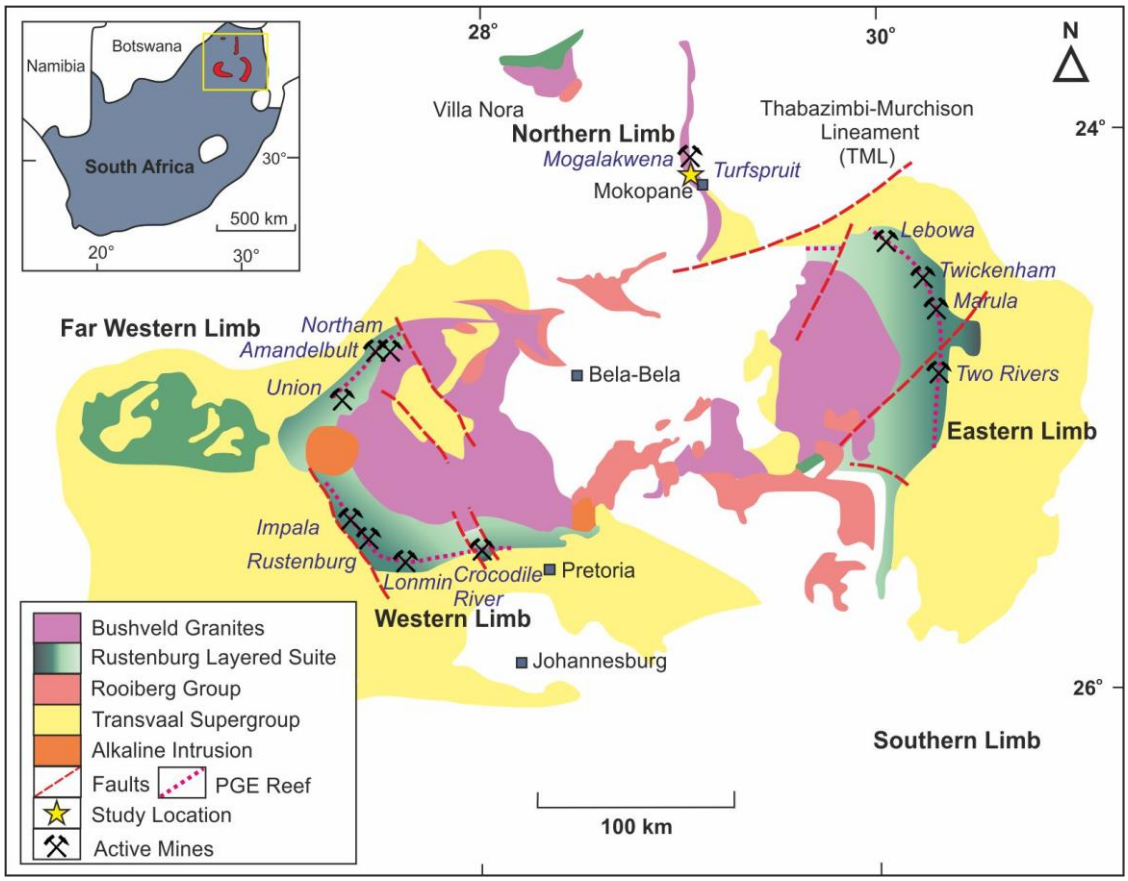

Figure 3.1: Regional geological map of the Bushveld Igneous Complex showing the various limbs and its location within South Africa (top left inset). Highlighted are the location of the study area and significant PGE mining operations. Modified after Eales & Cawthorn, 1996.

The segmented nature of the geographic exposure of the RLS has led to its division into five lobes or limbs (all noted in Figure 3.1): the strongly eroded far western limb; the near-symmetrical western and eastern limbs; the partially exposed southern limb and the nonconforming northern limb.

The country rocks surrounding the BIC are sediments of the Late Archean to Early Proterozoic, 2.67 to 2.07 Ga Transvaal Supergroup (Bekker et al., 2001). The sediments of the Transvaal Supergroup were deposited on top of Archean basement and are found in two structural basins known as the Transvaal and the Griqualand West basins (Bekker et al., 2001; see Figure 3.2 inset). An overview of the chronostratigraphy of the Transvaal Supergroup as preserved at these two locations is shown in Figure 3.2; including some attempts at stratigraphic correlations between the separate basins. The Bushveld Complex intruded predominantly within the confines of the Transvaal Basin and marks the upper boundary of the Transvaal Supergroup at this location; hence all following references to the Transvaal Supergroup refer solely to the stratigraphy as present in the Transvaal Basin.

The Transvaal Supergroup attains a maximum thickness of 12 km and comprises the Wolkberg, Chuinespoort and Pretoria Groups (see Figure 3.2). On the eastern and western limbs, the emplacement of the RLS occurred along the regional unconformity separating the overlying Rooiberg Group volcanics from the underlying Pretoria Group sediments (Cheney & Twist, 1991; Scoates & Freidman, 2008 and Kruger, 2005). The igneous layering has been observed to follow the original near-horizontal bedding planes (Eales & Cawthorn, 1996; Harris & Chaumba, 2001; Barnes & Maier, 2002). In contrast, on the northern limb the magmatic sequence of the RLS has a transgressive basal contact and moves over progressively older facies of the Transvaal Supergroup moving from south to north before abutting Archean granite and gneisses (van der Merwe, 1976; Eales & Cawthorn, 1996). The consequences of this igneous transgression on the observed stratigraphic and mineralisation associated with the RLS on the northern limb compared to the eastern and western limbs are covered in section 3.4 below.

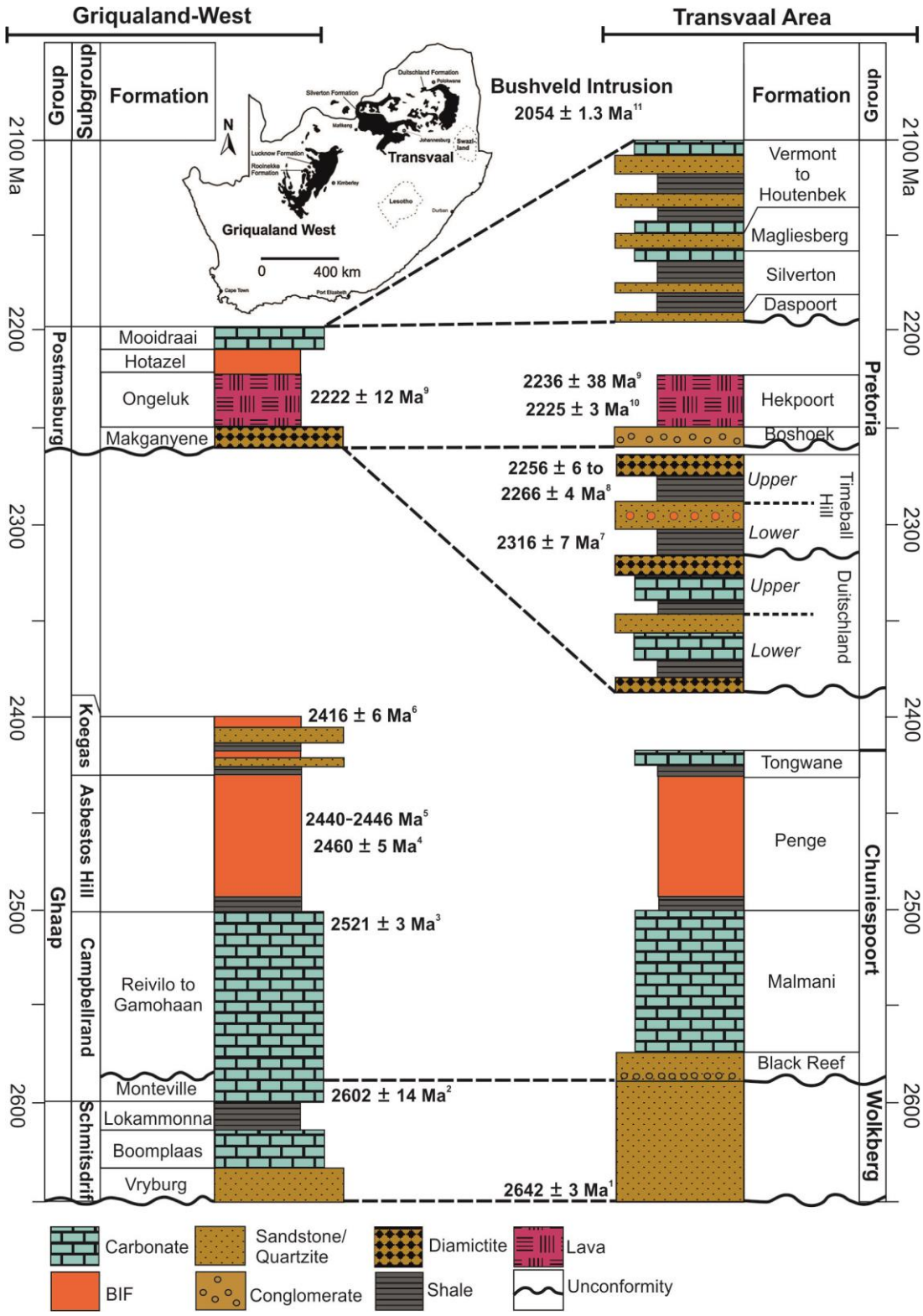

Figure 3.2: Chronostratigraphic columns of the Transvaal Supergroup as present in the presumed coeval Griqualand West and Transvaal sub-basins (see inset map). Highlighted are the levels of intrusion of the Bushveld Complex. Published ages are from: 1 - Walraven & Martini (1995); 2 – Altermann & Nelson (1998); 3 – Summer & Bowring (1996); 4 – Pickard (2003); 5 – Beukes & Gutzmer (2008); 6 – Gutzmer & Beukes (1998); 7 – Hannah et al., (2004); 8 – Rasmussen et al., (2013); 9 – Cornell et al., (1996); 10 – Dorland (2004) and 11 – Scoates & Friedman (2008). Modified after Schröder et al., (2016) and Frauenstein et al., (2009). Inset map of the basins taken from Frauenstein et al., (2009).

3.1 Evolution of the Bushveld Complex

The overall structure of the Bushveld Igneous Complex (BIC) remains controversial. Many key aspects pertaining to the structure of the BIC have yet to be definitively answered including: (A) identifying the location and nature of magma feeder zones; (B) establishing whether the magma was supplied from one large magma reservoir or several sub-chambers; (C) determining the true size and lateral extent of the Rustenburg Layered Suite (RLS). The latter point relates to the recent discovery of an ultramafic-mafic sequence of rocks beneath younger sedimentary rocks of the Waterberg Group beyond the current extent of the mapped outcrop of the northern limb (Kinnaird et al., 2017). In addition, it has long been speculated, based on geophysical evidence (see subsection 3.1.2) and outcropping rocks at Villa Nora, that the BIC extends beyond the northern limb. Prior to discussing the current structure of the BIC the palaeotectonic evolution of the Kaapvaal craton is described to outline the crustal architecture into which the BIC intruded.

3.1.1 Regional Paleotectonomagmatic History

The current configuration of southern Africa represents the end result of the amalgamation of a series of terranes which combined over a period from > 3.0 Ga to 1.8 Ga (Silver et al. 2004). An interpretation of the tectonomagmatic history over this time period by Silver et al. (2004), using mantle fabrics as revealed by seismic anisotropy, identified five major deformation phases, as depicted schematically in Figure 3.3. The overarching event is the tectonic juxtaposition of the Zimbabwe shield and Kaapvaal shield; with the intervening tectonic blocks experiencing high grade amphibolite (Pietersburg Greenstone Belt) to granulite metamorphism (in the Limpopo Belt).

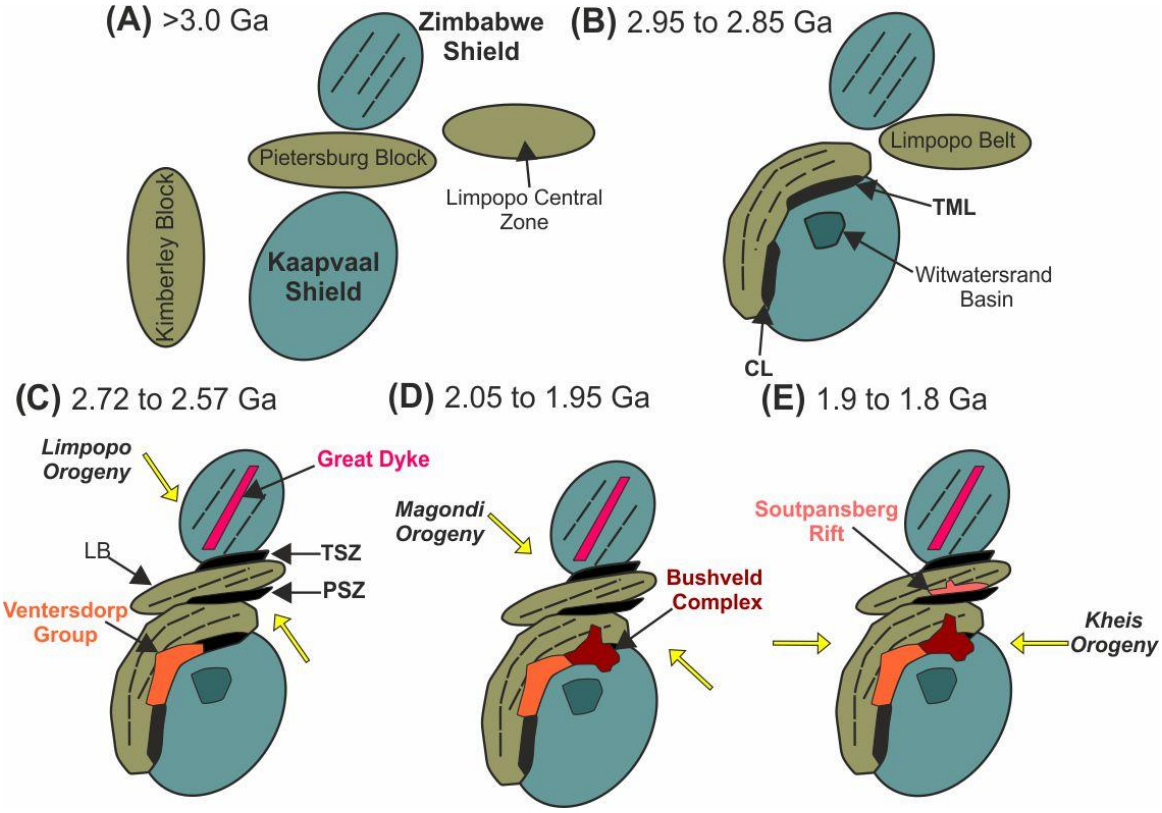

Figure 3.3: A schematic representation of the Palaeotectonic evolution of the Kaapvaal craton between >3.0 Ga and 1.8 Ga. Modified after Silver et al., (2004). Abbreviations: CL = Colesberg Lineament, LB = Limpopo Belt, PSZ = Palala Shear Zone, TSZ = Tiangle Shear Zone, TML = Thabazimbi-Murchison Lineament. Note: dashed black lines indicate the orientation of the dominant structural fabric and yellow arrows are orientated in the principal stress directions.

The Thabazimbi-Murchison Lineament (TML) structural lineament formed early in the palaeotectonic history (see Figure 3.3B). This crustal-scale (250 km) lineament represents a deep-seated shear zone, which formed around 2.9 Ga during the collision of the Pietersburg and Kimberly Blocks with the Kaapvaal Shield (see Figure 3.3B; Clarke et al., 2009, Zeh et al., 2013). The TML represents a long-lived and continuously reactivated structural feature, since its formation through to the Mesozoic (Good et al., 1997; Silver et al*.,* 2004). This timeframe spans the period before, during and after the intrusion of the BIC leading to speculation on its role in the emplacement of the BIC (Good & De Wit, 1997; Kruger, 2005). The role of the TML as a potential dyke-like feeder zone is supported by Kruger (2005), Silver et al., (2004), and Clarke et al., *(*2009).

At the time of the intrusion of the BIC (see Figure 3.3D) the Kaapvaal Craton was experiencing NW-SE directed compression known as the Magondi Orogeny (Silver et al., 2004 and Clarke et al., 2009). This collisional event is recorded in high-grade metamorphism in the Limpopo Belt and it may have resulted in the reactivation of shear zones, including the TML, regarded as areas of weakness in the crust (Clarke et al., 2009 and Silver et al., 2004). As shown in Figure 3.3, the BIC intruded across the TML i.e.

the eastern and western limbs intruded onto the northern edge of the Kaapvaal shield and the northern limb onto the southern edge of the Pietersburg Block. The importance of this observation was highlighted in McDonald & Holwell (2011) who noted that the crust and underlying sub-continental lithospheric mantle (SCLM) of the northern limb experienced a different geological history to that of the rest of the complex prior to their juxtaposition. This inherited different geochemical signature of the SCLM and crustal rocks either side of the TML could explain the observed discrepancies between the geochemistry of the northern limb (e.g. Pt:Pd ≈1) compared to that of the eastern and western limbs (e.g. Pt:Pd ≈2) as the degree of interconnectivity of the magma plumbing system feeding these limbs is poorly understood (McDonald & Holwell, 2011).

3.1.2 Geophysical Constraints on the BIC

The mirror image appearance of the surface outcrop of the eastern and western limbs of the BIC, as shown in Figure 3.1, and their centripetal dips have led many to suggest that they are connected at depth e.g. Hall (1932), Kruger (2005) and Cawthorn & Webb (2001). These observations are supported by remarkable similarities in the lithologies present including the appearance of distinctive thin marker horizons (e.g. cm-scale chromite stringers) and the location and characteristics of narrow mineralised horizons. Their contiguous nature was first suggested by Hall (1932) who described the intrusion as a lopolith. Similarly, Kruger (2005) described it as "*lobate, interconnected, wide and shallow, sill-like intrusion with upturned margins*". Other examples of lopolith intrusions include Skaergaard in Eastern Greenland and Sudbury in Canada, both of which host PGE deposits.

Gravity modelling has been used in order to constrain the 3D geometry of the Bushveld intrusion and to address questions of the degree of interconnectivity between the limbs. The regional Bouguer gravity anomaly data from the Bushveld Complex as presented in Cole et al., (2014) is reproduced in Figure 3.4A. In Figure 3.4A, the data shows that the limbs (as exposed on the surface) of the Bushveld Complex form positive gravity anomalies (see Figure 3.4B), while the intervening areas are equivalent to the background values outside the complex (Cole et al., 2014). This gravity response has been interpreted two ways: (1) the 'dipping sheet model' - where the limbs represent two separate entities that terminate at depth (Meyer & de Beer, 1987) and (2) a 'continuous Bushveld model' – where the limbs are connected at depth (see Figure 3.4C). The second model represents the more recent interpretation with more sophisticated gravitational modelling inferring the negative signal to result from crustal flexure and a depressed moho in response to crustal loading as shown in Figure 3.4C

(Cawthorn & Webb, 2001; Webb et al., 2011). The discovery of xenoliths characteristic of outcropping Critical Zone rocks in the Cretaceous Palmiegat kimberlite pipe (for location see Figure 3.4A and 3.4C below) located in the centre of the complex further supports the continuous Bushveld model (Webb et al., 2011).

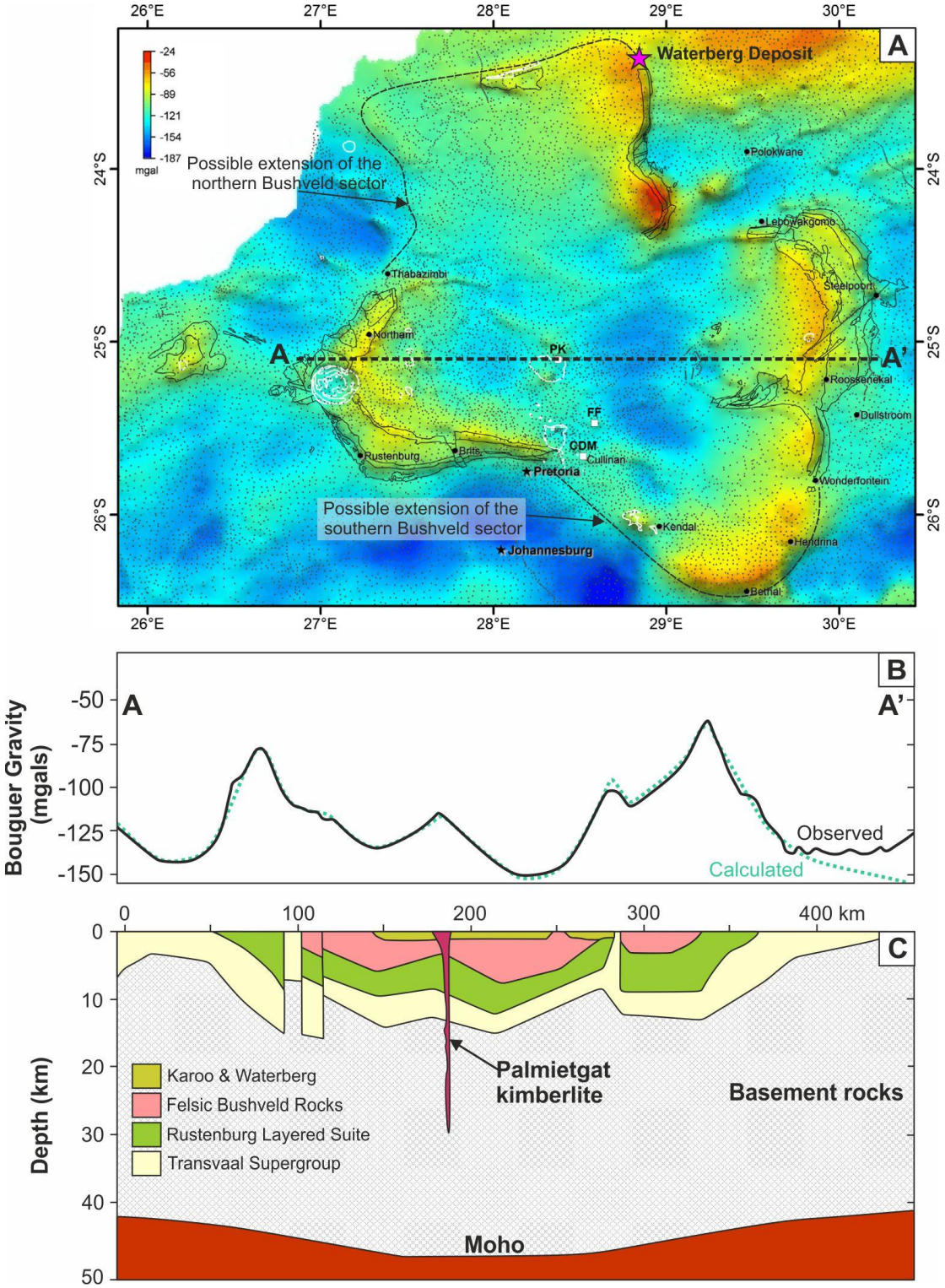

Figure 3.4: Geophysical interpretation of the structure of the Bushveld Complex. (A) A regional bouguer anomaly gravity map of the Bushveld Complex and surrounding areas taken from Cole et al., (2014). Note: black outlines highlight the mapped areas of the RLS and a pink star shows

the location of the Waterberg Ni-Cu-PGE deposit. Abbreviations: PK – Palmietgat kimberlite; FF – Fairfield borehole; CDM – Cullinan diamond mine. (B) An E-W striking bouguer anomaly cross-section across the Bushveld Complex. Note: data collected by the Council for Geoscience, South Africa and the calculated model by Webb et al., (2011). (C) A proposed interpretation of the observed bouguer anomaly by Webb et al., (2011).

The Bouguer gravity anomaly data shows positive anomalies outside of areas that have been traditionally mapped as Bushveld rocks. The recent discovery of the Waterberg Ni-Cu-PGE deposit, an approximate location highlighted in Figure 3.4A, north of the current known extent of the Bushveld rock on the northern limb (located on the Hout River Shear Zone) highlights how the extent of the RLS underneath younger cover is poorly understood. The interpretation of geophysical data may be significant for identifying previously unknown extensions of the complex, some of which may host PGE resources particularly in the Waterberg district and on the southern limb.

3.1.3 Dating the Bushveld Complex

Geochronological data has been used to constrain the sequence of emplacement and crystallisation history of the igneous rocks of the Bushveld Igneous Complex (BIC) in addition to providing provisional evidence for the co-evolution of the geographically separate limbs (Yudovskaya et al., 2013; Huthmann et al., 2016). A summary of the available published dates on BIC rocks using high precision U-Pb dating techniques are provided in Table 3.1 below.

An early felsic magmatic phase is recorded with the oldest dates on BIC rocks obtained for the subvolcanic intrusion of the Rashoop granophyre 2062 Ma (Harmer & Armstrong, 2000) followed by extrusive felsic volcanism that formed the Rooiberg group, 2061 and 2057 Ma (see Table 3.1; Walraven, 1997; Barnes & Maier, 2002). These dates immediately precede the intrusion of the Rustenburg Layered Suite (RLS) supporting suggestions that the Rooiberg volcanics formed the roof of the RLS magma chamber (Kruger, 2005).

A lower age limit of 2059 Ma for the emplacement of the RLS (on the eastern limb) was obtained in a study by Buick et al., (2001) who dated titanite from within a calc-silicate xenolith preserving the crystallisation age as opposed to cooling age. Combining this date with an upper age limit set as the date for the Rooiberg Group roof rocks (Walraven 1997) produces a well-constrained timeframe for emplacement and crystallisation of the RLS between 2055-2061 Ma (Walrave, 1997; Zeh et al., 2015). This short-lived emplacement history combined with the cumulative volume of magma as estimated by Cawthorn & Walraven (1998) are comparable to LIPs found worldwide, such as the Deccan traps (Wilson & Zeh, 2015).

The Merensky Reef mineralisation event has been dated in three relatively recent studies: (1) 2054.4 Ma by Scoates & Friedmann (2008); (2) 2055.09 Ma by Zeh et al (2015) and; (3) 2055.54 Ma by Mungall et al., (2016). These dates are within the error of each other (see Table 3.1). The Platreef mineralisation on the northern limb has been dated at 2056 Ma (Yudovskaya et al., 2013a); this date has a larger error associated with it (± 4.4 Ma) compared to the Merensky Reef data. It can therefore only be said that the Platreef mineralisation formed within a similar timeframe as that of the Merensky Reef; higher precision data is required to conclusively test whether they are contemporary. In the far north on the northern limb beneath a cover of younger Waterberg sediments (dated at 2045 Ma, Huthmann et al., 2016) the Main Zone hosted Waterberg sequence records an intrusion ages of between 2053 Ma and 2059 Ma and are within error of the published dates for the wider Bushveld rocks (Huthmann et al., 2016). The current northern limb dataset does support suggestions that the mafic rocks on the northern limb are coeval with those on the eastern and western limbs; however, the larger analytical errors on this data require the collection of more precise dates (i.e. within 100,000 years) to definitively verify this.

Table 3.1: A summary of the published dates for rocks of Bushveld Igneous Complex using high precision U-Pb methods. References are provided in the table.

Stratigraphic Unit	Age (Ma)	Method/Mineral	Reference
RLS – Critical Zone	2054.4 ± 2.8	U-Pb/zircon	Harmer & Armstrong (2000)
RLS (E. limb) – Calc-silicate	2058 ± 0.8	U-Pb/titanite	Buick et al ., (2001)
RLS – Merensky Reef	2054.4 ± 1.3	U-Pb/zircon	Scoates & Friedman (2008)
RLS – Platreef chromitite	2056.2 ± 4.4	U-Pb/zircon	Yudovskaya et al., (2013a)
RLS – Marginal Zone	2055.91 ± 0.25	U-Pb/zircon	Zeh et al., (2015)
RLS – UG2	2055.32 ± 0.30	U-Pb/zircon	Zeh et al., (2015)
RLS – Merensky Reef	2055.09 ± 0.36 and 2054.89	U-Pb/zircon	Zeh et al., (2015)
RLS – Lower Main Zone	2055.86 ± 0.15	U-Pb/zircon	Mungall et al., (2016)
RLS – Merensky Reef	2055.54 ± 0.27	U-Pb/zircon	Mungall et al., (2016)
RLS – UG1	2056.28 ± 0.15	U-Pb/zircon	Mungall et al., (2016)
RLS – MG4A/2A	2056.04 ± 0.15/ 2055.68 ± 0.20	U-Pb/zircon	Mungall et al., (2016)
Rashoop Granophyre	2061.8 ± 5.5	U-Pb/zircon	Harmer & Armstrong (2000)
Rooiberg Volcanics	2057.3 ± 3.8	U-Pb/zircon	Walraven (1997)
Rooiberg Volcanics	2060 ± 2.0	U-Pb/zircon	Walraven (1997)
Lebowa Granite Suite	2054 ± 2.0	U-Pb/zircon	Walraven & Hattingh (1993)
Northern limb - Waterberg Ni-Cu (PGE) deposit	2059 ± 3 and 2053 ± 5	U-Pb/zircon	Huthmann et al., (2016)

3.2 The Rustenburg Layered Suite

The Rustenburg Layered Suite (RLS) is the World's largest known layered intrusion covering an area of 65,000 km^2 with a thickness of 7 to 8 km (Eales & Cawthorn, 1996). It hosts 95% of the estimated global PGE reserves (USGS, 2016), in addition to significant Cr and V ore deposits (Viljoen, 2016).

The establishment of a regional stratigraphic framework for the RLS has greatly facilitated both the mining and scientific communities by enabling the prediction of the height within the intrusion of mineralised horizons and to rationally conceptualise a km-thick package of rocks. However, it has also fenced in our ideas and augmented assumptions that these stratigraphic units are identical along strike; whereas in reality significant local and regional variations exist. The following descriptions of the RLS stratigraphy are from the eastern and western limbs; the northern limb is discussed separately in section 3.3.

3.2.1 RLS Stratigraphy

A regional-scale stratigraphic framework for the RLS was originally devised by Hall (1932, see Figure 3.5A) who subdivided the intrusive package into five zones based on either the presence of a new cumulus mineral and/or the position of specific stratigraphic markers. The five zones (from base to top) are as follows: (1) the Marginal Zone composed of norites; (2) the Lower Zone, predominantly pyroxenites and harzburgites; (3) the Critical Zone characterised by cyclic units of chromite-pyroxenite-norite-anorthosite; (4) the Main Zone a homogenous sequence of gabbronorites and (5) the Upper Zone comprising anorthosites, ferrogabbros and magnetites. The thicknesses of these units, the location of key marker horizons (e.g. chromitite layers) and mineralised intervals are shown in Figure 3.5A. An example of the internal complexity of these zones is shown in Figure 3.5C where layering is present on the metre scale; this also represents an oversimplification with centimetre-scale layering common.

Radiogenic isotopic data, acquired >60 years later by Kruger (1994), provided quantitative support for these broad zonal subdivisons (see Figure 3.6B). The results of the study by Kruger (1994) indicate that the Lower Zone, Critical Zone and lower Main Zone formed during an early open-system 'integration stage' with repeated injections of fresh mafic magma. Whereas, the upper Main Zone and Upper Zone formed in a closed system 'differentiation stage' via fractional crystallisation, which produced a corresponding normal Fe-enrichment trend leading to economically exploitable magnetite mineralisation.

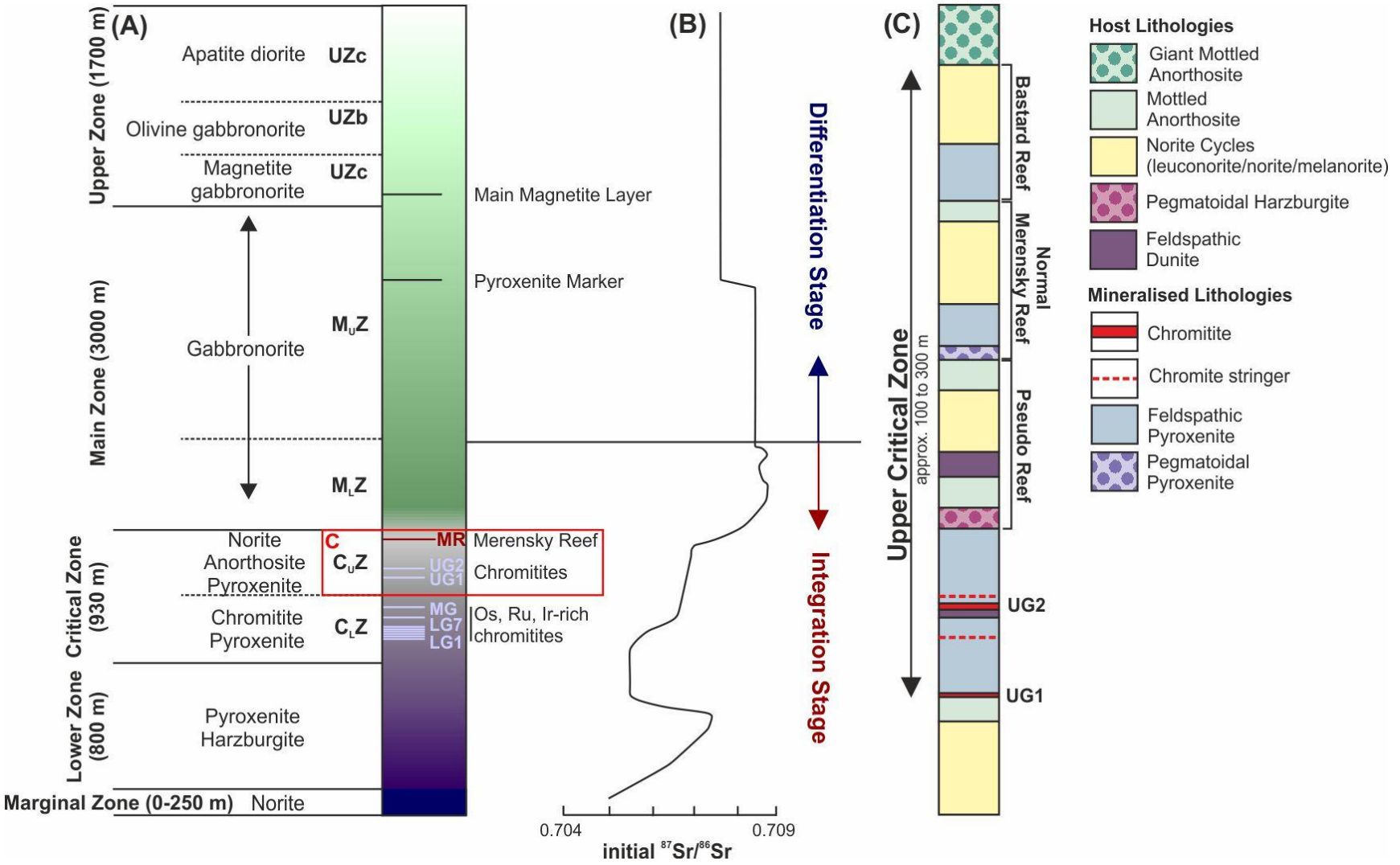

Figure 3.5: An overview of the Rustenburg Layered Suite (RLS) as exposed on the eastern and western limbs. (A) The RLS stratigraphic column modified after Eales & Cawthorn (1996); (B) Initial Sr isotope profile modified after Kruger (1994) and; (C) A detailed stratigraphic column of the Upper Critical Zone showing the stratigraphic interval from the Merensky Reef (normal-facies) to the UG2 chromitite as identified in the Northam Platinum mine (modified after Smith et al., 2013).

The stratigraphic units (or 'Zones') that constitute the RLS are not homogenously developed across the known-extent of the intrusion, rather they demonstrate lithological, mineralogical and thickness variations in both the vertical and horizontal directions. A full succession is present only in the northern sectors of the eastern (e.g. Steelpoort) and western limbs. Detailed studies on the stratigraphy and the geochemical, mineralogical and isotopic variations between these zones can be found in Eales & Cawthorn (1996), Barnes & Maier (2002) and Kruger (2005). A brief overview of the 'Zones' is provided below; the PGE mineralised Critical Zone is handled separately in section 3.2.2.

The Marginal Zone represents the base of the RLS and is found in contact zones with the floor rocks as sill-like intrusions into the immediate footwall country rocks (Sharpe, 1981; Harmer & Sharpe, 1985; Sharpe & Hulbert, 1985). The observed thickness of the Marginal Zone is highly variable from 0 to 800 m, it is extensively developed south and westward throughout the Complex (Eales & Cawthorn, 1996). The norites and feldspathic orthopyroxenites are typically finer grained than the overlying layered rocks and contain abundant country rock xenoliths which have been identified as belonging to the Transvaal Supergroup.

The Lower Zone rocks are present as apparently discontinuous trough-like bodies whose morphology and distribution is controlled by the floor rock topography (Cameron, 1978). The lithologies are dominated by orthopyroxene- and olivine-rich cumulates. The greatest thicknesses of Lower Zone appear in proximity to the Thabazimbi-Murchison Lineament (TML) including: 1,050 m on Nietverdiend in the far western limb and 1,300 m on Nooitgedacht in the Union section of the western limb (Teigler, 1990; Eales & Cawthorn, 1996). This is accompanied by an apparent thinning of the sequence southward and its absence east of the Rustenburg sections and south of the Steelpoort Fault. Geochemical studies on marginal rocks of the Lower Zone (and Lower Critical Zone) by Sharpe (1981) and Harmer & Sharpe (1985) have concluded that two compositionally different magmas were responsible for the genesis of the RLS: (1) high-Mg basaltic andesite (U-type of Naldrett, 2004) and (2) tholeiitic basalt (T type of Naldrett, 2004). The tholeiitic Mg-rich basaltic andesites, known as the B1 magma (for Bushveld 1, Harmer & Sharpe, 1985), represent the parental magma composition responsible for the Lower Zone and Lower Critical Zone (Barnes et al., 2010). The tholeiitic basalts are responsible for both the Upper Critical Zone (B2 magma) and the Main Zone (B3 magma); the B3 magma has a higher Mg# (62) compared to Mg# (55) of the B2 magma (Harmer & Sharpe, 1985; Barnes et al., 2010).

The Main Zone is up to 3 km thick (see Figure 3.5A) and is found across the Bushveld Complex including on the northern limb (van der Merwe, 1976; Ashwal et al., 2005). Lithologically the Main Zone is relatively homogenous dominated by gabbronorites with minor anorthosite and pyroxenite (Ashwal et al., 2005); layering is poorly developed when compared to the underlying cumulates. Kruger (2005) recommended that the Main Zone is further subdivided into a layered and heterogenous Lower Main Zone (M_LZ) and a differentiated Upper Main Zone (M_UZ) (shown in Figure 3.5A). This additional subdivision marks the change of magmatic regime from open to closed system behaviour as evidenced in a shift in the initial Sr isotope ratio followed by a steady-state value (see Figure 3.5B; Kruger 1994). The location of the boundary between the Main Zone and the overlying Upper Zone has been positioned by Kruger (1990) at the level of the 'pyroxenite marker', 2.5 km above the base of the Main Zone; corresponding to the aforementioned shift in initial Sr isotope ratio also noted by Sharpe (1985, see Figure 3.5B). In contrast, Molyneux (1974), Wagner & Brown (1968) and the South African Committee of Stratigraphy (1980) use the first appearance of magnetite, 660 m above the 'pyroxenite marker', as the position of the base of the UZ (Klemm et al., 1985; Eales & Cawthorn, 1996; Maier & Barnes, 1999) and this definition is applied in Figure 3.5A.

The Upper Zone forms the top 2.8 km of the intrusion; it is composed of noritic rocks at the base followed by gabboric rocks including gabbro, anorthosite and magnetite gabbro (von Gruenwaldt, 1973; Molyneux, 1974). Isotopic data indicates that the UZ represents a single influx of a new magma that mixed completely with the resident magma then differentiated *in situ*; hence the most differentiated rocks are present towards the top (Kruger, 2005). The Main Magnetite layer, shown in Figure 3.5A, located near the base of the Upper Zone is 2 m thick and is mined for its vanadium content (Harney & von Gruenewaldt, 1995).

3.2.2 The Critical Zone

The Critical Zone is further separated into the Upper Critical Zone and Lower Critical Zones (UCZ and LCZ, respectively) based on the first appearance of cumulus plagioclase. The UCZ and LCZ are characterised by well-developed modal layering consisting of chromite-pyroxenite-norites-anorthosite magmatic cycles; in general, eight cycles are recorded in UCZ and nine in the LCZ (Eales & Cawthorn, 1996). The UCZ hosts the stratiform PGE mineralisation of both the Merensky Reef and UG2 chromitite and as such represents the most economically significant division of the RLS (see Figure 3.5A). These PGE mineralised layers are found between the UG1 chromitite and the base of the Main Zone in a 100 to 300 m thick stratigraphic interval (see Figure 3.5A and

3.5C; Barnes & Maier, 2002). On the western limb, the stratigraphic interval between the UG2 chromitite and the Merensky Reef is characterised by depleted Cu/Pd ratios (< 100 to 400) compared to normal Critical Zone values of 4000 as identified in Naldrett et al., (2009). Historically, these reefs have been described as being present at consistent stratigraphic levels and continuous over 100's km strike length (Cawthorn et al., 2002). In reality, the Merensky Reef (and to a lesser extent the UG2 chromitite) vary in stratigraphic position and may have transgressive basal contacts accompanied by the development of 'thick' and 'thin' reef facies as outlined in Viljoen (2016) and briefly described below in sections 3.2.2.1 and 3.2.2.2 below.

3.2.2.1 Merensky Reef

The Merensky Cyclic Unit (MCU) is a 9 to 42 m thick sequence beginning with a 10 to 30 cm thick basal pyroxenite, hosting the Merensky Reef. The MCU is sandwiched, above and below, by the Bastard reef and the Pseudo reef respectively (see Figure 3.5C; Kruger, 2010; Viljoen & Schürmann, 1998; Viljoen, 1999). The Bastard Cyclic unit, bears a resemblance to the MCU, but the Bastard Reef at the base contains fewer sulphides with lower PGE tenors (Naldrett et al., 2009). The Merensky Reef typically comprises a 0.1 to 1.2 m thick, sulphide-bearing, pegmatoidal feldspathic orthopyroxenite, bounded by thin (1 to 10 cm) chromite stringers and carrying grades of 5 to 8 g/t (3PGE + Au; Cawthorn et al., 2002). An example of the basal chromitite of the Merensky Reef ('Normal' reef facies) is shown in Figure 3.6. Olivine-bearing lithologies associated with the mineralised interval are frequently observed in the northwestern sector (Viljoen & Schurmann, 1998) of the Bushveld Complex occurring intermittently in the south west (Naldrett et al., 2009). The footwall lithology varies depending on the reefs exact position but typically either the host pyroxenite or an anorthosite defining the top of the underlying cyclic sequence (the latter shown in the example in Figure 3.6).

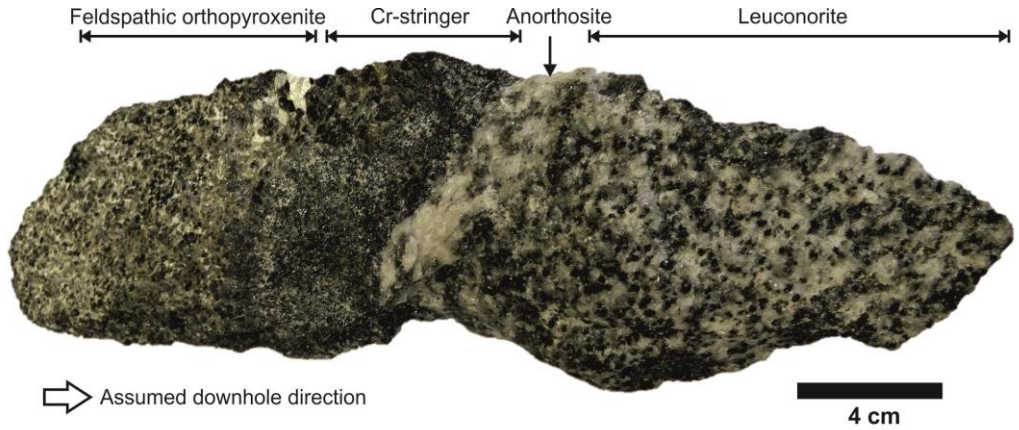

Figure: 3.6: An example of the 'normal' Merensky reef facies. Photograph of a sample of the Merensky Reef from the Frank Shaft, Rustenburg Platinum Mine collected by Iain McDonald for the Cardiff University teaching collection.

A summary of the various petrogenetic models proposed for the formation of the Merensky Reef are presented in Figure 2.9 (Chapter 2, section 2.4.1.1) and descriptions of the petrology of the Merensky Reef can be found in Ballhaus & Sylvester (2000), Barnes & Maier (2002), Seabrook et al., (2004), Li & Ripley, (2005), Wilson & Chunnett (2006) and Naldrett et al., (2009). In these studies the close association between the presence of interstitial sulphides (typically between 3 to 10 vol%; Lee, 1996 and Viljoen, 2016) and PGE enrichment have dominated ideas about the genesis of the Merensky Reef (von Gruenewaldt, 1979; Campbell et al., 1983; Naldrett et al., 1986). PGE-bearing sulphides may be present in the footwall rocks as much as 1 m below the lower chromite layer (Barnes & Maier, 2002), throughout the interval between the two chromite layers and up to several 10s of cm's above the upper chromite. The sulphide assemblage comprises pyrrhotite, pentlandite, chalcopyrite, pyrite and cubanite with lesser galena and sphalerite (Kinloch & Peyerl, 1990; Lee, 1996).

The Merensky Reef demonstrates both regional (interlimb) and local (intralimb) variations in the geological characteristics including: (1) stratigraphic position (2) host lithologies; (3) the footwall lithologies; (4) the number of chromite stringers between one and four and; (5) the degree of sulphide mineralisation. A schematic depiction of this variability is shown in Figure 3.7. Abnormalities in the structure and stratigraphic position of the Merensky Reef between different sectors of the Bushveld Complex have led to the distinction of two principal regional facies: (A) normal and (B) pothole (also known as contact) reef (see Figure 3.7).

The normal reef occupies the highest stratigraphic position and conformably rests on the footwall (Barnes & Maier, 2008); a typical example is shown in Figure 3.6. The 'thin' reef facies typically have a 3 to 10 cm separation between the upper and lower chromite stringers whereas the 'thick' reef facies have a 30 to 60 cm equivalent separation. Variation from one type to another occur over lateral distances of < 500 m and tend to show a relationship to structures such as faults and horst and graben structures that either pre-date or are contemporaneous with emplacement. The platinum-group mineral (PGM) assemblage associated with the normal reef facies is dominated by Pt-Pd sulphides (braggerite and cooperite; Kinloch, 1982).

The pothole reef has a transgressive contact with the footwall and consequently is found at a lower stratigraphic level than the normal reef by up to 30 m (Barnes & Maier, 2002). Pothole reefs characterise much of the northwestern sector described as 'regional pothole'. Where potholing is developed the Merensky Reef is much closer to the UG2 chromitite. The reef may be considerably thicker ranging from 0.5 to 7.0 m. The PGM

assemblage of the regional pothole is dominated by Pt-Fe alloys (92 %, Kinloch, 1982) and abnormally high PGE in solid solution in base-metal sulphdies (Viljoen, 2016).

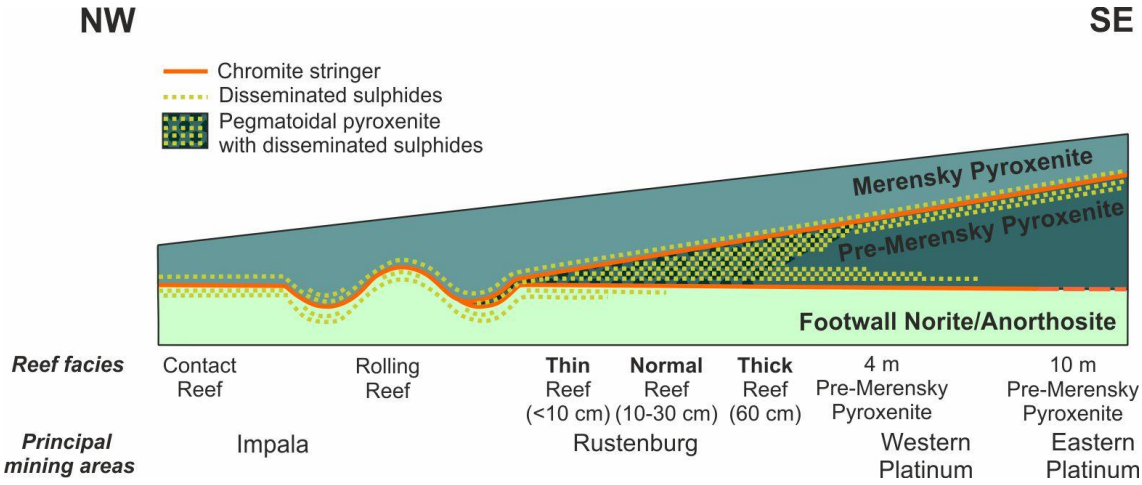

Figure 3.7: A SE-NW directed schematic representation of the variability in the thickness of the Pre-Merensky and Merensky pyroxenites from the southwestern sector of the Bushveld Complex. Thick reef facies dominate to the east and next to the Pilanesburg intrusive body in the extreme NW. Elsewhere, the reef types vary locally depending on structurally controlled irregularities in the Merensky footwall. Modified after Naldrett et al., (2009).

3.2.2.2 UG2 Chromitite

The UG2 chromitite is one of many monomineralic chromitite layers within the Critical Zone; the majority of chromitites are subeconomic because they are too thin. The UG2 chromitite is the exception with a thickness ranging from 0.6 to 2.5 m and carrying grades of between 7 to 9 g/t (4E) making it the only chromitite layer in the world to be mined primarily for PGEs (Lee, 1996; von Gruenewaldt *et al.,* 1986; Scoon & Teigler, 1994; Cawthorn, 2005; Osbahr et al., 2014). The petrology and stratigraphy of the UG2 unit is briefly summarised here; the chromitite is typically composed of 60 to 90 % chromite grains with 10 to 35 % oikocrysts of orthopyroxene and interstitial plagioclase (Barnes & Maier, 2002; Cawthorn, 2005; Viljoen, 2016). The hanging wall typically consists of a feldspathic orthopyroxenite (± olivine) with between two and four lead chromite-stringers. The footwall lithologies vary depending on location and may include a pegmatoidal feldspathic orthopyroxenite (± olivine), orthopyroxenite, anorthosite, leuconorite and norite (Hiemstra, 1985; Scoon & Mitchell, 2009).

Base-metal sulphides are present in low concentrations; the sulphide assemblage is dominated by pentlandite (cobalt-bearing) and chalcopyrite with lesser pyrrhotite, pyrite, arsenopyrite, bornite, chalcocite, covellite, galena and millerite (Vermaak, 1985). The platinum-group mineral (PGM) assemblage is composed of Pt-Pd sulphides (35 %),

laurite (30 %) with other PGMs including Pt-Fe alloys (21 %), Rh sulphides (11 %) and Pd alloys (3 %) (Kinloch, 1982; Viljoen, 2016).

3.3 The Northern Limb

The northern limb is separated from the eastern and western limbs by the Thabazimbi-Murchison Lineament (TML) a deep-seated and E-W orientated structural lineament (as discussed in section 3.2 above). A regional geological map of the > 100 km long northern limb highlighting the location of key farms is shown in Figure 3.8. Different locations along the northern limb are conventionally discussed by reference to the farm on which they occur. The northern limb has a sinous outcrop; south of the Ysterberg-Planknek fault the outcrop is NE trending with westwards dips of between 15° to 27° and to the north of this structural feature the outcrop is trending to the NW and dips are between 40° to 45° west at surface (see Figure 3.8). The limb is truncated to the south against Phanerozoic sediments of the Karoo Group by the Zebiedela fault.

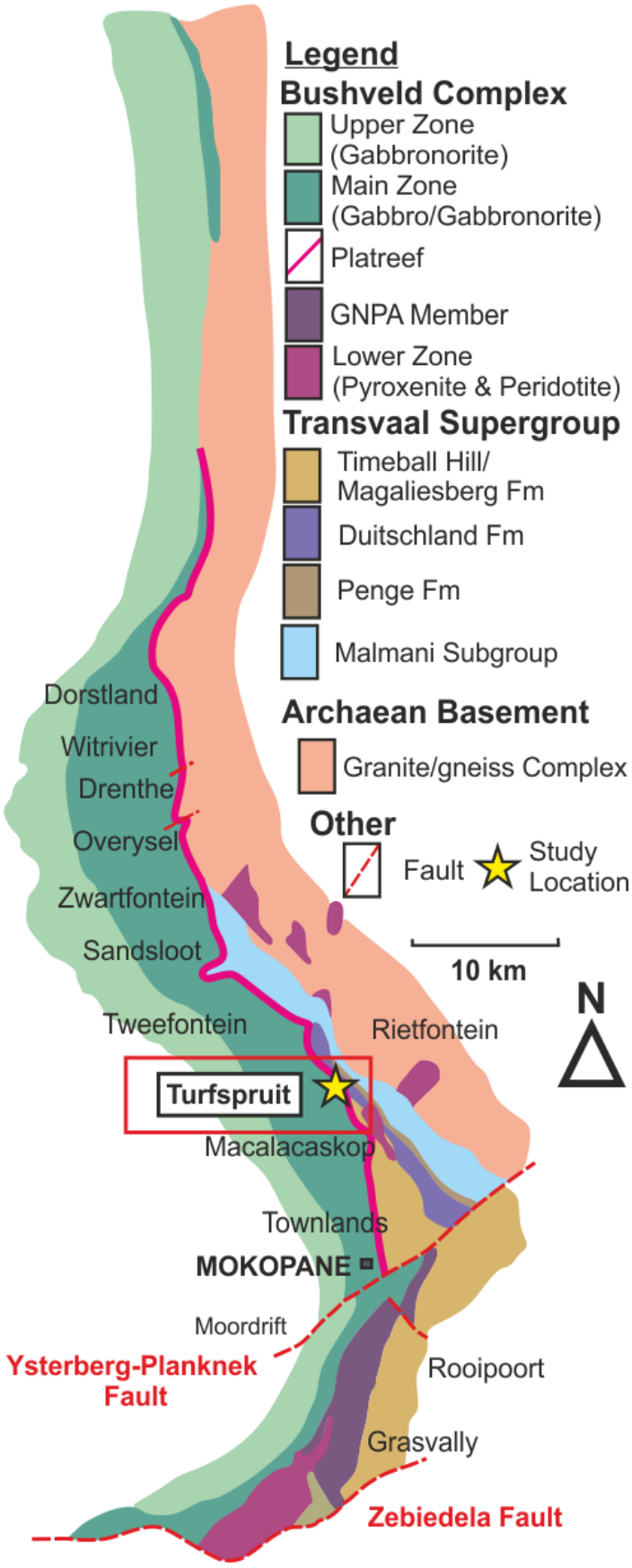

Figure 3.8: Regional geological map of the northern limb of the Bushveld Complex. Note: names refer to farm location as referred to in the text. Modified after Ashwal et al., (2005).

The Rustenburg Layered Suite (RLS) on the northern limb shows significant differences to the stratigraphy of the eastern and western limbs (see Figure 3.5) from the base of Main Zone downwards. The geology of the RLS on the northern limb is subdivided into two geographic areas north and south of the Ysterberg-Planknek Fault where the Platreef and Grasvally Norite-Pyroxenite-Anorthosite (GNPA) member are developed, respectively (see Figure 3.8). The stratigraphic position of PGE mineralisation on the northern limb in proximity to the base of the Main Zone has led to the proposal that both the GNPA member and Platreef represent the northern limb equivalents of the Upper Critical Zone as identified on the eastern and western limbs (e.g. White, 1994; Kinnaird, 2005; Maier et al., 2008; Yudovskaya et al., 2017b; Grobler et al., 2018). The distinct petrological characteristics of the northern limb have been ascribed to the transgressive nature of the basal unconformity resulting in crustal contamination of the magma.

3.3.1 Northern Limb Stratigraphy

In the southernmost part of the northern limb, immediately north of the Zebediela fault, a thick (up to 1600 m) series of ultramafic cumulates of Lower Zone affinity rocks are found across the properties Grasvally, Zoetfeld and Volspruit (Hulbert & von Gruenewaldt, 1982; see Figure 3.8). They outcrop over 5 km within the Grasvally Body and as series of isolated satellite bodies in the country rocks north of the Ysterberg-Planknek fault examples of which include the Uitloop and Zwartfontein intrusions (van der Merwe 1976; Yudovskaya et al., 2012). They host four major chromitite seams, which are mined for their chrome-content on the farm Grasvally. The Cr/Fe ratios in chromite grains from this location, typically >2, are the most primitive thus far found in the Bushveld Complex (Naldrett et al., 2008). In addition, the pyroxenes and olivines demonstrate the highest Mg/(Mg + Fe) ratios (up to 0.91) of any minerals in the Bushveld (McDonald *et al.,* 2009). It also hosts a Ni-PGE mineralised horizon, termed the Volspruit zone, in the Lower Pyroxenite (Hulbert and von Gruenewaldt, 1982; Tanner et al., 2018).

Stratigraphically above these ultramafic rocks is a PGE mineralised layered package of mafic cumulates known as the Grasvally Norite-Pyroxenite-Anorthosite (GNPA) member (Hulbert, 1983). The GNPA member represents a 400 to 800 m thick sequence of gabbronorites, norites, anorthosites, pyroxenites and PGE-rich chromitite that can be subdivided into three distinct stratigraphic units (de Klerk, 2005): the Lower Mafic Unit (LMU), the Lower Gabbronorite Unit (LGN) and the Mottled Anorthosite Unit (MANO). The 50 to 200 m thick LMU and the stratigraphically higher 200 to 400 m thick MANO contain PGE mineralised layers, the most important of which are the L3 chromitite in the LMU which displays lateral continuity and the M2 zone of the MANO (Maier et al., 2008).

The GNPA member stratigraphy cannot be traced northwards across the Ysterberg-Planknek fault (van der Merwe, 2008); north of Mokopane a mafic igneous stratigraphy continues but the mineralisation takes the form of the Platreef. A proposed model for the laterally continuous relationship between the Platreef and GNPA member by Smith (2014) is shown in Figure 3.9.

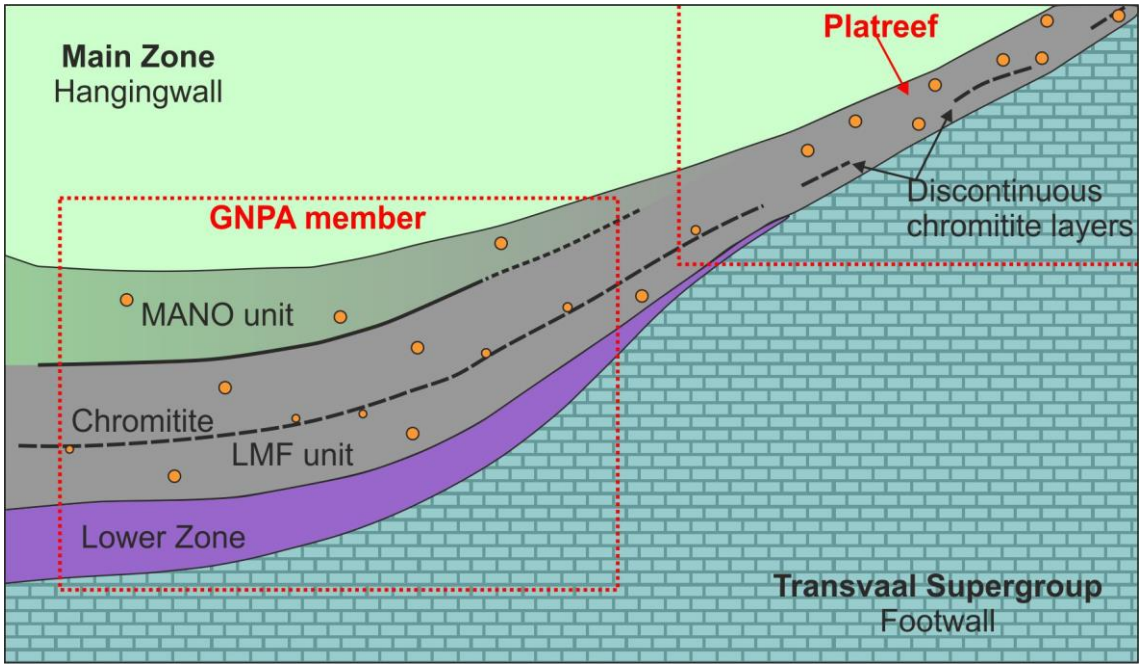

Figure 3.9: A schematic representation of the proposed relationship between the Platreef and GNPA member. Modified after Smith (2014). For abbreviations see text above.

The hanging wall of both the GNPA member and the Platreef is composed of Main Zone gabbronorites, up to 2 km thick (Hulbert, 1983; van der Merwe, 1978). The Main and Upper Zones of the northern limb have been studied by van der Merwe (1978) and more recently in Ashwal et al., (2005) and Roelofse & Ashwal (2012). Studies on the northern limb Main Zone record a few important discrepancies from the eastern and western limbs including: (1) the presence of a 200 m thick troctolitic horizon approximately halfway through the Main Zone (Bianca Kennedy *pers. commun*); (2) an absence of marker horizons (e.g. the pyroxenite marker) (Ashwal et al., 2005) and (3) a magmatic unconformity at the base of the Main Zone (Holwell et al., 2005; Holwell & Jordaan, 2006).

The contact between the top of the Platreef and the base of the Main Zone can be observed in open-pit exposures in the Mogalakwena mine. The contact is often defined by a distinctive mottled anorthosite recorded at Sandsloot by Holwell et al., (2005) and Weise et al., (2008) and by Kinnaird (2005) on Turfspruit. This marker horizon varies in thickness from 0.5 m to several meters and has been interpreted as a chilled horizon by Holwell et al., (2005) and Weise et al., (2008). Armitage et al., (2002) recorded an abrupt

change in the pyroxene composition between the Platreef (bronzite) and hanging wall (inverted pigeonite), leading them to suggest that the hanging wall formed from a separate magma. Naldrett (2005) identified intrusions of Main Zone gabbronorites that penetrated into the Platreef at Drenthe, this relationship was also noted by Holwell & Jordaan (2006) on Zwartfontein. All these observations support the interpretation that the Main Zone magma intruded after a significant hiatus from the emplacement of the Platreef pyroxenite (Holwell et al., 2005).

3.3.2 The Platreef

The definition of the Platreef, used in this study follows that proposed by Kinnaird & McDonald (2005): "*Mafic units enriched in Ni-Cu-PGE that occurs between the Archean granite-gneiss basement or the Transvaal Supergroup and the gabbros and gabbronorites of the Main Zone, north of the Planknek fault*". The Platreef varies in thickness along strike from 400 m thick in the south to < 50 m thick in the north (Kinnaird, 2004) with local thickening and thinning present over folds in the floor rocks (Kinnaird, 2008; Armitage, 2011). The Platreef has a 30 km strike length; north of Dorstland the Platreef is cut out by the transgressive nature of the Upper Zone which eliminates the Main Zone and rests against the granite-gneiss floor rocks (Armitage et al., 2002). The following descriptions on the Platreef principally relate to the shallow Platreef where the majority of the current literature is focused; an overview of the deep extensions as identified on Turfspruit are provided in Chapter 1.

The main lithologies identified in the Platreef are: pyroxenites, gabbronorites, norites, peridotites (of igneous and metamorphic origin), serpentinites and a variety of hybrid lithologies (e.g. parapyroxenites, McDonald & Holwell, 2011). The development of hybrid lithologies (of non-igneous origin) resulting from material transfer via partial melting, metasomatic and/or hydrothermal processes between the intrusion and either the footwall and/or xenoliths/autoliths are widely developed where the footwall rocks are composed of the Transvaal Supergroup sediments. There is a notable absence of significant chromitite layers although discontinuous chromite-stringers are present locally. The development of significant laterally continuous chromitite layers have been identified moving westwards from the surface exposure and with increasing depth (> 700m below surface) as noted on Akanani (Yudovskaya & Kinnaird, 2010) down-dip of Zwartfontein and in the Flatreef and deep Platreef on Turfspruit (Nodder, 2015; Grobler et al., 2018).

The basal contact of the Platreef is transgressive, as shown in Figure 3.8, moving northwards the intrusion rests against progressively older rocks belonging to the

Chuniespoort Group of the Transvaal Supergroup until, on the farm Overysel, it intersects Archean granite and gneisses. There is a broad range of chemical compositions in the rocks of the Chuniespoort group, including banded iron formations, shales, dolomites and limestones; for details see Figure 3.2. Consequently, the contamination signature along the strike length of the Platreef varies significantly depending on the mineralogy and volatile content of the country rocks. The Platreef is observed to contain numerous large rafts, up to 1,500m long and 100m thick, of the country rocks showing variable degrees of dissolution and assimilation (Gain & Mostert, 1982; Cawthorn et al. 1985 and Kinnaird et al., 2005). The composition of these country rock xenoliths broadly correlates to that of the directly underlying footwall suggesting that the contamination took place in situ. Geochemical and isotopic heterogeneity within the igneous rocks also supports shallow level contamination (Cawthorn et al., 1985).

Exploration and mining of the Platreef since the 1920's has focused on the central sector comprising the farms Tweefontein, Sandsloot, Vaalkop, Zwartfontein and Overysel (see Figure 3.8); this is also where research has focused (e.g. Buchanan et al., 1981; Buchanan & Rouse, 1984; Armitage et al., 2002; Holwell et al., 2005; Holwell et al., 2006; Holwell & McDonald, 2008; McDonald et al., 2009; Holwell et al., 2011; Yudovskaya & Kinnaird, 2010; van de Merwe, 2012). Mine development of mineralisation has historically been hindered by: (1) an apparent lack of stratigraphic markers e.g. chromite stringers to identify PGE mineralised layers (White, 1994); (2) variation in the host rocks from igneous lithologies to the immediate country rocks; (3) the sporadic and discontinuous occurrence of economic mineralisation with the grade, thickness and geological elevation varying over short distances (Cawthorn, 2010).

The Ni-Cu-PGE mineralisation is developed throughout the igneous pyroxenite units, the xenoliths, into the footwall and sometimes into the base of the Main Zone hangingwall (Holwell et al. 2006). This suggests that the mineralisation formed through the interaction of magmatic, metasomatic and hydrothermal processes (e.g., Harris & Chaumba, 2001; Sharman-Harris et al., 2005; Sharman et al., 2013). The majority of platinum group mineral (PGM) studies on the Platreef are concentrated on the near-surface mineralisation with samples derived from Turfspruit in the southern sector (Hutchinon & Kinnaird, 2008), the Sandsloot and Zwartfontein open pits (Armitage et al., 2002; Holwell et al., 2006; van der Merwe et al., 2008; Junge et al., 2018) in the central Platreef, and on Overysel further north (Holwell & McDonald, 2007). The ore has been observed to be mineralogically heterogeneous with the prevalence of semi-metal PGMs, predominantly Pt and Pd tellurides and bismuthotellurides and sperrylite, that are identified across all sectors (Kinloch, 1982; White, 1994; Armitage et al., 2002; Kinnaird et al., 2005, Holwell

et al., 2006; Holwell & McDonald, 2007; Hutchinson & McDonald, 2008; Yudovskaya et al., 2011; van der Merwe et al., 2012).

3.3.3 Petrogenesis of the Platreef Magma: Evolving Ideas

One of the key problems to address in any petrogenetic model of the Platreef is the imbalance of the very high chalcophile element and sulphide concentrations within the relatively thin series of mafic sills that make up the Platreef. This represents a mass balance paradox i.e. to achieve the measured PGE grades high R factors are needed requiring a very large body of magma to have been present, more than currently represented at the surface (details on the physiochemical processes involved are provided in Chapter 2). Kruger (2005) suggested that this magma reservoir could be the Main Zone, however as mentioned previously field relations discount this hypothesis with the evidence decisively showing that the Platreef was emplaced and solidified before the intrusion of the Main Zone magmas (Holwell et al., 2005; Holwell & Jordaan, 2006).

A role for crustal contamination in ore formation is frequently inferred based on the marginal position of the Platreef mineralisation; it is categorised as a contact-style deposit in numerous review papers on Ni-Cu-PGE deposits e.g. Maier, (2005), Naldrett (2004), Barnes & Ripley (2016). Multiple stable isotope studies on the Platreef have been used to constrain crustal contamination and its effect on the Ni-Cu-PGE mineralisation. Harris & Chaumba (2000) examined the $\delta^{18}O$ values of plagioclase and pyroxene from the Platreef at Sandsloot, finding considerable variation (< +10.3‰ in plagioclase and < +8.9‰ in pyroxene), suggesting local shallow crustal contamination by Transvaal dolomites.

A key geochemical tool used in the literature to establish the relative input of crustal material and trace the evolution of sulphur during ore-forming processes are sulphur isotopes; for details on S isotope systematics see Chapter 2 (section 2.4.2). Local sources of crustal sulphur are available from the Transvaal Supergroup, held in evaporite minerals in carbonate rocks of the Malmani and Duitschland Formation and as pyrite from shales in the Duitschland Formation. Several researchers including Buchanan *et al.,* (1981), Kruger (2005), Harris & Chaumba (2001), Armitage et al., (2002), and Sharman-Harris et al., (2005) have suggested that S saturation of the Platreef magma was triggered by the addition of S from sulphide-bearing lithologies in the Transvaal Supergroup. This deduction is based on the observed correlation between the $\delta^{34}S$ values of contaminated Platreef sulphides and the $\delta^{34}S$ values from partially assimilated country rock xenoliths and the directly underlying footwall as shown in Figure 3.10.

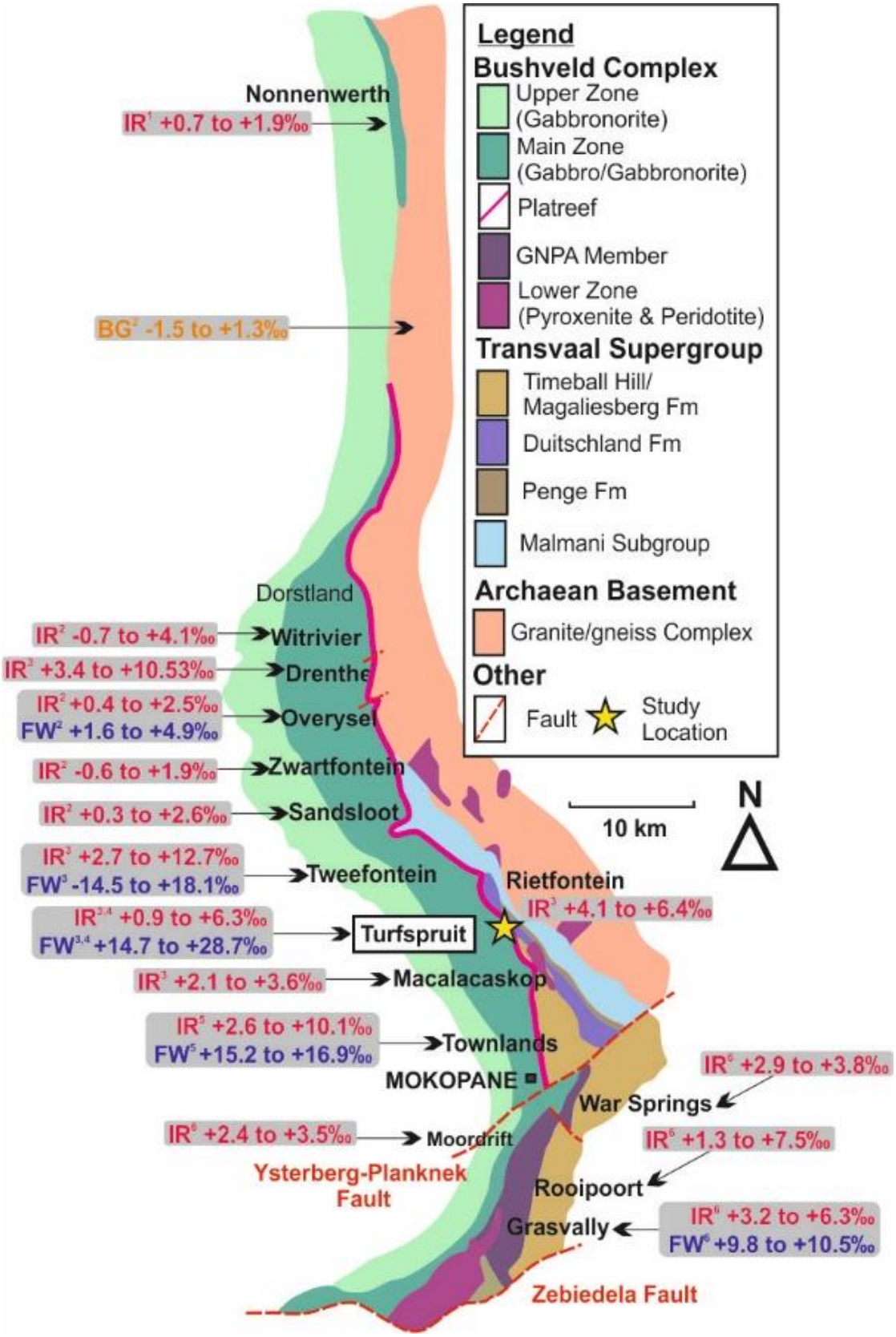

Figure 3.10: A regional geological map of the northern limb, highlighted are the locations of $\delta^{34}S$ isotope studies. Note: IR = igneous rocks, FW = footwall rocks and BG = basement granite. 1: Manyeruke PhD: (2) Holwell *et al.,* 2007: (3) Sharman-Harris *et al.,* 2005: (4) Sharman et al., 2013: (5) Manyeruke et al., 2005: (6) Smith *et al.,* 2016.

A more limited role of in situ crustal contamination in the Platreef ore genesis has been proposed by Holwell et al., (2007), McDonald & Holwell, (2007), Penniston-Dorland et al., (2008), Ihlenfeld & Keays, (2011), Yudovskaya et al., (2017a) whereby country rock S assimilation from the floor rocks and xenoliths adds little to the mineralisation and only locally elevates S contents. Small-scale (< 5 m) localised interaction with surrounding sedimentary rocks is supported in a study using mass independent fractionated (MIF) sulphur isotopes measured in the Platreef by Sharman-Harris et al., (2013) based on the distribution of anomalous and variable $\Delta^{33}S$ values (Penniston-Dorland *et al.,* 2008). In addition, magmatic $\delta^{34}S$ values (0 ± 2‰) have been identified across the strike length of the Platreef (see Figure 3.10) typically associated with an interpreted high temperature primary magmatic sulphide assemblage (pyrrhotite, pentlandite and chalcopyrite) (Holwell et al., 2006; Yudovskaya et al., 2017a).

Two orthomagmatic petrogenetic models for the origin of the Platreef mineralisation are frequently cited in the literature these are: (1) the Platreef represents a marginal extension of the Upper Critical Zone, in situ contamination by country rocks diluted the PGE tenor of the magmatic sulphides (Naldrett *et al.,* 2012, Maier *et al.,* 2008 and Cawthorn *et al.,* 2002); (2) the Platreef was emplaced with pre-formed sulphides containing high PGE tenor formed in a staging chamber (McDonald *et al.,* 2009, and Kinnaird, 2008).

Model 1 implies that the Platreef mineralisation is genetically related to the Merensky Reef of the Upper Critical Zone with the two deposits forming coevally and is supported by Naldrett et a., (2008); Maier et al., (2008), Yudovskaya et al., (2017a) and Grobler et al., (2018). In Naldrett et al., (2008) a conceptual model for this relationship was developed known as the ‘pudding basin’ model as shown in Figure 3.11. The Platreef is proposed to have formed by mixing of Critical Zone and Main Zone type magmas; a new influx of Upper Critical Zone magma results in over-pressurisation in the chamber causing the magma to escape up the margins of the intrusion. This idea is illustrated in nested pudding basins where the lower basin represents the floor of the chamber and the nested basin represents the roof (see Figure 3.11). Naldrett et al., (2008) go on to suggest that the Rustenburg Layered Suite (RLS) is compartmentalised into a series of variably sized “pudding basins”, each containing their own RLS stratigraphy. These are separated geographically and include one on the far western limb, one comprising the main western and eastern limbs and a third on the northern limb. Different rates of erosion on each limb determines the extent to which the RLS stratigraphy is preserved (see Figure 3.11B). If this model is correct the marginal mineralisation, seen at surface on the northern limb, is purely a preservation feature and that the layered series will be

present at depth. The discovery of UG2 ‘like’ chromitite on Turfspruit (Grobler et al., 2018) and Akanani (west of Mogalakwena) down dip of the surface mineralisation provide tentative evidence to support this model.

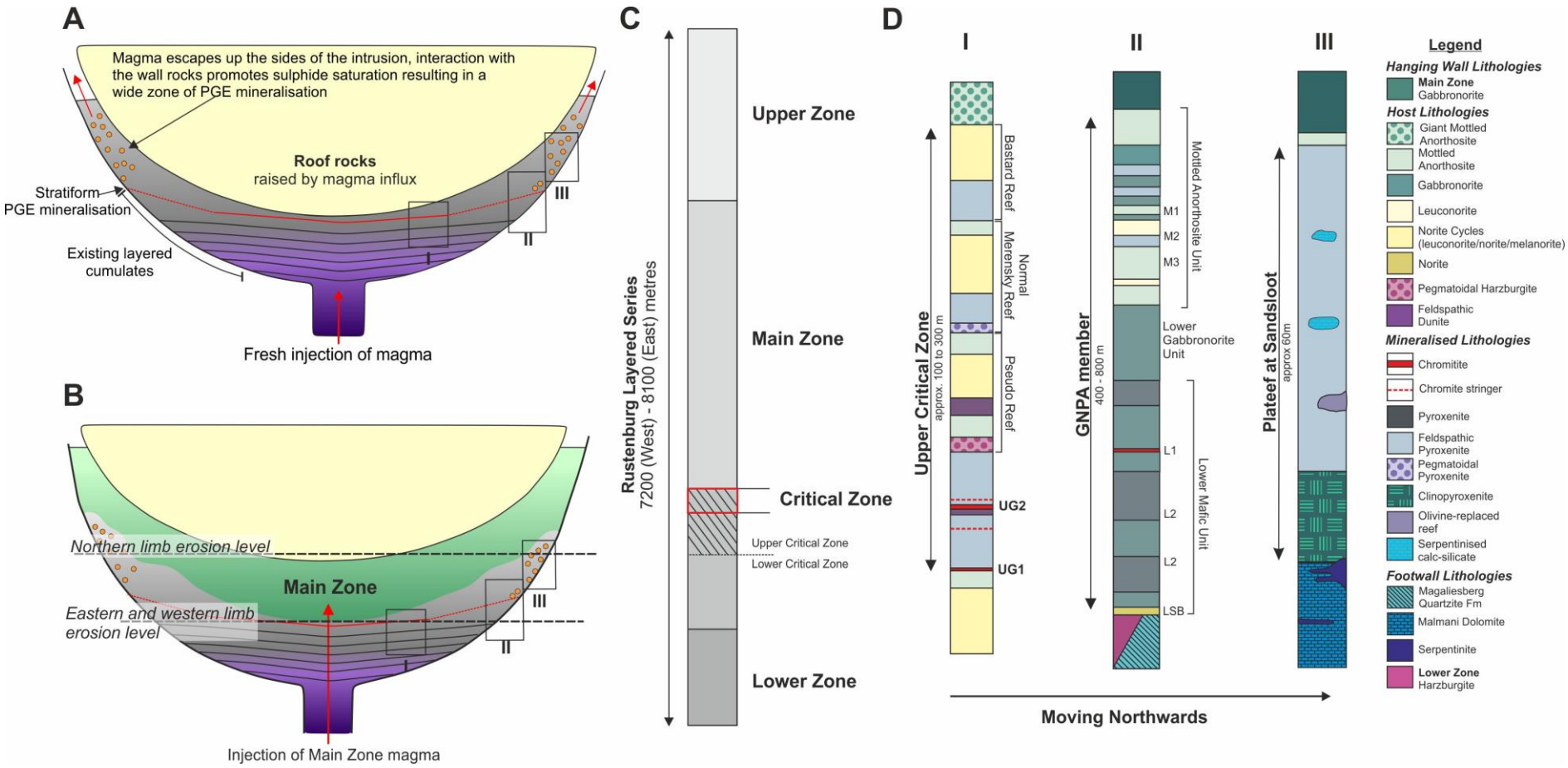

Figure 3.11: A schematic representation of the 'Pudding Basin Model' as proposed by Naldrett et al., (2008) whereby the Platreef represents a marginal facies of the Merensky Reef, developed where the magma is in contact with or intruded against the margin of the Bushveld Complex magma chamber. Note: In B the red line denotes the height of the erosion level. Modified after Naldrett et al., (2008).

Model 2 as developed in Holwell et al. (2007) and McDonald & Holwell (2007), envisages the concentration of sulphides in pre-Platreef staging chambers, which supplied the Lower Zone intrusions (see Figure 3.12A). The sulphides PGE content are upgraded by repeated interactions with fresh batches of undepleted Lower Zone magma, which leave the system depleted in chalcophile elements. Evidence for chalcophile element depleted Lower Zone cumulates has been identified on Zwartfontein by McDonald et al., (2008). Furthermore, trapped droplets of PGE-rich sulphides (> 100 ppm) preserved as inclusions in chromite grains analysed by Holwell et al., (2011) provide evidence for pre-enriched sulphides that were entrained in the magma during emplacement. The mineralised sulphides are subsequently expelled from the chamber as a crystal-sulphide mush, by an early pulse of Main Zone magma (see Figure 3.12B) and emplaced at higher stratigraphic levels. The sulphide content of the Platreef is locally elevated in areas where the footwall rocks are sulphide rich e.g. Turfspruit (see Figure 3.12C)

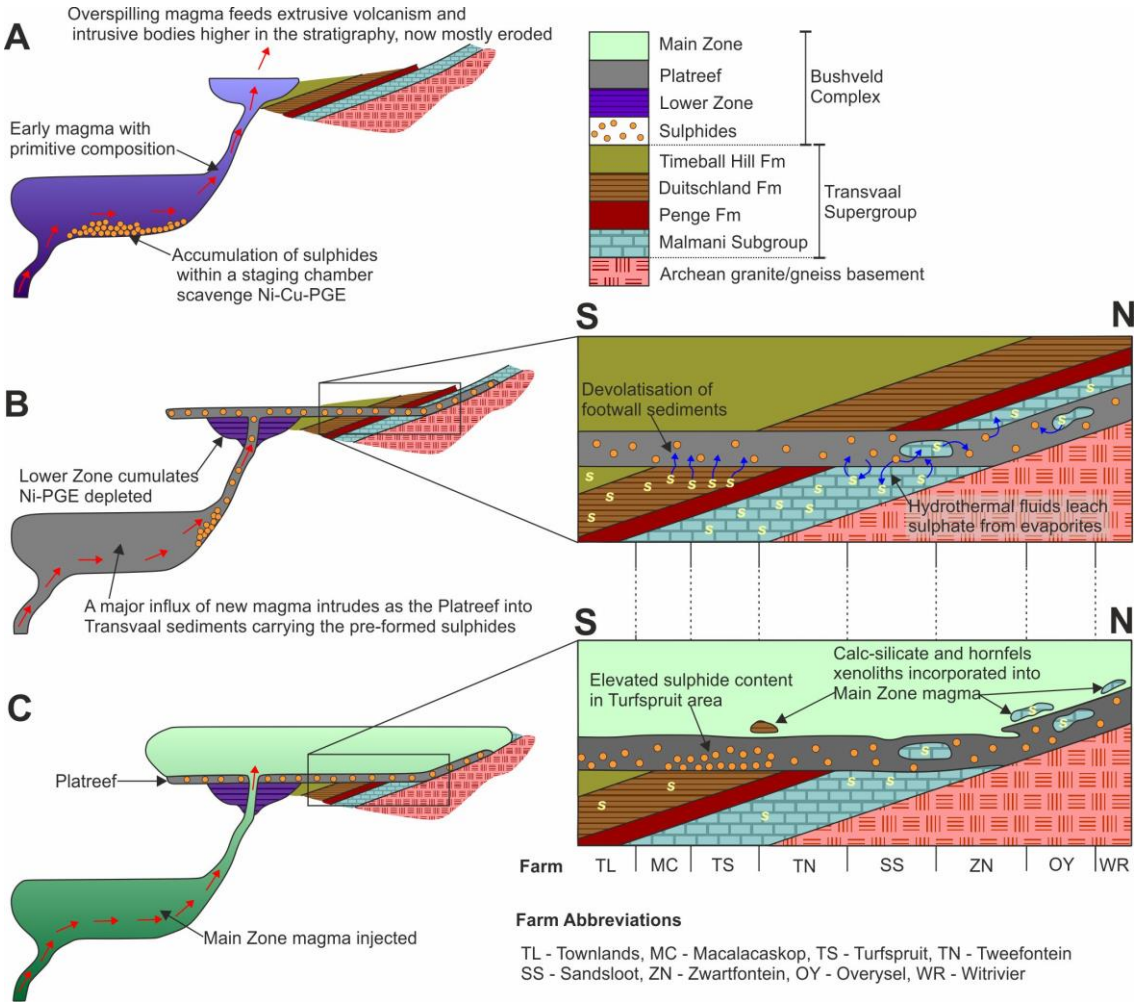

Figure 3.12: A petrogenetic model for the development of the sulphide-rich Platreef mineralisation at depth in a pre-Platreef staging chamber and emplacement at higher stratigraphic levels as a sill hosting pre-existing, high-tenor sulphides. Modified after Holwell et al., (2007) and McDonald & Holwell (2007).

Chapter 4

Methodology

4.0 Introduction

A range of quantitative analytical methods including: whole-rock geochemistry, in situ mineral chemistry and sulphur isotope geochemistry have been used in this study to critically assess the mineralisation and associated stratigraphy across the Turfspruit deposit. The following sections outline the various methods used to evaluate the rocks covering all stages of the study: initial logging and sampling protocols (4.1), country rock sampling (4.2), whole-rock geochemistry (4.3), in situ mineral chemistry (4.4), sulphur isotope geochemistry (4.5) and in situ PGE analysis (4.6). The results of this multi-disciplinary study are presented in appendices (A to F). The majority of these analyses were carried out at the analytical facilities at Cardiff University and supported by the funding from Ivanplats Pty Ltd. The sulphur isotope analysis was completed at the Scottish Universities Environmental Research Council (SUERC) Stable Isotope Facility at East Kilbride, Glasgow with funding provided by an isotope facility grant from the Natural Environment Research Council (NERC IP-1677-1116).

4.1 Core Logging and Sampling Methodology

The logging of drill core was conducted at the Ivanplats core yard facility located on the outskirts of Mokopane. The setup of core yard is shown in Figure 4.1. Logging was undertaken over the course of two fieldwork excursions; the first from the 06/05/2015 to 28/05/2015 and the second from the 21/07/2016 to the 12/08/2016.

Figure 4.1: The Ivanplats core yard facility in Mokopane, drill core logged in this study was kept either on logging benches or on the floor under shade.

The focus of the first visit to the core yard was on the deep Platreef drill holes following on from work completed by two previous Masters Students at Cardiff University; Geoff Smart (2013) and Suzanna Nodder (2015). Smart (2013) partially sampled drill holes UMT_345, UMT_345_D1 and UMT_336; he focussed on mineralised intersections of the core without looking in detail at their wider stratigraphic context. The drill holes UMT_345 and UMT_336 represent examples of 'thick' and 'thin' reef facies, respectively. Nodder (2015) conducted a more detailed analysis on UMT_336_D1 and compared the well-preserved magmatic layering to the Upper Critical Zone as described for the eastern and western limbs. As a consequence of this previous work the primary objective of this first visit was to understand the wider stratigraphic context of the mineralised samples collected by Smart (2013) through further sampling and more detailed logging of drill holes UMT_345 and UMT_345_D1.

The subsequent fieldtrip, focused on logging core from higher up in the stratigraphy in the Flatreef (UMT_233 and TMT_006) and near-surface Platreef (ATS_002). Thus enabling a comparison of the lithological and stratigraphic continuity moving across the deposit (W to E) in the up-dip direction. Similar to the drill holes sampled from the deep Platreef the Flatreef drill holes selected also represent 'thick' (TMT_006) and 'thin' (UMT_233) mineralisation facies.

In total, five diamond drill holes were partially logged and sampled for this study these are: UMT_345, UMT_345_D1, UMT_233, TMT_006_D2 and ATS_002 (see Chapter 1 Figure 1.8 for location and Appendix A).

4.1.1 Lithological Logging

Logging of each drill hole began either at the depth of the top contact with the Main Zone or at the beginning of the first mineralised mafic lithological unit. The logged interval ended either at the end-of-hole (EOH) or where the igneous rocks became unrecognisable due to contamination. The assay results for each drill hole logged were provided by Ivanplats to assist with the determination of logging and sampling intervals. A summary of the logged intervals for all drill holes studied is provided in Table 4.1.

Table 4.1: Logging intervals for each logged drill hole. Note: core size refers to the core diameter with BQ (36.5 mm), NQ (47.6 mm) and HQ (63.5 mm).

Section	Drill Hole	From (m)	To (m)	Interval (m)	No. Samples	Core Size	Author
Deep Platreef	**UMT_345**	1353.00	1596.20 (EOH)	243.20	16 (HS) 17 (GS)	NQ	Hannah Stephenson Geoff Smart
Deep Platreef	**UMT_345_D1**	1382.49	1535.75 (EOH)	153.26	20 (HS) 7 (GS)	NQ	Hannah Stephenson Geoff Smart
Deep Platreef	**UMT 336**	1020.00	1140.00	120.00	18	NQ	Geoff Smart
Deep Platreef	**UMT 336 D1**	994.00	1247.65	253.65	56	NQ	Suzanna Nodder
Normal Flatreef	**UMT_233**	794.47	904.66	110.19	18	NQ	Hannah Stephenson
Thick Flatreef	**TMT_006**	794.86	905.41	110.55	38	HQ	Hannah Stephenson
Platreef	**ATS_002**	91.00	175.59	84.59	9	BQ	Hannah Stephenson

As shown in Table 4.1, the size of the drill cores varies with the prefix reflecting the purpose for which each drill hole was drilled e.g. resource drilling (ATS), metallurgical testwork (TMT) and exploration drill holes (UMT). Typically, half core was logged; the other half having been sent for metallurgical test work and assaying by Ivanplats for resource characterisation. Where previous academic study/metallurgical testwork had reduced the core to a quarter of the original cylinder no sampling was permitted. This only significantly affected sampling of drill hole ATS_002 where the majority of the mineralised interval had already been sampled and was reduced to quarter core.

Lithological logging was conducted on a variety of scales from millimetres to meters. This adaptability was necessary in order to log both thick packages of relatively homogenous lithologies and to include important petrological features such as 1 to 2 mm thick chromite stringers. The logging codes used during the study are presented in Table 4.2. The information recorded whilst logging included: lithology, grain size, rock texture, contact type (always from the base), angle to core axis (of planar features e.g. contacts) and any observed alteration. In addition, the presence/absence (with a visually estimated abundance) of certain indicator minerals including plagioclase, phlogopite, chromite and sulphides was noted. Most of the igneous rocks logged were phaneritic and a typical grain size classification system was used (see Table 4.2 top left). Aphanitic rocks were observed in drill holes ATS_002 and TMT_006 corresponding to suspected metamorphosed sedimentary material (hornfels and serpentinised calc-silicate).

Table 4.2: Logging codes used to classify grain sizes, contact type and textures.

Grain Size	Size Range
Fine (F)	<=1 mm
Medium (M)	1 to 5 mm
Coarse (C)	5 to 10mm
Very Coarse (VC)	10 to 20 mm
Pegmatite (PEG)	20+ mm

Nature of Contact	Description
GRD	Gradational
IRR	Irregular
S	Sharp
SH	Sheared
UND	Undulating

Texture Label	Description
ALT	Altered
ASSIM	Assimilated
BAND	Banded
GRN	Granophyric
INEQ	Inequigranular
MAS	Massive
MOT	Mottled
PEG	Pegmatoidal
PK	Poikilitic
SP	Spotted
STR	Stringer
VT	Vari-textured

The lithological names assigned during logging conform to the approach favoured by many workers on the eastern and western limbs of the Bushveld Complex including Kruger & Marsh (1985) and on the northern limb by Harris & Chaumba (2001) and Hutchinson & Kinnaird (2005). This nomenclature is more qualitative than the Streckeisen (1976) IUGS scheme. This also conforms to the logging protocols used by Ivanplats geologists (Parker *et al.,* 2012). In practice, this means that a rock containing <20% modal interstitial plagioclase and 80% modal cumulate orthopyroxene is given the name feldspathic pyroxenite as opposed to a melanorite. Another example is the mottled anorthosite which in the IUGS system would be called a leucogabbronorite as it typically contains >10% mafic minerals. The terms mottled and spotted before anorthosite refer to the characteristic texture observed within these rocks throughout the Bushveld Complex.

4.1.2 Core Sampling Methodology

Core sampling was undertaken in order to collect samples for geochemical and mineralogical analysis. Quarter core samples, a minimum of 10 cm in length, were collected from logged sections of core. The length of samples was dependent on numerous factors including: the occurrence of natural breaks, the presence of contacts, the grain size, textural/compositional homogeneity etc. The selection of samples took into consideration multiple factors but essentially there are two types of samples:

1. Representative samples: typical of that particular lithology and therefore can be assumed to represent the larger, homogeneous bulk.

2. Targeted samples: to investigate specific variations within an inhomogeneous bulk. These variations include alteration, grade (high or low), petrological features of interest (e.g. chromite stringer), lithological contacts, interesting textures and evidence of assimilation.

The location of these samples in relation to the logged stratigraphy in each drill hole is presented in Chapter 5 (Figure 5.4) and a summary table outlining all the samples collected and the reasoning is presented in Appendix A.

4.2 Country Rock Sampling

The stratigraphy of the footwall sedimentary rocks of the Duitschland Formation was observed and sampled on the farms Duitschland (Grid reference: S 24°17'33.0" E 029°08'10.1") and De Hoop as shown in Figure 4.2. Sampling permission was sought from the landowners Al Thingwe Safaris (Duitschland) and Ivanplats (De Hoop); no sampling was conducted within the boundary of the Makapan Valley World Heritage Site. Country rock samples were collected using a geological hammer from exposed outcrops, whereas in areas of no outcrop float samples were collected. The aim of sampling was to collect representative samples from both the upper and lower parts of the Duitschland Formation succession. To achieve this two transects approximately perpendicular to the strike of the sedimentary bedding were walked across each locality (as shown in Figure 4.2). In total 37 samples were collected; 21 samples from Duitschland (prefix DTH) and 16 from De Hoop (prefix DHP); see Appendix B. In addition to the collection of samples, brief observations on the geology were made and structural measurements taken from in situ exposures, as shown in Figure 4.3 and Figure 4.4 (also see Appendix B).

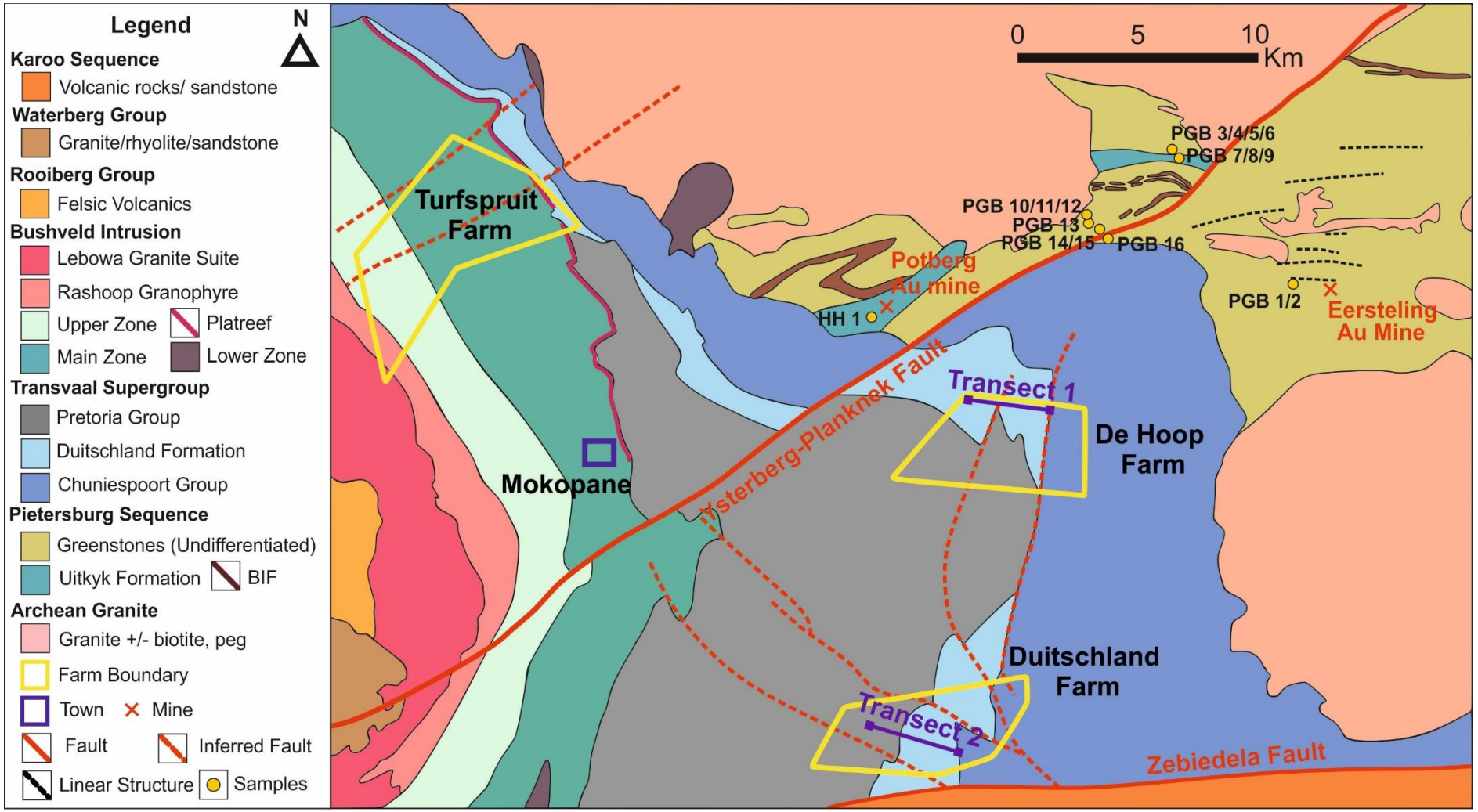

Figure 4.2: A regional geological map of the northern limb showing the location of farms De Hoop and Duitschland in relation to the Turfspruit locality. The sampling locations of all PGB samples are highlighted along with the two sampling transects walked on De Hoop and Duitschland farms. Modified after regional geological survey maps from the Department of Mines (1978) and Department of Mineral and Energy Affairs (1985) combined with geological details on the PGB based on mapping results collected by de Wit (1991) and de Wit et al., (1992).

The most complete succession of the Duitschland Formation stratigraphy was observed on Duitschland farm. At this locality a road orientated almost exactly perpendicular to the strike of the beds facilitated the access to rock exposures. The position and lithology of samples collected from this locality are shown in Figure 4.3. The strike of the sedimentary bedding is approximately NE-SW and dipping to the NW; a younging direction (NW) is given based on observed sedimentary structures.

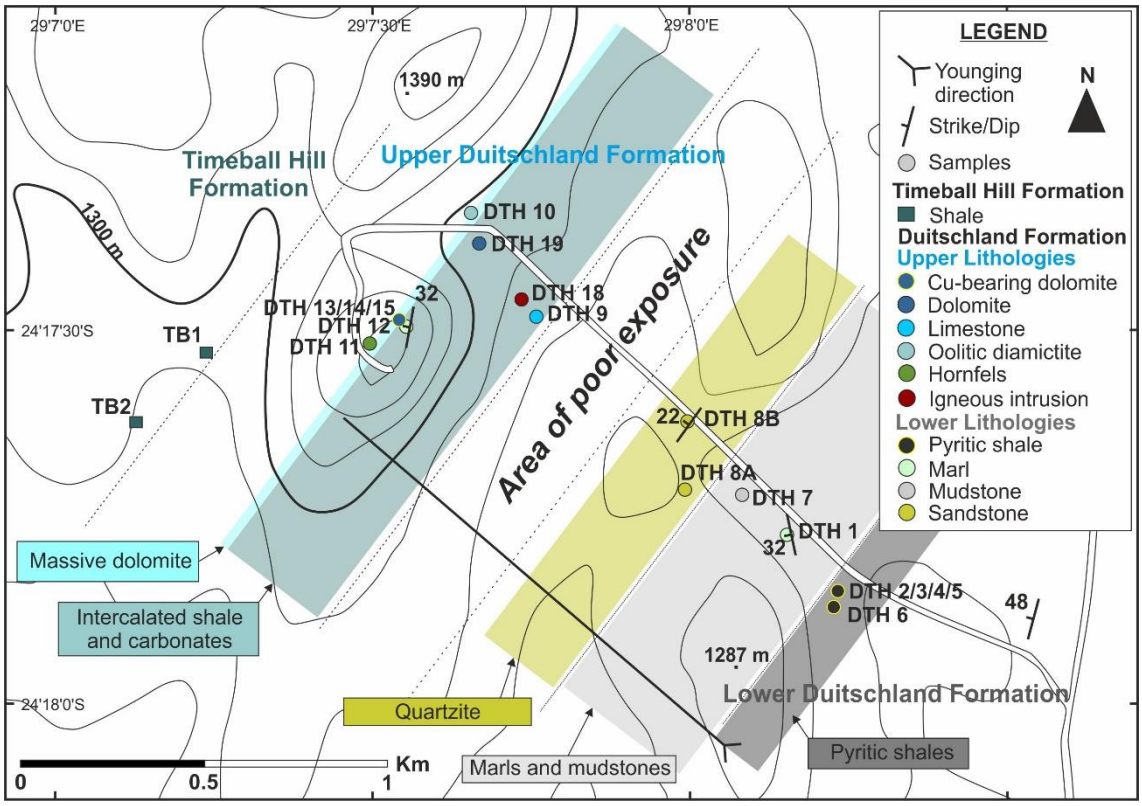

Figure 4.3: Topographic map of the traverse on Duitschland Farm showing the location of samples, structural measurements on sedimentary bedding and with geological boundaries inferred based on the surface geology. Note: samples with DTH are Duitschland Formation samples and TB are Timeball Hill shales.

On farm De Hoop only the shallow water facies forming the upper portion of the stratigraphy is exposed (Frauenstein et al., 2009); hence the more limited sampling from this locality as shown in Figure 4.4. At this location the strike of the bedding is more N-S orientated, reflecting the folding observed within the Transvaal Supergroup.

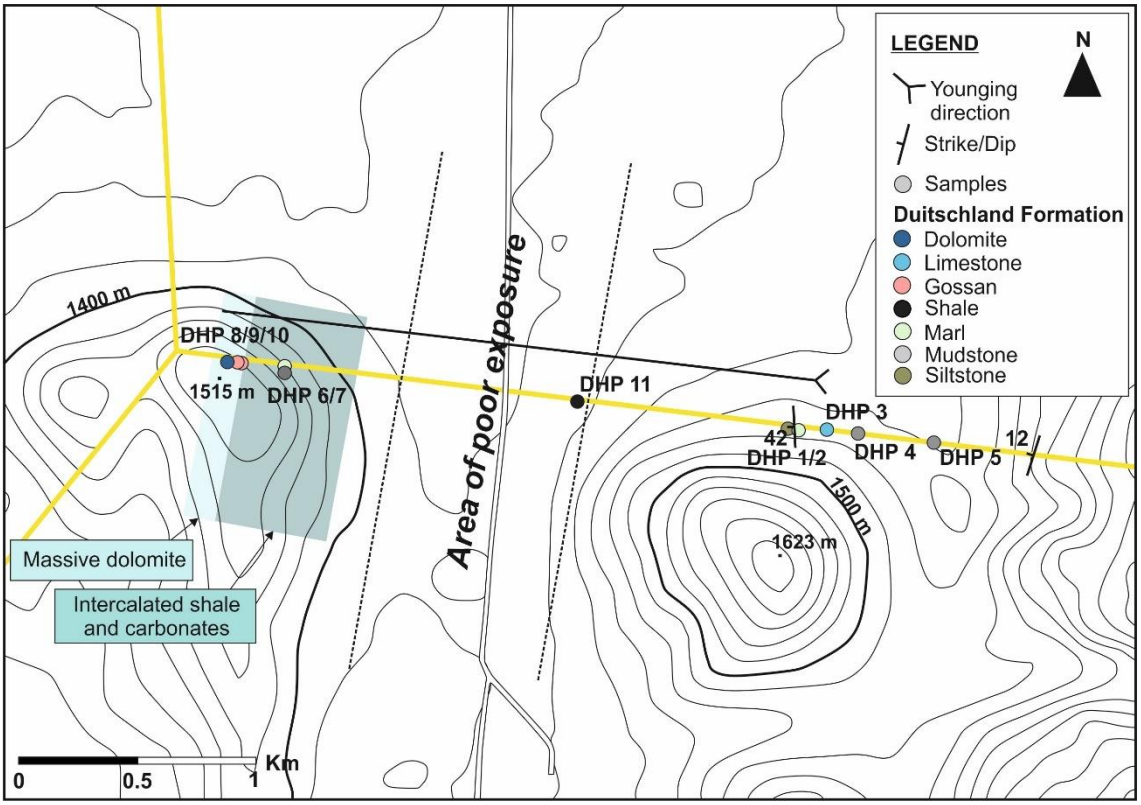

Figure 4.4: Topographic map of the traverse on De Hoop farm showing the location of samples (prefix DHP), structural measurements on sedimentary bedding and inferred geological boundaries based on surface geology.

Sampling of the Pietersburg Greenstone Belt (PGB) was undertaken over a period of two days (03/12/2016 to the 04/12/2016) by a group of co-workers led by Hannah Hughes and including Bianca Kennedy and Tshilisanani (Simon) Nethononda. The PGB samples were collected from exposures around the former gold mines located at Potberg and Eersterling (see Figure 4.2), in addition to sites at Geyser and Ysterberg. A total of 18 samples were collected including representative samples of the Ysterberg Formation banded iron formations, Uitkyk Formation conglomerates (including mineralised with buck shot/pyrite from Potberg), sandstones (some arkosic and quartzite) and Eersteling metavolcanics. A list of all the PGB samples collected including coordinates and a brief description are presented in Appendix B.

4.3 Whole-Rock Geochemistry

The major (wt% oxides) and trace element (ppm) composition of whole rock samples was analysed using both the JY Horiba Ultima 2 inductively-coupled plasma optical emission spectrometer (ICP-OES) and the Thermo Elemental X7 Series inductively-coupled mass spectrometer (ICP-MS) at Cardiff University.

4.3.1 Lithophile Element Analysis

A representative part (at least 20 g) of each sample was prepared for bulk geochemical analysis. Initial comminution to a powder, passing 125 μm, was undertaken in a two-stage process involving primary crushing through a hardened steel jaw crusher followed by milling in a planetary agate ball mill. A portion (2 g) of each comminuted sample was roasted for 90 mins at 900 °C and the loss on ignition (LOI) determined gravimetrically. A portion, 0.100 g, of the ignited sample powder mixed with 0.6 g of Li metaborate flux was melted using a Claisse Fluxy automated fusion system and subsequently dissolved in dilute HNO_3. The resulting solution was spiked with 1 ml of 100 ppm rhodium stock solution enabling calibration of the mass spectrometers. A detailed outline of this procedure is presented in McDonald & Viljoen (2006). The accuracy and precision of this method was measured through the introduction of certified reference materials (CRMs), reagent blanks and duplicates at the weighing stage. A complete table of results for both unknowns and standards analysed in this study is provided in Electronic Appendix B (for country rock samples) and Electronic Appendix C (for drill core samples).

4.3.2 PGE Ni-S Fire Assay

The precious metal (PGE and Au) content of the whole-rock powder, prepared as above, was analysed using Ni-sulphide fire assay followed by Te co-precipitation and ICP-MS as described in Huber *et al.* (2001) and McDonald & Viljoen (2006). This method analyses for ^{189}Os, ^{193}Ir, ^{99}Ru, ^{103}Rh, ^{195}Pt, ^{106}Pd, and ^{197}Au; Re is not recovered.

This method uses 15 g of sample combined with the following proportion of reagents: 6 g of $NaCO_3$, 12 g of borax, 0.9 g of sulphur, 1.08 g of carbonyl-purified Ni, and 1 g of silica. For chromite-rich samples the fusion mixture requires significant changes, as follows: 5 g sample 15 g $NaCO_3$, 30 g Li tetraborate, 0.9 ± 0.01 g sulphur 0.9 g, 1.08 ± 0.01 g carbonyl-putrified Ni, 10 g silica and 5 g NaOH. Furthermore, during this study certain modifications to this 'recipe' were made following failed experiments and insufficient sample sizes as shown in Table 4.3 below.

Table 4.3: Modifications to the 'normal' fusion mixture for various compositional criteria.

	< 15 g Sample	**> 7% LOI**	**< 50 wt% Silica**	**Blank**
Sample (g)	10	7.5	15	N/A
Silica (g)	5	2.5	2	10

The accuracy of the whole rock PGE analysis was constrained by measuring a mixture of low and high grade CRMs as presented in Table 4.4. The precision of the procedure was estimated by repeat analysis of a subset of samples and blanks analysed per assay batch. The raw PGE data are supplied in Electronic Appendix B (country rock samples) and Elctronic Appendix C (core samples).

Table 4.4: Certified values for the fire assay CRMs presented in increasing grade order.

Standard	^{189}Os	^{193}Ir	^{99}Ru	^{103}Rh	^{195}Pt	^{106}Pd	^{197}Au
Certified Values							
TDB1	0.10	0.15	0.30	0.70	5.8 ± 1.1	22.4 ± 1.4	6.3 ± 1.0
WITS1	1.40	1.50	5.50	1.30	11.80	7.60	4.90
WMG1	12.99	14.09	20.44	13.51	277.01	240.83	40.12
WPR1	13.00	13.50	22.00	13.40	285.00	235.00	43.00
SARM 64	-	52	240	80	475	210	18

4.4 Mineral Chemistry

Quantitative, in situ mineral compositional data was collected using the Cardiff University Zeiss (NTS S360) Sigma HD analytical field emission gun scanning electron microscope (FEG-SEM), fitted with two Oxford Instrument 150 mm^2 EDS detectors. Calibration of the spectra and standardisation of data was achieved through the use of two standard blocks: (1) an Astimex Standards mineral block (MINM25-53+FC) containing 53 naturally occurring minerals and; (2) the Micro-Analysis Consultants Ltd Universal Standard element block. The use of this extensive suite of external standards improves the detection limit on the major elements to 0.05 wt%; comparable to microprobe analyses. The results of this study are presented in Electronic Appendix D; additional information is provided in Appendix D.

Quantitative major element mineral data was collected using both EDS detectors and imaged with the in-lens Everhart-Thornley secondary electron detector (SE). The following operating conditions on the SEM were used for all quantitative analyses: 60 µm aperture, 20 kV accelerating voltage, 3.0 nA beam current, a magnification of 400 and a fixed working distance of 8.9 mm. Data acquisition, processing and spectrum analysis were performed using Oxford Instruments AZtec analytical software. The data acquisition settings used on all analyses were a 30 second dwell time and spectrum processing time 4. Analytical drift checks were performed every fifteen minutes on the Co reference standard. In addition, secondary mineral standards were analysed up to four times a day to monitor any drift on particular elements (see Table 4.5) ensuring accurate analyses with accepted totals ± 1.5% of the standard values. Different calibration standardisations were used for the different minerals analysed; a

list of the element standardisations used for the different minerals is shown in Table 4.5.

Table 4.5: Calibration and secondary standards used for quantitative SEM analyses.

Mineral	Calibration Standards	Secondary Standards
Pyroxene	Diopside (Si, Mg, Ca); Jadeite (Na); Rutile (Ti); Cr-Diopside (Cr); Olivine (Fe); Rhodonite (Mn); Albite (Al and Si)	Cr-diopside; Pyrope; Almandine
Plagioclase	Albite (Si, Na); Labradorite (Al, Ca); Orthoclase (K)	Plagioclase; Orthoclase
Olivine	Olivine (Mg, Si, Fe); Almandine (Fe); Diopside (Mg); Nickel metal (Ni)	Olivine; Pyrope
Spinel	Chromite (Cr, Al); Magnetite (Fe); Sphalerite (Zn); Pentlandite (Ni); Rhodonite (Mn); Periclase (Mg)	Chromite; Olivine; Pyrope

4.4.1 Multi-Element Maps

The automated acquisition of whole thin section multi-element maps using the Zeiss Sigma HD FEG-SEM operating at an accelerating voltage of 20 kV, a 2.5 nA beam current and a working distance of 8.9 mm. The acquisition specifications, set in the 'Map' function of the AZtec software, include a pixel size of 10 µm, a dwell time of 3 ms per pixel and a process time of 1.

4.5 Sulphur Isotope Analysis

Sulphur isotope analysis by conventional and in situ laser combustion methods was undertaken at the Scottish Universities Environmental Research Centre (SUERC) on a selection of core and country rock samples. In total 54 conventional and 116 in situ laser combustion analyses were performed on Fe-Ni-Cu sulphide minerals in samples of the Platreef (n = 7), Flatreef (n = 19), deep Platreef (n = 24), Duitschland Formation (n = 7) and Pietersburg Greenstone Belt (n = 7). The results are calculated as $\delta^{34}S$ values relative to the standard VCDT (Vienna Canyon Diablo Troilite), reported in standard "δ" notation and expressed in parts per thousand (per mil). Uncertainties on the $\delta^{34}S$ values are on the order of 0.01‰; errors >0.03‰ were rejected (total of 4 rejects). The raw data resulting from this study are presented in Appendix E.

The core samples analysed were chosen in order to achieve good coverage of the stratigraphy within each drill hole studied. Flatreef and deep Platreef samples were given priority over Platreef samples (ATS), where the current literature is focussed. A further consideration concerned the varying nature of the sulphides in terms of their host rock lithology, degree of alteration, morphology, composition and grain size as observed in reflected light studies; these factors also influenced the decision on the

method of analysis undertaken on each sulphide mineral. Some examples of the variety of sulphide morphologies analysed in this study are shown in Figure 4.5.

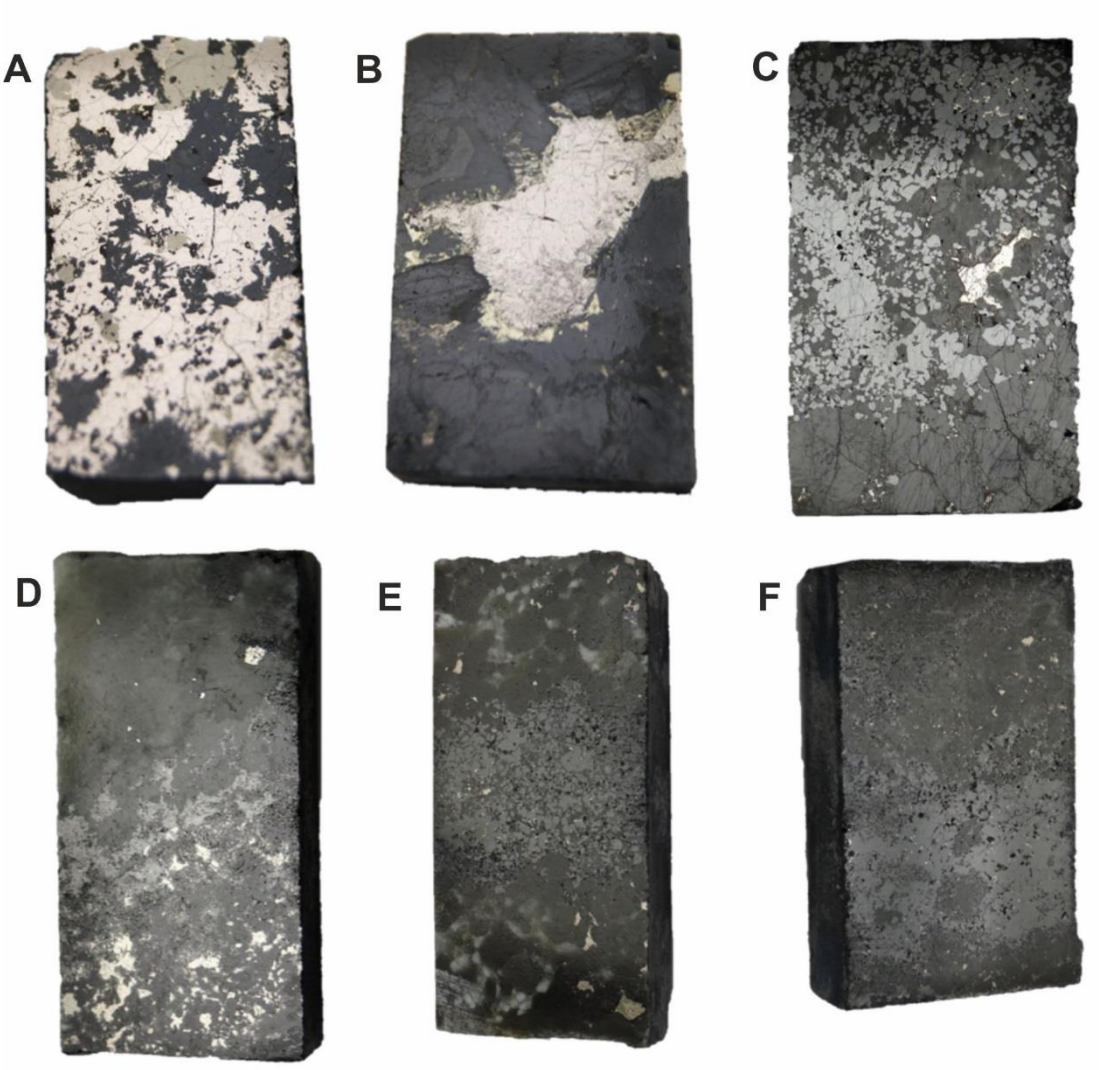

Figure 4.5: Normal light images of polished slabs (all approx. 4 x 2 cm) from selected core samples showing a variety of sulphide textures. (A and B) Coarse-grained to pegmatoidal sulphides where individual minerals can be identified by eye; example from samples ATS_07 and TMT_18, respectively. (C and D) Medium-grained sulphides where individual phases can be identified using a hand-lens; examples from GS20B and ATS_01A, respectively. (E and F) Medium-fine to fine grained sulphides where identification of phases requires the use of a light microscope: examples from 233_11A and 233_18A, respectively.

4.5.1 Conventional Sulphur Isotope Analysis

For conventional analysis a variety of methods of extraction were used to isolate sulphides from the rest of the sample. The method chosen was dependent primarily on the grain size of the sulphides present in each sample for example: (1) in medium grained samples, the sulphides are hand-picked from the coarse rejects and divided into chalcopyrite and combined pyrrhotite and pentlandite using a light microscope; (2) in coarse grained to pegmatoidal samples, where pyrrhotite and chalcopyrite can

be distinguished in hand specimen, the sulphide is collected as a powder using a micro-drill from a polished block and; (3) in fine-grained samples the sulphide is chemically extracted from whole-rock samples. The latter of these methods applies to the majority of the country rock samples where there are no visible sulphide minerals (i.e. <500 μm^2) prohibiting the isolation of sulphur by manual means. The exceptions include a pyrite-bearing conglomerate from the PGB (HH1 and HH2) and pyrite-bearing shales (DTH 2 to 6) and a chalcopyrite-bearing marble (HS_F_09) from the Duitschland Formation.

Whole-rock S concentrations are not measured in the geochemical analysis used in this study. In order to avoid wasting time and chemicals during the sulphur extraction process on samples with negligible sulphur contents the S concentration of the Duitschland Formation samples was tested using an Olympus hand-held X-ray fluorescence (XRF) system (for details on the methodology see Appendix E). Out of 44 samples tested eight contained detectable S concentrations ranging from 0.0082 to 0.1 wt% (see Table E1.1 in Appendix E). These samples were then prioritised for the whole-rock sulphur extraction process in addition to all PGB samples. The sulphur extraction method used in this study recovers only chromium-reducible sulphur (CRS) not the carbonate associated sulphur (CAS). The procedure is based on that as described in Zhabina & Volkov, (1978), Canfield et al. (1986), Tuttle et al. (1986), Hall et al. (1988), Newton et al. (1995), Nielsen & Hanken, (2002), Labidi et al. (2012) and Hughes (2015). In total, 37 experiments were completed from which 20 produced sufficient quantities of precipitate, at least 0.005g of Ag_2S, required for conventional analysis from a minimum of 50 g of initial sample material. Additional information on the samples and equipment set up and method can be found in Appendix E.

Upon analysis between 4 to 10 µg of prepared sample is combined with 150-200 µg of cuprous oxide and sealed in a glass tube using silica wool. The sample tube is placed into the sulphur line and combusted under vacuum at 1070 °C for 20 minutes; during this time the sample is converted to SO_2 gas. The sulphur line setup includes a dry ice/acetone slush trap at ≈ -80 °C, which removes any water. The released gases, SO_2 and minor CO_2, are collected in a cold finger. A standard n-pentane trap at ≈ -130 °C is used to isolate the SO_2 from the CO_2 and to remove any non-condensable gasses. The final stage involves measuring the 'clean' SO_2 content in the manometer cold finger and collecting the sample by freezing into a labelled and vacuumed sample tube ready for loading into the ThermoFisher Scientific MAT 253

dual inlet mass spectrometer. This procedure is described in detail in Robinson & Kusakabe (1975).

4.5.2 In Situ Laser Combustion

In situ laser combustion was used on samples containing visible sulphides prepared as polished blocks (see Figure 4.5). The samples are positioned in a sample chamber and put under vacuum before excess oxygen is added. The laser, a SPECTRON LASER 902Q CW Nd-YAG laser (1-W power), is used to ablate the surface of the sulphide guided using an optical microscope. The SO_2 gas released from the ablating sulphide is 'cleaned ' during transit through a sulphur line, analogous to that used in the conventional method, before entering the on-line VG Isotech SIRA II mass spectrometer. For additional information on the laser system design and operating conditions see Kelley & Fallick (1990) and Wagner et al. (2002).

4.5.3 Data Analysis

The raw values of $\delta^{66}SO_2$ are converted to a $\delta^{34}S$ value through calibration with international standards NBS-123 (certified +17.1‰) and IAEA-S-3 (certified -31.5‰), in addition to the SUERC internal lab standard CP-1 (certified -4.6‰). A correction factor is applied to the calculated $\delta^{34}S$ values for samples analysed using the laser-combustion method based on a small and predictable fractionation of the sulphur isotopic composition between the $\delta^{34}S$ of the SO_2 gas produced and the $\delta^{34}S$ of the sulphide mineral (Wagner et al., 2002). The $\delta^{34}S$ values are corrected by applying the following correction factors to the different mineral species: pyrrhotite +0.4, pentlandite +1.9, chalcopyrite +0.7 and pyrite +0.8.

Analytical precision and accuracy were determined through the use of a subset of duplicate unknown samples and by measuring international and internal standards. All data on repeated quality control analyses were within $2\sigma < \pm 0.2$ ‰ reproducibility.

4.6 PGM Identification Methodology

The PGE have higher atomic numbers than most common elements in silicate/sulphide ores and this property enables them to be observed using the scanning electron microscope (SEM); under backscattered electron imaging they are commonly the brightest minerals. A combination of manual and automated search techniques (for full details see Appendix F) were used to identify in excess of 1000 discrete platinum group minerals (PGM). The two SEMs available at Cardiff University were used in this study with automated analyses conducted on the Zeiss (NTS S360) Sigma HD FEG-SEM and manual PGM searches conducted on the FEI XL30 FEG-SEM. The Zeiss FEG-SEM is fitted with two Oxford Instruments 150 mm^2 EDS

detectors running Oxford Instruments AZtec software whilst the FEI FEG-SEM is fitted with one Oxford Instrument 15 mm^2 EDS detector and running Oxford Instrument INCA software.

The size, composition and textural setting was recorded for each individual PGM grain identified. The size of each PGM was measured on the SEM with the long (*a*) and short (*b*) axis recorded in micrometres; these measurements were then used to calculate the area of each grain assuming an elliptical shape ($A = \pi * a * b$) as used in Holwell et al., (2006).

All compositional data acquired is non-standardised and therefore semi-quantitative; EDS analyses were collected over a 20 second dwell time. PGM mineral names are assigned based on the normalised mineral At% data using mineral stoichiometry from Cabri (2002) as a reference.

Conventional PGM studies involve manual scanning of thin sections for bright PGM, following scan lines at a certain magnification, and are a time-consuming process. This is especially problematic in highly mineralized samples, (>4 g/t total PGE), where it may take >8 hours to manually record all the PGMs in a 1 cm^2 area of a thin section. This study has therefore developed a semi-automated technique using the Zeiss FEG-SEM at Cardiff University running the widely available Oxford Instruments AZtec software in an attempt to streamline this process.

Table 4.6: Comparing the performance of manual vs. automated PGM identification techniques and data acquisition.

	Manual	**Automated**	
		150x Mag	**300x Mag**
# Features	54	36	151
Time (hrs)	8	2	4
#PGM (+Au +Ag)	33	25	84
PGMs found/hour	4.125	12.5	21
Area of Features (μm^2)	135	559	1249
Area of PGM (μm^2)	26.24 (19%)	508.75 (91%)	889.21 (71%)

This semi-automated technique utilises the ‘Feature’ function on the AZtec software; a step-by-step guide to setting up an automated PGM search is provided in Appendix F and an example is shown in Figure 4.6. The process may be described as semi-automated as it still requires an initial manual identification step (ideally a cluster of PGM of different sizes) in order to calibrate the automated search and assess the range of sizes that the search is likely to find. In summary, this method involves setting up an automated scan of a thin section at a given magnification to identify ‘bright’

phases above a specified backscatter electron (BSE) intensity. During the scan any phases identified within the specified BSE intensity range are assigned a 'Feature' number (see Figure 4.6B) and a chemical and area analysis are performed. For the acquisition of this data the Zeiss FEG-SEM is set to operating conditions of 20 kV accelerating voltage, 1.2 nA beam current, a 60 µm aperture size and peak counting time of 20 seconds. In post-acquisition data analysis a chemical classification scheme can be applied to the Feature data, as shown in Figure 4.6C.

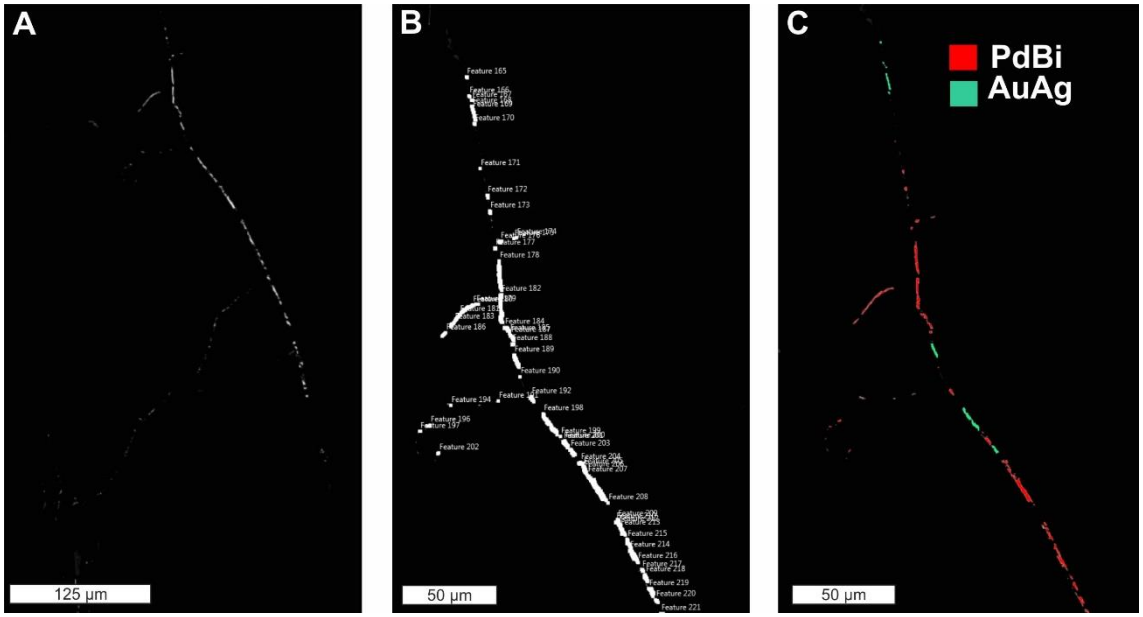

Figure 4.6: A complex PGM as highlighted using the Feature Map function on AZtec software. (A) PGM are the only mineral phases visible at high contrast and low brightness conditions. (B) The 'Feature map' identifies, highlights and numbers each unique PGM (91 shown in this cluster). (C) Feature map collects compositional information on each identified feature and assigns it a colour based on a pre-set compositional classification scheme.

The main advantages to this new technique are as follows: (1) fast acquisition of PGM data (improves search times by >50%); (2) more PGM are found per hour (see Table 4.6); (3) the automated search can run overnight reducing user time on the SEM; (4) the chemical classification enables distinction between PGM from other heavy minerals e.g. galena; (5) human error/bias inherent when manually scanning for PGM is removed. The main limitations of the method at present are: (1) the extreme brightness and contrast settings required for this to work mean that each PGM 'feature' found automatically must still be revisited manually in order to observe its host assemblage; (2) AZtec is more liable to crash with larger datasets such as acquired in this method; (3) laurite may be underestimated as it typically appears duller than the other PGMs and; (4) the resolution on polyphase PGM is lost and their composition is effective homogenised.

4.7 Laser Ablation ICP-MS

The PGE and trace element concentrations in sulphide minerals, prepared as polished thin sections, were measured using the New Wave Research UP213 UV laser system coupled to a Thermo X Series 2 ICP-MS at Cardiff University. The laser was operated using a frequency of 10 Hz generating ≈ 5 Jcm^2 for a 40 μm diameter beam with a penetration depth of 10 μm. The sample is ablated under a helium flow (~0.7 L min−1) the vapour released is combined with argon (0.65–0.75 L min^{-1}) and carried to the on line ICP-MS detecting both the element and their isotopes (Smith et al., 2014). Line analyses were used across selected sulphides and across sulphide-sulphide contacts using a scanning rate of 6 μm/s over a length of between 250 to 300 μm. Acquisition times ranged from 90 to 160s; with an initial 20 s gas blank and a 10 s washout at the end. The resulting time-resolved analysis (TRA) plots were analysed using the software PlasmaLab; for multiphase analyses the element peaks are used to distinguish between each sulphide phase traversed in the laser line (e.g. chalcopyrite and pentlandite).

The accuracy of the laser ablation mass-spectrometry (LA-ICP-MS) procedure was tested by analysing standard Po-727 T1 at the beginning, middle and end of each session on the laser (a certified synthetic FeS supplied by Memorial University, for details see Appendix F). Monitoring and calibration against isobaric interferences was achieved using a series of 5 synthetic Ni-Fe-S internal standards prepared from quenched sulphides. The analytical procedures and standards for the LA-ICP-MS technique at Cardiff University are outlined in Prichard et al., (2013) and Smith et al., (2014).

Chapter 5

Core Logging Results and the Turfspruit Stratigraphy

5.0 Introduction

The results of the lithological core logging are presented in the following chapter along with an interpretation of the observed stratigraphy. The Deep Platreef drill holes (UMT_345 and UMT_345_D1) were logged first followed by the Flatreef drill holes (UMT_233 and TMT_006) and finally the Platreef drill hole (ATS_002). Based on the results of previous studies at Turfspruit these drill holes represent a transition from relatively fresh and unaltered rocks at depth (e.g. Grobler & Nielsen, 2012; Nodder, 2015; Grobler & Dunnett, 2016; Yudovskaya et al., 2017a/b; Grobler et al., 2018) to highly contaminated rocks nearer the surface (Kinnaird, 2005; Sharman-Harris et al., 2005).

A wider context on the stratigraphic variability within the Turfspruit project area, beyond the scope of the five drill holes logged in the current study, was obtained by making observations on drill holes laid out from elsewhere in the deposit. A selection of images showing the variety of textures and skarn mineralogy observed in core from other drill holes are shown in Figure 5.1. The dominant protoliths of these skarn-type rocks are shale, quartzites and carbonates of the footwall Duitschland Formation sediments; the highly variable geochemical nature of the contaminant is reflected in the resulting range of skarn mineralogy. In addition, the varying degrees of partial melting and assimilation of the sediments means that in some areas original sedimentary layering is preserved (see Figure 5.1A and 5.1B) whereas in other places complete recrystallisation destroys any primary textures (see Figure 5.1C to 5.1F).

The mineralogy and textures observed are typical of high-temperature contact metamorphic skarn assemblages (see Figure 5.1C to 5.1E). The metamorphic mineral assemblage at Turfspruit can be found in Sluzhenikin et al., (2015). The most common mineralogical transformations observed are shale to pyroxene-cordierite-andalusite hornfels (see Figure 5.1D) and dolomite to clinopyroxene-garnet-montecellite calcsilicate (see Figure 5.1E). The presence of graphite, as shown in Figure 5.1A, indicates an organic carbon input possibly from stromatoilitic algal mats as found in the Duitschland Formation. In Grobler et al., (2018) it was noted that graphite locally forms on a decimetre-wide scale and they propose a method for their formation whereby CO_2 released by devolatising carbonates reacts with crystal mushes.

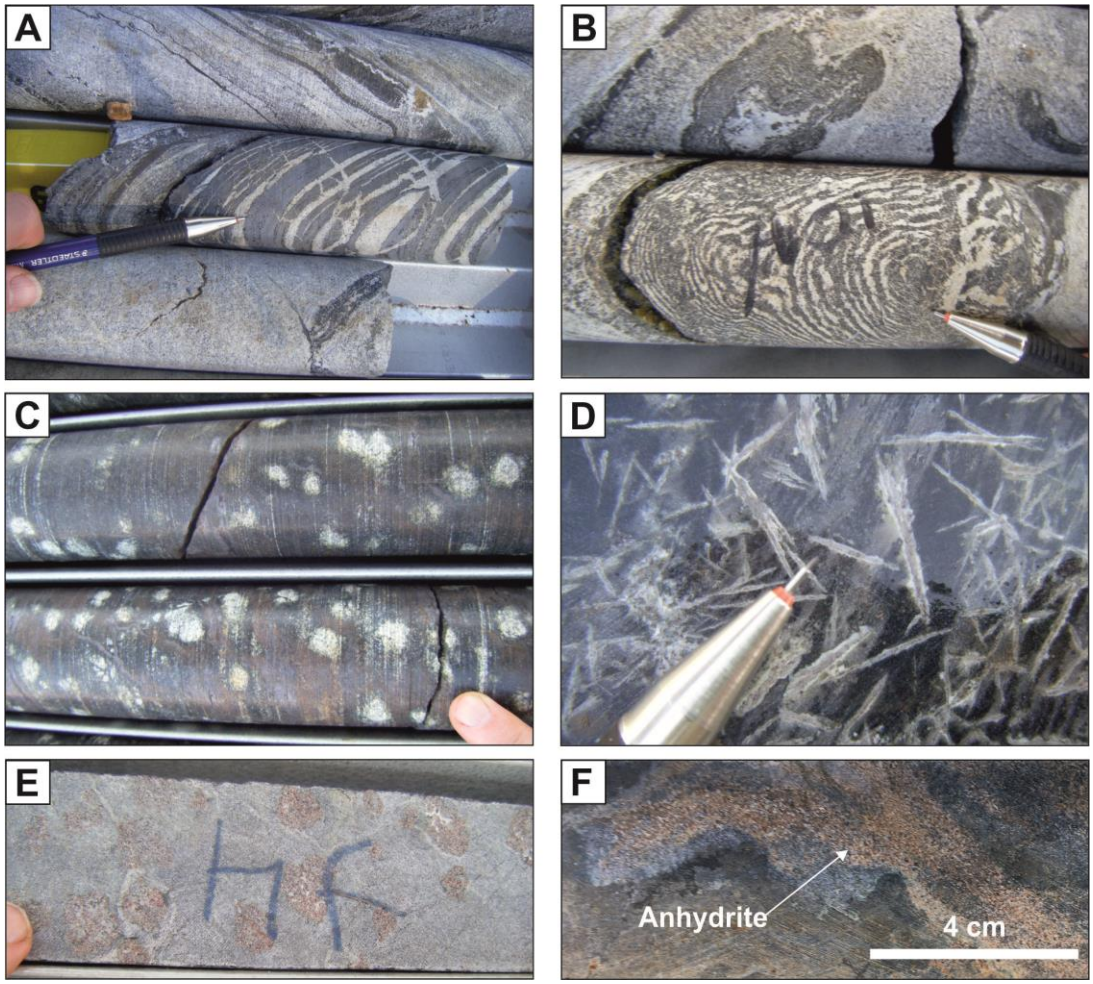

Figure 5.1: A selection of contact metamorphosed sedimentary xenoliths from random drill holes laid out in the Ivanplats core yard over the course of this study. (A) Graphite layers in metamorphosed country rock. (B) Relict textures (possibly domal stromatolities) preserved in a partially assimilated calc-silicate. (C) Black soapy texture with white, round, porphyroblasts of an unknown metamorphic mineral. (D) Coarse-grained (1.5 cm long) needle-like metamorphic minerals (possibly sillimanite/andalusite) in fine-grained hornfelsic matrix. (E) Coarse-grained (1 cm), red garnet porphyroblasts (probably almandine) in a fine-grained hornfels. (F) A partially assimilated anhedral mass of granular anhydrite. Note: the silver pencil tip (shown for scale) is 2 cm in length.

Contaminated rocks may also resemble igneous rocks; this has lead to the coining of terms such as parapyroxenites (clinopyroxene-rich) and paraharzburgites (dominated by serpentinised olivine) rock types (Gain & Mostert, 1982; White, 1994; Buchanan et al., 1981). These ‘para’ lithologies are usually feldspar- and/or clinopyroxene-rich, serpentinised, may contain elevated pyrrhotite-dominated sulphide concentrations and demonstrate textural (e.g. pegmatoidal, inequigranular) variability. Three examples of sediment-magma interaction are shown in Figure 5.2 below. In Figure 5.2A footwall calc-silicate preserving primary sedimentary layering is shown; the overlying igneous rocks are shown in Figure 5.2B. The igneous rocks have been affected by the partial assimilation of carbonate material and the release of

fluids/volatiles during magma/sediment interaction. This has resulted in a vari-textured rock consisting of coarse-grained orthopyroxene with interstitial areas composed of troctolite (plagioclase and high-Mg olivine) and coarse-grained sulphide accumulations. In contrast, sharp contacts between igneous rocks and hornfels were observed with minimal alteration of the igneous rocks, as shown in Figure 5.2C and 5.2D. In the examples shown in Figure 5.2C and Figure 5.2D the hornfels has been metamorphosed to such an extent that it has been transformed to monomineralic cordierite and has a purple colour. The contact between the hornfels and the noritic rocks as shown in Figure 5.2D is at 90° to the core axis and either side of the xenolith there is an increasing in the feldspar content possibly due to the assimilation of shales.

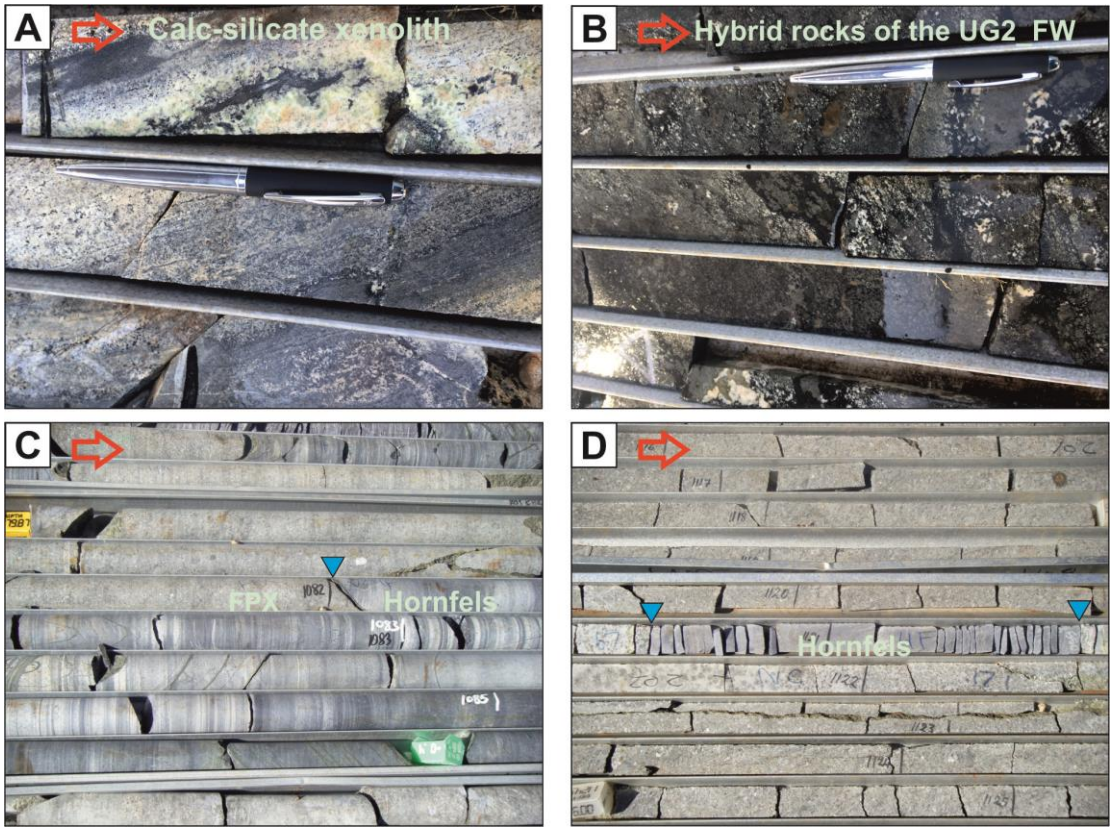

Figure 5.2: Examples of the contacts between the igneous rocks and metamorphosed country rocks. (A) Metamorphosed calc-silicate material retaining primary compositional banding at depths of between 1413 to 1415 m (UMT_094). (B) Alteration of igneous rocks over 5 metres above the calc-silicate shown in A; note the elevated plagioclase and olivine contents (UMT_094). (C) The contact between fine-grained hornfels and hybrid feldspathic pyroxenite. (D) Fine-grained hornfels completely transformed to monomineralic cordierite with sharp contacts to the igneous rocks. Note: red arrows point in the downhole direction, blue triangles are located on lithological contacts and each row in the core box is 1 m in length. Abbreviations: FPX – feldspathic pyroxenite.

5.1 Turfspruit Stratigraphic Framework

A stratigraphic framework for the Turfspruit deposit covering the interval from the base of the Main Zone down to the contaminated footwall lithologies has been developed

by geologists working on the project. The improved stratigraphic continuity of the Flatreef, compared to the Platreef, enabled the development of the original Turfspruit Cyclic Unit (TCU) nomenclature by Grobler & Nielsen (2012). This was the first attempt to correlate the observed rock sequence with the Upper Critical Zone (UCZ) of the eastern and western limbs of the Bushveld Complex. A more recent update of this stratigraphic framework by Grobler & Dunnett (2016) incorporates the discovery of a 'UG2-like' chromitite in the Deep Platreef and the TCU nomenclature is dropped in favour of the UCZ nomenclature. Details on the development of the lithostratigraphic framework can be found in Grobler & Dunnett (2016); the two versions of the stratigraphic framework for Turfspruit are shown in Figure 5.3 below.

The latest interpretation, Grobler & Dunnett (2016), is strongly influenced by the nomenclature of the eastern and western limbs of the Bushveld Complex; this represents the first time that the entire UCZ sequence has been applied to rocks on the northern limb. The main mineralised horizons of the Flatreef are correlated to the Merensky Cyclic Unit (MCU) of the UCZ based on the petrological and geochemical similarities of the T1m and T2U/T2L to the 'Bastard' and 'Merensky' reef, respectively (see Figure 5.3). The subdivision of the MCU into the M1 pegmatoidal pyroxenite/ harzburgite and the M2 feldspathic pyroxenite is based on the northeastern limb stratigraphy of the main Bushveld Complex as developed by Lee (1996). The deeper intercepted magmatic package hosts a patchily mineralised, massive to semi-massive 1 m thick chromitite unit that again in terms of its stratigraphic position and dominant mineralogy bears a resemblance to the UG2 chromitite as found elsewhere within the Bushveld Complex (Nodder, 2015; Grobler et al., 2018).

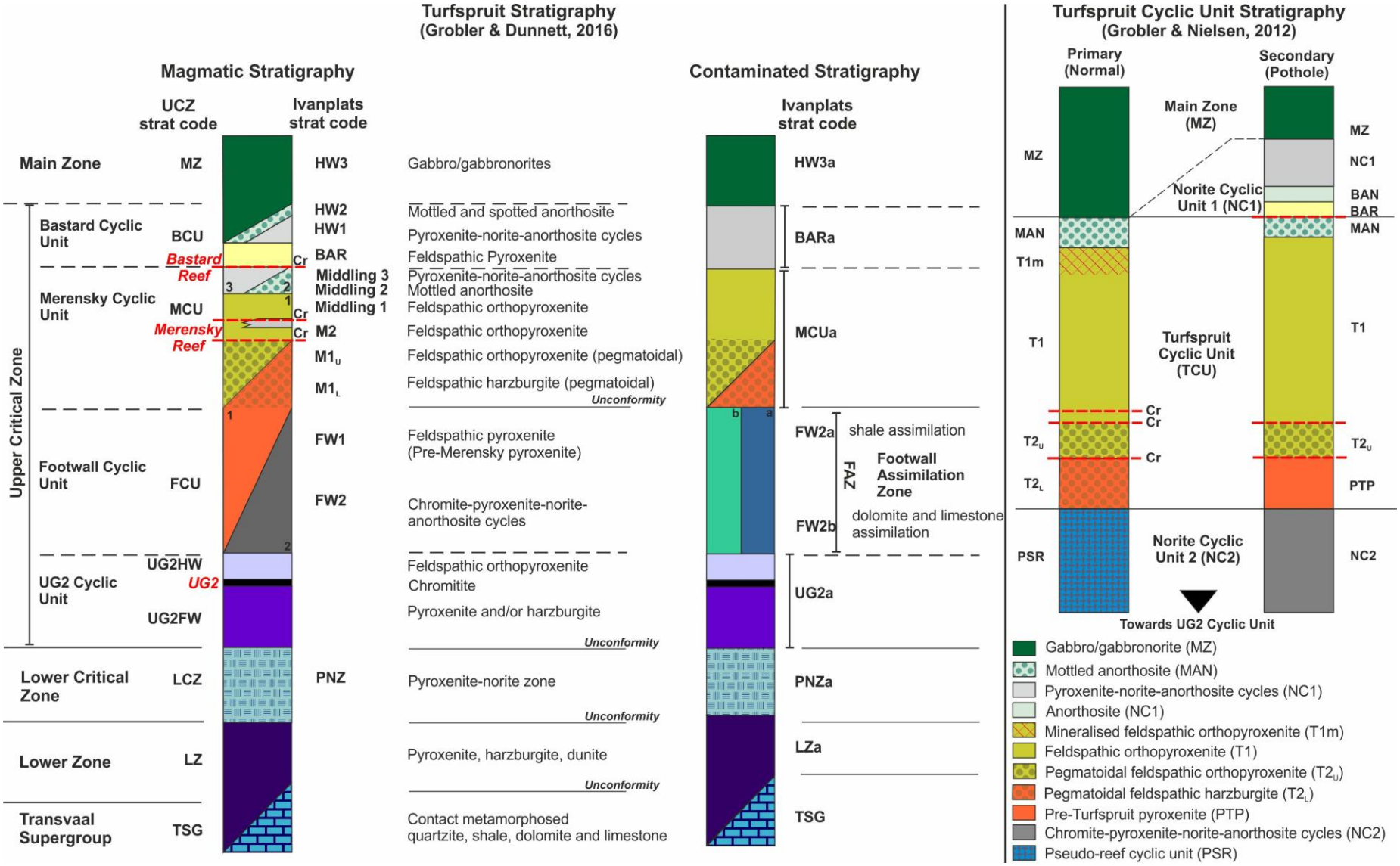

Figure 5.3: Stratigraphic framework used by Ivanplats Pty Ltd., to characterise the rocks on Turfspruit. The most recent version of Grobler & Dunnett (2016) is shown on the left and the original Grobler & Nielsen (2012) version is shown on the right.

5.2 Logging Results

The geological logging data, stratigraphic codes, sampling locations and grade profiles 3PGE (Pt+Pd+Rh) and Au for each drill hole logged in this study are shown in Figure 5.4. These drill holes are all positioned relative to one another using a common reference point, a mineralised chromite stringer above a pegmatoidal region, that can be identified within all drill holes. The mineralised interval boundaries are defined as > 2 g/t 3PGE and are named based on their relative stratigraphic position following Yudovskaya et al., (2017b).

The stratigraphic codes used in this study differ from the Grobler & Dunnett (2016) model, although the position of divisions broadly correlate (see Table 5.1). A conscious decision was made at the beginning of logging not to adopt the Grobler & Dunnett (2016) stratigraphic framework for Turfspruit because of the ambiguity of the relationship between the northern limb with the rest of the Bushveld Complex (for details see Chapter 3, section 3.3). The nomenclature used is similar to that adopted in Kinnaird (2005) and in Yudovskaya et al., (2017b) and in the earlier version Grobler & Nielsen (2012) where the names of stratigraphic units are more descriptive of the lithologies present and do not require any wider context to the Bushveld Complex. A brief description on the dominant geological characteristics of each stratigraphic unit are provided in Table 5.1.

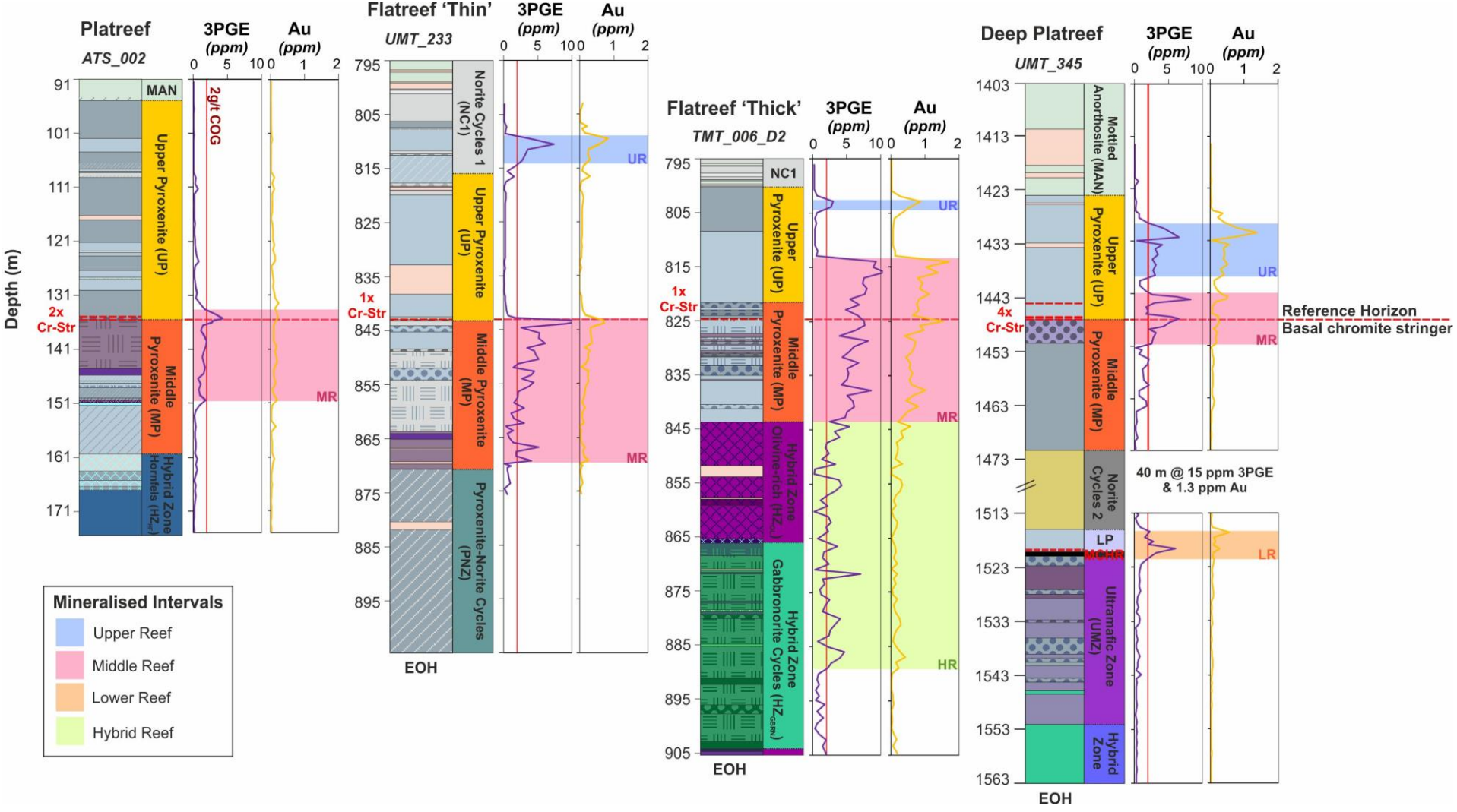

Figure 5.4: Geological logs, stratigraphic columns and grade profiles of 3PGE (Pt, Pd and Rh) and Au for each drill hole studied across the Turfspruit project area. The mineralised intervals identified within each drill hole are highlighted based on 1m composite data provided by Ivanplats Pty Ltd. Note: a geological key can be found in section 5.3 below at the beginning of each drill hole sub-section.

Table 5.1: Stratigraphic correlations between the Upper Critical Zone (UCZ) of the eastern and western limbs with the different Ivanplats models (Nielsen & Grobler, 2012 and Grobler & Dunnett, 2016) on Turfpsruit and the one developed in the current study.

UCZ		Nielsen & Grobler 2012 Code		Grobler & Dunnett 2016 Code		This Study	Ivanplats Geology Description	Distribution
Main Zone		MZ		HW3		MZ	Gabbronorites (up to 2 km thick)	All
Upper Critical Zone (UCZ)	**Bastard Cyclic Unit**	MAN		HW2		MAN	Mottled anorthosite (0.3 to 30 m thick[1])	ATS_002, UMT_345 & UMT_345_D1
		NC1		HW1		NC1	Pyroxenite-norite-anorthosite cyclic units	UMT_233 & TMT_006_D2
		BAR/T1m		BAR			Unmineralised feldspathic pyroxenite	UMT_233 (but mineralised)
	Merensky Cyclic Unit (MCU)	T1		MD3	Middling Units (MDU)	-	Pyroxenite-norite-anorthosite cyclic units	All
				MD2		-	Mottled anorthosite	None
				MD1		UP	Unmineralised feldspathic pyroxenite	All
				M2		UP	Mineralised feldspathic orthopyroxenite	TMT_006_D2, UMT_345 & UMT_345_D1
		T2U		$M1_U$		MP_U	Mineralised pegmatoidal orthopyroxenite	All
		T2L		$M1_L$			Mineralised pegmatoidal harzburgite	ATS_002, UMT_345 & UMT_345_D1
	Footwall Cyclic Unit	PTP		FW1		MP_L	Unmineralised orthopyroxenite/feldspathic orthopyroxenite	UMT_345 & UMT_345_D1
		NC2/PSR		FW2		NC2	Pyroxenite-norite-anorthosite cyclic unit (45 to 100 m thick)	UMT_345 & UMT_345_D1
	UG2 Cyclic Unit	UG2 HW	UG2CU	UG2 HW	UG2CU	LP	Mineralised feldspathic orthopyroxenite	UMT_345 & UMT_345_D1
		UG2		UG2		MCHR	1m thick massive to semi-massive chromitite	UMT_345 & UMT_345_D1
		UG2 FW		UG2 FW		UMZ	Pyroxenite and/or harzburgite	UMT_345 & UMT_345_D1
LCZ		-		PNZ		PNZ	Pyroxenite-Norite Zone	UMT_233
		-		FAZ		HZ_{OLWEBS}	Harzburite, troctolite, parapyroxenite with assimilation (limestone and dolomite contamination). Norite with assimilation (shale and quartzite contamination).	TMT_006_D2
						HZ_{GBRN}		TMT_006_D2
						HZ_{HF}		ATS_002
LZ		LZ		LZ		HZ_{FCPX}	Peridotite, harzburgite, dunite	UMT_345 & UMT_345_D1

5.3 Lithological Descriptions

Detailed descriptions of the lithologies present within each stratigraphic unit of the logged drill holes are given in the following sections. They are presented here in the downhole direction against convention; this approach is appropriate for this deposit because the top lithologies are more consistent and readily identifiable than the lower portions of the drill core. Therefore, moving downhole reflects decreasing confidence in the stratigraphic correlations; this approach is also used by Grobler et al., (2018) for this deposit. The stratigraphic units referred to from hereon in are those as outlined for the current study in Figure 5.4 and Table 5.1. Examples of the lithologies are shown in images from core boxes, these are all standard width (1 m) and hold up to 7 metres of core; in all figures shown no core loss was recorded.

5.3.1 Deep Platreef (UMT_345 and UMT_345_D1)

The Deep Platreef is found beneath 1400 m of gabbronorites belonging to the Main Zone (MZ). Logging of the entirety of the MZ was beyond the scope of this project, so an upper limit of the study was chosen at 50 m above the base of this unit. The Deep Platreef was logged in the drill holes UMT_345 and its deflection UMT_345_D1; the results of the geological logging are shown in Figure 5.5. The slight variation in the observed stratigraphy between UMT_345 and UMT_345_D1 could be related to the different orientation of drilling between the two holes. It is estimated that the separation between the mother and deflection hole at the end of hole is around 5.69 m.

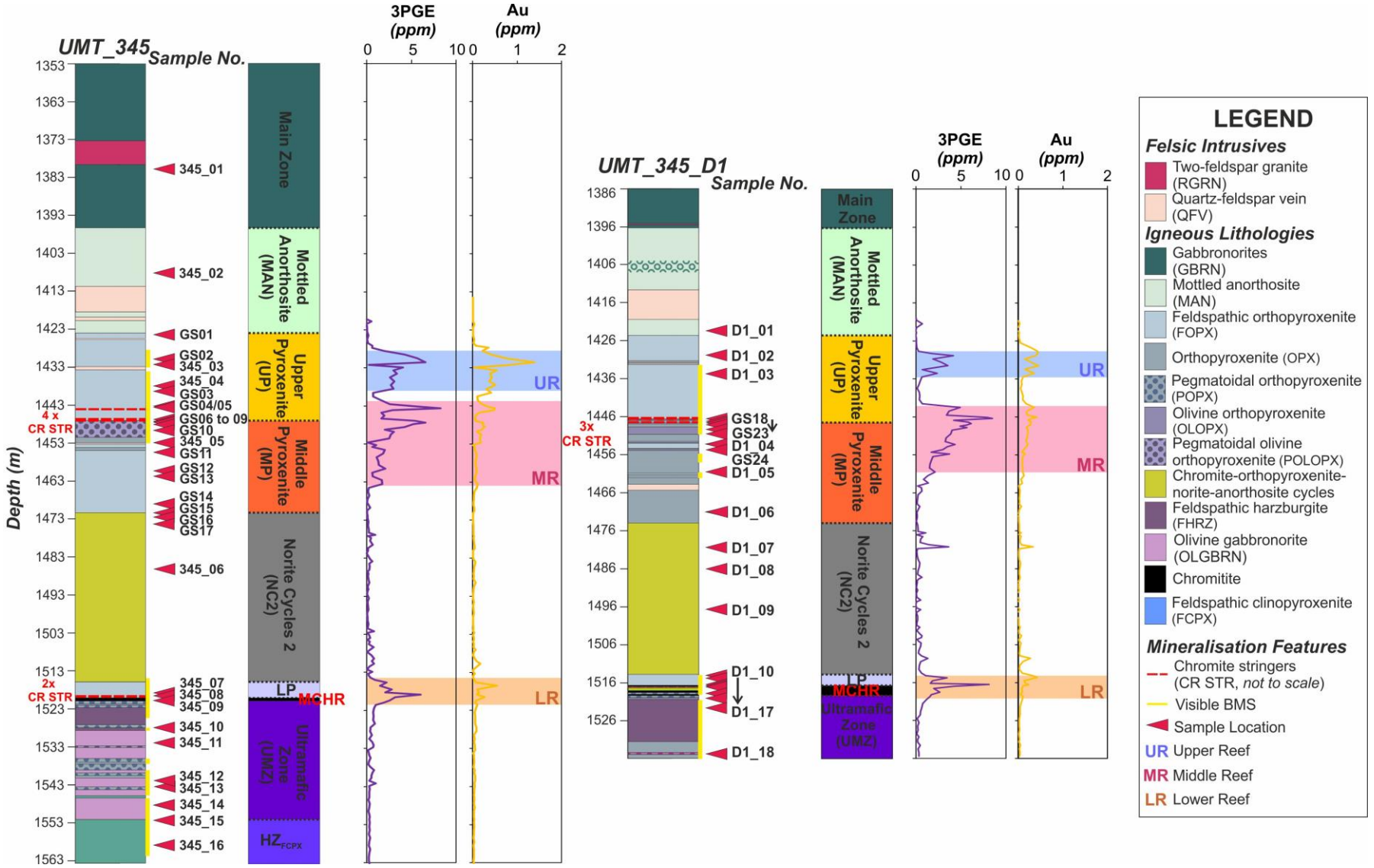

Figure 5.5: Geological logging data, sampling locations, stratigraphic codes and grade profiles for the Deep Platreef as sampled in drill holes UMT_345 and UMT_345_D1.

The MZ was logged from 1353 m to 1396.52 m in UMT_345, over this interval the rock consists of medium-grained gabbronorite to leucogabbronorite (see Figure 5.6). The texture of the gabbronorites is either homogenous as shown in Figure 5.6A or contains cm-scale bands varying proportions of leuco- to melanocratic minerals, see Figure 5.6B. Minor green alteration (see Figure 5.6B) is associated with thin (mm-scale) amphibole-rich veins some of which host fine to medium-grained base metal sulphides (BMS).

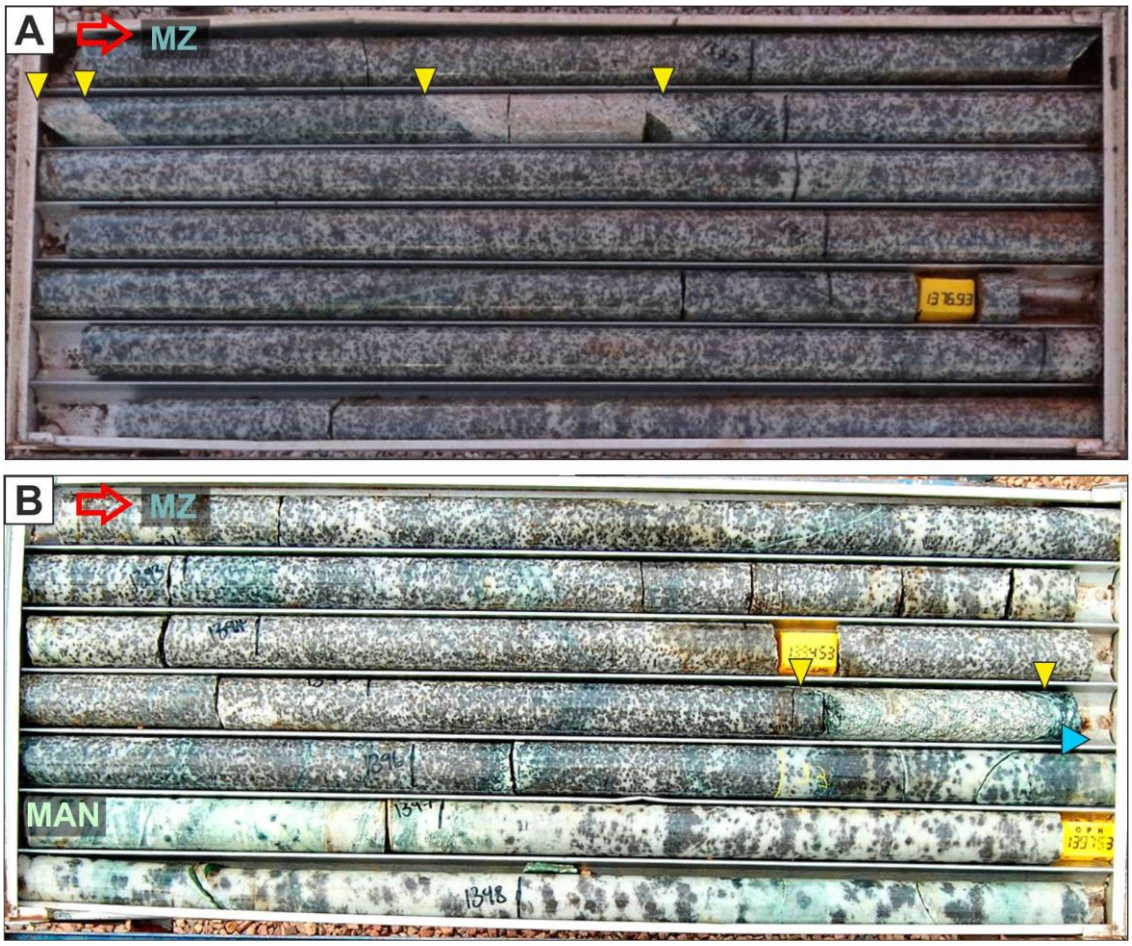

Figure 5.6: Lithological characteristics of the Main Zone unit in the Deep Platreef. (A) Core box 208 (UMT_345) from 1372.37 m to 1378.96 m showing homogenous gabbronorites intruded by granitic veins. (B) Core box 02 (UMT_345_D1) from 1391.89 to 1398.51 m showing the contact between the MZ and the MAN. Note: red arrows point in the downhole direction, yellow triangles point towards granite vein contacts and blue arrows are located on stratigraphic contacts.

The MZ gabbronorites are intruded by a medium-grained and varitextured, subsolvus (two-feldspar) granite. The intrusive contacts are sharp, planar and orientated at between 30° to 40° to the core axis (see Figures 5.6A). Compositionally the granite is composed of 60 vol% feldspar (plagioclase 40 vol% and alkali feldspar 30 vol%), 30 vol% quartz and 10 vol% mafic minerals. The thickness of these granitic intrusions varies from 0.05 m to 6.23 m. No felsic intrusives of this composition were identified below the MZ in this drill hole.

Beneath the MZ is a mottled anorthosite unit (MAN) that is 27.48 m thick (1396.52 m to 1424.00 m). The top contact of the MAN unit with the MZ is sharp but non-planar (see Figure 5.6B). Compositionally, the mottled anorthosite contains approximately between 10 to 40 vol% mafic mottles and 60 to 90 vol% cumulate plagioclase both of which are medium-grained. The mottles are composed of intercumulus pyroxenes, mainly clinopyroxene with lesser orthopyroxene, and they may host BMS. The size of the mottles varies from 1 cm to 5 cm; this variation is illustrated in Figure 5.7A. Where best developed the mottles appear regularly dispersed; moving towards the base of the unit (last 2 metres) the mottles become more elongate (see Figure 5.7B).

Figure 5.7: Lithological characteristics of the MAN unit in the Deep Platreef. (A) Core box 04 (UMT_345_D1) from 1405.13 to 1411.63 m highlighting the variation in size of the mottles within the MAN unit. (B) Core box 215 (UMT_345) from 1418.55 to 1425.19 m showing the basal contact of the MAN with the top of the UP. Note: red arrows indicate the downhole direction, blue triangles point to stratigraphic changes and yellow triangles point to felsic intrusive contacts.

The MAN unit is intruded by a 6.67 m thick quartz-feldspar intrusive (labelled QFV for quartz-feldspar vein), as shown in Figure 5.8A. The QFV is composed of approximately 60 vol% plagioclase and 40 vol% quartz with varying grain sizes from fine to pegmatoidal (mostly coarse-grained) and is varitextured ranging from graphic (see Figure 5.8B) to an immature granular texture (see Figure 5.8C). The contacts between the MAN and QFV

are sharp and orientated at an angle of ≈40° to the core axis (see Figure 5.7B and Figure 5.8C). The plagioclase in the MAN directly adjacent to the QFV appears hydrothermal altered with a pale green colour resulting from the presence of saussurite minerals (see Figure 5.8C).

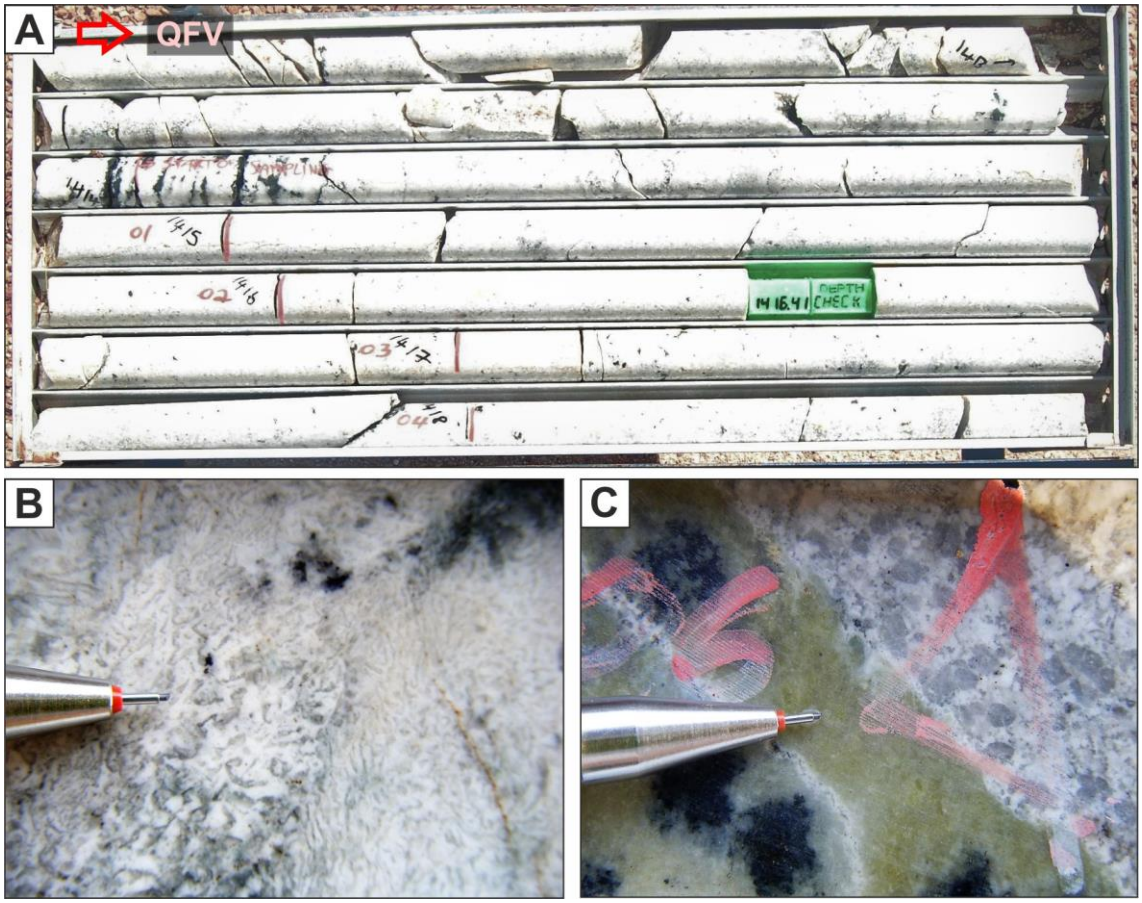

Figure 5.8: Lithological characteristics of the quartz-feldspar vein intruding the MAN unit in the Deep Platreef. (A) Core Box 214 from UMT_345 (1412.10 to 1418.55 m) containing entirely the QFV. (B) A close up of the graphic texture between quartz and plagioclase that characterises parts of the QFV. (C) A close-up of the contact between the QFV and the MAN highlighting the saussuritization of the plagioclase in the MAN unit. Note: red arrows indicate the downhole direction and the silver pencil tip (shown for scale) is 2 cm in length.

The top contact of the Upper Pyroxenite (UP) with the MAN is shown in Figure 5.7B above. The contact represents a sharp compositional change at 90° to the core axis, however on the cm-scale the contact appears irregular and undulating as opposed to planar. Directly below the contact the first 20 to 30 cm of the UP has an altered appearance, as shown in Figure 5.9A. At this locality the UP is fine-grained with the exception of very-coarse grained clinopyroxene oikocrysts creating a poikilitic and inequigranular texture (see Figure 5.9A). Medium-grained phlogopite, as shown in Figure 5.9A, was also identified in this altered section.

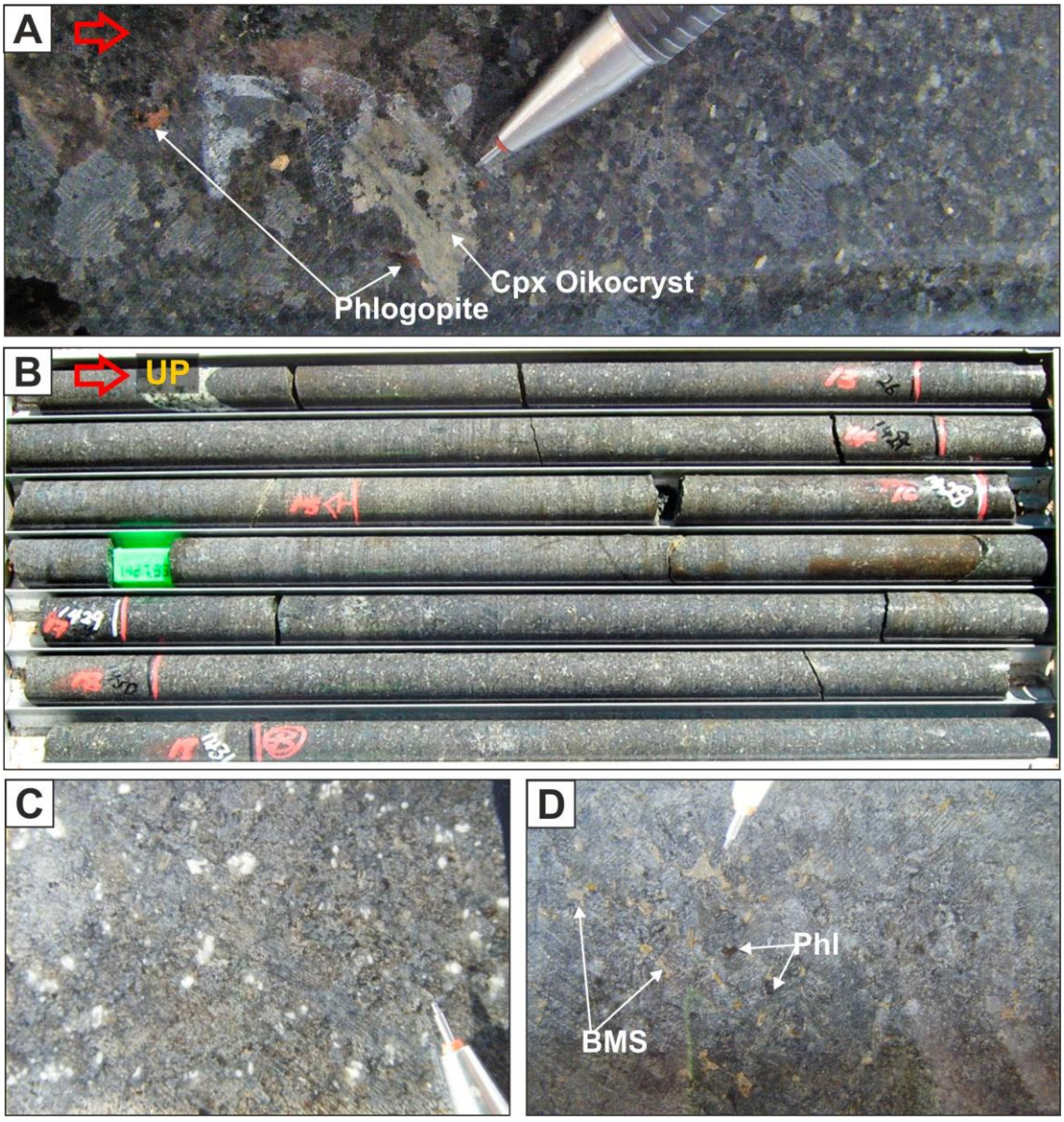

Figure 5.9: Lithological characteristics of the UP unit in the Deep Platreef. (A) The top 10 cm of the UP in UMT_345_D1, showing coarse-grained clinopyroxene (Cpx) oikocrysts and medium-grained phlogopite (Phl). (B) Core box 216 (UMT_345) from 1425.19 to 1431.75 m, illustrating the massive nature of the UP. (C) A close-up of the typical texture of the non-mineralised feldspathic orthopyroxenite. (D) A mineralised section of the UP with interstitial medium-grained base metal sulphides (BMS) with minor associated Phl. Note: red arrows indicate the downhole direction and the silver pencil tip (shown for scale) is 2 cm in length.

The majority of the UP is composed of a massive, homogenous, medium-grained feldspathic orthopyroxenite (FOPX), as shown in Figure 5.9B. The FOPX is composed of approximately 80 vol% cumulate orthopyroxene, 10 to 20 vol% interstitial plagioclase and <10 vol% interstitial clinopyroxene. Orthopyroxene is present as subhedral cumulus crystals whereas clinopyroxene typically forms anhedral oikocrysts. Plagioclase is always found interstitially as anhedral, intercumulus grains that often appear either a fuzzy white colour (see Figure 5.9C) or translucent indicating the early stages of

saussuritization. The interstitial assemblage shows the greatest compositional variation with the plagioclase abundance varying from 5 to 20 vol% and increasing up to 40 vol% over shorter intervals and BMS contributing up to 5 vol% of the interstitial material over specific intervals.

Although initially barren of visible BMS, moving downhole the abundance of BMS increases with observed concentrations varying from 1 to 5 vol% over significant intervals (> 10 metres; see Figure 5.5). Typically, the BMS are fine to medium-grained, interstitial and consist of fractionated pyrrhotite, pentlandite and chalcopyrite (in order of abundance; see Figure 5.9D). The first appearance of BMS in UMT_345 is at 1427.88 m (3.88 m from the top contact) and continues to a depth of 1445 m; an interval of 17.12 m corresponding to the Upper Reef as shown in Figure 5.5. The presence of BMS is interrupted by a quartz-feldspathic veins (QFV) at between 1432.53 to 1433.34 m (0.81 m thick).

The UP is cross-cut by infrequent QFV, examples of which are shown in Appendix A (section A.4). These are similar in terms of their composition and texture to those found in the MAN unit above. In the UP they vary in thickness from 0.81 m to 0.04 m. The contacts between the UP and the QFV are orientated at ≈ 50° to the core axis. The contact morphology varies from straight and planar to undulating and irregular. The contact relationships also provide evidence for the mode of emplacement of the QFV as an intrusion with the contact showing apophysis and the entrainment of the host rock. There is often evidence of felsic alteration of the host UP on either side of the vein with varying degrees of alteration of orthopyroxene to tremolite and plagioclase to sausserite minerals, accompanied by elevated phlogopite contents.

The first chromite-stringer or '1st CR-STR' is intersected at a depth of 1443.45 m (see Figure 5.10A and 5.10C). The 1st CR-STR is 1 cm thick and consists of 90% chromite with 10% interstitial orthopyroxene and plagioclase. The location of this chromite stringer corresponds to the beginning of the second mineralised interval, the Middle Reef as shown in Figure 5.5. The 2nd CR-STR is located three metres below the first at 1446.65 m.

The 2nd CR-STR is 1 cm thick and composed of 85 vol% chromite with 10 vol% interstitial plagioclase and around 5 vol% BMS. It is separated from the 3rd CR-STR by a noritic (>20 vol% plagioclase) region with disseminated chromite (see Figure 5.10B and 5.10D).The 3rd CR-STR is similar in appearance and composition to the 2nd CR-STR, however it is thicker at 2 cm. Below the 3rd CR-STR the plagioclase content increases to 50 vol% over a 40 cm before returning to 20 vol% upon reaching the 4th CR-STR. There

is a slight variation in the deflection hole (UMT_345_D1) with this noritic unit leading up to the 4th CR-STR appearing varitextured with pegmatoidal regions concentrating the plagioclase content (see Figure 5.10B and 5.10E).

The 4th CR-STR, located at 1447.20 to 1447.24 m, is the thickest at 4 cm and was observed to be magnetic (all previous stringers non-magnetic). Compositionally, it is more disseminated with ≈70% chromite and 30% a mixture of plagioclase, orthopyroxene and clinopyroxene. This final chromite stringer marks the base of the UP unit and the beginning of the Middle Pyroxenite (MP) unit; specifically the upper part (MP_U) defined as having a pegmatoidal texture ± olivine.

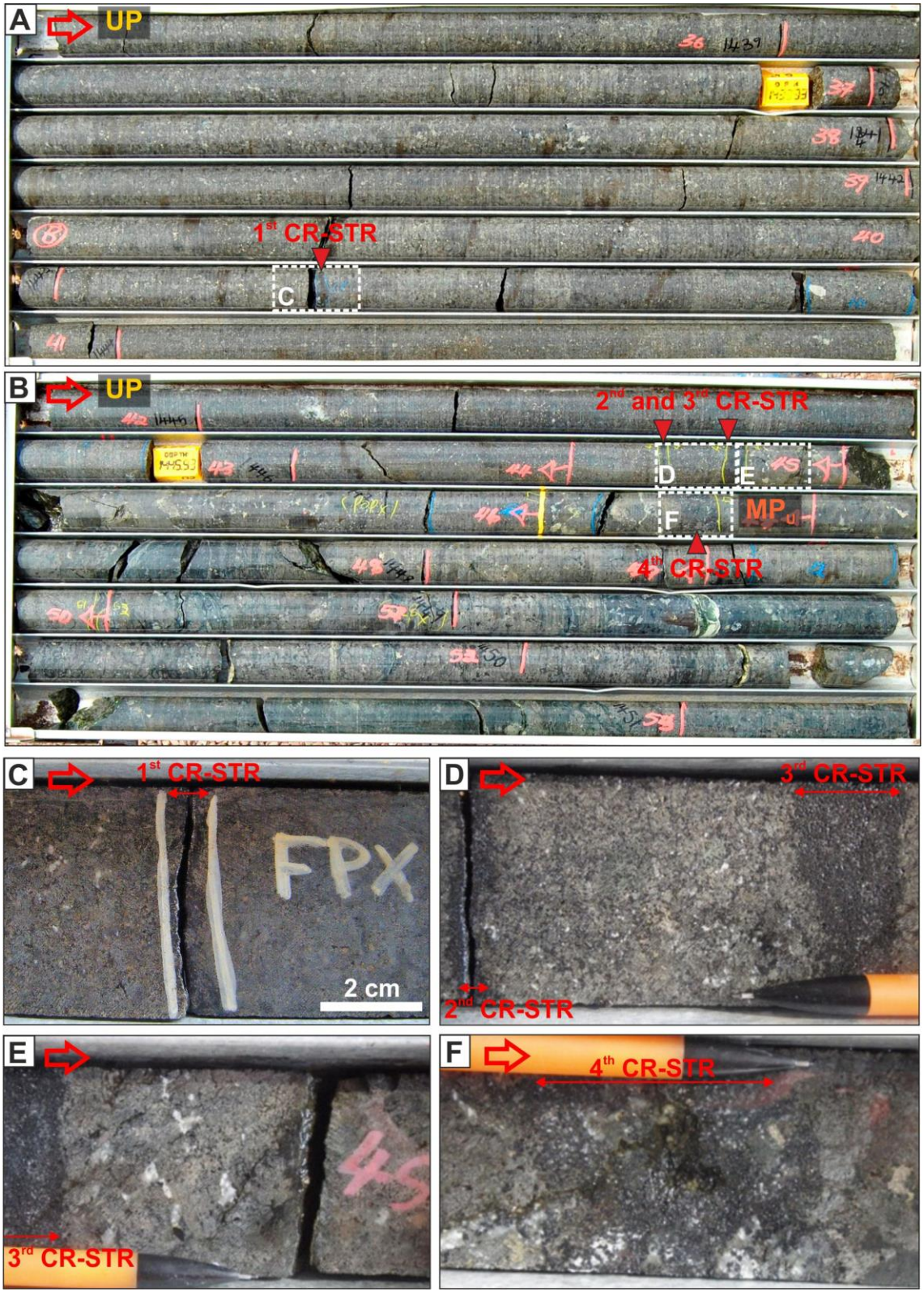

Figure 5.10: Lithological characteristics across the transition from the UP to the MP stratigraphic units. All photos taken from drill hole UMT_345_D1. (A) Core box 09 (1438.22 to 1444.84 m) hosting the UP and the 1st CR-STR. (B) Core box 10 (1444.84 to 1451.24 m) containing the 2nd, 3rd and 4th CR-STR and the contact between the UP and the MP. (C to F) Close up pictures of the chromite stringers as identified in A and B, respectively. Note: red arrows indicate the downhole direction, red triangles point to chromite stringers and the black pencil tip (shown for scale) is 2 cm in length.

The base of the UP is marked by the transition to pegmatoidal grain sizes accompanied by the first appearance of olivine. In UMT_345 and UMT_345_D1 the top of the pegmatoid is marked by the basal chromite stringer (4th CR-STR), as mentioned above. The first 4.41 m of the MP, from 1447.23 to 1451.64 m, is composed of a pegmatoidal feldspathic harzburgite; assigned the MP_U stratigraphic code (see Figure 5.11A and 5.11B). The feldspathic harzburgite consists of approximately 60% orthopyroxene with varying concentrations of olivine 20 to 40%, plagioclase <10% and BMS up to 10%. Texturally, this unit is defined by orthopyroxene oikocrysts surrounding medium-grained, anhedral, serpentinised olivine chadacrysts (see Figure 5.11A). Where enclosed entirely by orthopyroxene olivine appears smaller than where they are found interstitially with plagioclase. The BMS are medium to coarse grained and form blebs of pyrrhotite, pentlandite and chalcopyrite given in order of abundance. The olivine content gradually disappears and grades into a 1.5 m thick varitextured orthopyroxenite up to a 0.35 m thick QFV at 1453.12 m (see Figure 5.11C).

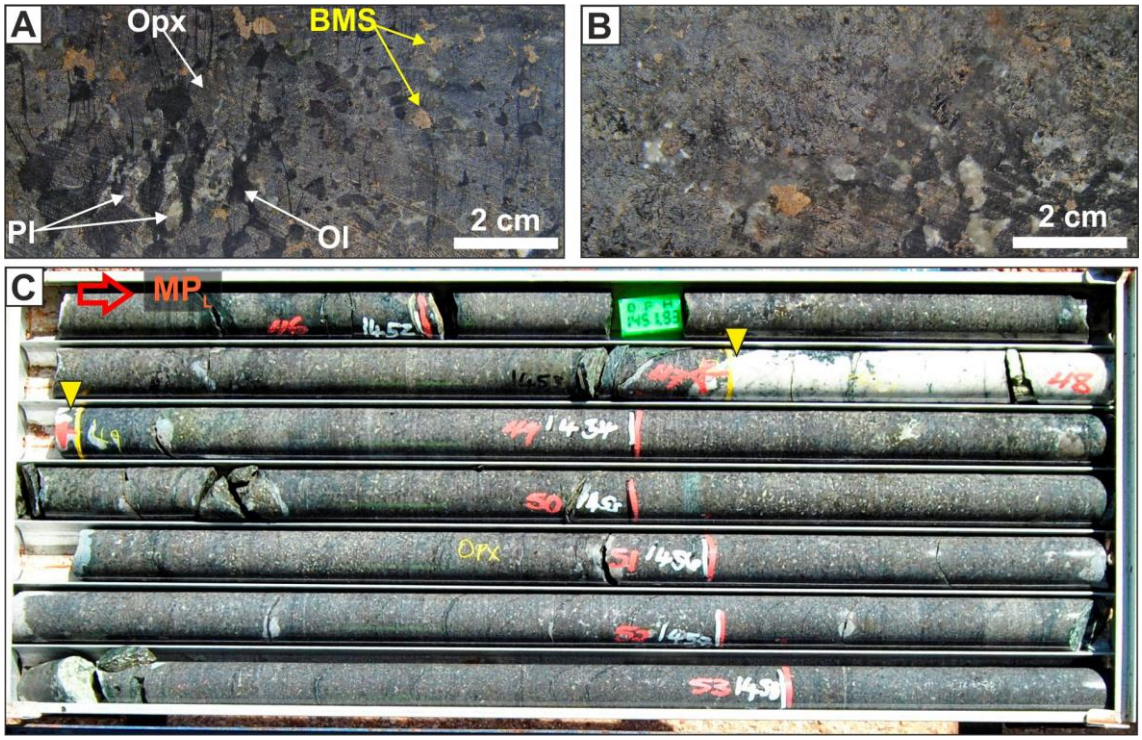

Figure 5.11: Lithological characteristics of the MP unit in the Deep Platreef. All core boxes from UMT_345. (A and B) Examples of the pegmatoidal olivine orthopyroxenite. (C) Core box 220 (1451.65 to 1458.30 m) containing the massive lower feldspathic orthopyroxenite. Note: the red arrow points in the downhole direction and yellow triangles point to intrusive contacts.

The lower part of the MP unit (MP_L), from 1453.47 m (see Figure 5.11C) to the basal contact, is a relatively homogenous, unmineralized, massive orthopyroxenite. This orthopyroxenite has varying plagioclase content (0 to 10 vol%) varying over the metre-scale. The contact between the MP and the Norite Cycles 2 (NC2) unit is orientated at

90° to the core axis and is quite sharp, as shown in Figure 5.12. The contact is defined by: (1) an increase in the plagioclase content (>20 %); (2) the first appearance of plagioclase as a cumulus mineral phase and (3) the development of cyclical compositional layering.

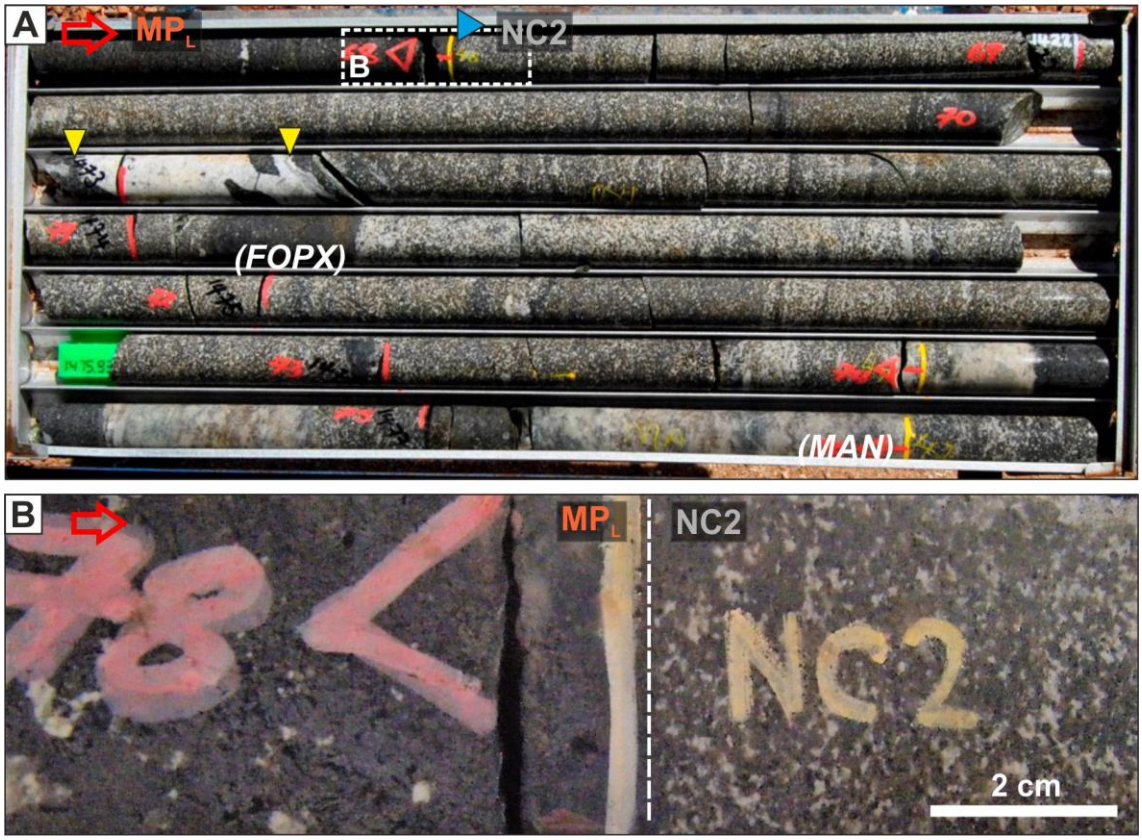

Figure 5.12: Lithological characteristics of the contact between the MP_L and the NC2 units in the Deep Platreef. (A) Core box 223 (UMT_345) from 1471.07 to 1477.57 m, showing the top contact of the NC2 with the overlying MP_L. (B) A close up of the contact between the MP_L and NC2. Note: red arrow points in the downhole direction, blue triangles mark stratigraphic contacts and yellow triangles point to felsic intrusive contacts.

The NC2 unit represents a thick sequence (up to 45 m) of repetitive cycles recording a complete and incomplete sequences of chromite-pyroxenite (+/- BMS)-norite-anorthosite (+/- mottles). The norites are typically medium-grained and equigranular with cumulate and intercumulus orthopyroxene and plagioclase with minor clinopyroxene. The cycles range in thickness from <0.10 to >3 m; approximately 58 cycles were recorded in UMT_345 and 53 in UMT_345_D1 so the average cycles are < 1 m in thickness. Some of the best examples of these cycles are preserved in drill hole UMT_336_D1 and polished core from here is shown in Figure 5.13. Rarely is a whole cycle preserved more typically the normal fractionation sequence is disrupted by either injections of new magma (felsic and mafic compositions) that are planar (see Figure 5.13) or irregular (e.g. ball and flame structures see Figure 5.14B) suggesting crystal slumps.

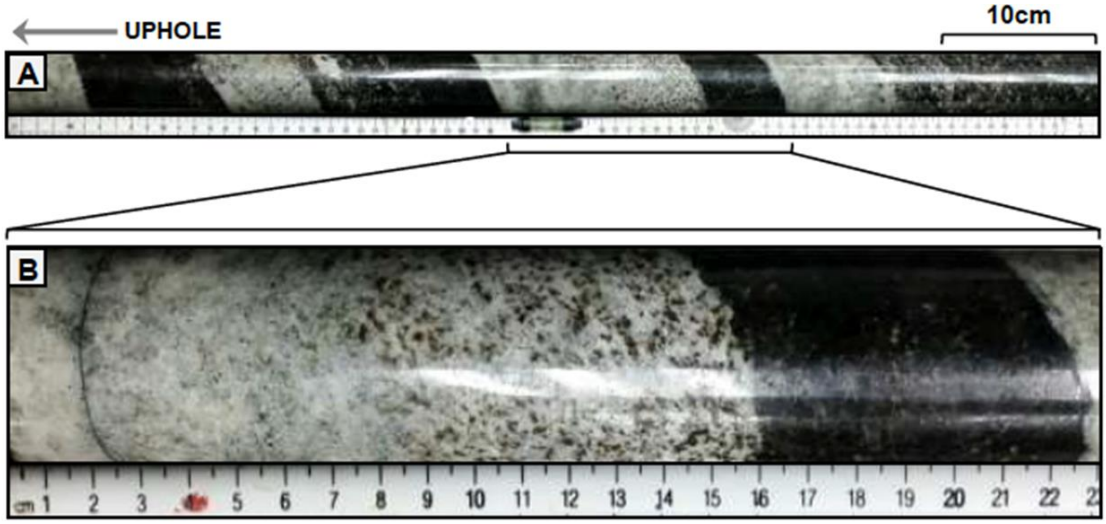

Figure 5.13: Type-examples of the magmatic cycles recorded in the NC2 unit recording steady-state normal fractionation patterns. (A) Polished core from UMT 336 D1 at 1157.68 to 1158.45 m showing four norite cycles. (B) Close up photograph of polished core at 1158.00 to 1158.22 m showing a single norite cycle. Photos from Nodder, (2015).

The base of these cycles are typically sharp and may be planar with a 1 to 2 mm thick chromite stringer on the basal contact (see Figure 5.14A and 5.14C) although irregular and undulating contacts are also observed as shown in Figure 5.14B. The basal orthopyroxenite typically hosts BMS mineralisation that carries PGE grade; these units are too thin to be economically extracted.

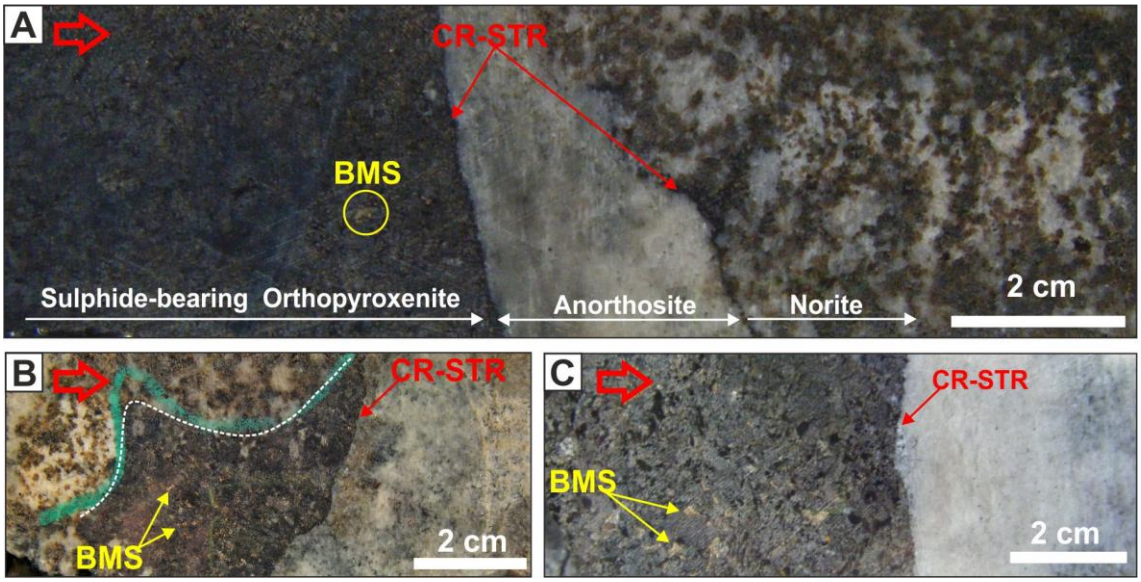

Figure 5.14: Lithological characteristics of the BMS mineralised base of cycles in the NC2 unit in the Deep Platreef. (A) Chromite stringers (CR-STR) present on the basal contact of the pyroxenite and on the contact between anorthosite and norite. (B) An irregularly shaped orthopyroxenite unit hosting BMS at 10 vol%; example of a ball and flame structure possibly representing a slump. (C) A sharp planar contact between anorthosite and sulphide-bearing orthopyroxenite. Note: red arrows point in the downhole direction.

The base of the NC2 unit is represented by a gradational loss of cyclicity accompanied by the dominance of pyroxenitic over noritic lithologies. Over the transitional interval,

from 1515.85 to 1518.91 m, feldspathic orthopyroxenite and norites are interlayered and there is an increase in BMS and disseminated chromite. This unit is known as the Lower Pyroxenite (LP) and is relatively thin compared to other stratigraphic units at 4.09 m; it marks the beginning of the Lower Reef mineralised interval as shown in Figure 5.5. This interval is varitextured between poikilitic and pegmatoidal with coarse-grained pyroxenite bands and medium-grained norites. Over short intervals, up to 30 cm's, the LP is quite compositionally diverse with elevated olivine (up to 20%) and clinopyroxene (up to 40 %). The base of the LP is marked by the presence of two lead chromite stingers; the first chromite stinger appears discontinuous, however the basal chromite stringer is 6 mm thick followed by a coarse-grained feldspathic orhtopyroxenite with medium-grained interstitial BMS above the top contact of the Main Chromitite unit (MCHR, see Figure 5.15).

The Main Chromitite (MCHR) unit as present in UMT_345 forms a continuous layer 1.09 m thick as shown in Figure 5.15. Chromite is present as fine-grained disseminations comprising between 60 to 80 vol%. A significant silicate proportion (up to 40 vol%) is composed of predominantly pegmatoidal orthopyroxene oikocrysts (containing chromite chadacrysts) and interstitial plagioclase. Locally chromite forms dense concentrations producing a schlieren texture where pegmatoidal orthopyroxene oikiocrysts are present. Calcite veins are common (see Figure 5.15) orientated at ≈ 80 to 90° to the core axis that range in thickness from 3 to 8 mm. The undulating base of the MCHR unit at 1521.13 m is shown in Figure 5.15, in contact with fluid altered orthopyroxenite with serpentinised olivine.

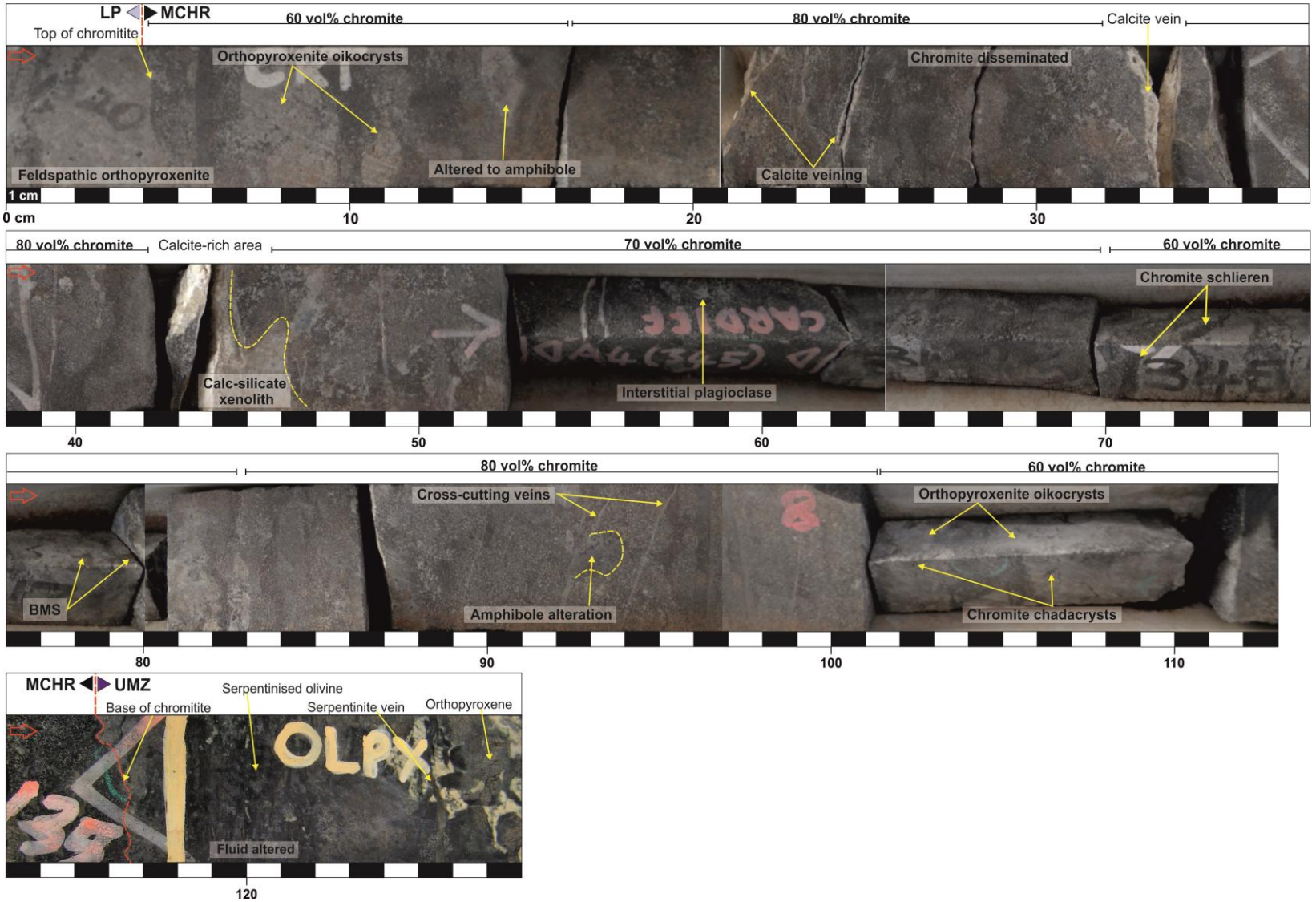

Figure 5.15: Lithological characteristics of the MCHR unit as present in drill hole UMT_345 in the Deep Platreef. Note: red arrows point in the downhole direction.

The Ultramafic Zone (UMZ) underlying the MCHR unit consists of a mixture of lithologies, see examples in Figure 5.16, dominated by a feldspathic harzburgite (see Figure 5.16A), pegmatoidal orthopyroxenite, olivine orthopyroxenite and olivine gabbronorites (see Figure 5.16C). The BMS are unevenly distributed and localised over intervals of around a metre thick where they can be up to 10 vol% (more typically between 2 to 5 vol%) and their presence typically corresponds with a spike in PGE grade. The composition of the feldspathic harzburgite is variable but commonly contains olivine (up to 40 vol%), orthopyroxene (up to 50 vol%), plagioclase (5 vol%) and BMS (5 vol%) and is frequently pegmatoidal (see Figure 5.16A). The olivine content is strongly serpentinised and cross-cutting magnetite veins are common. The pyroxenite-dominated lithologies are typically pegmatoidal. There are a range of sulphide textures observed within this unit including net-textured (see Figure 5.16B); massive pods in pegmatoidal regions and medium-grained interstitial (see Figure 5.16C).

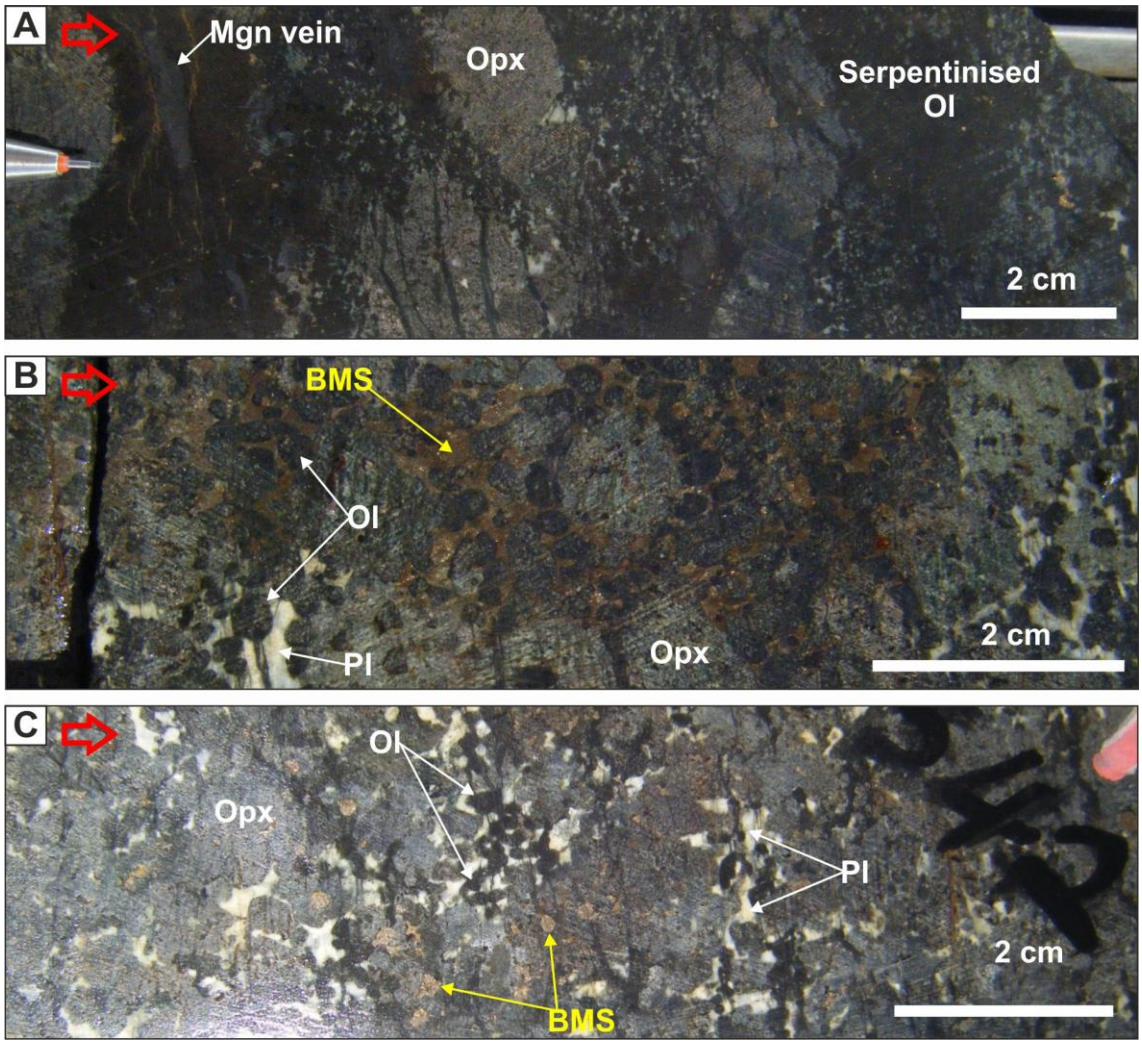

Figure 5.16: Lithological characteristics of the compositionally heterogenous UMZ in the Deep Platreef. (A) An example of feldspathic harzburgite with coarse-grained orthopyroxene (Opx) and fine-grained olivine (Ol). (B) Sulphide-rich olivine gabbronorite. (C) Olivine gabbronorite

comprising coarse-grained pyroxenes concentrating the sulphides and with interstitial medium-grained troctolite. Note: red arrows point in the downhole direction.

An overview of the olivine gabbronorite at the base of the UMZ as intersected in the deeper drill hole (UMT_345; from 1543.4 to 1551.21m) are shown in Figure 5.17A. They consist of coarse-grained orthopyroxene and clinopyroxene with interstitial sulphide and medium-grained rounded olivine in the interstitial regions (see Figure 5.16C); this rock type is similar in appearance to the mineralised harzburgite F zone rocks at Waterberg (Huthmann et al,. 2018).

In UMT_345, the last 45 meters to the end of the hole at 1596.20 m are composed of a homogenous fine to medium grained feldspathic clinopyroxenite (FCPX) known as the Hybrid Zone (HZ_{FCPX}). This has a pseudo-porphyry texture defined by coarse-grained, green clinopyroxene (see Figure 5.17C); the rest of the rock is composed of medium-grained orthopyroxene (creating a brown-sugar texture, see Figure 5.17C) and interstitial plagioclase. Medium-grained interstitial BMS are heterogenously distributed and more common towards the top contact. A xenolith or interlayer of this unit is present in the overlying UMZ from 1543.4 to 1544.98 m (an interval of 1.58 m). This can be explained in three ways: (1) the younger UMZ unit bifurcated during emplacement above the HZ_{FCPX}; (2) the HZ_{FCPX} intruded later, out-of-sequence, bifurcating the pre-existing UMZ lithology; (3) the intrusion of the UMZ lithology is interrupted by another pulse of HZ_{FCPX} magma. Model 1 considered by the author to be the most likely with evidence for bifurcating lithologies in the Bushveld Complex observed elsewhere such as at the Dwars River UG1 chromitite outcrop (see Chapter 3 section 3.2). Compositionally the rock contains orthopyroxene (40 vol%), plagioclase (40 vol%) and clinopyroxene (20 vol%) and an inequigranular texture dominates.

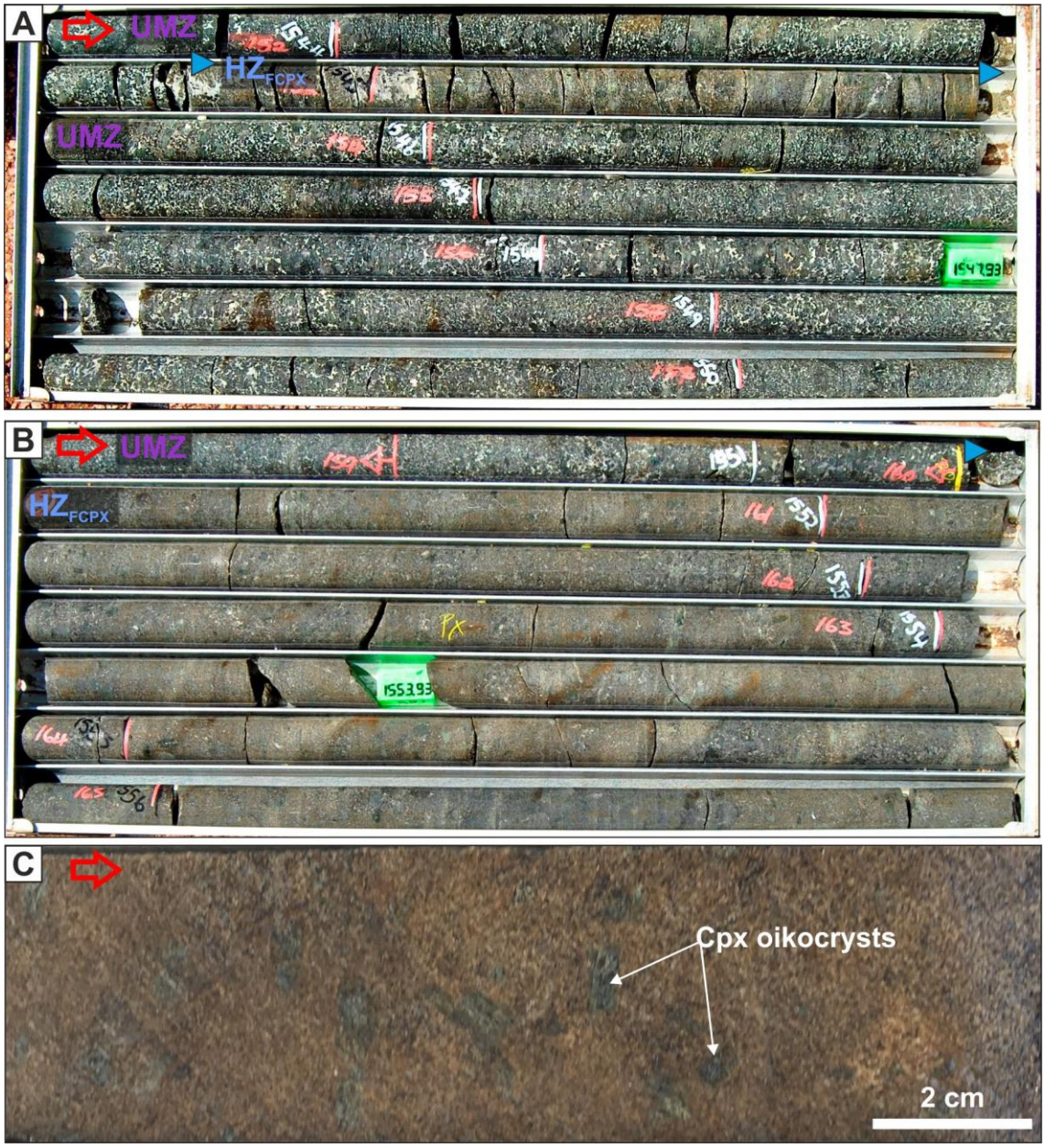

Figure 5.17: Lithological characteristics of the HZ_{FCPX} unit in the Deep Platreef. All photos from UMT_345. (A) Core box 234 from 1543.71 to 1550.28 m, hosting the base of the UMZ and an interlayer of the HZ_{FCPX} unit. (B) Core box 235 from 1550.28 to 1556.83. (C) Representative texture of the HZ (GBR) unit with a pseudo-porphyry texture. Note: red arrows point in the downhole direction and blue arrows mark stratigraphic contacts.

5.3.2 The Thick Flatreef (TMT_006_D2)

The results of the geological logging of the Thick Flatreef as sampled in TMT_006_D2 are shown in Figure 5.19; the entire drill hole was logged. TMT_006_D2 is a deflection hole and as such the first stratigraphic unit intercepted is the Norite Cycle 1 unit (NC1).

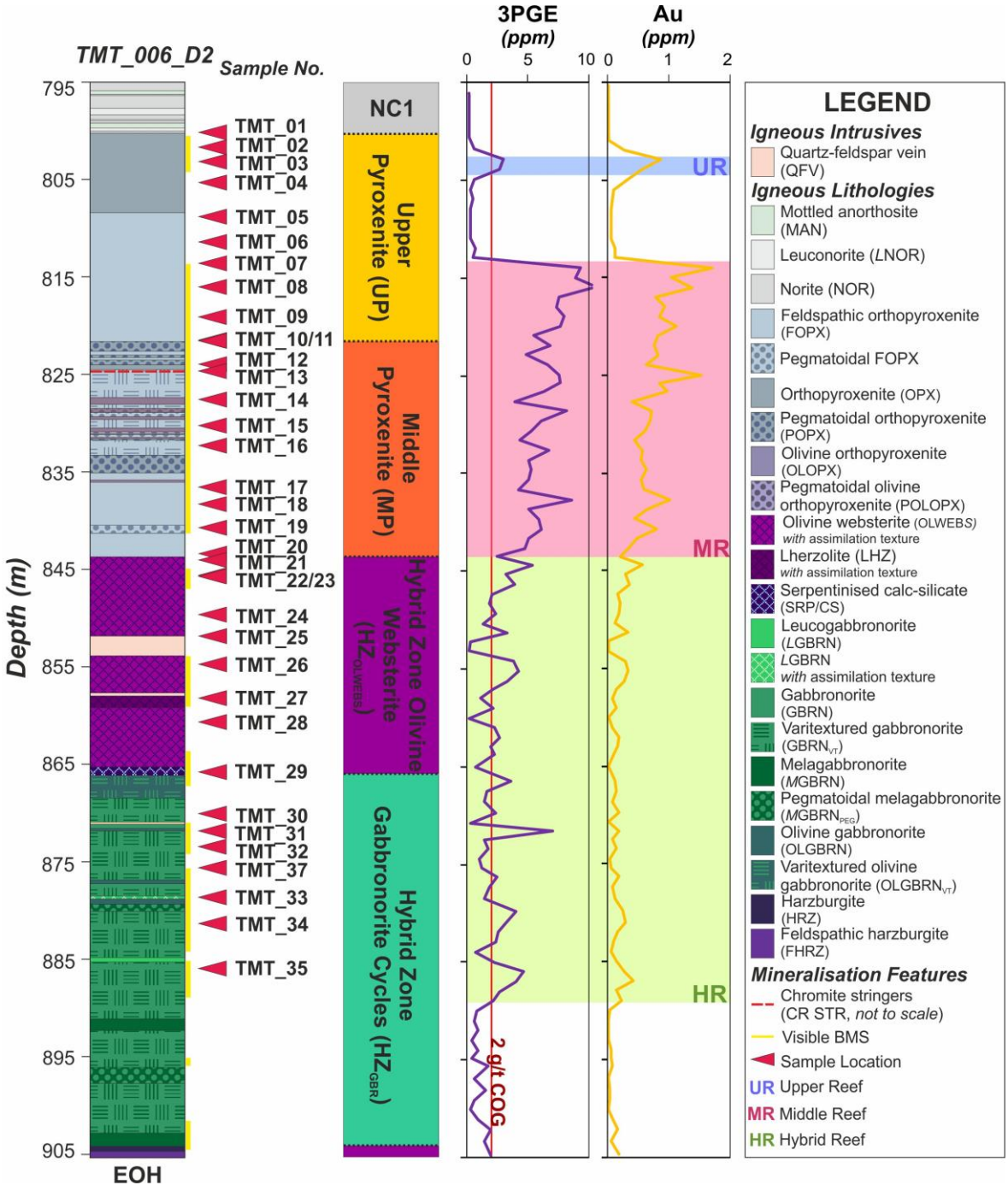

Figure 5.18: Geological logging data, sampling locations, stratigraphic codes and grade profiles for the Thick Flatreef as sampled in the deflection drill hole TMT_006_D2. Note: grade data is based on 1 m composites and provided by Ivanplats Pty Ltd.

The NC1 unit as recovered in TMT_006_D2 is 5.32 m thick; over this interval eight cycles are reasonably well developed. A typical cycle in this unit is composed of norite-leuconorite-anorthosite (with mottles); notably no chromite or base metal sulphides (BMS) were observed at the base of the cycles as characterises the NC2 unit of the Deep Platreef. This corresponds to an absence of grade within this unit as shown in Figure 5.18.

The contact between the base of the NC1 and the Upper Pyroxenite (UP) is gradational. The first 8.15 m of the UP is composed of orthopyroxenite with a pseudo-porphyry texture resulting from the presence of coarser-grained clinopyroxene. On the whole the UP is very similar in appearance as described for the Deep Platreef; typical features are shown in Appendix A (section A.5). BMS are present within the UP unit over specific intervals; the first interval of sulphide mineralisation is present from 800.44 to 804.15 m (a total of 3.71 m) the assemblage is dominated by pyrrhotite found interstitial in abundances up to 10 vol%. This corresponds to the Upper Reef mineralised interval (see Figure 5.18) with the appearance of grade directly corresponding to the presence of visible BMS. This is followed by an interval of 9.43 m of no visible BMS and is correspondingly barren of mineralisation. This barren interval contains regularly-spaced chlorite/serpentinite veining orientated at between 70 and 80 ° to the core axis.

At 808.33 m the plagioclase level increases to between 10 to 20 vol% and the dominant lithology is feldspathic orthopyroxenite. BMS reappears at 813.58 m and are continuously present to 841.26 m (a total of >27 m) with visual estimates on the abundance varying from <5 to 20 vol%. The highest concentrations (20 vol %) of interstitial BMS are on the contact between the UP and the Middle Pyroxenite (MP) at 821.55 m.

The transition to the MP is gradual and distinguished by an increase in grain size from medium to coarse-grained feldspathic orthopyroxenite. In contrast to the Deep Platreef there are no lead stringers into the MP; chromite is present near this contact (at 823.96 m and 824.64 m) but as disseminations as opposed to a continuous layer. The MP is varitextured with massive, pegmatoidal and poikilitic textures observed in addition to more localised sections with an assimilation overprint.

Pegmatoidal regions, ranging from 20 to 100 cm in thickness, are regularly developed (for examples see Appendix A section A.5). These pegmatoids can be dominated by feldspar or orthopyroxene. In the feldspar-dominated pegmatoid the feldspar has a strained appearance and the surrounding orthopyroxene grains appear fragmented with green (amphibole) alteration on their edges. This indicates that this pegmatoid may be related to late-stage felsic fluids. In contrast, the orthopyroxene pegmatoids appear primary magmatic. These pegmatoidal regions often concentrate BMS dominated by pyrrhotite into massive pods or as medium-grained and interstitial.

Olivine-bearing lithologies are irregularly identified and typically adjacent to mafic pegmatoids and/or fine-grained serpentinite calc-silicate xenoliths as shown in Figure 5.19. Compositionally they are composed of 80 vol% orthopyroxene, 5 to 10 vol%

olivine, 5 vol% plagioclase and up to 10 vol% BMS (see Figure 5.19B) and are logged as olivine orthopyroxenite. Texturally, the olivine orthopyroxenites are poikilitic with fine to medium grained olivine chadacrysts enclosed in medium to coarse-grained orthopyroxene oikocrysts (see Figure 5.19B). They contain significantly less and finer grained olivine than the equivalent unit in the Deep Platreef.

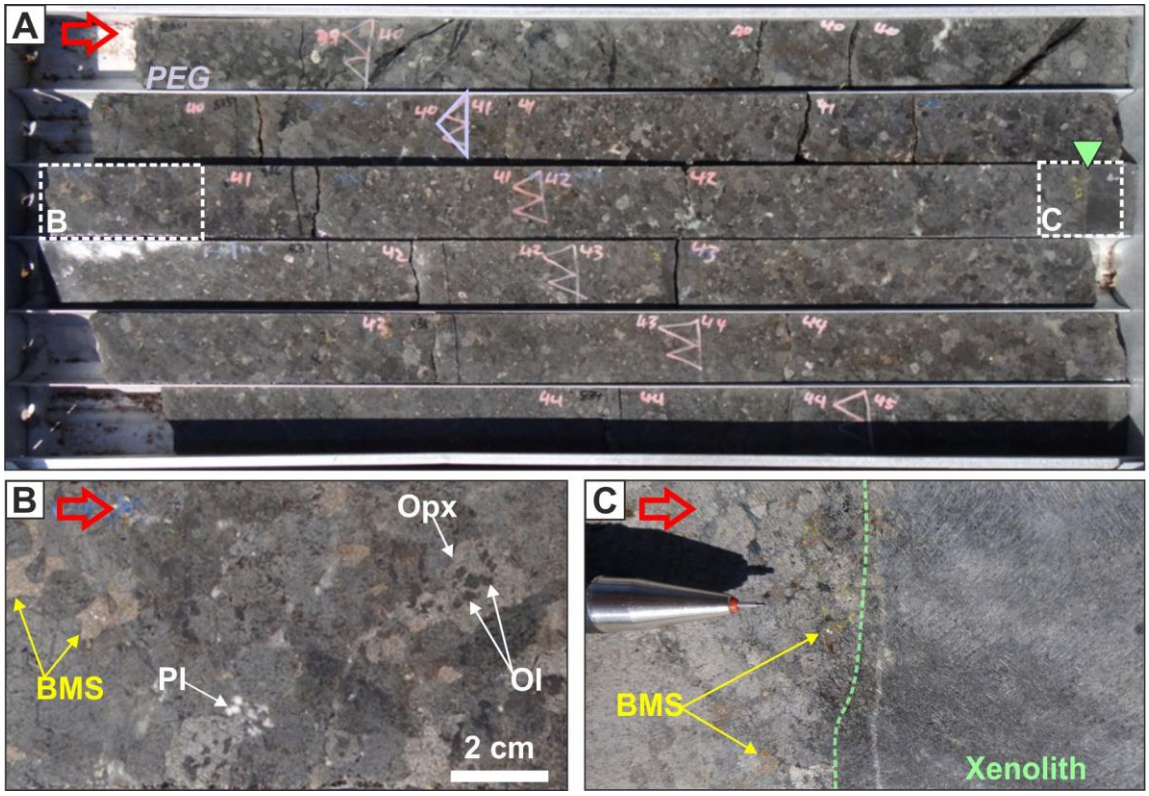

Figure 5.19: Lithological characteristics of the MP unit of the Thick Flatreef. (A) Core box containing core from 834 to 839 m. (B) Olivine orthopyroxenite showing a typical poikilitic texture. (C) The sharp contact between xenolith and the MP unit. Note: red arrow points in the downhole direction, lilac triangles denote pegmatoidal intervals, the green triangle points to a xenolith contact and the silver pencil tip (shown for scale) is 2 cm in length.

Towards the base of the MP there are thin units (1.5 cm and 7 cm thick) of fine-grained, black, serpentinite interpreted as assimilated country rock of calc-silicate composition (see Figure 5.19C). The thicker serpentinite unit is located on the contact between the MP and the underlying olivine-websterite Hybrid Zone (HZ_{OLWEBS}) at 843.86 m. The grade decreases significantly across this boundary from an average of >5 g/t in the UP and MP to <5 g/t (3 PGE + Au) in the HZ_{OLWEBS} unit, as shown on Figure 5.18**.** This corresponds to significant changes in the observed lithologies from predominantly magmatic pyroxenites to parapyroxenites with a strong assimilation overprint hence the use of the term 'Hybrid Zone'. They are described as olivine websterite because the dominant minerals are clinopyroxene and olivine.

The grade profile for the HZ_{OLWEBS} is spiky (see Figure 5.18); this corresponds to the more patchy occurrence of visible BMS and generally lower concentrations (1 to 5 vol%). Elevated BMS concentrations of up to 10 vol% are present from 845.58 to 847 m (a total of 1.48 m) corresponding to an interval of fine-grained disseminated chromite (up to 70 vol% chromite) within a clinopyroxenite. Fine-grained wispy pyrrhotite-dominated BMS with a brassy appearance are associated with serpentinised areas (see Figure 5.20A). The grade profile for the HZ_{OLWEBS} is interrupted by the intrusion of a 2.04 m thick medium-grained granitic vein.

The olivine content within the parapyroxenites is erratically distributed and ranges from 10 vol% to 100 vol%; for examples see Figure 5.20. The presence of olivine is accompanied by a strong serpentinite overprint often forming wispy veins (see Figure 5.20). Massive serpentinites often accompany olivine; they have irregularly shaped contacts with the parapyroxenites that may be convex (see Figure 5.20A) or concave (see Figure 5.20B). Plagioclase is a minor component within the HZ_{OLWEBS} with concentrations typically <5 vol%.

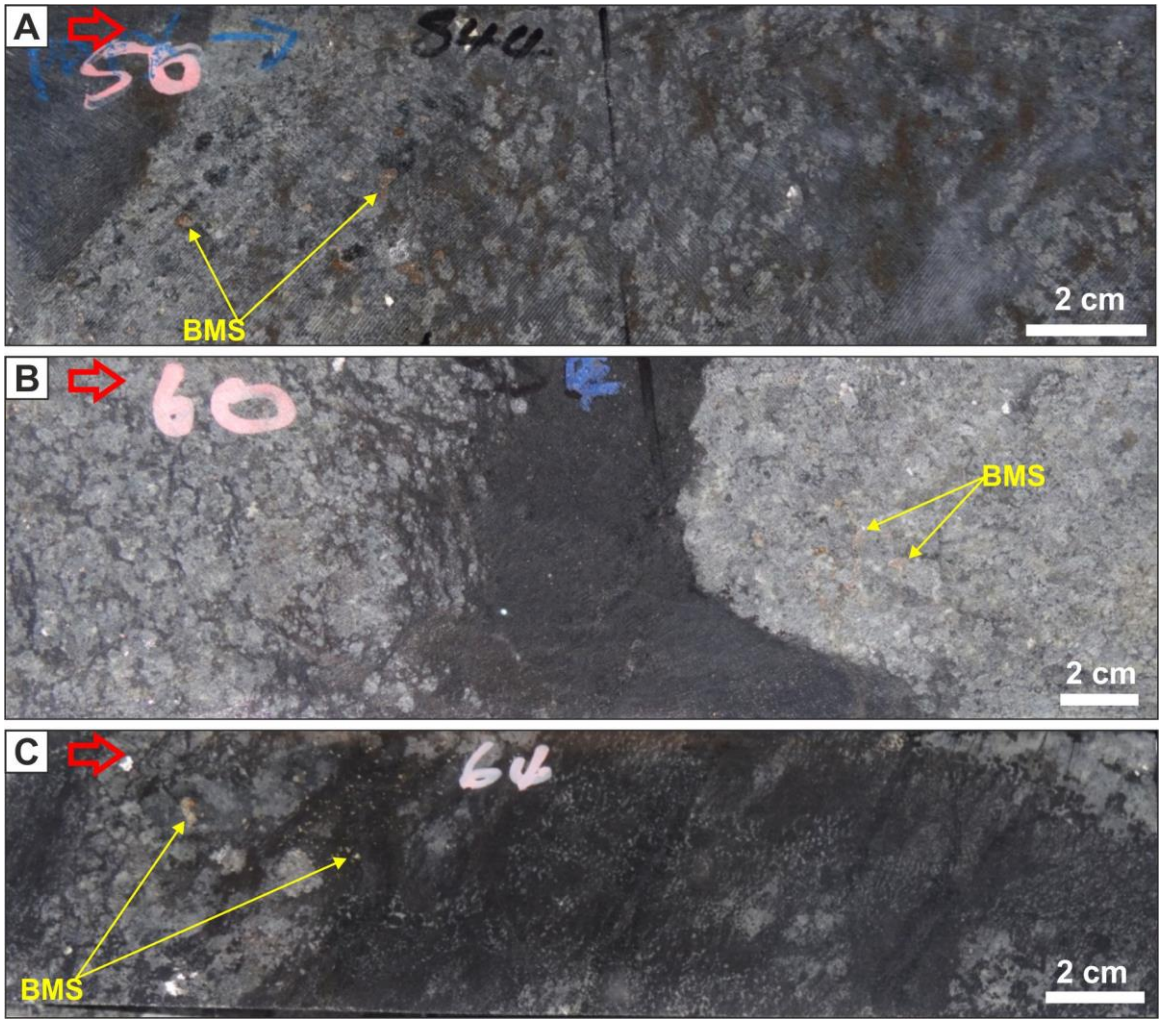

Figure 5.20: Lithological characteristics of the strongly altered HZ_{OLWEBS} unit in the Thick Flatreef.

(A) Parapyroxenite showing significant alteration with wispy serpentinite and BMS; in the top left corner is a strongly serpentinised xenolith. (B) A concave contact between a dense serpentinite and parapyroxenite. (C) Fine-grained subhedral olivine concentrate BMS, nearby parapyroxenite altered. Note: red arrows point in the downhole direction.

The base of the HZ_{OLWEBS} is marked by the presence of a 0.87 m thick interval of serpentinization, highlighted in Figure 5.21A; beneath this there is an increasing felsic component, less olivine and less serpentinization. This marks a noticeable change in the contamination style at a depth of 866 m extending to 902.7 m an interval of 36.7 m.

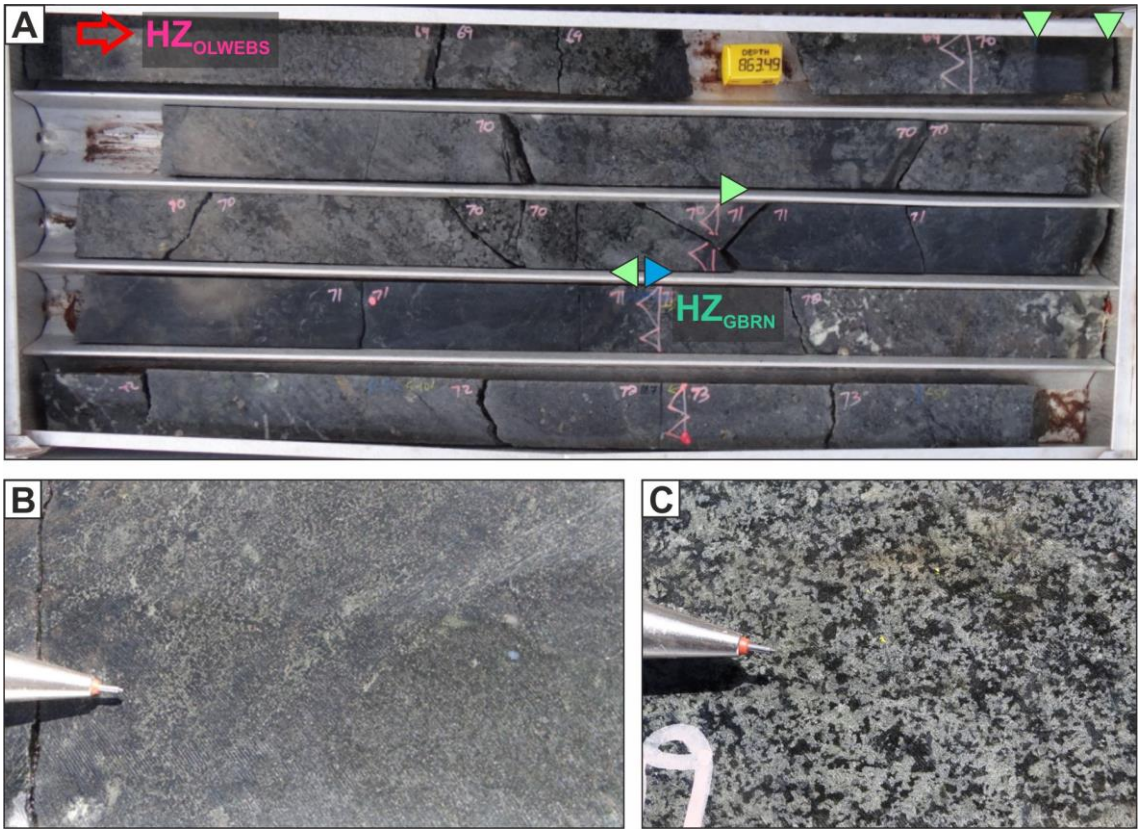

Figure 5.21: Lithological characteristics of the contact between the HZ_{OLWEBS} unit and the HZ_{GBRN} unit in the Thick Flatreef. (A) Core box containing core from 883 to 887 m showing the contact between the HZ_{OLWEBS} and HZ_{GBRN}. (B) Close up of the texture of the fine-grained serpentinite. (C) Example of an assimilation texture in the parapyroxenites directly above serpentinite. Note: red arrows point in the downhole direction, green triangles point to xenoliths, blue triangles are located on stratigraphic contacts and the silver pencil tip (shown for scale) is 2 cm in length.

The gabbronoritic rocks of the Gabbronorite Hybrid Zone (HZ_{GBRN}) are varitextured as demonstrated in Figure 5.22; orthopyroxene is typically fine to medium grained whereas clinopyroxene is typically coarse-grained to pegmatoidal and found in clusters or as bands (see Figure 5.22B). Compositionally the gabbronorites range from leuco- to melanogabbronorites; other lithologies present include parapyroxenites (in the top few metres of the unit) and rare olivine gabbronorite. The pyrrhotite-dominated sulphides form interstitially to coarse-grained clinopyroxene found in bands (see Figure 5.22B) or as coalesced masses in the finer-grained parts (see Figure 5.22C). This unit contains

phlogopite and sulphide-bearing quartz-feldspar veins similar in appearance to those previously identified in the Deep Platreef. One interval of fine-grained disseminated chromite was identified in a clinopyroxenite (see Figure 5.22E); the accumulations of chromite are noticeably finer-grained than those in the Deep Platreef.

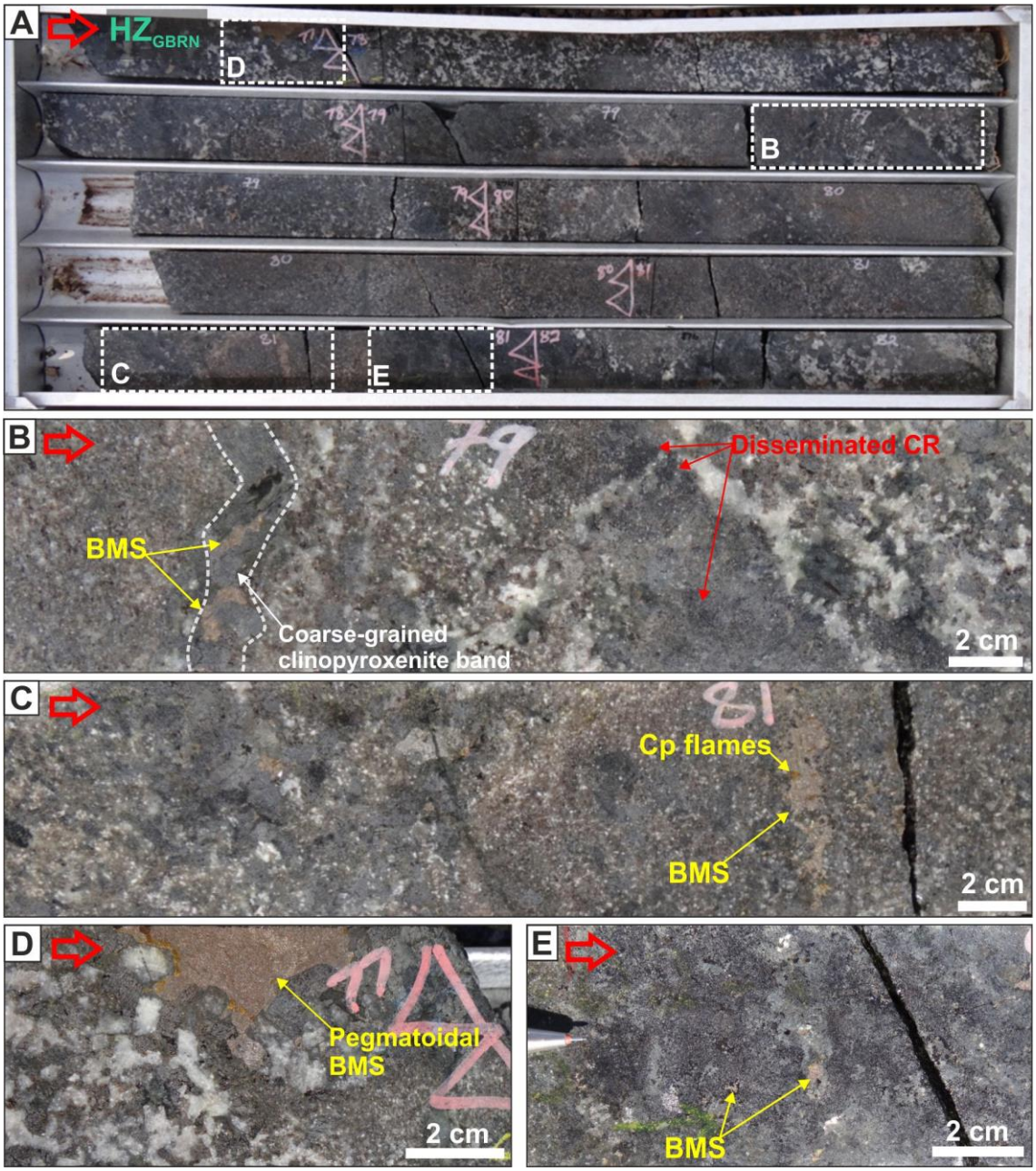

Figure 5.22: Lithological characteristics of the HZ_{GBRN} unit in the Thick Flatreef. The textural settings of medium to pegmatoidal BMS are also highlighted. (A) Core box hosting the vari-textured gabbronorite rocks of the HZ_{GBRN} from 872 to 876 m. (B) Coarse-grained clinopyroxene bands concentrates BMS, finer grained disseminated chromite in a fine-grained gabbronorite. (C) A band of pyrrhotite-dominated sulphide with flames of chalcopyrite on edges hosted in fine grained gabbronorite. (D) A pyrrhotite-dominated pegmatoidal sulphide in leucogabbronorite. (E) Disseminated fine-grained chromite and blebby BMS in clinopyroxenite. Note: red arrows point in the downhole direction.

5.3.3 The Normal Flatreef (UMT_233)

The results of the geological logging of drill hole UMT_233 intersecting the Normal Flatreef are shown in Figure 5.23. The first unit logged in UMT_233 was the Norite Cycles 1 (NC1) unit beneath the Main Zone (the contact was not logged).

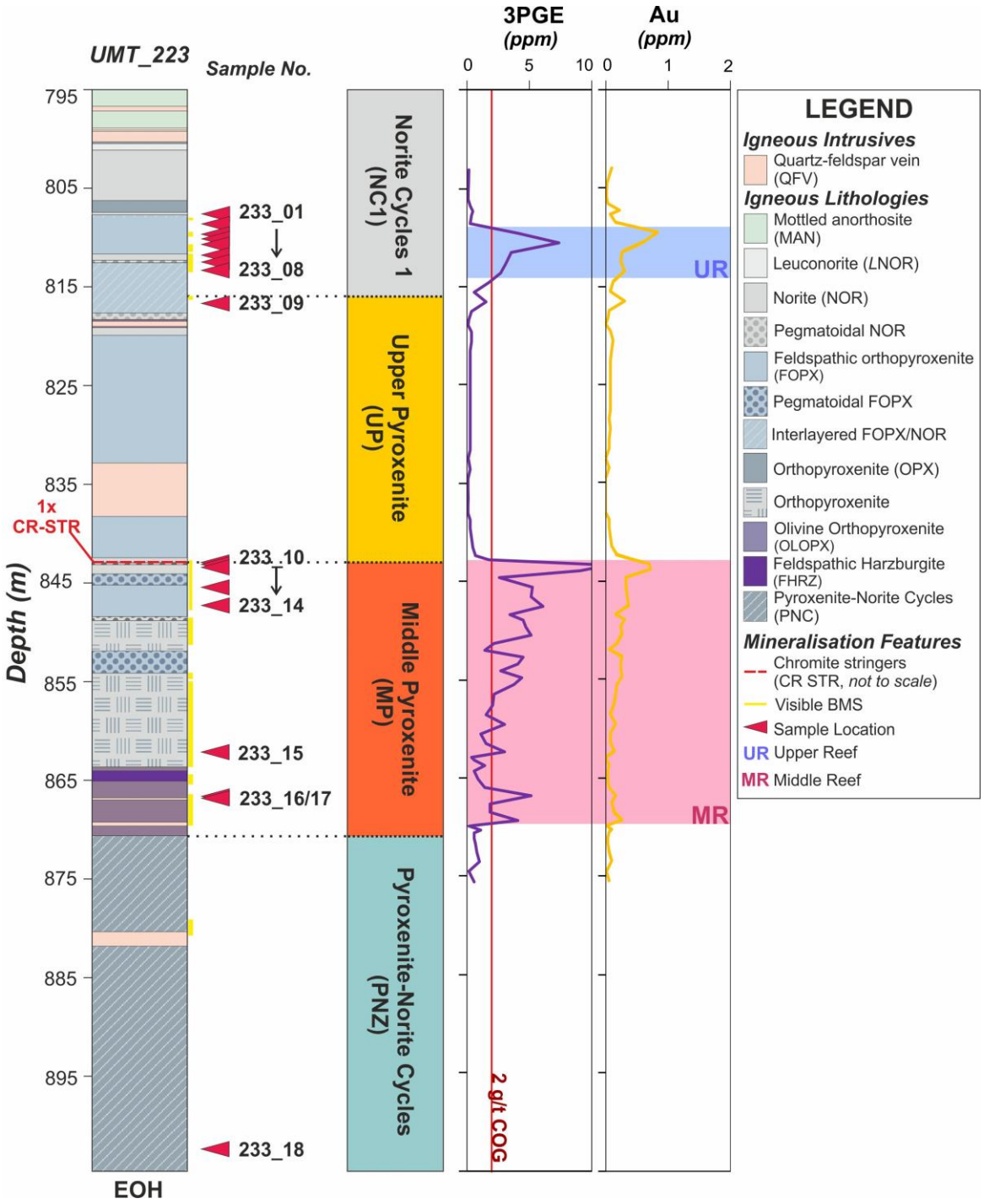

Figure 5.23: Downhole lithological log, sampling locations, stratigraphic divisions and grade profiles for the Normal Flatreef as sampled in UMT_233. Note: grade data is based on 1 m composites and provided by Ivanplats Pty Ltd.

The NC1 unit in UMT_233 hosts the first significant mineralised intersection; the Upper Reef (see Figure 5.23). The norite cycles in this drill hole are poorly developed when compared to the cycles of the NC2 as identified in the Deep Platreef. A complete norite cycle includes orthopyroxenite-norite-leuconorite-mottled anorthosite ranging from 30 cm to 1 m in thickness. The rock types are medium-grained to pegmatoidal and typically contain between 1 to 2 vol% base metal sulphides (BMS). At one location a fabric is developed defined by the preferential orientation of orthopyroxene laths. These norite cycles are developed over the first 13.5 m of the NC1 unit logged; the last 7.3 m is composed of dominant feldspathic orthopyroxenite containing intervals of more noritic composition as shown in Figure 5.24.

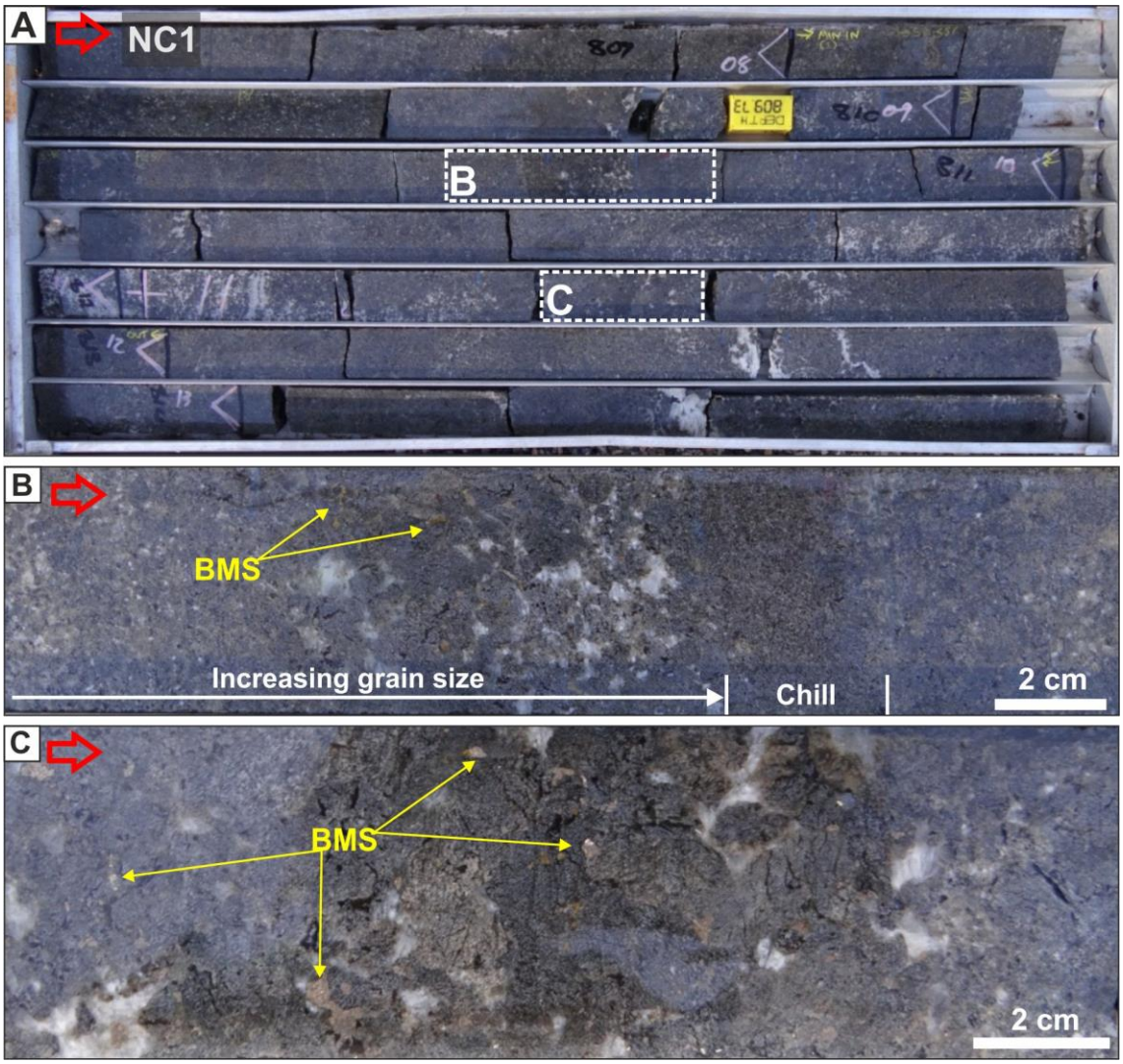

Figure 5.24: Lithological characteristics of the NC1 unit in the Normal Flatreef hosting the Upper Reef mineralisation event. (A) Core box sampling core from 809 to 814 m. (B) Fine-medium-coarse grained feldspathic orthopyroxenite. The location of a possible magmatic chill horizon is also shown. (C) Coarse-grained noritite rocks hosting medium-grained interstitial sulphides.

The lower part of the NC1 unit hosts the mineralisation; this corresponds with the presence of elevated BMS concentrations between 5 to 10 vol% that are medium-

grained and hosted in the interstitial assemblage. Unlike in the Deep Platreef and the Thick Flatreef, the BMS are not homogenously concentrated throughout the unit but are concentrated in intervals up to a metre thick with no visible sulphides in between. Texturally, this feldspathic orthopyroxenite is inequigranular with a range of grain sizes varying from fine to pegmatoidal over quite short distances e.g. 10 cm; the fine-grained sizes appear as chilled rocks (see Figure 5.24). Medium-grained phlogopite is present towards the base of this unit associated with the presence of amphibole and felsic veins. The transition from the NC1 to the Upper Pyroxenite (UP) is gradual and is recorded by a decrease in the noritic component and the development of a more homogenous texture.

The UP unit has been described previously in other drill holes, however unlike other localities it is not mineralised in UMT_233. This may be the result of the low BMS concentrations, typically absent or between 1 to 2 vol%, recorded in this stratigraphic unit. The UP is intruded by a 5.43 m thick medium-grained white granite composed of 60 vol% plagioclase, 30 vol% quartz and 10 vol% magnetite/amphibole. The contacts between the granite and the UP are sharp, straight and orientated at 90° to the core axis and there is evidence of chilling of the granite and evidence of fluid alteration of the pyroxenite on the contacts, resulting in the formation of olivine (see Appendix A for images). Towards the basal contact of the UP unit the feldspar concentration increases to ≈ 30 vol% (see Figure 5.25A) this corresponds with an increase in the BMS abundance to 5 vol%. The base of the UP is defined by a 2 cm thick chromite stringer (see Figure 5.25B) comprising 60 vol% fine-grained chromite grains and the remaining 40 vol% is composed of the interstitial plagioclase and orthopyroxene. The base of the chromite stringer marks the top of the 20 m thick middle reef mineralised interval and the beginning of the Middle Pyroxenite (MP) unit.

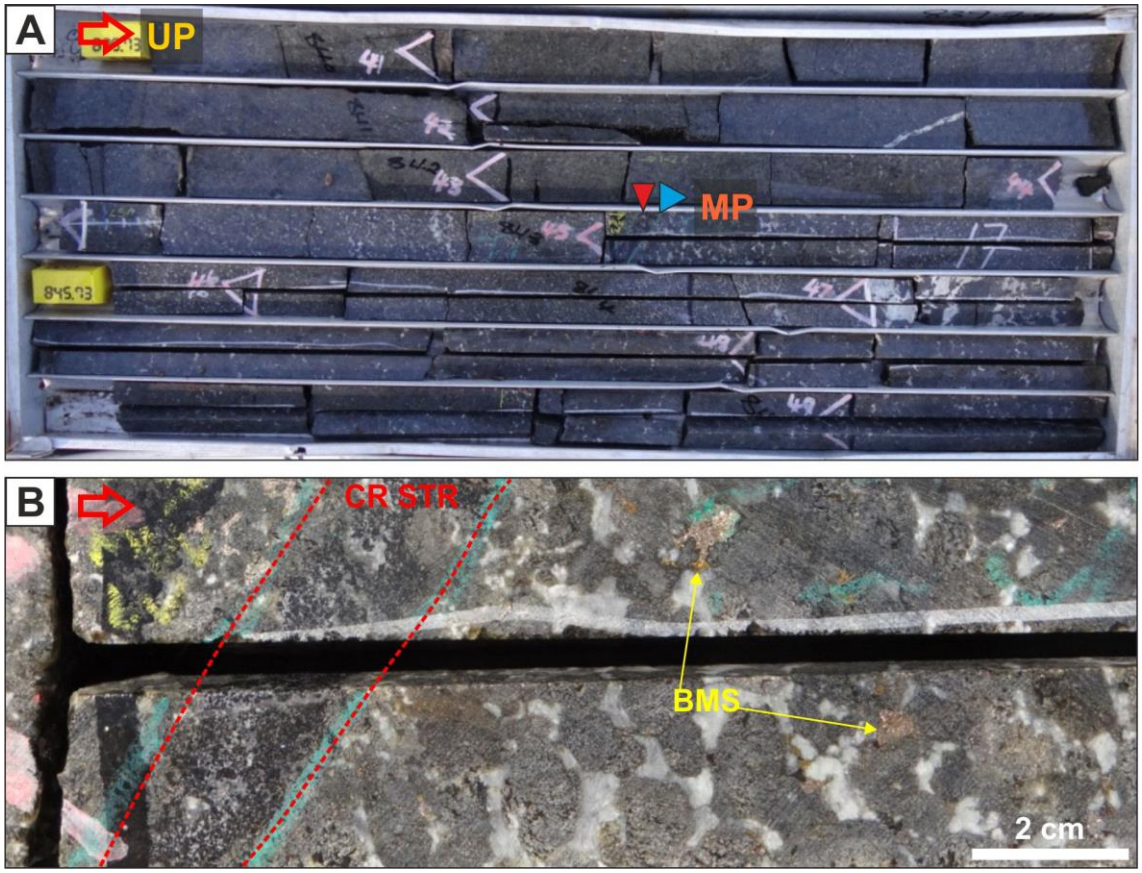

Figure 5.25: Lithological characteristics of the contact between the UP and the MP hosting the Middle Reef mineralisation event in the Normal Flatreef (UMT_233). (A) Core box from 840 m to 845 m containing the contact between the UP and MP stratigraphic units. (B) A close up of the chromite stringer with coarse-grained norite of the MP unit below. Note: red arrow points in the downhole direction, red triangle is positioned on a chromite-stringer and blue triangle marks a stratigraphic contact.

The MP unit beneath the chromite stringer is a coarse-grained norite composed of 60 vol% orthopyroxene, 35 vol% plagioclase and 5 vol% interstitial BMS. There is a notable absence of olivine and higher feldspar contents compared to the equivalent interval in the Deep Platreef drill holes. The BMS concentrations remains elevated at between 5 to 10 vol% over an interval of 5.21 m before returning to background concentrations. Moving downhole away from the chromite stringer the MP unit unit displays textural and compositional heterogeneity consisting of interlayered norites and pyroxenites with the pyroxenites typically coarse-grained and the norites medium-grained.

Olivine in the MP unit is present from 864 m to 871 m (see Figure 5.26); this corresponds to the presence of two quartz-feldspar veins (see Figure 5.26B) analogous in appearance to those as described for the Deep Platreef. The olivine-bearing lithology is a feldspathic harzburgite, as shown in Figure 5.26C, comprised of 50 vol% olivine, 40 vol% orthopyroxene, 5 vol% feldspar and 5 vol% BMS. This lithology is mineralised hosting 2.9 ppm (3PGE + Au) over a 3 m interval.

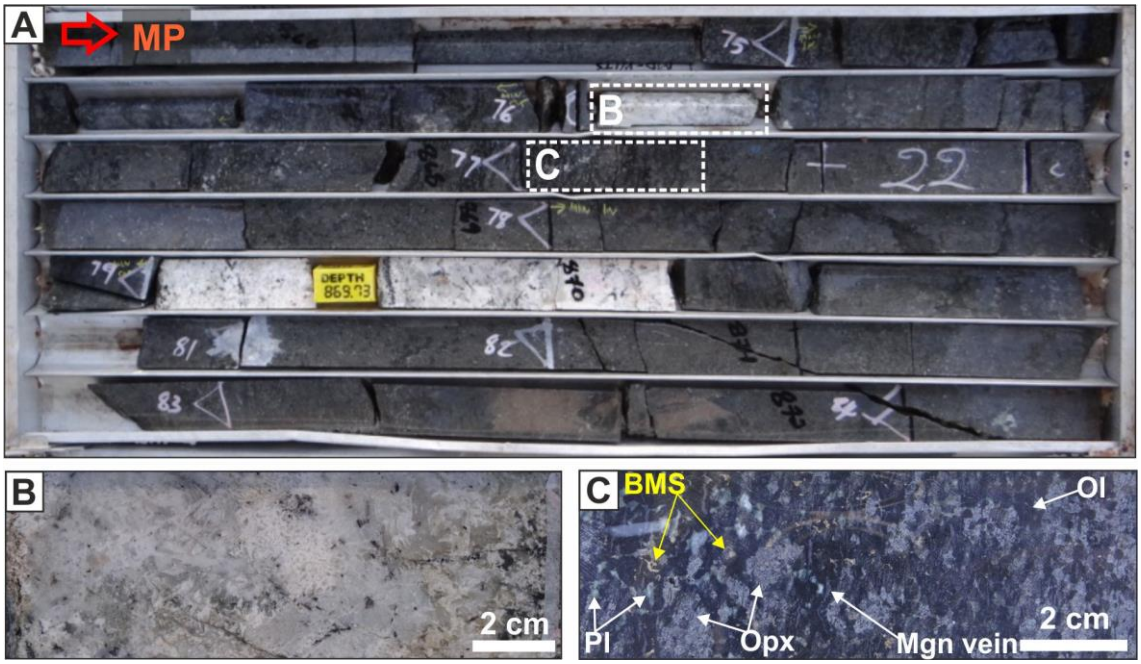

Figure 5.26: Lithological characteristics of mineralised feldspathic harzburgite within the MP unit in the Normal Flatreef (UMT_233). (A) Core box sampling core from 866 m to 872 m. (B) Close up of the QFV with a graphic texture. (C) Mineralogical characteristics of the mineralised feldspathic harzburgite. Note: red arrow points in the downhole direction.

The occurrence of olivine-bearing lithologies in close spatial proximity to late-stage veins may be a coincidence or could indicate that the olivine formed from via fluid flux melting of orthopyroxene. The source of the hydrothermal fluids required for this reaction would be from the QFV. In the examples shown here the leaching of metals from the pyroxenites by the same fluids causing the olivine transformation could act to cause this slight elevated PGE contents over a restricted interval. This observation of a close spatial association between these rock types accompanied by elevated grade above background values is not unique to this location but is observed in a few separate drill holes.

The last logged unit in this drill hole is a thick interval (33.66 m) known as the pyroxenite-norite zone (PNZ). The PNZ is characterised by poorly differentiated pyroxenite and norite that form a weak banded texture (see Figure 5.27). This unit contains BMS that are typically concentrated in the coarse-grained pyroxenite bands. Massive pods of pyrrhotite-dominated sulphides are found in intruding quartz-feldspar veins (see Figure 5.27A). The PNZ was observed to contain one disseminated band of chromite as shown in Figure 5.27C.

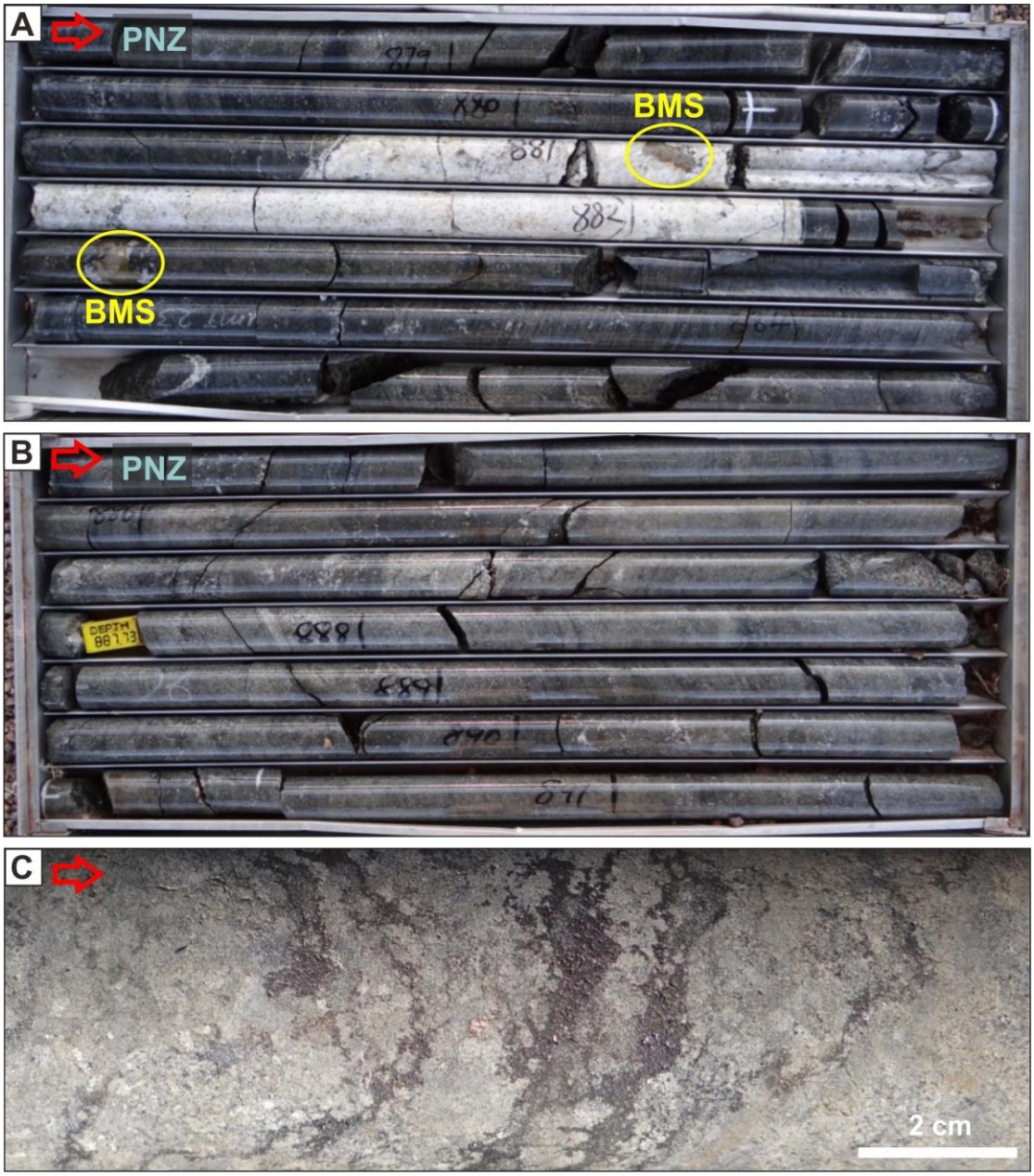

Figure 5.27: Lithological characteristics of the PNZ unit in the Normal Flatreef. (A) Massive pods of BMS associated with QFV intrusions. (B) An overview of the weak banding in the PNZ as sampled from 885 m to 891 m. (C) Banded chromite disseminations in the PNZ. Note: red arrow points in the downhole direction.

5.3.4 The Platreef (ATS_002)

The results of the geological logging of drill hole ATS_002 intersecting the Platreef are shown in Figure 5.28. The first unit logged in the Platreef drill hole was the mottled anorthosite (MAN) unit at a depth of 91 m.

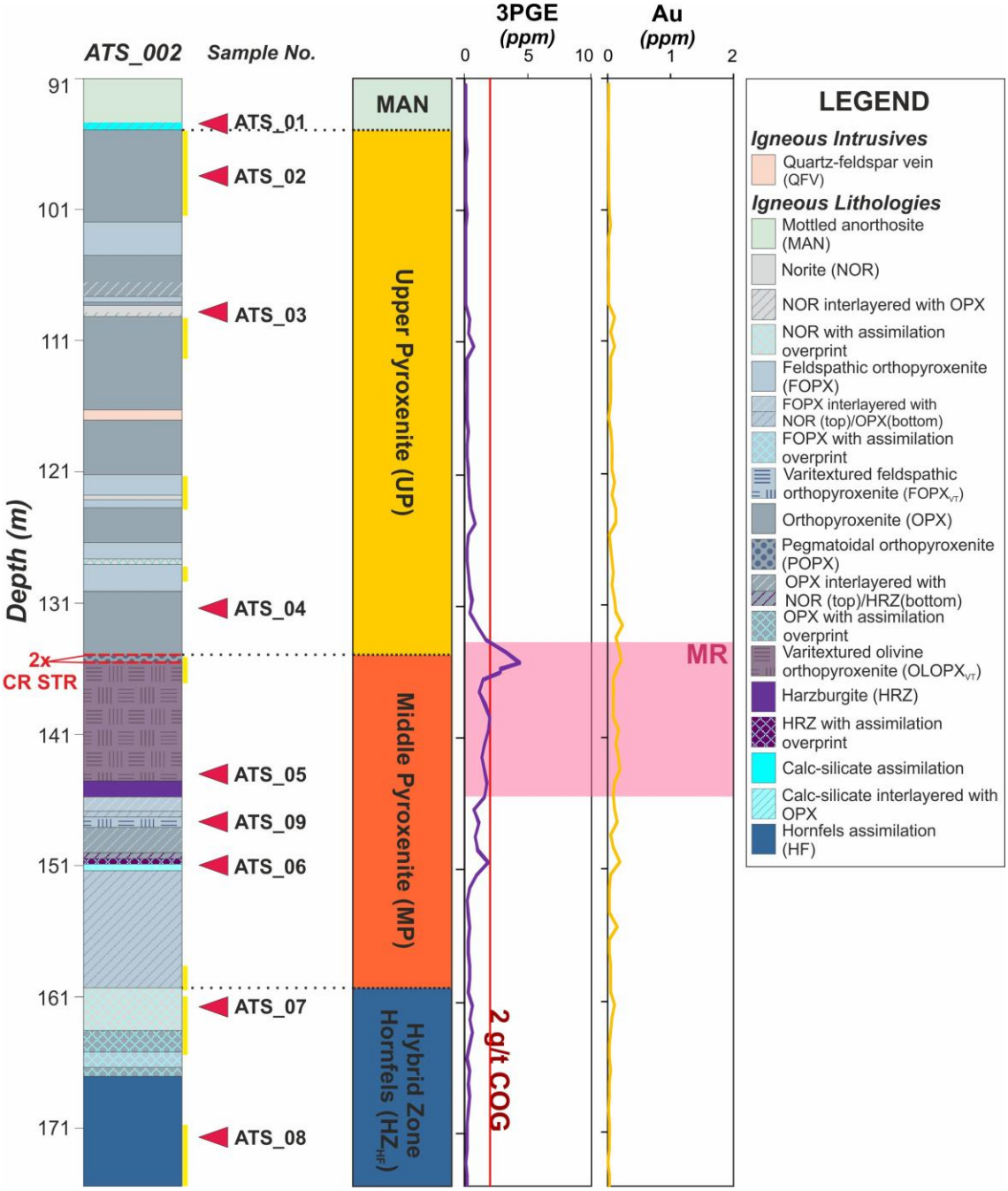

Figure 5.28: A downhole lithological column showing the sampling locations, a stratigraphic column and grade profiles from drill hole ATS_002.

The MAN unit in the Platreef is similar in appearance to the equivalent unit as observed in the Deep Platreef. The basal contact of the MAN with the Upper Pyroxenite (UP) is shown in Figure 5.29A. The contact is less sharp than the same contact as observed in the Deep Platreef and is orientated at 55° to the core axis. A close up of the contact between the MAN unit and the UP is shown in Figure 5.29B; in this image one can see a mottle forming on the mixing front between the anorthosite and the pyroxenite.

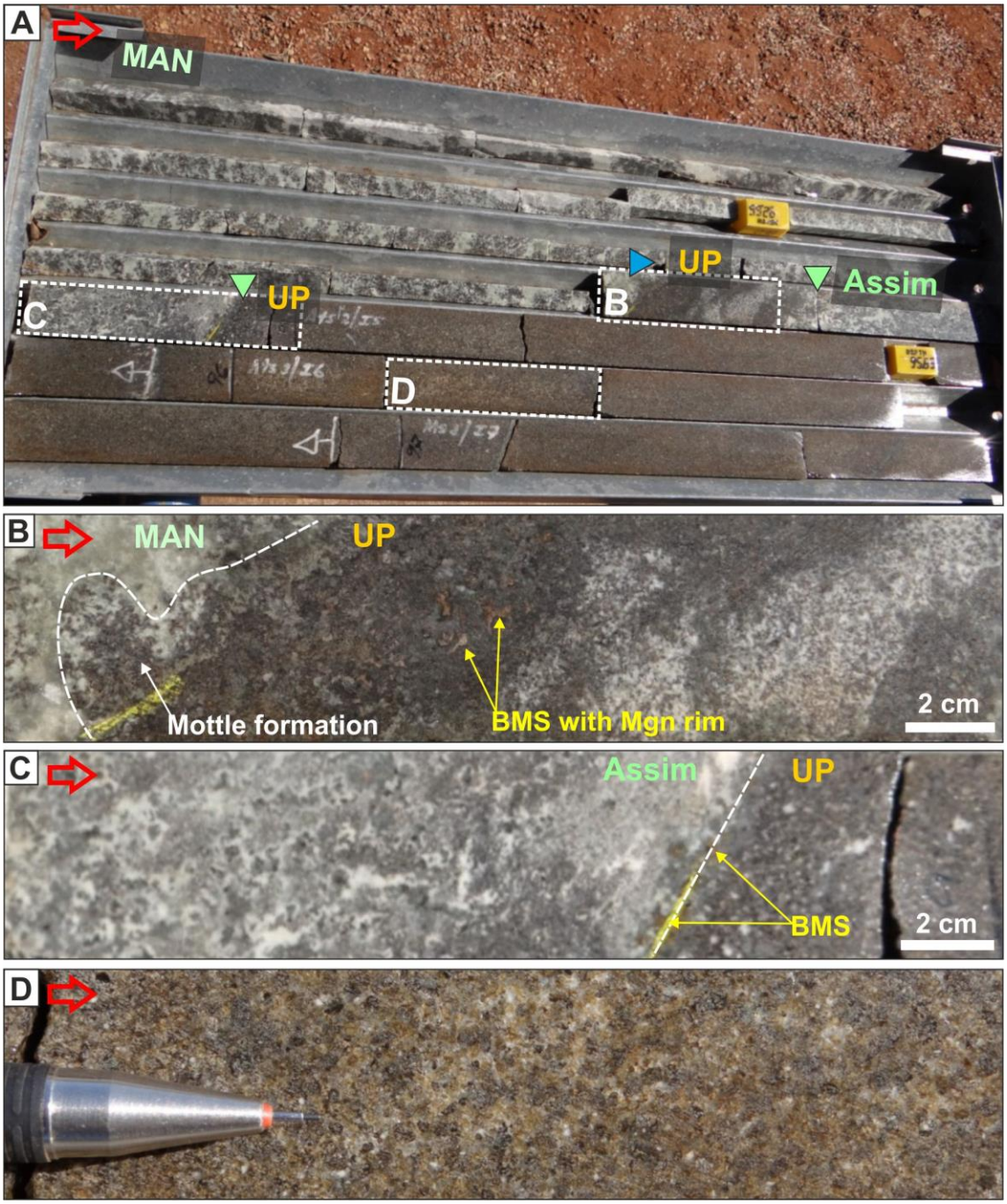

Figure 5.29: Lithological characteristics of the contact between the MAN unit and the UP unit in the Platreef. (A) An overview of the core box containing core from 91 to 97 m. (B) A close up of the contact between the MAN and UP units. (C) The second contact between calc-silicate skarn and the UP unit. (D) Fine-grained feldspathic orthopyroxenite of the UP. Note: red arrows point in the downhole direction, blue triangles are located on stratigraphic contacts and green arrows point to assimilated sedimentary material. Note: red arrows point in the downhole direction, blue triangles are located on stratigraphic contacts, green triangles point to assimilation contacts and the silver pencil tip (shown for scale) is 2 cm in length.

The UP in direct contact with the MAN contains up to 10 vol% base-metal sulphide (BMS) over a distance of a few cm dominated by medium-grained blebby pyrrhotite with rims of magnetite. The silicate assemblage of the UP at this location is composed of a mixture of noritic and pyroxenitic lithologies and is fine to fine-medium grained (see Figure

5.29B). The UP unit here represents a slither that is 24 cm in length and separated from the rest of the unit by a skarn-type lithology, possibly a calc-silicate xenolith or autolith that may have once been the roof of the intrusion (see Figure 5.29C). The basal contact of this assimilated sedimentary material and the top of the UP unit is orientated at 60° to the core axis and again magnetite and BMS are concentrated on this contact.

Initially, the top of the UP unit is composed of orthopyroxenite that is fine-grained with an equigranular 'brown sugar' texture (see Figure 5.29D). The grain size increases to medium-grained with depth over an interval of 6.41 m. Compositionally this unit is quite homogenous with the largest variation observed in the feldspar contents from 5 to 40 vol% (see Figure 5.30A). A localised noritic interval showing grain size reduction and elongation resulting from either localised shearing or fluid alteration is shown in Figure 5.30B. Between 130.4 to 135.07m at specific intervals, the orthopyroxene grains showed evidence for a preferred orientation (90° to the core axis) imparting a weak fabric on the rock; as seen in the NC1 unit of UMT_233.

Figure 5.30: Lithological characteristics of the UP unit as sampled in the Platreef. (A) Core box containing UP unit from 104 to 111 m. (B) Evidence of shearing/fluid alteration of a leuconorite. Note: red arrows point in the downhole direction.

Base metal sulphides (BMS) are heterogeneously distributed in the UP, large intervals contain no BMS; where present they are up to 5 vol% and are typically medium-grained and interstitial apart from one locality where net-textured BMS were identified. In all settings the BMS are compositionally dominated by pyrrhotite (≈ 90 vol%). The base of the UP unit is marked by the presence of two chromite stringers (see Figure 5.31).

The 1st chromite stringer, identified at 135.07 m, is 8 mm thick, fine to fine-medium grained consisting of euhedral chromite grains and containing 5 vol% interstitial sulphides (see Figure 5.31A). The 2nd chromite stringer is less well developed than the 1st. It is located at 135.54 m, is 7 mm thick, orientated at 80° to the core axis and contains fine-grained, interstitial BMS comprising <5 vol% (see Figure 5.31B). The intervening silicate rocks between the two chromite-stringers is a 0.5 m thick pegmatoidal orthopyroxenite (without olivine) containing between 5 to 10 vol% sulphides (pyrrhotite > chalcopyrite). These chromite-stringers mark the beginning of the first mineralised interval within the Platreef which has been correlated to the Middle Reef (see Figure 5.28) as identified elsewhere across the deposit.

Figure 5.31: Lithological characteristics of chromite stringers on the contact between the UP and MP units in the Platreef. (A) An overview of the core box hosting the chromite stringers. (B) A close up of the 1st chromite stringer. (C) A close up of the 2nd chromite stringer. Note: red arrows point in the downhole direction, red triangles are situated on chromite-stringers and blue triangles point to stratigraphic contacts.

The top 10 m of the MP unit is characterised by olivine-bearing lithologies including olivine orthopyroxenite and harzburgite. The olivine is typically medium-grained and enclosed in coarse-grained orthopyroxene oikocrysts; serpentinization is prevalent. This unit best resembles the lithologies as observed in the Deep Platreef compared to the Flatreef drill holes. The lower part of the unit (known as MP_L) is dominated by orthopyroxenites. Locally, these display an assimilation overprint and partially assimilated lithologies are identified, some examples are shown in Figure 5.32. Olivine is present in a feldspathic harzburgite over a limited interval adjacent to assimilated material as shown in Figure 5.32B.

Figure 5.32: Calc-silicate xenoliths partially assimilated within the MP unit in the Platreef. (A) Core box hosting assimilated sedimentary material. (B) Close up of the feldspathic harzburgite in contact with assimilated country rock. (C) A xenolith of country rock enclosed in parapyroxenites. Note: red arrows point in the downhole direction and green triangles point to assimilation contacts.

The last unit logged in the drill hole is a fine-grained, foliated hornfels as shown in Figure 5.33; logged as the Hornfels Hybrid Zone (HZ_{HF}). The foliation of the hornfels is made visible by the presence of pyrrhotite-dominated sulphides with a rim of magnetite, as shown in Figure 5.33B. The fact that this fabric is not preserved in the igneous rocks attest to the different origin of this lithology as metamorphosed footwall sediments.

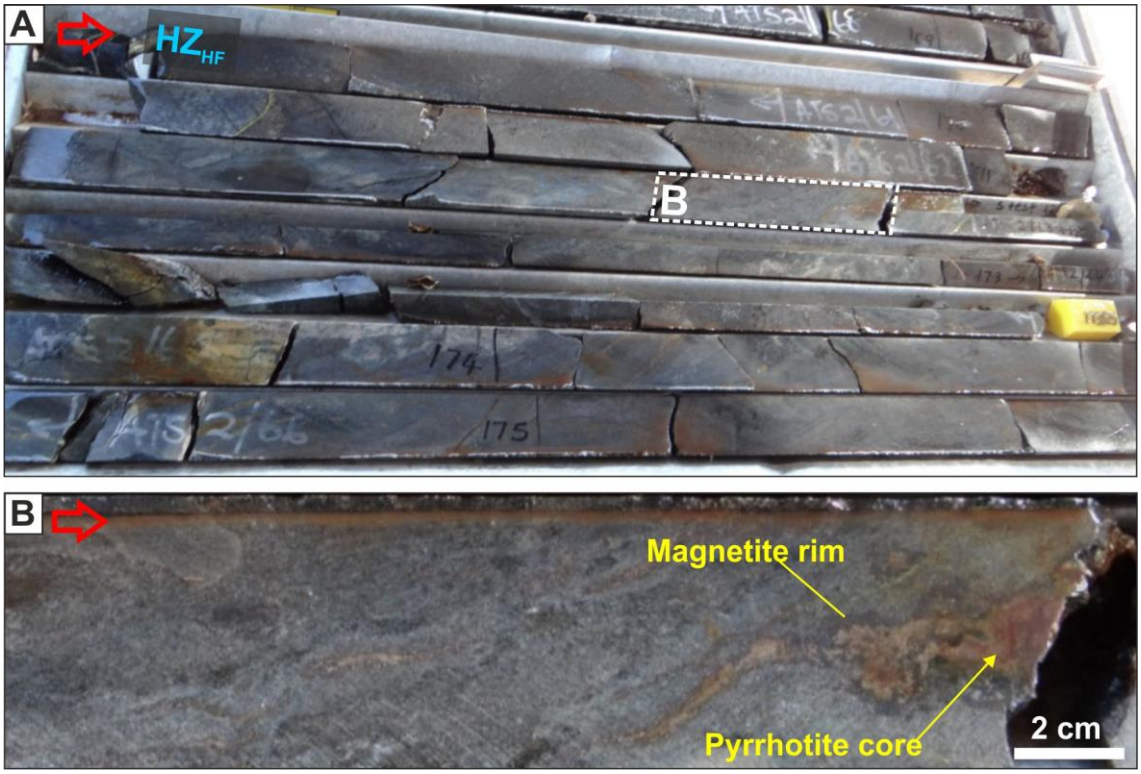

Figure 5.33: Lithological characteristics of the HZ_{HF} unit in the Platreef (ATS_002). (A) Core box containing fine-grained hornfels at depths of between 170 to 175 m (B) Pyrrhotite with magnetite crystallised on edges highlights a foliation identified in the hornfels. Note: red arrows point in the downhole direction.

Chapter 6

Country Rock Geochemistry

6.0 Introduction

Country rock sampling was undertaken on localities at a distance of ≈10 km away from the Bushveld intrusion; as such the geochemistry of the lithologies present should be relatively unaltered by the intrusions thermal aureole. The work presented in this chapter was completed in order to understand the lithological variability of the footwall and basement rocks to the Platreef magmatic event on Turfspruit and to provide quantitative geochemical data on their primary compositions. The geochemical data will be used to distinguish between fresh and contaminated magmatic rocks at Turfspruit and to constrain the background Au and PGE concentrations of the hinterland. The location of samples collected as part of this study are shown in Figure 6.1; a description of the sampling technique can be found in Chapter 4 (section 4.2). A detailed methodology for the preparation and analysis of samples for multi-element and precious metal analysis is provided in Chapter 4 (section 4.3).

Xenoliths and interlayers of the sedimentary footwall rocks of the Duitschland Formation (DF) are found sporadically in drill holes intersecting the Platreef across the Turfspruit licence area; some examples of these are shown in Chapter 5 (see Figure 5.1). The analysis of xenoliths within the Platreef as conducted in Sharman-Harris et al., (2005) are unlikely to provide data that are representative of true 'end-member' compositions, given devolatilization and alteration effects during contact metamorphism by the Bushveld Complex magmas.

The DF stratigraphy represents a 1000 m thick shallowing basin with deep marine shales in the lower section and shallow marine sediments including limestone and stromatolites in the upper section. The majority of the literature on the DF are focused on understanding the stratigraphy from a paleoclimate and paleoenvironmental perspective. The DF was deposited over an important time period in the Earth's history known as the 'Great Oxidation Event' where the Earth's atmosphere changed from anoxic to oxic conditions. Multi-element isotopic studies on the stratigraphy including $\delta^{13}C$, $\delta^{18}O$, and ^{34}S have identified this event within the DF (Bekker et al., 2001; Guo et al., 2009). As far as the current author is aware no comprehensive geochemical dataset including trace and precious metals exists for these sediments at these locations. New DF samples were collected along transects through the well-established stratigraphy on the Duitschland and De Hoop Farms; details on the sampling are provided in Chapter 4 section 4.2 and an overview is shown in Figure 6.1.

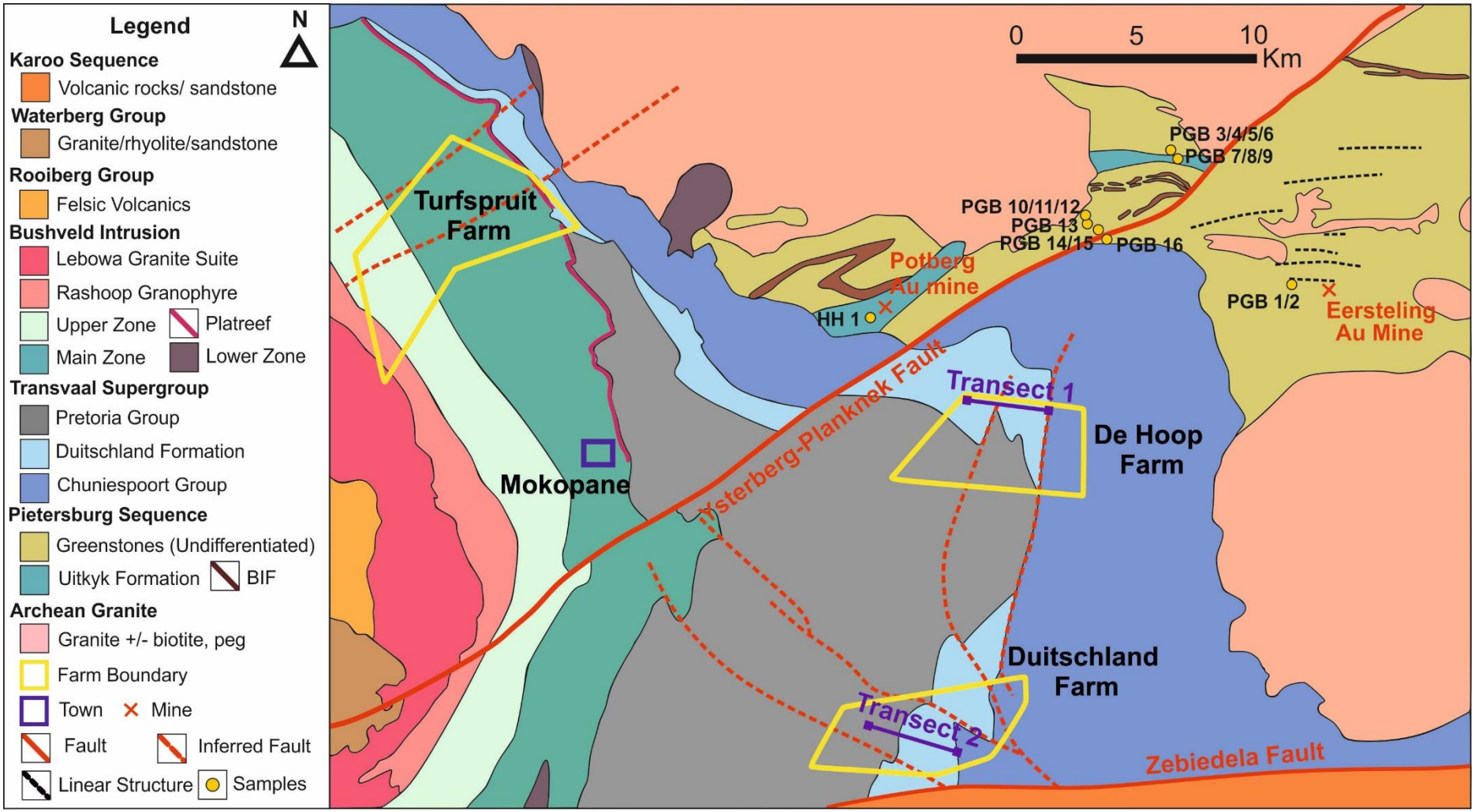

Figure 6.1: Regional geological map of the northern limb of the Bushveld Complex highlighting the location of country rock sampling locations in the PGB and as transects walked on farms De Hoop and Duitschland. Modified after regional geological survey maps from the Department of Mines (1978) and Department of Mineral and Energy Affairs (1985) combined with geological details on the PGB based on mapping results collected by de Wit (1991) and de Wit et al., (1992).

An investigation into the Pietersburg Greenstone Belt (PGB) was conducted based on evidence from field observations (see Figure 6.1 and 6.2) and from previous mapping studies (de Wit, 1991) that appear to suggest that the PGB extends westwards beneath the Transvaal Supergroup sediments. The PGB is composed of two tectonosedimentary sequences divided into a basal greenstone sequence (>3450 Ma), interpreted by De Wit (1991) as obducted oceanic crust and a upper sedimentary cover (ID-TIMS on Uitkyk Formation detrital zircon >2957 Ma, de Wit et al., 1993). Details on the stratigraphy are presented in SACS (1980) and it was remapped by de Wit (1991).

If the PGB continues beneath the Transvaal cover then the Platreef magma has to interact with the PGB before emplacement at higher stratigraphic levels. The PGB hosts known gold mineralisation with the Eersteling gold mine, the first gold discovery in South Africa, and artisanal workings on a placer gold deposit hosted in a metaconglomerate at Potberg (see Figure 6.1). Greenstone belts around the World are known to host some economic deposits Ni-Cu-PGE deposits, typically at the base of komatiite flows (e.g. Munni Munni). No komatiites have been identified in the PGB, however the PGB is poorly studied. To the current authors knowledge there have been no geochemical studies on the PGB rocks.

Figure 6.2: View looking south westwards towards the Transvaal Supergroup onlapping the Pietersburg Greenstone Belt. Photo taken from the Eersteling gold mine location as shown in Figure 6.1.

6.1 Duitschland Formation Lithological Descriptions

The following section provides descriptions of the Duitschland Formation (DF) outcrop as observed whilst walking along two transects on farms Duitschland and De Hoop (see Figure 6.1). The best exposure and thickest sequence of the DF was found at the type-

locality, farm Duitchland; consequently the majority of the following descriptions are based on this locality. Details on the De Hoop locality including field photos and sample locations, are provided in Appendix B.

A ≈2 km long transect, orientated approximately SE to NW, was walked on Duitschland farm beginning in the basal pyritic shales of the Lower DF moving up succession to the massive dolomites at the top of the Upper DF (see Figure 6.3). A topographic map of farm Duitschland is provided in Figure 6.3 (for GPS coordinates of sample locations see Appendix B); the sediments define two ridges with an intervening flat-lying valley of poor exposure. The strike of the ridges matches that of the bedding; structural measurements from the bedding planes gave an average dip of 34° towards 280° (based on six measurements, see Appendix B).

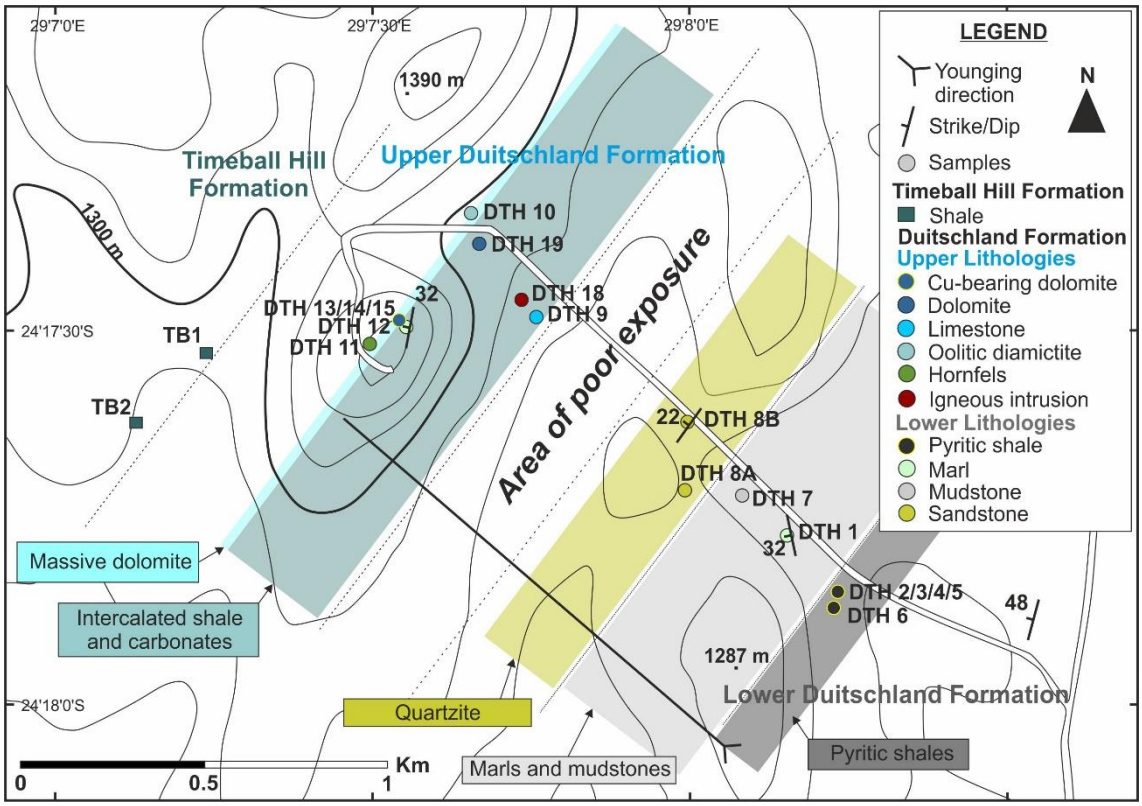

Figure 6.3: Topographic map of farm Duitschland, showing sample locations and the inferred outcrop extent of certain lithological units based on field observations.

The lower part of the DF, comprising the deep water facies, is characterised by relatively poor, patchy exposure in a flat-lying topographic low. No in situ outcrop was found and samples of the pyrite-bearing, carbonaceous shales and laminated mudstones were collected from float samples, as shown in Figure 6.4A. The shales are black to grey in colour and show mm-scale laminations (sometimes showing cross-bedding) with minor pyrite present as 1 to 2 mm subspherical nodules concentrated on laminations defining

the contact between darker (shales) and lighter (silty) layers, as highlighted in Figure 6.4B. The concentration of pyrite in these rocks doesn't appear to be very high with a visual estimate of 0.5 vol%. Moving up-sequence these shales grade into a fine-grained marl, exposed in a road cutting, with a light green tinge and no visible pyrite (see Figure 6.4C). The top of the lower part of the DF consists of fine to medium grained arenaceous sandstones (see Figure 6.4D). These sandstones have a good outcrop exposure and display sedimentary structures including cross-bedding, which indicated that they are the correct way-up (see Figure 6.4D).

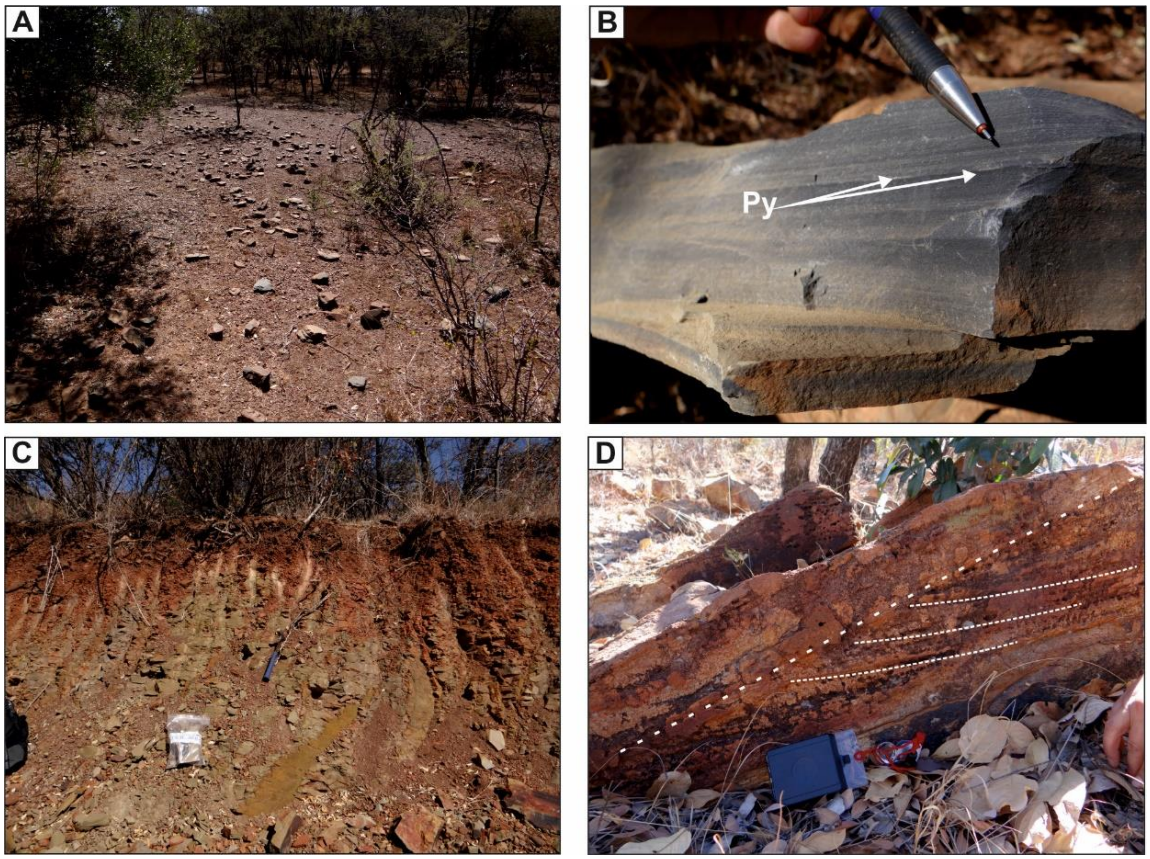

Figure 6.4: Lithological characteristics of the siliciclastic Lower Duitschland Formation. (A) Lower DF shales identified in flaggy float samples. (B) Parallel laminations in a dark mudstone, the presence of pyrite along these laminar planes is highlighted. (C) A small roadside quarry exposing a marly-mudstone above the pyrititc shales. (D) Cross-bedding in an arenaceous sandstone.

The transition from the Lower DF to Upper DF is within a region of poor exposure approximately 400 m in thickness (on surface). The base of the Upper DF as identified in the field is characterised by interbedded carbonates and shales (see Figure 6.5A) with a gradual increase in carbonate content moving up dip. The carbonates are varicoloured from grey to pink and compositionally range between limestones and dolomites. They typically show laterally-orientated mm-scale crenulations and have a characteristic weathering with rain-runoff ridges (see Figure 6.5B). An oolitic matrix-supported breccia (possible diamictite) was also identified in this interval (see Figure 6.5C). This consists

of an ooid matrix (ooids sub-millimetre in size) supporting sub-angular clasts of dolomite, sandstone, quartzite and rounded ironstones. The clasts are poorly sorted and range in size from 2 mm to 200 mm. This intercalated unit is intruded by a mafic igneous intrusion (unknown whether sill or dyke) approximately 15 m wide. The top of the Upper DF is well exposed on the large ridge at the NW end of the transect shown in Figure 6.3; the slopes of this ridge are covered in loose boulders. It is characterised by a massive, ivory coloured dolomite (see Figure 6.5E), which on exposed surfaces has a characteristic 'elephant skin' weathered texture (see Figure 6.5F). On fresh surfaces the dolomites have a sugary texture potentially indicative of having been recrystallised. Sulphides have been identified within the dolomites at this stratigraphic level and they are described in detail in Martini (1979); they include disseminated chalcopyrite, bornite and chalcosite with accessory galena, molybdenite, tennantite, mawsonite and a mercury-silver alloy. This mineralisation has been interpreted by Martini (1979) to represent a typical stratabound syngenetic deposit. No primary sulphides were identified in this study, however green and blue secondary oxide staining was observed (see Figure 6.5F).

Moving further north-westwards away from the prominent Upper DF dolomitic topographic ridge sediments of the younger Timeball Hill Formation outcrop in a topographic low (see far left side of Figure 6.3). The lower units of Timeball Hill Formation were observed as laminated, purple-brown ferruginous shales/mudstones. Two samples of the Timeball Hill shales were collected for reference (shown as TB1 and TB2 in Figure 6.3).

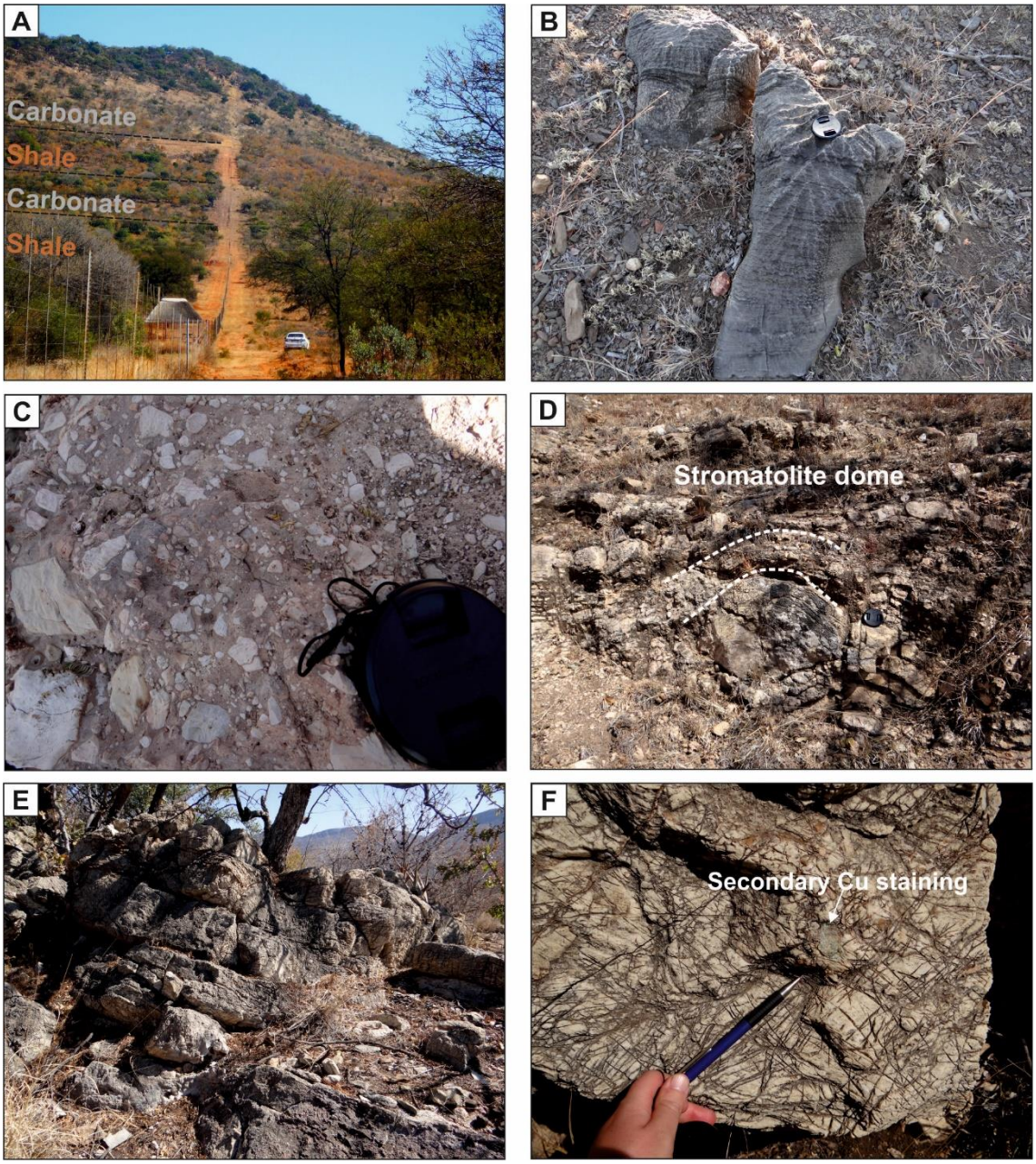

Figure 6.5: Lithological characteristics of the carbonate-dominated Upper Duitschland Formation. (A) Interbedded shale (orange soil) and carbonate (grey soil) lithologies observed in hillside on De Hoop. (B) Millimetre-scale crenulations in a typical grey limestone outcrop with rain runoff grooves. (C) Oolitic limestone forms the matrix with suspended angular clasts proposed to represent a diamictite. (D) Limestone with stromatolite domes on the decimetre scale. (E) Massive dolomite exposure on top of the second ridge on farm Duitschland in the north west. (F) An example of elephant skin weathering on the surface of white dolomite with secondary copper staining.

6.2 Pietersburg Greenstone Belt Lithological Descriptions

The stratigraphic units of the Pietersburg Greenstone Belt (PGB) were not systematically sampled along transects as described previously when sampling the Duitschland Formation. Instead a sampling strategy was adopted to try and collect representative samples from each of the stratigraphic units as outlined in SACS (1981) and mapped by

De Wit (1991). The reason for this change in sampling strategy is that the DF is assumed to have affected the magma in situ; it will therefore impart a variable signature depending at what stratigraphic height within the sedimentary sequence the magma intruded. Any interaction between the basement rocks and the magma is presumed to have occurred at depth and pre-emplacement; signatures from the PGB are more likely to have been homogenised and a more general characterisation of these rocks is more appropriate.

The location of PGB samples obtained for this study are shown in Figure 6.1 and GPS coordinates are provided in Appendix B. The metavolcanics of the Eersteling Formation were sampled in proximity to the closed mine workings at the Eersteling monument. An example of the sheared and blocky nature of the metavolcanic outcrop is shown in Figure 6.6A. The banded iron formations (BIF) that characterise the Ysterberg Formation were sampled from float (see Figure 6.6B). These BIFs are layered and contain a significant chert component (up to 50 vol%). The majority of samples collected are metasedimentary rocks from the Uitkyk Formation consisting of a mixture of fine- and coarse-grained metasediments in addition to a mineralised (pyrite-bearing) and unmineralised conglomerate. In hand specimen these sediments often have a slight green colour to them as shown in the matrix of the metaconglomerate in Figure 6.6C; this is probably a result of greenschist facies metamorphism. The Potberg mine was highlighted for investigation because of the known gold mineralisation and unlike the Eersteling gold mine outcrops were accessible (see Figure 6.6D). The mineralisation of the Potberg gold mine is hosted in a coarse-grained metaconglomerate. The matrix is rich in clay mineral and carries rounded pyrite clasts, ranging in size from < 1 mm to 5 mm; as shown in Figure 6.6E. The dominant silicate clasts are composed of sub-rounded quartzite and they range in size from <1 cm to >20 cm (see Figure 6.6E).

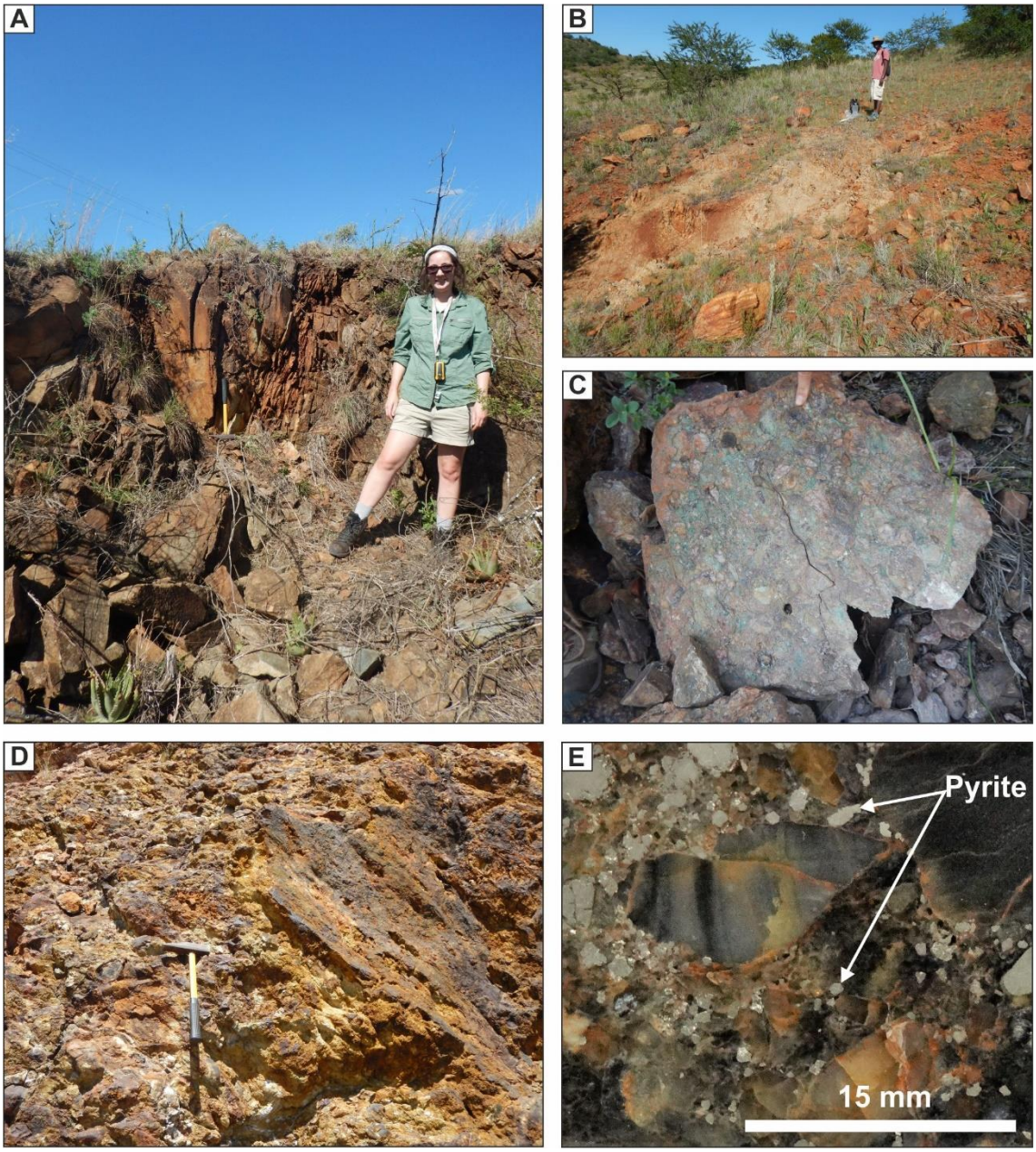

Figure 6.6: Lithological characteristics of the Pietersburg Greenstone Belt. (A) Outcrop of sheared metavolcanics rocks of the Eersteling Formation. (B) Float samples of the Ysterberg Formation BIFs. (C) Metaconglomerate from the Uitkyk Formation with a strong-green coloured matrix. (D) A iron-stained outcrop of the pyrite-bearing mineralised conglomerate. (E) Polished rock section of the mineralised Potberg metaconglomerate.

6.3 Geochemical Results

The results of major and trace element analysis on the country rock samples are presented in the following section; the raw data is provided in Electronic Appendix B.

6.3.1 Lithophile Element Geochemistry

The major element geochemistry of the different lithologies sampled from the Duitschland Formation (DF) are presented in Figure 6.7 (A-D). Based on the data shown in Figure 6.7 the lithologies of the DF can be subdivided into two main compositional

groups; carbonates and silicates. A further subdivision can be applied to both groups with the carbonates subdivided into limestone and dolomites (see Figure 6.7B) and a subdivision based on grain size i.e. coarse- and fine-grained (see Figure 6.7C) for the siliciclastic rocks.

Previous geochemical studies on the Platreef magmatic rocks have used the ratio of CaO/Al_2O_3 as a contamination proxy (Kinnaird, 2005). Magmatic rocks crystallising orthopyroxene and plagioclase, the major minerals in the PGE mineralised feldspathic orthopyroxenites of the Platreef, should have CaO/Al_2O_3 values within the range of 0.6 to 1.0 (Kinnaird, 2005). Excursions to the right indicate contamination by a Ca-rich source (e.g. dolomite) and those to the left indicate the influence of an Al-rich source (e.g. shale). This contamination proxy was tested using the geochemical data collected from the DF sediments, the results are shown in Figure 6.7A. The carbonate samples plot significantly above the magmatic range with CaO/Al_2O_3 values >10. The siliciclastic samples typically plot below the magmatic range with CaO/Al_2O_3 values <0.5. The difference between the magmatic range and the siliciclastic samples is smaller and one sample of the pyritic shale has a CaO/Al_2O_3 value of 0.8, which overlaps with the magmatic range. The results here show that any carbonate material introduced in to the magma (via partial melting or devolatisation) from the upper DF will significantly elevate the CaO/Al_2O_3 ratio. In contrast, any shale assimilation by the magma will likely result in a less dramatic shift because the CaO/Al_2O_3 values of shales are nearer to those of magmatic compositions.

The highest total REE concentrations (>120 ppm) are observed in the fine-grained lithologies including the shales, mudstones and marls (see Figure 6.7D). The concentration in the carbonates is significantly lower (< 50 ppm). The implication of this is that mafic igneous rocks showing elevated REE concentrations are more likely to have been contaminated with shales than carbonates.

The distinct major element geochemically variability identified here should help constrain the level of intrusion of the Platreef magma into the DF floor rocks on Turfspruit. The distinct lithogeochemistry of the DF sediments will impart a strongly contrasting and heterogenous geochemical contamination signature on the magma depending on whether it is emplaced into the siliciclastic-dominated Lower DF or the carbonate-dominated Upper DF. The Pietersburg Greenstone Belt major element data is not presented here because any potential interaction with the Platreef magma would occur at depth where homogenisation at magmatic temperatures would make it undistinguishable from magmatic rocks.

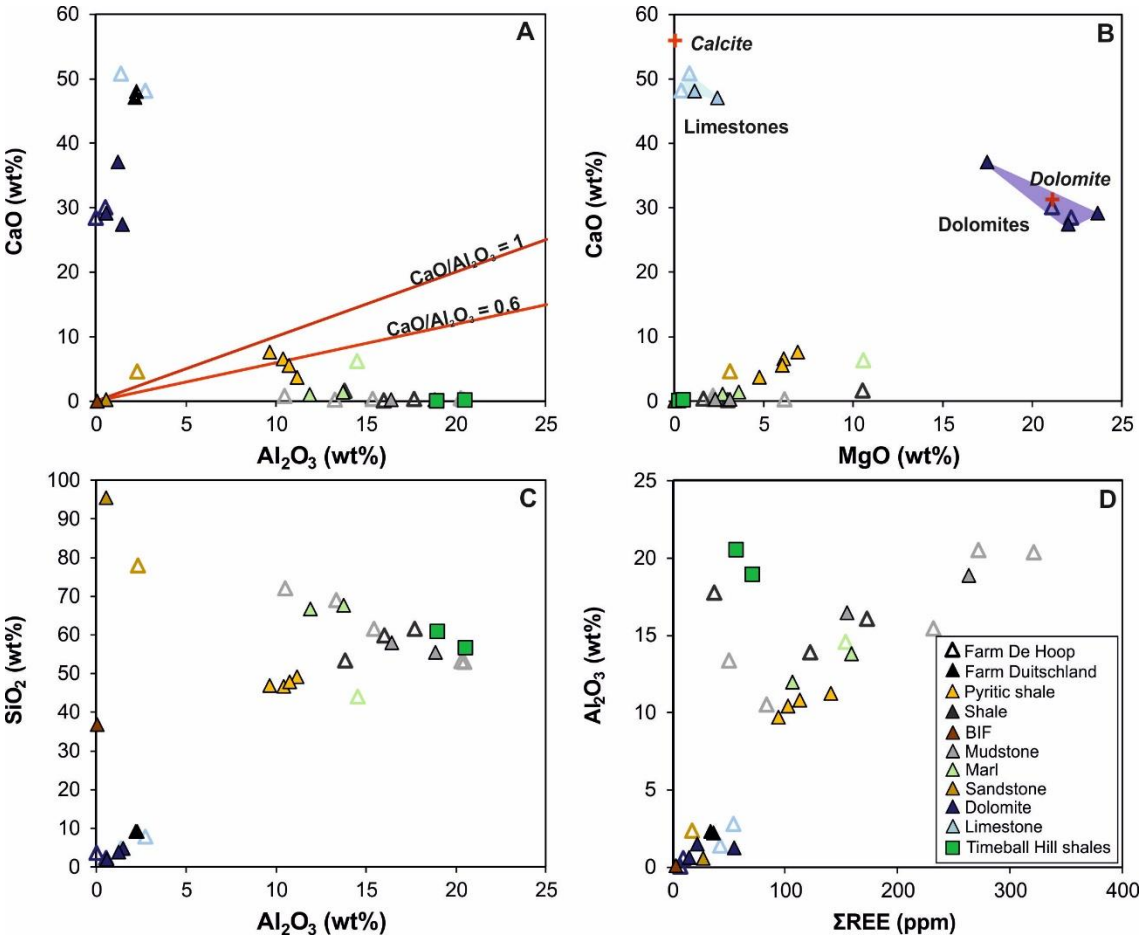

Figure 6.7: Major element bivariate plots of the Duitschland Formation samples from farm Duitschland. (A) CaO (wt%) vs. Al_2O_3 (wt%); (B) CaO (wt%) vs. MgO (wt%), end-member compositions of dolomite and calcite are plotted as a reference (data from Deer, Howie and Zussman, 1992); (C) SiO_2 (wt%) vs. Al_2O_3 (wt%); (D) Al_2O_3 (wt%) vs. ΣREE (ppm).

6.3.2. Chondrite-Normalised Rare Earth Element data

Chondrite-normalised rare earth element (REE) plots for the Duitschland Formation (DF) and Pietersburg Greenstone Belt (PGB) samples are presented in Figure 6.8 (A-D). The REE patterns for samples of the DF all have similar patterns with strong fractionation between the light REE (LREE, La to Sm) and the heavy REE (HREE, Gd to Lu). The main difference between the varying lithologies is in the concentration of REE, which are higher in the fine-grained silicates of both the Lower and Upper DF (by an order of magnitude) compared to the carbonates lithologies in the Upper DF. The lowest REE concentrations are identified in the Cu-stained dolomites from the Upper part of the DF. The most fractionated REE profile (La_N/Yb_N = 15.3) was obtained from a sandstone sample, which has a negative sloping profile and a slight negative Ce anomaly (Ce/Ce* 0.56). The least fractionated profile was identified for a BIF float sample (La_N/Yb_N = 3.86); this sample is anomalous and may represent actually be from the stratigraphically lower Penge Iron Formation. There appears to be a slightly more pronounced negative Eu

anomaly (Eu/Eu* of 0.58) in silicates from the Upper DF compared to the Lower DF; with the exception of the one BIF sample (Eu/Eu* of 0.51).

The two shale samples of the Timeball Hill Formation (see Figure 6.8A), stratigraphically above the DF in the Transvaal Supergroup, have bow-shaped profiles with a decrease in LREE to Gd then a gently positive slope for the HREE; they have an average La_N/Yb_N of 2.48. The HREE content of these shales are elevated above the DF shales indicative that they may derive from a different source region.

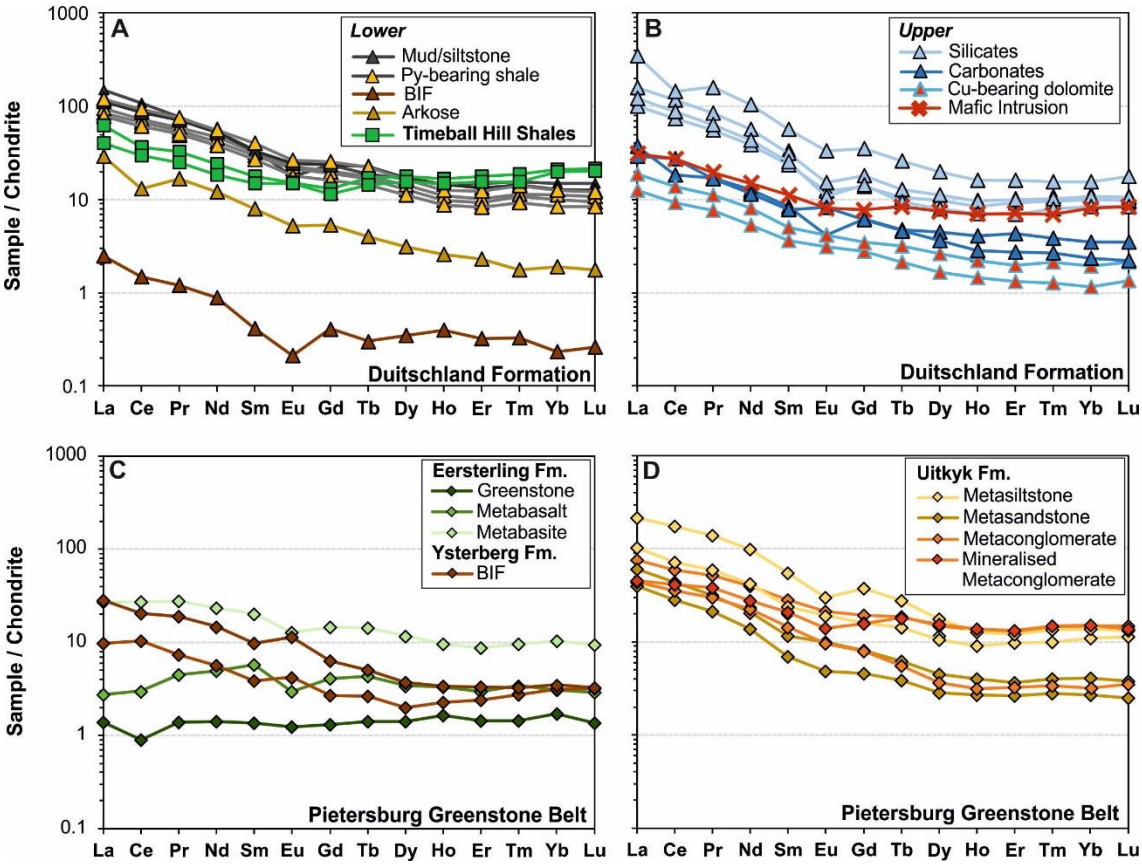

Figure 6.8: Chondrite normalised REE plots for: (A) the Lower Duitschland Formation; (B) the Upper Duitschland Formation; (C) the Eersteling and Ysterberg Formation of the Pietersburg Greenstone belt and (D) the Uitkyk Formation of the Pietersburg Greenstone Belt. Normalisation factors from McDonough & Sun (1995).

The PGB samples have been divided into metavolcanic and BIF samples from the Eersteling and Ysterburg Formation, respectively (Figure 6.8C) and the metasiliciclastic rocks of the Uitkyk Formation (Figure 6.8D). The Eersteling metavolcanic rocks have relatively flat-lying REE profiles; a greenstone sample (PGB 1) has near chondritic values (La_N/Yb_N = 1.19). In contrast, the Uitkyk Formation sedimentary samples (Figure 6.8D) are enriched in the LREE over the HREE; with the finer-grained lithologies showing stronger LREE:HREE fractionation (e.g. metasiltstone La_N/Yb_N = 14.79) compared to coarser-grained sediments (e.g. metaconglomerates La_N/Yb_N = 5.14). The Potberg

mineralised metaconglomerate has a bow-shaped profile showing slightly elevated HREE concentrations and consequently has the lowest La_N/Yb_N value of 3.03.

6.3.3 Multi-Element Spidergrams

Primitive-mantle normalised trace element spidergrams for the Duitschland Formation (DF) are presented in Figure 6.9 (A-B) and compared to the results from the proposed least contaminated (Figure 6.9C) and most contaminated (Figure 6.9D) magmatic rocks on Turfspruit. The highest concentrations of the trace elements are found in the shale-dominated lithologies of both the Duitschland and Timeball Hill Formations (see Figure 6.9A). All the Lower DF samples have similar patterns with strong negative Nb, Ta, Sr and Ti anomalies. In contrast, the Timeball Hill shales have elevated Zr and Hf concentrations. The trace element profiles for the Upper DF samples are shown in Figure 6.9B, the silicate lithologies contain higher concentrations of the trace elements than the carbonate sediments.

The trace element spidergrams of the Deep Platreef (Figure 6.9C) and Platreef (Figure 6.9D) are provided for comparison with the older country rocks. All the magmatic rocks have a strong negative Nb and Ta anomaly of a similar order of magnitude as seen in the DF rocks. This signature is seen throughout the Bushveld Complex cumulate rocks (Barnes & Maier, 2002) and the modelled parental magma compositions (Harmer & Sharpe, 1985) and it is therefore difficult to attribute this to a particular contamination event. In Figure 6.9C, the pattern for the quartz-feldspar vein is very similar, in terms of concentration and overall shape, to the shales of the DF with elevated LILE, negative Sr and negative Ti. This LILE enrichment is also imparted on the mafic/ultramafic magmatic rocks particularly in the Middle Pyroxenite unit recorded in the Deep Platreef (>100 x mantle) but can also be seen in the Platreef rocks. The assimilated hornfels lithologies identified in the contaminated Platreef are enriched in LILE and show strong negative anomalies in all high field strength elements.

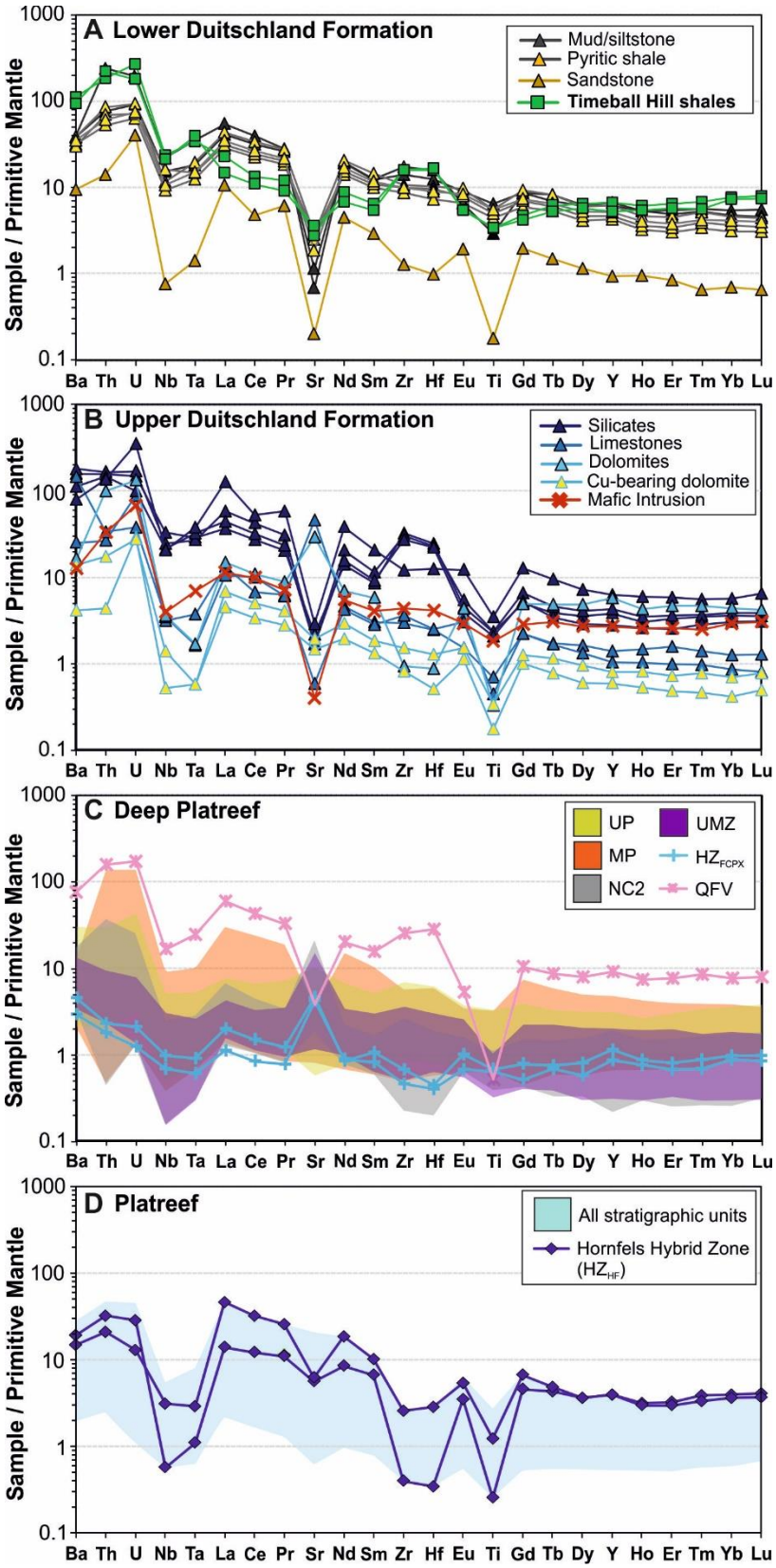

Figure 6.9: Multi-element spidergrams for: (A) the Lower Duitschland Formation; (B) the Upper Duitschland Formation; (C) magmatic rocks from the Deep Platreef on Turfspruit; (D) magmatic rocks from the Platreef on Turfspruit. All data collected in this study. Mantle normalisation factors from McDonough & Sun (1995).

The primitive mantle normalised trace element distribution in the PGB rocks are shown in Figure 6.10. The metavolcanic rocks don't have a negative Nb and Ta anomaly (see Figure 6.10A) indicative that they were derived from uncontaminated mantle melts e.g. the trace element profiles are similar to those typical of average MORB. The Ysterberg BIF samples have a very spiky profile with strong negative anomalies in the high field strength elements and Sr. The metasedimentary rocks of the Uitkyk Formation have higher overall concentrations in the incompatible elements reflected in a gently sloping profile (see Figure 6.10B) compared to a relatively flat-lying profile for the metavolcanics. They record a moderate negative Nb and Ta anomaly, a strong negative Sr anomaly and a moderate negative Ti anomaly; in addition, the pyrite-bearing mineralised metaconglomerate sample from Potberg has elevated U over Th (see Figure 6.10B).

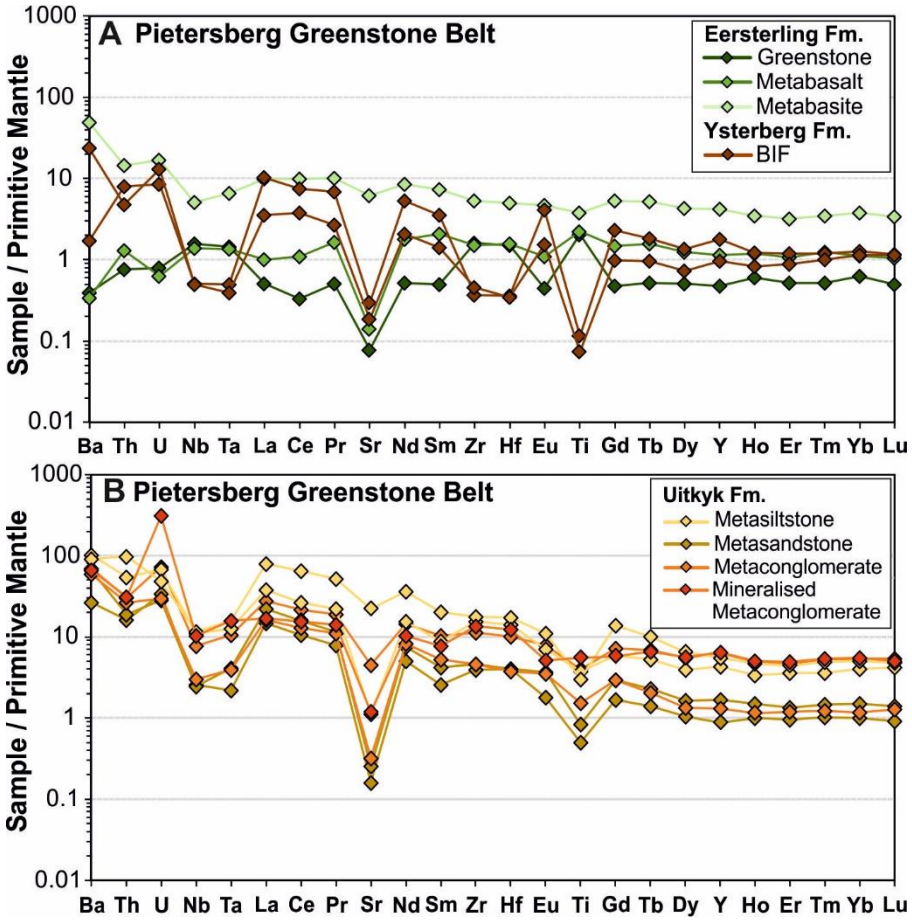

Figure 6.10: Multi-element spidergrams for the Pietersburg Greenstone Belt (PGB) samples. (A) Eersteling Formation volcanics and banded iron formations of the Ysterberg Formation; (B) Uitkyk Formation metasedimentary rocks. Mantle normalisation factors from McDonough & Sun (1995).

6.3.4 Chondrite-Normalised Ni-Cu-PGE data

A selection of samples of the Duitschland Formation (DF) and Pietersburg Greenstone Belt (PGB) were chosen for Ni-sulphide fire assay to test their precious metal (Ni-Cu-PGE-Au) budget a summary of the results is shown in Table 6.1.

Table 6.1: Whole-rock Ni-Cu-PGE-Au data for the Duitschland Formation and Pietersburg Greenstone Belt compared to selected reference examples from similar geological settings, in addition to the modelled compositions of the Bushveld parental magmas. References: (1) Park et al., 2012; (2) Siebert et al., 2015; (3) Maier et al., 2009. (4) Barnes et al., 2010.

		Ni	Os	Ir	Ru	Rh	Pt	Pd	Au	Cu		
Sample	**Lithology**	**ppm**	**ppb**							**ppm**	**Pt/Pd**	**Cu/Pd**
Duitschland Formation (This Study)												
DTH_15	Dolomite	9	0.05	0.23	0.45	0.78	7.71	9.34	11.13	486	0.8	52.0
DHP_10	Dolomite	17	0.03	0.07	0.24	0.58	5.30	3.93	3.61	31	1.3	7.9
DHP_12	Dolomite	25	0.02	0.05	0.12	0.41	2.37	1.36	2.21	50	1.7	36.9
DTH_18	Igneous Intrusive	706	0.05	0.25	1.13	1.10	11.80	5.58	4.25	129	2.1	23.1
DTH_2	Shale	56	0.23	0.29	0.60	0.87	5.78	3.96	1.63	123	1.5	31.1
DTH_3	Shale	152	0.24	0.77	2.45	3.04	29.84	58.27	5.71	193	0.5	3.3
DTH_4	Shale	86	0.10	0.24	0.43	0.43	13.30	10.32	2.51	348	1.3	33.7
DTH_6	Shale	69	0.10	0.20	0.16	0.40	4.01	2.14	3.19	235	1.9	109.9
DHP_11	Shale	610	0.02	0.15	0.32	1.02	9.19	5.60	9.54	31	1.6	5.6
DTH_7	Shaly mudstone	81	0.09	0.19	0.16	0.32	4.68	2.08	1.14	160	2.3	76.8
Upper Continental Crust[1]		-	-	0.02	0.03	0.02	0.60	0.53	-	-	1.1	-
Witwatersrand Black Shales (average)[2]		-	4.12	0.18	0.24	0.12	1.09	2.10	-	-	0.5	-
Pietersburg Greenstone Belt (This Study)												
PGB_16	BIF	262	0.07	0.10	0.11	0.41	8.50	2.59	3.67	161	3.3	62.4
HH_1	Mineralised Metaconglomerate	11	0.12	0.17	0.52	0.53	9.49	9.90	3920	97	1.0	9.8
PGB_5	Metabasalt	157	1.18	0.70	0.84	0.44	11.33	4.96	2.37	99	2.3	19.9
PGB_13	Meta-basite/amphibolite	150	0.09	0.23	0.51	1.23	10.67	5.68	1.27	56	1.9	9.9
PGB_2	Metaconglomerate	971	1.45	1.58	2.46	0.44	4.17	1.54	1.18	49	2.7	31.5
PGB_4	Metasandstone	68	0.33	0.48	0.88	0.37	3.09	1.49	1.79	15	2.1	9.8
Baberton Greenstone Belt												
Komati (average)[3]		1496	1.68	1.11	2.63	0.65	5.00	4.42	1.35	54	1.1	12.2
Fig Tree Group - Greywacke (average)[2]		-	0.34	0.26	0.69	0.22	1.58	1.52	-	-	1.0	-
Fig Tree Group - Siltstone[2]		-	0.53	0.44	0.93	0.34	2.66	3.37	-	-	0.8	-
Fig Tree Group - Black shales (average)[2]		-	0.64	0.55	1.49	0.57	3.00	3.51	-	-	0.9	-
Rustenburg Layered Suite Parental Magmas (Barnes et al., 2010)												
B1 (average)[4]		284	0.50	0.54	1.90	1.78	19.36	13.99	2.72	51	1.4	3.6
B2 (average)[4]		106	0.11	0.21	0.89	0.77	9.54	5.21	1.90	76	1.8	14.6
B3 (average)[4]		133	0.23	0.3	1.23	0.74	12.71	3.28	0.89	46	3.9	14.1

In Table 6.1 a comparison is made between the chalcophile element concentrations of the Duitschland Formation (DF) sediments and the Pietersburg Greenstone Belt (PGB) to similar geological units at different localities and with the modelled parental magma compositions of the Bushveld magmatic rocks. The DF sediments contain elevated PGE concentrations by up to two orders of magnitude compared to the average upper continental crust as estimated in Park et al., (2012) using PGE data on loess from around the world. This is illustrated in the chondrite-normalised PGE profiles of the DF in Figure 6.11A. The profiles for the shale lithologies consistently peak on Pd, whereas the dolomitic compositions peak on gold and are typically flat-lying from Rh to Pd. The highest PGE concentrations in the DF are recorded in the lower DF shales and mudstones with ΣPGE concentrations ranging from 7 to 95 ppb (average 27 ppb), with the highest values recorded in the pyrite-bearing samples. The upper DF dolomites and limestones have lower total PGE concentration of between 4 and 19 ppb (average 11 ppb). In comparison the parental magmas of the Bushveld Complex have estimated total PGE concentrations of 41, 19 and 19 ppb for the B1, B2 and B3 (see Table 6.1). The Pd_N/Ir_N ratio is highly variable within the shales varying from 8.4 to 60; the range in Pd_N/Ir_N is smaller in the carbonates with values of 20.7 to 44.4.

The PGE concentrations in the DF shales are comparable to the concentrations of the proposed parental B1, B2 and B3 magmas of the Bushveld Complex (see Table 6.1). As a comparison the PGE profiles of the proposed least contaminated magmatic rocks of the Deep Platreef and most contaminated magmatic rocks Platreef on Turfspruit are shown in Figure 6.11C and 6.11D. In Figure 6.11D the two hornfels samples have very similar PGE patterns and concentrations to the shales as shown in Figure 6.11A. Ultimately, both the DF and PGB do not contain enough PGE to have significantly contributed to the precious metal endowment of the Bushveld magmas on the northern limb (see Figure 6.11C and 6.11D).

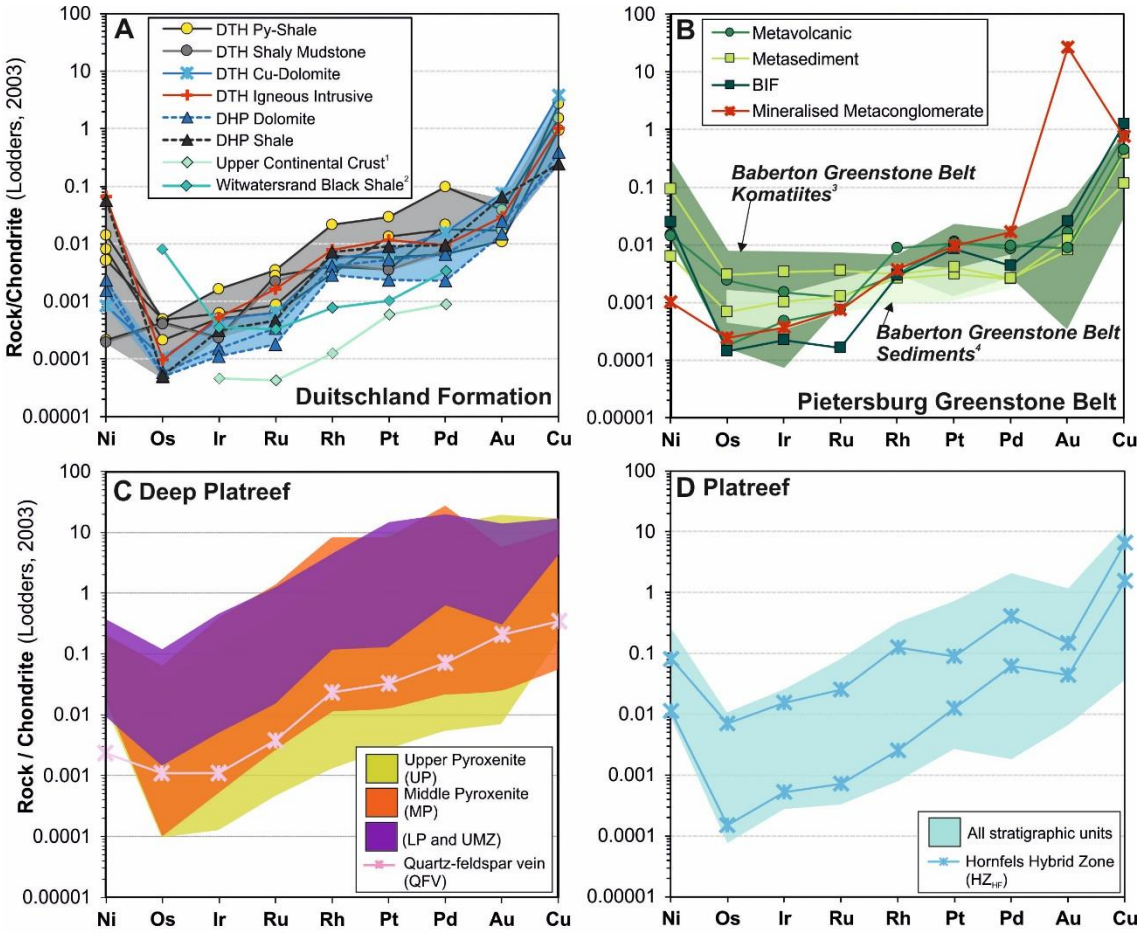

Figure 6.11: Chondrite-normalised Ni-Cu-PGE-Au profiles for: (A) the Duitschland Formation; (B) the Pietersburg Greenstone Belt; (C) the relatively 'uncontaminated' stratigraphic units of the Deep Platreef on Turfspruit and; (D) the 'contaminated' shallow Platreef on Turfspruit. Note: all unreferenced data was collected in this study. Normalisation factors from Lodders (2003). Source: [1]Park et al., 2012. [2]Siebert et al., 2005. [3]Maier et al., 2009.

The PGB samples have relatively flat profiles (see Figure 6.11B) when compared to the Duitschland Formation samples (see Figure 6.11A). The least fractionated samples are from the unmineralised metasediments of the Uitkyk Formation with an average Pd_N/Ir_N of 3.0; the shape and concentration of the PGE profile are similar to the Baberton Greenstone Belt sediments. The Au mineralised metaconglomerate from the Potberg mine shows the greatest fractionation with a Pd_N/Ir_N value of 46; the PGE profile for this sample peaks at gold with a concentration of 3920 ppb. The komatites of the Baberton Greenstone belt (BGB) peak on Pt, this is more pronounced than for the PGB samples which have relatively flat-lying profiles from Rh to Pd and elevated Au.

Chapter 7

Whole-Rock Geochemistry: Core Samples

7.0 Introduction

The results of a whole-rock geochemical study on all samples collected from drill holes across the Turfspruit deposit are reported in this chapter. The raw geochemical datasets are provided in Electronic Appendix C with additional information provided in Appendix C. A description of the analytical methodology can be found in Chapter 4 (section 4.3). These geochemical datasets illustrate the lithostratigraphic variability throughout the project area and can provide insight into the magmatic lineage of the parental magmas and the degree to which they are contaminated.

7.1 Downhole Geochemical Profiles

Geochemical variability with depth can be used to understand the controls on the observed stratigraphy and localisation of mineralised intervals. In the following section a selection of major and trace elements from the whole-rock geochemical dataset are plotted against depth for all drill holes sampled across the Turfspruit deposit.

In addition, a selection of major and trace element ratios are included that have proved useful in other studies on Bushveld rocks for identifying: (1) the magmatic lineage of the rocks i.e. Main Zone vs Critical Zone based on distinct Cr/MgO ratios (Seabrook et al., 2005) and; (2) crustal contamination of the magmatic rocks as evidenced in the Platreef on Turfspruit in excursions above and below the magmatic range of CaO/Al_2O_3 ratios (0.6 to 1.0) expected for magmas crystallising orthopyroxene and plagioclase (Kinnaird, 2005).

7.1.1 Deep Platreef (UMT_345)

The downhole geochemical profiles for a selection of major elements and major element ratios for the Deep Platreef as sampled in drill hole UMT_345 are provided in Figure 7.1; the downhole geochemical profiles of the deflection drill hole UMT_345_D1 are presented in Appendix C. The geochemical profiles are characterised by intervals with consistent values and others of geochemical complexity. The intervals showing the greatest geochemical variability correspond to lithostratigraphic contacts. There is no systematic variability observed in the major element concentrations in any of the depth profiles shown in Figure 7.1; this matches observations on the drill core of a distinct lack of cyclicity in the mineralised lithologies present within the Deep Platreef (see Chapter 5).

The majority of contacts between lithostratigraphic units are characterised by different silicate composition i.e. moving from a plagioclase-dominated to orthopyroxene-dominated lithologies. This change in the modal mineralogy is expressed on the

geochemical profile as an anticorrelation between CaO and Al_2O_3 with MgO and $Fe_2O_3^T$. This observation applies for the following lithostratigraphic contacts: (1) Mottled Anorthosite (MAN) and Upper Pyroxenite (UP) units; (2) Middle Pyroxenite (MP) and Norite Cycles 2 (NC2); and (3) the NC2 and the Lower Pyroxenite unit (LP). The exceptions to this are on contacts defined by the presence of chromitites, including: (1) on the contact between the base of the UP and the top of MP; and (2) between the LP unit and the Main Chromitite (MCHR).

The contact between the base of the UP unit and the top of the Middle Pyroxenite (MP) is characterised by the presence of chromite stringers and pegmatoidal olivine-bearing lithologies. Samples bearing chromite stringers have the lowest SiO_2 contents (< 50 wt%) and the highest $Fe_2O_3^T$ (up to 24 wt%); and elevated Cr/MgO (up to 3541). This interval also has slightly elevated Al_2O_3 and CaO corresponding to interstitial plagioclase and clinopyroxene (see Chapter 8). The pegmatoidal olivine orthopyroxenite/harzburgite records the highest MgO of all stratigraphic units at >28 wt%. The decrease in MgO content below this to values <20 wt% was identified within strongly altered samples (with elevated LOI values up to 4 wt%). The MgO content gradually returns to values of ≈25 wt% in the orthopyroxenite in the lower part of the MP unit.

The MCHR unit is recorded by a strong negative shift in SiO_2 (and SiO_2/Al_2O_3) and a moderate negative shift in MgO (and Mg#). The only negative LOI values (-0.19 to -0.93 wt%) are recorded for the MCHR unit indicating the presence of significant iron. The major elements of the Ultramafic Zone (UMZ) are highly variable; the greatest range in values are observed for MgO (9 to 27 wt%) and Al_2O_3 (3 to 18 wt%) reflecting the varying proportions of orthopyroxene, olivine and plagioclase. The highest MgO values are found directly beneath the MCHR in the pegmatoidal feldspathic harzburgite. At the basal contact between the UMZ and the Feldspathic Clinopyroxenite Hybrid Zone (HZ_{FCPX}) no significant geochemical shifts are observed.

The CaO/Al_2O_3 ratio fluctuates between 0.15 to 2.50, with the majority of samples within the magmatic range (0.6 to1.0) as outlined in Kinnaird (2005; see Figure 7.1G). The highest values (1.45 to 2.50) are observed on the contact between the UP and MP units and appear to correlate with the appearance of chromite with clinopyroxene as an interstitial phase. Internally in the UMZ unit there are a number of spikes in CaO/Al_2O_3 ratio (1.07 to 1.8). The NC2 unit is characterised by lower CaO/Al_2O_3 ratios with an average value of 0.58 and a tight range from 0.50 to 0.70.

The majority of samples of pyroxenite lithologies have Cr/MgO values that plot within the Critical Zone range as defined by Seabrook et al., (2005; see Figure 7.1H). Excursions outside of the Critical Zone range are found in the lowermost portions of the drill hole in the UMZ stratigraphic unit, directly beneath the MCHR (see Figure 7.1H). The top of the UMZ is composed of harzburgite and pegmatoidal orthopyroxenite which record very low Cr/MgO ratios of 20, 11 and 76 that are significantly below the Critical Zone range. The Cr contents are too low for them to represent 'true' magmatic ultramafic rocks; they have been contaminated to form a para-igneous rock as described in Harris & Chaumba (2001). The Main Zone sample analysed has a Cr/MgO value of 71, slightly above that of 60 outlined in Seabrook et al., (2005) for this unit.

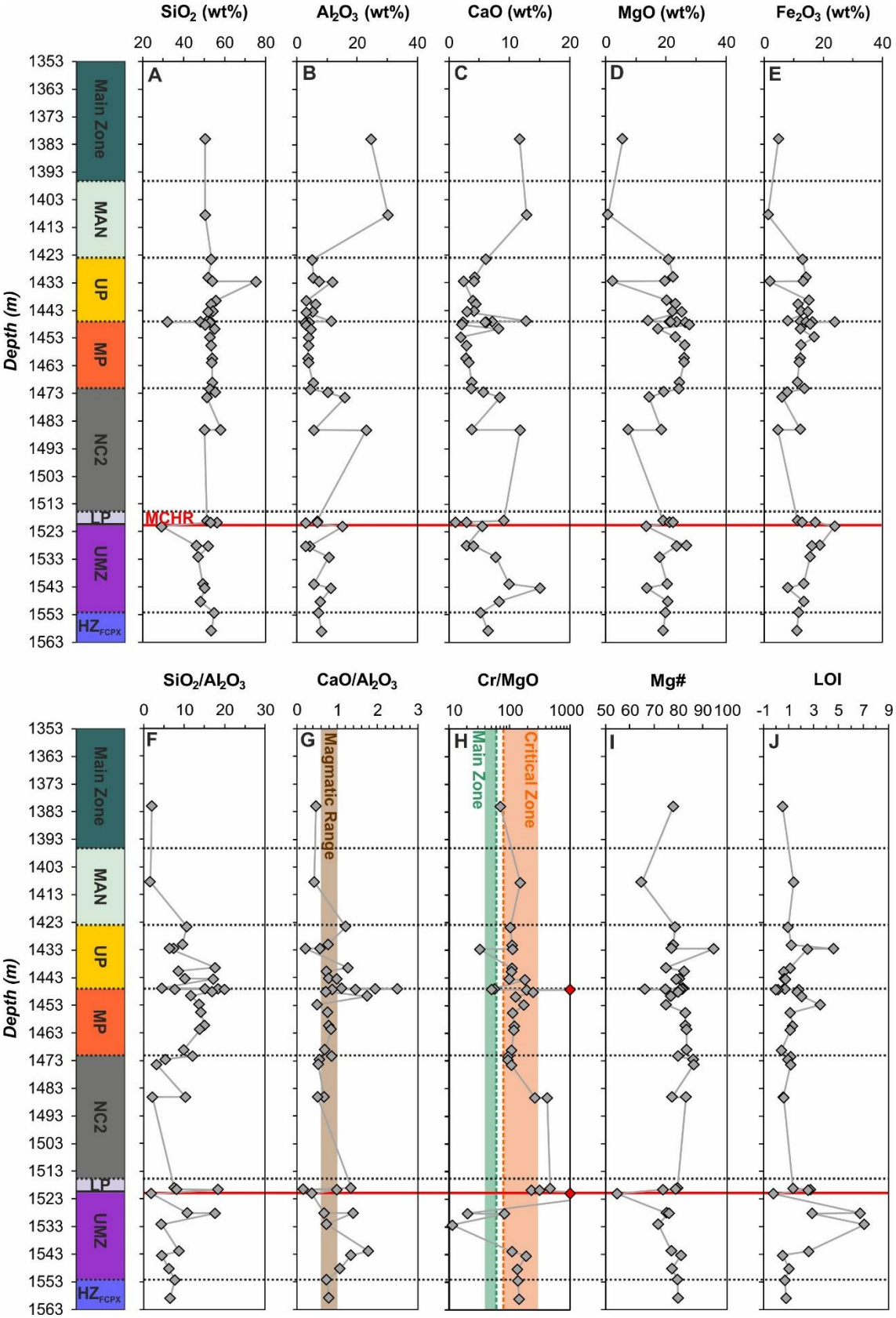

Figure 7.1: Major element geochemical profiles with depth in the Deep Platreef as sampled in drill hole UMT_345. (A) SiO_2 wt%; (B) Al_2O_3 wt%; (C) CaO wt%; (D) MgO wt%; (E) $Fe_2O_3^T$ wt%; (F) SiO_2/Al_2O_3; (G) CaO/Al_2O_3; (H) Cr/MgO; (I) Mg# (calculated as 100*Mg/(Mg+Fe)); and (J) LOI wt%.

The observed anticorrelation between MgO and both Al_2O_3 and CaO suggests that the major element variability is controlled primarily by the modal mineralogy. This is illustrated in Figure 7.2A and 7.2B, where average mineral compositions of orthopyroxene, plagioclase, clinopyroxene and olivine (measured in this study; see Chapter 8, section 8.2) for this drill hole are plotted along with the whole-rock geochemical data. In Figure 7.2A and 7.2B the majority of the whole-rock data plot between orthopyroxene-plagioclase-clinopyroxene end-members. The presence of olivine is recorded in both the pegmatoidal upper part of the MP unit (MP_U) and within the UMZ; neither of these units have any data that plots towards the apex defined by the olivine composition. The whole-rock data for the UP and MP are quite tightly clustered near the orthopyroxene composition; in contrast, the more litholgoically diverse NC2, UMZ and LP units have a larger spread of data.

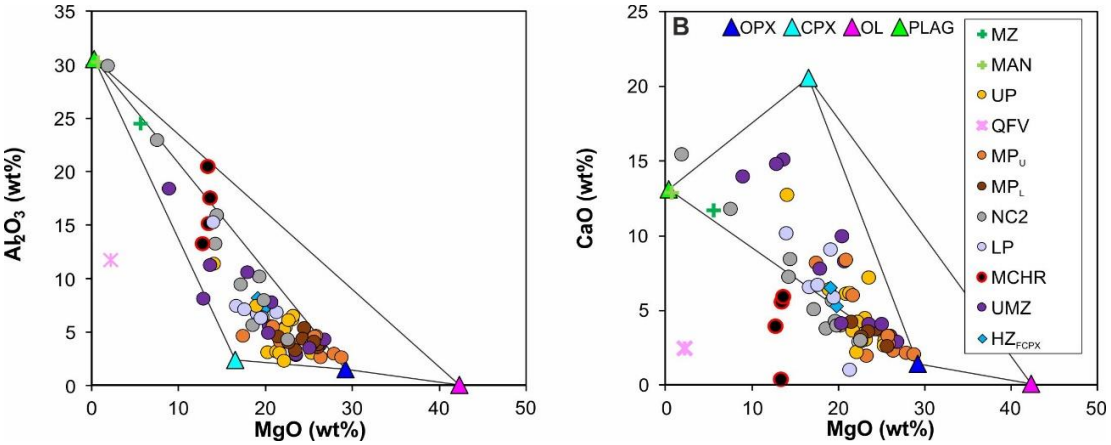

Figure 7.2: Whole-rock major element bivariate plots combined with end-member mineral compositional data as analysed in sampled from the Deep Platreef. (A) Al_2O_3 (wt%) vs. MgO (wt%). (B) CaO (wt%) vs MgO (wt%). Note: whole-rock data from drill holes UMT_345 and UMT_345_D1 is combined.

The trace and precious metal down hole geochemical profiles for drill hole UMT_345 are shown in Figure 7.3. The profiles show similar trends as the major elements with the variability restricted to stratigraphic contacts and no fractionation trends are observed.

The Cr, TiO_2 and V concentrations vary sympathetically and all peak in samples containing visible chromite mineralisation (see Figure 7.3A to 7.3C). The background Cr content increases moving down hole from the hanging wall lithologies of the Main Zone and the MAN at < 500 ppm to the pyroxenite units which have consistent Cr contents of approximately 2500 ppm (without visible chromite; see Figure 7.3A). The four chromite stringers at the base of the UP contact result in elevated Cr values up to 74,727 ppm; a similar value to the Merensky Reef chromitite as measured at Impala

(Barnes & Maier, 2002). Moving downhole from the MP unit to the NC2 unit there is a change from a consistent background Cr levels to a more variable signature reflecting the rapidly changing modal mineralogy characteristic of the NC2 unit. The overall highest Cr content was recorded in the MCHR unit at 169,872 ppm; this value is relatively low in comparison to the UG2 chromitite which typically contains >200,000 ppm (Barnes & Maier, 2002) and reflects the more disseminated nature of the MCHR unit with a significant proportion of silicate gangue minerals. The Cr content decreases by three orders of magnitude from the MCHR unit to the UMZ unit. The top of the UMZ unit has Cr contents ranging from 51 to 167 ppm this increases moving downhole to values > 2000 ppm. This represents an anticorrelation with the observed lithologies which appear more ultramafic (harzburgites) directly below the MCHR unit and become more mafic (olivine gabbronorites) with depth.

The Sr profile, shows the highest concentrations (>250 ppm) in stratigraphic units where plagioclase-dominated rock types are present i.e. in the Main Zone, MAN and in the anorthositic portions of the NC2 unit. The one elevated Zr peak (268 ppm) corresponds to a sample of the quartz-feldspar vein (QFV) analysed from the UP unit.

The 3PGE data (Pt, Pd and Rh, see Figure 7.3F) shows three consistent elevated peaks corresponding to the Upper, Middle and Lower reefs as outlined in Chapter 5. The data collected in this study (shown as points in Figures 7.3F to 7.3G) display a strong nugget effect compared to the Ivanplats 1 m composite data; this is accentuated in the UMZ unit because of the heterogenous distribution of sulphides and preferential sampling of sulphide-bearing samples.

The Upper Reef mineralisation event is 11 m thick at 4.2 ppm 3PGE accompanied by a significant peak in Au (up to 1.4 ppm). This interval corresponds with elevated Ni + Cu concentration >3500 ppm and has average Pt/Pd and Cu/Pd ratios of 1.5 and 1160, respectively. The Pt/Pd ratio within the Upper Reef decreases from 1.9 at the top of the interval to 1.4 at the base. The beginning of the mineralised interval is marked by a significant decrease in the Cu/Pd ratio from 6009 above the mineralised interval to 2437 at the top of the Upper Reef. In Grobler et al., (2018) this mineralisation event is equated to the Bastard reef, the application of this in the current study was avoided because of the lack of the presence of a chromite stringer at the base of the mineralised interval and because the grade is at the same magnitude as the Middle Reef.

The Middle Reef mineralisation event is thicker at 14 m and only slightly higher grade at 4.5 ppm 3PGE and isn't accompanied by any significant Au peak. At the level of

the 4th chromite stringer, which marks the contact between the UP and MP stratigraphic units the Pt/Pd ratio increase from an average of 0.6 in the pegmatoidal upper part of the MP unit below the chromite stringer to an average of 1.6 above. In the Merensky Reef, as analysed in Naldrett et al., (2009), the Pt/Pd ratios decrease from 3-4 on the basal chromite stringer to 1-2 moving upwards to the top of the mineralised interval. In the Middle Reef the Cu/Pd ratio decreases moving upward through this mineralisation event with an average value of 807.

The Lower Reef mineralisation event is ≈ 6m thick at 4 ppm (3PGE); the mineralised interval begins in the LP unit and ends at the base of the MCHR unit. The mineralisation is top loaded; the grade drops off sharply to < 2 ppm within 2 m into the footwall rocks of the UMZ unit, but elevated grades extend into the overlying feldspathic orthopyroxenite of the LP unit. The Pt/Pd ratio increases from an average of 0.46 in the footwall rocks of the UMZ unit to an average of 1.44 in the mineralised interval. This is accompanied by a decrease in the Cu/Pd ratio from an average of 4052 in the footwall to an average of 1394 in the mineralised interval.

The Pt/Pd ratio has an overall trend of decreasing with depth, with local deviations from this occurring above stratigraphic contacts, suggesting that these formed from new replenishing magma pulse. The Cu/Pd ratio below the MCHR unit, in both the UMZ and HZ_{FCPX} units, has an average value of ≈4000; this Cu/Pd ratio is equivalent to the average of the Critical Zone crystallising plagioclase and orthopyroxene as identified in Naldrett et al., (2009). The Cu/Pd ratio is most variable within the NC2 unit, varying from low values (550) similar to the mineralised interval to higher values (7684) as identified in the hanging wall MAN unit.

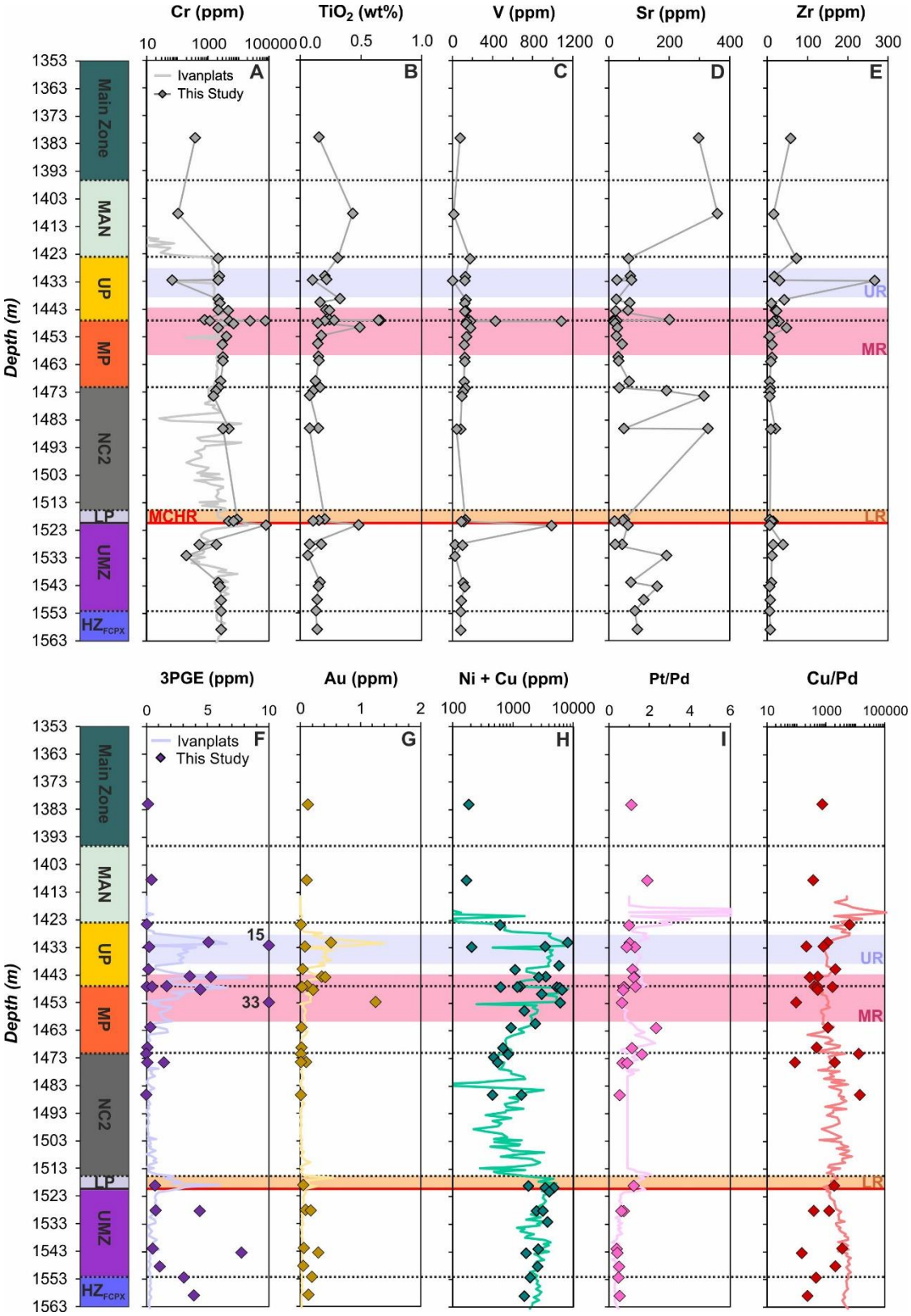

Figure 7.3: Trace element geochemical profiles with depth in the Deep Platreef as sampled in drill hole UMT_345. (A) Cr (ppm); (B) TiO_2 (wt%); (C) V (ppm); (D) Sr (ppm); (E) Zr (ppm); (F) 3PGE (ppm); (G) Au (ppm); (H) Ni + Cu (ppm); (I) Pt/Pd; (J) Cu/Pd. Note: lines without points represent data provided by Ivanplats Pty Ltd., and points are data collected in the current study. 3PGE = Pt + Pd + Rh. UR = Upper Reef, MR = Middle Reef and LR = Lower Reef.

Further investigation into the distribution of the base metals, Ni and Cu, is necessary because of the similarity in their distribution with that of the PGE grade. Ni can partition into both silicate minerals (orthopyroxene and olivine) and sulphides whereas Cu resides strongly in sulphides. A strong correlation between Cu and Ni indicates that the Ni is predominantly hosted in sulphides. R-squared values (R^2) values are used as an assessment of the strength of correlation as follows: (1) >0.8 indicating a strong correlation; (2) >0.6 a moderate correlation and; (3) <0.6 a weak correlation.

The relationship between Ni and MgO is shown in Figure 7.4A. There is no linear correlation, rather there appears to be an significant increase in the Ni content at between 20 to 30 wt% MgO, within the range of compositions recorded in the pyroxenite units. Also shown in Figure 7.4A are whole rock Ni and MgO data from Upper Critical Zone (UCZ) rocks of the eastern and western limbs of the Bushveld Complex as measured by Godel et al., (2011) and Maier et al., (2013). In comparison to the UCZ data, the data from the Deep Platreef plots at much higher Ni contents (> 5000 ppm) and lower MgO (wt%). In Figure 7.4B, a very strong correlation between Ni and Cu is evidenced suggesting that Ni is predominantly hosted in sulphides particularly in the pyroxenite units (i.e. the UP, MP and LP units) where the R^2 values are between 0.97 to 0.98. These pyroxenite host the Upper, Middle and part of the Lower Reef mineralisation, respectively; this highlights the close control of sulphides on concentrating the PGE mineralisation. In contrast, samples from the UMZ and HZ_{FCPX} units show a weaker correlation (R^2 = 0.37 in the HZ_{FCPX}) over a more restricted range of Ni and Cu concentrations (see Figure 7.4B).

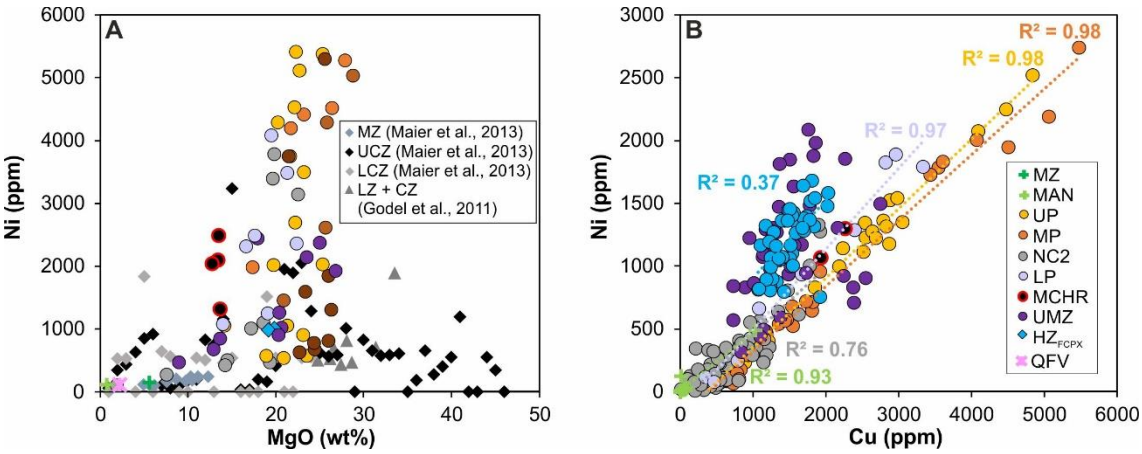

Figure 7.4: Bivariate plots demonstrating the distribution of Ni between silicate and sulphide minerals in the Deep Platreef. (A) Ni (ppm) vs MgO (wt%) based on combined data from drill holes UMT_345 and UMT_345_D1. (B) Ni (ppm) vs Cu (ppm) plotted according to stratigraphic unit using 1 m composite data provided by Ivanplats Pty Ltd.

7.1.2 'Thick' Flatreef (TMT_006_D2)

The major element geochemical depth profiles for the Thick Flatreef as sampled in drill hole TMT_006_D2 are provided in Figure 7.5 (A-J). The major element geochemical variations are relatively consistent throughout the Upper Pyroxenite (UP) and the Middle Pyroxenite (MP) units. The geochemical profiles, downhole from the base of the MP unit (i.e. at depths > 845 m), becomes more variable within both the Olivine Websterite and Gabbronorite Hybrid Zones (HZ_{OLWEBS} and HZ_{GBRN}); this reflects the heterogenous nature of the lithologies that make up these stratigraphic units.

Minor geochemical variations are recorded within the UP unit including a slight decrease in CaO and increase in MgO moving downhole away from the top contact; this corresponds with the visual observation of poikilitic clinopyroxene at this level. In addition, there is a slight decrease in the $Fe_2O_3^T$ content from the top contact of the UP unit to 815 m; this change can be attributed to a downhole decrease in the abundance of pyrrhotite-dominated sulphides over this interval. Towards the base of the MP unit there is a decrease in the MgO and $Fe_2O_3^T$ accompanied by an increase in Al_2O_3 indicative of the more noritic composition of the lithologies on the contact with the underlying stratigraphic unit.

All Cr/MgO ratios in the UP and MP units plot either within or above the Critical Zone field as defined in Seabrook et al., (2005). The highest Cr/MgO ratios, above the Critical Zone range, are identified in samples containing disseminated chromite (up to 498). The average MgO content (and Mg#) are higher than the equivalent pyroxenite units of the Deep Platreef, although the Cr/MgO ratios are lower. This could indicate that either the Thick Flatreef pyroxenites crystallised from a compositionally more primitive magma or that the Mg-budget of the magma has been elevated through the addition of dolomitic material. The majority of the CaO/Al_2O_3 values within the UP and MP units fall within the magmatic range (see Figure 7.7F and 7.7G). Exceptions to this are principally found in olivine-bearing lithologies of the MP unit hosting the highest CaO/Al_2O_3 (up to 2.0) and SiO_2/Al_2O_3 (29) concentrations.

On the contact between the MP unit and the HZ_{OLWEBS} unit there are positive spikes in CaO, MgO, $Fe_2O_3^T$, $CaO:Al_2O_3$ and LOI accompanied by a reduction in SiO_2. Compared to the other stratigraphic units the lithologies within the HZ_{OLWEBS} unit demonstrate the greatest variation in SiO_2, $Fe_2O_3^T$, MgO, CaO, Mg# and $CaO:Al_2O_3$. The $CaO:Al_2O_3$ ratio downhole profile (see Figure 7.7G) is very spiky with the majority of data plotting above the magmatic range (up to 3.3) indicative of the assimilation of

carbonate material. Overall, the Cr/MgO ratio decreases significantly moving from the MP unit to the HZ_{OLWEBS} unit; although elevated Cr/MgO ratios (up to 2036) are recorded in samples containing visible disseminated chromite. The bulk rock Mg# remains high despite the low Cr/MgO and elevated $CaO:Al_2O_3$ suggesting that Mg is also being added from a non-igneous source; based on the results of the geochemical study on the footwall rocks of the Duitschland Formation this is most likely due to the assimilation of dolomite.

The sample on the contact between the HZ_{OLWEBS} unit and the HZ_{GBRN} represents metamorphosed country rock. This is characterised by low $CaO:Al_2O_3$ (0.1), negligible Cr/MgO (0.03), and very high whole-rock Mg# (92); indicating that the protolith was a highly magnesian dolomite. In the geochemical profile the sample above the country rock contain elevated $CaO:Al_2O_3$ ratios (3.3); these rocks are parapyroxenite lithologies rich in clinopyroxene and tremolite (see Chapter 8, section 8.1.2).

The HZ_{GBRN} records moderate geochemical variability in the major element concentrations; a result of the varying abundances of plagioclase, clinopyroxene and orthopyroxene that make up this unit (see Chapter 5, section 5.3.2). The majority of the data plots within the Main Zone Cr/MgO range (see Figure 7.5H); the dominant lithology within this unit are gabbronorites and they have an average Cr/MgO of 71 (excluding samples with visible chromite). The highest Cr/MgO value of 2132 corresponds the presence of disseminated chromite in a clinopyroxenite which also records the highest CaO/Al_2O_3 value within this unit of 2.06.

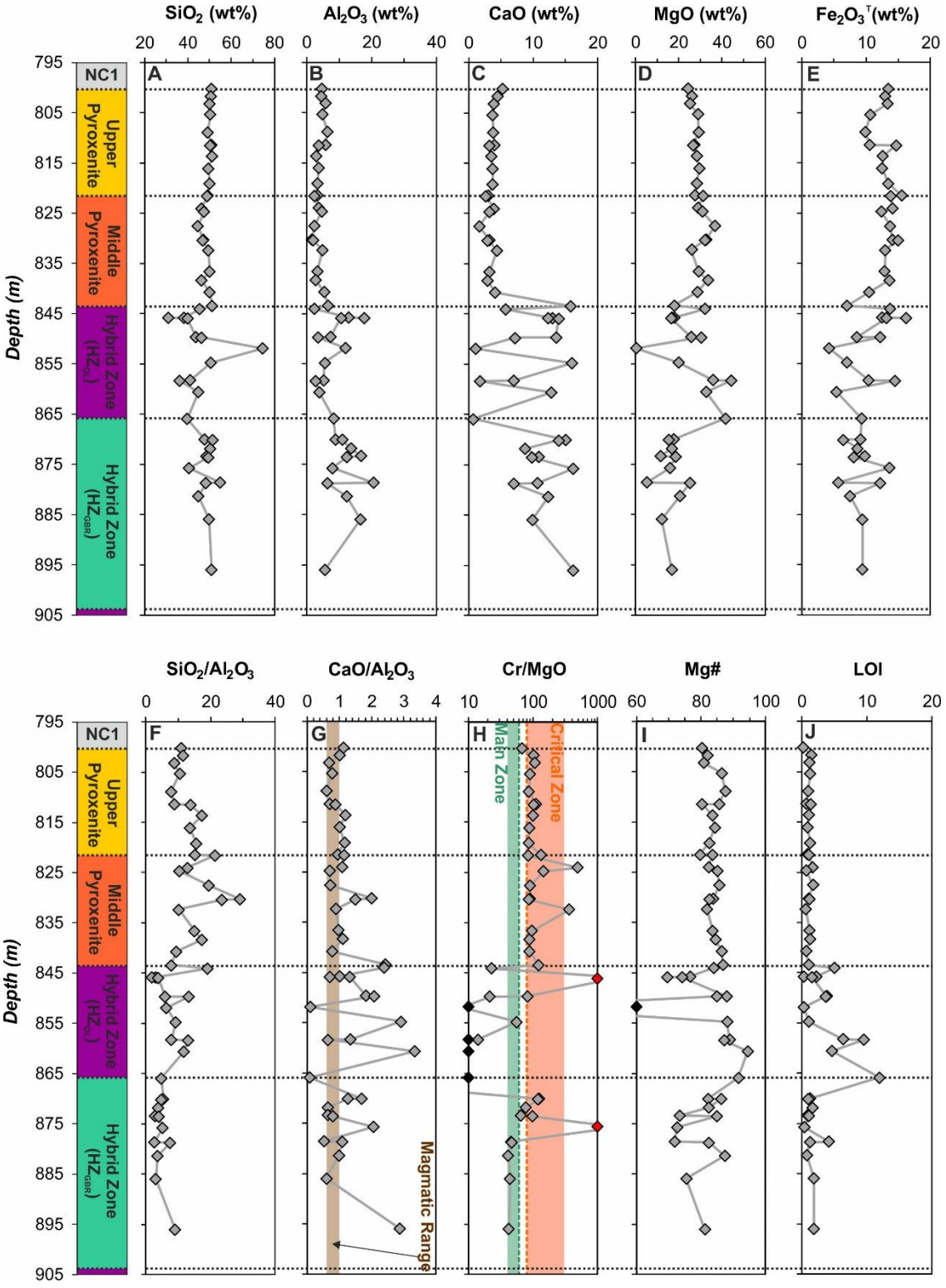

Figure 7.5: Major element geochemical profiles with depth in the Thick Flatreef as sampled in drill hole TMT_006_D2. (A) SiO_2 (wt%); (B) Al_2O_3 (wt%); (C) CaO (wt%); (D) MgO (wt%); (E) Fe_2O_3 (wt%); (F) SiO_2/Al_2O_3; (G) CaO/Al_2O_3; (H) Cr/MgO; (I) Mg# (calculated as 100*Mg/(Mg+Fe)); and (J) LOI wt%.

In Figure 7.6 the whole-rock major element data for the Thick Flatreef are plotted relative to the average compositions for the principal rock-forming minerals. The

whole-rock data for the UP and MP units plot within the orthopyroxene-olivine-plagioclase field and are tightly clustered around the orthopyroxene composition as observed in equivalent units of the Deep Platreef (see Figure 7.2). The results are shifted towards higher MgO concentrations compared to the equivalent units in the Deep Platreef. The MP unit shows slightly greater spread of data into the olivine-rich field, this is recorded in the mineralogy. In contrast, the HZ_{OLWEBS} and the HZ_{GBRN} data show greater scatter. The scatter of the HZ_{OLWEBS} data is spread between olivine and clinopyroxene reflecting the observed mineralogy; a few samples plot at elevated MgO content outside of the mineral composition fields. The majority of the HZ_{GBRN} data plots in the space between the end-members clinopyroxene-orthopyroxene-plagioclase and shows quite a large scatter reflecting the varying proportion of these minerals in the samples analysed.

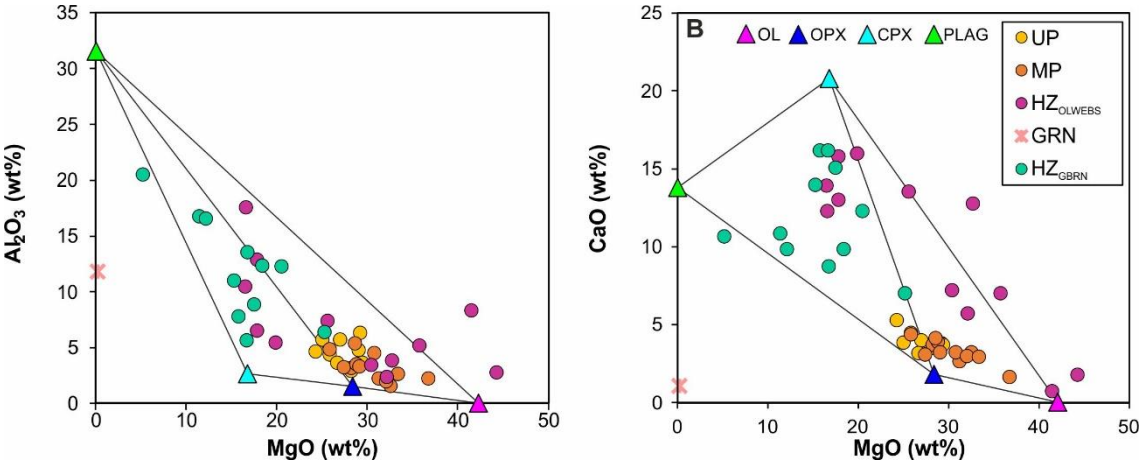

Figure 7.6: Whole-rock major element bivariate plots combined with end-member mineral compositional data as analysed in sampled from the Thick Flatreef (TMT_006_D2). (A) Al_2O_3 (wt%) vs. MgO (wt%). (B) CaO (wt%) vs MgO (wt%).

The trace and precious element depth profiles for the Thick Flatreef are presented in Figure 7.7 (A-J). The downhole pattern of the elements Cr, TiO_2 and V broadly reflect one another and peak in samples containing visible chromite mineralisation. The background Cr concentrations of the UP and MP units are relatively homogenous averaging ≈ 2000 ppm. The highest Cr contents are found in the HZ_{OLWEBS} (33829 ppm) and the HZ_{GBRN} (33636 ppm) where there are significant visible disseminated chromite present; these values are significantly lower than those compared to the Main Chromitite unit of the Deep Platreef (169872 ppm). The average Cr contents of the HZ_{OLWEBS} and HZ_{GBRN} (excluding chromitites) of 931 and 1144 ppm, respectively are significantly lower than the overlying pyroxenite units. The low Cr and high MgO contents in the HZ_{OLWEBS} further attests to the assimilation of dolomite.

The grade profiles of 3PGE (Pt, Pd and Rh) and Au are shown in Figure 7.7F and 7.7G; they demonstrate a strong correlation in terms of their distribution patterns. The nugget effect between the samples analysed in this study compared to the Ivanplats composite data is less pronounced than in the Deep Platreef. The reason for this is that the sulphide minerals in the Thick Flatreef are omnipresent rather than being concentrated over specific intervals.

The first mineralised interval, the Upper Reef at the top of the UP unit is identified over two metres averaging 3.4 ppm (3PGE) and 0.7 ppm Au. The peak in grade corresponds with elevated Pt/Pd ratios (1.9 to 2.1), lower Cu/Pd ratios (average 2466) and high Ni and Cu concentrations (7075 ppm). The highest Cu/Pd values are observed above this mineralised interval on the contact between the UP and NC1 unit at 23333.

The second mineralisation event, the Middle Reef, is separated from the first by an interval of ≈ 4 metres with no grade; this barren interval lacks sulphide mineralisation as observed in the core and indicated in the Ni + Cu profile (average 1332 ppm, see Figure 7.7H). The Pt/Pd and Cu/Pd downhole profiles (see Figure 7.7I and 7.7J) demonstrate some variability at this depth. The sulphide-poor zone is characterised by elevated Pt/Pd (average 3.0) and undepleted Cu/Pd ratios (at 10429) indicative of injection of a fresh magma injection. The Middle Reef, begins in the middle of the UP unit (813.5 m) and continues until the base of the MP unit (a distance of 30 m). Over this distance the grade achieves an average value of 7 ppm (3 PGE per metre) and 0.8 ppm Au. The maxium grade is recorded over the first few metres with up to 10 ppm (3PGE/metre) and 1.4 ppm Au corresponding to very high Ni and Cu contents (>10,000 ppm). This mineralisation event traverses the UP/MP and the MP/HZ_{OLWEBS} lithostratigraphic contacts, however there is a drop off in the average grade associated with the latter contact. The Pt/Pd ratio for this mineralisation is around unity (up to 1.2 in the first few metres) and the Cu/Pd ratio averages 989 (with a range from 650 to 1381).

The mineralisation below the level of the MP unit is termed ‘Hybrid Reef’ despite the continuation of elevated grade; the reason for this distinction are twofold: (1) there is a significant decrease in grade, from an average of 7 ppm to 3 ppm per metre, and; (2) the mineralisation in the HZ_{OLWEBS} is less consistent with a spiky profile. In the HZ_{OLWEBS} the mineralisation is disrupted by intervals that are barren, these correspond to either the intrusion of a granitic vein or interlayers of country rock. There is a

significant decrease in the average Ni and Cu content moving from the pyroxenite units into the HZ_{OLWEBS} and the HZ_{GBRN} with values of 3747 and 3417 ppm, respectively.

There is an overall very slight decrease in the Pt/Pd ratio with depth (see Figure 7.7I); although the stratigraphic units of the MP, HZ_{OLWEBS} and HZ_{GBRN} have similar average average Pt/Pd values of 1.00, 0.94 and 0.88, respectively. In contrast, the Cu/Pd ratio increases slightly with depth from the MP unit downwards (see Figure 7.7J) with average Cu/Pd ratio in the HZ_{OLWEBS} and HZ_{GBRN} of 1710. The average Cu/Pd value for each stratigraphic unit is lower than primitive mantle (approximately 7000; Barnes & Maier, 2002).

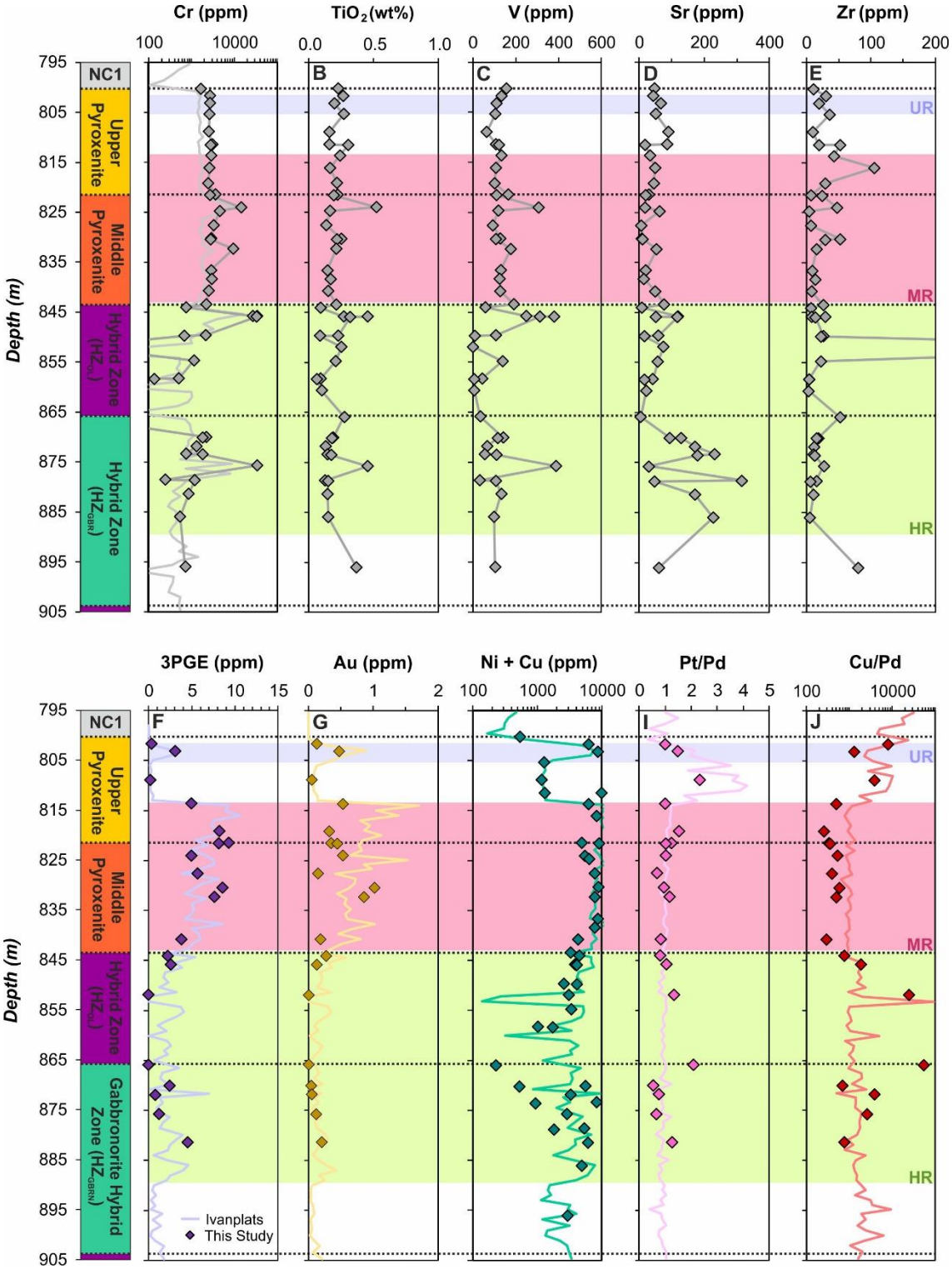

Figure 7.7: Trace element geochemical profiles with depth in the Thick Flatreef drill hole TMT_006_D2. (A) Cr (ppm); (B) TiO_2 (wt%); (C) V (ppm); (D) Sr (ppm); (E) Zr (ppm); (F) 3PGE (ppm); (G) Au (ppm); (H) Ni + Cu (ppm); (I) Pt/Pd; (J) Cu/Pd. Note: lines without points represent data provided by Ivanplats Pty Ltd., and points are data collected in the current study. 3PGE = Pt + Pd + Rh. UR = Upper Reef, MR = Middle Reef and HR = Hybrid Reef.

In Figure 7.8A there is no linear correlation between the Ni concentration and MgO wt%; similar to the Deep Platreef the Ni content increases dramatically in the pyroxenite units containing between 25 to 35 wt% MgO. The Ni concentrations are

signifcantly higher (up to 10013 ppm) than in the Upper Critical Zone of the eastern and western limbs of the Bushveld Complex; this probably reflects the elevated sulphide mineralisation in the Thick Flatreef (see Figure 7.8A). In Figure 7.8B the Ni and Cu show a strong correlation in the UP, MP and HZ_{GBRN} startigraphic units with R^2 values of 0.93, 0.84 and 0.89, respectively. A moderate correlation is observed in the HZ_{OLWEBS} containing significant olivine with a slightly lower R^2 value of 0.64 (see Figure 7.8B).

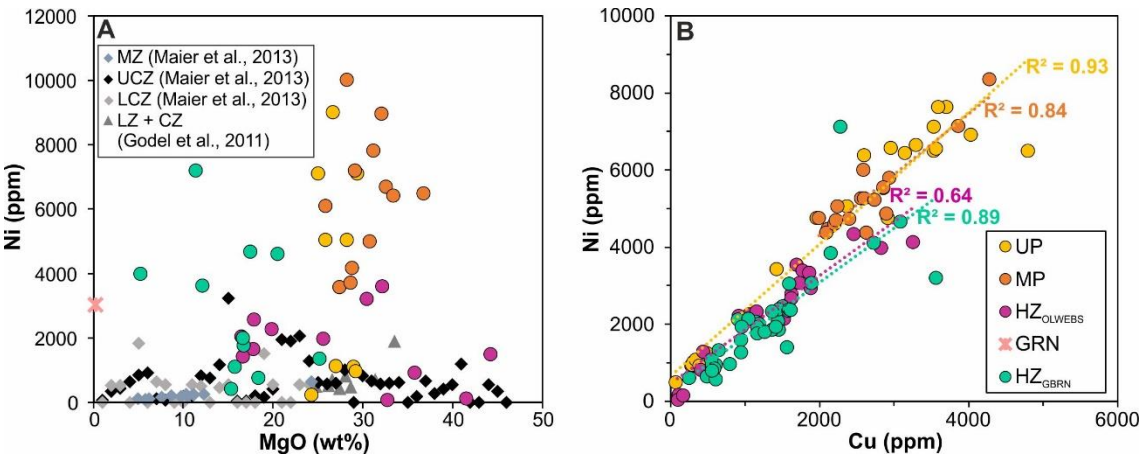

Figure 7.8: Bivariate plots demonstrating the distribution of Ni between silicate and sulphide minerals in the Thick Flatreef (TMT_006_D2). (A) Ni (ppm) vs MgO (wt%); data from this study, for other references see image. (B) Ni (ppm) vs Cu (ppm); data provided by Ivanplats Pty Ltd.

7.1.3 'Normal Flatreef' (UMT_233)

Geochemical depth profiles for the Normal Flatreef as sampled in UMT_233 are shown in Figure 7.9 (A-J). The first logged stratigraphic unit, the Norite Cycle 1 (NC1) unit shows minor variability in the concentrations of the major elements (see Figure 7.9) with the largest excursions observed in the Al_2O_3 content (and SiO_2:Al_2O_3) reflecting the heterogeneity in the distribution of plagioclase in this unit. The first sample of the NC1 unit records the highest LOI value at 12 wt% corresponding to a sample of norite with elongated orthopyroxene crystals; all other samples fall below 1 wt%. The CaO:Al_2O_3 values of the NC1 unit all plot within the magmatic range. The Cr/MgO values in the NC1 unit vary between 52 and 95 with an average of 68 generally fall between the Main Zone and Critical Zone range as defined in Seabrook et al., (2005).

The top of the Middle Pyroxenite (MP) unit is characterised by a decrease in Al_2O_3 and CaO moving down from the top contact with the UP unit, which is marked by the presence of a well-defined chromite stringer. The majority of samples from the MP unit are fresh with low LOI values; the one sample with an elevated LOI value (4 wt%) represents a serpentinised feldspathic harzburgite sample above a quartz-feldspar

vein (QFV). The highest SiO_2, Al_2O_3 and CaO concentrations are recorded in the QFV. Samples from the top of the MP unit plot within the Critical Zone range of Cr/MgO values and have magmatic CaO/Al_2O_3 ratios. In contrast, samples taken from the bottom part of the MP unit plot above and below the Critical Zone range of Cr/MgO; the lowest values (between 71 and 79) are recorded in medium-grained interlayered pyroxenite and norite lithologies and the highest value of 559 from a feldspathic harzburgitic sample. The CaO/Al_2O_3 ratio for these rocks varies from 0.79 to 1.62, so some samples are slightly elevated above the magmatic range. The two samples from the Pyroxenite-Norite Zone (PNZ), which is chromite-bearing, record the lowest bulk Mg# (65-73) and highest Cr/MgO ratio of 1529.

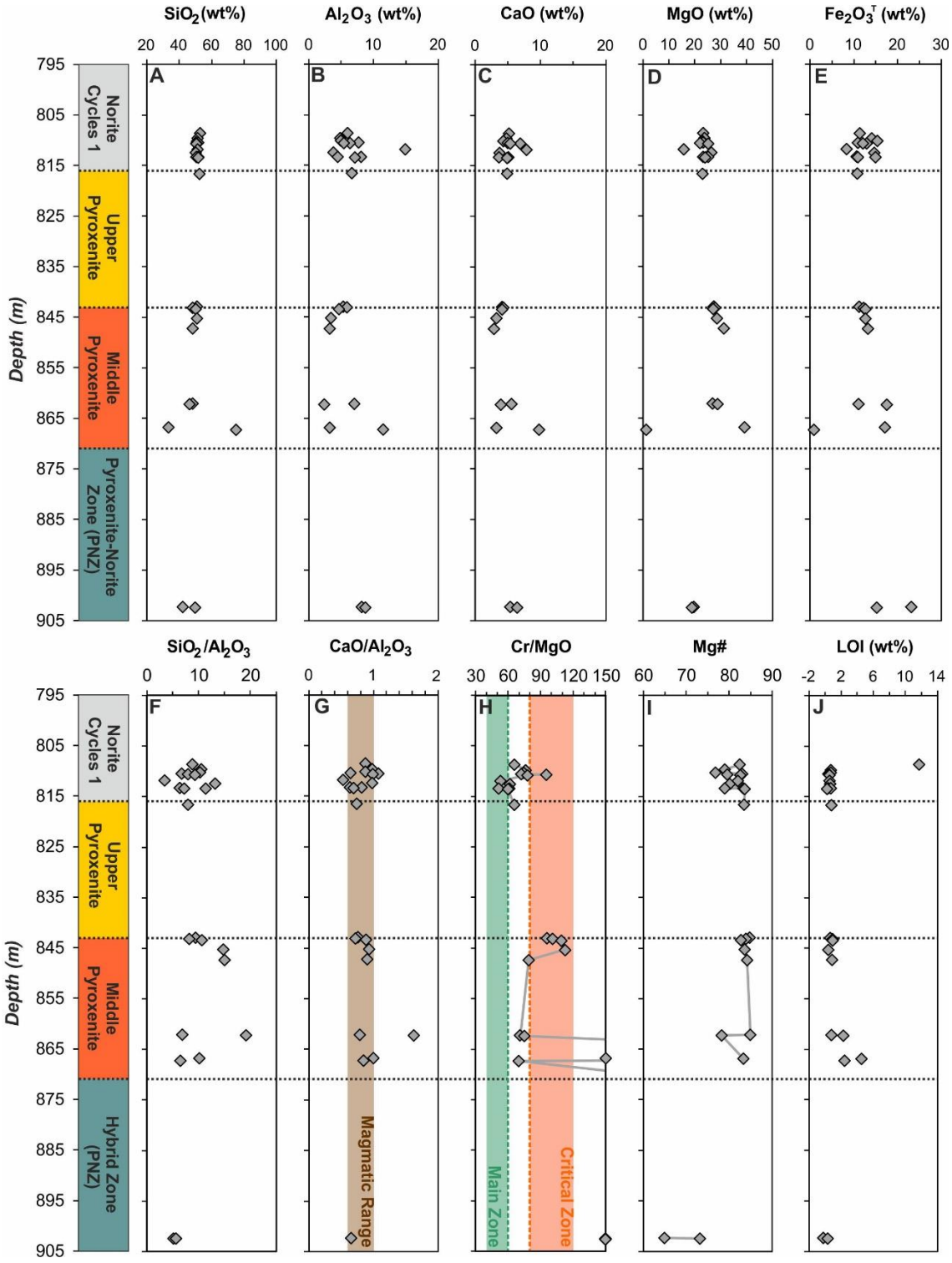

Figure 7.9: Major element geochemical variations with depth in the Normal Flatreef as sampled in drill hole UMT_233. (A) SiO_2 wt%; (B) Al_2O_3 wt%; (C) CaO wt%; (D) MgO wt%; (E) Fe_2O_3 wt%; (F) SiO_2/Al_2O_3; (G) CaO/Al_2O_3; (H) Cr/MgO; (I) Mg# (calculated as 100*Mg/(Mg+Fe)); and (J) LOI wt%.

The major element data is plotted in respect of the average major mineral compositions in Figures 7.10A and 7.10B. The majority of the data from the NC1, UP and MP units plot nearest to the orthopyroxene end-member composition. The NC1

data is spread along the orthopyroxene-plagioclase tie line (see Figure 7.10A). The UP and MP data are spread between orthopyroxene and olivine end-member compositions. The chromite-hosting PNZ unit has elevated clinopyroxene content shifting the data points away from the orthopyroxene-plagioclase tie line. Two data points plot outside of the field defined by the end-member major mineral compositions; these are a QFV and the feldspathic harzburgite in the lower part of the MP unit.

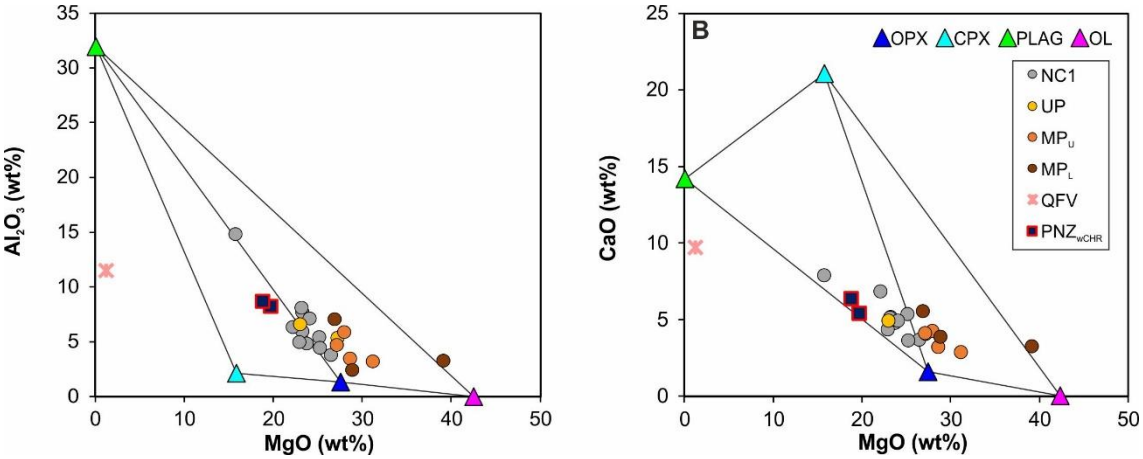

Figure 7.10: Whole-rock major element bivariate plots combined with end-member mineral compositional data as analysed in sampled from the Normal Flatreef (UMT_233). (A) Al_2O_3 (wt%) vs. MgO (wt%). (B) CaO (wt%) vs MgO (wt%).

The trace and precious element depth profiles are presented in Figure 7.11 (A-J); please note that the Cr and 3PGE + Au grade data provided by Ivanplats only covers up to the beginning of the Pyroxenite-Norite Zone (PNZ) unit. The Cr content of the UP unit is consistent at around 1460 ppm with the exception of intervals intruded by granite (10 ppm Cr). There is a narrow spike in the Cr content, up to 4330 ppm, on the contact between the UP and MP units corresponding to the presence of a well-defined chromite stringer (note: the stringer itself not analysed) before returning to a background value of 1460 ppm. A second positive spike in Cr is identified towards the base of the MP unit corresponding to a anomalous sample of harzburgitic composition (21899 ppm Cr). The background Cr contents of the pyroxenite units are considerably lower than in equivalent units moving down-dip in both the Thick Flatreef (2000 ppm) and Deep Platreef (2500 ppm).

The highest Zr value (382 ppm) is recorded in a quartz-feldspar vein sample from the MP unit. A slight elevation in the Zr content is recorded on the contact between the UP and NC1 units; this sample appears strongly altered to amphibole with coarse-grained phlogopite (also showing a peak in TiO_2). The Sr profile records elevated plagioclase content in the NC1 unit compared to the pyroxenite-dominated units. There is a slight decrease in the Sr content moving downhole from the chromite-

stringer on the contact between the UP and MP units this reflects the more noritic composition at the top of the MP unit.

The first mineralised interval, the Upper Reef, is hosted in the NC1 unit; unlike in the other drill holes studied where it is hosted in the UP unit. It is 5 m thick averaging 4 ppm 3PGE per metre with slightly elevated Au concentrations (up to 0.8 ppm) and corresponding raised levels of Ni and Cu. The Ni and Cu content in the NC1, as analysed in samples from this study, forms two populations at different orders of magnitude (100's ppm compared to 1000's ppm); this illustrates the observed heterogeneity of the sulphide distribution within this unit. In the Ivanplats data this variability is smoothed because of the larger sample sizes. There is a small peak in the Pt/Pd ratio (3.29) of the unmineralised hangingwall norites preceeding the Upper Reef event. The mineralised interval has an average Pt/Pd ratio of 1.2 and a Cu/Pd ratio of 824.

The UP unit is unmineralised with low concentrations of Ni and Cu and characterised by elevated Pt/Pd (average 2.61) and Cu/Pd (1396) ratios compared to the mineralised stratigraphic units above and below. The Pt/Pd and Cu/Pd ratios decreases sharply over an interval of 4 m towards the top contact with the NC1 unit and on the bottom contact with the MP unit.

The Middle Reef appears abruptly on the contact between the UP and MP units; this corresponds to a sharp peak in the Pt/Pd ratio to 8.67 which rapidly decreases downhole to an average value of 1.31. The mineralisation is bottom-loaded with no mineralisation in the hanging wall. The mineralised interval is 20 m thick and contains an average of grade of 4.5 ppm (3PGE) with a minor peak in Au (up to 0.7 ppm) on the top contact. The 3PGE grade, Ni and Cu concentrations decrease gradually moving downhole from the top contact. The MP unit has a spiky Cu/Pd profile ranging from a low of 545 at the top of the mineralised interval to 11038 at the base of the unit with an overall pattern of increasing Cu/Pd with depth.There is no significant mineralisation below the MP unit; the chromitite found in the PNZ unit doesn't contain grade, has a low Pt/Pd ratio (0.83) and high Cu/Pd (1769).

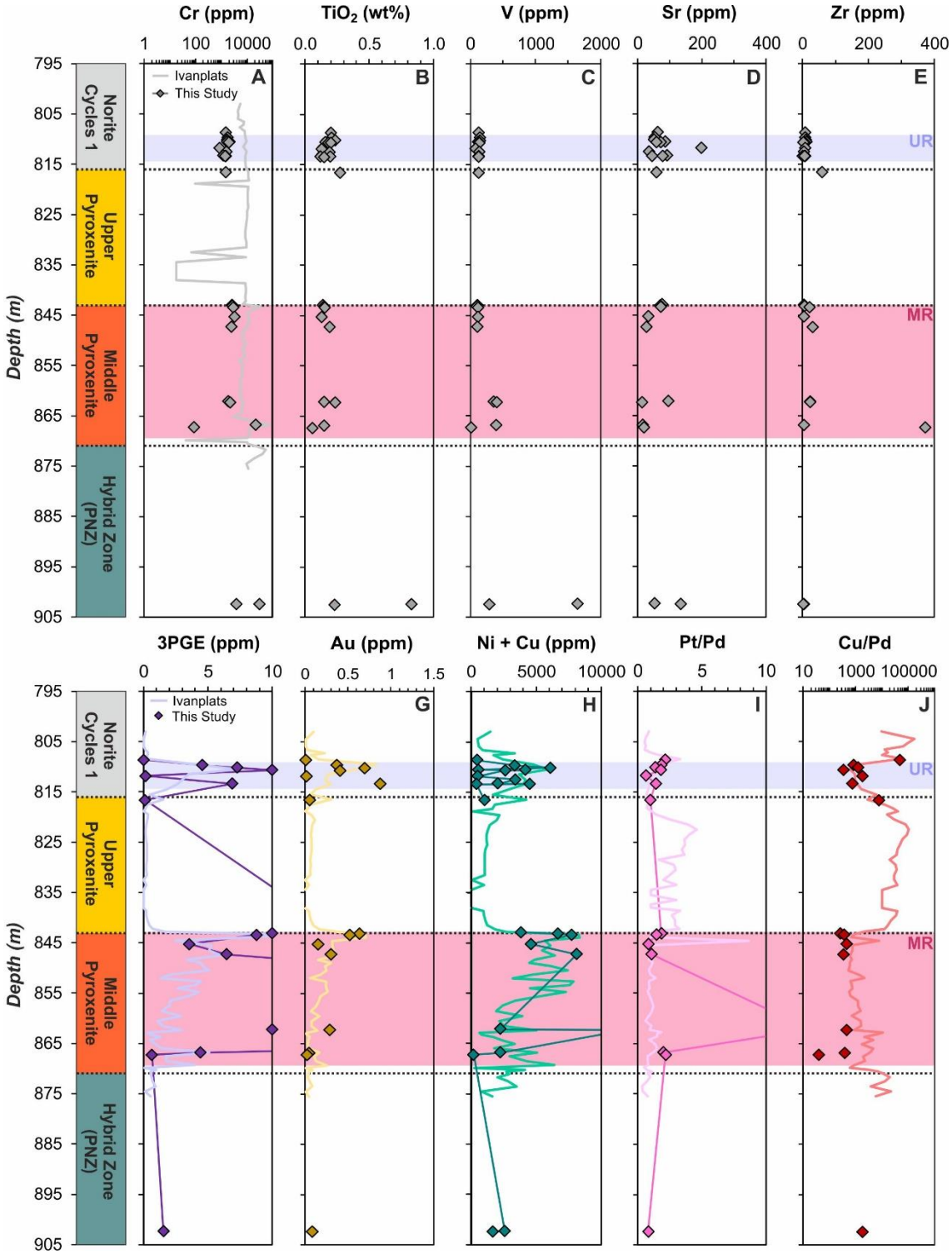

Figure 7.11: Trace element geochemical profiles with depth in the Normal Flatreef as sampled in drill hole UMT_233. (A) Cr (ppm); (B) TiO_2 (wt%); (C) V (ppm); (D) Sr (ppm); (E) Zr (ppm); (F) 3PGE (ppm); (G) Au (ppm); (H) Ni + Cu (ppm); (I) Pt/Pd; (J) Cu/Pd. Note: lines without points represent data provided by Ivanplats Pty Ltd., and points are data collected in the current study. 3PGE = Pt + Pd + Rh. UR = Upper Reef and MR = Middle Reef.

In Figure 7.12A, no relationship is observed between Ni and MgO; this matches observations on the other drill holes. All stratigraphic units show a strong correlation

between Ni and Cu (see Figure 7.12B) with a minimum R^2 value of 0.85 recorded in the MP and a maximum R^2 value of 0.99 recorded in the NC1 unit. This again demonstrates that the majority of Ni is hosted in sulphides as opposed to silicate minerals.

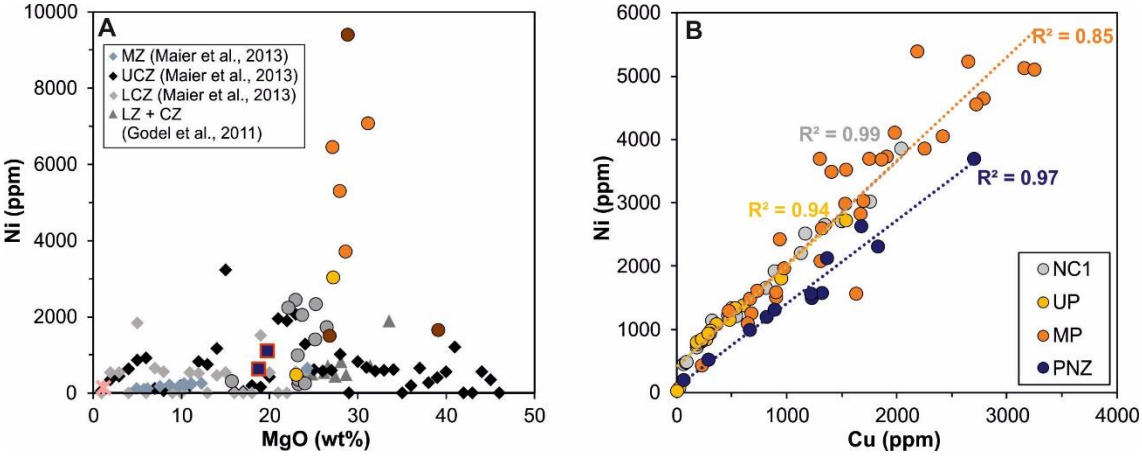

Figure 7.12: Bivariate plots demonstrating the distribution of Ni between silicate and sulphide minerals in the Normal Flatreef (UMT_233). (A) Ni (ppm) vs MgO (wt%), data from this study. (B) Ni (ppm) vs Cu (ppm), data provided by Ivanplats Pty Ltd.

7.1.4 Platreef (ATS_002)

The Platreef, as sampled in drill hole ATS_002, is found nearest to the surface with the mafic/ultramafic rocks hosting mineralisation beginning at 91m depth; based on its location and from observations on the drill core it is expected that crustal contamination may have a significant effect on the downhole major element profiles, the results are shown in Figure 7.13 (A-J).

The contact between the Mottled Anorthosite (MAN) and the Upper Pyroxenite (UP) units demonstrates significant geochemical variability in the major elements (see Figure 7.13A to 7.13E). This corresponds to observation in drill core of the interaction of compositionally distinct magmas. The pyroxenite has elevated $Fe_2O_3^T$ which matches the observed high concentrations of magnetite and pyrrhotite-dominated sulphide mineralisation.

All samples from the UP unit have relatively consistent SiO_2, bulk Mg#, CaO/Al_2O_3 and LOI values; the variability is observed between CaO, Al_2O_3 and MgO which indicate the formation of plagioclase or pyroxene as recorded in the lithological logging. The Middle Pyroxenite (MP) unit demonstrates more internal geochemical variability. The suspected assimilated country rock material (ATS_06Y) is characterised by elevated Al_2O_3 (20 wt%) and CaO (12 wt%) accompanied by recording the lowest SiO_2/Al_2O_3 ratio (2.2) of the drill hole.

The Cr/MgO profile is highly variable and more samples plot in the Main Zone range (see Figure 7.13H) including samples from the MAN, UP and MP unit. The sample from the MP unit with low Cr/MgO (16) ratio has a harzburgitic composition and was identified directly above the assimilated country rock material as outlined above. Three samples plot within the Cr/MgO range of the Critical Zone and these all represent feldspathic orthopyroxenite compositions.

The majority of the data plots within or just below the magmatic range of CaO/Al_2O_3 values with a range of 0.5 to 1.5; this is surprising considering that the Platreef is proposed to represent the most contaminated drill hole and suggests that the composition of the country rock must be more shale-dominated (see Chapter 6). The one sample that plots above the magmatic range at 1.51 is identified at the base of the logged interval in the Hornfels Hybrid Zone (HZ_{HF}).

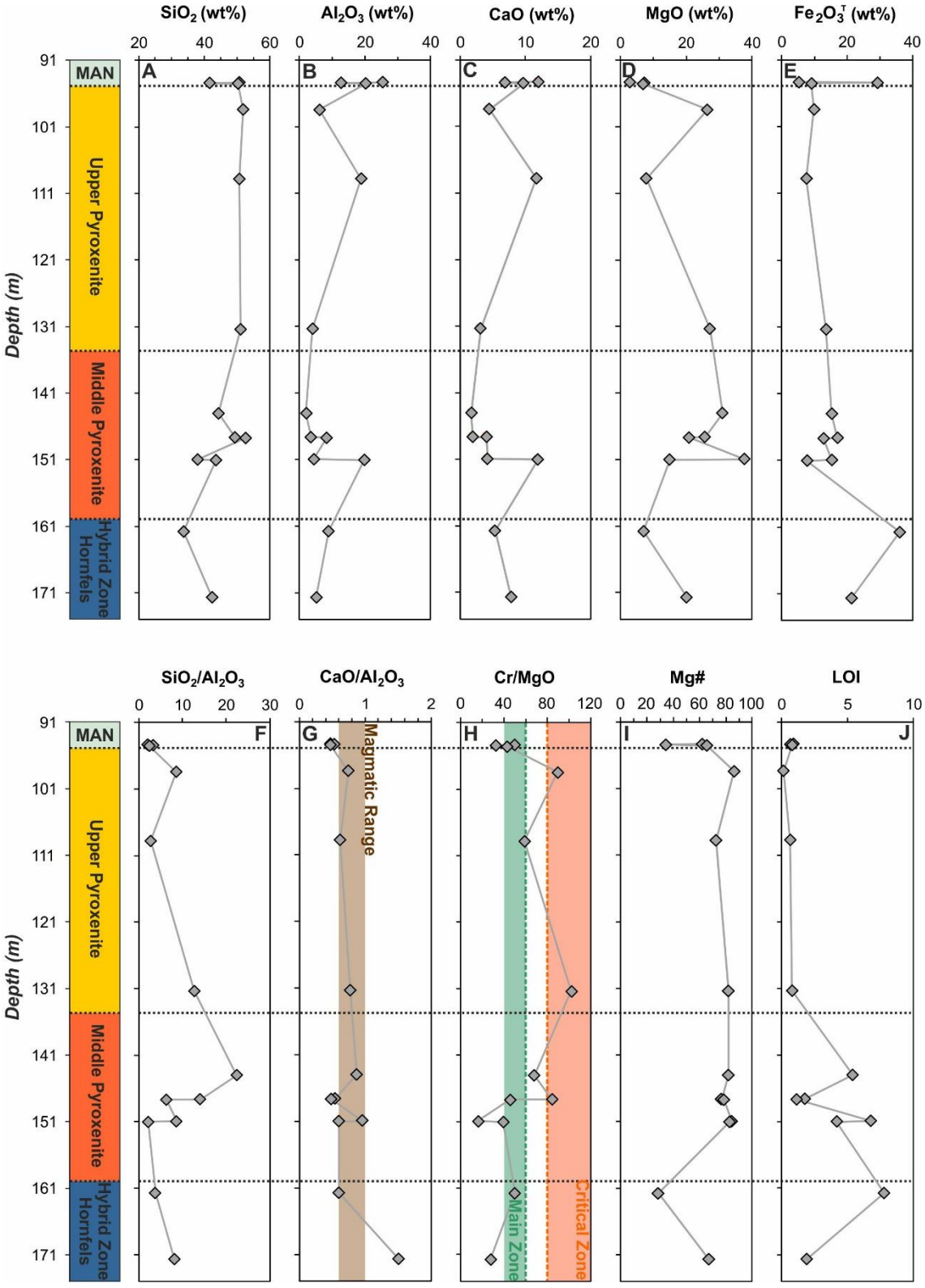

Figure 7.13: Major element geochemical variations with depth in the Platreef as sampled in drill hole ATS_002. (A) SiO_2 wt%; (B) Al_2O_3 wt%; (C) CaO wt%; (D) MgO wt%; (E) Fe_2O_3 wt%; (F) SiO_2/Al_2O_3; (G) CaO/Al_2O_3; (H) Cr/MgO; (I) Mg# (calculated as 100*Mg/(Mg+Fe)); and (J) LOI wt%.

In Figure 7.14, the major element data shows a much greater scatter between the major mineral compositions than in previous drill holes shown. The majority of the data from the UP and MP units plot within the orthopyroxene-olivine-plagioclase field and are nearest the orthopyroxene composition. The MAN samples plot along the plagioclase-orthopyroxene tie line at low MgO contents. The Hybrid Zone samples principally fall within the orthopyroxene-plagioclase-clinopyroxene field but demonstrate large compositional variability.

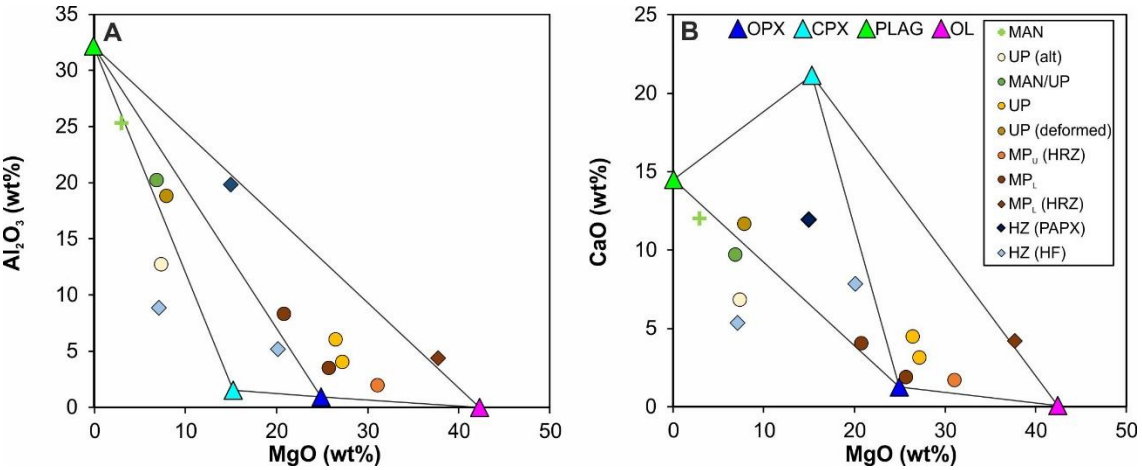

Figure 7.14: Whole-rock major element bivariate plots combined with end-member mineral compositional data as analysed in sampled from the Platreef (ATS_002). (A) Al_2O_3 (wt%) vs. MgO (wt%). (B) CaO (wt%) vs MgO (wt%).

The trace and precious element depth profiles for the Platreef are presented in Figure 7.15 (A-J). The Cr content is initially low in the Mottled Anorthosite (MAN) unit (≈ 200 ppm) and there is a sharp increase on the contact with the UP unit, which has an average of 2100 ppm; this value is only slightly lower than the average 2500 ppm in the Deep Platreef. The low Cr content in samples recording the interaction between the MAN and the UP units are accompanied by elevated TiO_2 (up to 0.58 wt%); in all other drill holes these two elements show a good correlation. The presence of abundant opaque minerals on this contact may be hosting the TiO_2 in either ilmenite or Ti-magnetite. The trace element profiles (Figure 7.15A to 7.15E) become very erratic from 146 m downwards, reflecting increasing levels of contamination.

Only one economic mineralisation event (see Figure 7.15F) is identified in drill hole located on the contact between the UP and MP units; this location can be correlated with the Middle Reef event as identified in the Deep Platreef and Flatreef drill holes. The mineralised interval is 7 m thick and contains 3 ppm (3PGE per metre) with corresponding elevated Ni and Cu concentrations but no enrichment in Au. The grade is bottom-loaded; similar to as observed for this event in the Flatreef drill holes. A

restricted interval (3 m) in the hangingwall directly above the mineralised interval is characterised by an elevated Pt/Pd (2) and lower Cu/Pd ratios than the units above and below. Within the Middle Reef the average Pt/Pd ratio is 0.9 and an average Cu/Pd of 1380.

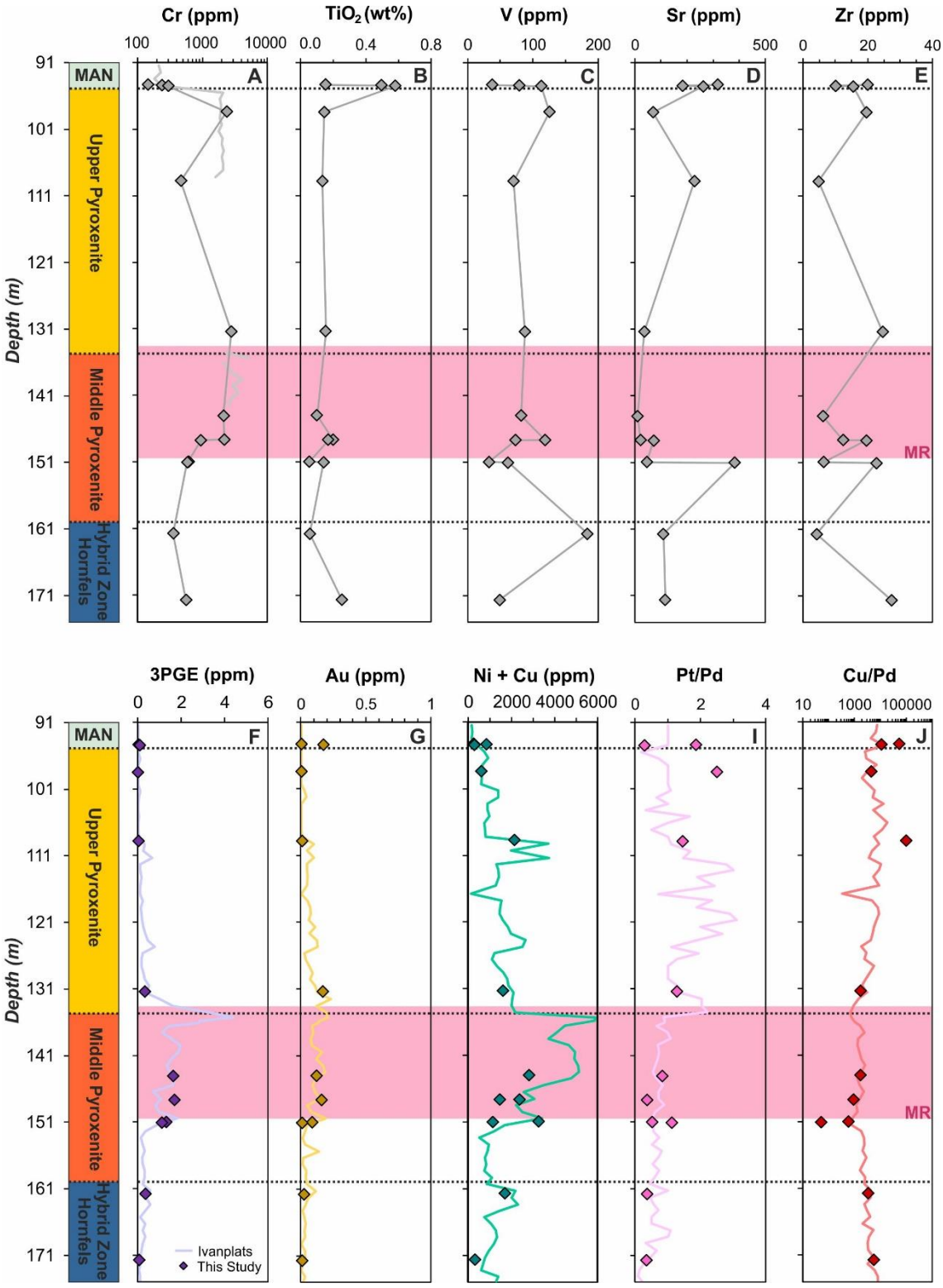

Figure 7.15: Trace element geochemical profiles with depth in the Platreef as sampled in drill hole ATS_002. (A) Cr (ppm); (B) TiO_2 (wt%); (C) V (ppm); (D) Sr (ppm); (E) Zr (ppm); (F) 3PGE (ppm); (G) Au (ppm); (H) Ni + Cu (ppm); (I) Pt/Pd; (J) Cu/Pd. Note: lines without points represent data provided by Ivanplats Pty Ltd., and points are data collected in the current study. 3PGE = Pt + Pd + Rh and MR = Middle Reef.

In Figure 7.16A the Ni concentration doesn't show a strong peak at intermediate MgO values as observed in all other drill holes; the Ni values in this drill hole are significantly lower than the concentrations observed elsewhere on Turfspruit i.e. up to 10,013 ppm the Thick Flatreef drill hole. This supports observations on the sulphide mineral assemblage which appeared to be dominated by pyrrhotite with only minor pentlandite and chalcopyrite identified in the core. In the UP and MP units the Ni and Cu show a good linear correlation (see Figure 7.16B) suggesting that their distribution is controlled by the presence of sulphides; in the HZ_{HF} this correlation is weaker with R^2 values of 0.58 indicative of a decoupling of these elements from the sulphides.

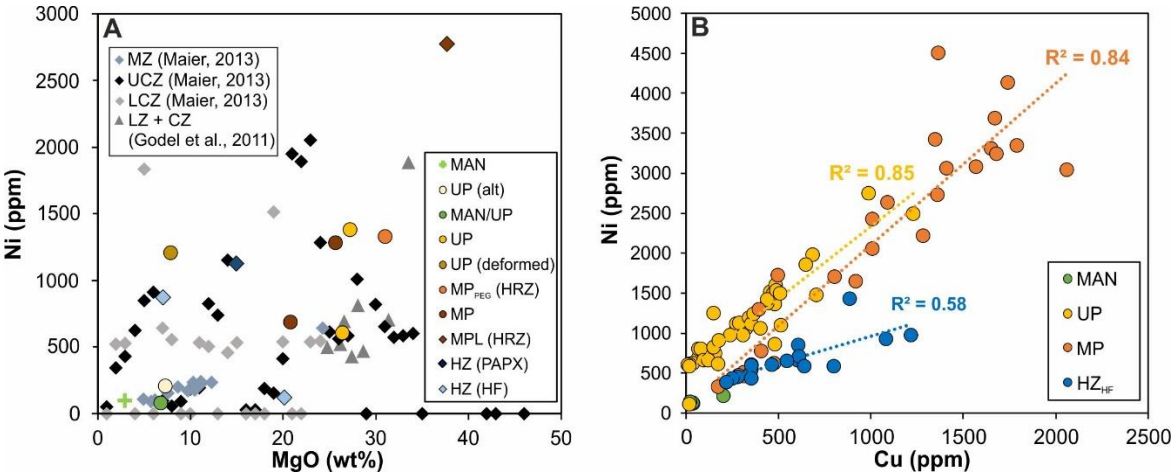

Figure 7.16: Bivariate plots demonstrating the distribution of Ni between silicate and sulphide minerals in the Platreef (ATS_002). (A) Ni (ppm) vs MgO (wt%), data from this study. (B) Ni (ppm) vs Cu (ppm), data provided by Ivanplats Pty Ltd.

7.2 Rare Earth Element Geochemistry

The following section presents chondrite-normalised whole-rock rare earth element (REE) data; the REE are frequently referenced as light REE (LREE; from La to Sm) and heavy REE (HREE; from Gd to Lu). The REE patterns from a variety of Bushveld rocks analysed in other studies are shown in Figure 7.17A to 7.17C; in addition, the REE patterns of the footwall rocks of the Duitschland Formation as obtained in the current study are shown in Figure 7.17D.

The Upper Critical Zone (UCZ) REE patterns are characterised by a strong positive Eu anomaly (Eu/Eu* 3.68) resulting from cumulate plagioclase and LREE enrichment (Ce_N/Sm_N 3.3; Maier & Barnes, 1998; see Figure 7.17A). In comparison, the Main Zone cumulates are more REE enriched and have a more moderate positive Eu

anomaly (Eu/Eu* 2.11) (see Figure 7.17A). Positive Eu anomalies are identified in rocks containing early formed plagioclase as a cumulate phase.

Geochemical modelling of the Merensky Reef from the western limb of the Bushveld Complex by Wilson & Chunnett (2006) noted the trapped liquids can have a significant effect on the observed REE patterns. In rocks where the trapped melt is < 3% the REE patterns are mainly controlled by the abundance of cumulus mineral phases (Wilson & Chunnett, 2006). The dominant feldspathic orthopyroxenites observed in the current study have an orthocumulate texture with >10 % interstitial space (see Chapter 8) meaning that the trapped liquids are likely to affect the REE patterns.

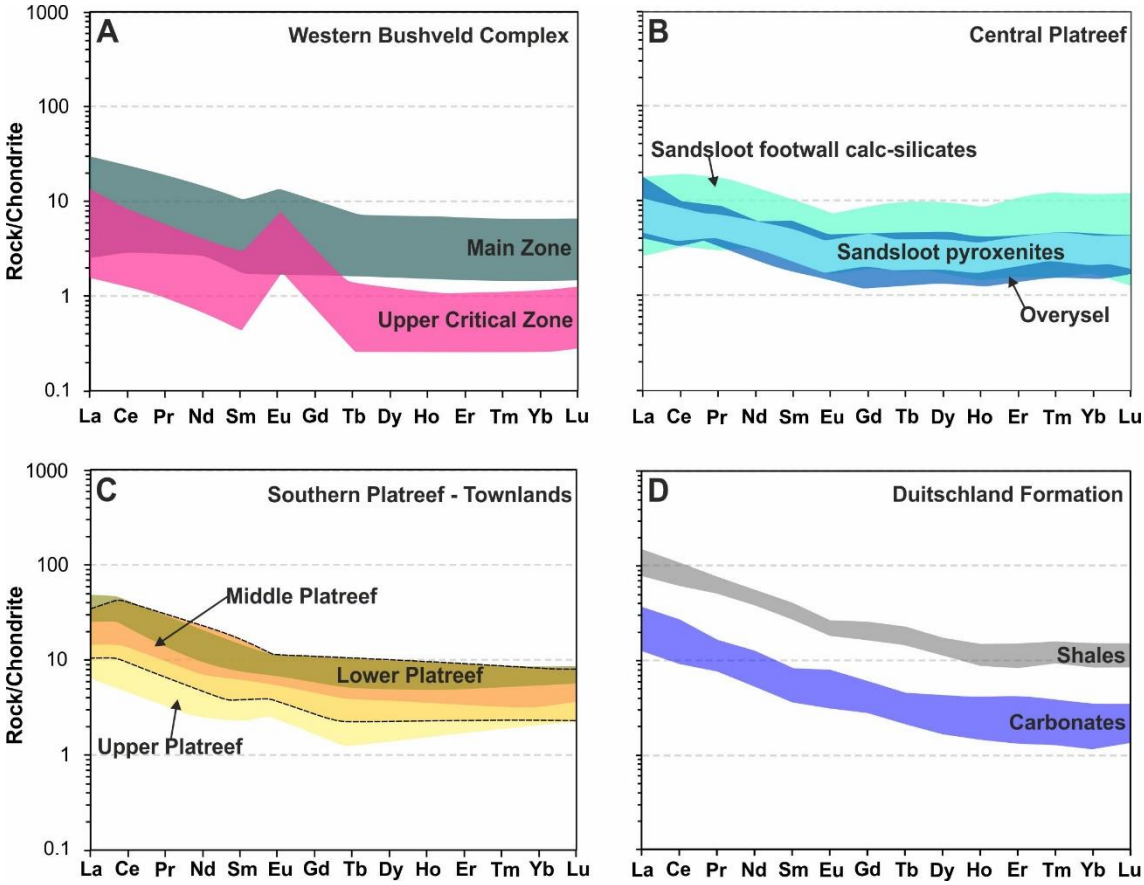

Figure 7.17: Chondrite-normalised REE patterns for proposed equivalent stratigraphic units within the Bushveld Complex and the footwall Duitschland Formation sediments. (A) Western Bushveld Complex data from Maier & Barnes (1998). (B) Sandsloot and Overysel data in the Central Platreef from Holwell & McDonald (2006). (C) The Upper, Middle and Lower Platreef as identified on Townlands in the southern Platreef by Manyeruke et al., (2005). (D) Shale- and carbonate-dominated lithologies of the Duitschland Formation (data from this study). Normalisation factors from Sun & McDonough (1995).

The Platreef pyroxenites from the shallow and contaminated portions of the central Platreef at Sandsloot and southern Platreef at Townlands are shown in Figure 7.17B and 7.17C, respectively. The dominant feldspathic pyroxenites of the Platreef rocks

have interstitial plagioclase crystallising from a trapped liquid and this typically imparts a negative Eu* signature as opposed to the positive Eu* in cumulate plagioclase from the UCZ (see Figure 7.17A). At Sandsloot the REE patterns are characterised by small negative Eu anomalies (Eu/Eu* 0.72-0.93; McDonald et al., 2005) and LREE enrichment (see Figure 7.17B). A similar pattern is identified in the southern Platreef on Townlands by Manyeruke et al., (2005) in all three pyroxenite packages as shown in Figure 7.17C. The 'Lower' Platreef (see Figure 7.17C) is the most fractionated (Ce_N/Sm_N 2.7-3.1; Manyeruke et al., 2005) which is an unexpected result if they are considered to have been formed sequentially from a progressively more fractionated magma; in all layers the HREE are relatively unfractionated. The total REE concentrations are slightly higher in the southern Platreef compared to the central; this may reflect a difference in the footwall lithologies. The footwall on Sandsloot is composed of dolomites of the Malmani Group whereas on Townlands the Platreef intrudes hornfels, quartzites and calcsilicates of the Silverton Formation. The REE patterns of the Duitschland Formation sediments as shown in Figure 7.17D indicate that the shales are enriched in REE over carbonate lithologies. This variability in the REE concentration between different sediment-types may account for the differences in REE concentrations observed along the strike of the Platreef. The two dominant rock types in the DF both show similar patterns defined by a strong fractionation trend between the LREE and the HREE. The shales show a small negative Eu anomaly whereas the carbonates have a moderate positive Eu anomaly (for more details see Chapter 6).

7.2.1 Deep Platreef (UMT_345 and UMT_345_D1)

The Deep Platreef chondrite-normalised REE patterns, grouped according to their stratigraphic unit are presented in Figure 7.18 (A-F). The Main Zone and Mottled Anorthosite (MAN) units have similar LREE patterns and both have a moderate +ve Eu anomaly (Eu/Eu* 1.6 and 2.6, respectively) as shown in Figure 7.18A. The Main Zone has higher HREE concentrations compared to the MAN (see Figure 7.18A); in the Main Zone the HREE are flat-lying (Gd_N/Yb_N 1.3) whereas in the MAN they are relatively depleted (Gd_N/Yb_N 2.7). The REE profile for the sample of the MAN unit is the most fractionated of all samples from the Deep Platreef. The Main Zone data for this study plots within the field of the Main Zone as identified in Barnes & Maier (2002) with comparable Eu/Eu* values.

The pyroxenite-dominated lithologies of the Upper (UP), Middle (MP) and Lower (LP) Pyroxenite units are all dominated by gentle U-shaped profiles (see Figure 7.18B and 7.18C). The HREE have a gently positive gradient (Gd_N/Lu_N 0.9) suggesting

incorporation in orthopyroxene; similar patterns are identified in Platreef rocks by Holwell & McDonald (2006, see Figure 7.17C). In both the UP and MP units a subset of samples have a positive curve in the LREE from La to Nd before dropping to a –ve Eu anomaly (Eu/Eu* 0.8). This is particularly evident in phlogopite-bearing feldspathic orthopyroxenite from the UP and in the pegmatoidal olivine-bearing units in the upper mineralised part of MP unit (see Figure 7.18B). The observed pattern is similar to the known REE-pattern of the mineral monazite; this has been identified in interstitial areas associated with quartz and phlogopite. Holwell & McDonald (2006) recorded moderately positive Eu anomaly values for the Platreef pyroxenites of 1.35 and pyroxenites from the Merensky Reef have minor negative Eu anomalies (Eu/Eu* 0.75-0.91).

The quartz-feldspar vein (QFV) within the UP unit, as shown in Figure 7.18B, has a strongly fractionated REE pattern (La_N/Yb_N 7.5). It also has a strong negative europium anomaly (Eu/Eu* 0.4) suggesting that it represents a residual liquid from which plagioclase has been separated. This matches the petrology of the QFV which is dominated by alkali feldspar and quartz as opposed to plagioclase (for more details see Chapter 8). The overall appearance of the REE profile is similar to that of the mineral apatite, which has been identified in the petrological studies; suggesting that this mineral has a dominant control on the REE profile.

The Norite Cycles 2 (NC2) unit is characterised by two REE patterns based on the dominant lithology (see Figure 7.18D): (1) the ultramafic pyroxenites have U-shaped profiles with negative Eu anomalies (Eu/Eu* 0.8) and; (2) the mafic leuconorites and anorthosites have more fractionated profiles (up to La_N/Yb_N 12.1), similar to that of the MAN unit, with moderate positive Eu anomalies (Eu/Eu* 2.8). The highest concentrations of REE are found within a sulphide-rich and PGE mineralised pyroxenite within this unit (see Figure 7.18D).

The Main Chromitite (MCHR) unit has a gently negative sloping REE profile (La_N/Yb_N 2.9) with no appreciable Eu anomaly (Eu/Eu* 1.1) comparable to pyroxenites from the UG2 chromitite (Eu/Eu* 0.99-1.38; Maier & Barnes, 1998). The Ultramafic Zone (UMZ) lithologies also have gentle negatively sloping profiles with a narrow range of LREE concentrations and a broader range of HREE concentrations. This reflects the dominance of orthopyroxene and olivine in the lithologies accommodating the HREE but not LREE. A range of fractionation trends are observed with La_N/Yb_N varying from 1.8 to 8.3; in addition, moderate negative and positive Eu anomalies (Eu/Eu* 0.7 to

1.9) are found in the UMZ unit. The Feldspathic Clinopyroxenite Hybrid Zone (HZ_{FCPX}) has a relatively flat-lying profile with no appreciable Eu anomaly (Eu/Eu* 1.1).

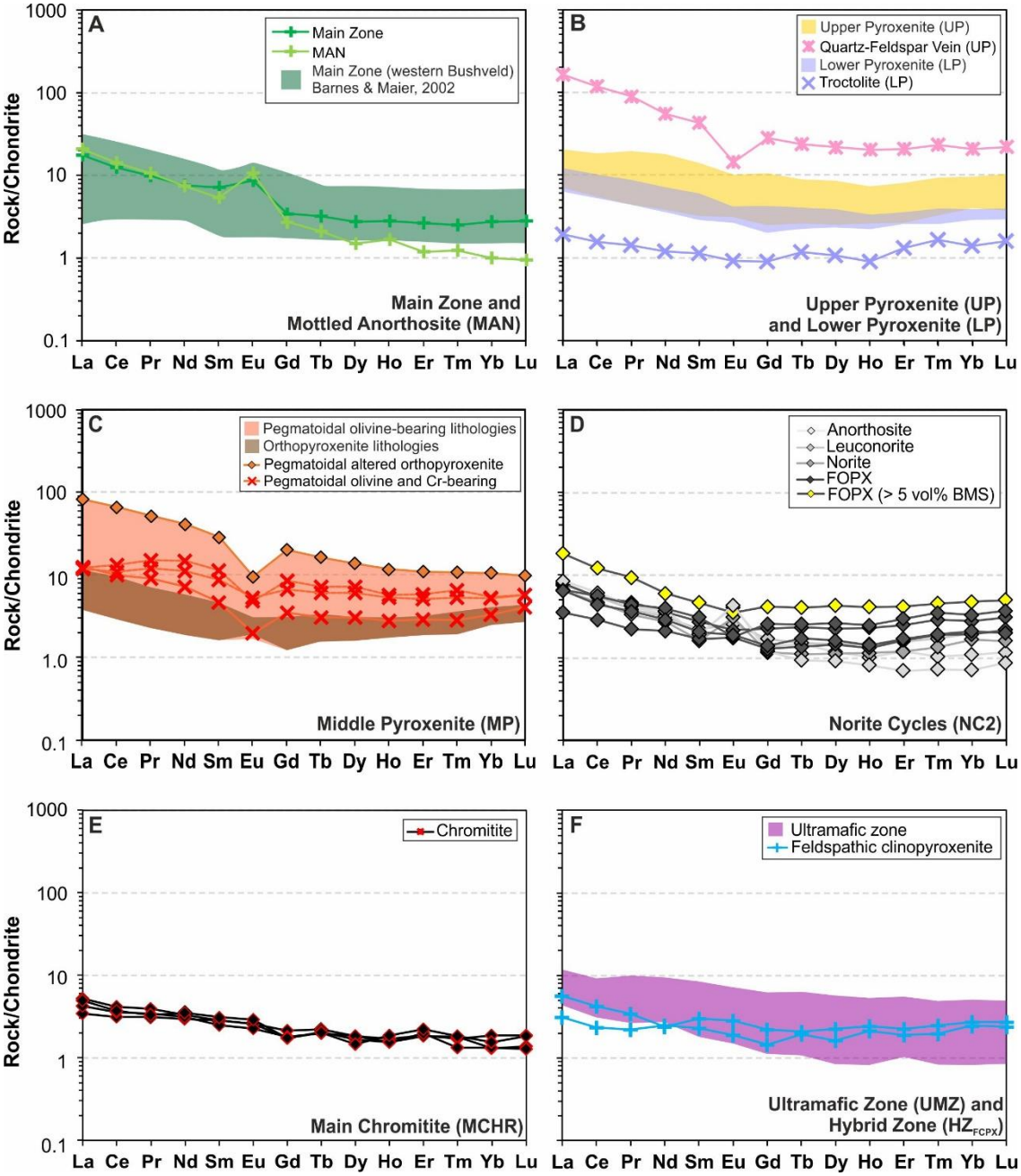

Figure 7.18: A series of chondrite-normalised REE spidergrams for the lithostratigraphic units of the Deep Platreef, as sampled in UMT_345 and UMT_345_D1. Normalisation factors from Sun & McDonough (1995).

7.2.2 'Thick' Flatreef (TMT_006_D2)

The Thick Flatreef chondrite-normalised REE profiles for the different stratigraphic units are presented in Figure 7.19. The pyroxenite dominated lithostratigraphic units of the Upper (UP) and Middle Pyroxenite (MP) units have a restricted range in REE concentrations as shown in Figure 7.19A and 7.19B. The REE pattern is similar to that as observed for equivalent units in the Deep Platreef; U-shaped with moderate

positive and negative Eu anomalies (Eu/Eu* 1.65 to 0.51). The highest REE concentrations in the UP unit were identified in samples containing phlogopite (highlighted in Figure 7.19A), suggesting the presence of a more evolved interstitial melt; all values fall within the range as observed in the Deep Platreef. In Figure 7.19B the REE data for the MP unit are compared to the equivalent unit in the Deep Platreef; this shows that the field for the MP unit in the Deep Platreef spans a much broader concentration range that is shifted towards higher REE concentrations. The cumulate and interstitial mineralogy in the Thick Flatreef is simpler compared to the Deep Platreef (i.e. no olivine and no alkali-feldspar-quartz-monazite assemblage, respectively); and there is less serpentinization and talc/tremolite alteration at this interval compared to the Deep Platreef.

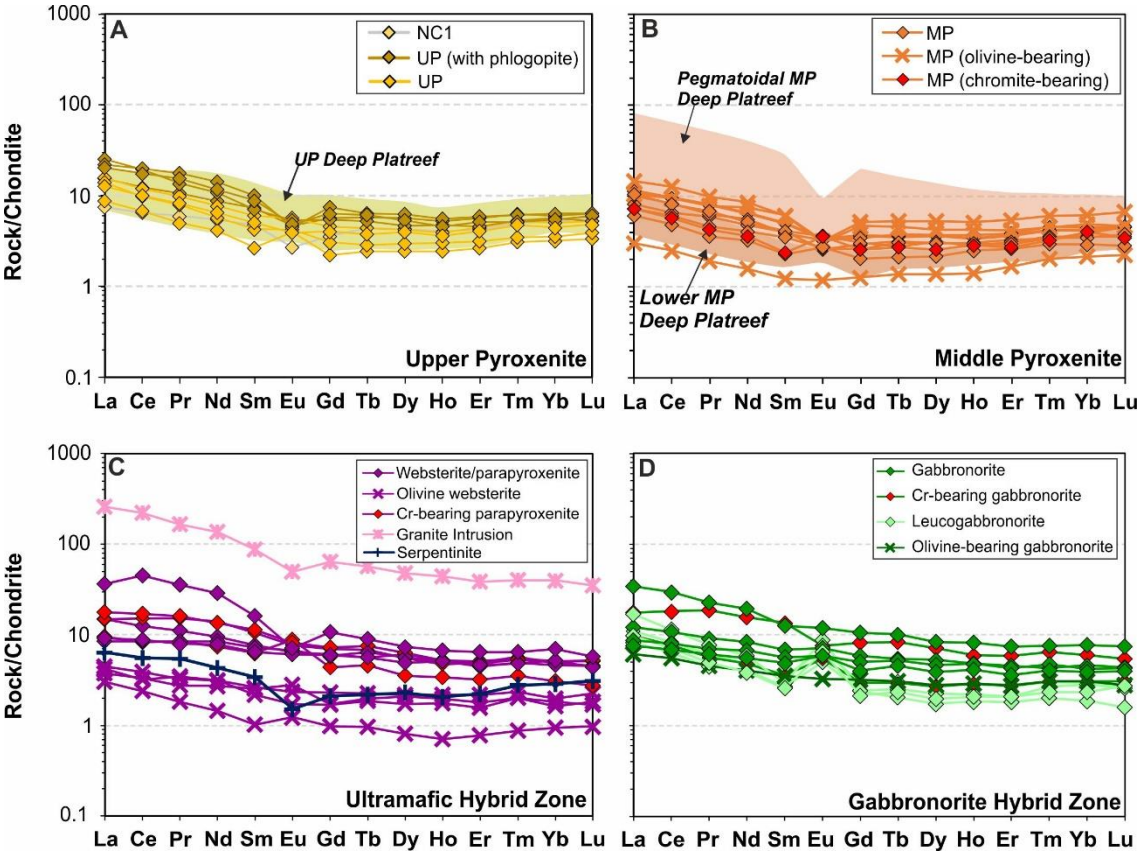

Figure 7.19: A series of chondrite-normalised REE spidergrams for the different stratigraphic units in the Thick Flatreef as sampled in drill hole TMT_006_D2. Normalisation values from Sun & McDonough (1995).

The REE patterns for the Olivine Websterite Hybrid Zone (HZ_{OLWEBS}; see Figure 7.19C) are spread over a larger range of concentrations compared to the pyroxenite-dominated units. The mineral apatite was identified as an accessory phase in the HZ_{OLWEBS} unit and will cause LREE enrichment. The lowest concentration of REE are found in samples containing olivine, which have gently sloping patterns from LREE to HREE (average La_N/Yb_N of 2.5). The one autolith sample analysed (labelled

serpentinite) has a slightly bow-shaped profile with decreasing LREE (La_N/Sm_N 1.86), negative Eu anomaly (Eu/Eu* 0.55) followed by a gently rising HREE profile (Gd_N/Yb_N 0.73). In contrast, the Gabbronorite Hybrid Zone (HZ_{GBRN}) REE profiles (see Figure 7.19D) record gently sloping to flat-lying REE patterns. In comparison to the pyroxenite-dominated lithostratigraphic units the HREE do not have a gently positive slope; a response to the lower orthopyroxene and higher plagioclase content. The elevated plagioclase content in this stratigraphic unit is also expressed in a moderate positive Eu anomaly (Eu/Eu* 3.26).

7.2.3 'Normal' Flatreef (UMT_233)

The chondrite-normalised REE patterns for the different stratigraphic units in the Normal Flatreef as sampled in UMT_233 are shown in Figure 7.20. The Norite Cycle 1 (NC1), Upper Pyroxenite (UP) and Middle Pyroxenite (MP) stratigraphic units have U-shaped profiles as described previously (see Figure 7.20A, 7.20B and 7.20C). The Pyroxenite-Norite Zone (PNZ) unit with chromite mineralisation shows a different pattern (see Figure 7.20D) with a flat-lying LREE (La_N/Sm_N 1.41), a strong positive Eu anomaly (Eu/Eu* 4.7) and HREE enrichment (Gd_N/Yb_N 0.50). The highest REE values and strongest fractionation (La_N/Yb_N 35) are found in the quartz-feldspar vein (QFV; see Figure 7.20C) with a strong negative europium anomaly (Eu/Eu* 0.17).

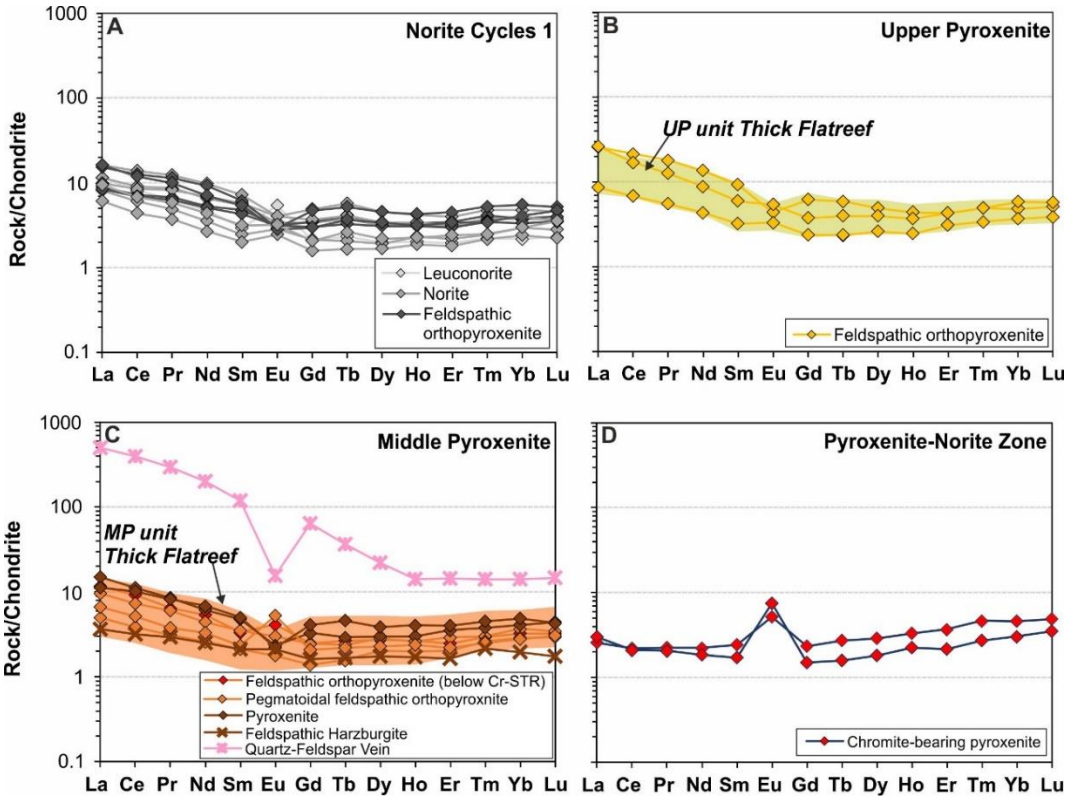

Figure 7.20: A series of chondrite-normalised REE spidergrams for the different stratigraphic units in the Normal Flatreef as sampled drill hole UMT_233. Normalisation values from Sun & McDonough (1995).

7.2.4 Platreef (ATS_002)

In the Platreef drill hole, as sampled in ATS_002, the Mottled Anorthosite (MAN) unit has the most fractionated profile with La_N/Yb_N of 30 (compared to an average of 7) and demonstrates similar characteristics to the equivalent unit in the Deep Platreef (see Figure 7.21A). The pyroxenites of the Upper Pyroxenite (UP, see Figure 7.21B) and Middle Pyroxenite (MP, see Figure 7.21C) units have trough-shaped profile with LREE enrichment and a slight positive slope in the HREE; these patterns resemble equivalent units in the other drill holes as noted previously. At the base of the MP unit the samples with evidence of calc-silicate assimilation are compared to the carbonates of the Duitschland Formation (DF) (see Figure 7.21D); both the REE concentrations and overall shape of the profile are comparable. The Hornfelsed Hybrid Zone (HZ_{HF}) samples (see Figure 7.21D) show LREE enrichment (La_N/Sm_N 3.5 to 12.6), moderate negative Eu anomaly (0.63) and relatively flat-lying HREE (Gd_N/Yb_N 1.2 to 1.8); their overall pattern resembles that of the DF shales as shown in Figure 7.21D.

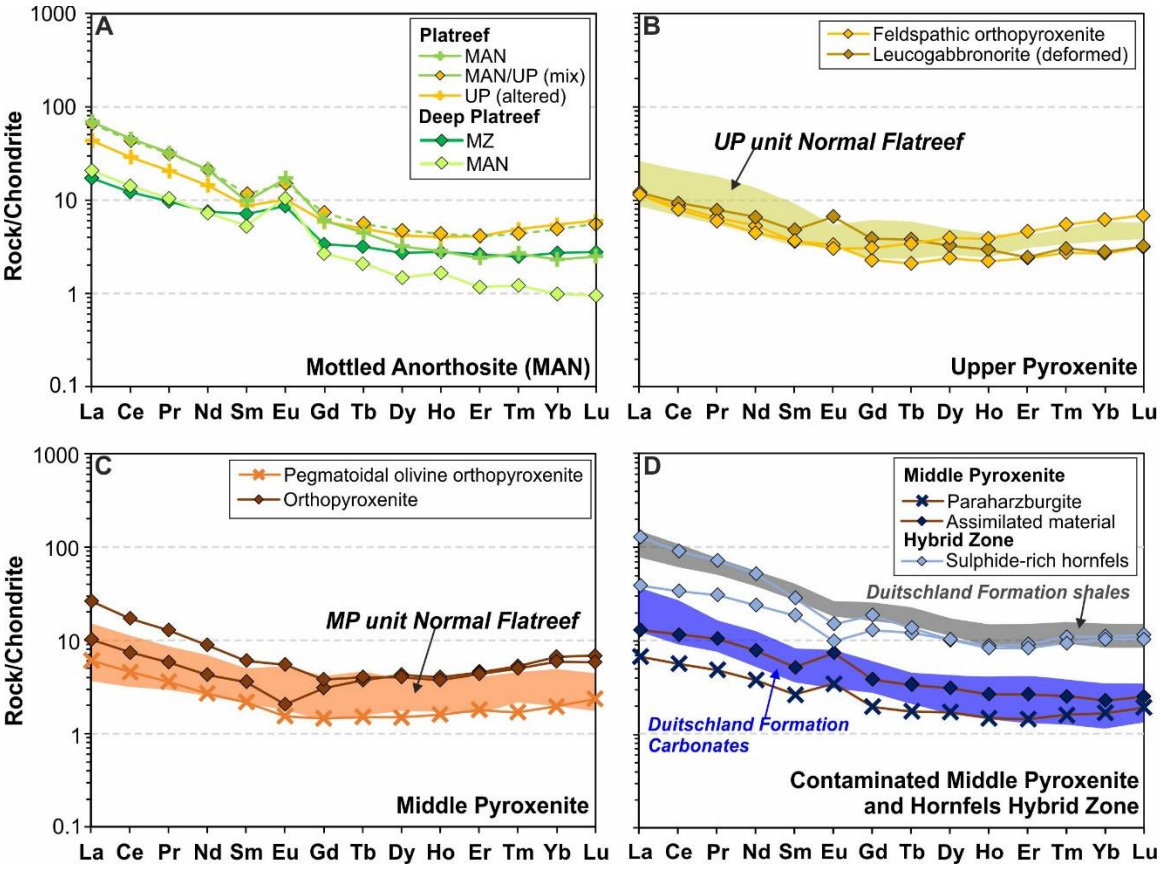

Figure 7.21: A series of chondrite-normalised REE spidergrams for the different stratigraphic units in the Platreef as sampled in drill hole ATS_002. Normalisation values from Sun & McDonough (1995).

7.2.5 Ce/Sm Ratios (All drill holes)

The Ce/Sm ratio (used as a proxy for LREE fractionation) has proved to be effective at tracing the magmatic lineage of the Bushveld rocks on the western limb as shown in a study on the Union section by Maier & Barnes (1998). In Maier & Barnes (1998) they recognised that the Ce/Sm ratio increases systematically with depth moving from the Main Zone to the Lower Zone (see Figure 7.22A); for example, the Critical Zone has a higher Ce/Sm ratio (average 13.6) compared to that of the Main Zone (average 8.97). The Ce/Sm data from this study are plotted relative to the fields (based on the range of Ce/Sm values) of the Main Zone and Critical Zone in Figure 7.22C to 7.22F. In addition, the Ce/Sm values of the two potential contamination sources, namely the footwall Duitschland Formation sediments and basement rocks of the Pietersburg Greenstone Belt (for details see Chapter 6), are plotted in Figure 7.22B.

The majority of the Ce/Sm values for all stratigraphic units in all drill holes across the Turfspruit deposit plot within the Main Zone field, although there is variable degrees of scatter across the Main Zone-Critical Zone boundary. The one sample of Main Zone analysed from the Deep Platreef (see Figure 7.22C) plots within the Main Zone field (Ce/Sm = 7.16). In contrast, the directly underlying Mottled Anorthosite (MAN) unit plots within the Critical Zone field in both the Deep Platreef (Ce/Sm = 11.07) and Platreef (Ce/Sm = 10.96; see Figure 7.22F). In the Deep Platreef the stratigraphic units of the upper part of the drill hole, the Upper (UP) and Middle Pyroxenite (MP) units, have higher concentrations and lower Ce/Sm ratios (average 7.54) than in the lower NC2 unit (average 10.57). The PGE mineralised Main Chromitite (MCHR; see Figure 7.22C) unit doesn't conform to this overall trend as it contains low concentrations of REE and has an average Ce/Sm value of 5.20 significantly lower than the average of the UG2 chromitite of 12.3 (Maier & Barnes, 1998; see Figure 7.22A). This stratigraphic trend is also observed in the Normal Flatreef with the highest stratigraphic unit, the NC1 recording lower Ce/Sm ratios (average 8.26) than the MP unit (average 9.30). This increase in Ce/Sm ratio with depth matches observations by Maier & Barnes (1998) and is also noted in the Platreef pyroxenite packages directly south of Turfspruit on Townlands by Manyeruke et al., (2005). In the Thick Flatreef (see Figure 7.22E) this pattern is not observed with the lower stratigraphic units of the Olivine Websterite Hybrid Zone (HZ_{OLWEBS}) and the Gabbronorite Hybrid Zone (HZ_{GBRN}) plotting at lower Ce/Sm ratios with average values of 7.0 and 8.7, respectively. Interestingly, the average HZ_{GBRN} value is very similar to that of the average Main Zone as identified in Maier & Barnes (1998).

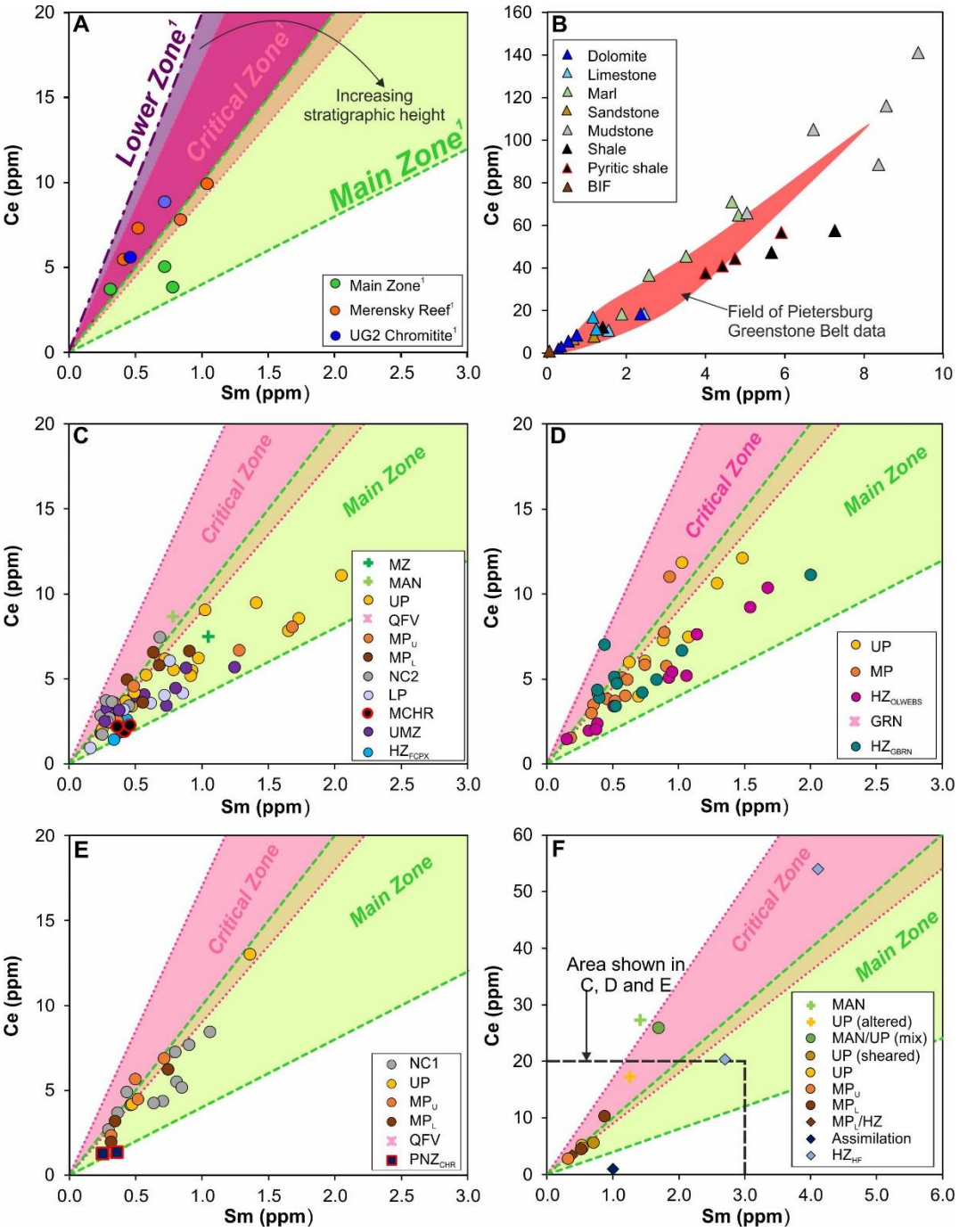

Figure 7.22: Bivariate plots of whole-rock Ce vs Sm; (A) the range of values from the Lower, Critical and Main Zone cumulates from the Union section (western limb Bushveld Complex) are plotted as fields and specific samples are plotted from the PGE mineralised Merensky Reef and UG2 chromitite; (B) Duitschland Formation and Pietersburg Greenstone Belt sediments, from samples collected in this study; (C) Deep Platreef, combined data from UMT_345 and UMT_345_D1; (D) Thick Flatreef, TMT_006_D2; (E) Normal Flatreef, UMT_233. (D) Platreef, ATS_002. Source: [1]Maier & Barnes, 1998.

The Ce/Sm ratio of the Duitschland Formation footwall sediments, as shown in Figure 7.22B, varies from 7.7 to 15.6 (average 10.9). This range covers both the Critical Zone and Main Zone fields with the average falling in between the two (see Figure 7.22D); however the range of concentrations are significantly higher in particular the Ce

concentration in mudstones (up to 141.07 ppm). In contrast, the carbonate lithologies dolomite and limestone plot within the same range of concentrations of Ce and Sm as the magmatic rocks. This means that in terms of using Ce/Sm to identify a in situ contamination signature of the Platreef by the DF the Ce/Sm ratio isn't very useful because the ranges overlap; however the assimilation of fine-grained siliciclastic sediments will result in anomalously high Ce (> 20 ppm) and Sm (> 3 ppm) concentrations. This is observed in the most contaminated drill hole of the shallow Platreef, as shown in Figure 7.22D where most data plots near the Critical Zone-Main Zone boundary, however the range of concentrations of Ce (up to 54.02 ppm) and Sm (up to 4.02 ppm) are elevated above those recorded in the deeper drill holes. The Pieterburg Greenstone Belt samples show a similar distribution pattern to the DF samples (see Figure 7.22B).

In the Deep Platreef and Flatreef drill holes, the observed distribution of Ce/Sm values within the Main Zone field cannot be explained by in situ contamination from the DF sediments; this presents a problem for correlating the stratigraphy to that of the Critical Zone. On the northern limb it is established that the Main Zone intruded after the Platreef had cooled and solidified (see Chapter 3, section 3.3), this implies that the Main Zone REE signature is inherited in the parental magma. A Main Zone signature in the Ce/Sm ratios was also noticed in a similar study on the mafic/ultramafic Grasvally Norite-Pyroxenite-Anorthosite (GNPA) member to the south of the Ysterberg-Planknek fault (see Chapter 3, section 3.3.1). In the GNPA member each stratigraphic unit recorded an average Ce/Sm ratio of between 9.6 to 10.4 (Smith, 2014). To account for this Smith (2014) propose either the mixing of the two parental magmas (B1 with the B2/B3 magmas) or via contamination of the Critical Zone magma with shales and quartzites of the footwall rocks.

7.2.6 Incompatible Element Ratios (all drill holes)

The degree of crustal contamination of the Platreef magma can also be examined using primitive mantle normalised incompatible element ratios. A combination of low $(Nb/Th)_{PM}$ ratios (<1) and elevated $(Th/Yb)_{PM}$ ratios (>5) define a field of crustal contamination of a mantle-derived magma (Lightfoot & Hawkesworth, 1988; Lightfoot et al., 1990; Ihlenfeld & Keays, 2011). In Figure 7.23 the $(Nb/Th)_{PM}$ ratio is plotted against the $(Th/Yb)_{PM}$ ratio for all the samples collected across Turfspruit deposit. The ratios for the two end-members are plotted for comparison these are: (1) an uncontaminated mantle mantle melt typified by N-Morb or ocean island basalt from Mauna Loa and (2) the footwall sediments of the Duitschand Formation (DF).

The DF sediments are characterised by very low $(Nb/Th)_{PM}$ ratios (0.04 to 0.2) and high $(Th/Yb)_{PM}$ ratios (10.4 to 56.8). The Turfspruit magmatic rocks in all drill holes (see Figure 7.23) studied have low $(Nb/Th)_{PM}$ ratios (0.02 to 1.9) and elevated $(Th/Yb)_{PM}$ (0.4 to 56.8). The majority of the data plot at low $(Nb/Th)_{PM}$ ratios and this reflects the negative Nb-Ta anomalies as observed in primitive mantle-normalised multi-element spidergrams (provided in Appendix C). A significant proportion of all the data in all drill holes plot within the contaminated magma field, this represents a homogenous signature that must have been inherited into the parental magma before emplacement. The field of Platreef data from a study on Overysel, Sandsloot and Tweefontein by Ihlenfeld & Keays (2011; see Figure 7.23) further implies that this was a regional event affecting all localities along the strike of the Platreef.

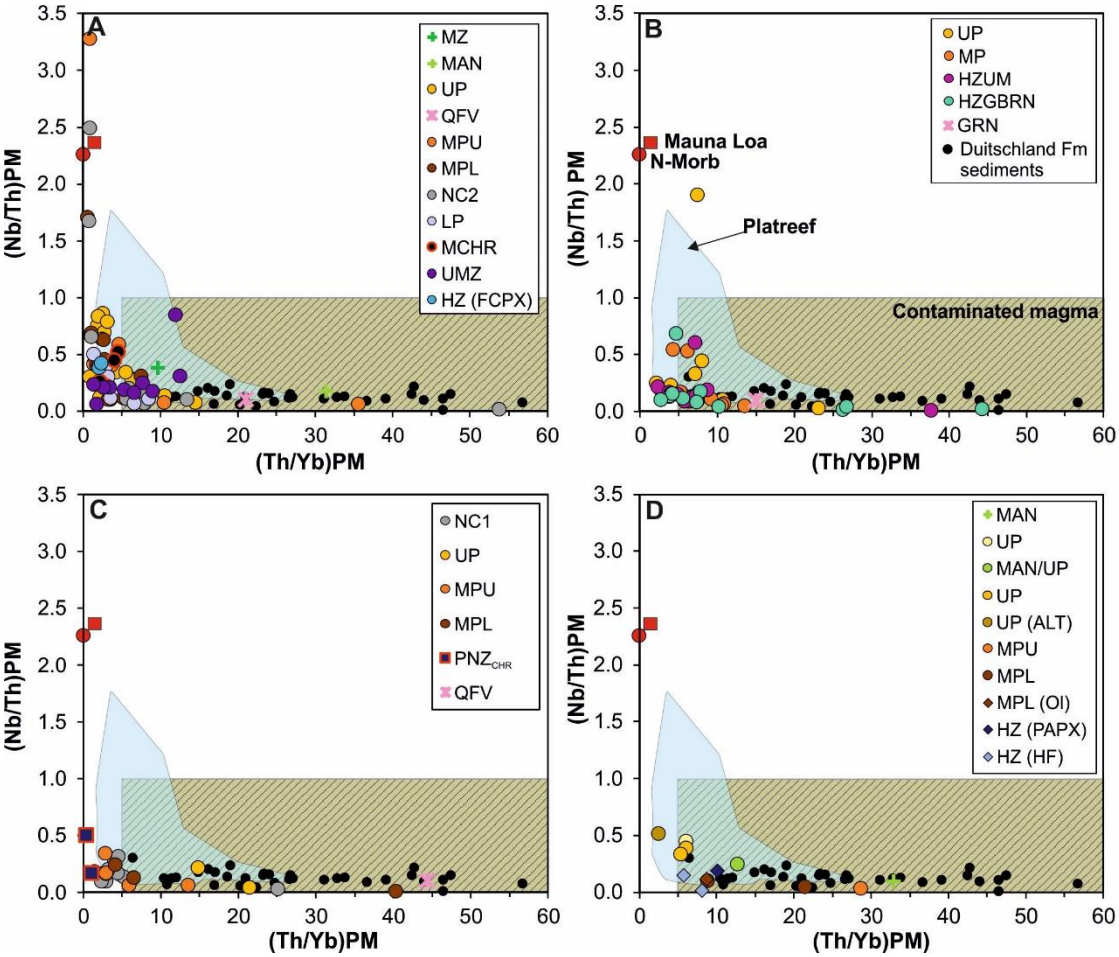

Figure 7.23: Plot of $(Nb/Th)_{PM}$ vs. $(Th/Yb)_{PM}$ from: (A) the Deep Platreef, combined data from UMT_345 and UMT_345_D1; (B) the Thick Flatreef, TMT_006_D2; (C) the Normal Flatreef, UMT_233; (D) the Platreef, ATS_002. The blue area of Platreef samples is based on the results from Ihlenfeld & Keays (2011). Sources: Duitschland Formation obtained in this study; average compositions of N-Morb, Mauna Loa are from Ihlenfeld & Keays (2011). Normalisation factors from McDonough & Sun (1995).

7.3 Platinum-Group Element Geochemistry

The whole-rock platinum-group element (PGE) geochemistry of a subset of samples was analysed in this study using the method of Ni-S fire assay, as detailed in Chapter 4. The most economically important of the PGEs are Pt, Pd and Rh (for details see Chapter 1), they are referred to in this section as 3PGE; if gold is included it is added on as 3PGE + Au. PGE geochemical data are frequently divided into the subgroups PPGE (Rh, Pt and Pd) and IPGE (Os, Ir, Ru) based on their similar physical and chemical properties (Barnes et al., 1985) and in the following discussion these terms will be used.

A summary of the distribution of the 3PGE + Au between the different drill holes analysed in this study are shown in Figure 7.24A. The same set of elements are also presented for the parental Bushveld magmas and their crystallisation products as represented by the cumulates of the Main Zone and Upper Critical Zone (UCZ) in Figure 7.24B. In Figure 7.24C, a direct comparison is made between the mineralised intervals of the Merensky Reef with the Middle Reef and the UG2 chromitite with the Lower Reef as sampled in the Main Chromitite (MCHR) unit; these units are proposed to be equivalent in Nodder (2015) and Grobler et al., (2018).

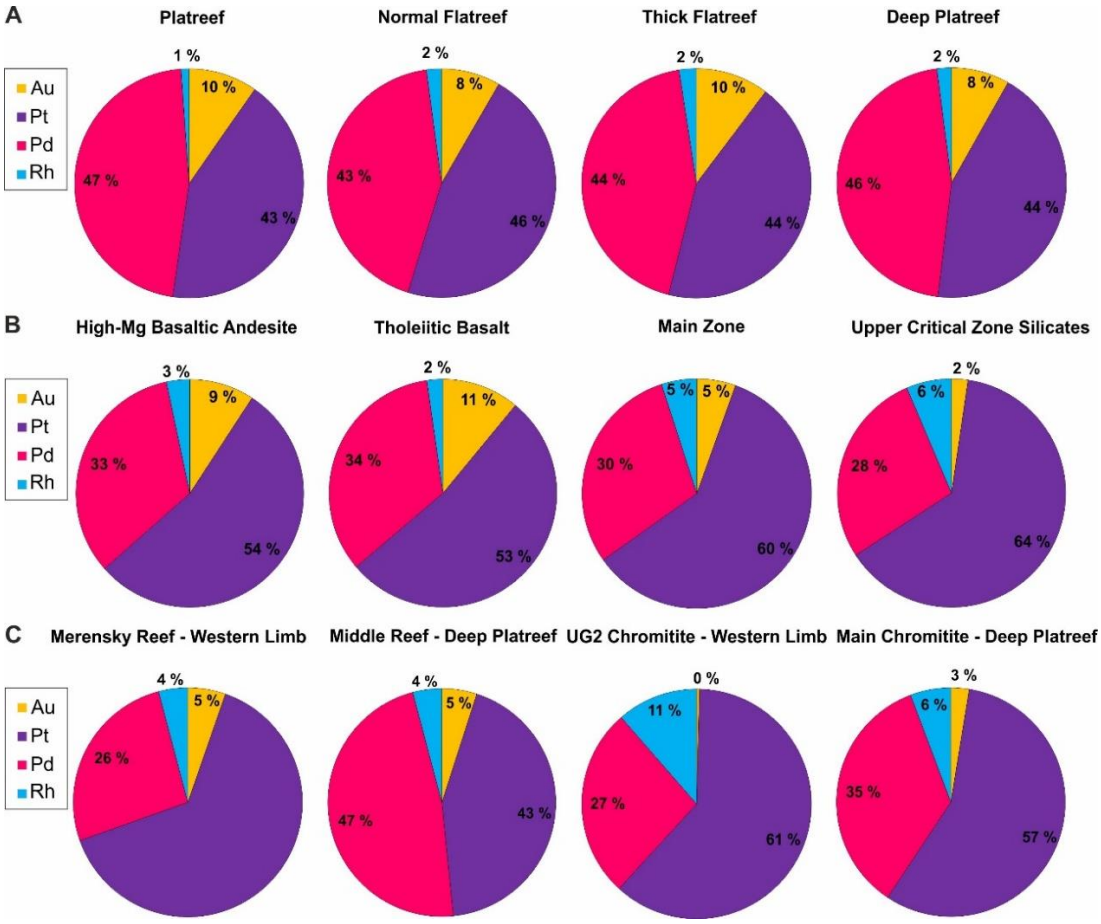

Figure 7.24: A series of pie charts showing the distribution of the 3PGE + Au (expressed as

a % of the summed total) as analysed in the current study and from elsewhere in the Bushveld Complex. (A) An overview of the Turfspruit locality moving progressively down-dip from left to right. (B) The theoretical compositions of the parental magma and measured Bushveld cumulate data. (C) Comparing proposed equivalent mineralised intervals as found in the Deep Platreef on Turfspruit with the Merensky Reef and UG2 Chromitite from the western limb. Source: Turfspruit data in (A and C) from Ivanplats Pty Ltd and all other Bushveld data as shown in (B and C) from Barnes & Maier (2002)

Despite the compositional and mineralogical heterogeneity observed between the drill holes sampling the different zones of the Platreef orebody on Turfspruit the relative proportions of the economic elements are remarkably similar (see Figure 7.24A). This contradicts the suggestion in Maier et al., (2008) that Pd-rich zones found on the margins (i.e. the Platreef) will transition to Pt-rich reefs down dip (i.e. the Deep Platreef). In comparison, both the modelled parental magma compositions and analysed Bushveld cumulates, as shown in Figure 7.24B, have Pt:Pd ratios of ≈2. The cumulates of the UCZ and Main Zone have slightly higher Rh and lower Au compared to the Turfspruit rocks. In Figure 7.24C the PGE deportment of the Middle Reef shows the characteristic Pd-dominated signature as found elsewhere along the Platreef, which is distinct from the Pt-rich Merensky Reef as identified elsewhere. The MCHR unit is compared to the UG2 chromitite in Figure 7.24C, it is similarly Pt-rich as the UG2 but contains lesser Rh and higher Pd and Au contents.

The whole-rock 6PGE data collected in this study is presented in Figure 7.25 as a series of bivariate diagrams to illustrate the various geochemical behaviour of the PGE. The relationship between Cu/Pd and Pd is shown in Figure 7.25A, this is often used as a proxy to illustrate the distribution of Pd into sulphides (e.g. Maier et al., 1996; Barnes & Maier, 2002; Ihlenfeld & Keays, 2011; Barnes & Ripley, 2016); a line is drawn to show the Cu/Pd ratio of the primitive mantle. The data from across the Turfspruit deposit shows a negative linear relationship with all drill holes containing points that are both depleted and enriched relative to mantle Cu/Pd values; with the exception of the Platreef drill hole the majority of the data plots on the enriched side of this line. The highest Pd content and lowest Cu/Pd values are obtained in the Deep Platreef so this drill hole should contain the highest Pd tenor sulphides.

In all drill holes, the IPGE and PPGE show a positive linear trend (R^2 values from 0.6 to 0.9, see Figure 7.25B) suggesting a close correlation between these geochemically distinct subgroups of PGE with similar geochemical/physical mechanisms governing their concentration. The effect of the chrome content of the rock, a proxy for magmatic compositions (i.e. Critical Zone parental magma has 1400 ppm Cr, Barnes & Maier, 2002), on the PGE concentrations in the rock is shown Figure 7.25C. The PGE

concentration increases dramatically where the chromite contents exceeds ≈ 2000 ppm (see Figure 7.25C); this value represents the background chrome content of the pyroxenite units hosting the Upper and Middle Reef mineralised intervals in the majority of the drill holes as shown in the downhole profiles presented in section 7.2. The PGE grade does not increase sympathetically with increasing the Cr content above 2000 ppm; the PGE grade appears to drop off steadily at Cr contents >5000 ppm and this includes the PGE mineralisation associated with the MCHR unit.

The effect of crustal contamination on the grade is shown in Figure 7.25D where the ΣPGE is plotted against the CaO/Al_2O_3 ratio of the whole-rock sample. The highest grades typically plot within the range of magmatic values (0.6 to 1.0); the grade outside of this range drops off sharply. There are a couple of outliers to this and these represent hydrothermally altered samples. This confirms earlier suggestions (e.g. Holwell et al., 2007) that contamination of the magma has the effect of diluting the primary grade.

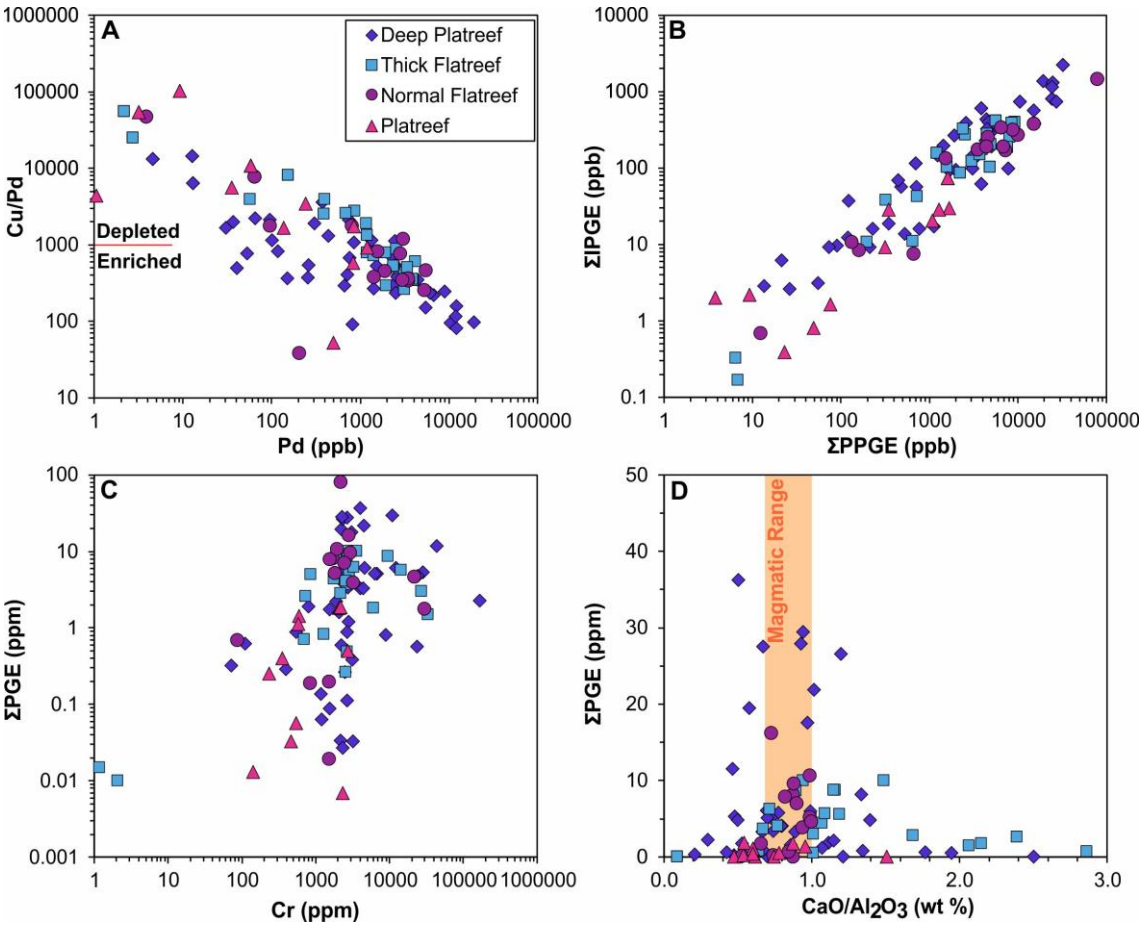

Figure 7.25: Bivariate plots for the PGE data for all drill holes sampled across the Turfspruit deposit. (A) Cu/Pd vs. Pd (ppb); (B) ΣIPGE (ppb) vs ΣPPGE (ppb); (C) ΣPGE (ppm) vs Cr (ppm); (D) ΣPGE (ppm) vs CaO/Al_2O_3.

7.3.1 Chondrite-normalised Ni-Cu-PGE-Au profiles

The chondrite-normalised Ni-Cu-PGE patterns for the different lithostratigraphic units of the Deep Platreef are shown in Figure 7.26. All stratigraphic units exhibit fractionated PGE profiles with elevated PPGE over IPGE resulting in a positive slope that typically peaks on Pd. The exceptions to this are the samples of the Main Zone, Mottled Anorthosite (MAN) and of a quartz-feldspar veins (QFV) all of which peak on Au (see Figure 7.26A and 7.26B, respectively).

The Main Zone and MAN units immediately above the ultramafic lithologies of the Deep Platreef have elevated 6PGE concentrations and are depleted in Ni and Cu in comparison to the average Main Zone as calculated in Barnes & Maier (2002, see Figure 7.26A). The MAN unit PGE profile is more fractionated than the Main Zone profile (Pd/Ir 12.0 and 8.4, respectively) and increases steadily from Ni to Pt before decreasing slightly to Pd and peaking on Au. The Main Zone profile increases from Os to Rh, with negative Pt increasing steadily to Pd before also peaking on Au.

The pyroxenite-dominated units of the Upper Pyroxenite (UP) and the Middle Pyroxenite (MP) have very similar PGE patterns (average Pd/Ir ratios of 48 and 37, respectively) and ranges of concentrations (average ΣPGE 7 and 8 ppm, respectively; see Figure 7.26B and 7.26C). The UP profiles peak on both Au and Pd (Figure 7.26B) and have a wide range in grade (ΣPGE from 0.03 to 19.46 ppm). The highest PGE grade sample from the UP is from the Upper Reef mineralisation event hosted in hydrothermally altered feldspathic orthopyroxenite above a quartz-feldspar vein and this sample also hosts 3.5 ppm Au. The Upper Reef is correlated with the Bastard Reef mineralisation in Nodder (2015) and Grobler et al., (2018); PGE data for the Bastard reef from the Impala platinum mine as measured in Maier & Barnes (2008) is shown in Figure 7.26B. The Upper Reef mineralisation contains significantly higher grade than the Bastard Reef; particularly PPGE with a maximum sample value of 24.4 ppm in the Upper Reef compared to 0.78 ppm in the Bastard Reef. The Upper Reef also contains elevated gold concentrations compared to the Bastard Reef with an average value of 1.5 ppm compared to an average of 0.06 ppm, respectively.

The MP unit has been divided into the upper pegmatoidal lithologies hosting the Middle Reef mineralisation event and the lower unmineralized orthopyroxenite-dominated lithologies in Figure 7.26C. Overall, the MP unit Ni-Cu-PGE profiles increase steadily from Os to Rh, are flat-lying to Pt then increases sharply to Pd with negative Au. In comparison, the Merensky Reef, peaks on Pt and has higher IPGE concentrations (western limb average ΣIPGE of 0.57 ppm). The highest PGE

concentrations in the Merensky Reef samples shown in Figure 7.26C are from the chromite stringers. In contrast, the highest PGE concentrations analysed in this study were from a pegmatoidal orthopyroxenite at the base of the mineralised section that has elevated REE concentrations. The Pt/Pd ratio of the Middle Reef samples analysed in this study vary from 0.5 to 2.3 (average of 1) compared to the Merensky Reef samples (excluding chromitites) of between 1.5 to 2.8.

The Ni-Cu-PGE profiles of the Norite Cycles 2 (NC2) unit are shown in Figure 7.26D; the dominant control on grade is the host rock lithology. The sulphide-mineralised pyroxenite lithologies, typically identified at the base of magmatic cycles, may contain elevated grade (up to ΣPGE 27 ppm) comparable to the highest grades found in the Middle Reef mineralisation. This attests to the formation of these cycles from new influxes of primitive magma. The rock types with higher plagioclase contents contain less grade and it's this dilution which makes this unit uneconomical to exploit.

The highest PGE grades (up to 29 ppm ΣPGE) measured in this study are recorded in the silicate rocks of the Lower Pyroxenite (LP) unit (see Figure 7.26E), which hosts the beginning of the Lower Reef mineralisation event (see Figure 7.3F). The LP unit chondrite-normalised Ni-Cu-PGE profiles have less negative Os concentrations than observed in the other pyroxenite units higher up in the stratigraphy and higher average IPGE contents at 0.95 ppm. The PGE profile of the disseminated chromite-bearing sample from the LP unit steadily increase from Os to Pd before decreasing to Au whereas the sulphide-rich sample increases to Pt then is flat-lying to Au. The Pt/Pd ratio varies between 1.7 to 1.2 and the Pd_N/Ir_N ratio between 41 and 73 for the sulphide-rich and chromite-bearing samples, respectively. Compared to the average UG2 chromitite of the eastern and western limbs the LP unit contains equivalent concentrations of the IPGE but has elevated PPGE concentrations (Barnes & Maier, 2002). The average PPGE grade for the two LP unit samples is 26 ppm compared to the average for the western limb of 4.5 ppm. The two samples of the Main Chromitite (MCHR) unit shown in Figure 7.26, were taken from the Deep Platreef drill hole UMT_336_D1 as studied by Nodder (2015). The patterns are similar to the UG2 chromitite and demonstrate less enrichment in the PPGE than observed in the LP unit. The main differences between the MCHR unit and the UG2 chromitite are the enrichment in Pd over Pt and elevated Ni and Cu content in the former.

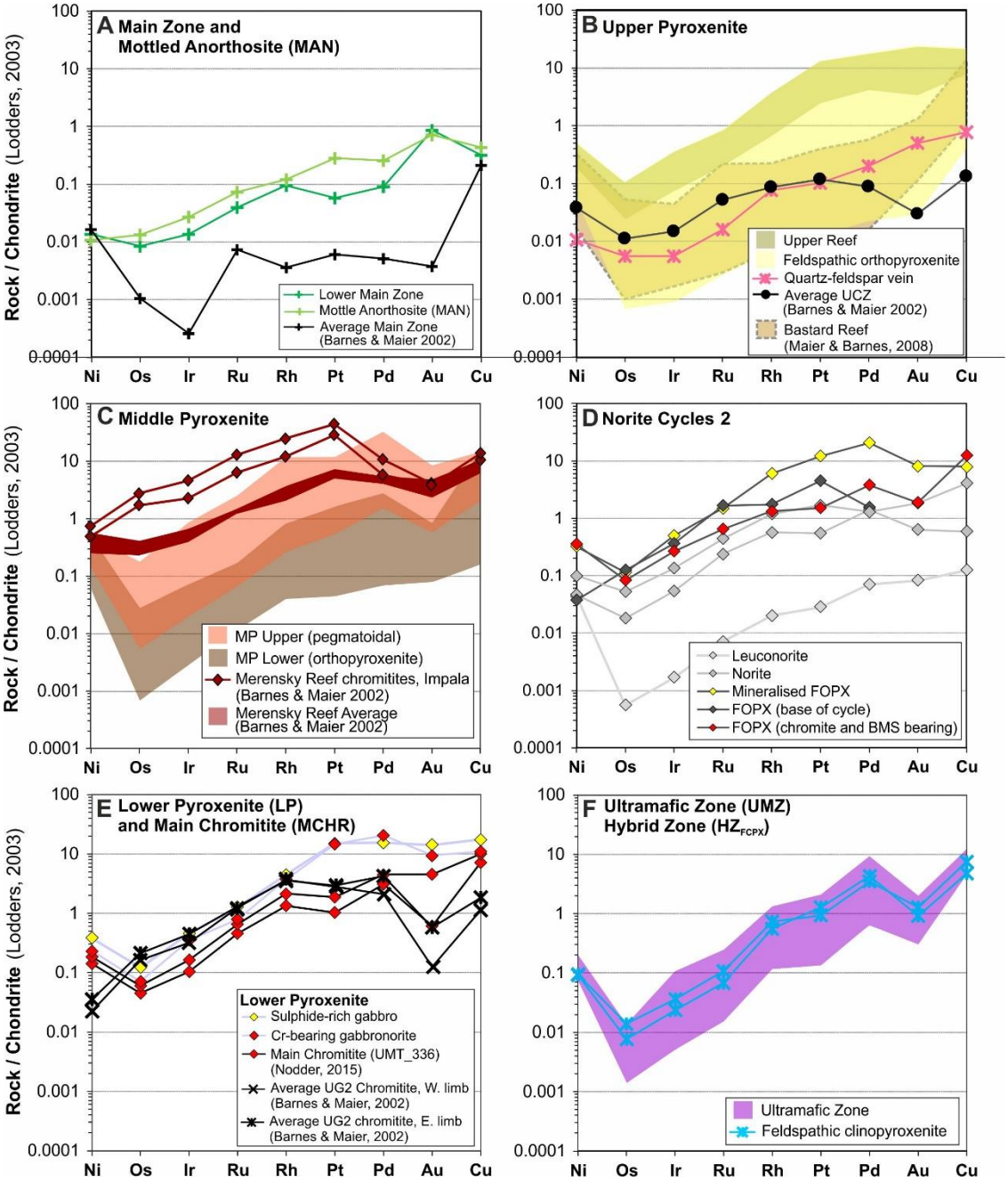

Figure 7.26: Chondrite-normalised Ni-Cu-PGE plots for the different lithostratigraphic units of the Deep Platreef (combined data from UMT_345 and UMT_345_D1). Normalisation factors from Lodders (2003).

The chondrite-normalised Ni-Cu-PGE profiles for the Thick Flatreef are shown in Figure 7.27. The PGE patterns demonstrate remarkable similarity in all stratigraphic units, despite the significant lithological variability; the patterns are characterised by negative Os, positive Pd, negative Au and positive Ni and Cu anomalies. The obvious exceptions to this are samples of the granite vein and country rock (serpentinite); both of which show strongly fractionated and depleted profiles (see Figure 7.27C).

The Upper Pyroxenite (UP) unit, as shown in Figure 7.27A, has been divided into samples that are sulphide-poor (<5 vol%) and sulphide-rich (>5 vol%); corresponding

to a drop of an order of magnitude in grade. The shape of these PGE patterns are similar however, the sulphide-rich pattern peaks on Pd and sulphide-poor samples on Au. The Middle Pyroxenite (MP) unit, has a narrow range of PGE grade and all samples show a similar pattern rising from Os to Pt then flattening out to Pd before a negative anomaly in Au. In Figure 7.27A and 7.27B, the UP and MP data of the thick Flatreef are compared to the profiles of the equivalent stratigraphic units observed in the Deep Platreef. The spread of grades for the same units in the Deep Platreef are much greater compared to the Thick Flatreef where the grades remain consistent in all samples analysed.

The Ni-Cu-PGE profiles for the Olivine Websterite Hybrid Zone (HZ_{OLWEBS}; see Figure 7.27C) and Gabbronorite Hybrid Zone (HZ_{GBRN}; see Figure 7.27D) are similar showing fractionated profiles with a peak on Pd. The average Pd/Ir ratio is highest in the HZ_{GBRN} (67.3) corresponding with the more evolved host rock lithologies compared to those in the HZ_{OLWEBS} (45.8). The spread of grades analysed in the HZ_{GBRN} is larger than observed in the UP and MP units and reflects the heterogenous distribution of sulphides and the spiky downhole grade profile (see Figure 7.7F).

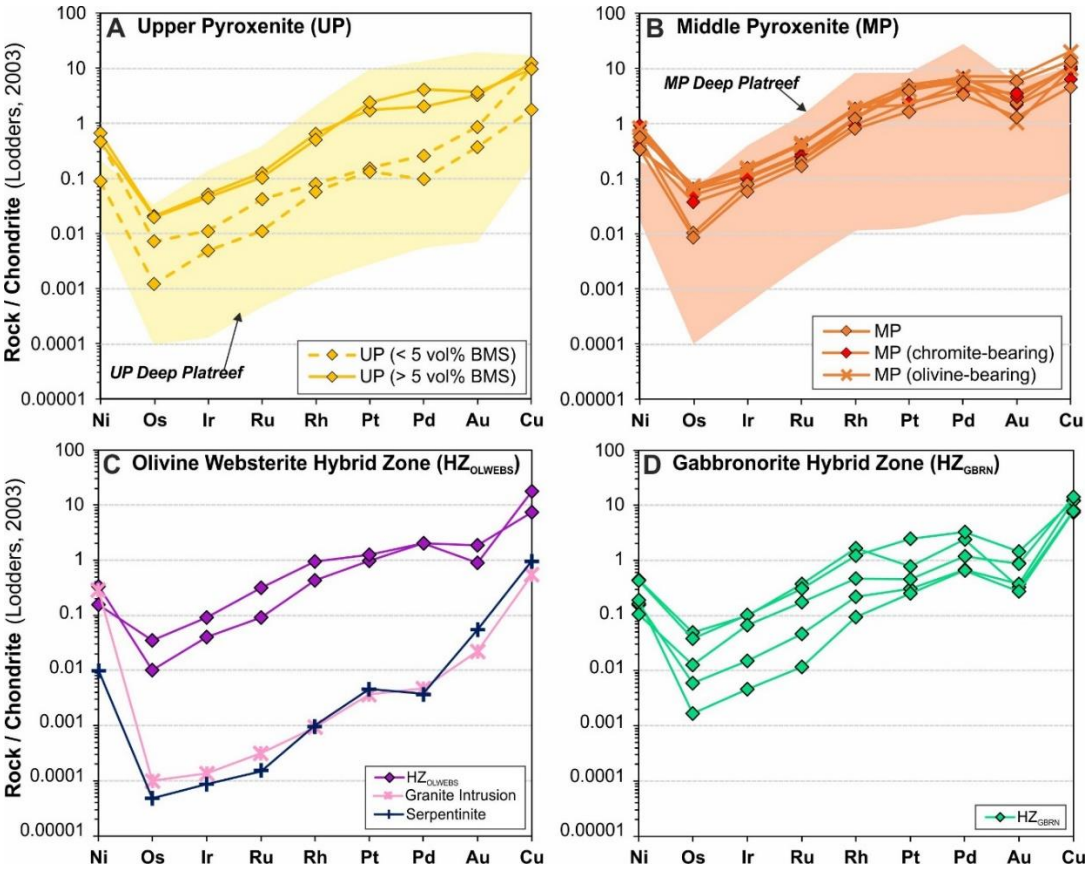

Figure 7.27: Chondrite-normalised Ni-Cu-PGE profiles for the different stratigraphic units in the Thick Flatreef as sampled in drill hole TMT_006_D2. Normalisation factors from Lodders (2003).

The Normal Flatreef chondrite-normalised Ni-Cu-PGE profiles are presented in Figure 7.28A and 7.28B. The profiles for the Norite Cycle 1 (NC1) unit are divided into sulphide-poor (< 5 vol%) and sulphide-rich (> 5 vol%) samples (see Figure 7.28A); similar to the division of the UP unit in the Thick Flatreef. The sulphide-rich NC1 samples peak on Pt then are flat-lying to Au (see Figure 7.28A). There is an order of magnitude difference in the grade between the sulphide-rich and sulphide-poor samples, reflecting the importance of sulphides in concentrating the PGE. One sulphide-poor sample peaks on Au, similar to observations in the UP unit of the Thick Flatreef (see Figure 7.27A).

The one sample analysed from the Upper Pyroxenite (UP) unit in this drill hole contains the lowest concentration of PGE (ΣPGE 0.14 ppm; see Figure 7.28B). This is unusual for this stratigraphic unit which is mineralised in the Deep Platreef and Thick Flatreef drill holes and may be the result of hydrothermal alteration with the sample analysed containing abundant phlogopite and is relatively sulphur-poor.

The majority of samples analysed from the Middle Pyroxenite (MP; see Figure 7.28B) unit have similar PGE profiles that demonstrate less fractionation between Pt and Pd than observed in the previous drill holes. The highly mineralised pegmatoidal portion of the MP unit, directly below the chromite stringer on the contact between the UP and MP units, has a Pt/Pd ratio of 1.8. An unexpected result was obtained for a sample of sulphide-rich from the lower portion of the MP unit which shows significant enrichment in both Pt (Pt/Pd 13.43) accompanied by a peak in Ir. The elevated Pt and Ir peaks are most likely accommodated in an arsenide PGM phase in the platarsite (PtAsS) – irarsite (IrAsS) solid solution. The quartz-feldspar vein (QFV) analysed in the MP unit has a unique profile compared to the granitic intrusions analysed in the Thick Flatreef (see Figure 7.27C) and the Deep Platreef (see Figure 7.26B) drill holes. The QFVs analysed in the other drill holes have similar profiles that show a gradual increase up to a peak in Au; the QFV as shown in Figure 7.28B peaks on Pt (with a slight positive anomaly in Ir) and is depleted in Cu and Au. The chromite-bearing sample from the Pyroxenite-Norite Zone (PNZ_{CHR}; see Figure 7.28B) shows a similar fractionated PGE pattern to the MP unit but is less mineralised. The profile rises steadily from Os to a peak on Pd and a negative anomaly on Au.

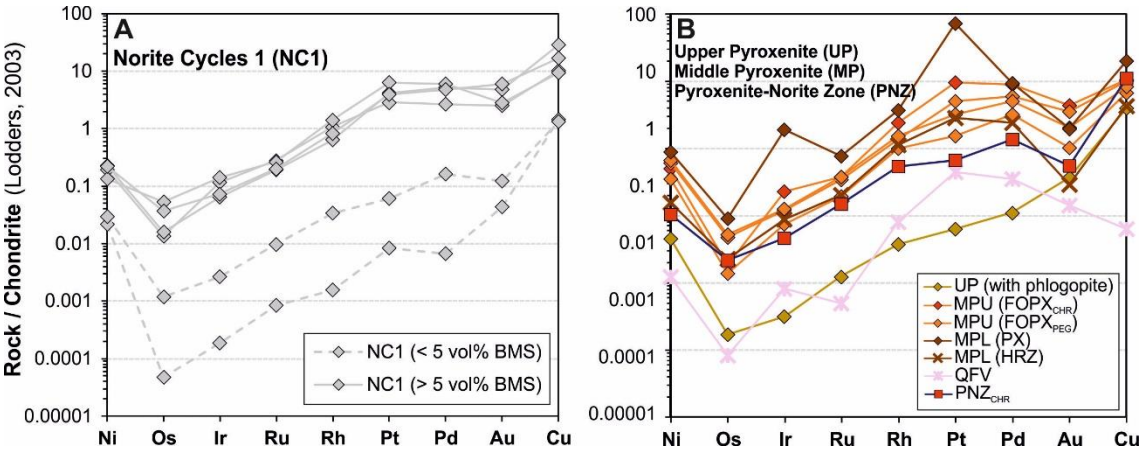

Figure 7.28: Chondrite-normalised Ni-Cu-PGE profiles for the different stratigraphic units of the Normal Flatreef as sampled in drill hole UMT_233. Normalisation factors from Lodders (2003).

Chondrite-normalised Ni-Cu-PGE profiles for the Platreef as sampled in ATS_002 are presented in Figure 7.29. Overall, the PGE profiles for the Platreef demonstrate a larger spread in grade at lower concentrations (particularly in IPGE) than in the other drill holes analysed across the Turfspruit deposit. The profiles observed in each stratigraphic unit also display more variability in their patterns than observed previously. All samples contain elevated Ni and Cu content and have negative Os concentrations; although the overall Ni contents (between 0.01 and 0.1 relative to chondrite) are lower than those measured in the previous drill holes (between 0.1 and 1.0 relative to chondrite).

The Ni-Cu-PGE profile for a sample analysed from the Mottled Anorthosite (MAN) unit is characterised by low concentrations and moderate fractionation (Pd/Ir 8.9; see Figure 7.29A). Directly below the MAN unit, a sample collected from the contact zone with the underlying Upper Pyroxenite (UP) unit has a strongly fractionated (Pd/Ir 174) PGE profile with elevated PPGE and Au (two orders of magnitude more) contents relative to the fresh MAN unit (see Figure 7.29A). Pd and Au are some of the most mobile PGEs (as outlined in Chapter 2 section 2.2.6) possibly indicative of hydrothermal activity on this contact.

The UP unit shows three variable profiles (see Figure 7.29B) that are unique to this unit within this drill hole: (1) a steady increase from Os to a peak on Au (Pd_N/Ir_N 92); (2) a stepped PGE profile with an overall increase from Os to Au (Pd_N/Ir_N 77) and elevated Cu; and (3) a weakly fractionated (Pd_N/Ir_N 7.4), low grade PGE profile with a peak on Ru. The Middle Pyroxenite (MP) unit contains the only economic PGE grade measured in the samples from this drill hole (see Figure 7.29C), which based on the stratigraphic position is correlated with the Middle Reef as identified in the other drill holes. The PGE profiles for the MP unit are characterised by a continuous positive

gradient from Os to a peak in Pd followed by negative Au concentrations and elevated Cu. The most fractionated sample is a feldspathic orthopyroxenite sample from the MP_L unit with a (Pd_N/Ir_N 225). The two samples of the Hornfelsed Hybrid Zone (HZ_{HF}) display an order of magnitude difference in grade; both are moderately fractionated (Pd_N/Ir_N 33 and 146, respectively), peak on Pd have negative Au and elevated Cu (see Figure 7.29D).

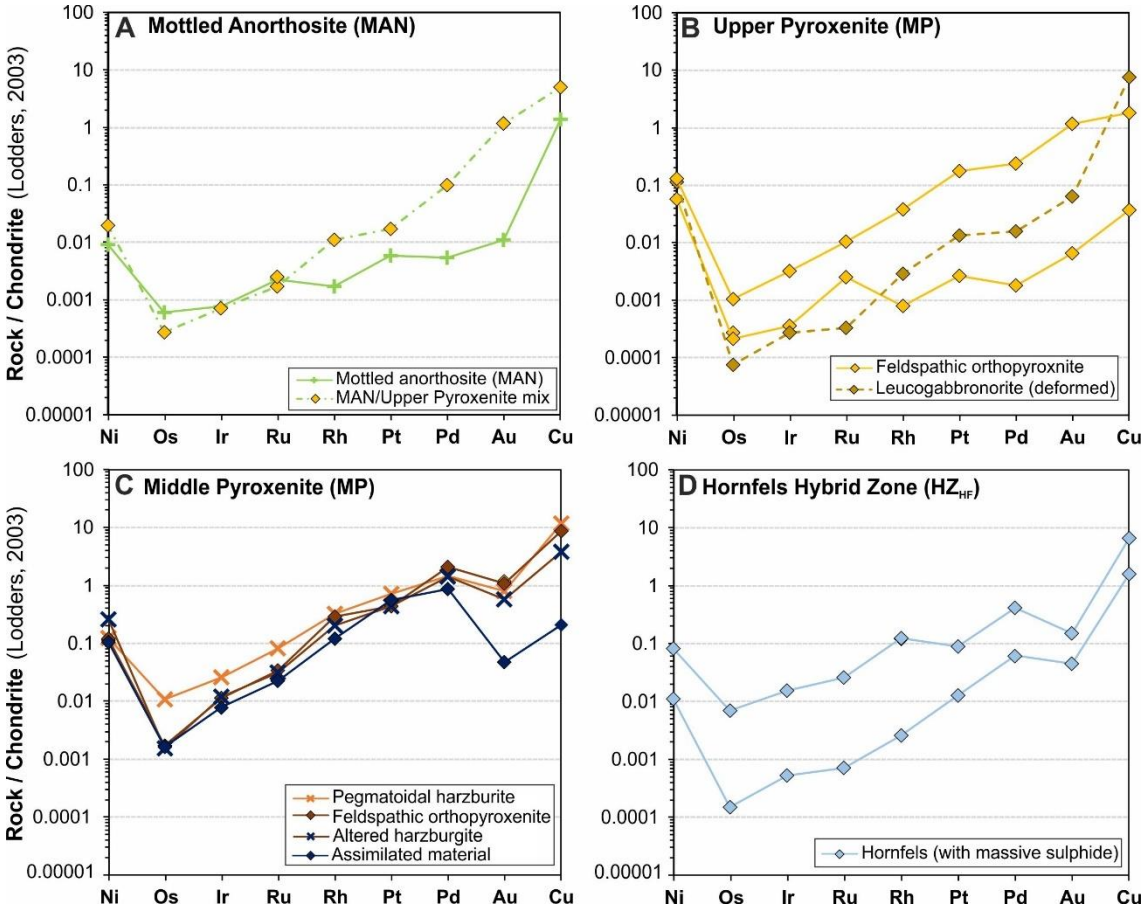

Figure 7.29: Chondrite-normalised Ni-Cu-PGE profiles for the different stratigraphic units of the Platreef as sampled in drill hole ATS_002. Normalisation factors from Lodders (2003).

Chapter 8

Mineralogy and Mineral Chemistry

8.0 Introduction

The mineral assemblages, mineral textures and mineral chemistry as presented in this chapter are based on work completed on polished thin sections of the drill core samples (see Figures 8.1 and 8.2, below). A description of the analytical methods used in this section can be found in Chapter 4 (section 4.4). Mineralogical descriptions are presented first (section 8.1) followed by quantitative mineral chemistry data (section 8.2). Additional photomicrographs and descriptions can be found in Appendix D. A full set of quantitative mineral compositional data is provided in Electronic Appendix D.

The mineralogy of the Platreef on Turfspruit has been studied previously by Hutchinson & Kinnaird (2005), Sharman-Harris et al., (2005), McDonald et al., (2005), Hutchinson & McDonald (2008), Pronost et al., (2008) and Yudovskaya et al., (2014). Recently, the focus has shifted to the Flatreef with mineral studies by Yudovskaya et al., (2017) and Beukes et al., (2018). The main focus of this work is, therefore, on the unstudied Deep Platreef where the stratigraphy has been previously identified as being the least contaminated and in principle the minerals should retain the most primary magmatic composition (see Chapter 5).

8.1 Mineralogical Observations

The majority of the lithological units identified in this study contain varying proportions of the minerals (in order of abundance); orthopyroxene, plagioclase, clinopyroxene and olivine. The main visible accessory minerals include chromite, base metal sulphides (BMS), quartz and phlogopite. The most common alteration products of the mafic minerals include; serpentinite (± magnetite), talc, chlorite, tremolite and other amphiboles. Plagioclase is frequently observed to be undergoing alteration to: albite, prehnite, pumpellyite and sericite. A summary of the visually estimated modal abundances of these minerals in each drill hole studied is provided in Figures 8.1 and 8.2.

A variety of igneous and hybrid textures are observed in the drill core including: massive, pegmatoidal, poikilitic, pseudoporphyry, equigranular and inequigranular. The most common oikocryst minerals are clinopyroxene, plagioclase and occasionally orthopyroxene. The grain sizes vary from fine (<1 mm) to very coarse (>10 mm) grained.

As with the lithological descriptions, the mineralogy here will be described according to stratigraphic units beginning from the top in a downhole direction; for an explanation of this decision please refer to Chapter 5 (section 5.2). The descriptions are

accompanied by numerous photomicrographs highlighting key observations; a guide to the abbreviations used in the annotation of these figures is provided in Table 8.1 below. In addition, please note: (1) thin sections with the prefix GS were sampled in the study Smart (2013); (2) the prefix HS denotes samples collected in the current study and; (3) red arrows on figures point in the downhole direction.

Table 8.1: A list of abbreviations for common annotations used on thin section photomicrographs.

Primary Silicate Minerals		Secondary Alteration		Opaque Minerals		Microscope Settings	
Opx	Orthopyroxene	**Amp**	Amphibole	**BMS**	Base metal sulphides	**PPL**	Plane polarised light
Cpx	Clinopyroxene	**Hbl**	Hornblende	**Po**	Pyrrhotite	**XP**	Crossed polars
Ol	Olivine	**Act**	Actinolite	**Pn**	Pentlandite	**RFL**	Reflected light
Pl	Plagioclase	**Serp**	Serpentine	**Cp**	Chalcopyrite	**BSE**	Back-scattered electron
Qtz	Quartz	**Cc**	Calcite	**Cb**	Cubanite		
Phl	Phlogopite	**Apt**	Apatite	**Py**	Pyrite		
		Chl	Chlorite	**Cr**	Chromite		
				Mgn	Magnetite		

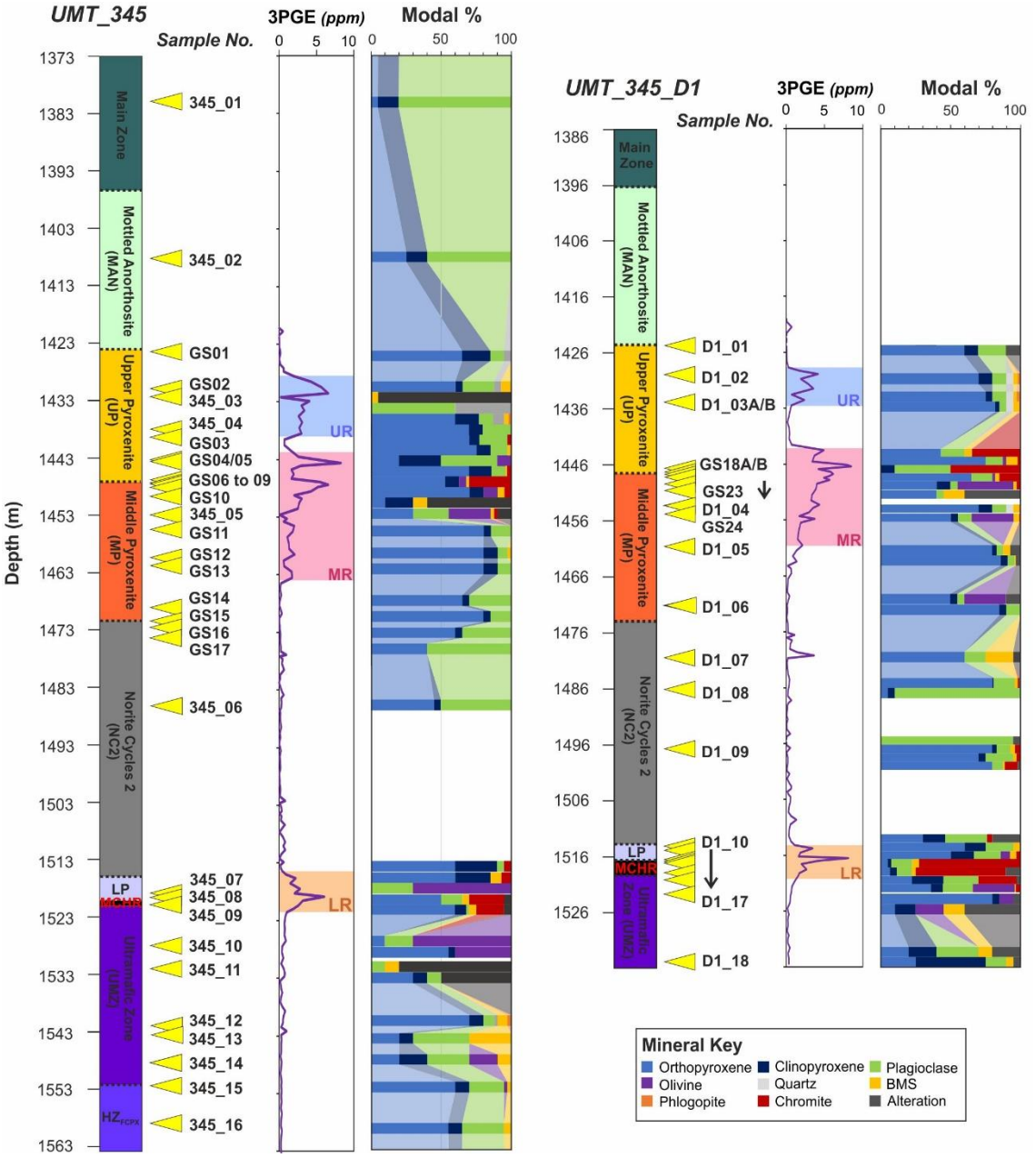

Figure 8.1: Downhole profiles showing the stratigraphy, thin section depth, grade (Pt, Pd, Rh) and visually estimated petrographic modes for thin sections from the Deep Platreef drill holes UMT_345 and UMT_345_D1, respectively.

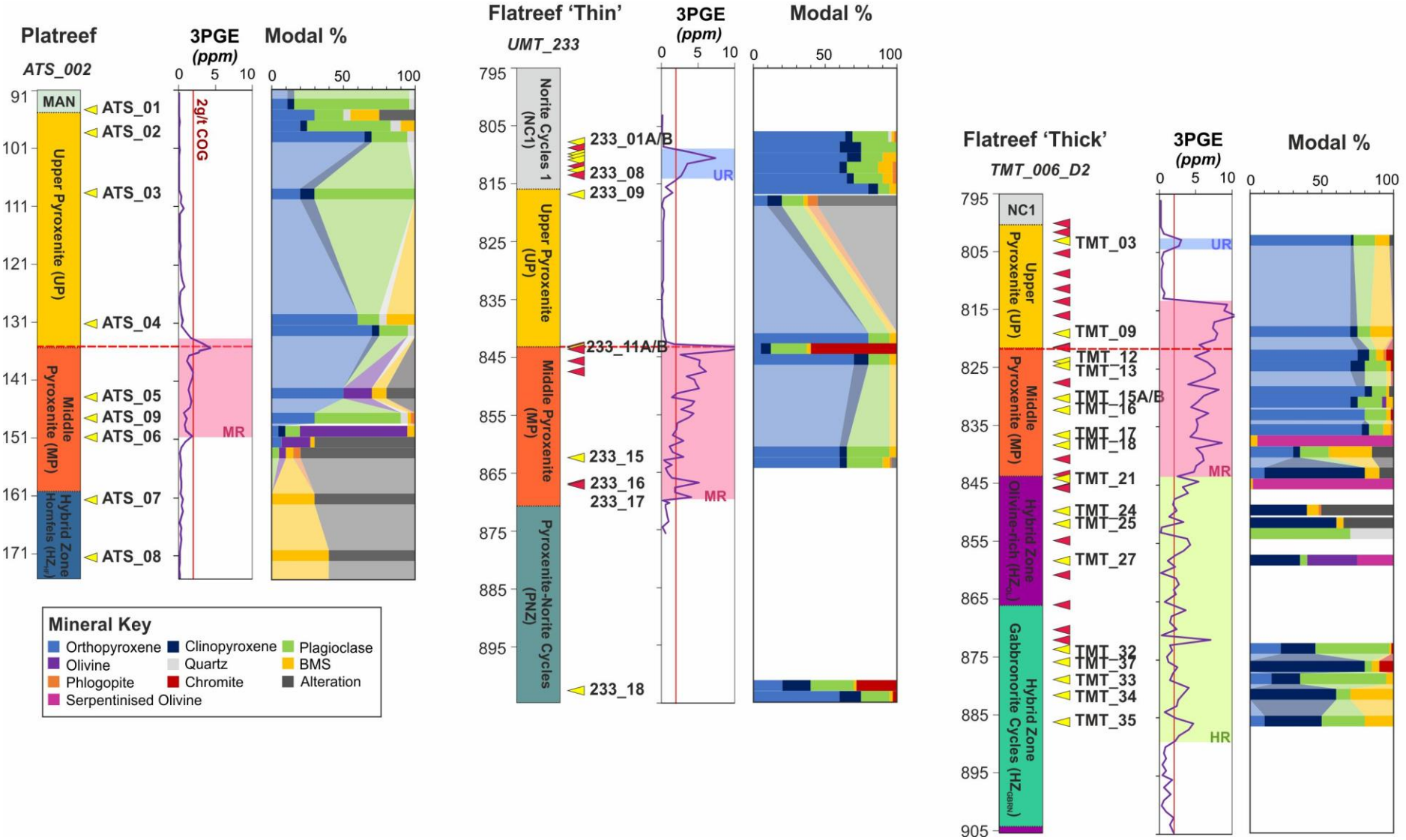

Figure 8.2: Downhole profiles showing the stratigraphy, thin section depth, grade (Pt, Pd, Rh) and visually estimated petrographic modes for thin sections from the Platreef and Flatreef drill holes studied.

8.1.1 Deep Platreef Mineralogy

An overview of the Deep Platreef mineralogy as observed in thin sections from the drill holes UMT_345 and UMT_345_D1 are shown in Figure 8.1. Representative photomicrographs and descriptions of the Main Zone gabbronorite as sampled directly above the Platreef are shown in Appendix D (Figure D.1).

The Mottled Anorthosite (MAN) unit, as presented in Figure 8.3(A-C), can be compositionally divided into pyroxene-dominated mottles and the host adcumulate anorthosite. The pyroxene mottles are composed of anhedral ortho- and clinopyroxene oikocrysts that have grown to very coarse to pegmatoidal sizes (>10 mm), as shown in Figure 8.3A and 8.3C. These oikocrysts contain sub- to euhedral plagioclase laths ranging in size from < 1 mm up to 2 mm (long axis). The composition of the pyroxene mottles shows a slight zoning with the centre of the mottles composed of orthopyroxene with clinopyroxene on the edge. The contact between the two pyroxenes is irregular and embayed. The clinopyroxene side of the contact typically contains numerous anhedral inclusions of the orthopyroxene whereas no clinopyroxene inclusions were observed in the orthopyroxene. Evidence for the exsolution of clinopyroxene from orthopyroxene is also observed (see Figure 8.3B and 8.3C) on the contact between the anorthosite and the orthopyroxene oikocryst. The anorthosite component is composed of predominantly acicular, sub- to euhedral, fine to medium grained laths of plagioclase. These show evidence of minor seriticisation (see top left-hand side of Figure 8.3C).

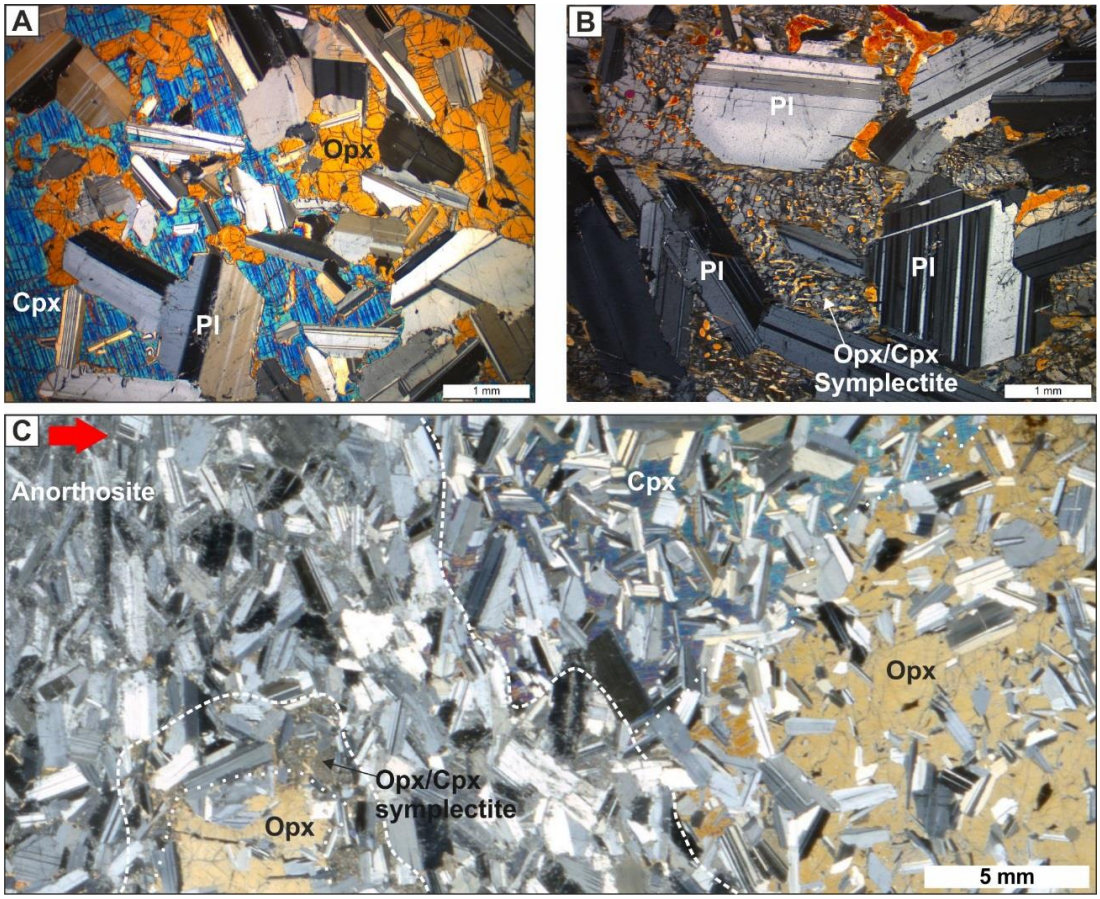

Figure 8.3: Photomicrographs of the MAN unit as sampled in thin section HS_345_02. *All images in XP.* (A) A pyroxene mottle with an ophitic texture, showing the contact between orthopyroxene and clinopyroxene. (B) Interstitial orthopyroxene exsolving clinopyroxene on edge of mottle. (C) Overview of the relationship between the mottles (denoted by dashed white lines) and the anorthosite. Note: red arrow points in the downhole direction.

The top of the Upper Pyroxenite (UP) unit was sampled in thin sections GS1A (UMT_345) and D1_01 (UMT_345_D1) located 50 and 10 cm away from the MAN unit, respectively. The sample nearest to the contact (D1_01) is strongly altered with amphibole minerals growing on the edges of medium-grained orthopyroxene grains (see Figure 8.4A) and interstitial plagioclase being altered to chlorite and other saussuritization minerals (see Figure 8.4A). Additionally, the orthopyroxenes have a slight anomalous dark blue colour to their extinction indicating alteration by chlorite minerals (see Figure 8.4B) and light brown amphiboles can be seen developed along cleavage planes (see Figure 8.4A). Moving away from this contact, sample GS1A is significantly less altered. The cumulate mineral assemblage is dominated by fine to medium grained (< 1 mm to 3 mm) equant orthopyroxene crystals. The interstitial areas contain plagioclase, quartz, phlogopite and minor Na-rich plagioclase. Clinopyroxene is present as coarse to very coarse oikocrysts with an abundance of very fine rutile inclusions (see Figure 8.4C). The interstitial quartz decreases in abundance in the downhole direction.

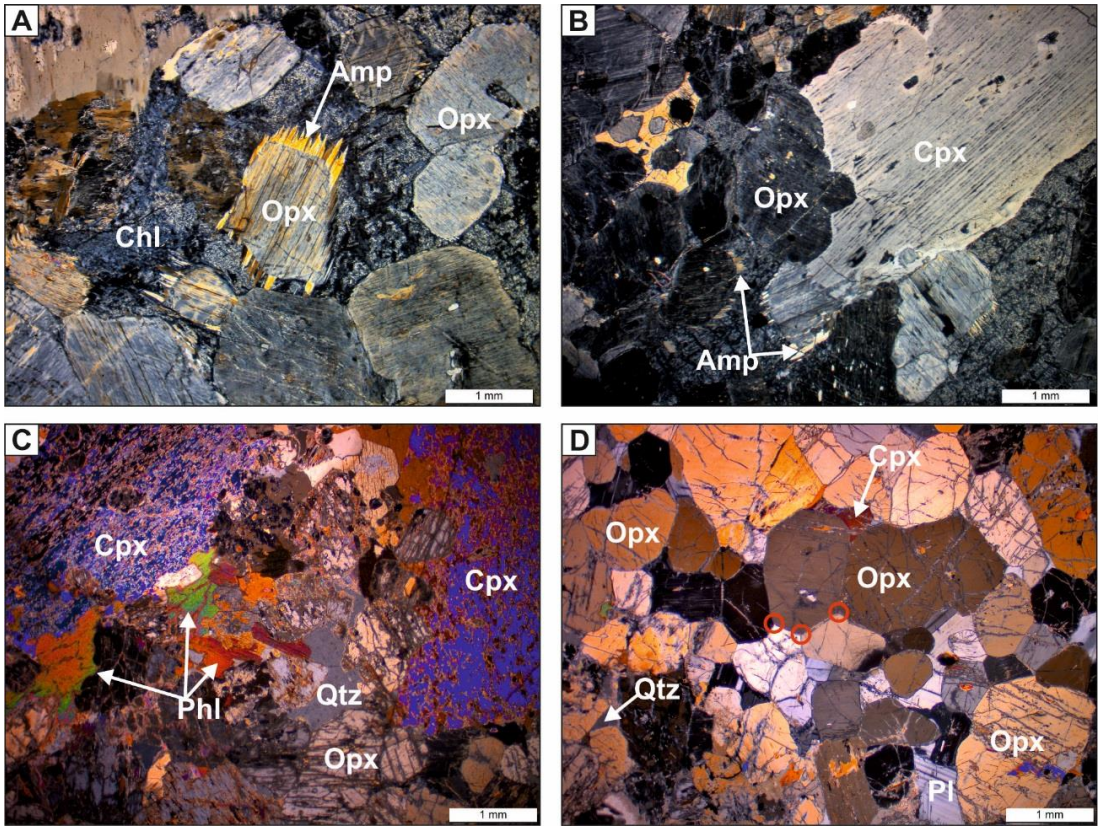

Figure 8.4: Photomicrographs showing features of the UP unit within 50 cm of the MAN contact. All images in XP. (A) Medium grained orthopyroxene undergoing alteration to amphibole and chlorite (D1_01). (B) Coarse-grained clinopyroxene oikocryst and medium-grained altered orthopyroxene (D1_01). (C) Clinopyroxene oikocrysts with cumulate orthopyroxene and interstitial phlogopite and quartz (GS1A). (D) Fine to medium grained orthopyroxene demonstrating a polygonal texture with interstitial plagioclase (GS1A).

Moving down from the top contact the UP feldspathic orthopyroxenite has an orthocumulate texture dominated by cumulus orthopyroxene (>70 modal%) and interstitial plagioclase (varying between 5 to 20 modal%) with minor amounts of clinopyroxene (<5 to 10 modal%) present as oikocrysts. The orthopyroxene forms as equant and short to elongated crystals of medium to coarse grain size (typically between 3 to 7 mm) that are randomly orientated (see Figure 8.5B and 8.5C). The interstitial assemblage of the UP unit is more variable than the cumulate assemblage consisting of: clinopyroxene, plagioclase, quartz, phlogopite and base metal sulphides (BMS). Clinopyroxene oikocrysts, grow to very coarse grain sizes (up to 15 mm; see Figure 8.5A) and impart a pseudo-porphyritic texture on the rock. The clinopyroxene contains chadacrysts of anhedral, medium-grained orthopyroxene and exsolution lamellae of orthopyroxene may also be present (see Figure 8.5A). Plagioclase is the dominant interstitial phase and is usually medium-grained (between 2 to 5 mm) and shows well-developed lamellae twinning (see Figure 8.5D). Sometimes the plagioclase has a patchy appearance due to the development of alteration minerals such as talc and tremolite (see Figure 8.5D). Quartz is also frequently identified as an

interstitial phase and forms sharp contacts when next to plagioclase (see Figure 8.5B and C). The presence of quartz is frequently accompanied by anhedral, fine to medium grained (< 1 mm to 3 mm) phlogopite. Finally, a fractionated BMS assemblage of pyrrhotite, pentlandite and chalcopyrite (in order of abundance; see Figure 8.5E and 8.5F) are also found interstitially and are spatially associated with the presence of phlogopite and quartz (see Figure 8.5C and 8.5E). The BMS are frequently medium-grained (1 to 5 mm in size) and surrounded by an alteration rim of talc, tremolite and quartz. In addition, using the enhanced microscope capabilities of an SEM, monazite grains pitted with inclusions of galena were identified within these alteration pockets near to BMS. Examples of the quartz-feldspar veins (QFV) intruding the UP unit are provided in Appendix D.

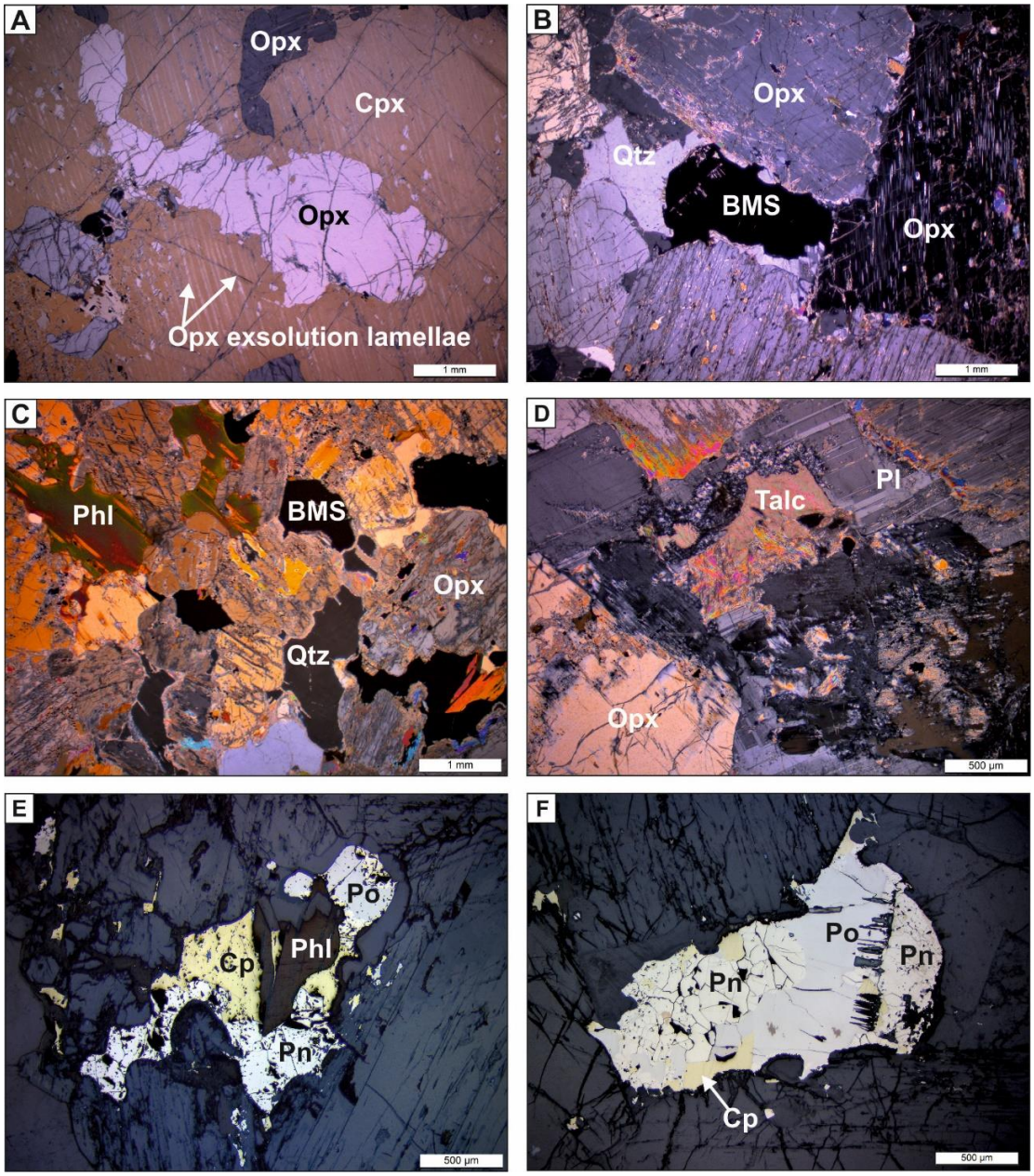

Figure 8.5: Photomicrographs showing typical mineralogical features of the UP unit in the Deep Platreef. *Images A to D in XP and E to F in RFL.* (A) Clinopyroxene oikocryst with orthopyroxene chadacrysts and exsolution lamellae (345_04). (B) Interstitial area hosting quartz and BMS (345_04). (C) Quartz-phlogopite-base metal sulphide interstitial assemblage to orthopyroxene cumulates (D1_03A). (D) Talc alteration patch in interstitial plagioclase (GS3A). (E) Medium-grained interstitial base metal sulphide with a close spatial association to phlogopite (D1_03A). (F) Medium-grained BMS in a quartz dominated interstitial space (345_04).

The basal part of the UP unit is characterised by the presence of four chromite stringers; the 1st chromite stringer marks the beginning of the Middle Reef mineralised interval (see Figure 8.1) and the 4th chromite stringer lies on the contact between the UP and Middle Pyroxenite (MP) units.

The 3rd chromite stringer was sampled in thin sections GS18A (top) and GS18B (base); features of which are shown in Figure 8.6. The chromite stinger is composed of disseminated, euhedral, fine-grained chromite (70 %) and interstitial plagioclase (30 %) with minor BMS (see Figure 8.6A and 8.6B). The chromite grains are frequently pitted (see Figure 8.6C and 8.6D) containing micron-sized inclusions of oxide minerals, base metal sulphides and silicates (plagioclase). Multiple small pits (<200 µm) in chromite grains create a 'sieve' texture and this is typically developed around a fracture in the chromite grain; sulphides infilling are commonly monomineralic chalcopyrite. Singular, larger (up to 500 µm) sized holes in the chromite containing polyphase BMS consisting of pyrrhotite, pentlandite and chalcopyrite are also found; these are interpreted as melt inclusions based on the negative crystal shapes imposed by the spinel structure (as discussed in Holwell et al., 2011).

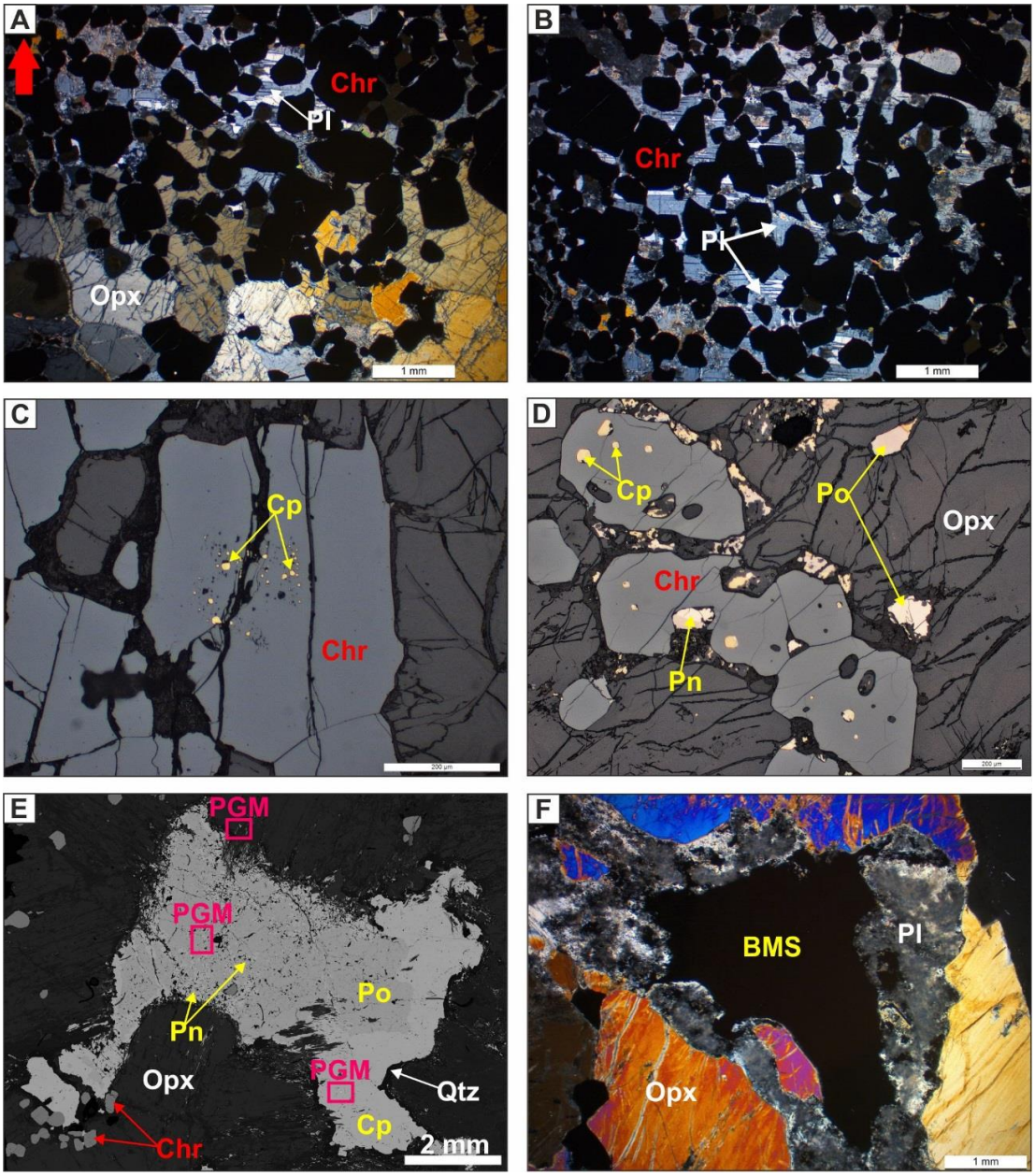

Figure 8.6: Photomicrographs showing petrological features of the 3rd chromite stringer as sampled in UMT_345_D1. *Images A, B and F are in XP*; *C and D are in RFL; and E is in BSE*. (A) The top contact of the 3rd chromite stringer (GS18A). (B) The middle of the 3rd chromite stringer (GS18B). (C) Sieve-textured chromite containing micron-scale inclusions of chalcopyrite and plagioclase (GS18B). (D) Disseminated chromite grains with multiple inclusions in the underlying orthopyroxene pegmatoid (GS19B). (E) A very coarse grained BMS hosting numerous PGM phases in both the sulphide and in alteration minerals on the sulphides edge (GS18B). (F) A coarse-grained BMS hosted in interstitial plagioclase undergoing alteration (GS19A).

The pegmatoidal orthopyroxenite beneath the 3rd chromite stringer, is shown in Figure 8.6D to 8.6F. It hosts medium to coarse-grained BMS comprising pyrrhotite, pentlandite and chalcopyrite (in order of abundance) some of which host multiple occurrences of visible platinum-group minerals (PGMs, see Figure 8.6E). Disseminated chromite grains within this lithology are shown in Figure 8.6D; the

chromite grains appear more rounded and embayed than in the chromite stringer and contain multiple rounded sulphide inclusions.

Petrological features of the 4th chromite stringer on the bottom contact of the UP unit, as sampled in GS8A (UMT_345) and GS20A/GS20B (top/base, respectively; UMT_345_D1), are shown in Figure 8.7. The chromite grains are found as both euhedral grains but also as annealed clusters; the latter texture is not seen in the first three chromite occurrences (see Figure 8.7A to 8.7D). The 4th chromite stringer as sampled in these two drill holes demonstrates some visible differences. In UMT_345 (GS8A) the chromitite is massive (80 % chromite) and the interstitial silicate is composed of clinopyroxene (see Figure 8.7A) with minor BMS at triple junctions. In UMT_345_D1 (GS20A/B) the chromite stringer is more disseminated in appearance (50 modal% chromite) and the dominant interstitial silicate minerals are plagioclase with lesser clinopyroxene (see Figure 8.7C). The annealed texture of chromite grains is only partially developed in GS20A; where found the annealed chromite grains demonstrate an interstitial morphology with plagioclase (see Figure 8.7C and 8.7D). The fine- to medium-grained euhedral chromite grains in GS20A may have ilmenite exsolution needles and/or contain inclusions of oxide minerals (see Figure 8.7F) and polyphase sulphide melt inclusions (see Figure 8.7E and 8.7F; no sieve-textured chromite grains were identified).

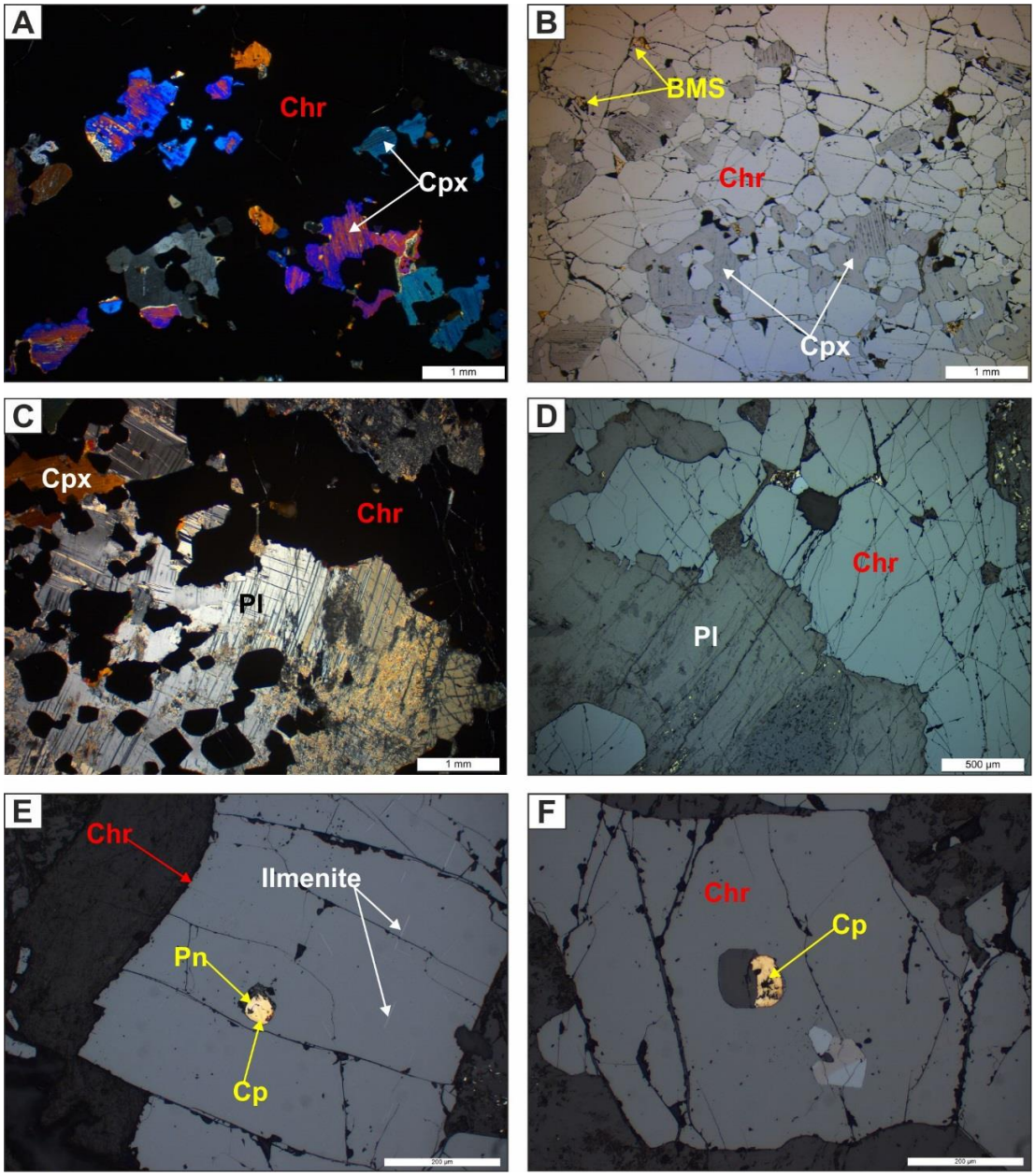

Figure 8.7: Photomicrographs showing petrological features of the 4th chromite stringer. *Images A and C are in XP, all others are in RFL. (*A and B) Annealed chromite at base of chromite-stringer with interstitial clinopyroxene (GS8A). (C and D) Annealed chromite with interstitial edges to plagioclase (GS20A). (E) Chromite grain exsolving ilmenite needles (GS20). (F) A polyphase sulphide-silicate inclusion in a chromite grain (GS20).

The base of the 4th chromite-stringer and top of the Middle Pyroxenite (MP) unit in the Deep Platreef are shown in Figure 8.8A; the contact is concave and the chromitite extends down into the MP unit. The lithologies present in the top of the MP unit are distinct from the UP unit and are marked by the first appearance of olivine and a dominant pegmatoidal texture; representative examples of the textures and mineralogy are shown in Figure 8.8.

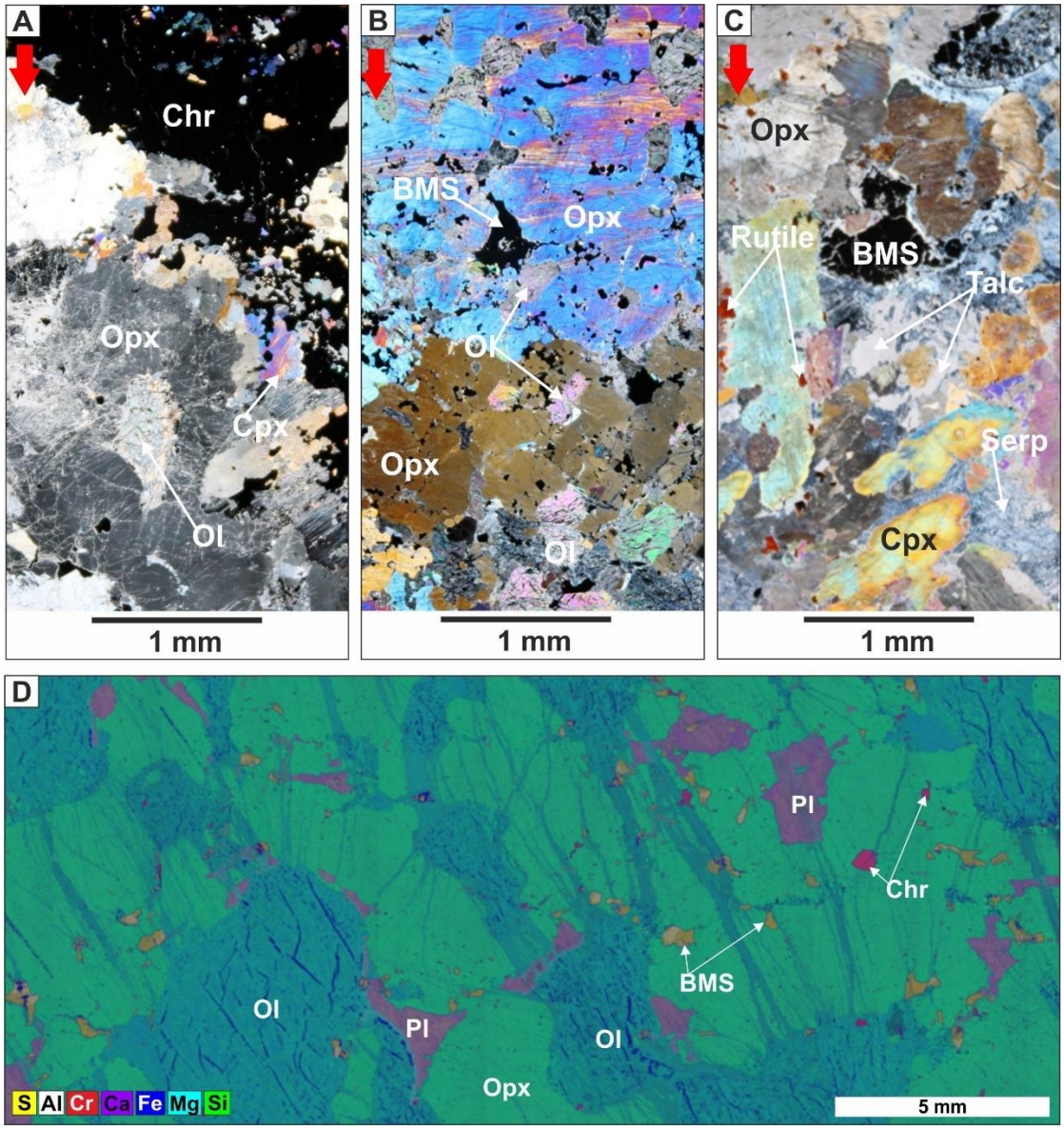

Figure 8.8: Whole-thin section photomicrographs showing petrological characteristics of the top (5 m) of the MP unit in the Deep Platreef. *Images A to C in XP and D is an EDS multi-element map.* (A) Base of the 4th chromite stringer on the contact between the UP and MP units showing the first appearance of olivine (GS8A). (B) Pegmatoidal orthopyroxene oikocryst hosting olivine chadacrysts, chromite and BMS are disseminated (GS9A). (C) Altered pegmatoidal olivine orthopyroxenite (GS10A). (D) Pegmatoidal feldspathic harzburgite (GS22A).

The overview provided in Figure 8.8 illustrates how the olivine content and its textural setting varies within this unit. In the olivine orthopyroxenite shown in Figure 8.8A and 8.8B the olivine (up to 10 modal%, medium-grained) is hosted as chadacrysts in a pegmatoidal orthopyroxene oikocryst that also hosts fine-grained, disseminated chromite and medium-grained BMS (see Figure 8.9C and 8.9D). The olivine causes deformation cracks in the orthopyroxene crystal, which are preferentially exploited by serpentinising fluids. Moving downhole the degree of alteration increases and two alteration styles are observed (1) serpentinization (with magnetite veins) dominants

in olivine-bearing lithologies (see Figure 8.8D) and (2) talc-tremolite (± rutile, ± serpentinisation) alteration in pegmatoidal olivine pyroxenite (see Figure 8.8C). In the feldspathic harzburgite the olivine content is up to 50 modal% with between 10 to 15% plagioclase (see Figure 8.8D). Where olivine has been completely serpentinised sulphide minerals may be concentrated in the relict olivine left after serpentinisation suggesting that some sulphide was mobile in the serpentinising fluids (see Figure 8.9A and 8.9B).

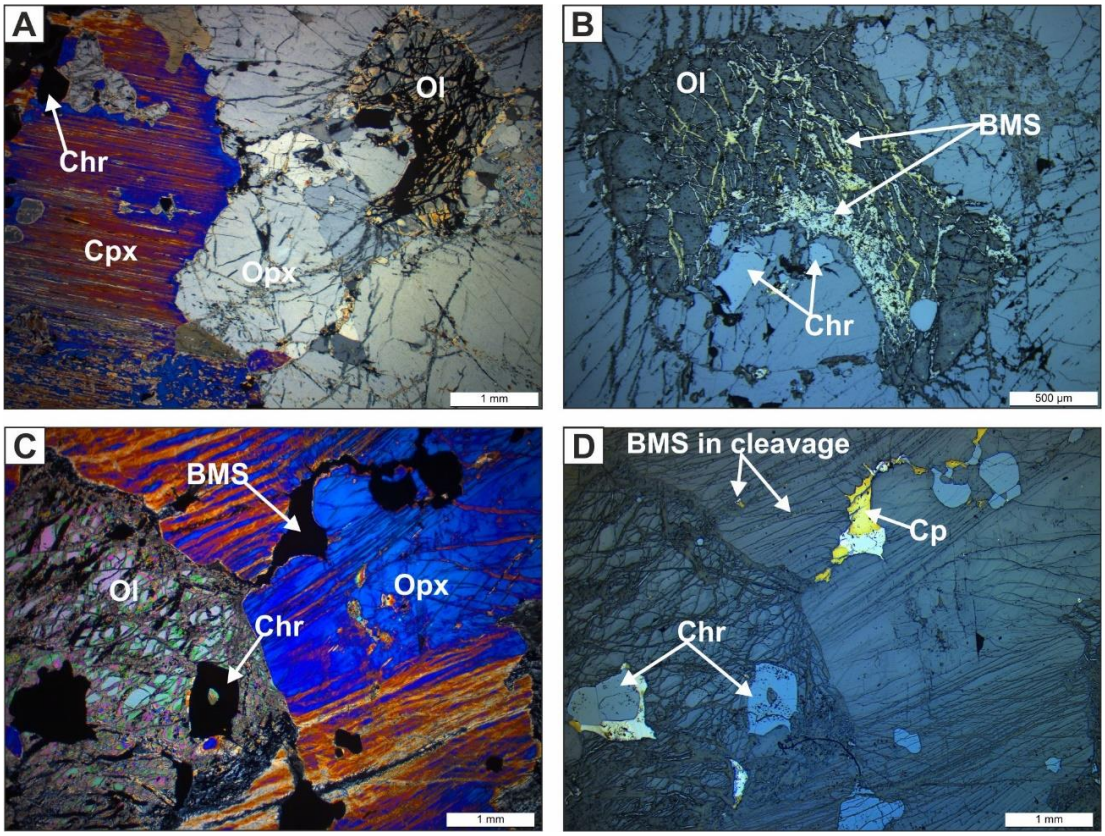

Figure 8.9: Photomicrographs showing mineralogical features of the top of the MP unit. *Images A, C and E in XP; B, D and E in RFL. (A)* Clinopyroxene on the contact between the 4th chromite stringer and the pegmatoidal olivine orthopyroxenite (GS8A). (B) BMS in alteration veins (possibly talc) in replaced olivine grain (GS8A). (C) Medium-coarse grained olivine with inclusions of chromite and base metal sulphides (GS9A). (D) Fine-grained base metal sulphides and chromite grains hosted within both olivine and orthopyroxene (GS9A).

Petrological features of typical lithologies within the Norite Cycles 2 (NC2) unit are shown in Figure 8.10. Plagioclase is the dominant mineral and is present as cumulate laths that are fine- to medium-grained; these may be aligned to form a weak fabric, particularly in anorthosites. Orthopyroxene is present both interstitially (see Figure 8.10A) and as a cumulate phase (see Figure 8.10C). Interstitial orthopyroxene to cumulate plagioclase is unusual and is not expected in a normal fractionating magma; however, it is also observed in the mottled anorthosite unit. Clinopyroxene is present as exsolutions from orthopyroxene (see Figure 8.10A) and as a minor interstitial

phase (see Figure 8.10B); locally it may be present as oikocrysts. An example of a base of a typical norite cycle is shown in Figure 8.10C; the contact shown is between an anorthosite and feldspathic orthopyroxenite with a chromite stringer located directly on this boundary. The chromite stringer is fine grained and thin, one or two grains width; the chromite grains sit within embayments on the edges of the orthopyroxene grains.

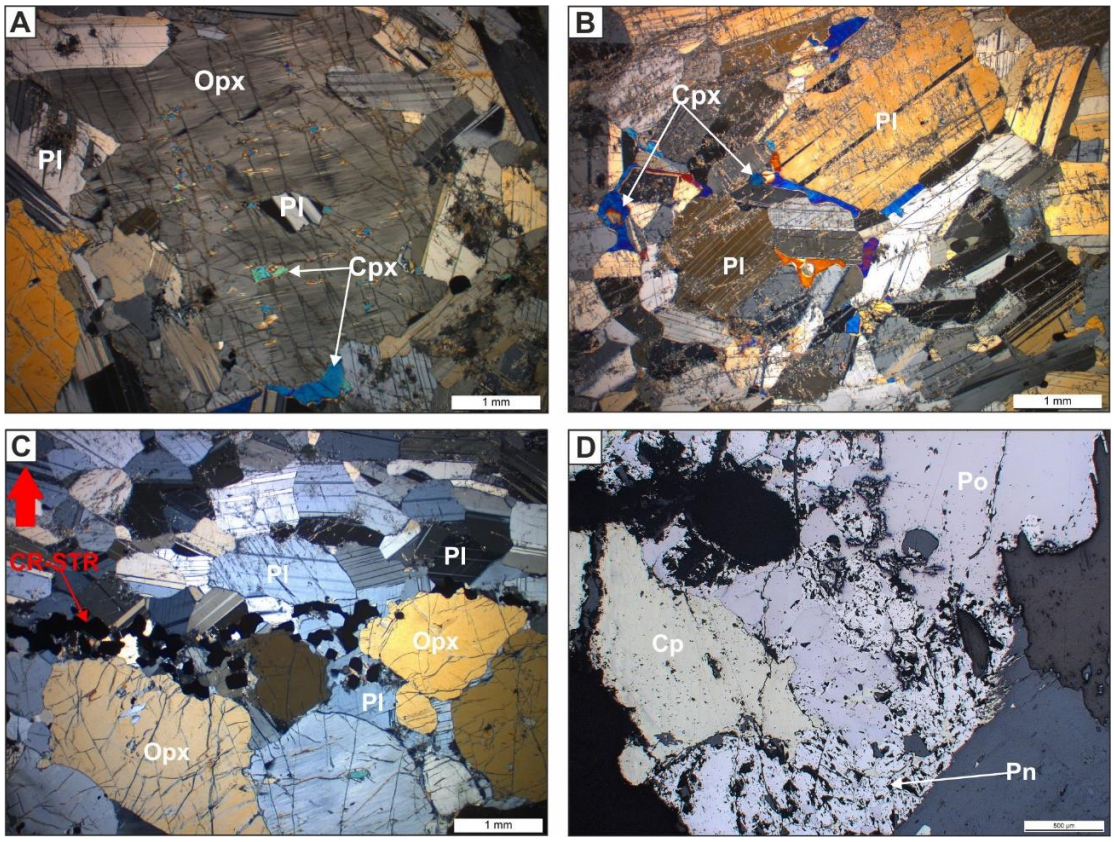

Figure 8.10: Photomicrographs showing typical petrological features of the NC2 unit as sampled in the Deep Platreef. *Note: Images A to C in XP and D in RFL.* (A) Interstitial orthopyroxene in norite (345_06). (B) Minor interstitial clinopyroxene on edges of plagioclase in anorthosite (345_06). (C) Base of a norite cycle with a chromite stringer (D1_08A). (D) A pegmatoidal BMS within a feldspathic orthopyroxenite (D1_07).

Evidence for disruption of the normal fractionation sequence in the norite cycles was noted in Chapter 5 and a detailed example is shown here in Figure 8.11. In Figure 8.11A a mafic pyroxenite body has intruded into an anorthosite providing evidence for the occasional out-of-sequence emplacement and intrusive formation of these rocks. Petrological features supporting an intrusive origin of the pyroxenite shown in Figure 8.11 include: (1) presence of a chilled margin of the pyroxenite (see Figure 8.11D) and (2) chromite-stringers on the base and top of the pyroxenite intrusion (see Figure 8.11A and 8.11B). Similar intrusions are noted in the NC2 unit within the Deep Platreef drill hole UMT_336 by Nodder (2015). The example shown in Figure 8.11 represents the best example identified in UMT_345_D1.

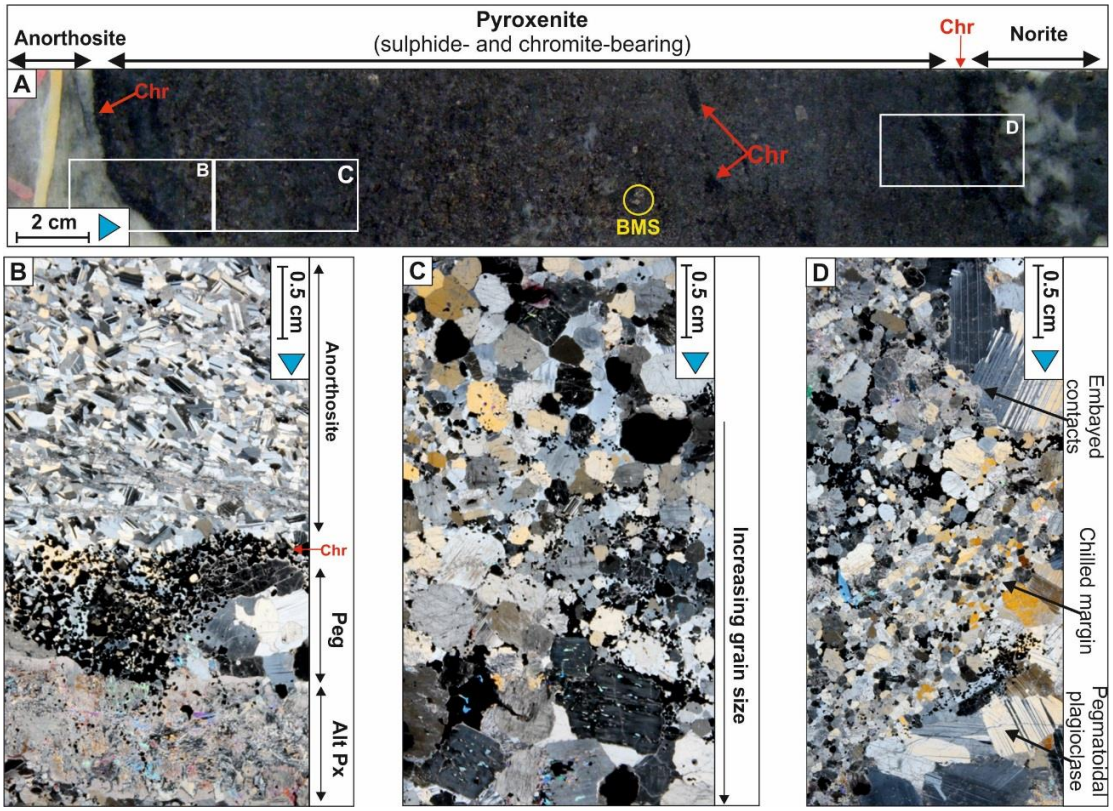

Figure 8.11: Petrological features of an intrusive, out-of-sequence pyroxenite within the NC2 unit in the Deep Platreef as sampled in D1_09. *Note: blue arrows point in downhole direction.* (A) A chromite and sulphide-bearing mafic intrusion in the NC2 unit. (B) Top contact of a discontinuous pyroxenite, the contact is marked by the formation of chromite preceded by a calcite alteration vein. (C) Moving away from the contact the grain size increases. (D) The pyroxenite on the basal contact is also finer grained where the footwall is a coarse grained leuconorite.

The Lower Pyroxenite (LP) unit is compositionally and texturally heterogenous over short distances (on the cm-scale); the LP unit hosts the beginning of the Lower Reef mineralisation. The presence of disseminated chromite and interstitial BMS with visible PGM represent mineralogical expressions of this mineralisation (see Figure 8.12 and 8.13D to 8.13E). The mineralogy is variable with clinopyroxene and olivine minor over the entire interval but significant locally; this is best demonstrated using samples collected over a 30 cm interval in drill hole UMT_345_D1 as shown in Figure 8.12.

Clinopyroxene is predominantly present as an interstitial phase forming medium- to coarse-grained oikocrysts (see Figure 8.12B) or as irregular exsolutions on the edge of orthopyroxene grains. Plagioclase is consistently present as an interstitial phase ranging in abundance from 5 % (see Figure 8.12A) to 35 % (see Figure 8.12C).

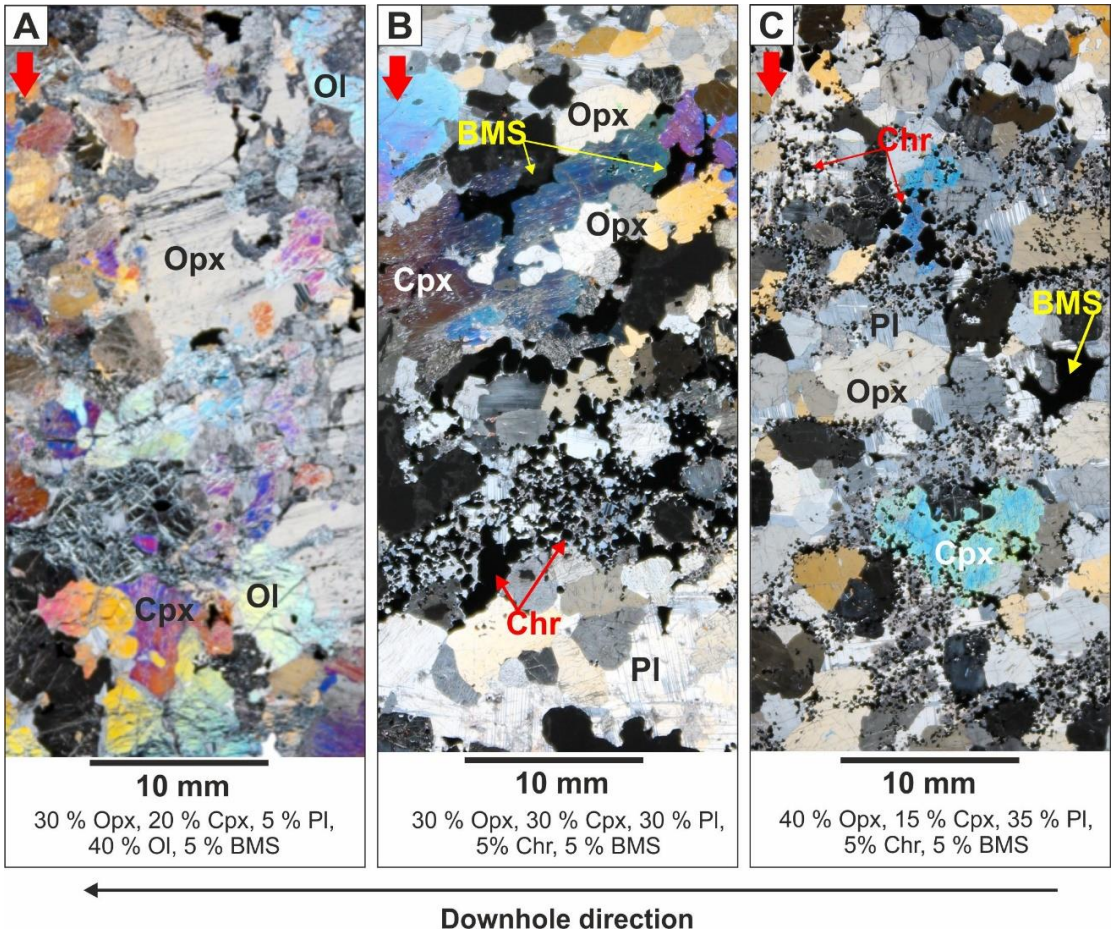

Figure 8.12: Photomicrographs demonstrating the small-scale (over 30 cm) lithological variability within the LP unit in the Deep Platreef. *All images in XP, mineral abundances are based on visual estimations*. (A) Olivine sampled in (D1_12F). (B) Gabbronorite with disseminated chromite and BMS mineralisation (D1_12A). (C) Medium-grained gabbronorite with disseminated chromite and BMS (D1_12C). Note: red arrows point in the downhole direction.

Detailed petrological features of the LP unit lithologies are shown below in Figure 8.13. The dominant mineral orthopyroxene, is typically found as either pegmatoidal oikocrysts (see Figure 8.13A and 8.12A) or as medium-grained cumulate grains (see Figure 8.13B and 8.12C). Where found as cumulate minerals as shown in Figure 8.12 (B to C) the size of the orthopyroxene varies from medium to coarse grained; the grain edges appear corroded and embayed and are surrounded by clinopyroxene and chromite found within interstitial plagioclase. This assemblage may be indicative of a late-stage melt causing the dissolution of the orthopyroxene and promoting the formation of chromite grains. Further evidence for this is shown in Figure 8.13B where a cumulate equant orthopyroxene grain contains melt pockets of clinopyroxene and plagioclase. Chromite forms in rounded embayments on the edge of the orthopyroxene in contact with plagioclase (see Figure 8.13B). Coarse-grained clinopyroxene is locally found (see Figure 8.13B and Figure 8.13C). Disseminated

chromite is a characteristic of this unit, as noted above it is typically found in the plagioclase portion as opposed to being enclosed in pyroxenes suggesting possibly a later stage of formation. An interstitial massive accumulation of annealed chromite is shown in Figure 8.13E; again, this is evidence for the later-stage of crystallisation of chromite.

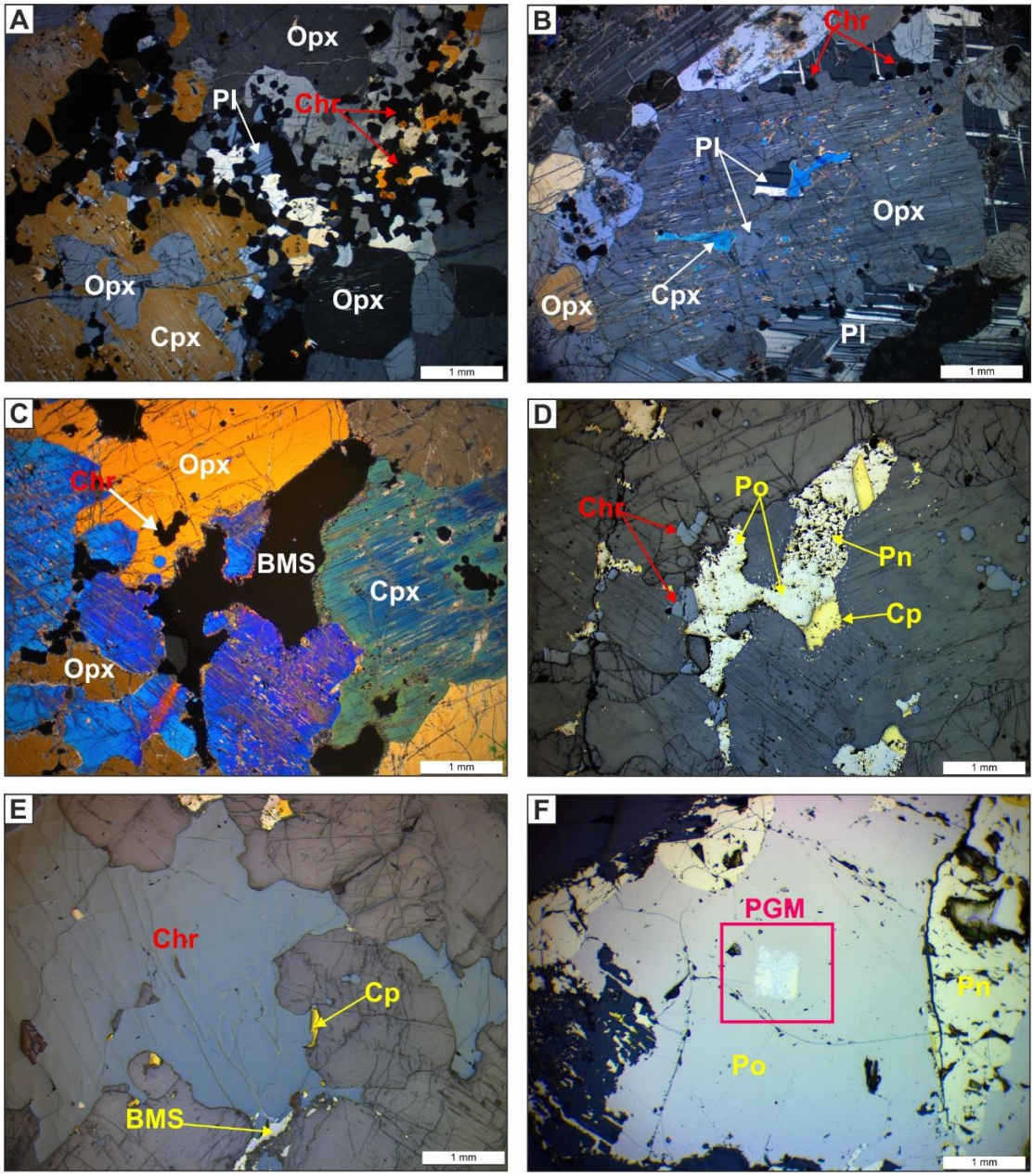

Figure 8.13: Photomicrographs showing textural details of the LP unit. Images *A-C are in XP; E and H are in RFL.* (A) Reactionary relationships between clinopyroxene oikocryst, embayed/resorbed orthopyroxene and fine-grained chromite (345_08A). (B) A former cumulate orthopyroxene crystal that is out of equilibrium with anhedral inclusions of clinopyroxene and plagioclase and corroded edges in contact with plagioclase and crystallising chromite. (C) Clinopyroxene oikocryst hosting fine-grained chromite and medium to coarse-grained interstitial base metal sulphides (D1_12A). (D) An interstitial polyphase BMS composed of Po-Pn-Cp (D1_12A). (E) A massive annealed accumulation of chromite with an interstitial texture. (F) A symplectite, cubic PGM hosted in pyrrhotite.

Medium- to coarse-grained interstitial base metal sulphides are dominated by pyrrhotite (50 %), pentlandite (40 %) with minor chalcopyrite (10 %). Pyrrhotite was observed to contain visible PGM, typically as exsolved symplectites. The BMS assemblage typically has sharp contacts with the silicates and appears relatively unaltered.

The gabbronorite lithologies, as shown in Figure 8.12 for the deflection hole UMT_345_D1, were not identified in drill hole UMT_345; in addition, the olivine occurrence in UMT_345 differs as shown in Figure 8.14. In UMT_345 olivine is present as a thin (5 cm thick) troctolite comprising olivine (60 %) and plagioclase (40 %; see Figure 8.14). The troctolite appears fresh and unaltered, the plagioclase is interstitial, and the olivine grains are fine to medium-grained and group together to form a polygonal equilibrium texture with 120° contacts indicative of insitu recrystallisation under magmatic conditions. The olivines are finer grained on the contact with the orthopyroxenite where they may be enclosed as chadacrysts in orthopyroxene suggesting that the recrystallisation event occurred at the same time as the formation of the overlying lithology. The protolith of the troctolite is unknown; troctolites horizons are found in other layered intrusions including in Stillwater (Boudreau, 1999) and associated with gabbronorite rocks. Rocks of similar composition and texture are described from another Turfspruit borehole (UMT_083) by Marquis (2015) but in a unit equivalent to the Feldspathic Clinopyroxenite Hybrid Zone (HZ_{FCPX}).

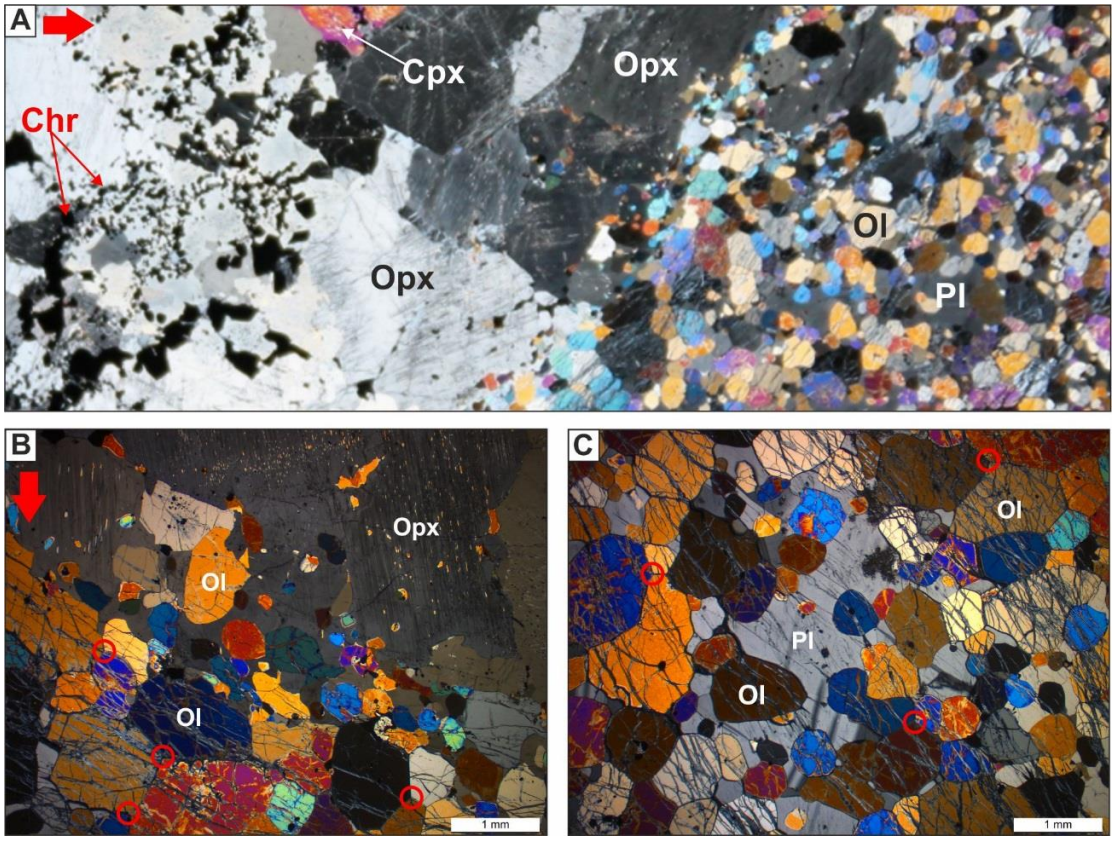

Figure 8.14: Photomicrographs showing the petrological characteristics of the troctolite lithology in the LP unit. *All images in XP and from sample 345_08B.* (A) The contact between orthopyroxenite and troctolite. (B) A close up of the contact between the troctolitic and overlying orthopyroxenite. (C) Olivine grains within the troctolite have an equilibrium texture, red circles denote 120° triple junctions.

The top contact of the Main Chromitite (MCHR) unit was sampled in thin section D1_13; features of which are shown in Figure 8.15 and an overview of the thin section in Figure 8.16A. The silicate assemblage directly above the chromitite is composed of fine to medium grained orthopyroxenite displaying an equilibrated texture with 120° interfacial angles (see Figure 8.15C). No silicate interstitial phase is present; instead this space is occupied by fractionated BMS dominated by pyrrhotite (50 %), pentlandite (30 %), chalcopyrite (18 %) and minor cubanite (2 %; see Figure 8.15A). The edges of orthopyroxene grains in contact with BMS are undergoing alteration to amphibole minerals (see Figure 8.15B). This densely packed orthopyroxenite contains one large accumulation (3 x 2 mm) of annealed chromite grains that has been dislocated from the top of the underlying chromitite (see Figure 8.16A).

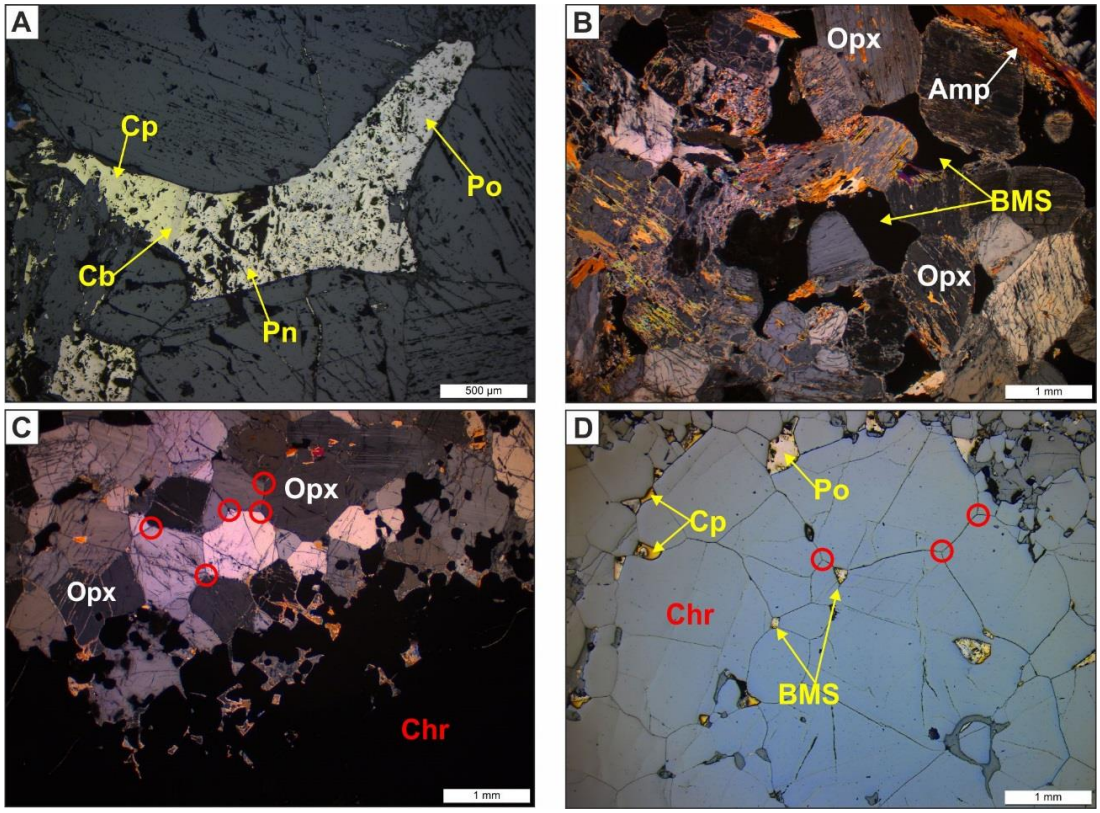

Figure 8.15: Photomicrographs showing mineralogical features of the top of the MCHR unit. *Images A and D in RFL; B and C in XP and all from sample D1_13.* (A) Medium-grained, interstitial and polyphase BMS. (B) Cumulate orthopyroxene with interstitial BMS and amphibole alteration on the orthopyroxene edges. (C) The top contact of the MCHR with the base of the LP unit characterised by annealed orthopyroxenes and chromite grains. (D) Fractionated base metal sulphides are concentrated into the triple junctions of annealed chromite grains.

The top of the chromitite in UMT_345_D1 has an annealed texture with fine to medium-grained chromite grains trapping fractionated BMS at triple junctions (see Figure 8.15D). This annealed chromitite extends for 5 mm away from the top contact before it becomes more disseminated, as shown in Figure 8.16A. An overview of the mineralogical and textural characteristics of the MCHR unit are shown in Figure 8.16. One of the dominant mineralogical features of the MCHR unit are the varying proportions of silicate minerals to chromite grains as shown in Figure 8.16B and 8.16C.

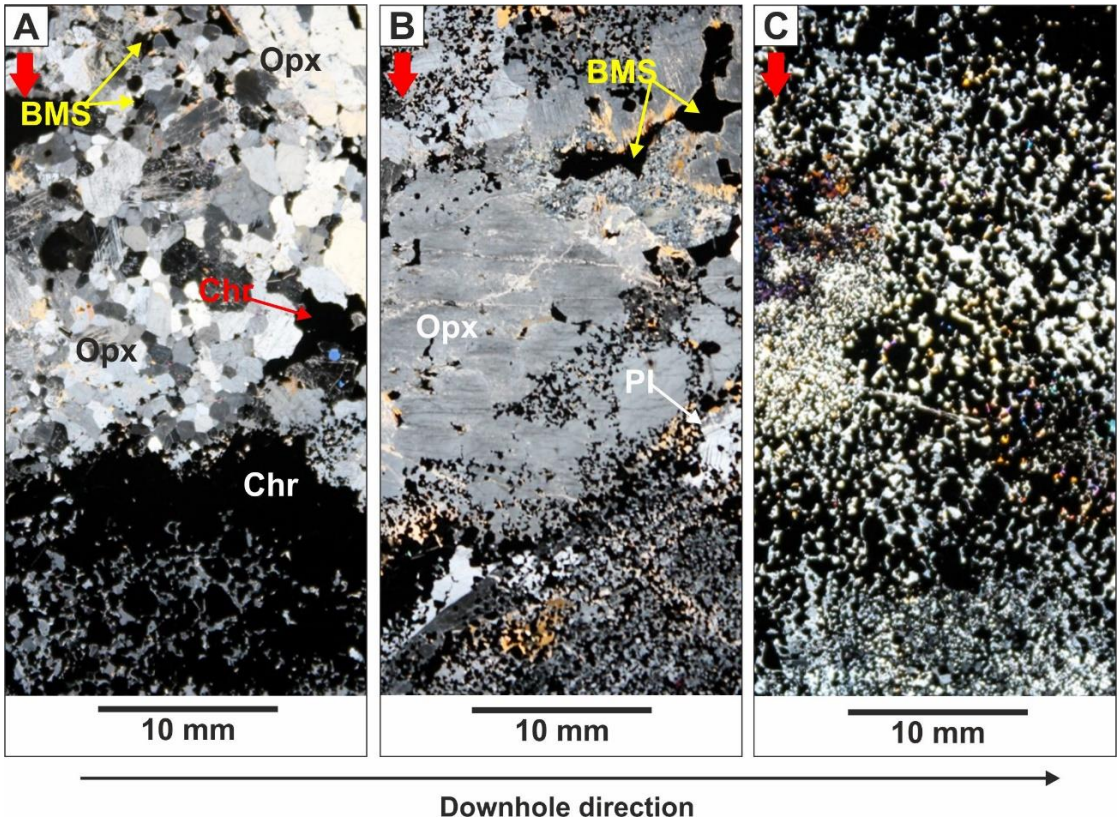

Figure 8.16: Photomicrographs showing the varying proportions of silicate minerals and chromite grains within the MCHR unit. A*ll images in XP*. (A) The top contact of the MCHR with the LP unit (D1_13). (B) Coarse-grained, poikilitic orthopyroxene with disseminated chromite (345_09). (C) Massive chromitite with varying chromite grain sizes (D1_14B). Note: red arrows point in the downhole direction.

The range of silicate minerals associated with the chromitites are shown in Figure 8.17. The dominant mineral varies locally from interstitial plagioclase (see Figure 8.17C) and clinopyroxene (see Figure 8.17B) to pegmatoidal and poikilitic orthopyroxene (see Figure 8.17A and 8.17E). Hydrous alteration minerals including amphibole and chlorite have a patchy distribution and where identified they often accompany medium- to coarse-grained BMS (see Figure 8.17D and 8.17E). The chromite grains demonstrate a bimodal size distribution between fine and medium-grained (up to 2 mm); the medium-sized grains are predominantly found where the interstitial mineral is plagioclase whereas the fine-sized grains, < 1 mm, are typically found within clinopyroxene-dominated interstitial spaces (see Figure 8.17C) or where enclosed in coarse-grained orthopyroxene oikocrysts (see Figure 8.16B).

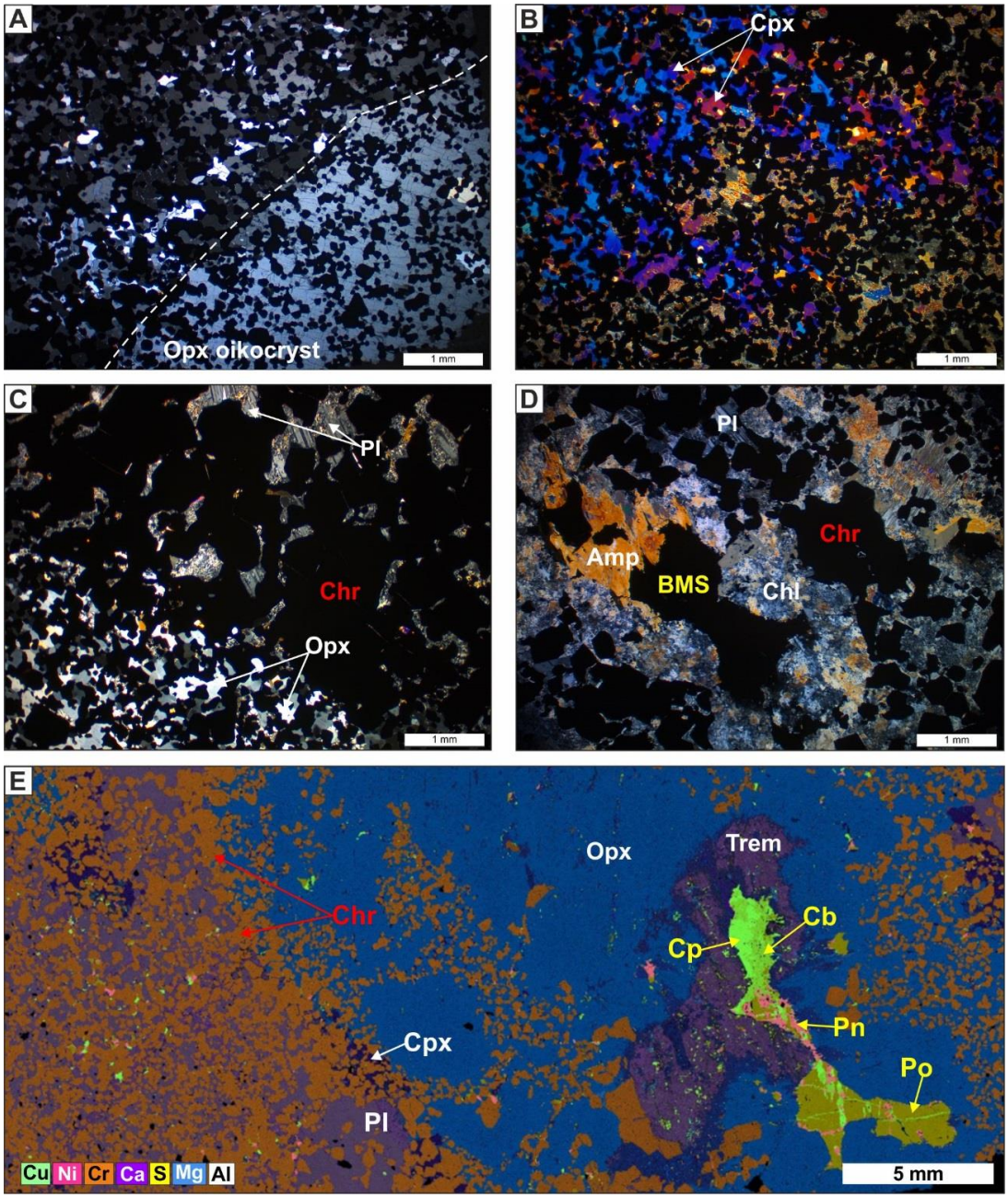

Figure 8.17: Photomicrographs illustrating the mineralogical and textural variability of the MCHR unit. *Images A to D are in XP and E is an EDS multi-element map.* (A) A close up of the fine-grained chromitite showing the contact between a large orthopyroxene oikocryst (on right hand side in optical continuity) and the slight increase in chromite grain size where not cemented (D1_14A). (B) Fine-grained (< 1 mm) chromite grains with interstitial clinopyroxene and alteration amphiboles (D1_14A). (C) Variations in the grain size of chromite dependent on the composition of the interstitial phase e.g. plagioclase (top right) compared to orthopyroxene (bottom left) (D1_14A). (D) Medium-grained BMS in altered silicates mostly composed of amphibole and chlorite. (E) Showing the distribution of chromite and BMS in a sample of disseminated chromitite (345_09).

An overview of the distribution of the base metal sulphide (BMS) assemblage within the MCHR unit is shown in Figure 8.18; they can contribute up to 5 vol% of the rock. BMS are found in a range of textural settings including: interstitial to chromite (see Figure 8.18A), as sulphide melt inclusions in chromite grains (see Figure 8.18B),

along fractures in chromite grains (see Figure 8.18C), and interstitial to the silicate assemblage (see Figure 8.18D). When located interstitial to chromite the BMS assemblage (see Figure 8.18A) is dominated by pentlandite (50 vol%), pyrrhotite (30 vol%), chalcopyrite (30 vol%); with accessory cubanite as lamellae and euhedral pyrite replacing pyrrhotite. The identification of sulphide melt inclusions in chromite grains, identified using criteria as outlined in Holwell et al., (2011), corresponds to the observation in the chromite stringers higher up in the stratigraphy on the UP/MP contact. This supports early sulphide saturation. Medium- to coarse-grained sulphides were identified in the silicate mineral where they may appear fresh (see Figure 8.18D) or altered by silicate alteration minerals. Where hosted in the silicate-assemblage the BMS are frequently more complex mineralogically and texturally than when surrounded by chromite grains, an example is shown in Figure 8.18D.

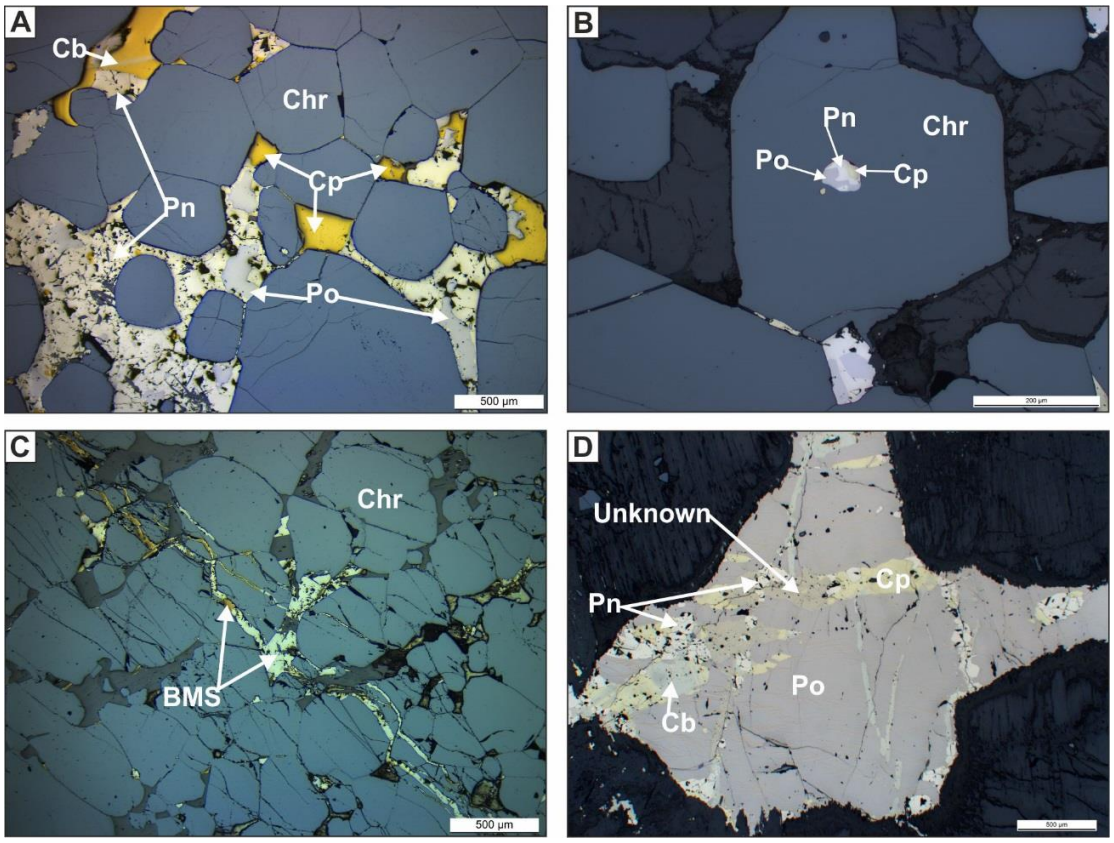

Figure 8.18: Photomicrographs of the base metal sulphide assemblage within the MCHR unit. *All images are in RFL.* (A) Interstitial fractionated sulphides including pentlandite-chalcopyrite-pyrrhotite-cubanite entirely fill the pore space between sub to euhedral chromite grains (D1_14C). (B) Sulphide inclusion in a euhedral chromite grain filled with fractionated BMS (D1_14A). (C) Fractionated BMS in veins cross-cutting fractured subhedral chromite grains (D1_14A). (D) A complex, coarse-grained fractionated BMS composed of pyrrhotite-pentlandite-chalcopyrite-cubanite and an unidentified sulphide phase (345_09).

There is a great variety in the proportion of minerals and textures observed in the Ultramafic Zone (UMZ). In general, the average grain size is coarser in this

stratigraphic unit than any other previously mentioned with pegmatoidal and poikilitic textures dominating the upper part of the UMZ unit directly beneath the MCHR unit. The content of the dominant minerals olivine (up to 70 %), orthopyroxene (up to 80%), clinopyroxene (up to 50%) and plagioclase (up to 40 %) vary significantly and over small distances; the variety of textures observed suggest that the rock is not in chemical equilibrium. Orthopyroxene is frequently developed as pegmatoidal oikocrysts enveloping fine- to medium-grained rounded olivine. Olivine is located in a range of textural settings (see Figure 8.19) including: (1) enclosed in orthopyroxene (see Figure 8.19A); (2) enclosed in a pegmatoidal clinopyroxene oikocryst (see Figure 8.19); (3) as chains of multiple, rounded grains in interstitial plagioclase forming troctolite (see Figure 8.19B). Where identified together olivine-orthopyroxene-clinopyroxene-spinel often display a disequilibrium texture; unstable crystals are readily apparent from their embayed and corroded forms (see Figure 8.19D). Serpentinisation (with magnetite veining) of olivine and talc-tremolite alteration of orthopyroxene affect minerals within the same sample (see Figure 8.20B). The presence of euhedral, medium-grained amphibole (hornblende) with oscillatory zoning attests to multiple hydrothermal fluid events of different compositions (see Figure 8.20A).

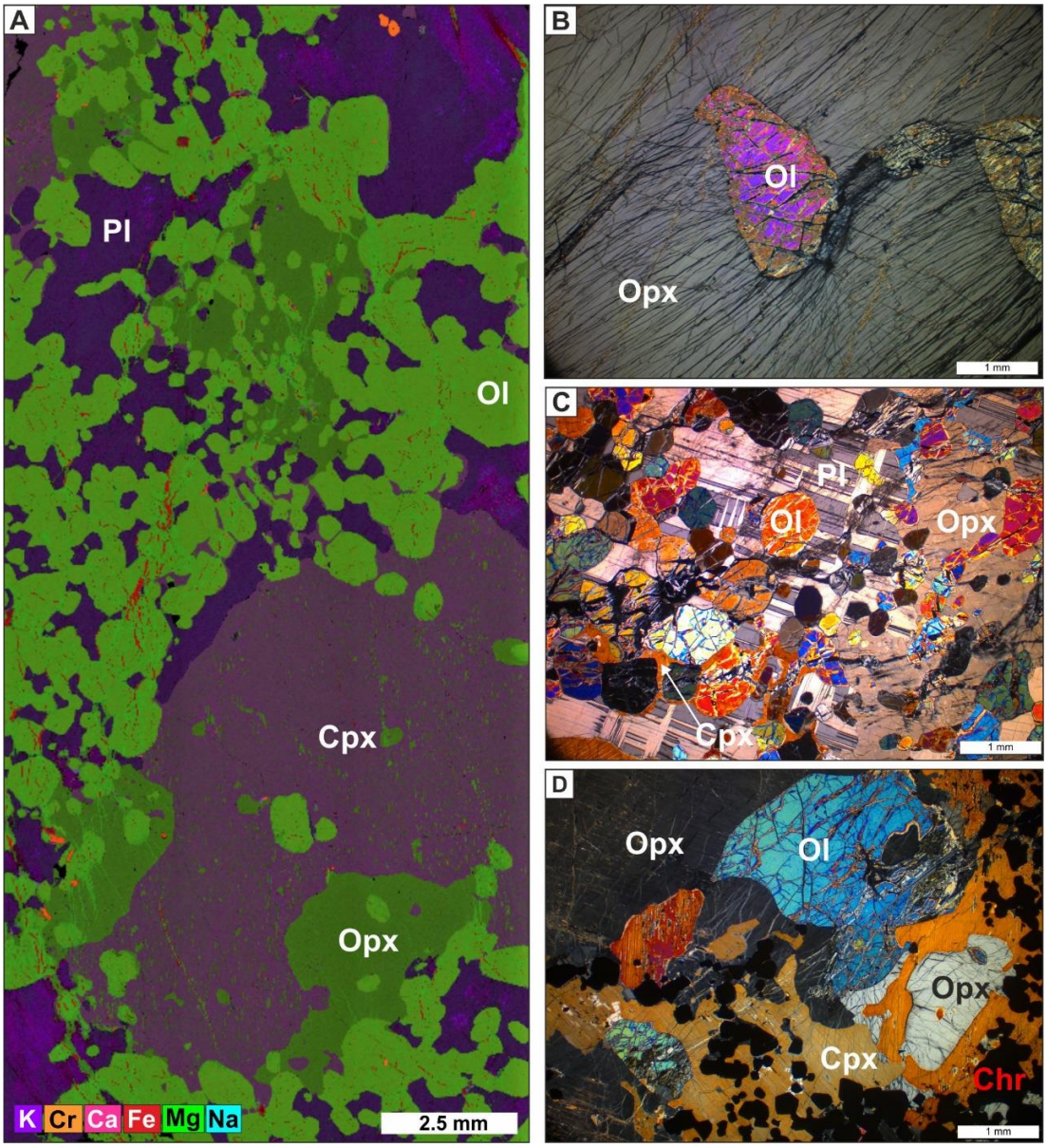

Figure 8.19: Mineralogical characteristics of the UMZ unit. *All images from sample D1_16; image A is a EDS multi-element map; and B to D are in XP.* (A) Illustrating the various textural settings of olivine forming interstitial troctolite and as inclusions orthopyroxene and clinopyroxene oikocrysts. (B) A partially resorbed olivine enclosed in orthopyroxene causing deformation of the crystal. (C) Fine- to medium-grained olivine in troctolite and as chadacryst on edge of an orthopyroxene oikocryst. (D) Olivine-clinopyroxene-orthopyroxene-spinel in disequilibrium.

Moving downhole away from the MCHR unit the mineralogy of the UMZ changes with a decrease in olivine content and an increase in plagioclase (up to 40 %) and the development of feldspathic orthopyroxenite and olivine gabbronorite lithologies. These mafic lithologies are significantly less altered than the ultramafic ones higher up in the stratigraphy and there is a reappearance of quartz and phlogopite as interstitial phases (see Figure 8.20C). Small (µm-sized) and anhedral accumulations of calcite are irregularly identified in the UMZ unit and these are interpreted as

xenocrysts of original carbonate material. Where plagioclase is most abundant it appears as a cumulate phase with a tabular form or in pegmatoidal noritic pockets. These pegmatoidal occurrences often concentrate accumulations of BMS that are dominated by the mineral cubanite (see Figure 8.20D).

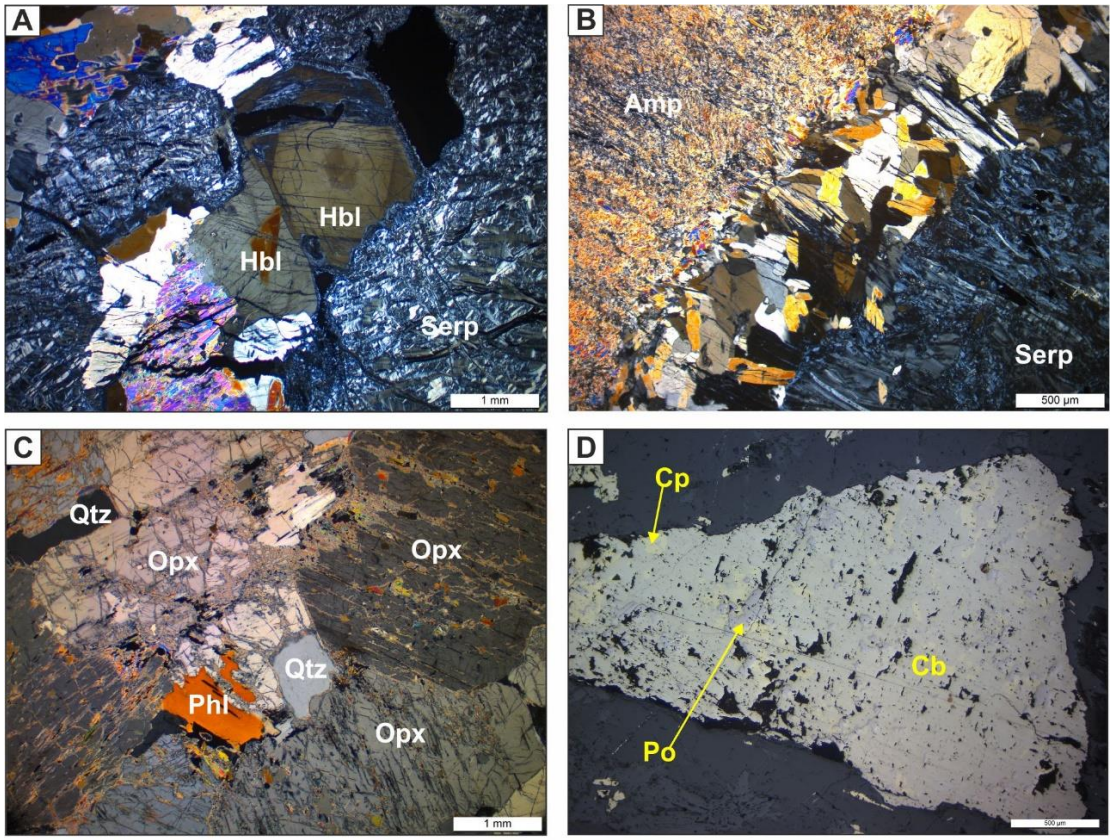

Figure 8.20: Photomicrographs showing the alteration and base metal sulphide assemblages of the UMZ unit. *Images A to C in XP; D in RFL.* (A) Zoned hornblende identified in a serpentinite alteration pathway (345_11). (B) Contact between amphibole-dominated and serpentinite-dominated alteration (345_11). (C) Medium-grained orthopyroxene with interstitial quartz and phlogopite, a similar assemblage as identified in the UP unit (345_12). (D) A pegmatoidal sulphide dominated by cubanite with relict anhedral pyrrhotite and chalcopyrite (345_13).

The base metal sulphide (BMS) assemblage within the UMZ is concentrated over localised intervals e.g. 10 cm but where found they can be abundant (up to 30 %). The BMS have a range of grain sizes from medium to pegmatoidal, and compositionally they vary from being pyrrhotite- to cubanite-dominated (see Figure 8.20D) and may host coarse-grained visible PGM.

Mineralogical features of the Feldspathic Clinopyroxenite Hybrid Zone (HZ_{FCPX}) unit are shown in Figure 8.21. The rock has an inequigranular, pseudo-porphyry texture with grain size ranging from fine-to coarse-grained; it is the finest grained rock observed in this drill hole. The cumulate minerals are fine- to medium-grained rounded orthopyroxene (60 %) and partially resorbed olivine (< 1%, see Figure 8.21A). The

dominant interstitial phase is plagioclase (30 %) with heterogeneously distributed BMS (locally up to 5 %, see Figure 8.21C). Clinopyroxene is present as coarse-grained oikocrysts enclosing rounded and corroded orthopyroxene chadacrysts (see Figure 8.21B). The BMS assemblage comprises pyrrhotite (50 %), pentlandite (40 %) and chalcopyrite (10 %); the BMS fully occupy the interstitial space i.e. no plagioclase present. The lithologies appear relatively unaltered, however patches of unassimilated calcite were identified, as shown in Figure 8.21D.

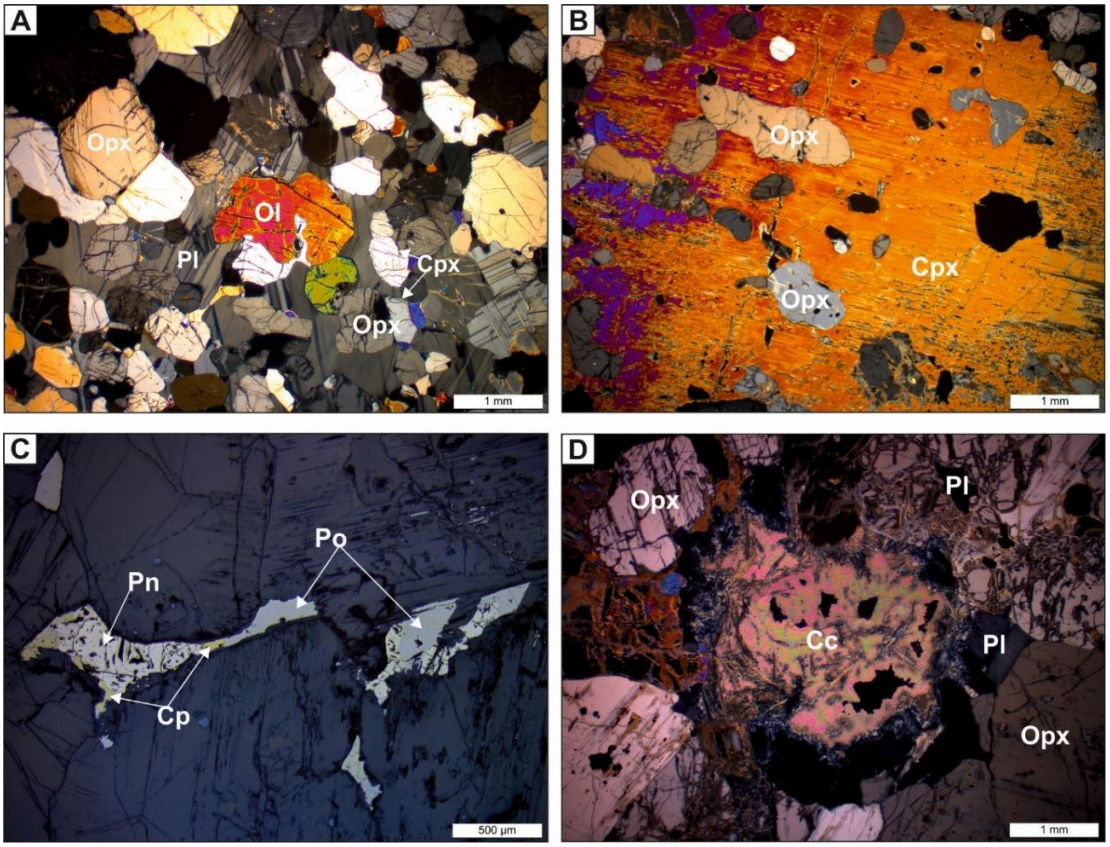

Figure 8.21: Photomicrograhs of mineralogical features of the HZ_{FCPX} in UMT_345. *Images A, B and D in XP; C in RFL*. (A) A representative texture of the HZ_{FCPX} unit (345_15). (B) A large clinopyroxene oikocryst enclosing resorbed and relict orthopyroxene grains (345_15). (C) The interstitial BMS assemblage within this unit (345_15). (D) An unassimilated xenolith of calcite, surrounded by a rim of serpentinite (345_16).

8.1.2 Thick Flatreef Mineralogy

The first mineralised interval, the Upper Reef, hosted in the Upper Pyroxenite (UP) unit was sampled in sample TMT_03 (see Figure 8.22). Orthopyroxene is the only cumulate mineral; it is present as medium-grained, equant grains with rounded edges. The interstitial assemblage is composed of medium-grained plagioclase and base metal sulphides (BMS); these minerals do not share interstitial spaces and are found exclusive to one another. Where plagioclase is present as an interstitial phase the orthopyroxene grains have corroded edges and contain anhedral holes of plagioclase, quartz and phlogopite.

Sulphides are locally concentrated to 10 vol%; the presence of BMS is accompanied by amphibole alteration of the surrounding orthopyroxenes and into the pentlandite portion of the sulphides (see Figure 8.22A and 8.22C). The BMS assemblage present of pyrrhotite (70 vol%) and granular pentlandite (30 vol%) crystallised from monosulphide solid solution and no intermediate solid solution crystallisation phases (chalcopyrite) are present.

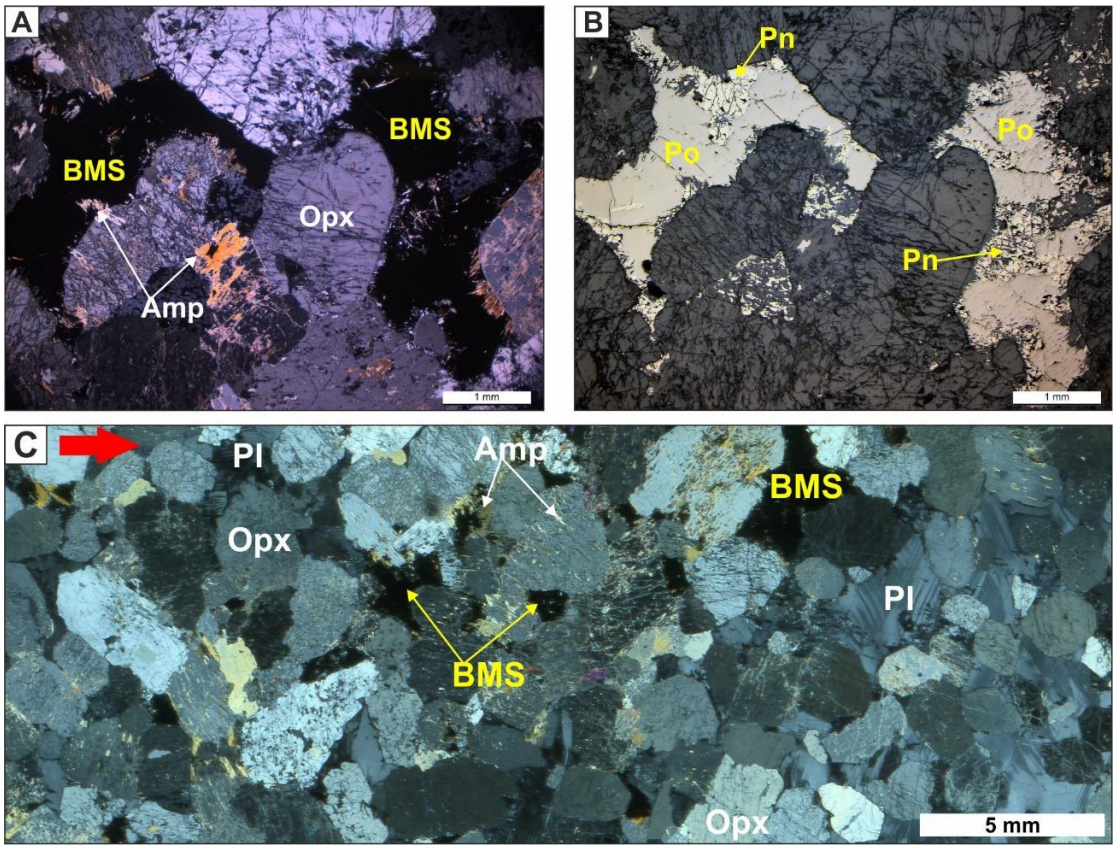

Figure 8.22: Photomicrographs of the Upper Reef in the UP unit in the Thick Flatreef. *Images A and C in XP and B in RFL*. All images from sample TMT_03. (A) Interstitial BMS entirely fill the space between orthopyroxene crystals with amphibole alteration on their edges. (B) The BMS are dominated by pyrrhotite and pentlandite with a notable absence of chalcopyrite. (C) A whole thin section photomicrograph showing the concentration of sulphide mineralisation and amphibole alteration in a band across the section. Note: red arrow points in the downhole direction.

The second mineralised interval, the Middle Reef, as identified in the UP unit was sampled in TMT_09 located 2.5 m above the basal contact of the UP unit. Orthopyroxene is still the only cumulate mineral identified; it is present as medium- to coarse- (2 to 7 mm), equant grains. The edges of the orthopyroxene minerals are scalloped where in contact with interstitial plagioclase; talc and phlogopite alteration penetrates along cleavage planes. The interstitial assemblage is composed of plagioclase, BMS (10 %), clinopyroxene and quartz. Clinopyroxene is present as coarse-grained (5 to 7 mm) oikocrysts and contain chadacrysts of anhedral

orthopyroxene and phlogopite. The BMS are medium- to coarse-grained (2 to 6 mm) and composed of pyrrhotite (60 %), pentlandite (25 %) and chalcopyrite (15 %)

The Middle Pyroxenite (MP) unit demonstrates more texturally variability than the UP unit; although they are compositionally similar. Typical examples of the coarse- to pegmatoidal textures and mineralogy of this unit are shown in Figure 8.23. This stratigraphic contact differs in its appearance from that observed in the Deep Platreef by the lower quantity of olivine and poorly developed chromite stringers.

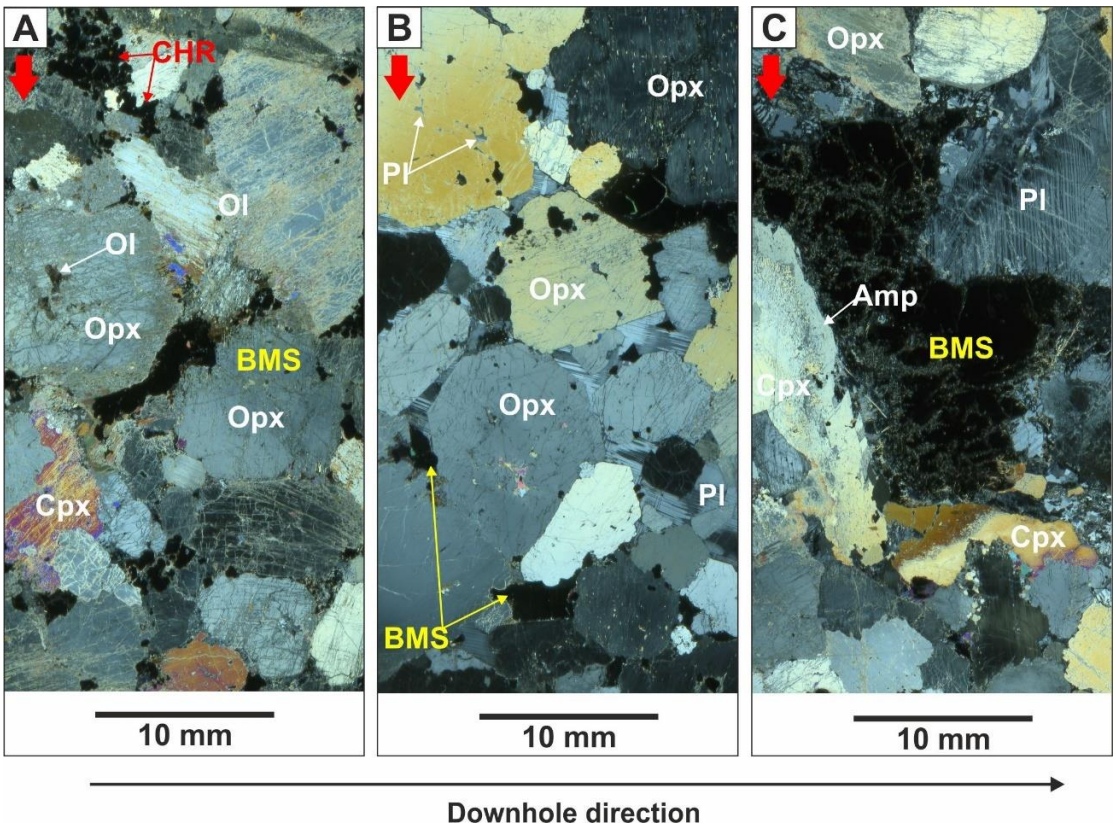

Figure 8.23: Whole-thin section photomicrographs showing the dominant textures and mineral associations within the MP unit. *All transmitted light images taken in XP*. (A) The beginning of the MP unit with minor chromite disseminated interstitially to coarse-grained orthopyroxene oikocrysts with olivine chadacrysts (TMT_12). (B) Typical coarse-grained feldspathic orthopyroxenite (TMT_15A). (C) A pegmatoidal BMS concentrated in a felsic pocket in orthopyroxenite (TMT_18). Note: red arrows point in the downhole direction.

Detailed photomicrographs of the silicate assemblage within the MP unit are shown in Figure 8.24. The MP unit is composed of predominantly orthopyroxene present as sub- to euhedral medium to pegmatoidal grains. Olivine is present in low concentrations (< 10 %) and only identified over short (cm-scale) intervals (see Figure 8.23A). Where found, the olivine is fine- to medium-grained, anhedral and hosted as chadacrysts in orthopyroxene oikocrysts (see Figure 8.24A and 8.24B). The orthopyroxene grains were observed to have an undulose extinction and there is

evidence of solid state grain boundary migration as shown in Figure 8.24C with the formation of subgrains on the grain boundary (highlighted using a dashed white line). Further modification on grain margins is recorded in the sample shown in Figure 8.24D with grain margin recrystallisation of the orthopyroxene in contact with clinopyroxene located beneath the felsic (and hydrous phase) pocket hosting pegmatoidal BMS. Recrystallisation on grain boundaries of original crystals into smaller sub-grains typical is a response to post-crystallisation stress and the resulting features are sometimes referred to as 'core-and-mantle microstructure' (Vernon, 2004) The main interstitial phase is plagioclase (5 to 20%) with minor clinopyroxene (up to 10 %) and BMS (typically 5% locally up to 30%). Where found clinopyroxene often appears as an exsolution on the edge of orthopyroxene (see Figure 8.23A and 8.24D).

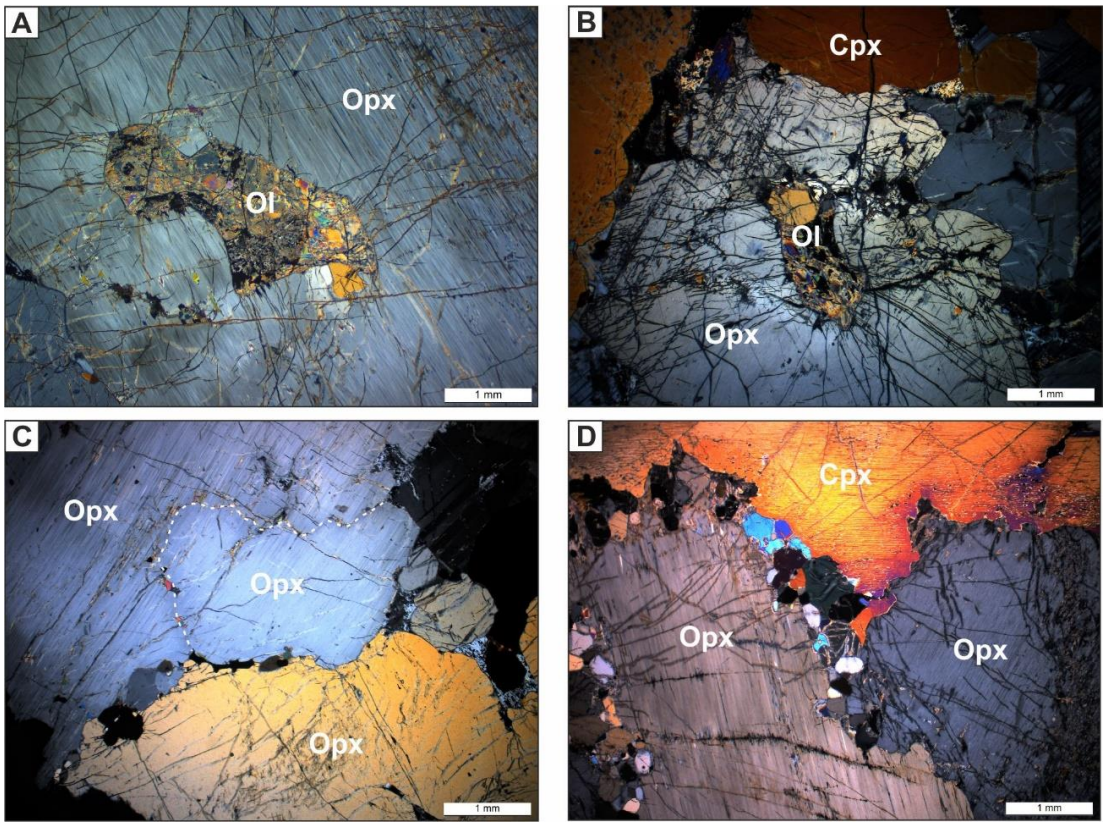

Figure 8.24: Photomicrographs showing petrological characteristics of the MP unit in the Thick Flatreef. *All transmitted light images in XP.* (A) Anhedral relict olivine enclosed in orthopyroxene (TMT_15B). (B) Fine-grained relict olivine showing an atoll texture with orthopyroxene (TMT_15B). (C) Orthopyroxene showing an overgrowth texture as denoted by a dashed white line (TMT_16). (D) Triple junction between two orthopyroxene and one clinopyroxene grain with grain size reduction on contact (TMT_18).

Characteristics of the chromite and BMS mineralisation within the MP unit, part of the Middle Reef mineralisation event, are shown in Figure 8.23 and Figure 8.25. In Figure

8.23 an overview of the distribution of BMS is given and this shows that the occurrence varies from medium-grained interstitial to pegmatoidal (see Figure 8.23C).

The first visible occurrence of chromite crystallisation in the drill hole was sampled in TMT_12 (for overview see Figure 8.23A) and characteristics are shown in Figure 8.25A to 8.25D. The chromite grains are interstitial and found as clusters of euhedral grains that are fine- to medium-grained. A close spatial association is observed between the chromite grains and euhedral, fine-grained perovskite (visual identification, see Figure 8.25C); this mineral association is not identified in any other drill hole. Perovskite ($CaTiO_3$) typically occurs in basic or alkaline igneous rocks, however it may also be present in metamorphosed impure limestones (Deer, Howie & Zussman, 1992). The chromite is also spatially associated with interstitial medium- to coarse-grained BMS (see Figure 8.25B and 8.25D). Phlogopite is concentrated on the edge of the BMS and has penetrated into the cleavage of the surrounding pyroxenes (see Figure 8.25A). The BMS are composed of an assemblage of pyrrhotite (60 %), pentlandite (10 %) and chalcopyrite (30 %); although a coarse-grained sulphide in the middle of the thin section is dominated by chalcopyrite (80 %).

A second occurrence of fine-grained (< 500 μm) chromite (TMT_13) appears disseminated in interstitial plagioclase and in embayments on the edges of orthopyroxene where in contact with plagioclase (similar to that observed in the Deep Platreef in the Lower Pyroxenite unit, see Figure 8.13B). In the latter setting a fine film of plagioclase typically separates the chromite from orthopyroxene indicative of solid-liquid interaction. Fragments of BMS are also present on the edges of orthopyroxene suggesting they are mobile in later stage melt. In TMT_13 the BMS are present as medium to coarse-grained, interstitial and composed of pyrrhotite (40 %), pentlandite (40 %) and chalcopyrite (20 %). Oxide mineral exsolution from the chromite grains is identified in all examples sampled and this typically takes the form of ilmenite laths (see Figure 8.25E).

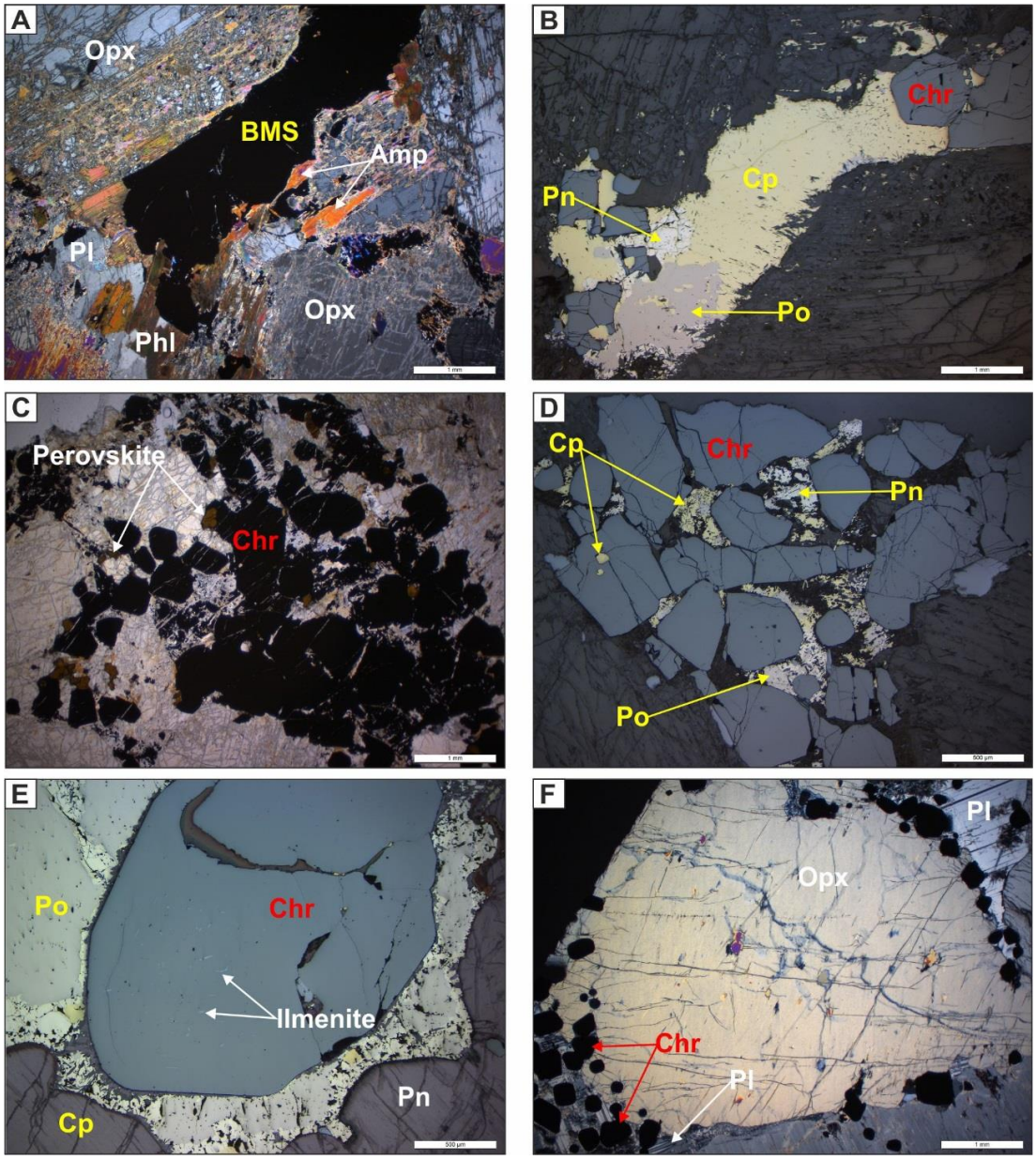

Figure 8.25: Photomicrographs of the mineralisation of the Middle Reef in the MP unit in the Thick Flatreef. *Transmitted light images A and F in XP; B, D and E in RFL and; C in PPL.* (A and B) Interstitial BMS with phlogopite on the edges and associated with chromite (TMT_12). (C and D) Interstitial accumulations of chromite, perovskite and BMS (TMT_12). (E) Exsolution of ilmenite from euhedral chromite grain (TMT_16). (F) Chromite grains nucleating on the edge of orthopyroxene where in contact with plagioclase (TMT_13).

Towards the base of the MP unit, the appearance of serpentinised autoliths results in alteration (see Figure 8.26). The contact between the pegmatoidal orthopyroxenite and a serpentinised autolith is shown in Figure 8.26; it is irregular and characterised by a sharp compositional and textural change. The pegmatoidal orthopyroxenite has extensive talc alteration and medium-grained tremolite grains are developed (see Figure 8.26C). A coarse-grained BMS present above the contact is dominated by pyrrhotite (90 %) with islands of granular pentlandite (5 %) and minor chalcopyrite (5

%) on the edges; in addition, medium-grained apatite minerals are identified on the edges of the BMS (see Figure 8.26A).

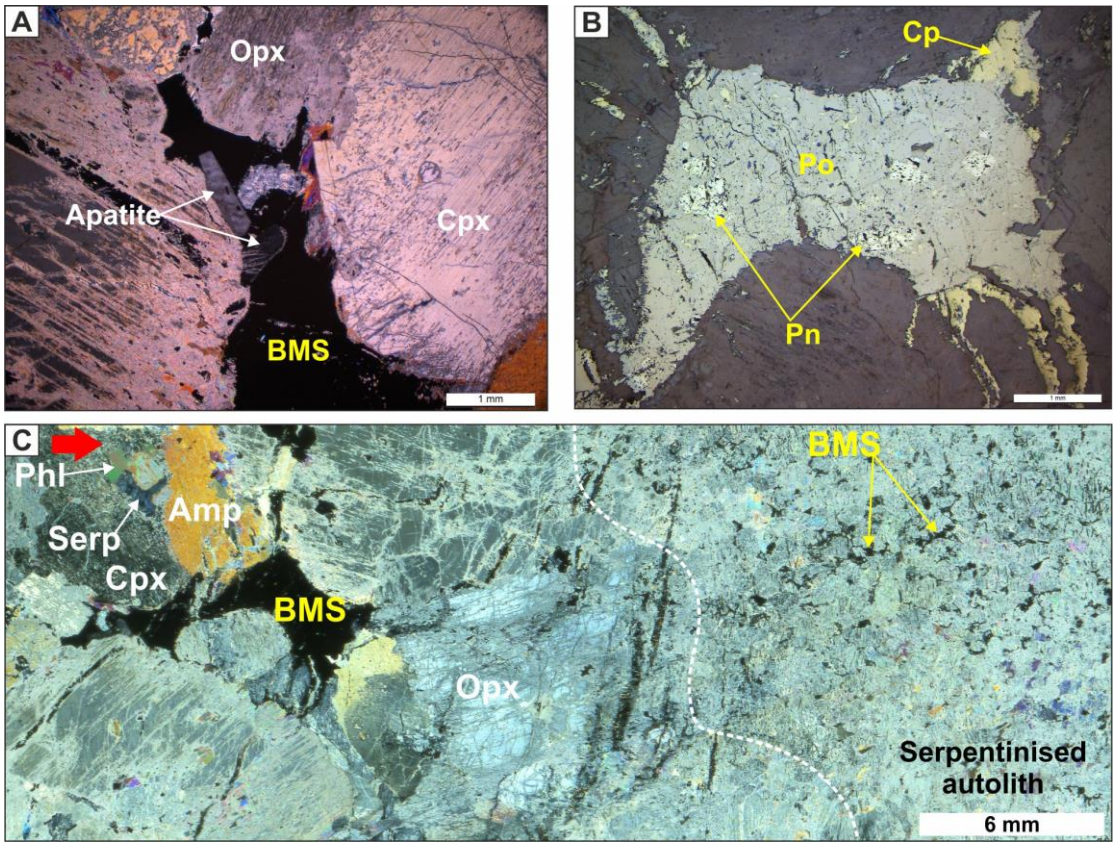

Figure 8.26: Photomicrographs of the MP unit showing mineralogical and textural features resulting from assimilation. *Transmitted light images A and C in XP and image B is in RFL. All images from sample TMT_17.* (A) Fine-grained apatite on the edges of a BMS. (B) Pegmatoidal pyrrhotite-dominated BMS. (C) Contact between pegmatoidal orthopyroxene and a recrystallised autolith of country rock. Note: red arrows point in the downhole direction.

The Olivine Websterite Hybrid Zone (HZ_{OLWEBS}) unit is characterised by a very altered appearance resulting from the assimilation of country rock material. Examples of the textures and mineralogy within the HZ_{OLWEBS} unit are shown in Figure 8.27. The nature of the contaminant is the same as shown in Figure 8.26 from the MP unit with fine-grained densely packed serpentinised olivines and interstitial BMS. The contact between the olivine-dominated lithology and the overlying parapyroxenites is variable from relatively sharp (see Figure 8.27A) to more diffusive (see Figure 8.27B) and irregular (see 8.27C).

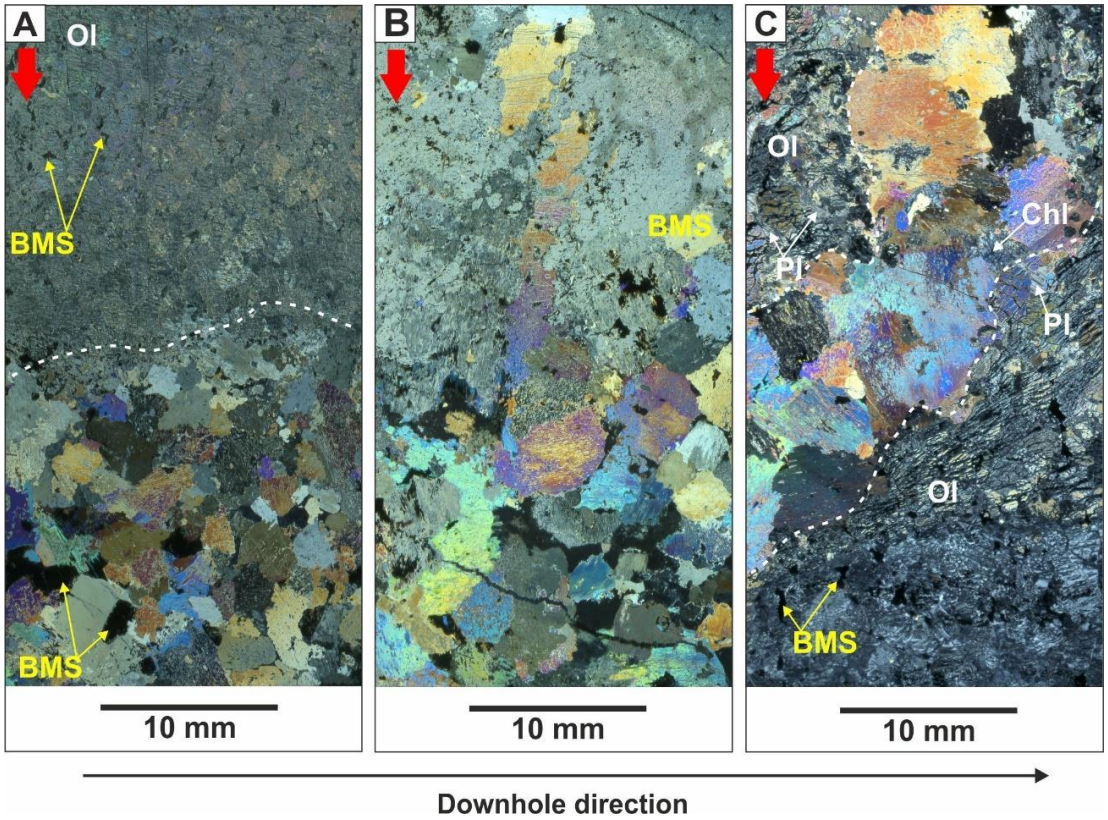

Figure 8.27: Whole thin-section photomicrographs showing contacts between country rock autoliths and parapyroxenites of the HZ_{OLWEBS} unit. *All transmitted light images in XP*. (A) A sharp contact between parapyroxenite and a sepentinised autolith (TMT_21). (B) Irregular contact between parapyroxenite and alteration from assimilation (TMT_24). (3) An irregular interaction between clinopyroxenite and serpentinite (TMT_27). Note: red arrows point in the downhole direction.

The strongly serpentinised olivine-dominated lithologies are interpreted to be of metamorphic origin and are proposed to be derived from the assimilation of impure carbonate material present in the footwall Duitschland Formation sediments. The formation of forsteritic olivine from carbonate sedimentary rocks is known to occur in contact metamorphic environments; this transformation can be achieved by the following isochemical reactions under hydrous (eq. 8.1) and anhydrous conditions (eq. 8.2), as outlined in Deer, Howie & Zussman (1992):

$$Ca_2Mg_5Si_8O_{22}(OH)_2 + 11CaMg(CO_3)_2 = 8Mg_2SiO_4 + 13CaCO_3 + 9CO_2 + H_2O \quad \textbf{Equation 8.1}$$

$$CaMgSi_2O_6 + 3CaMg(CO_3)_2 = 2Mg_2SiO_4 + 4CaCO_3 + 2CO_2 \quad \textbf{Equation 8.2}$$

The presence of both diopside (see Figure 8.28A) and tremolite (see Figure 8.28B) silicate mineral assemblages indicates that both these conditions may have been in operation. The metamorphosed olivine-bearing lithologies may host significant sulphides (up to 5 vol%) present interstitial to the olivine grains and typically composed of pyrrhotite, pentlandite and chalcopyrite (see Figure 8.28C and 8.28D). This sulphide mineral assemblage can be described as typical of high temperature

magmatic deposits (e.g. Fleet, 2006) despite the non-magmatic origin of their host rock.

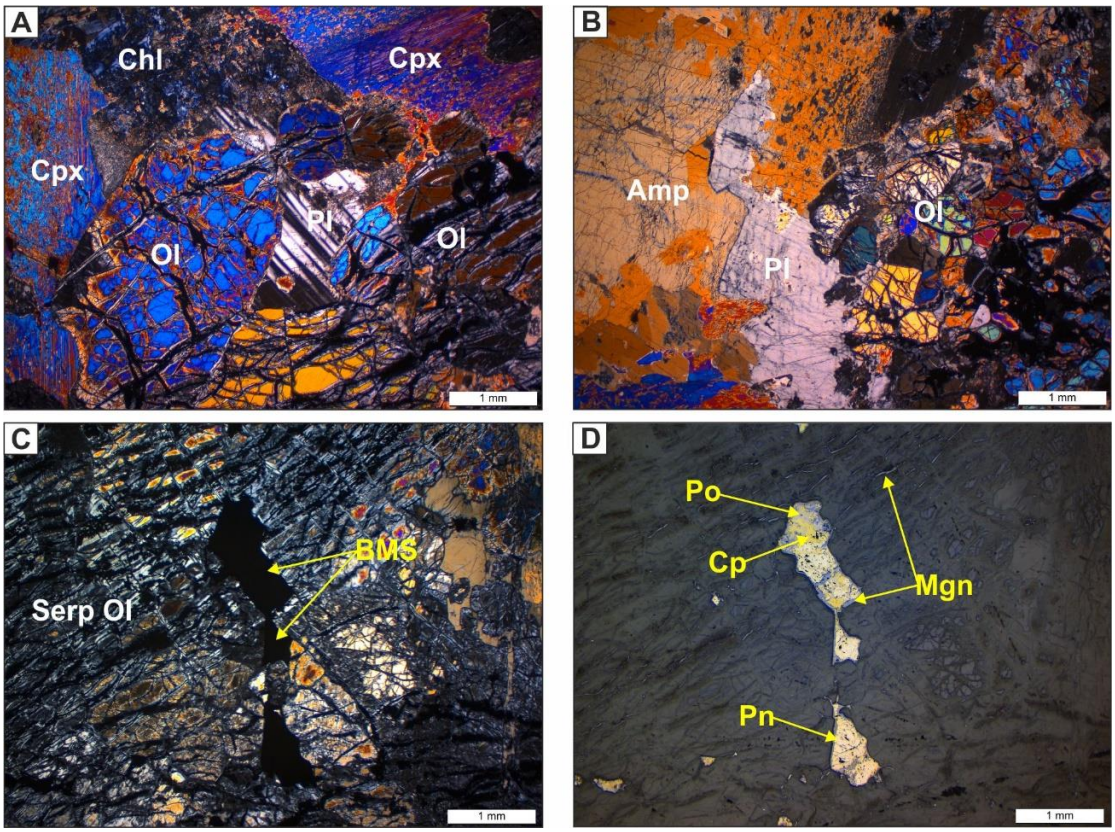

Figure 8.28: Photomicrographs showing petrological features of the HZ_{OLWEBS} zone. *Transmitted light images A to C in XP and D is in RFL.* All images from sample TMT_27. (A) A medium-grained olivine-plagioclase-clinopyroxene (diopside) assemblage. (B) Contact between olivine-plagioclase-amphibole (tremolite-composition). (C and D) Interstitial BMS hosted in strongly serpentinised olivine.

The Gabbronorite Hybrid Zone (HZ_{GBRN}) marks the first appearance of cumulate plagioclase and clinopyroxene over the logged interval of this drill hole. Similar to the HZ_{OLWEBS} unit, the HZ_{GBRN} unit demonstrates both lithological and textural heterogeneity and the features described in the samples below may be representative of relatively short intervals.

An example of the range in sizes of the minerals that make up the rocks of the HZ_{GBRN} unit are shown in Figure 8.29A where medium-grained cumulate laths of plagioclase are in contact with pegmatoidal clinopyroxene grains. This contact is irregular but not erosional with the clinopyroxene enveloping plagioclase laths. The medium-grained leucogabbronorite host rock is composed of 60 vol% plagioclase, 20 vol% orthopyroxene and 20 vol% clinopyroxene. In addition to forming pegmatoidal accumulations the clinopyroxene also forms interstitially as oikocrysts enclosing fine-grained plagioclase laths (see Figure 8.29B) and on the corroded edges of orthopyroxene grains (see Figure 8.29C). The orthopyroxene grains appear unstable

and are frequently anhedral and pitted with plagioclase, chromite and clinopyroxene creating embayed edges as shown in Figure 8.29C. Talc- and serpentinite- alteration minerals are present in patches and do not appear to significantly affect the surrounding silicate mineral assemblage (see Figure 8.29D).

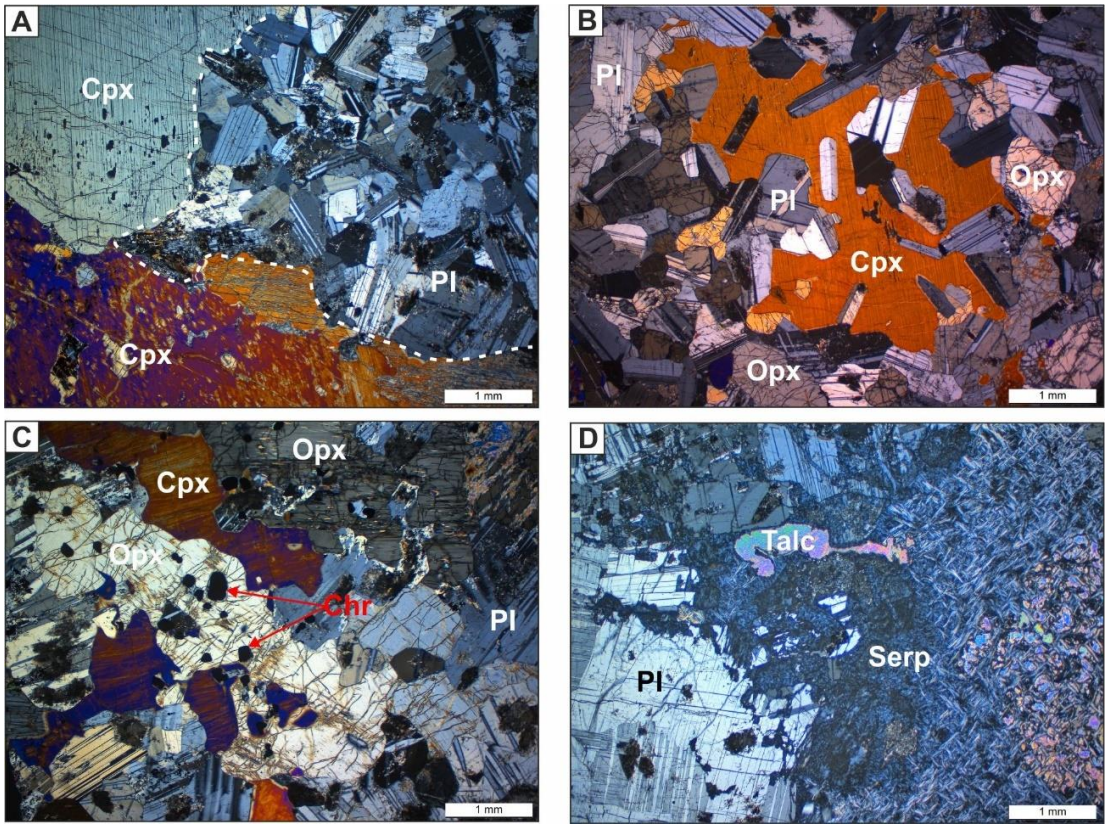

Figure 8.29: Photomicrographs showing key mineralogical features of the HZ_{GBRN}. *All transmitted light images in XP.* (A) The contact (dashed white line) between a fine- to medium grained anorthosite and pegmatoidal clinopyroxene grains which form a band across the sample (TMT_32A). (B) Medium-grained clinopyroxene oikocryst (TMT_32A). (C) Anhedral, corroded orthopyroxene surrounded by leucogabbro (TMT_32A). (D) Alteration pocket consisting of talc and serpentinite (TMT_32B).

Observations on the drill core noted the preferential concentration of BMS within very-coarse to pegmatoidal clusters of clinopyroxene; an example of this texture is shown in Figure 8.30. The clinopyroxene grains show signs of solid-state deformation with undulose extinctions and fine-grained recrystallisation on grain boundaries (see Figure 8.30B). Plagioclase is present as medium- to coarse-grained tabular crystals (see Figure 8.30A) and minor orthopyroxene are present as strongly resorbed grains (see Figure 8.30C). The pegmatoidal clinopyroxene grains enclose a very coarse grained (16 mm) polyphase sulphide comprising pyrrhotite (40 vol%), pentlandite (55 vol%) and chalcopyrite (5 vol%, see Figure 8.30D) observed to host visible PGM.

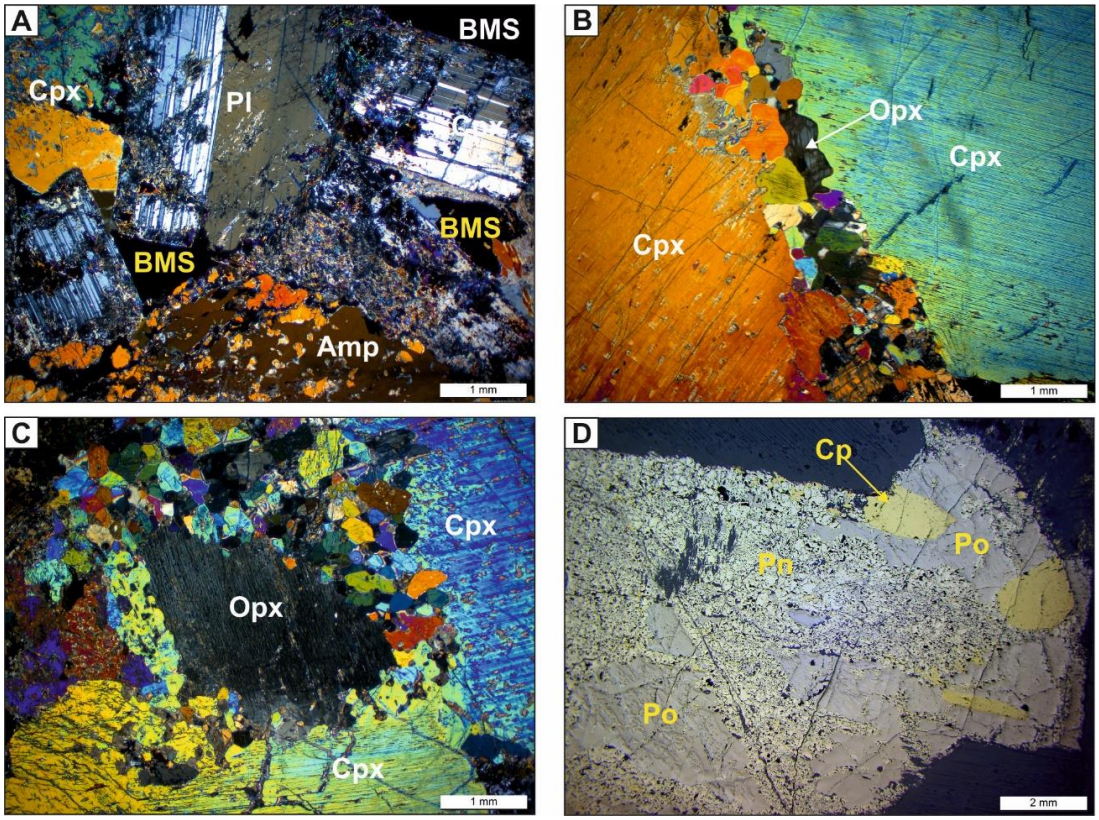

Figure 8.30: Photomicrographs of characteristics of sulphide-bearing clinopyroxenite bands in the HZ_{GBRN} unit. *Transmitted light images A-C in XP and D-F in reflected light.* All photos from sample TMT_34. (A) Plagioclase present as a cumulate phase. (B) Fine-grained recrystallisation on the contact between two pegmatoidal clinopyroxene grains, relict orthopyroxene also identified here. (C) Strongly resorbed orthopyroxene surrounded by fine-grained recrystallised clinopyroxene. (D) Very-coarse grained, fractionated BMS comprising pyrrhotite, pentlandite and chalcopyrite.

8.1.3 Normal Flatreef Mineralogy

The first Norite Cycle (NC1) unit was sampled extensively (eight samples) in the Normal Flatreef because this is the only drill hole studied where this unit hosts the Upper Reef mineralisation event; it can be divided into an upper noritic cyclic portion (non-mineralised) and the mineralised basal feldspathic orthopyroxenite (see Chapter 5 section 5.3.3).

One sample was collected from the upper portion of the NC1 unit; this sampled an interval where orientated, elongated coarse-grained orthopyroxene defined a weak linear fabric, as shown in Figure 8.31. In this sample plagioclase and clinopyroxene are present as oikocrysts and do not define any fabric. The orthopyroxene grains show evidence of deformation with undulose extinctions and localised recrystallization on grain boundaries; as shown in Figure 8.31C. In the fine-grained recrystallised grain boundary plagioclase is identified in thin wedges in pressure shadows between orthopyroxene grains, as shown in Figure 8.31B and 8.31C, potentially indicating the infiltration of late-stage felsic fluids. This is further supported by the presence of relict,

corroded orthopyroxene through resorption by a melt forming clinopyroxene and plagioclase.

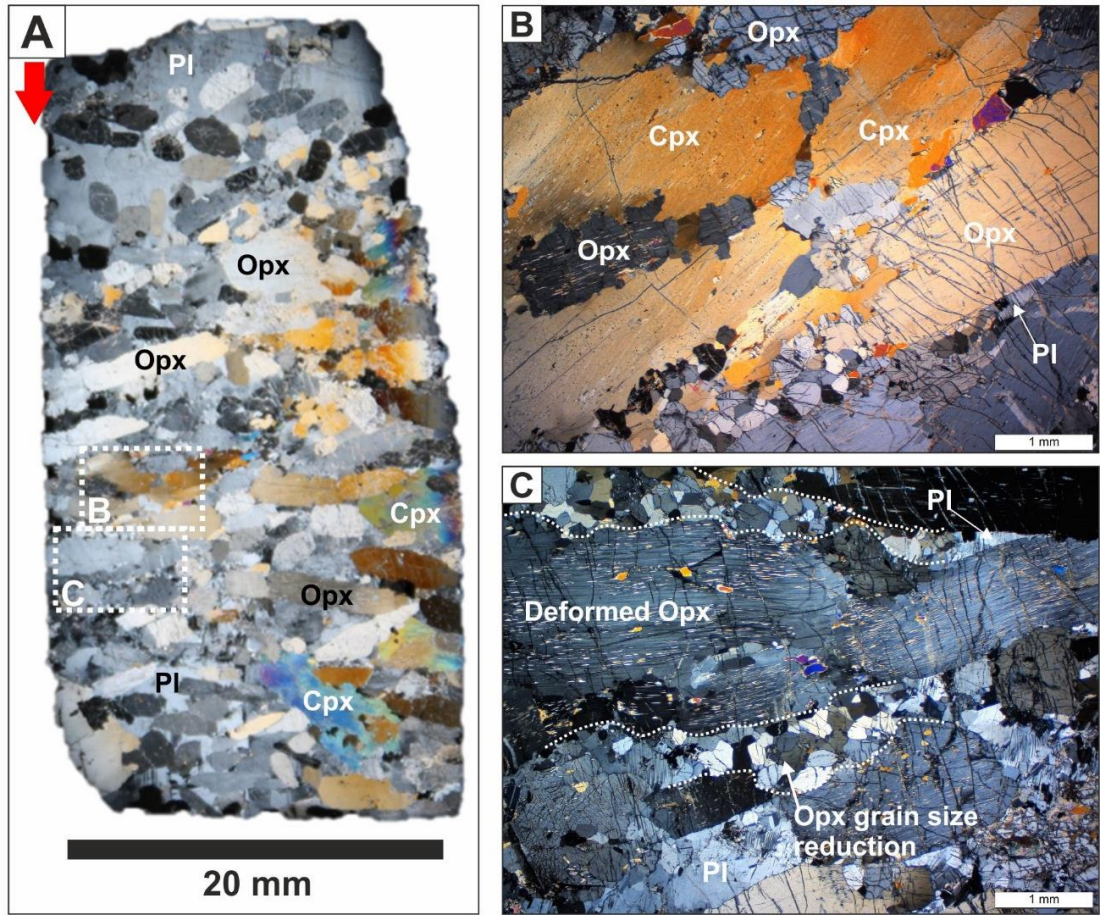

Figure 8.31: Photomicrographs showing orientated, elongated orthopyroxene grains within the NC1 unit. *All transmitted light images in XP from sample 233_01B.* (A) An overview of thin section 233_01B. (B) Coarse-grained clinopyroxene corroding a relict orthopyroxene grain. (C) Coarse-grained deformed orthopyroxene crystal with fine-grained recrystallized orthopyroxene on edges showing triple junctions indicative of in situ growth. Note: red arrows point in the downhole direction.

The feldspathic orthopyroxenite in the lower part of the NC1 unit was observed to be texturally heterogenous with grain sizes varying from fine (< 1 mm) to pegmatoidal (> 20 mm). Examples of the grain size variability over relatively short intervals (a few metres) within the unit are shown in Figure 8.32. This textural heterogeneity is absent in similar lithologies from the upper portions of the Deep Platreef and Thick Flatreef drill holes studied. The identification of these textures was therefore, considered to be important in understanding the formation of the NC1 unit mineralisation.

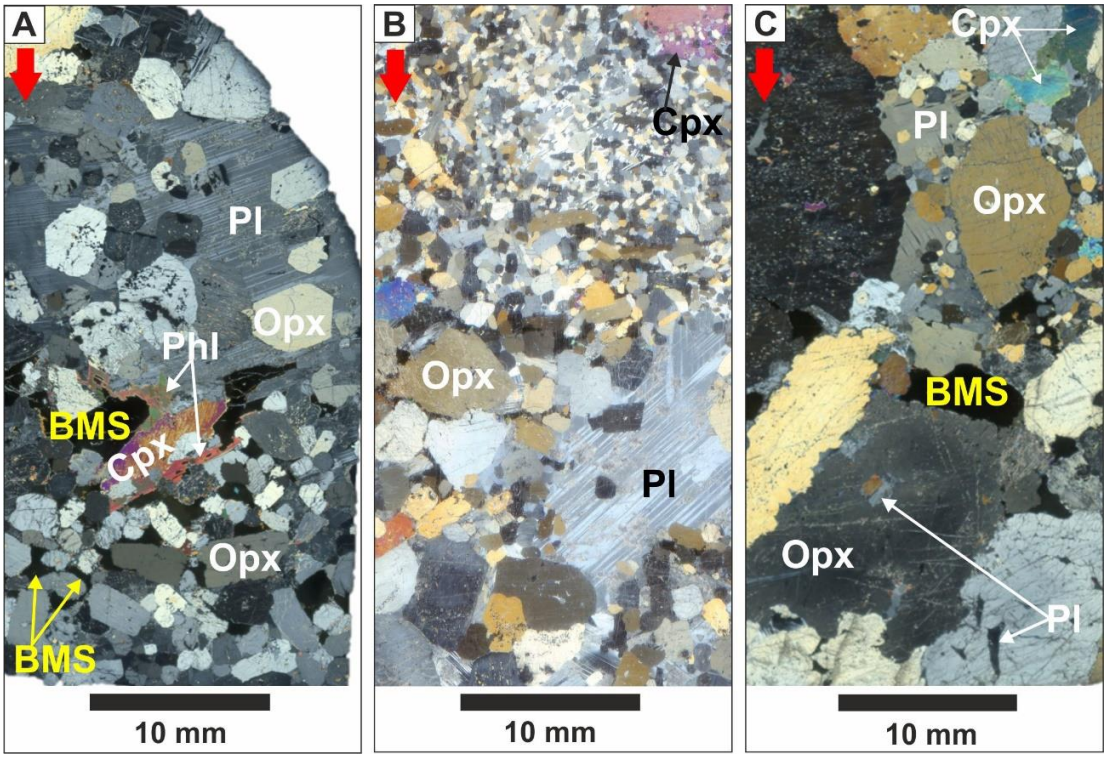

Figure 8.32: Whole-thin section photomicrographs illustrating the grain size heterogeneity within the NC1 unit in the Normal Flatreef. *All transmitted light images in XP*. (A) Medium to coarse grain sizes in sample 233_04; note the continuity of the twinning in the plagioclase-rich region which also hosts euhedral orthopyroxenes. (B) Fine- to coarse-grained orthopyroxene and a very coarse felsic pocket (233_05A). (C) Medium-grained to pegmatoidal grain sizes (233_07). Note: red arrows point in the downhole direction.

Details on the silicate mineralogy of the NC1 unit are shown in Figure 8.33. An example of a cumulate, medium-grained, deformed orthopyroxene grain containing an anhedral inclusion of quartz and phlogopite indicating that it crystallised in the presence of evolved fluids in the upper part of the NC1 unit is shown in Figure 8.33A. In the feldspathic orthopyroxenite dominated lower part of the NC1 unit pegmatoidal orthopyroxene have scalloped edges and contain multiple anhedral inclusions of plagioclase and clinopyroxene (see Figure 8.32C and 8.33B). Plagioclase is often found in pegmatoidal leucocratic pockets (see Figure 8.32A and 8.32B) as oikocrysts; these may contain euhedral, medium-grained orthopyroxene crystals with exsolved chromite grains (see Figure 8.33C). Fine-grained norite is found over short intervals (a few centimetres, see Figure 8.32B) the interstitial plagioclase often shows optical continuity and the norite locally develops into monomineralic, equant orthopyroxene clusters with a polygonal texture (see Figure 8.33D)

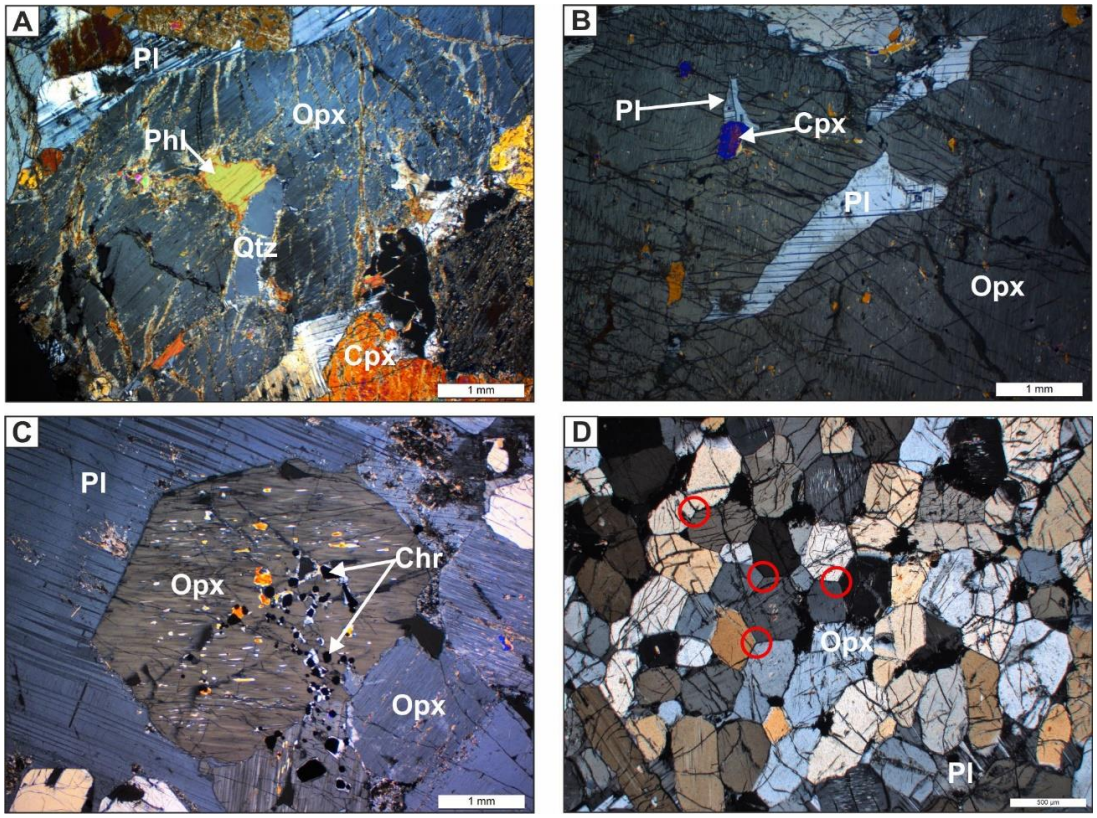

Figure 8.33: Photomicrographs showing features of the dominant silicate minerals present in the NC1 unit. *All transmitted light images in XP.* (A) Orthopyroxene with polyphase anhedral inclusions of quartz and phlogopite (233_01A). (B) Pegmatoidal orthopyroxene hosting anhedral inclusions of plagioclase and clinopyroxene (233_07). (C) Euhedral orthopyroxene enclosed in a plagioclase oikocryst (233_04). (D) Monomineralic, fine-grained orthopyroxene with a polygonal texture, red circles are placed on 120° triple junctions (233_05B).

The mineralised base metal sulphide (BMS) assemblage present over the Upper Reef interval consists of pyrrhotite (≈ 60 vol%), pentlandite (≈30 vol%) and chalcopyrite (≈10 vol%). The BMS are not distributed homogenously throughout this unit; rather, they are concentrated in specific areas that appear to be controlled by the textures of the rock as opposed to any cyclicity. Examples of the BMS assemblage within the NC1 unit are shown in Figure 8.34. In one sample the BMS are net-textured, as shown in Figure 8.34A and 8.34B; although they are predominantly found interstitially and are medium- to coarse-grained (see Figure 8.34C and 8.34D). A spatial association with medium- to coarse-grained phlogopite was frequently observed as shown in Figure 8.32A and 8.34D; this mineralogical association is also identified in the Upper Reef of the Deep Platreef.

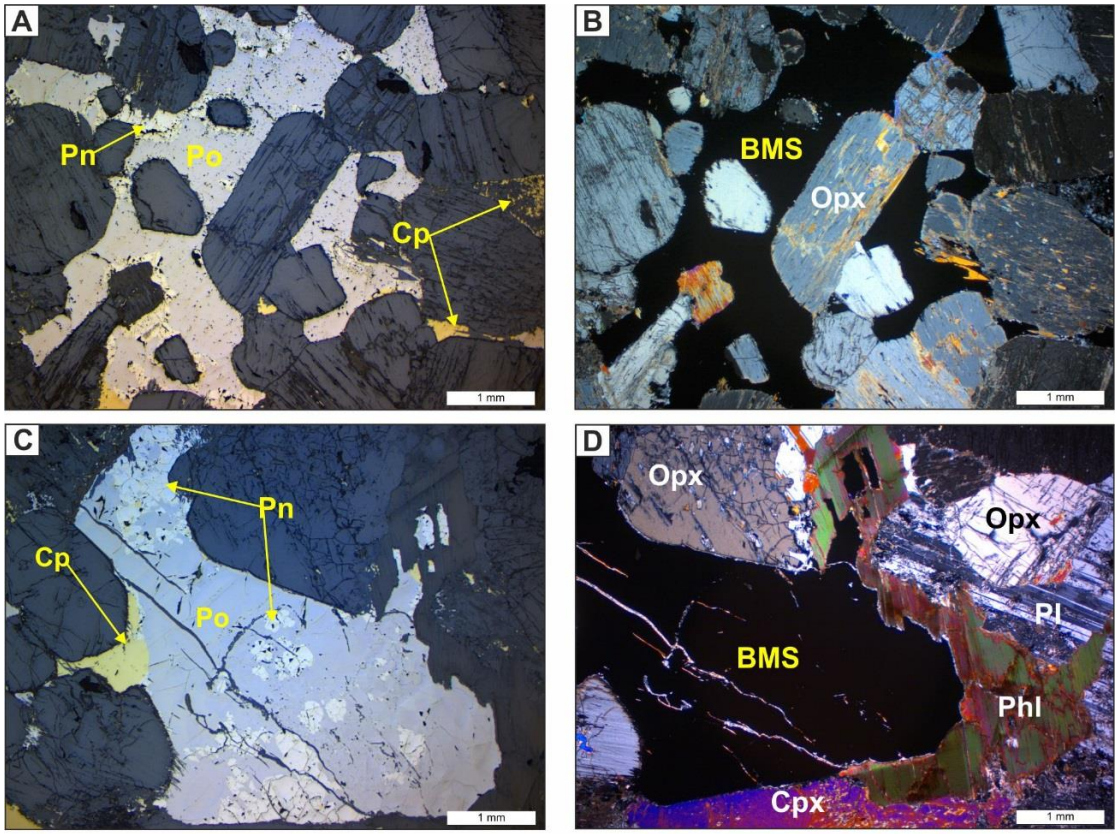

Figure 8.34: Photomicrographs showing characteristics of the BMS assemblage of the lower part NC1 unit hosting the Upper Reef mineralisation event. *Images A, C, and E are in RFL; transmitted light images B, D and F in XP.* (A and B) Net-textured BMS surround rounded equant orthopyroxene grains (233_03). (C and D) Coarse-grained, interstitial BMS spatially associated with medium-grained phlogopite (233_05B).

The chromite-stringer at the base of the UP unit marks the beginning of the Middle Reef mineralisation event. The mineralogical characteristics of the chromite stringer are provided in Figure 8.35; it consists of disseminated chromite (50 %) with interstitial plagioclase (30 %; see Figure 8.35A), clinopyroxene (10 %) and orthopyroxene (10 %; see Figure 8.35B).

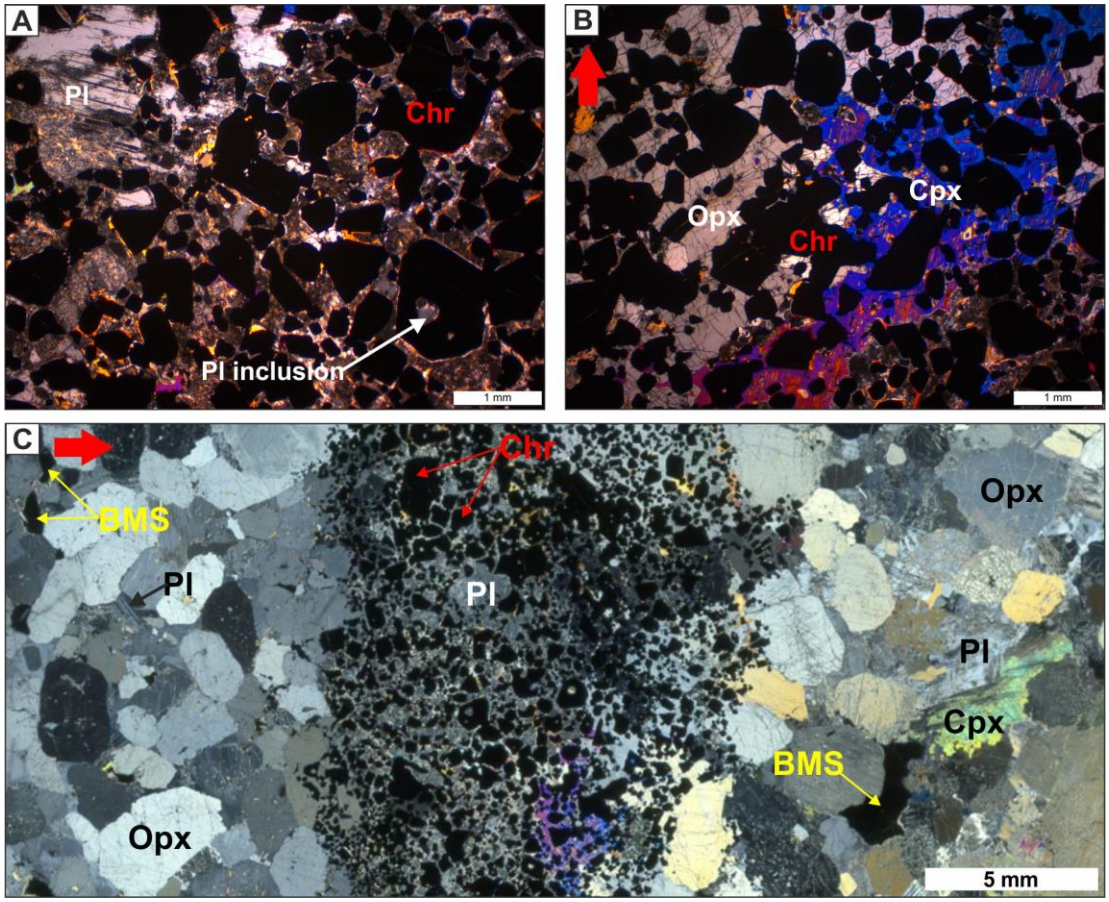

Figure 8.35: Photomicrographs of the chromite-stringer on the contact between the UP and MP units hosting the Middle Reef mineralisation event (as sampled in 233_11A). *All transmitted light images in XP*. (A) Interstitial plagioclase surrounding euhedral chromite grains. (B) Interstitial orthopyroxene and clinopyroxene hosting fine-grained chromite grains. (C) Overview of sample 233_11A hosting the chromite stringer, red arrow points in the downhole direction.

The contacts between the chromitite and the top and bottom silicates are transitional; there is also no increase in grain size directly below the chromitite as observed in the previous two drill holes. On the top contact of the chromite stringer orthopyroxene appears as overgrowths enclosing the chromite grains. The chromite-stringer is poor in BMS; where present they are either found as: inclusions (< 200 µm) associated with fractured chromite grains; mobilised in fractures in chromite grains; interstitial to chromite grains or; as fragments in the interstitial silicates. The chromite grains are typically fine- to medium-grained and euhedral; they may contain isolated inclusions infilled by either plagioclase or BMS.

Pegmatoidal textures are developed 4 cm below the chromite stringer along with a more typical appearance of the MP unit; although it is compositionally more noritic than observed elsewhere. Orthopyroxene dominates the silicate assemblage (70 modal%) as pegmatoidal and frequently euhedral grains. The orthopyroxene grains may contain anhedral inclusions of plagioclase and exsolutions of clinopyroxene on

grain margins in contact with interstitial plagioclase (similar to that shown in Figure 8.23 for the Thick Flatreef).

The mineralogical features of the a clinopyroxenite from the Pyroxenite-Norite Zone (PNZ, sample 233_18), hosting a band of chromitite can be found in Appendix C. The banding of the chromitite is formed by localised annealing of chromite grains. The grain sizes observed range from fine- to medium-grained (up to 2 mm). The chromitite hosts up to 5 % BMS typically interstitial to annealed chromite grains. Orthopyroxene is present as fine-grained subhedral laths that often have corroded edges; they are typically present as accumulations of recrystallised grains with polygonal contacts or as corroded elongate grains in a plagioclase oikocryst.

8.1.4 Platreef Mineralogy

The top contact of the Upper Pyroxenite (UP) unit with the Mottled Anorthosite (MAN) unit was sampled in ATS_01A and ATS_01B; these samples are located on the contact and 40 mm downhole, respectively. A summary of mineralogical features of these thin sections are shown in Figure 8.36 below. In Figure 8.36A, the important lithostratigraphic contact between the base of the MAN unit and top of the UP unit is shown. There is a fine-grained chlorite-alteration front developed on this contact (see Figure 8.36A) indicative of hydrothermal activity. The UP unit on this contact includes orthopyroxene with interstitial plagioclase and is sulphide-rich (see yellow colour in Figure 8.36B) comprising monomineralic pyrrhotite spatially associated with magnetite (see red colour in Figure 8.36B). Moving downhole away from this contact the mineralogy completely changes with plagioclase present as cumulate-laths with interstitial orthopyroxene (similar to the MAN unit; see Figure 8.36C). In the middle of the rock section shown in Figure 8.36C and 8.36D is a four millimetre thick band of medium-grained orthopyroxene grains, orientated ≈ perpendicular to the core axis. This pyroxenite-band is sulphide-rich (see yellow colour in Figure 8.36D) and on the downhole side are concentrated medium-grained apatite (bright pink in Figure 8.36D) and ilmenite (red in Figure 8.36D). In summary, these sections highlight the complexity of this intrusive contact with significant changes in the grain size, mineralogy and crystallisation sequence over short distances.

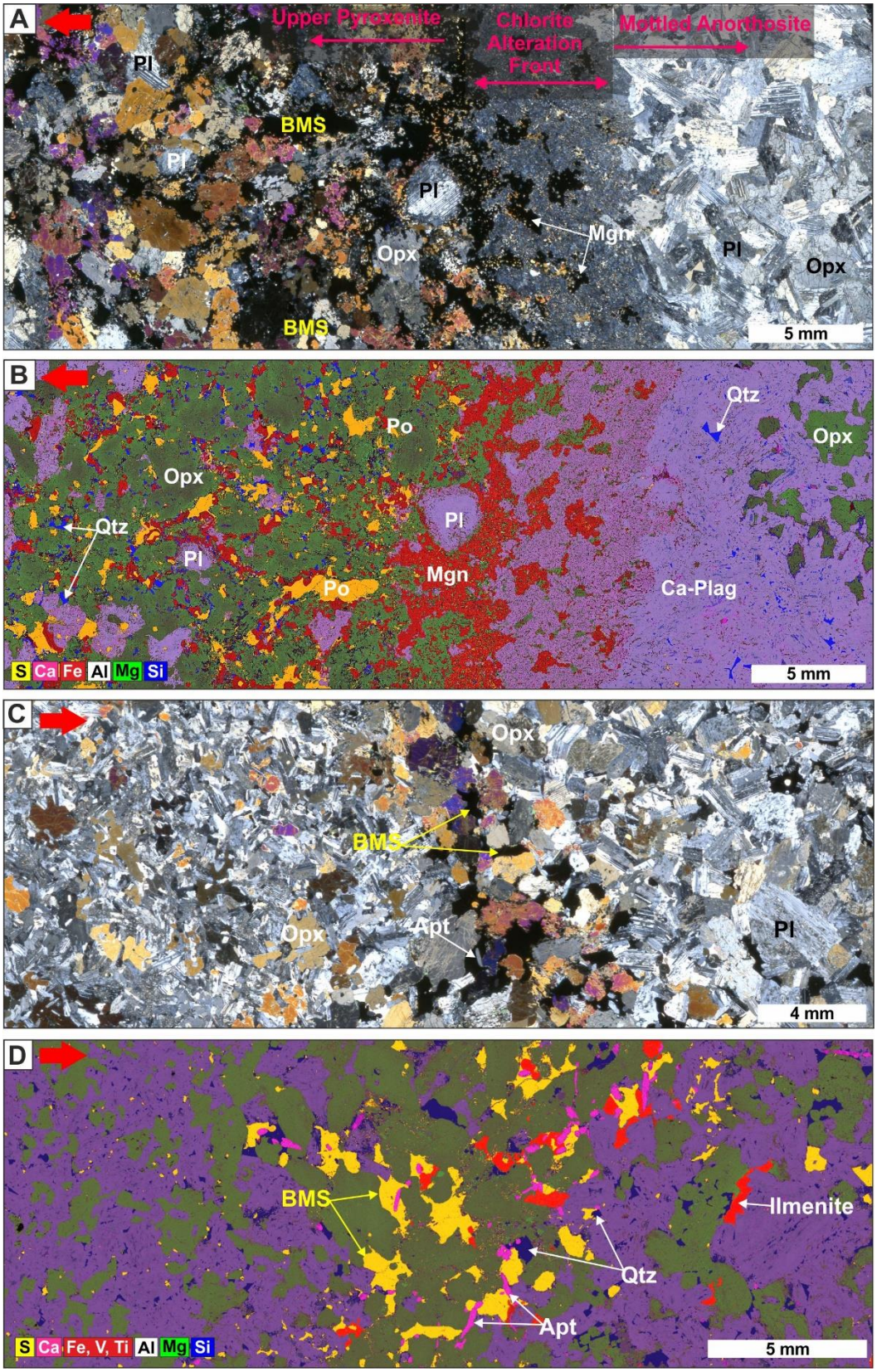

Figure 8.36: The mineralogy of the contact between the MAN and UP units. *Transmitted light images A and C are in XP; images B and D are EDS multi-element maps.* (A and B) Sample ATS_01A. (C and D) Sample ATS_01B. Note: red arrows point in the downhole direction.

The basal 10 mm of the MAN unit is composed of cumulate plagioclase (80 vol%) and interstitial orthopyroxene (11 vol%), clinopyroxene (5 vol%) and quartz (4 vol%). The plagioclase is medium-grained and forms euhedral, equant laths. Orthopyroxene is present interstitially as shown in Figure 8.37A; the plagioclase laths have embayed edges in contact with orthopyroxene. Over this interval the 'mottle' texture is poorly developed with the pyroxene content present as isolated interstitial oikocrysts forming a subophitic texture as shown in Figure 8.37A.

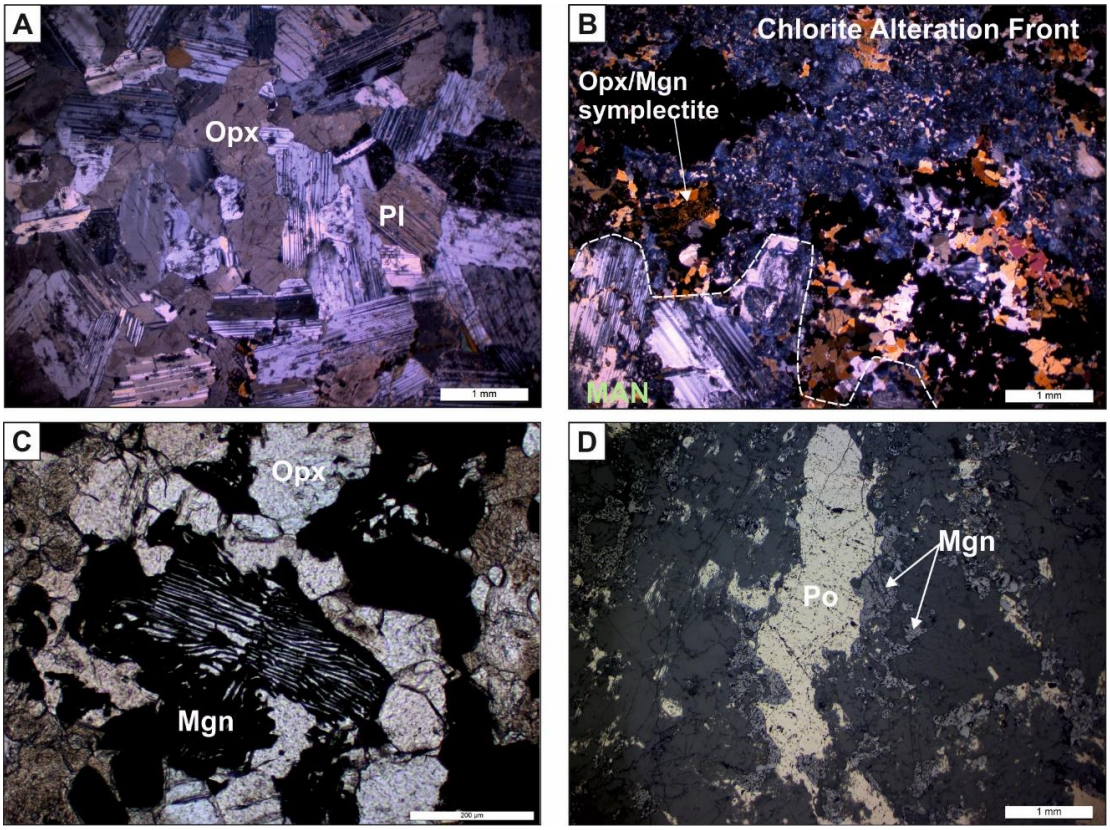

Figure 8.37: Photomicrographs showing the mineralogical changes across the MAN/UP contact. *Note: transmitted light images A and B in XP; C in PPL and D in RFL.* All images from thin section ATS_01A. (A) Subophitic texture between orthopyroxene and plagioclase at the base of the MAN unit. (B) The contact between the base of the MAN unit and the fine-grained chlorite alteration front. (C) Fine-grained orthopyroxene and magnetite symplectite in the chlorite alteration front. (D) Medium-grained pyrrhotite-dominated sulphide in the UP with magnetite on edges.

The contact between the MAN and the UP is defined by a 6 mm thick band of fine-grained alteration that gives a cloudy appearance (see Figure 8.36A and 8.37B). This alteration has an irregular boundary with the anorthosite and appears to truncate some of the plagioclase laths (see Figure 8.37B). The dominant alteration mineral has an anomalous blue colour indicating the presence of chlorite (see Figure 8.37B). This altered layer also contains fine-grained orthopyroxene and magnetite; in places these minerals form a vermicular symplectite texture (see Figure 8.37C). A band of magnetite (up to 2 mm thick) is concentrated on the base of the contact (UP side).

Behind this the altered pyroxenite contains abundant monomineralic sulphides (up to 20 %) composed of pyrrhotite that are fine to medium grained (<1 to 3 mm; see Figure 8.37D) and typically have a close spatial association with magnetite.

Moving downhole from the MAN/UP contact by 40 mm there is a significant change in mineralogy including the reappearance of leucocratic compositions and the development of a pyroxenite band concentrating BMS (see Figure 8.36A and 8.36B). Medium-grained apatite (see Figure 8.38C) and ilmenite are concentrated on the coarser-grained downhole side of the pyroxenite band suggesting that this may be acting as a barrier to fluids or late-stage melts. The pyroxenite band is 7 mm thick and contains up to 40 modal% BMS that are pyrrhotite-dominated (see Figure 8.38C and 8.38D).

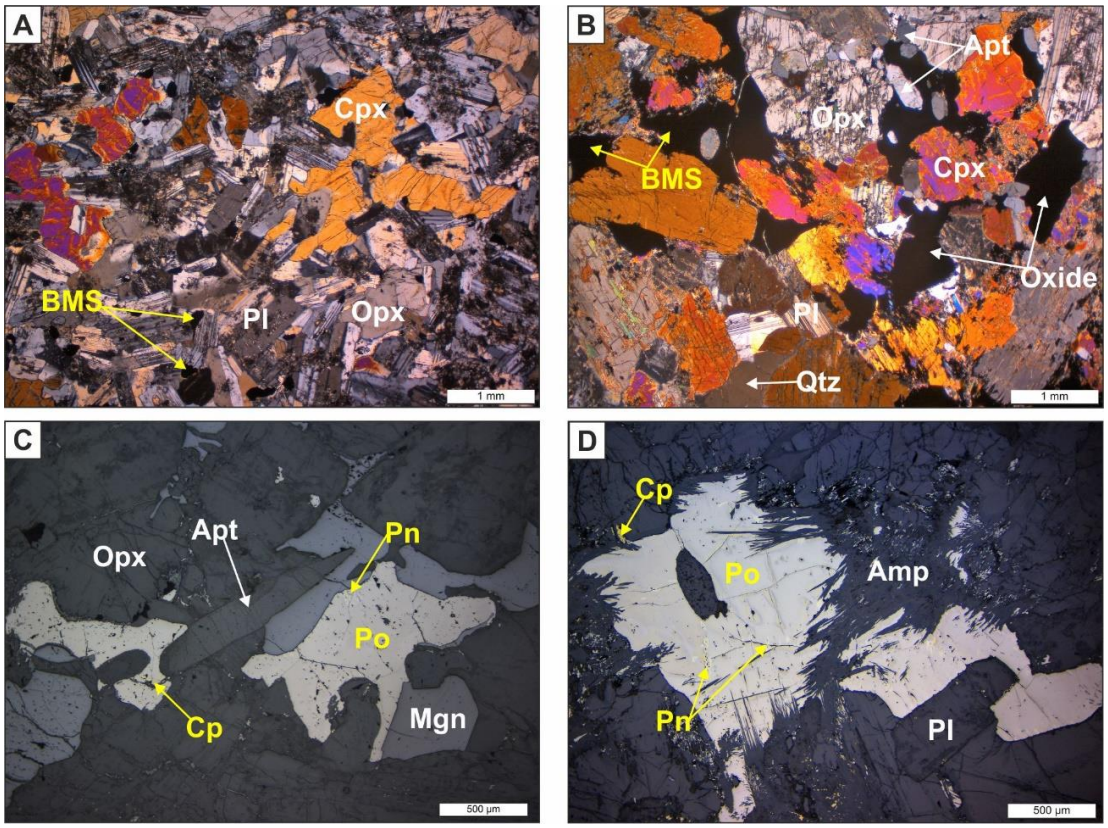

Figure 8.38: Photomicrographs of mineralogical features at a distance of 40 mm away from the MAN/UP contact as sampled in ATS_01B. *Transmitted light images A and B are in XP; C and D in RFL*. (A) Fine- to medium-grained leucogabbronorite on the uphole side of the pyroxenite band. (B) Pyroxenite-band containing interstitial quartz, BMS and medium-grained apatite. (C) Pyrrhotite-dominated, medium-grained sulphides showing a close spatial association with magnetite and apatite. (D) Pyrrhotite-dominated, medium-grained sulphides with amphibole alteration on edges.

The UP unit, is finer-grained (< 1 to 2 mm) than that observed in both the Flatreef drill holes and in the Deep Platreef (see Figure 8.39); also unlike elsewhere the UP unit here is PGE-poor despite the presence of BMS (see Figure 8.39D). The UP unit at

this locality typically comprises cumulate orthopyroxene (70 %) and interstitial plagioclase (20 %), clinopyroxene (5 %) and quartz (up to 5 %). The fine- to medium grained cumulate orthopyroxene is present as equant (see Figure 8.39B) and elongate grains that locally demonstrate a preferred orientation. Plagioclase is the dominant interstitial mineral, clinopyroxene is present as medium-grained oikocrysts (see Figure 8.39A) and BMS are locally significant forming interstitially or net-textured (see Figure 8.39C and 8.39D). The BMS identified reflect the crystallisation of MSS and are dominated by pyrrhotite (90 %) and pentlandite (10 %); no ISS crystallisation products identified. Apatite and quartz are found in close spatial association with the BMS within the sample shown in Figure 8.39D.

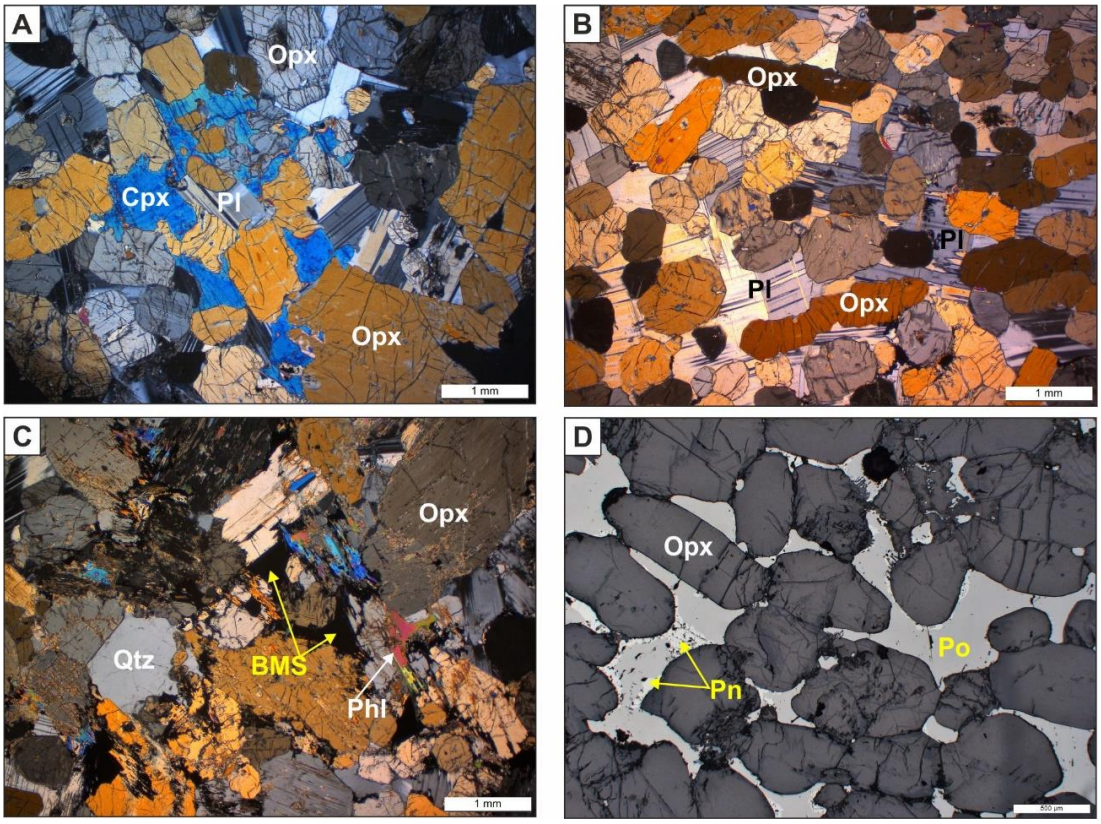

Figure 8.39: Photomicrographs showing sulphide-poor and sulphide-rich samples from the UP unit. *Transmitted light images A, B and C in XP; D is in RFL.* (A) Medium-grained clinopyroxene oikocrysts in feldspathic orthopyroxenite (ATS_02). (B) Typical fine-grained feldspathic orthopyroxenite (ATS_04B). (C) Sulphides associated with interstitial phlogopite-quartz and apatite (ATS_04A). (D) Pyrrhotite-dominated sulphides with pentlandite forming on silicate grain boundaries (ATS_04A).

Evidence for localised movement and/or intense fluid alteration in the upper part of the UP unit was identified in sample ATS_03. This sample, from a more leucocratic interval of gabbroic composition within the UP unit, demonstrates significant grain size reduction (see Figure 8.40A) of the original cumulate minerals of plagioclase, clinopyroxene and orthopyroxene (see Figure 8.40B, 8.40C,and 8.40D). The relict

medium-sized grains preserved are proposed to represent the original grains from which the finer grains formed. The mechanism by which this was achieved is proposed to be due to strain-related deformation processes. The evidence for this is in the preservation of deformed plagioclase twins and a kink in the orthopyroxene grain coupled with an undulose extinction.

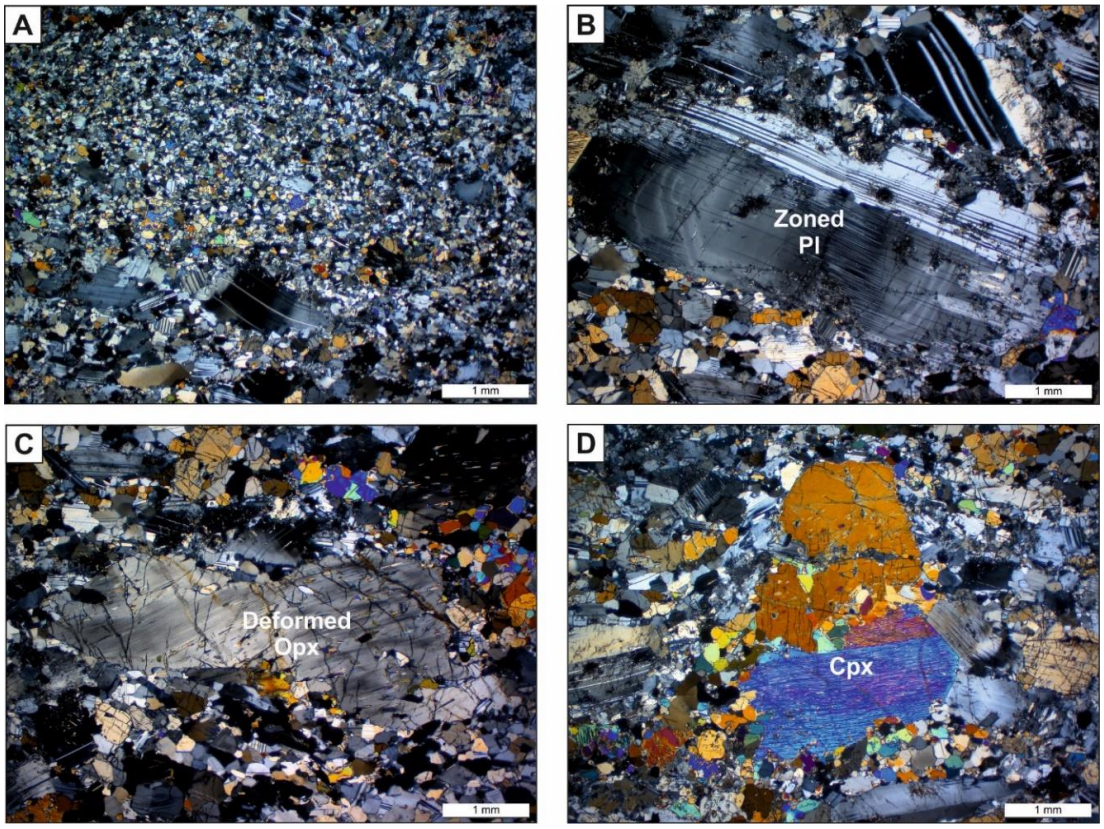

Figure 8.40: Evidence of localised deformation preserved in a thin leucocratic lithology within the UP unit. *All transmitted light images are in XP from sample ATS_03.* (A) Very fine grained leucogabbronorite. (B) A relict zoned, coarse-grained plagioclase. (C) A relict medium-grained orthopyroxene with an undulose extinction. (D) A relict clinopyroxene grain surrounded by very fine-grained leucogabbronorite.

The Middle Pyroxenite (MP) unit, hosting the Middle Reef mineralisation event (see Figure 8.2), was sampled in ATS_05. Detailed mineralogical features of this sample, a pegmatoidal olivine orthopyroxenite, are shown in Figure 8.41. The pegmatoidal upper portion of the MP unit, as shown in Figure 8.41 is composed of orthopyroxene oikocrysts enclosing medium-grained olivine (see Figure 8.41B) and medium- to coarse-grained BMS (see Figure 8.41E). The BMS assemblage is composed of pyrrhotite (80 %), pentlandite (15 %) and minor chalcopyrite (5 %, see Figure 8.42C). It is noticeably chalcopyrite poor compared to equivalent units identified elsewhere throughout the deposit. There is observed a spatial association between the presence of BMS and hydrous minerals as shown in Figure 8.41A. Extensive fluid alteration is evidenced by the presence of mm-thick amphibole veins around relict orthopyroxene

(see Figure 8.41D) and serpentinite veins cross-cutting olivine (even where enclosed by orthopyroxene, see Figure 8.41E). With increasing depth, the olivine content disappears; an example of the feldspathic orthopyroxenite lithologies within the MP unit are shown in Appendix D.

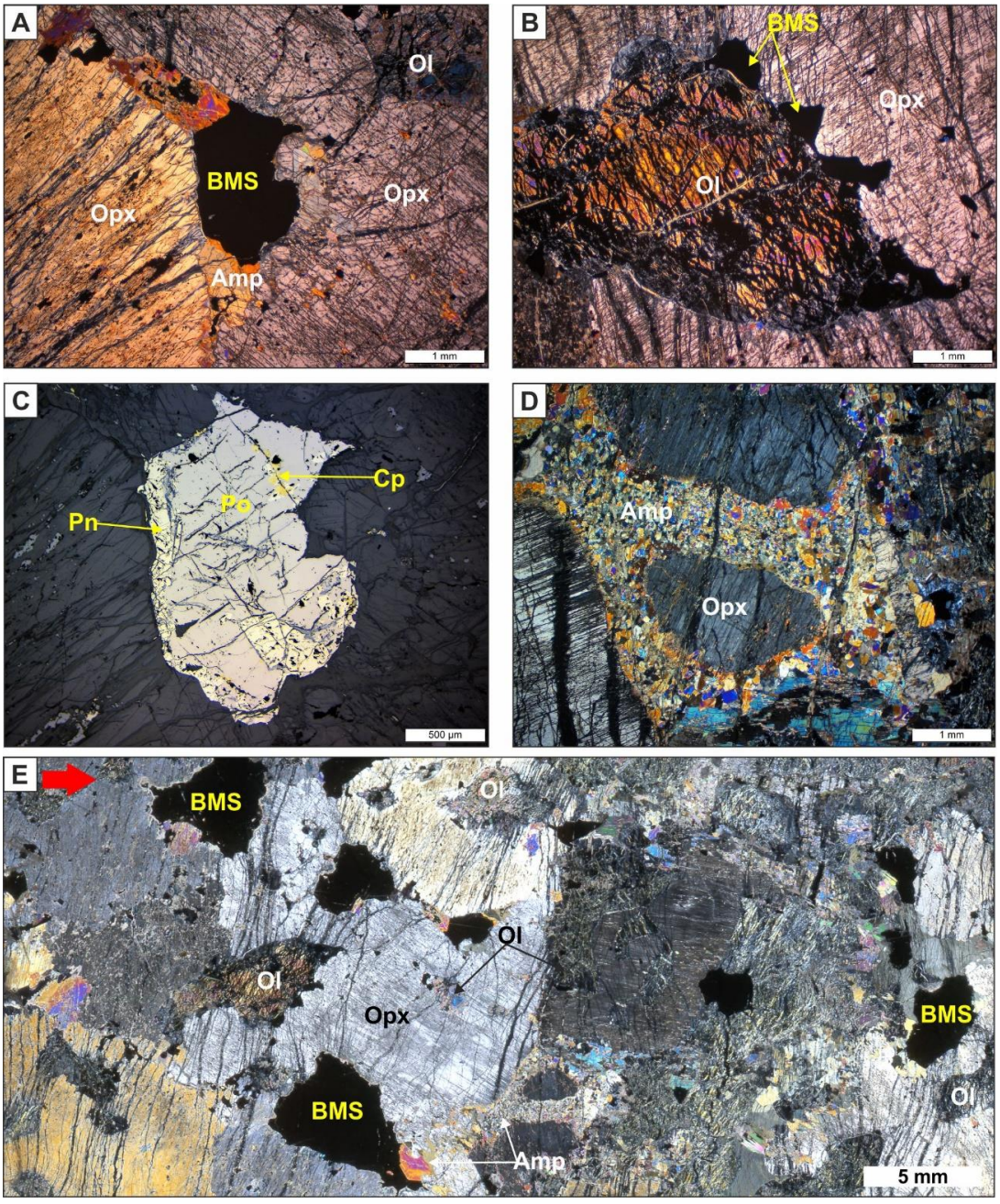

Figure 8.41: Photomicrographs showing the mineralogical characteristics of the pegmatoidal olivine orthopyroxenite in the MP unit hosting the Middle Reef mineralisation event. *Transmitted light images A, B, D and E are in XP and C in RFL; all from sample ATS_05.* (A) BMS located between two coarse-grained orthopyroxene grains and spatially associated with amphibole in pressure shadows. (B) Olivine and orthopyroxene with BMS located on the contact. (C) An example of the pyrrhotite-dominated sulphide assemblage with only minor pentlandite and chalcopyrite. (D) A 1 mm thick, fine-grained amphibole vein found on orthopyroxene grain boundaries. (E) A whole-thin section overview highlighting the distribution of olivine and the BMS. Note: red arrow points in the down hole direction.

The Hornfels Hybrid Zone (HZ_{HF}) unit is composed of fine-grained lithologies dominated by an assimilation overprint. This unit is also characterised by massive sulphide accumulations dominated by pyrrhotite as illustrated in Figure 8.42A and 8.42B but are low grade. In Figure 8.42B the massive pyrrhotite is crystallising magnetite on the contact with the silicates similar to the textures observed at the top of the drill hole on the MAN/UP contact. The fine-grain size of the ground mass restricted mineral identification but finely disseminated calcite and quartz were discernible.

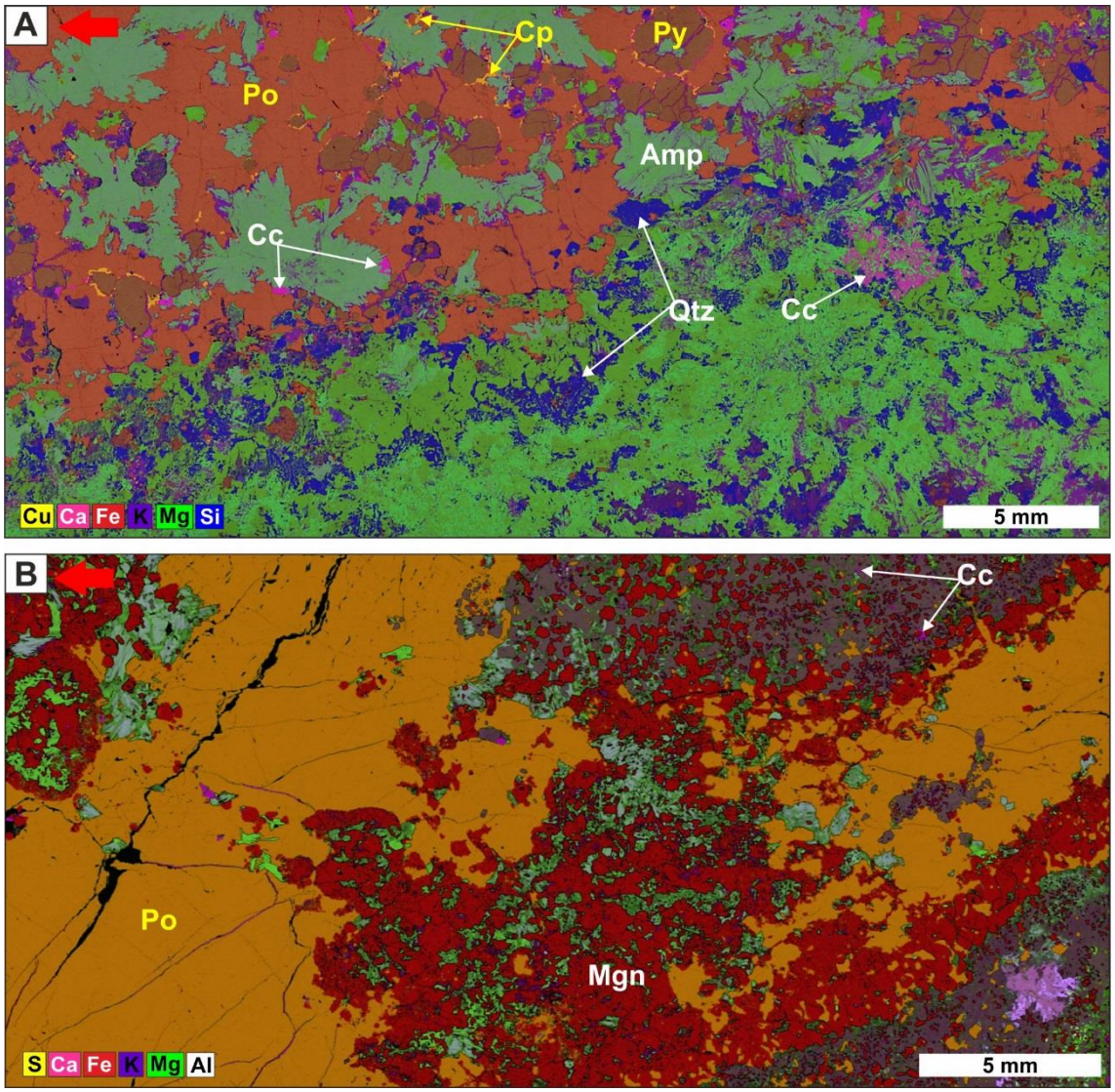

Figure 8.42: EDS multi-element maps of the massive sulphides within the HZ_{HF} unit. (A) Massive pyrrhotite, with euhedral pyrite and minor chalcopyrite associated with amphiboles and quartz (ATS_07). (B) Massive pyrrhotite with magnetite on edge and a fine-grained silicate matrix (ATS_08). Note: red arrow points in the down hole direction.

8.2 Mineral Chemistry

The compositions of the minerals olivine, orthopyroxene, clinopyroxene, plagioclase and chromite were analysed from selected samples across the drill holes studied. A

summary table of the compositional data of the main silicate minerals analysed in this study is provided below in Table 8.2.

Table 8.2: Mineral compositions for the major silicate minerals from drill holes sampled across the Turfspruit deposit.

Stratigraphy	Orthopyroxene		Clinopyroxene		Plagioclase	Olivine
Deep Platreef (UMT_345 and UMT_345_D1)						
Main Zone	En_{69}	$Mg\#_{71}$	Wo_{44-45}	$Mg\#_{78-79}$	An_{70-74}	
MAN	En_{63-70}	$Mg\#_{65-72}$	Wo_{26-44}	$Mg\#_{69-74}$	An_{65-73}	
QFV					An_{0-18}	
UP	En_{56-79}	$Mg\#_{59-82}$	Wo_{35-46}	$Mg\#_{79-85}$	An_{0-96}	
MP	En_{76-86}	$Mg\#_{77-87}$	Wo_{37-46}	$Mg\#_{80-87}$	An_{52-81}	Fo_{80-83}
NC2	En_{78-83}	$Mg\#_{81-85}$	Wo_{42-49}	$Mg\#_{80-87}$	An_{46-83}	
LP	En_{78-86}	$Mg\#_{83-87}$	Wo_{38-46}	$Mg\#_{82-87}$	An_{57-98}	Fo_{81-86}
MCHR	En_{79-88}	$Mg\#_{81-89}$	Wo_{27-48}	$Mg\#_{83-96}$	An_{59-78}	
UMZ	En_{75-82}	$Mg\#_{76-83}$	Wo_{36-45}	$Mg\#_{80-86}$	An_{39-77}	Fo_{80-82}
HZ_{FCPX}	En_{79-82}	$Mg\#_{81-84}$	Wo_{39-45}	$Mg\#_{82-86}$	An_{54-72}	
Thick Flatreef (TMT_006)						
MP	En_{75-78}	$Mg\#_{77-80}$	Wo_{35-45}	$Mg\#_{81-84}$	An_{49-63}	
HZ_{GBRN}	En_{69-83}	$Mg\#_{76-85}$	Wo_{40-46}	$Mg\#_{79-89}$	An_{64-78}	
Normal Flatreef (UMT_233)						
NC1	En_{74-78}	$Mg\#_{77-81}$	Wo_{44-45}	$Mg\#_{82-84}$	An_{40-71}	
MP	En_{77-80}	$Mg\#_{80-83}$	Wo_{44-45}	$Mg\#_{86-87}$	An_{68-77}	
PNZ_{CHR}	En_{70-77}	$Mg\#_{72-79}$	Wo_{40-46}	$Mg\#_{79-88}$	An_{71-76}	
Platreef (ATS_002)						
MAN/UP	En_{59-63}	$Mg\#_{60-65}$	Wo_{44}	$Mg\#_{74}$	An_{72-79}	
UP	En_{68-77}	$Mg\#_{73-79}$	Wo_{41-45}	$Mg\#_{78-80}$	An_{65-74}	
MP						Fo_{80-81}

8.2.1 Major Silicate Mineral Chemistry

The results of the pyroxene analyses are plotted in the system Wollastonite (Wo)-Enstatite (En)-Ferrosilite (Fs) (see Figure 8.43); samples from the Deep Platreef are presented in Figure 8.43A and the combined data from the Flatreef and Platreef drill holes in Figure 8.43B. Mineral compositional data from elsewhere in the Bushveld Complex are presented as fields for comparison (see Figure 8.43C for references); the data collected in this study shows a good correlation with the results of previous studies.

The majority of the orthopyroxene compositions plot in the enstatite field and within the range of $Mg\#_{75-85}$. In the Deep Platreef the upper part of the stratigraphy plots at lower $Mg\#_{59-72}$ compared to the lower ultramafic parts of the stratigraphy which plot to higher $Mg\#_{>75}$ (see Figure 8.43A). One orthopyroxene analysis from the Upper Pyroxenite (UP) unit plots within the pigeonite field (sample GS7A); this sample also records an anomalously low An content An_{57}. The Flatreef orthopyroxene

compositional data from the pyroxenite-dominated units plot in a tight cluster and have $Mg\#_{75-80}$ (see Figure 8.43B); these are comparable to the Deep Platreef values but demonstrate less variability. In the Flatreef, the Gabbronorite Hybrid Zone (HZ_{GBRN}) records the highest and largest range in orthopyroxene composition with $Mg\#_{69-83}$. Orthopyroxene from the Mottled Anorthosite unit in the Platreef records slightly lower $Mg\#_{60-65}$ compared to the equivalent unit as sampled in the Deep Platreef with $Mg\#_{65-72}$; this probably reflects the texture of the orthopyroxene in the Platreef as sub-ophitic and therefore open to trapped liquid shift (e.g. Barnes, 1986 and Meurer et al., 1999) compared to the ophitic texture in the Deep Platreef.

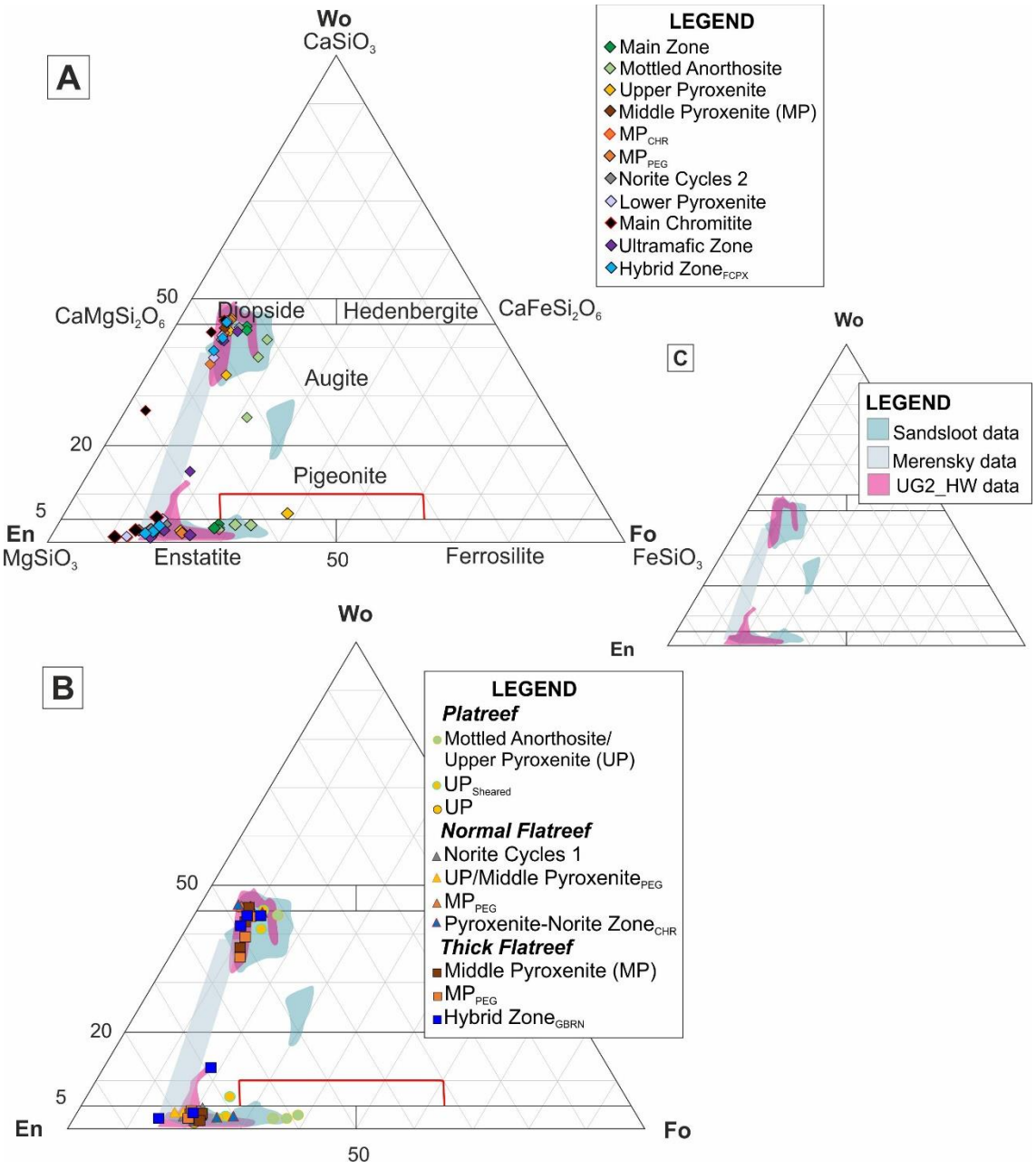

Figure 8.43: Ternary diagram showing the pyroxene compositional data plotted according to stratigraphic unit as identified in: (A) the Deep Platreef; (B) the combined Flatreef (Normal and

Thick facies) and Platreef; (C) Mineral compositional fields for selected locations from the Bushveld Complex including; Sandsloot data from McDonald et al., (2005); Merensky Reef data from Cawthorn et al., (1985) and Buchanan et al., (1981) and UG2 hanging wall data from Mondal & Mathez (2007). Note: the results plotted represent the mean, minimum (En) and maximum (En) values for each stratigraphic unit.

The clinopyroxene compositions plot within the diopside and augite fields (see Figure 8.43) with a few outliers representing solid solutions. In the Deep Platreef there is a transition from augite compositions within the Main Zone and Mottled Anorthosite (MAN) units to diopside compositions with higher Mg# and Wo contents moving down the stratigraphic units (see Figure 8.43A). The spread of data for the MAN along an exsolution line matches the observed textures (see Figure 8.3). The Thick Flatreef clinopyroxene data plots along an exsolution line, particularly in the Middle Pyroxenite (MP) unit (see Figure 8.43B); this compositional variability in clinopyroxene compared to the restricted range in orthopyroxene compositions reflects their variable textural setting and mineral associations as shown in Figure 8.23. In contrast, the Norite Cycle 1 and MP unit data for the Normal Flatreef are tightly clustered and plot within the diopside field and this reflects their more mature development as oikocrysts. Clinopyroxene compositional data for the MAN unit in the Platreef plots within the augite field but nearer to the diopside tie-line than in the equivalent unit of the Deep Platreef.

The results from the plagioclase analyses are plotted in the system Anorthite (An)-Albite (Ab)-Orthoclase (Or) (see Figure 8.44). There is a large spread of data, however the majority of the mean values (excluding the quartz-feldspar vein, QFV) have compositions between labradorite and bytownite.

In the Deep Platreef stratigraphic units where plagioclase is present as a cumulate mineral e.g. in the Main Zone, MAN and Norite Cycles 2 units, the range of values observed are more restricted and typically fall within the labradorite/bytownite compositions (see Figure 8.44A). The almost pure albite identified in the Upper Pyroxenite (UP) unit of the Deep Platreef was identified in a sample in proximity to the QFV intruding this unit (see Figure 8.44A). The interstitial areas of the UP unit host an array of minerals including plagioclase, quartz, base metal sulphides, phlogopite and monazite suggesting either hydrothermal fluids have percolated through it or it represents an evolved interstitial melt.

The plagioclase compositions for the Flatreef are less variable than those measured in samples from the Deep Platreef (see Figure 8.44B). In the Thick Flatreef dataset the majority of the Gabbronorite Hybrid Zone (HZ_{GBRN}) data plots within the bytownite field (Ca-rich) this corresponds with the dominance of Ca-bearing pyroxenes

compared to the dominant labradorite composition of the Middle Pyroxenite (MP) unit where orthopyroxene dominates. In the Normal Flatreef samples the largest range of anorthite concentrations is recorded in the NC1 unit (sample 233_04). The andesine compositions (An_{40}), analysed in this unit corresponds to a sample where plagioclase is present as a pegmatoidal oikocryst and other interstitial phases present include phlogopite and quartz; these minerals are also found in samples from the UP unit of Deep Platreef which show andesine plagioclase compositions indicating the presence of a more evolved melt.

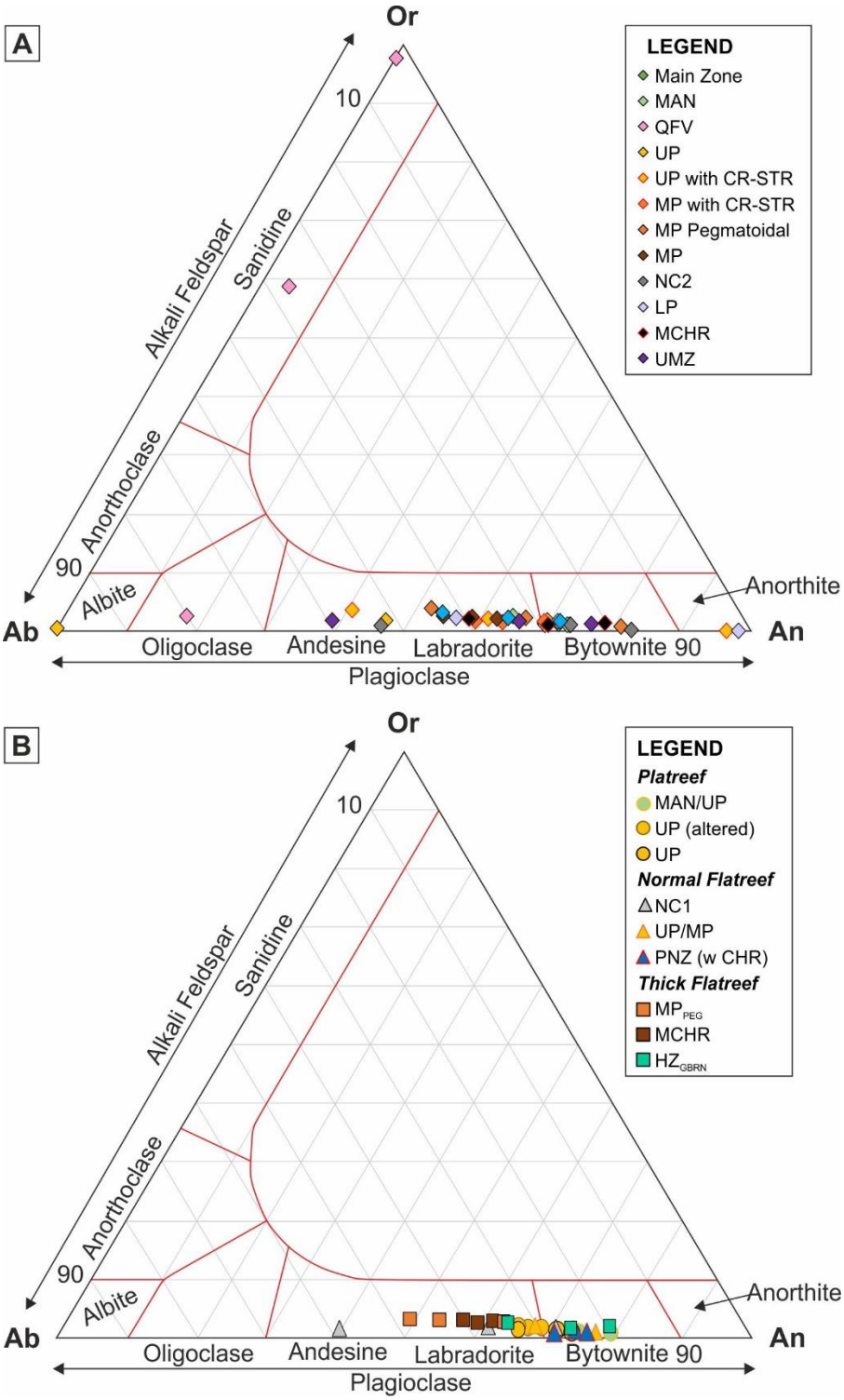

Figure 8.44: Ternary diagram showing the plagioclase compositional data plotted according to stratigraphic unit as identified in: (A) the Deep Platreef and; (B) the combined Flatreef (Normal and Thick facies) and Platreef. Note: the data presented represents the mean, minimum (An) and maximum (An) recorded for each stratigraphic unit.

8.2.2 Downhole Mineral Chemistry Profiles for the Deep Platreef

The variations in the mineral chemistry of the major silicate minerals with depth in the Deep Platreef are shown in Figure 8.45 and Figure 8.46 for drill holes UMT_345 and

UMT_345_D1, respectively. Overall these downhole plots don't demonstrate any systematic trends in mineral composition with changes in stratigraphic height; rather the variability is restricted to intervals where chromite is found. Mg-numbers (Mg# = Mg/(Mg + Fe)) exceeding 80 in orthopyroxene are typically identified in samples containing chromite as expected due to Fe-Mg exchange between the minerals. Similarly, high Mg#(Opx) are reported for the Akanani deposit, $Mg\#_{83-84}$, located along strike and at an equivalent depth (Yudovskaya & Kinnaird, 2010).

All orthopyroxene (n=6) analysed from the Main Zone sample (345_01) returned a consistent $Mg\#_{71}$. This value falls outside the range measured by McDonald & Holwell (2011) of $Mg\#_{60-63}$ on Overysel but corresponds with the range of Lower Main Zone on the eastern and western Bushveld Complex $Mg\#_{62-75}$ (Eales & Cawthorn, 1996; Mitchell, 1990). Orthopyroxene analyses from the underlying Mottled Anorthosite (MAN) unit returned $Mg\#_{65-72}$ with an average of $Mg\#_{68}$ slightly lower than the Main Zone values above; this suggests that the effects of trapped liquid shift was more pronounced in the MAN unit which corresponds to the presence of orthopyroxene as coarse-grained oikocrysts. A similar variability is also recorded in the anorthite content between the Main Zone (An_{70-74}) compared to the MAN unit (An_{65-73}).

The orthopyroxene-dominated lithologies of the Upper (UP), Middle (MP) and Lower (LP) Pyroxenite units have a broadly similar mineral chemistry. The average Mg# of orthopyroxene from these units increases slightly with increasing depth from $Mg\#_{79}$ in the UP to $Mg\#_{82}$ in the MP and LP units; these values are within the range of the orthopyroxene from the Upper Critical Zone (UCZ) $Mg\#_{78-84}$ (Eales & Cawthorn, 1996; Maier & Eales, 1994). The plagioclase is hosted interstitially in these lithologies and as such a wider range in the An content (compared to the orthopyroxene data) is observed. The average An content also broadly increases down hole from the UP to the LP unit with average values of An_{56}, An_{66} and An_{72}, respectively. In the UP and MP units the average anorthite content is below the range as recorded for the UCZ, An_{68-85} (Eales & Cawthorn, 1996; Maier & Eales, 1994). The interstitial assemblage of the UP unit has been affected by the late-stage intrusion of quartz-feldspar veins as outlined above. Similarly, low anorthite values of An_{55} are identified directly south of Turfspruit on the farm Townlands by Manyeruke et al., (2005).

The presence of olivine is restricted to certain stratigraphic intervals, as described previously in section 8.1.1, and shown in the modal abundance plots in Figure 8.45 and 8.46. The composition of olivine was determined from samples of the Middle Pyroxenite (MP; GS9A, GS22A and GS24A), Lower Pyroxenite (LP; 345_08B and

D1_12) and Ultramafic Zone (UMZ; 345_10B, 345_14, D1_16B, D1_17B). The olivine from these stratigraphic units are all magnesian-rich with the range in forsterite content from Fo_{80-86} with an average value of Fo_{81}; this range of data is similar to values obtained from the Akanani project, Fo_{82-83} (Yudovskaya & Kinnaird, 2010) located along strike and at an equivalent depth to the Deep Platreef on Turfspruit. The highest Fo value (Fo_{86}) was obtained from the recrystallised troctolite from the LP unit (as shown in Figure 8.14).

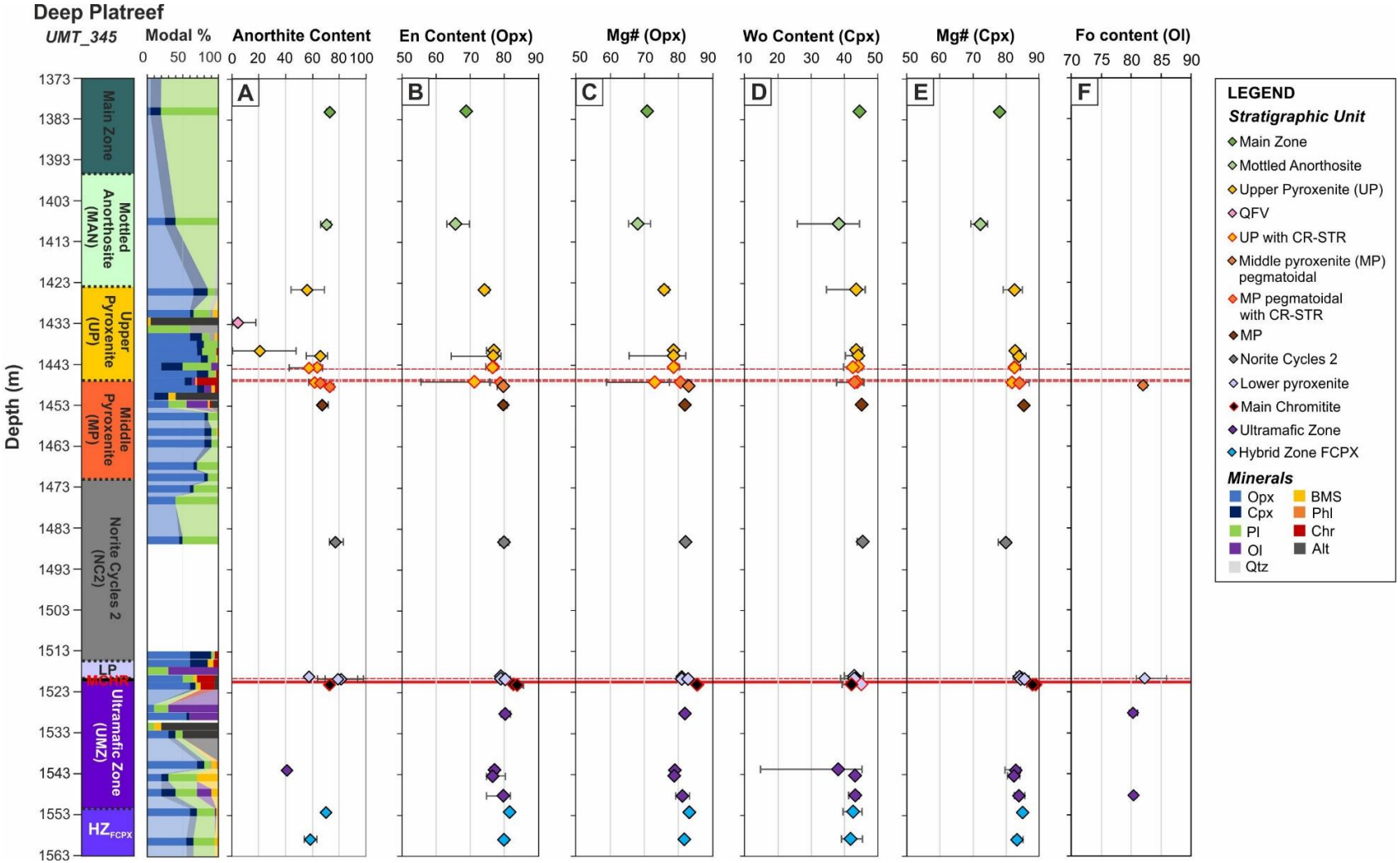

Figure 8.45: Downhole mineral chemistry profiles for the major elements within the Deep Platreef as sampled in drill hole UMT_345. The average mineral compositions for each sample are plotted with error bars depicting the range of values obtained for each sample. (A) An content of plagioclase. (B) En content of orthopyroxene. (C) Mg# of orthopyroxene. (D) Wo content of clinopyroxene. (E) Mg# of clinopyroxene. (F) Fosterite (Fo) content of olivine. Note: Mg# = Mg/(Mg+Fe).

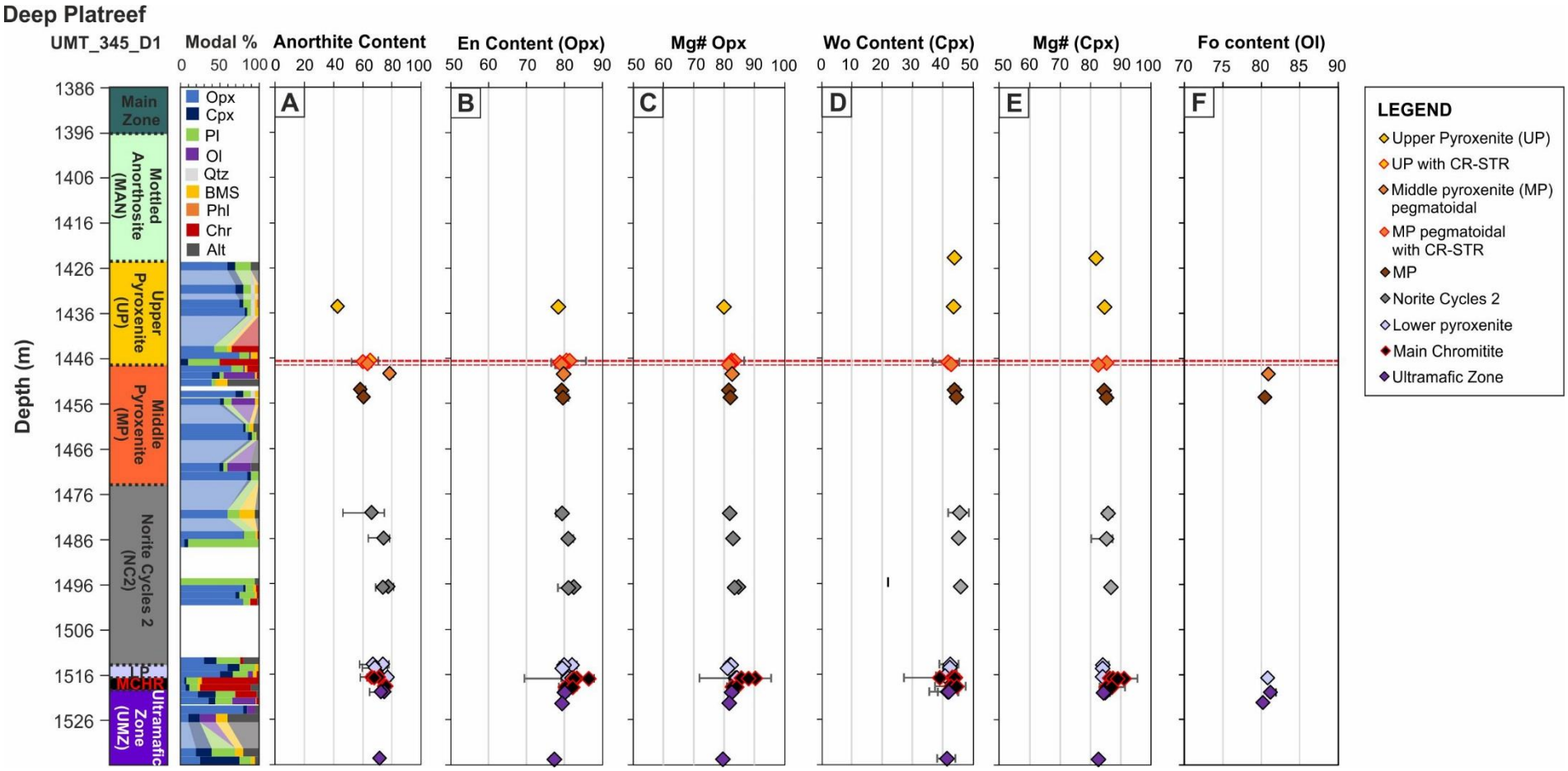

Figure 8.46: Downhole mineral chemistry profiles for the major elements within the Deep Platreef as sampled in drill hole UMT_345_D1. The average mineral compositions for each sample are plotted with error bars depicting the range of values obtained for each sample. (A) An content of plagioclase. (B) En content of orthopyroxene. (C) Mg# of orthopyroxene. (D) Wo content of clinopyroxene. (E) Mg# of clinopyroxene. (F) Forsterite (Fo) content of olivine. Note: Mg# = Mg/(Mg+Fe).

8.2.3 Chromite Chemistry of the Deep Platreef

Chromite grains are identified in a variety of lithological settings within the Deep Platreef including as thin stringers, disseminations, massive seams and on lithological contacts. The chromite chemistry was analysed in 13 samples covering all the different geological settings observed; a summary of the results are shown in Table 8.3.

Table 8.3: Chromite compositions from the various chromite occurrences in the Deep Platreef. Note: data presented as minimum, maximum and (average).

	Sample	Strat Unit	Lithology	Morphology	TiO_2 (wt%)	Cr_2O_3 (wt%)	Al_2O_3 (wt%)	MgO (wt%)
UMT_345	GS8A (n=11)	UP/ MP_{PEG}	Feldspathic orthopyroxenite	4th Cr-STR	0.8-3.9 (2.9)	30.8-35.8 (33.7)	9.1-16.3 (10.8)	3.8-7.3 (5.7)
	GS9A (n=11)	MP_{PEG}	Pegmatoidal olivine orthopyroxenite	Disseminated	0.8-1.6 (1.2)	28.2-34.8 (32.7)	13.9-18.8 (15.7)	4.6-8.1 (6.4)
	345_08A /B	LP	Poikilitic orthopyroxenite	Disseminated	1.2-1.9 (1.5)	25.8-35.5 (33.1)	9.8-14.3 (12.8)	4.5-7.0 (6.0)
UMT_345_D1	GS18A/B (n=24)	UP	Feldspathic orthopyroxenite	3rd Cr-STR	0.7-2.3 (1.5)	40.5 - 44.0 (41.61)	6.8-16.2 (12.4)	2.6-9.1 (6.6)
	GS19A (n=7)	MP_{PEG}	Pegmatoidal feldspathic orthopyroxnite	Disseminated	0.7-2.4 (1.8)	34.0-41.2 (36.6)	10.8-17.9 (13.2)	4.9-7.9 (6.1)
	GS20A (n=7)	UP/MP	Chromite stringer with interstitial plagioclase	4th Cr-STR	2.8-3.8 (3.0)	36.8-38.6 (37.4)	10.5-11.0 (10.8)	6.2-6.4 (6.3)
	GS21A (n=8)	MP_{PEG}	Pegmatoidal olivine orthopyroxenite	Disseminated	0.9-2.3 (2.0)	36.8-41.1 (38.4)	12.1-15.3 (12.7)	6.2-7.2 (7.8)
	D1_08A (n=11)	NC2	On anorthosite/ orthopyroxenite contact	Cr-STR	1.2-2.7 (1.6)	30.0-36.7 (33.3)	7.2-13.5 (11.0)	2.8-6.6 (5.4)
	D1_09CA (n=8)	NC2	On anorthosite/ orthopyroxenite contact	Cr-STR	0.8-1.1 (0.9)	33.6-34.6 (34.0)	15.1-16.0 (15.4)	6.7-7.6 (7.2)
	D1_13 (n=20)	MCHR	Top contact of MCHR unit	Annealed Chromitite	1.2-2.7 (1.6)	33.8-39.5 (36.7)	6.5-16.1 (14.3)	1.8-9.0 (8.2)
	D1_14A (n=27)	MCHR	Middle of the chromitite	Chromitite disseminated	0.8-1.6 (1.0)	37.6-38.8 (38.1)	15.7-16.7 (16.4)	7.9-10.5 (9.1)

The results of the chromite analyses are plotted according to stratigraphy on a ternary diagram in Figure 8.47A relative to fields defined in Barnes & Roeder (2001) from a global database on layered intrusions and chromitites. The majority of the data from this study plots within the boundaries of both of these fields. In Figure 8.47B, the Deep Platreef chromite chemistry is compared to chromite occurrences within the Bushveld Complex including localities along strike and up-dip from Turfspruit within the Platreef and of the exceptionally mineralised stratiform chromite layers of the Merensky Reef and UG2 chromitite (see Figure 8.48C for references).

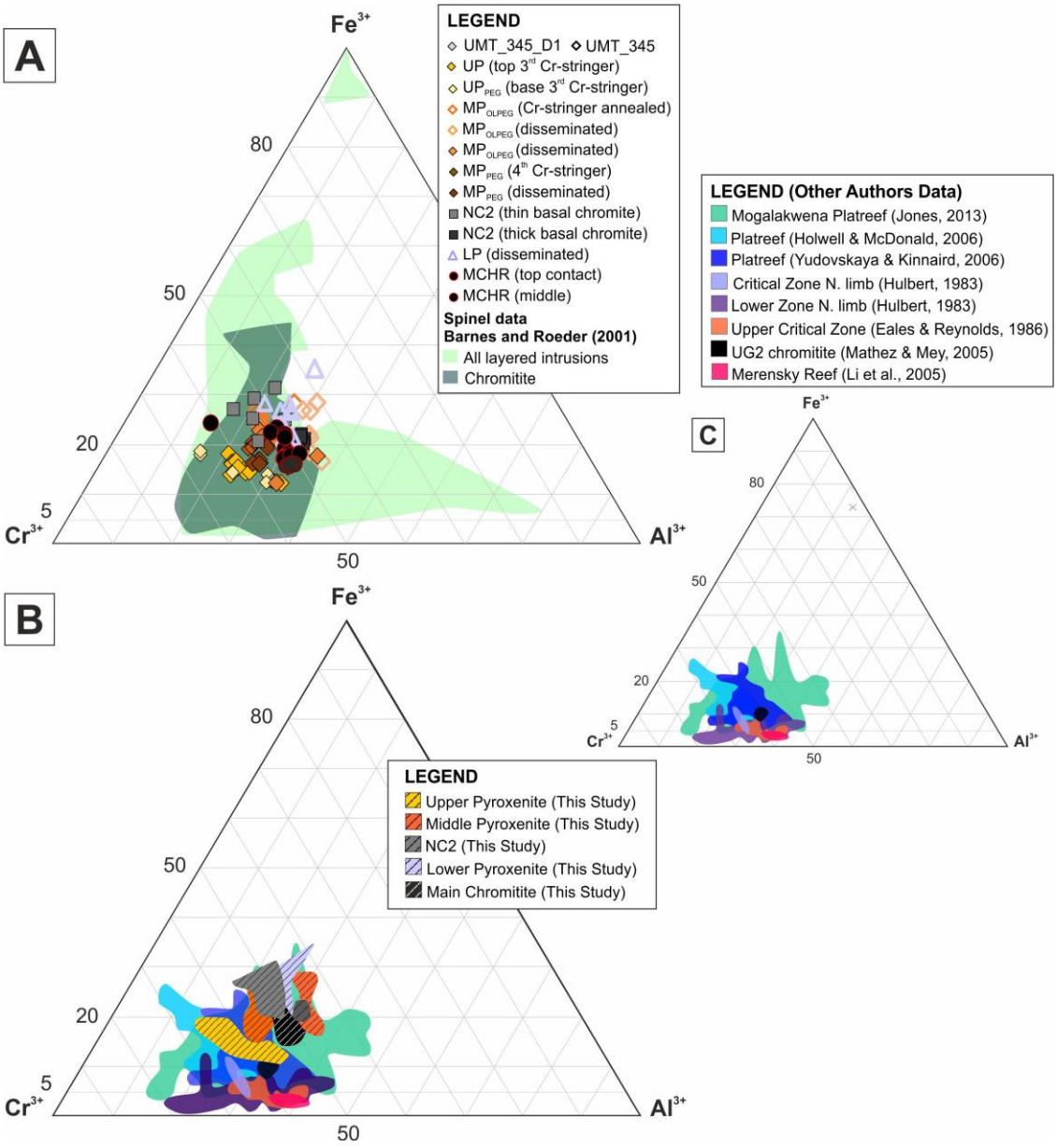

Figure 8.47: Ternary plot showing the chromite chemistry as represented by the trivalent ions Cr-Al-Fe^{3+}. (A) Data collected in the current study is compared to data typical of layered intrusions and chromitites. (B) A comparison of the chromite composition as determined in this study to other localities of the Bushveld Complex. (C) Fields of chromite compositions as analysed in other studies on rocks from the Bushveld Complex, for references see figure.

The chromite compositions analysed in the current study all plot within the range of compositions as recorded along strike in the Platreef analysed in studies by Holwell & McDonald (2006), Yudovskaya & Kinnaird (2010) and Jones (2013). In comparison to the Upper Critical Zone hosted Merensky Reef and UG2 chromitite data the results of this study contain elevated Fe^{3+}. The lowest Fe^{3+} contents (6.43 to 8.77) are recorded in the 3rd chromite stringer (shown by the Upper Pyroxenite field in Figure 8.47B); this value is still significantly elevated above those recorded in the Merensky

reef by Li et al., (2005) of between 1.49 and 1.71 Fe^{3+}. The Middle Pyroxenite data of this study plots in two separate fields as shown in Figure 8.47; the elevated Al^{3+} data are from disseminated chromite occurrences in the pegmatoidal olivine-bearing footwall lithologies of the 4th chromite stringer and the chromite grains within the 4th chromite stringers plot at higher Cr^{3+} values.

The Cr_2O_3 content of chromite grains analysed in this study ranges from 25.8 to 44.0 wt%. The highest Cr_2O_3 value was obtained from the top of the 3rd chromite stringer where the interstitial mineral is plagioclase. The lowest value was measured in the LP unit where the chromite is enclosed in an orthopyroxene oikocryst. The average Cr_2O_3 wt% of the UG2 chromitite is 42.8 wt% (McClaren & DeVilliers, 1982), in comparison the proposed equivalent Main Chromitite (MCHR) unit in the Deep Platreef has an average Cr_2O_3 of 38.1 wt%.

The TiO_2 content of the chromite grains ranges from 0.7 to 3.9 wt% with an average of 1.6 wt%; this range of TiO_2 concentrations is comparable the 0.31 to 4.45 wt% measured in Jones (2013) on chromite grains in the Platreef from Overysel, Sandsloot and Zwartfontein. The highest TiO_2 value was identified in the annealed chromite seam on the contact between the Upper Pyroxenite (UP) and the Middle Pyroxenite (MP). This corresponds to the presence of exsolutions of ilmenite identified in section 8.1.1 (see Figure 8.7). The TiO_2 concentration of the Merensky Reef chromitites as presented in Li et al., (2005) varies from 0.55 to 0.74 wt% significantly lower than the values recorded in the Middle Reef chromite grains in the UP and MP samples. The lowest TiO_2 values are present as disseminated grains in the MCHR unit with an average of 1.0 wt%, this is similar but still elevated above the 0.78 wt% TiO_2 recorded for the UG2 chromitite (McClaren & DeVilliers, 1982).

Chapter 9

Sulphur Isotope Geochemistry

9.0 Introduction

The application of sulphur isotopes has been established in the literature on Ni-Cu-PGE deposits as a very effective means of identifying crustal input into a magma; for an overview see Chapter 2 (section 2.4.2). This is largely because of the significant differences that may be present in the sulphur isotopic compositions between igneous and sedimentary rock types. A narrow range of $\delta^{34}S$ values are expected for igneous rocks, 0 ± 2 ‰, centred on mantle values; whereas crustal rocks can exhibit a wide range in values typically within +/- 50 ‰. The identification of a crustal signature in magmatic rocks raises questions over the timing of sulphur saturation and consequently ore genesis (for more details see Chapter 2 section 2.2.3).

This study presents both mineralogical and bulk rock sulphur isotope data ($\delta^{34}S$ values) from variably contaminated magmatic rocks in drill holes sampling the different sectors of the Turfspruit deposit. The observed stratigraphic variability between the Platreef-Flatreef-Deep Platreef sectors of the orebody are interpreted to result from varying degrees of crustal contamination with the Platreef and Deep Platreef interpreted as representing 'contaminated' and 'magmatic' end-members, respectively. A complimentary sulphur isotope study on the country rocks of the Duitschland Formation (DF) and Pietersburg Greenstone Belt (PGB) was performed on samples collected beyond the contact aureole of the northern limb. A detailed outline of the sample preparation and analytical methodology is presented in Chapter 4 (section 4.5) and Appendix E; further information on the observed stratigraphy and sampling of the DF and PGB are provided in Chapter 6. The location of the samples used in the current study are shown in Figure 9.1 relative to the logged stratigraphy of the drill holes under investigation. The main objectives of this sulphur isotope study are as follows: (1) to determine the variability in sulphur isotope composition across the Turfspruit licence area; (2) to characterise the isotopic signature of the stratigraphic units with individual drill holes; (3) to establish 'unaltered' end-member values for both the shales and carbonate lithologies of the footwall; (4) establish the S isotope signature of the basement rocks. It is hoped that the results will enable a semi-quantitative assessment on the degree and timing of crustal contamination and its role in either ore genesis or modification.

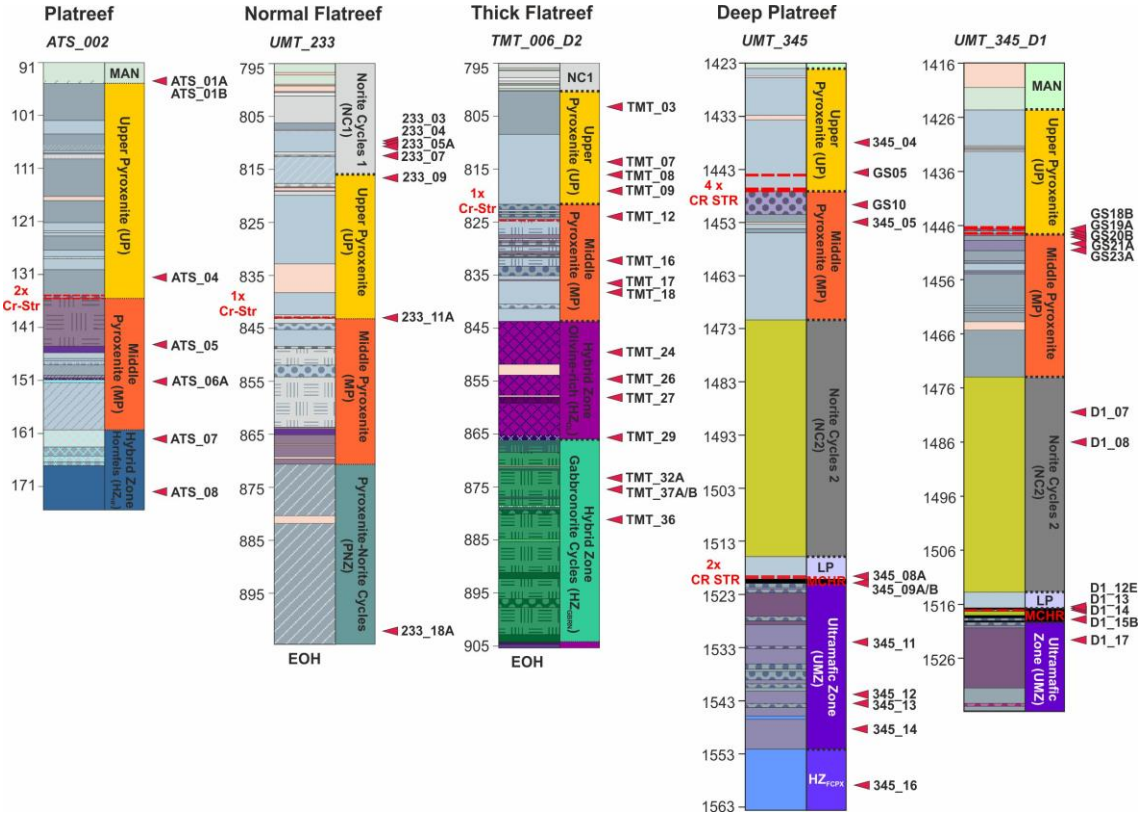

Figure 9.1: Stratigraphic logs of the drill holes under investigation with the location of samples analysed for their sulphur isotope compositions highlighted.

9.1 Sulphur Isotope Results

The results of 145 laser and conventional S isotope analyses on 71 samples from across the Turfspruit deposit and associated country rocks are summarised in Figure 9.2. A full list of the results is provided in Appendix E. The sulphide minerals analysed include pyrrhotite, pentlandite, chalcopyrite, cubanite and pyrite; in addition to bulk rock sulphur extracted as Ag_2S from whole-rock samples.

The magmatic rocks as sampled in drill holes across the project area show a zonal variation in the distribution of S isotopic compositions. The Flatreef drill holes have average $\delta^{34}S$ values on the upper limit of the magmatic range +2.0 ‰ (UMT_233) and +2.2 ‰ (TMT_006_D2). In contrast, the average $\delta^{34}S$ values for the Platreef and Deep Platreef are significantly elevated above the mantle range at +10.2 ‰ and +5.2 ‰, respectively.

The restricted amount of data shown in Figure 9.2 for the country rock samples reflects the low S concentrations contained within these rocks and the difficulty encountered in isolating S from whole rock samples. The bulk rock S extraction method used in this study only recovers chromium reducible sulphur (CRS; for details on the method see Appendix E). This means that any S present in the rocks as

sulphate, carbonate associated sulphur (CAS), was not recovered and this restricts the ability of this study to fully characterise the S isotope signature of the Duitschland Formation. Furthermore, upon analysis some of the PGB samples were identified as having been contaminated with organic material, introduced during the S extraction process (for details see Appendix E); consequently, the data collected for these samples has been classified as invalid (as such they are excluded from Figure 9.2).

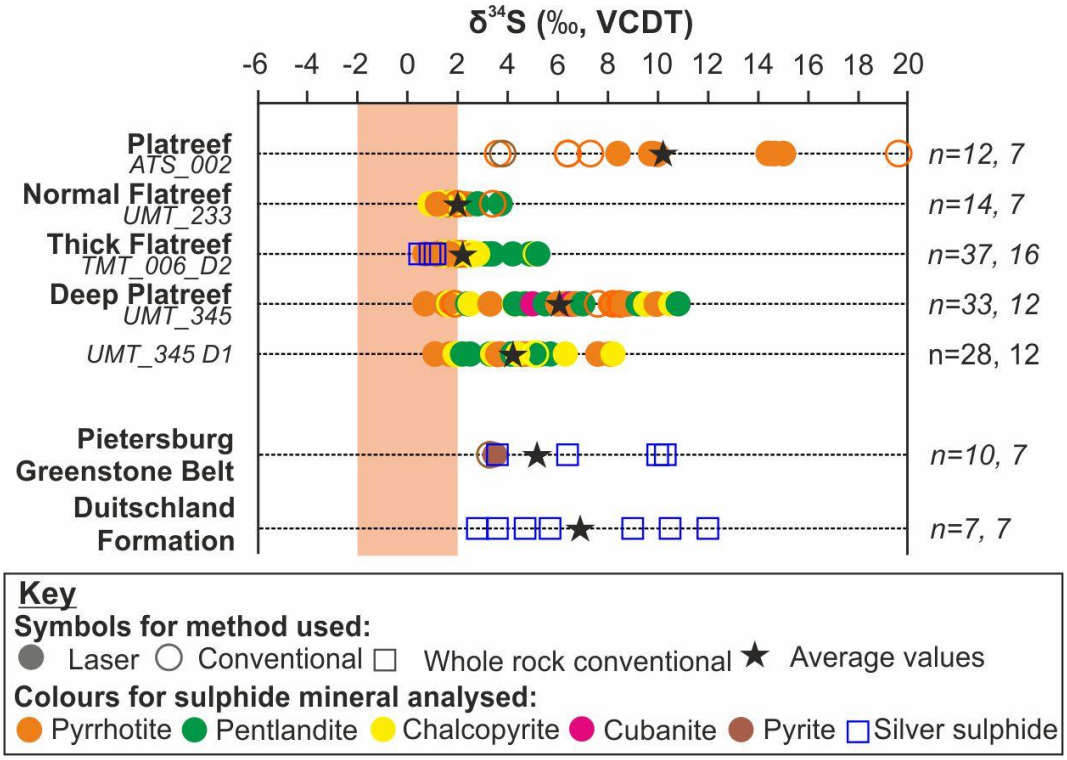

Figure 9.2: A summary of all the $\delta^{34}S$ isotope data collected as part of the current study. Note: n is for count with the #analyses followed by the #samples. Orange region indicates the magmatic range of $\delta^{34}S$ values. Symbols denote the analytical method used: filled in circles are laser analyses, open circles are conventional analyses on drilled out sulphides and open squares are whole-rock conventional analyses on sulphides prepared as silver sulphide.

All sulphides analysed returned positive $\delta^{34}S$ values with no negative results obtained (see Figure 9.2 and Figure 9.3); the sulphur isotope signature at the Turfspruit locality is therefore characterised by +ve $\delta^{34}S$ values. A summary of the statistics of the sulphur isotope data are provided in Figure 9.3 and Table 9.1. The largest range in $\delta^{34}S$ values (16 ‰) was identified in the samples analysed from the Platreef (ATS_002; see Figure 9.2 and Table 9.1). The heaviest $\delta^{34}S$ value recorded, +19.6 ‰, is higher than any $\delta^{34}S$ value obtained for the crustal rocks of either the PGB or the Duitschland Formation as analysed in the current study. The narrowest range of $\delta^{34}S$ values are identified in the drill holes that intersect the Flatreef deposit (see Figure 9.3 and Table 9.1); this is interesting because these two drill holes show significant differences in their relative S concentrations and in the observed

stratigraphy (see Figure 9.1). The Deep Platreef, (UMT_345 and UMT_345_D1) has an intermediate range of 10.1 ‰; this is unexpected considering that the logged stratigraphy has been interpreted as hosting essentially primary magmatic sulphide mineralisation in stratiform layers.

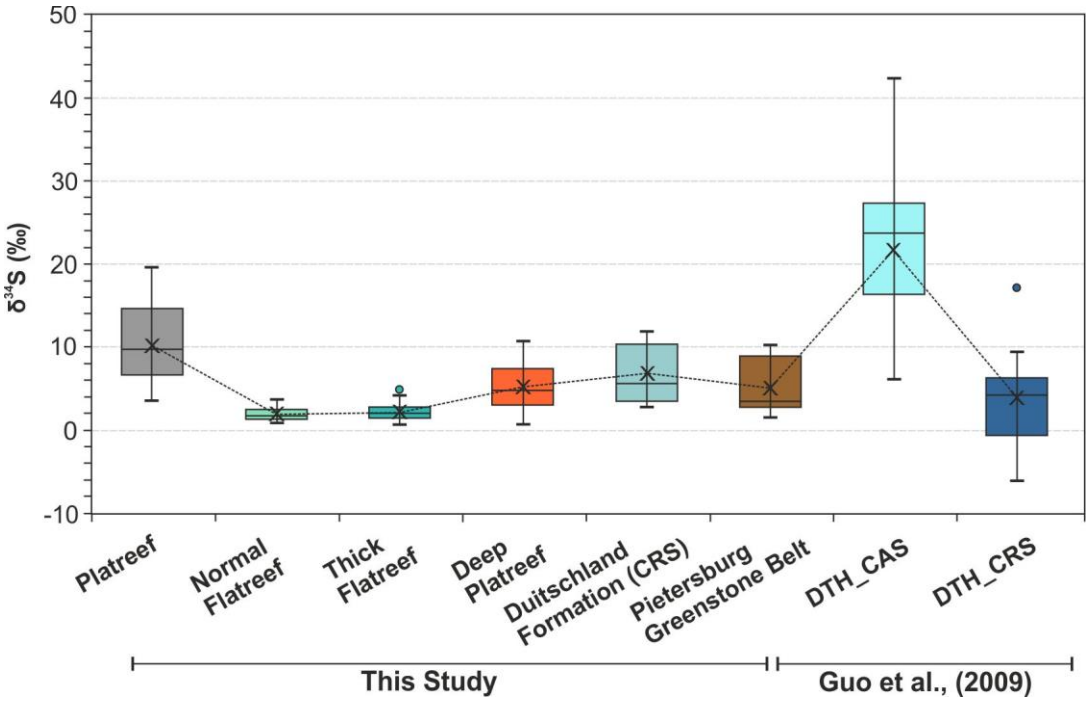

Figure 9.3: Box and whisker plot comparing the statistics of the $\delta^{34}S$ values recorded for the Turfspruit igneous rocks and country rocks. Note: the horizontal line within each box represents the median, the X represents the mean, the base of the box is positioned on the median of the 1st quartile, the top of the box is positioned on the median of the 3rd quartile and the vertical lines extend to the minimum and maximum values. Note: DTH – Duitschland, CRS – chromium reducible sulphide and CAS – carbonate associated sulphur.

Table 9.1: Statistical analysis of $\delta^{34}S$ values grouped according to their location within the Turfspruit deposit.

	Min	*Max*	*Range*	*Average*	*Std.dev*	*Count #Analyses*	*Count #Samples*
Deep Platreef	0.7	10.8	10.1	5.2	2.6	61	24
Thick Flatreef	0.5	5.2	4.7	2.2	1.1	50	18
Normal Flatreef	0.9	3.7	2.8	2.0	0.8	14	7
Platreef	3.6	19.6	16.0	10.2	4.7	12	7

A comparison of the results of the current study (Figure 9.4B) with that of previous S isotope studies on Turfspruit (Figure 9.4A) show that the current dataset is skewed to more magmatic values than have been previously identified at Turfspruit. The Platreef sulphides analysed in this study contain $\delta^{34}S$ values within the range reported by Sharman-Harris et al., (2005) and Sharman et al., (2013). The Flatreef samples

analysed in this study extend the range of measured $\delta^{34}S$ values to more magmatic and contaminated values compared to the limited study by Yudovskaya et al., (2017a). There is no comparative study on a Deep Platreef drill hole, however the range of $\delta^{34}S$ values observed are similar to the combined range of the Flatreef and Lower Zone rocks as analysed by Yudovskaya et al., (2017a). Lower Zone rocks were not identified in the Deep Platreef drill hole logged in the current study.

In Figure 9.4C, the country rock data on the Duitschland Formation (DF) and the Pietersburg Greenstone Belt (PGB) are plotted and supplemented by data from a more extensive study by Guo et al., (2009). The database collected by Guo et al., (2009) includes carbonate associated sulphur (CAS) data, a reservoir of S in the country rocks not analysed in this study. The addition of this data was necessary because none of the samples analysed in this study (chromium reducible sulphide, CRS) recorded heavy enough values to account for those obtained within the Platreef drill hole. The results of the Guo et al., (2009) study reveal a sharp jump to $\delta^{34}S$ enriched values (+11.8 to +42.3 ‰) at 700 m above the base of the DF. This is hinted at in the data collected in this study with dolomites from the upper part of the Duitschland stratigraphy containing sulphides up to +11.9 ‰; the heaviest $\delta^{34}S$ values i.e. > +12 ‰ must be contained in the sulphate component of the DF.

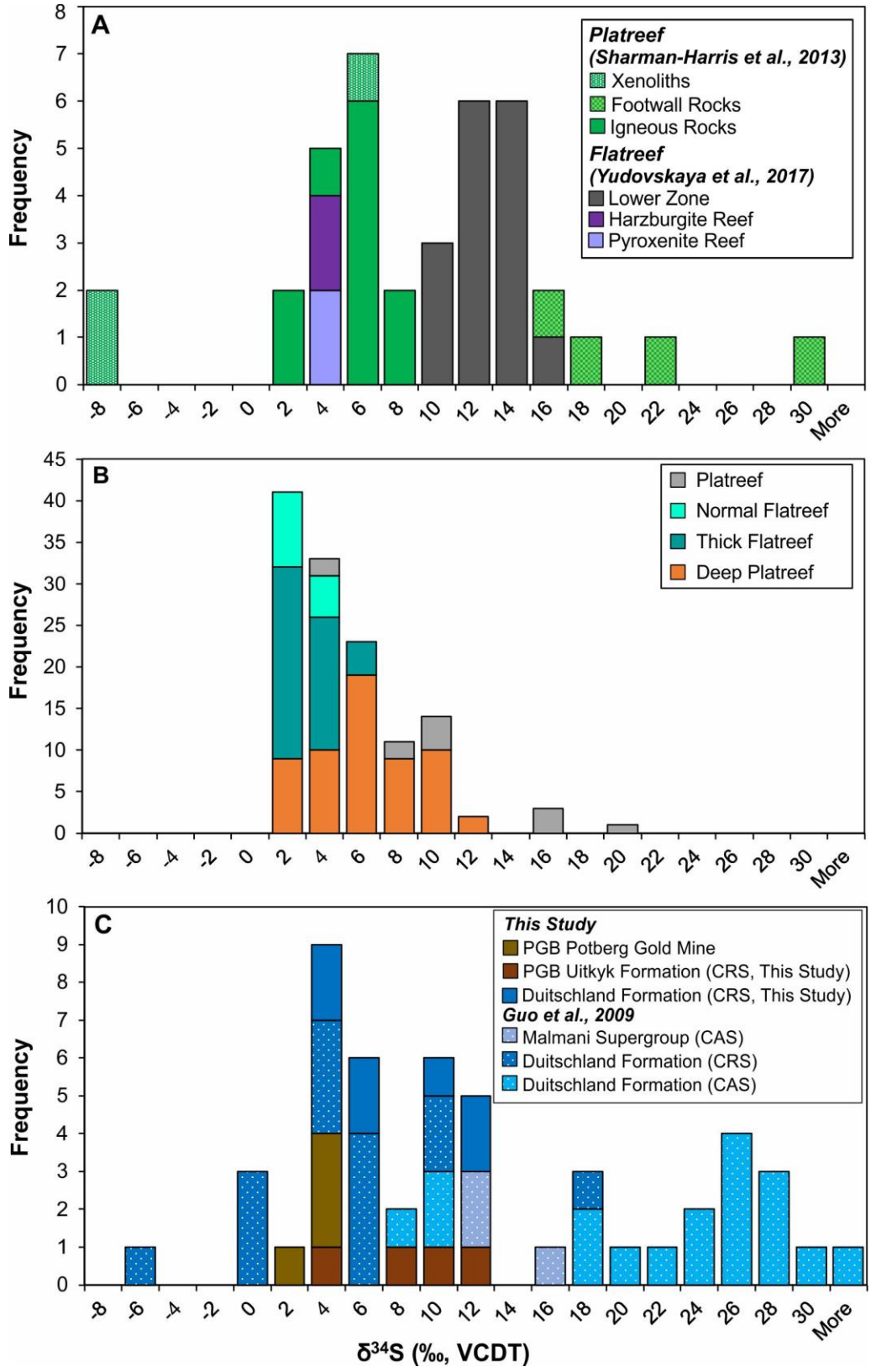

Figure 9.4: Histograms comparing the results of the current sulphur isotope study with previous studies at the Turfspruit locality and on the Duitschland Formation. (A) A histogram showing the range of sulphur isotope compositions for the Platreef and Flatreef on Turfspruit as measured in previous S isotope studies at this location, for references see image. (B) A histogram highlighting the zonal variability in sulphur isotopic compositions between the

different sectors of the orebody as collected in the current study from across the Turfspruit deposit. (C) The range in country rock sulphur isotopic compositions for the Duitschland Formation and PGB, see reference in image.

9.1.1 Footwall and Basement Rocks

The Duitschland Formation (DF) samples analysed in this study record heavy $\delta^{34}S$ values (see Figure 9.4C). The heaviest $\delta^{34}S$ value, +11.9 ‰ was identified in copper-oxide stained dolomite from the carbonate-dominated Upper DF. Pyrite in the shales from the Lower DF have a range of $\delta^{34}S$ values from +2.7 to +4.6 ‰. These values are lower than the $\delta^{34}S$ value of +8.2 ‰ recorded for the pyritic shales by Sharman-Harris et al., (2005). In summary, the 'Upper' carbonate-dominated sequence of the DF typically contains $\delta^{34}S$ values >10 ‰ and the 'Lower' shale-dominated sequence is characterised by $\delta^{34}S$ values <10 ‰; as shown in Figure 9.5 below plotted using Guo et al., (2009) data and further supported by the findings in the current study.

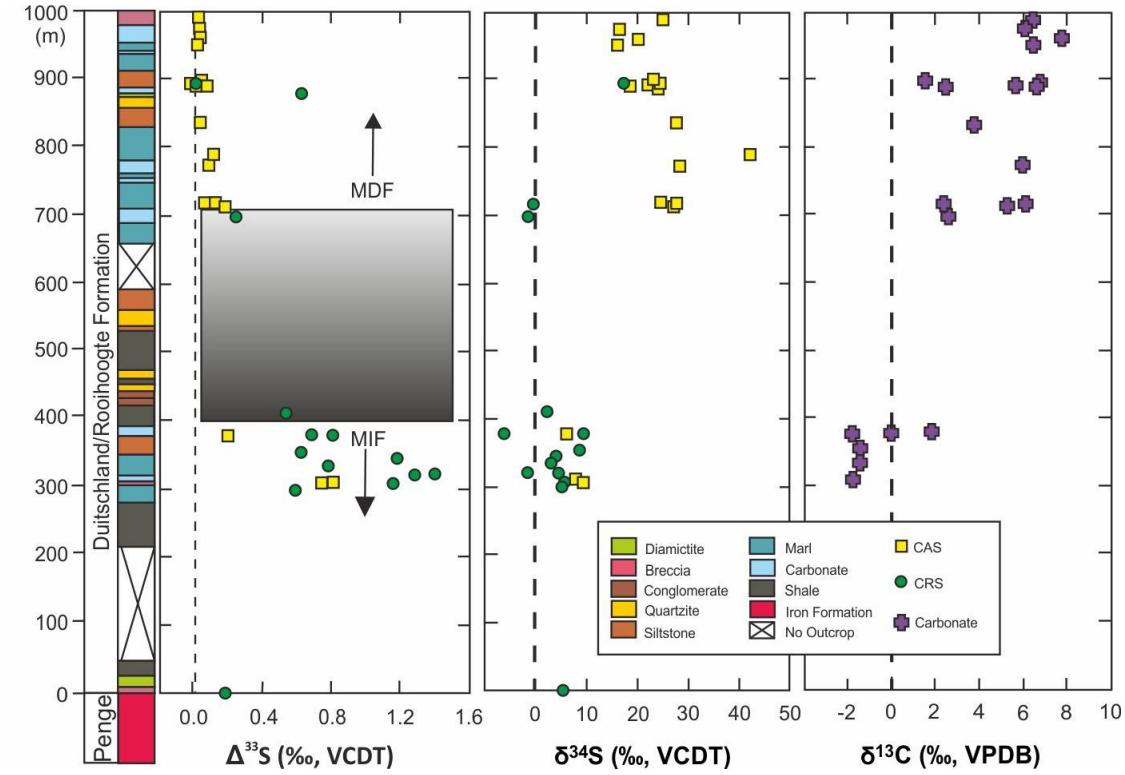

Figure 9.5: Isotopic profiles of $\Delta^{33}S$, $\delta^{34}S$ and $\delta^{13}C$ plotted against the Duitschland Formation stratigraphy. Modified after Guo et al., (2009).

The Pietersburg Greenstone Belt (PGB) samples also record heavy $\delta^{34}S$ values of +6.3‰ for a metavolcanic sample from the Uitkyk Formation and +1.5 to +3.4‰ in pyrite grains from the mineralised metaconglomerate at the Potberg mine locality. There are no other S-isotope databases on the PGB rocks so these values cannot be compared to other studies, however as the PGB rocks are older than 2.47 Ga they are expected to have $\delta^{34}S$ values in the range of 0 ± 5 ‰.

The sulphur isotopic composition of the PGB is indistinguishable from that of the Duitschland Formation sediments; the variability of the isotopic signature observed within the analysed magmatic rocks is best accounted for via in situ contamination from the Duitschland Formation. Any input from the PGB would have taken place at depth resulting in a more homogenous contamination signature. In order to asses any role of the PGB in triggering S saturation at an early stage within a staging chamber one would need to adopt a multiple sulphur isotope approach with the determination of mass-independent values of $\Delta^{33}S$ to supplement mass-dependent $\delta^{34}S$ values. The PGB is old enough (>2.45 Ga) to record non-zero $\Delta^{33}S$ values; a multiple isotope studies on the Platreef by Sharman et al., (2013) have shown that a non-zero $\Delta^{33}S$ signature is preserved at Turfspruit ($\Delta^{33}S$ 0.17 to 0.58 ‰). In Sharman et al., (2013) the non-zero $\Delta^{33}S$ values are interpreted to derive from pre-emplacement into the Lower DF, however the PGB represents another potential source of crustal S contamination and there is no available $\Delta^{33}S$ data to rule this out.

9.1.2 Downhole Sulphur Isotope Profiles

The $\delta^{34}S$ values measured in this study for drill holes across the Turfspruit project area are plotted with depth in Figure 9.6 in order to assess the effects of changes in stratigraphic height on the isotopic composition. There are distinct trends observed in the different drill holes, these are described below.

The Platreef profile, shown in Figure 9.6, records a gradual decrease in $\delta^{34}S$ values from the top of the Upper Pyroxenite (+14.4 ‰) unit to the base of the Middle Pyroxenite unit before returning to heavy $\delta^{34}S$ values at the base of the logged interval. Moving from the top contact downhole the change in sulphur isotope signature is more gradual decreasing by 11.4 ‰ over an interval of 67 m; in contrast moving from the base upwards the decrease in sulphur isotope values by 16 ‰ occurs over a much smaller interval of 10 m. This suggests that the majority of the Platreef has been affected by the roof contamination event, assuming diffusive mass transfer of S from the wall rocks to intrusion. Contaminated isotopic signatures at the base of the Platreef have been observed in other studies on the Platreef by Penniston-Dorland et al., (2008) and Sharman-Harris et al., (2005). This is the first time that heavy non-magmatic $\delta^{34}S$ values (+14.4 to +15 ‰) have been recorded on the top contact of the Platreef. This finding contradicts the conclusion of Sharman-Harris et al., (2005) that contaminated isotopic signatures within the Platreef decrease steadily moving away from the floor contact. It also supports the idea that the roof of the Platreef was originally composed of Transvaal Supergroup sediments prior to the intrusion of the Main Zone.

The two Flatreef drill holes shown in Figure 9.6 display remarkable uniformity with only minor positive deviations (up to +5.2 ‰) from magmatic values suggesting that there is no lithological control on the S isotope values.

The $\delta^{34}S$ profile for the Deep Platreef samples shows increasing isotopic composition with depth (see Figure 9.6). This overall trend is disrupted by several positive fluctuations at restricted stratigraphic intervals. The first positive shift to elevated $\delta^{34}S$ values +3.4 to +5.1 ‰, occurs between 1440 and 1460 m. This depth corresponds to the first appearance of chromite stringers and olivine-bearing lithologies relating to the Middle Reef mineralisation event. In drill hole UMT_345_D1 sample D1_08A from the Norite Cycles 2 unit (NC2) also records heavy $\delta^{34}S$ values of +7.2 to +7.7 ‰ from a feldspathic orthopyroxenite at the base of a norite cycle. This is surprising as these 'magmatic' cycles preserve a typical fractionated sequence of chromite stringer-pyroxenite-norite-anorthosite and should contain magmatic sulphides. From the level of 1520 m downwards there is a systematic increase in the $\delta^{34}S$ values with depth.

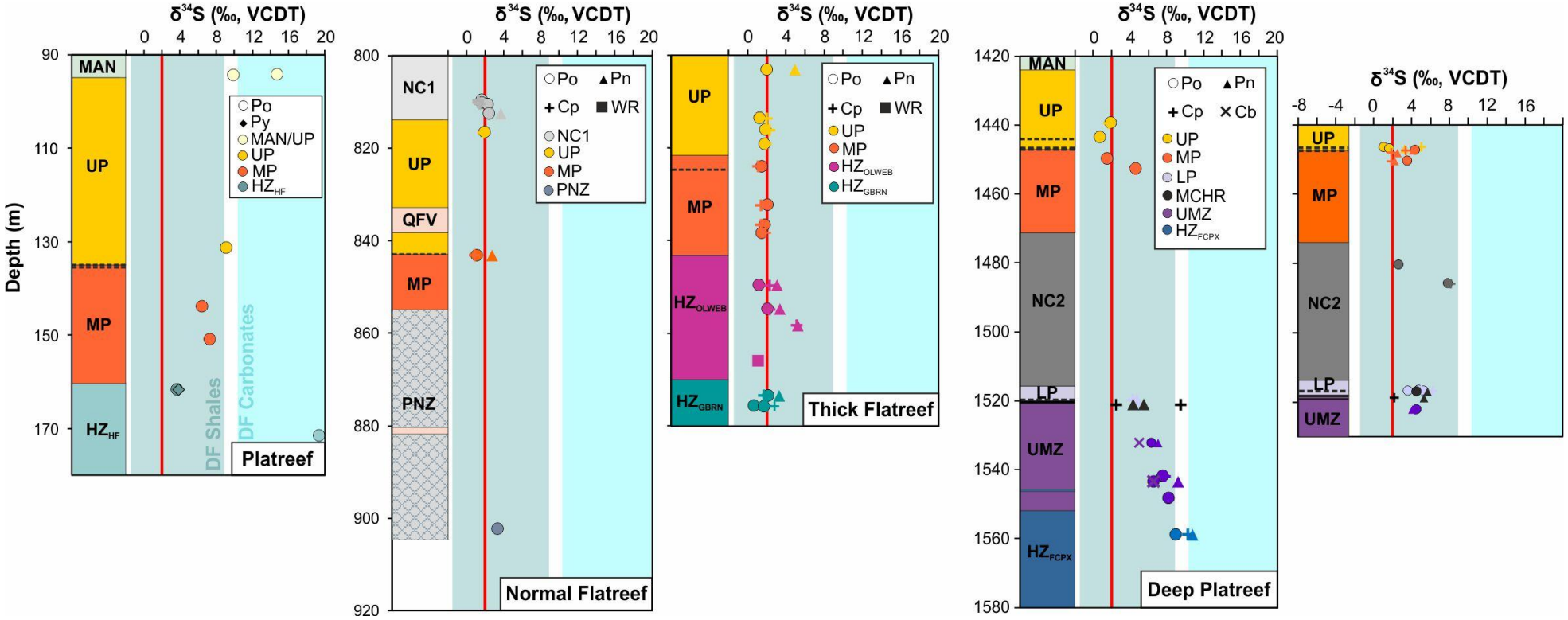

Figure 9.6: Downhole $\delta^{34}S$ isotope profiles for all drill holes across the Turfspruit project area. From left to right: the Platreef (ATS_002), Normal Flatreef (UMT_233), Thick Flatreef (TMT_006_D2) and the Deep Platreef (UMT_345 and UMT_345_D1). Note: the shaded dark green and light blue fields represent the range of $\delta^{34}S$ values for the shale- and carbonate-dominated lithlogies in the Duitschland Formation (DF), respectively.

9.1.3 Platreef (ATS_002)

Sulphides analysed from the Platreef all contain $\delta^{34}S$ values that are consistently and significantly heavier than the mantle range (± 0 to 2 ‰) with a mean value of +10.23 ‰. The sulphide assemblage is dominated by pyrrhotite (>95 vol%) with minor pentlandite, chalcopyrite and pyrite. Texturally, pyrrhotite exhibits a range of morphologies including net-textured, interstitial, massive and blebby (examples are shown in Figure 9.7). Pentlandite and chalcopyrite typically form on the edges of the pyrrhotite in contact with the surrounding silicates; whereas pyrite (identified only in one sample) is found as euhedral grains within massive pyrrhotite (see Figure 9.7E). This sulphide assemblage is unique to this drill hole; in all other drill holes studied pyrrhotite, pentlandite and chalcopyrite are more evenly distributed.

The heaviest $\delta^{34}S$ values were obtained in sample ATS_08 at +19.6 ‰ in a foliated hornfels from the Hybrid Zone (HZ_{HF}) at the end of the logged interval (see Figure 9.6). This expands the highest range of hornfels values at Turfspruit as previously identified at +18.1 ‰ (Sharman et al., 2013). The massive pyrrhotite analysed is rimmed by magnetite and no other sulphide mineral phases are present (see Figure 9.7F); this mineralogical feature is also observed in sample ATS_01A (see Figure 9.7A), located at the top of the Upper Pyroxenite (UP) unit, recording the second heaviest $\delta^{34}S$ values of +15 ‰. Moving 4 cm downhole the sulphides are medium-grained interstitial and closely associated with ilmenite and apatite; they are still dominated by pyrrhotite with heavy $\delta^{34}S$ values of +9.8 ‰ containing some flame exsolutions of pentlandite (see Figure 9.7B). Towards the base of the UP unit and hosted in a quartz- and apatite-bearing feldspathic orthopyroxenite net-textured, pyrrhotite-dominated sulphides records only slightly lighter values of +8.4 ‰ (see Figure 9.7C). In the mineralised harzburgite of the Middle Pyroxenite (MP) unit the sulphides are present as coarse-grained blebs consisting of a pyrrhotite core with a blocky pentlandite rim (see Figure 9.7D); despite being mineralised these sulphides still record a heavy contaminated signature ranging from +6.4 to +7.3 ‰ (combined Po and Pn). The lightest values in the Platreef samples were obtained from a massive sulphide in the hornfels Hybrid Zone (HZ_{HF}) with values of +3.6 ‰ pyrrhotite and +3.8 ‰ pyrite in sample ATS_07 (see Figure 9.7E).

Many of the mineralogical features observed in samples from this drill hole are also recorded by Holwell et al., (2007) in parts of the reef and footwall that have experienced extensive fluid interaction including; less consistent sulphide textures, lack of well-defined phase zonation and the development of magnetite in close association with sulphides. However, the sulphides analysed in Holwell et al., (2007) don't contain the same heavy $\delta^{34}S$ signature and it is suggested that the presence of fine-grained calcite

and apatite in the host rock indicates the presence of a carbonate and chlorine-rich fluid derived from the de-volatisation and melting of the Duitschland Fomation sediments.

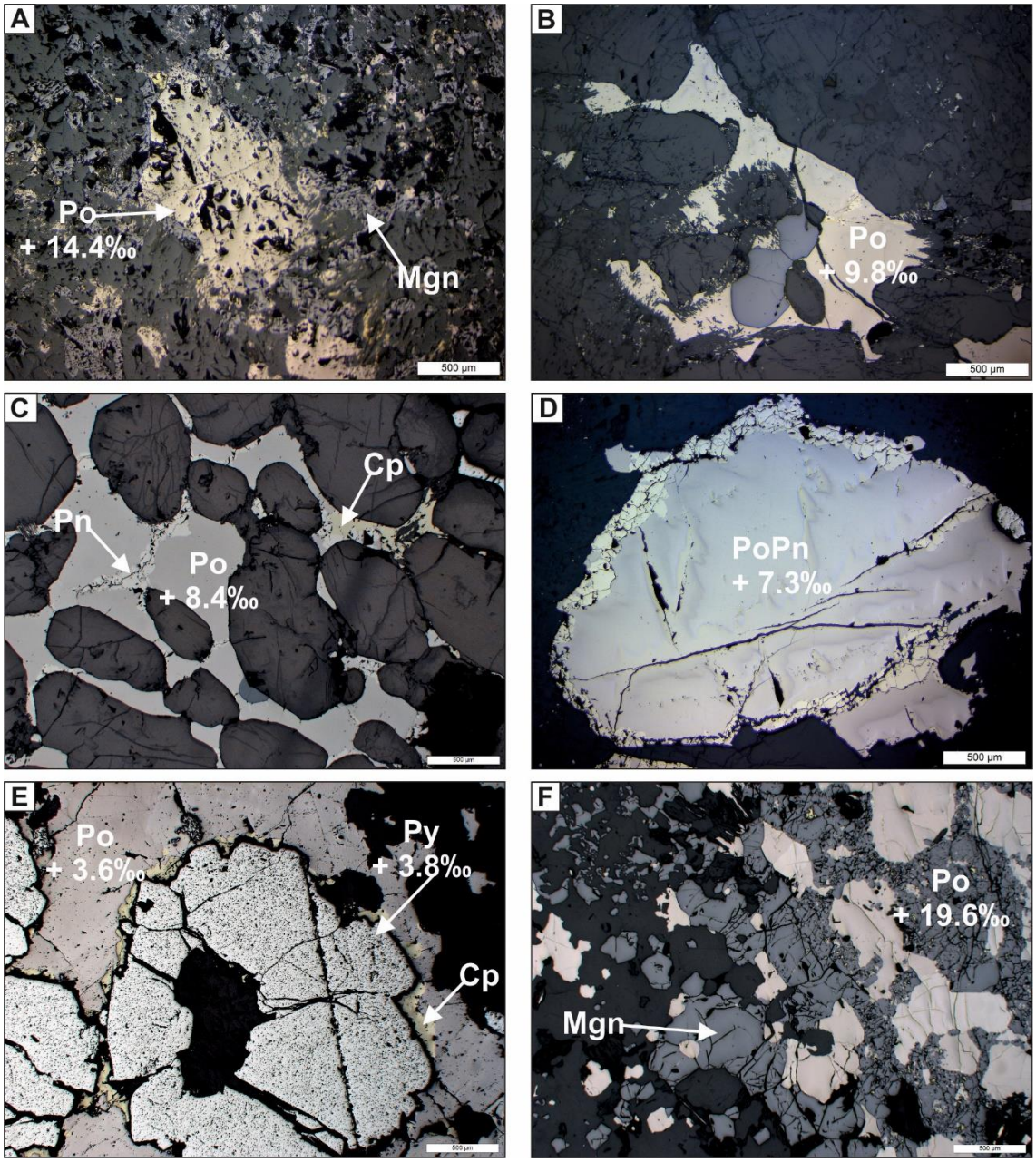

Figure 9.7: Reflected light images showing the composition and morphology of sulphides analysed for their isotopic composition in the Platreef (ATS_002). (A) ATS_01A; medium-grained Po dominated sulphides with a rim of magnetite. (B) ATS_01B; medium-grained Po-rich sulphide. (C) ATS_04; net-textured Po with minor Pn and Cp interstitial to rounded orthopyroxene grains. (D) ATS_06; medium grained Po-dominated sulphide with Pn as a rim. (E) ATS_07; massive Po-dominated sulphide with subhedral Py with Cp on the rim. (F) ATS_08; massive Po-dominated sulphide with extensive magnetite crystallisation on the edges. Note: Po, pyrrhotite; Pn, pentlandite; Cp, chalcopyrite; Py, pyrite; Mgn, magnetite.

9.1.4 Flatreef (UMT_233 and TMT_006_D2)

The Flatreef demonstrate significantly less isotopic variation than observed in the Platreef (see Figure 9.5); 64% of the analysed samples containing a magmatic isotopic

composition. The two drill holes studied sample the Normal (UMT_233) and Thick Flatreef (TMT_006_D2) which have notable geochemical and mineralogical differences as outlined in previous chapters (7 and 8). The sulphur isotopes do not reflect this heterogeneity suggesting that processes affecting the composition of the rocks are acting independently of the sulphides.

The PGE mineralised Norite Cycle 1 (NC1) and Middle Pyroxenite (MP) units of the Normal Flatreef, preserved in the top section of UMT_233, contains sulphides with $\delta^{34}S$ values ranging from +1.3 to +3.7 ‰; examples of sulphides analysed from these units are shown in Figure 9.8A to 9.8C.

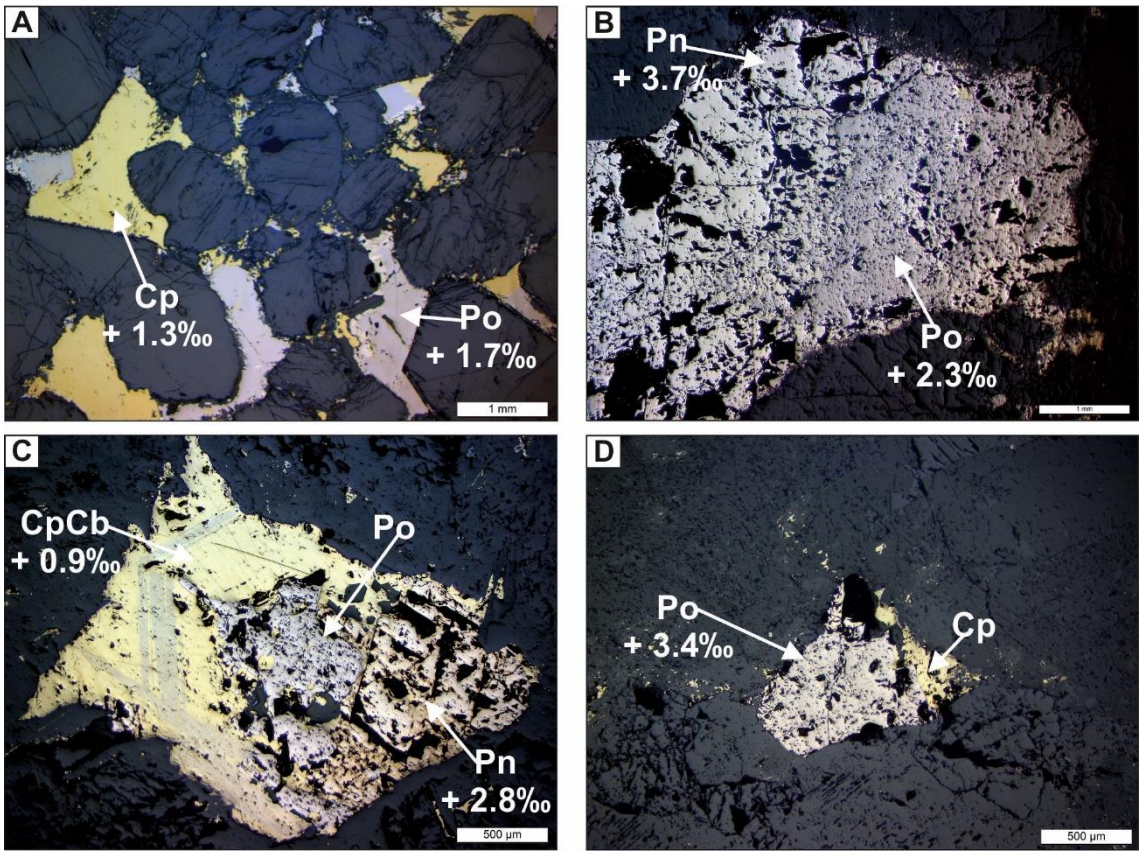

Figure 9.8: Reflected light images showing the composition and morphology of sulphides analysed for their isotopic composition in the Normal Flatreef (UMT_233). (A) 233_04; Po and Cp rich with minor Pn interstitial sulphides. (B) 233_07; blocky Pn- and Po coarse-grained sulphide. (C) 233_11A; medium-grained sulphide dominated by Cp (with lamellae of Cb) with blocky Pn and minor Po. (D) 233_18A; fine-grained bleb of Po sulphide with minor Cp on edge. Note: Po, pyrrhotite; Pn, pentlandite; Cp, chalcopyrite; Cb, cubanite.

The sulphide assemblage at this location is characterised by medium-grained, interstitial pyrrhotite, pentlandite and chalcopyrite in approximately equal proportions; cubanite is observed as lamellae in chalcopyrite in the MP unit where chromite present (see Figure 9.8C). This represents a typical high temperature primary magmatic sulphide assemblage with only minor evidence of alteration on the sulphide/silicate contact. The

heaviest $\delta^{34}S$ value (+ 3.7 ‰) falls outside the magmatic range was identified in a sample with a pegmatoidal silicate assemblage and the sulphide is dominated by blocky pentlandite indicative that it cooled slowly. Towards the base of the drill hole, a chromite-rich interval within the pyroxenite-norite zone (PNZ) hosts sulphides with slightly elevated values of +3.4 ‰ (see Figure 9.8D). In this unit the sulphide assemblage is dominated by fine to medium-fine grained (<1 to 3 mm) sulphides consisting of pyrrhotite (50 vol%), chalcopyrite (30 vol%) and pentlandite (20 vol%).

The Thick Flatreef, sampled in drill hole TMT_006, records a transition with depth from relatively pristine pyroxenites in the upper part of the stratigraphy, the Upper (UP) and Middle Pyroxenite (MP) units, to a texturally and compositionally heterogenous Olivine Websterite (HZ_{OLWEBS}) and Gabbronorite Hybrid Zone (HZ_{GBRN}) in the lower portion (see Figure 9.1). This transition as observed petrologically is not translated into any significant variations in the sulphur isotope compositions recorded. In all stratigraphic units the heaviest $\delta^{34}S$ values are recorded consistently in pentlandite, this variation between coexisting sulphides ranges from + 0.1 to +2.9 ‰; this disequilibrium is indicative of isotopic fractionation between coexisting sulphide minerals possibly at quite low temperatures (Thode, 1970).

The UP and MP units contains nearly uninterrupted grade and elevated S concentrations (5 to 20 vol %) over a 44m interval. In the UP unit the majority (75%) of the values record a magmatic signature with an average value of +2.3 ‰. One sample with a slightly elevated value for blocky pentlandite at +4.9 ‰ (see Figure 9.9A) was identified on the top contact of the UP with the Norite Cycle unit (NC1). The silicate assemblage of the MP unit is coarser-grained than the UP unit and frequently pegmatoidal; this increase in grain size is reflected in the sulphide assemblage. Four samples analysed from the MP unit contain $\delta^{34}S$ values from +1.1 to +2.1 ‰ (see Figure 9.9B and 9.9C).

The range of $\delta^{34}S$ values obtained for the contaminated HZ_{OLWEBS} is wider (+0.9 to +5.2 ‰) than those recorded in the relative fresh pyroxenite units. The lithologies present in this unit show variable degrees of alteration by either amphibole-rich (see Figure 9.9D) or serpentinising fluids (see Figure 9.9E). The $\delta^{34}S$ composition of a sample proposed to represent metamorphosed country rock was tested and returned a magmatic value of +0.9 to +1.1 ‰.

The sulphides within the HZ_{GBRN}, are heterogeneously distributed and often form massive accumulations. The sulphides are dominated pyrrhotite (50 vol%), pentlandite (25 vol%) and chalcopyrite (25 vol%) with only minor amphibole alteration on the edges of the

sulphides (see Figure 9.8F). The $\delta^{34}S$ values range from between +0.7 to +4.2 ‰; pentlandite is observed to contain consistently heavier $\delta^{34}S$ values (see Figure 9.9A, 9.9D, 9.9E and 9.9F).

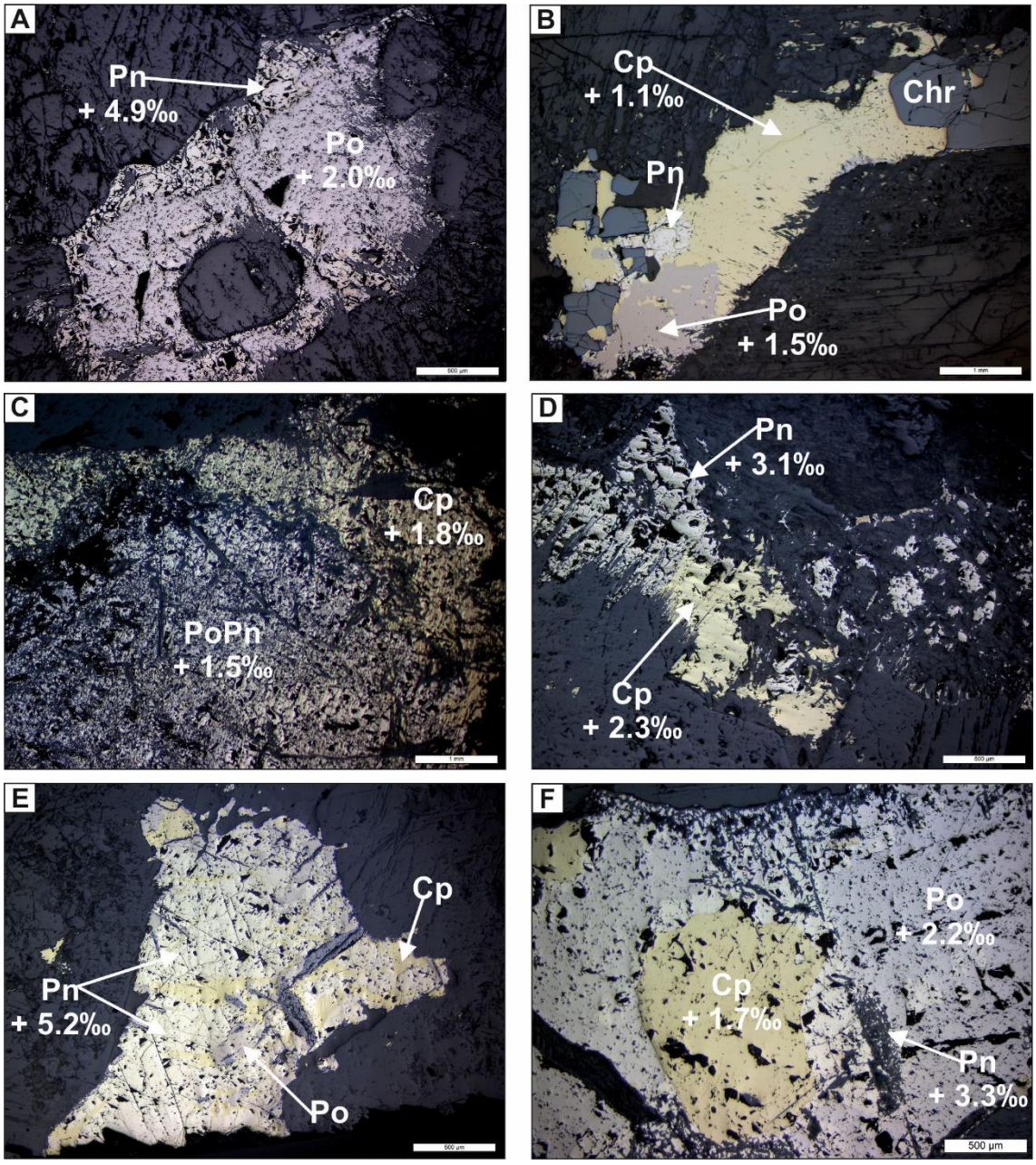

Figure 9.9: Reflected light images showing the composition and morphology of sulphides analysed for their isotopic composition in the Thick Flatreef (TMT_006). (A) Medium-grained, Po-dominated sulphide with a blocky Pn rim (TMT_03); (B) Cp-rich sulphide with minor Po and Pn (TMT_12); (C) A coarse-grained sulphide with a Po and Pn rich core and an edge of Cp showing strong penetrative alteration by amphiboles (TMT_18); (D) A strongly altered Pn and Cp interstitial medium-grained sulphide (TMT_24); (E) A Pn-dominated sulphide with minor Po and Cp showing an altered texture with magnetite forming along fractures (TMT_27); (F) Cp enclosed in Pn and Po (TMT_32A). For abbreviations see Figure 9.6.

9.1.5 Deep Platreef (UMT_345 and UMT_345_D1)

Moving down-dip from the surface Platreef to the Deep Platreef on Turfspruit is proposed to represent a transition from a contaminated to a magmatic stratigraphy in Nodder (2015) and Grobler et al., (2018). The downhole S isotope profile as shown in Figure 9.6 indicates increasing crustal contamination with depth in the Deep Platreef and the range of the $\delta^{34}S$ values are significantly higher compared to samples from the Flatreef. This brings into question the 'primary magmatic' origin of the stratigraphy and related mineralisation.

Sulphides in the top stratigraphic units of the Deep Platreef, the Upper Pyroxenite (UP) and Middle Pyroxenite (MP), do record a dominant magmatic signature, examples of the sulphide mineralogy and textures present within these units are shown in Figure 9.10. The sulphides in these units are typically medium-grained, interstitial and composed of pyrrhotite, pentlandite and chalcopyrite. In the UP unit the sulphides have sharp contacts with the host silicate minerals and they record the lightest $\delta^{34}S$ values (+0.7 to +1.9‰). The sulphides associated with the chromite stringers on the contact between the UP and MP units records slightly elevated $\delta^{34}S$ value (up to +4.4 ‰, see Figure 9.10B to 9.10D); they show evidence of secondary remobilisation of sulphides (or S loss) as shown by the fragmented edges of the coarse-grained sulphide in Figure 9.10B.

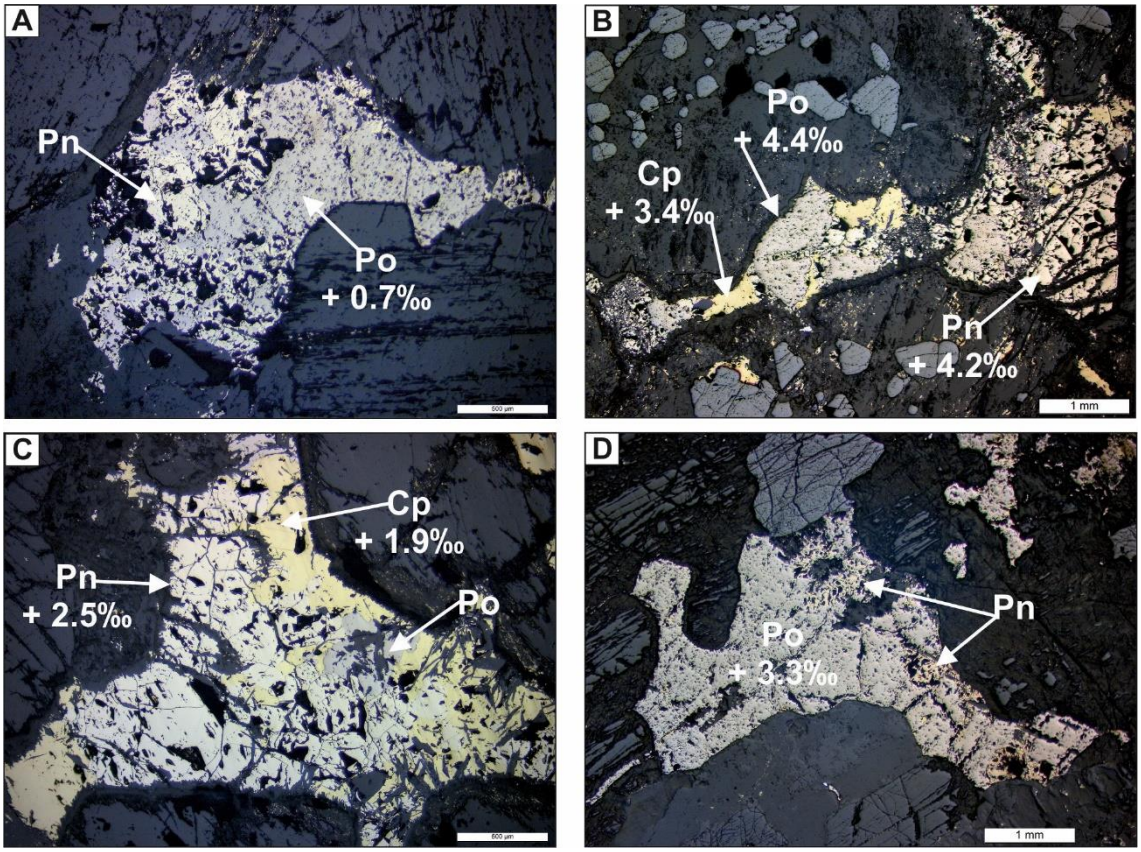

Figure 9.10: Reflected light images showing the composition and morphologies of selected sulphides analysed for their isotopic composition from the Upper and Middle Pyroxenite units of

the Deep Platreef (UMT 345 and UMT_345_D1). (A) Medium-grained interstitial sulphide composed of Po and blocky Pn, GS5A; (B) Coarse-grained interstitial sulphide composed of blocky Pn, Po and Cp, GS20B; (C) Medium-grained interstitial sulphide composed of blocky Pn and Cp with minor Po, GS21A. (D) Interstitial, Po-dominated sulphide with minor blocky Pn 345_05. For abbreviations see Figure 9.7.

In the lower part of the Deep Platreef stratigraphic sequence, i.e. from the Lower Pyroxenite unit to the basal Feldspathic Clinopyroxenite Hybrid Zone (HZ_{FCPX}) an increasing component of heavy $\delta^{34}S$ values are recorded. Non-magmatic $\delta^{34}S$ values are identified in the mineralised Main Chromitite (MCHR) unit hosting the Lower Reef mineralised interval. The sulphide assemblage within this unit comprises pyrrhotite, pentlandite, chalcopyrite and cubanite and they are typically found as an interstitial phase to the host silicate assemblage (see Figure 9.11A) and to chromite grains (see Figure 9.11B). In both settings the sulphides contain moderately heavy $\delta^{34}S$ values relative to the mantle range.

The sulphide assemblage of the Ultramafic Zone (UMZ) is heterogeneously distributed and a range of sulphide textures are observed including massive (see Figure 9.11C), blebby and interstitial. The range of $\delta^{34}S$ values obtained for this unit are all heavier than the mantle range and vary from +4.4 to +9.2‰. The sulphide assemblage shown in Figure 9.11C appears in disequilibrium with significant cubanite and chalcopyrite that have diffusive boundaries with pyrrhotite and pentlandite. Magnetite forms a minor rim on the edge of the sulphide indicating the presence of oxidising fluids may be promoting this reaction through sulphur loss.

The basal unit logged in the Deep Platreef, the Feldspathic Clinopyroxenite Hybrid Zone (HZ_{FCPX}) contains variable amounts of heterogeneously distributed interstitial sulphides (typically < 5 vol%) comprising pyrrhotite, pentlandite and chalcopyrite (see Figure 9.11D). The sulphides in this unit record the heaviest $\delta^{34}S$ values ranging from +8.5 to +10.8 ‰; they do not show evidence of hydrothermal alteration on the edges of the sulphides with sharp contacts between the sulphides and the cumulate silicates. This suggests that the contamination of a heavy crustal sulphur isotope signature was imparted early in the sulphides crystallisation history. These heavy $\delta^{34}S$ values are comparable to those noted by Yudovskaya et al., (2017a) in ultramafic rocks of ‘Lower Zone’ affinity (+9 to +14.2 ‰), however in this drill hole there are no intervening sediments separating the magmatic stratigraphy.

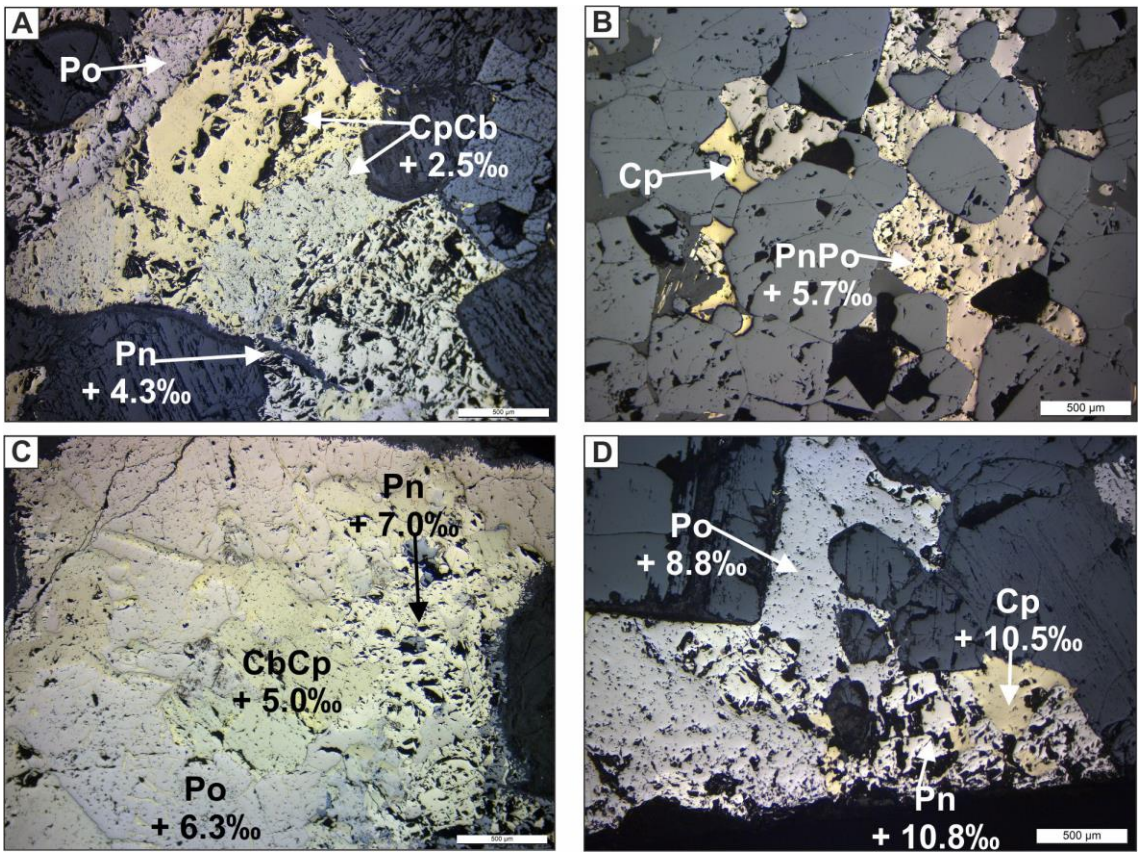

Figure 9.11: Reflected light images showing the composition and morphologies of selected sulphides analysed for their isotopic composition from the Main Chromitite (A and B), Ultramafic Zone (C) and Feldspathic Clinopyroxenite Hybrid Zone (D) stratigraphic units of the Deep Platreef. (A) A coarse-grained, interstitial sulphide dominated by Cp and Cb with Pn and Po on edges (345_09); (B) Po, Pn and Cp located interstitially to chromite grains (D1_14); (C) Massive sulphide consisting of patchy Po with veins of Cp and Cb (345_11). (D) A coarse-grained interstitial polyphase BMS (345_16). For abbreviations see Figure 9.6.

9.2 Sulphur Isotope Values vs Geochemical Contamination Indices

The prevalence of non-magmatic $\delta^{34}S$ signatures in the Platreef and Deep Platreef drill holes requires some input from externally derived S into the magmatic system. Two geochemical contamination proxies; the bulk rock $CaO:Al_2O_3$ and in situ S/Se ratios on sulphides have been previously used to measure contamination effects and/or alteration of sulphide minerals in the Platreef and the GNPA member (e.g. Kinnaird 2005; Holwell et al., 2007; Smith et al., 2014) and these are plotted against the S isotope data to see if any correlations can be observed. The varying scales of these data should indicate whether contamination processes are operating on a mineralogical scale affecting sulphides or are having a greater influence on the rock mass.

The major element ratio $CaO:Al_2O_3$, has been identified as an effective means of identifying and classifying the nature of crustal contamination in the Platreef at Turfspruit (see Chapter 7). The $\delta^{34}S$ values of pyrrhotite are plotted against the bulk rock $CaO:Al_2O_3$ in Figure 9.12. Pyrrhotite analyses are used because they are the most common sulphide

observed in all drill holes analysed (chalcopyrite and pentlandite demonstrate similar patterns).

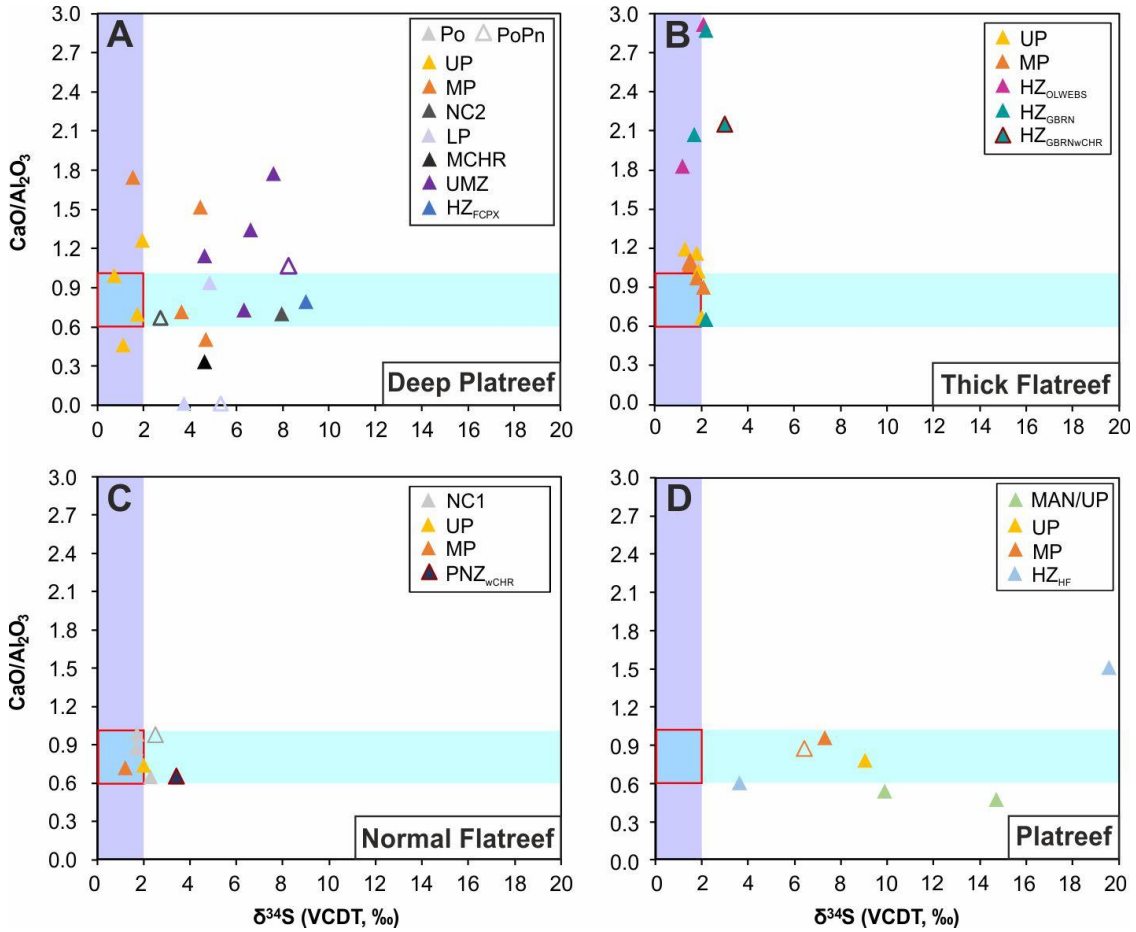

Figure 9.12: Bivariate plots of $\delta^{34}S$ values in pyrrhotite vs. CaO/Al_2O_3 for all drill holes. Note: vertical and horizontal fields indicate the magmatic range of $\delta^{34}S$ and CaO/Al_2O_3 values, respectively and a red box highlights the intersection of the fields.

The largest spread of data on both axes is seen in the Deep Platreef (Figure 9.12A) there is no systematic correlation observed between the two datasets. The samples with the most contaminated $\delta^{34}S$ value in the Deep Platreef plot within the "magmatic" range of $CaO:Al_2O_3$. In the Thick Flatreef there is strong geochemical evidence for the assimilation of carbonate material in the HZ_{OLWEBS} and the HZ_{GBRN} with elevated $CaO:Al_2O_3$ ratios (> 1); however there is no corresponding enrichment in heavy $\delta^{34}S$ values. This implies either that the carbonate material assimilated in these units didn't contain any S to exchange with the magma or that formation of a sulphide melt postdates the devolatisation of the assimilated dolomites. The latter opens the possibility that the sulphide melt is not genetically related to the host rocks but percolated downwards, potentially from the UP and MP units, and settled in the Hybrid Zone due to the elevated porosity created by volume decrease resulting from the formation of forsterite after dolomite (Olszak-Humienik & Jablonski, 2014). A good correlation is observed in the

Normal Flatreef between the two parameters with all samples plotting in a tight cluster on the edge of the magmatic values for both these parameters (see Figure 9.12C). In contrast, the Platreef data (Figure 9.12D) shows that the most contaminated samples all lie outside of the magmatic field based on $CaO:Al_2O_3$. There is a discrepancy, however with the isotopic composition suggesting that these samples were contaminated by sulphate-bearing sediments whereas the $CaO:Al_2O_3$ ratio indicating a mixed signal involving input from both shales and carbonates.

S/Se ratios are established as a useful tool for identifying any crustal influence on sulphides in Ni-Cu-PGE deposits (Quefferus & Barnes, 2002). The mantle has a restricted range in bulk rock S/Se ratio values at between 2850 to 4350 (Eckstrand & Hulbert, 1987) whereas crustal rocks have bulk rock S/Se ratios of 3500 to 100,000 (Yamamoto, 1976). Therefore, magmatic rocks containing S/Se ratios elevated above mantle values are interpreted to result from contamination via S-rich sedimentary rocks. The S/Se ratios used can be either for whole rock samples or in situ on sulphide minerals; the latter data is presented here as S and Se are not analysed in the whole-rock geochemical method used in this study.

The in situ S isotope data has been combined with in situ S/Se ratios, obtained via laser ablation mass spectrometry (LA-ICP-MS), where possible on the same grain in Figure 9.13. The majority of samples plot within the mantle range of S/Se ratios or below it; the latter suggestive of S loss. This suggests minimal crustal input at odds with the $\delta^{34}S$ data, particularly for the Deep Platreef samples. A similar disparity between these two parameters was observed by Smith (2014) for the Grasvally Norite-Pyroxenite-Anorthosite member and is accounted for by magmatic or low-temperature processes modifying the S/Se ratio and/or the $\delta^{34}S$ of the sulphide liquid.

Only two samples plot above the mantle S/Se range; (1) a chalcopyrite analysis from the UP unit of the Deep Platreef records a S/Se ratio of 5107 and; (2) a pyrrhotite analysed from the top of the UP in the Platreef records a S/Se of 16615. The elevated S/Se values in the Platreef sample confirms the heavy $\delta^{34}S$ value measured and supports that the sulphide is highly contaminated. The one elevated S/Se ratio in the Deep Platreef contains a magmatic signature and this anomalous result is likely the result of co-existing galena and sphalerite identified in sulphides from this unit, a feature noted elsewhere at the locality Volspruit of the northern limb by Tanner et al., (2018).

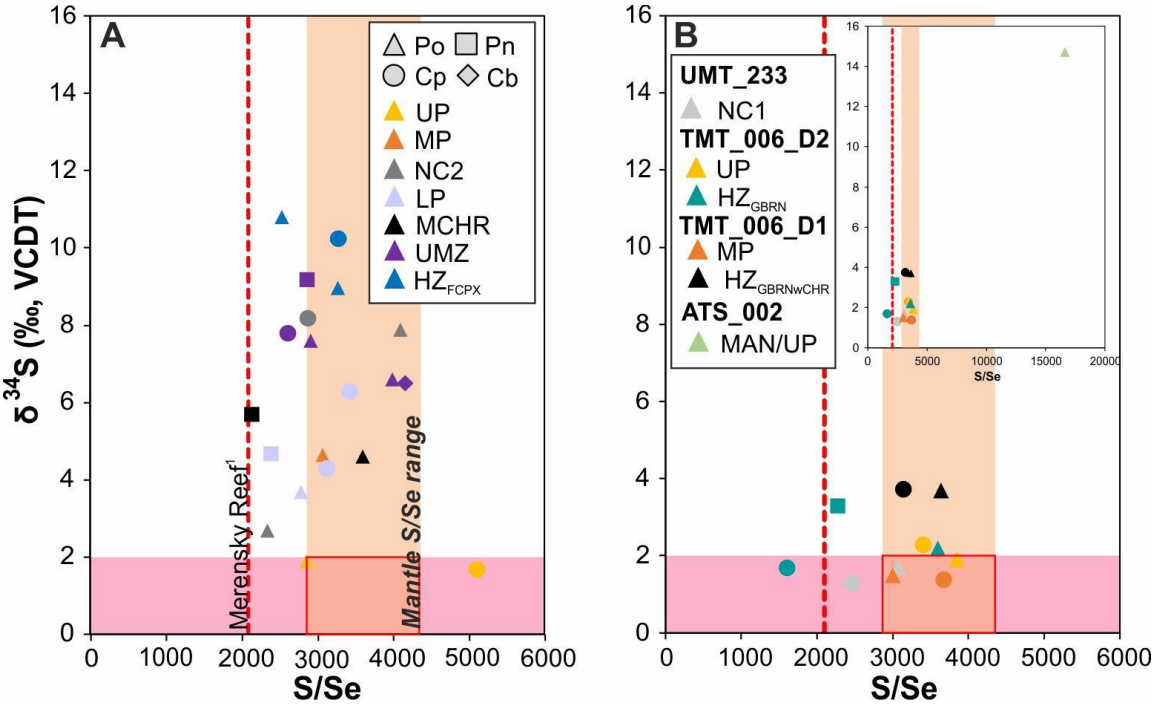

Figure 9.13: Bivariate plots of $\delta^{34}S$ vs in situ S/Se for all drill holes studied. (A) Deep Platreef data from UMT_345 and UMT_345_D1. (B) Flatreef data from the Normal (UMT_233) and Thick reef facies; inset plot shows the result of one analysis from the Platreef. Note: Merensky reef value of 2080 from Naldrett et al., (2009).

Naldrett et al., (2009) recorded a relatively consistent S/Se ratio in sulphides of the Merensky Reef, which they interpreted as indicative that the primary sulphide content was retained with minimal S loss through alteration. In contrast, the same data plotted for the UG2 chromitite showed significant scatter; reflecting the highly altered appearance of sulphides with pyrrhotite replaced by pyrite. The results of this study also show significant variability in the S/Se ratio within stratigraphic units and this is suggested to result from secondary hydrothermal remobilisation of sulphur.

9.3 Modelling of Crustal Contamination

The non-magmatic $\delta^{34}S$ values obtained in this study for sulphides in the Platreef and Deep Platreef indicate that the intruding magmas were contaminated with crustally-derived sulphur with an isotopically heavy $\delta^{34}S$ signature. The heterogeneity of the S isotope signature varying with stratigraphic level indicates that the dominant source of this crustal sulphur is from the immediate footwall rocks of the Duitschland Formation. The degree of S assimilated from the Duitschland Formation into the magmatic system can be modelled using the two-component mixing model of Lesher & Burnham (2001) and Ripley & Li (2003) shown in Equation 9.1:

$$\delta^{34}Smix = \frac{\delta^{34}S_c f_c C_c^S + \delta^{34}S_m f_m C_m^S}{f_c C_c^S + f_m C_m^S} \quad \textbf{Equation 9.1}$$

where $\delta^{34}S_{mix}$ is the contaminated magma; $\delta^{34}S_C$ and $\delta^{34}S_M$ are the isotopic compositions of the contaminant and starting magma, respectively; f_c and f_m are the fractional abundance of the contaminant and magma, respectively; and C_c^s and C_m^s are the concentrations of S in the contaminant and magma, respectively.

Typically, users of this model input data from single samples and extrapolate the results across an entire deposit (e.g. Holwell et al., 2007; Yudovskaya et al., 2017a). The zonal distribution of isotopic variability at this location suggests that crustal contamination occurred in situ and the dominant contaminant is therefore the footwall and roof sediments. The Duitschland Formation (DF) is not homogenous; it represents a layered sedimentary sequence with different lithologies containing different concentrations of sulphur and varying isotopic compositions. To model an in situ signature a range of scenarios are modelled as shown in Figure 9.14.

The uncontaminated mantle-derived magma was estimated to contain 250 ppm sulphur and to have an $\delta^{34}S$ isotopic composition of 0 ‰. The range of S concentrations for the DF modelled in Figure 9.14 are based on numerous lines of evidence. The maximum S concentration (1.0 wt%) are based on whole rock S concentrations measured by Klein & Beukes (1989) from carbonates and shales of the Transvaal Supergroup. They measured S concentrations of between 0.02 to 17 wt% in limestones and dolomites and between 0.2 to 20 wt% in shales. The maximum values of these ranges are found in 1 in 10 samples with the majority falling between 0.2 and 3.0 wt%. The minimum modelled S concentration (0.05 wt%) is based on the results of XRF data collected on whole rocks sample pulps completed as part of the sample preparation (see Appendix E) with values measured from 0.008 to 0.158 wt%. The intermediate concentrations of 0.5 wt% and 0.1 wt% are based on visual estimations of the pyrite content in the shales. The models, as shown in Figure 9.14, consider a maximum of 20% assimilation; this was chosen as an arbitrary value and is possibly too high.

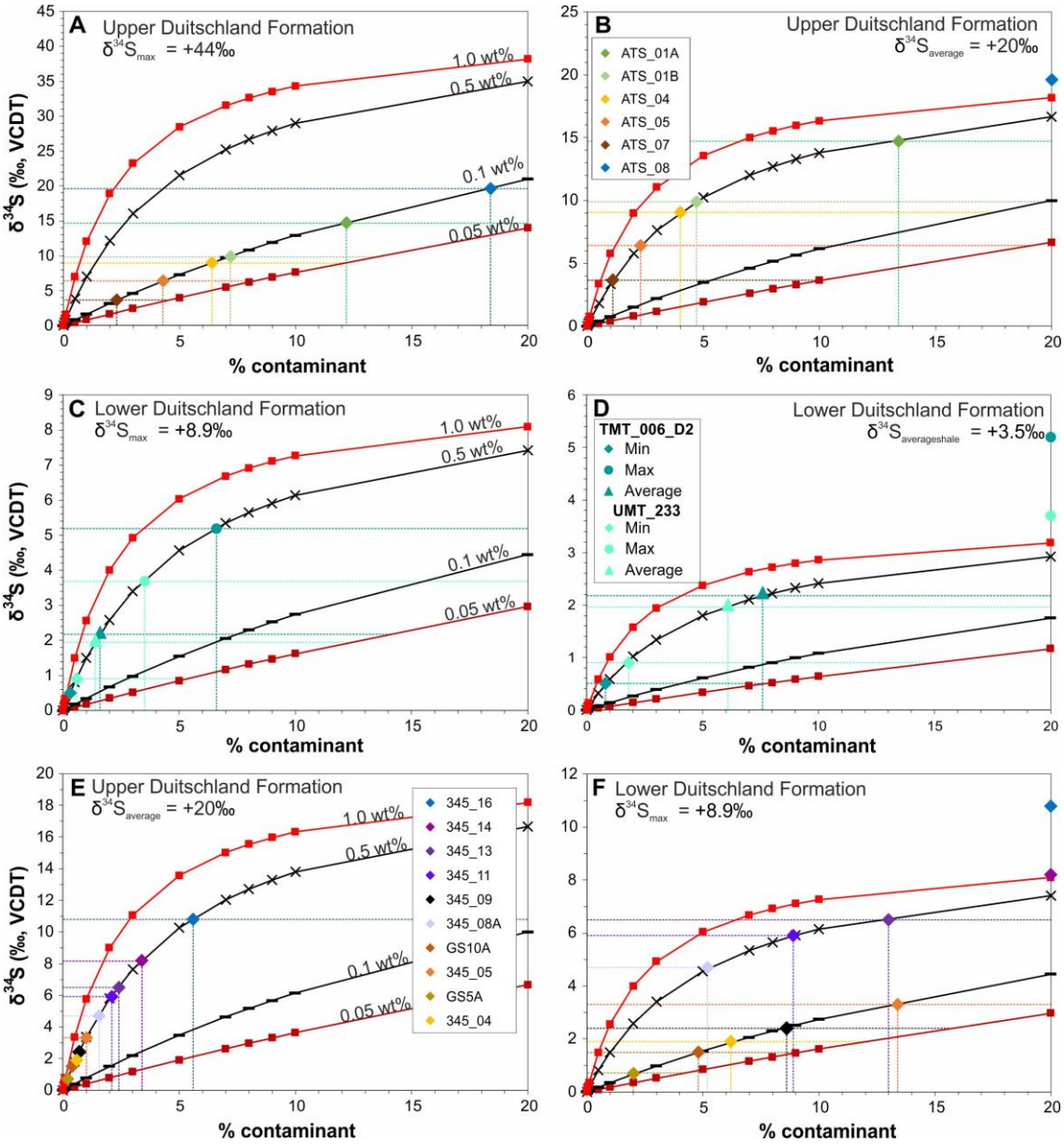

Figure 9.14: A series of simple two-end member mixing models between a mantle melt (starting values of 250 ppm S and $\delta^{34}S$ of 0.0 ‰) and contaminating Duitschland Formation sediments with a range of isotopic compositions and S concentrations modelled. (A, B) Platreef data modelled considering the maximum and average $\delta^{34}S$ value obtained from the Upper Duitschland Formation in Guo et al., (2009). (C, D) Flatreef data modelled considering the maximum and average $\delta^{34}S$ value measured in the Lower Duitschland Formation in this study. (E, F) Deep Platreef data modelled considering the maximum $\delta^{34}S$ value obtained via CAS in Guo et al., (2009). (F) Deep Platreef data modelled considering the maximum $\delta^{34}S$ value measured in this study as CRS.

The Duitschland Formation (DF) has variable isotopic signatures that can broadly be split into; (1) Lower DF with a mean CRS $\delta^{34}S$ value of +3.5 ‰ for the pyritic shales and a range of compositions up to +8.9 ‰; (2) the Upper DF with a mean CAS $\delta^{34}S$ value of +20 ‰ and a range from +11.8 to +44‰ (Guo et al., 2009).

The Platreef contamination is modelled using CAS $\delta^{34}S$ values from the Upper DF stratigraphy, as shown in Figure 9.14A and 9.14B. All of the observed values can be satisfied using the maximum $\delta^{34}S$ value of + 44‰ (Guo et al., 2009) and assuming S concentrations in carbonates at 0.1 wt%. The results estimate the assimilation of between 2 to 18 % of contaminant. In Figure 9.13B, the average CAS value for the Upper DF of +20‰ is modelled and fails to satisfy all the sample values. These results show that the Platreef must have intruded into the Upper DF stratigraphy effectively fixing the level of intrusion for this sector of the deposit.

The Normal and Thick Flatreef are modelled together because of the limited range in $\delta^{34}S$ values measured in this location and considering the range of isotopic compositions within the Lower DF (see Figure 9.14C and 9.14D). All sample isotopic compositions can be satisfied by modelling the highest $\delta^{34}S$ value of +8.9‰ with the % assimilated material ranging from <1 % to 6.5 % (see Figure 9.13C). Modelling of the average shale composition of the Lower DF (see Figure 9.13D) fails to account for two samples with $\delta^{34}S$ values > +3.0‰.

The Deep Platreef was modelled for both the Upper and Lower DF isotopic compositions. In Figure 9.14F, the heaviest value for the Lower DF do not satisfy all measured $\delta^{34}S$ values in the samples with two not plotting on the modelled line within the 20% assimilation cut off. All recorded $\delta^{34}S$ values can be achieved through decreasing contamination, 0.2 to 5.6% assimilation, assuming the average $\delta^{34}S$ value of +20 ‰ in the Upper DF.

Chapter 10

PGE Hosts: Base Metal Sulphides and Platinum-Group Minerals

10.0 Introduction

PGE enrichment in rocks can be expressed in either the formation of discrete, micron-scale platinum-group minerals (PGM) or in solid solution in sulphides and to a lesser extent chromite. Details on the partitioning behaviour of PGE between these mineral phases can be found in the literature review in Chapter 2 (section 2.3). Determining the relative contribution of PGE hosted in sulphides vs. PGM to the overall PGE deportment for the different stratigraphic units of the Deep Platreef is the focus of the current chapter.

10.1 Trace Elements in Base Metal Sulphides

The base metal sulphide (BMS) assemblages of pyrrhotite, pentlandite, chalcopyrite ± cubanite as identified in samples from this study were analysed using laser-ablation mass spectrometry (LA-ICP-MS) to establish their PGE and semi-metal budget. A detailed methodology for the LA-ICP-MS facility at Cardiff University is outlined Chapter 4 (section 4.7) and the raw data presented in Electronic Appendix F. The results of this study reveal PGE in both solid solution and as semi-metal rich inclusions (based on corresponding peaks of PGE and a semi-metal e.g. Te and As). The following PGE isotopes are presented ^{189}Os, ^{193}Ir, ^{99}Ru, ^{103}Rh, ^{106}Pd and ^{195}Pt and concentrations are reported to three significant figures. Attempts were made to analyse individual sulphide minerals however some of the data collected represents mixed BMS analyses with significant deviations in the Ni, Fe and Cu concentrations from stoichiometric.

In total, twenty-three samples from the Deep Platreef were analysed covering all logged stratigraphic units with the focus on samples hosting mineralisation. Six samples from the Flatreef were analysed; one from Normal Flatreef (UMT_233) and five from the Thick Flatreef (TMT_006). In addition, pyrrhotite from two samples (ATS_01A and ATS_08) from the top and base of the logged interval within the shallow Platreef, were chosen for analysis.

10.1.1 Trace Elements in Pentlandite

Pentlandite was observed in all stratigraphic units in the Deep Platreef and Flatreef (both ‘Normal’ and ‘Thick’ reef facies) but was present in insignificant quantities in samples from the shallow Platreef. Pentlandite is known to be a significant carrier of Pd and Rh in its crystal lattice with values on the scale of 100’s ppm identified in similar studies (e.g. Cabri & Laflamme, 1981; Godel et al., 2007; Holwell & McDonald, 2010; Osbahr et al., 2013, 2014; Junge et al., 2014, 2015, 2018). The pentlandite grains measured in this study contain the highest concentrations of all PGE compared to the

other sulphide minerals analysed; a summary of the results of LA-ICP-MS analyses on pentlandite are presented in Table 10.1 below.

Pentlandite accommodates Ni and can typically contain around 1 wt% of Co (see Figure 10.1). The pentlandites of the Turfspruit project area in general contain less Co than pentlandite from the Merensky Reef as analysed in Godel et al., (2007, see Figure 10.1B). The Co content in the Merensky Reef pentlandite varies from 5000 to 14000 ppm and in comparison, the Co content of the pentlandites measured in this study varies between 6 to 13191 ppm with an average of around 4500 ppm. The average Co contents of the three mineralised pyroxenite packages on Turfspruit varies from 4500 to 4800 ppm significantly lower than those of the Merensky Reef. The Pd and Co concentrations in pentlandites from the Merensky Reef display a positive correlation (see Figure 10.1A), whereas there is no observed correlation between these elements on Turfspruit. The relationship is non-linear with the highest Pd contents between 4000 to 6000 ppm Co, dropping off sharply above and below this range.

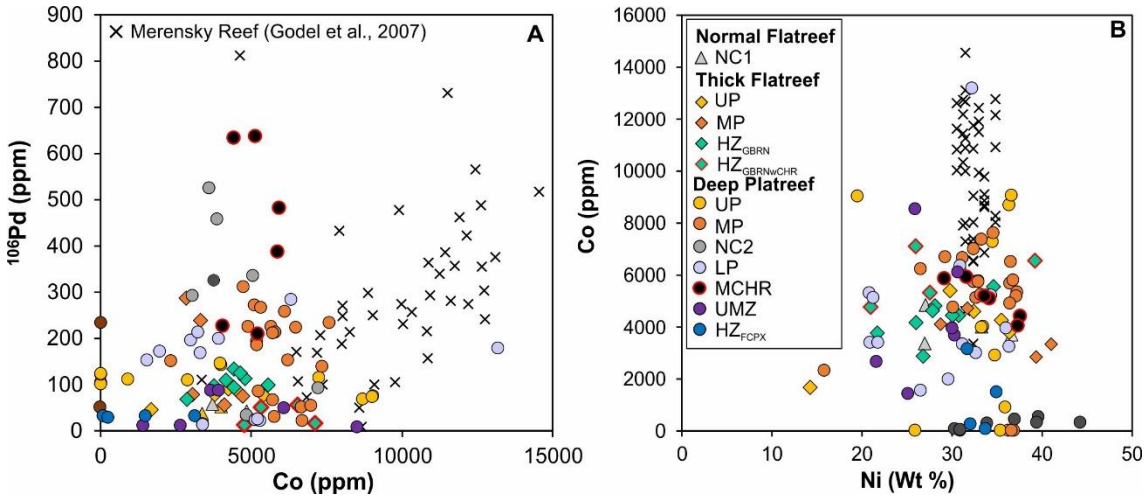

Figure 10.1: Bivariate diagrams of: (A) Pd (ppm) vs Co (ppm) and; (B) Co vs Ni concentrations in pentlandite. Note: black crosses represents Merensky Reef data from Godel et al., (2007).

Table 10.1: Trace element data collected on pentlandite from the different stratigraphic units from the Deep Platreef, Normal and Thick Flatreef. Note: the data shown are average values calculated for each stratigraphic unit are denoted by subscript AV.

	Count	Pd^{106} in Pn (ppm)				ΣPGE$_{AV}$	ΣPPGE$_{AV}$	ΣIPGE$_{AV}$	PPGE/IPGE	S/Se$_{AV}$	ΣAsSb$_{AV}$	ΣTeBi$_{AV}$	Co
		Min	Max	Range	Average	ppm					ppm		ppm
Deep Platreef													
UP	18	21.5	310	289	112	147	130	16.9	7.69	2179	0.36	4.07	4700
MP	17	31.0	271	240	184	264	218	46.1	4.74	1796	3.87	3.86	4838
NC2	7	33.6	525	492	294	310	304	6.13	49.6	2632	0.13	2.10	4494
LP	13	12.9	284	271	128	153	139	13.6	10.2	2453	6.15	4.03	4541
MCHR	6	211	638	427	430	618	545	73.6	7.40	2121	0.11	1.56	5097
UMZ	6	8.50	87.6	79.1	42.3	52.3	48.9	3.32	14.7	2826	25.3	5.05	4387
HZ_{FCPX}	4	28.0	32.7	4.74	31.3	32.0	31.7	0.23	137	2533	18.0	1.27	1249
Normal Flatreef													
NC1	4	36.4	58.6	22.2	47.5	59.1	52.3	6.87	7.61	1990	0.07	5.75	3984
Thick Flatreef													
UP	5	46.3	89.9	43.6	74.9	104	93.3	11.0	8.50	2408	0.00	0.30	3941
Middle Reef	5	56.3	287	231	147	206	179	27.5	6.50	2157	0.00	1.15	3617
Hybrid Reef (GBRN)	8	67.4	134	66.4	105	124	117	6.18	19.0	2785	0.00	0.75	4337
Hybrid Reef (wCHR)	4	12.3	56.3	44.0	34.0	39.6	35.5	4.05	8.77	2179	2.06	4.50	5938

Palladium follows Ni and Co (interpreted as solid solution behaviour) in every pentlandite grain analysed during this study. The samples from the Deep Platreef and Flatreef contain a significant range in concentrations from 8 to > 600 ppm, as shown in Figure 10.2A and 10.2B. The distribution of grade between the different sectors of the Platreef on Turfspruit are shown in Figure 10.2A; the highest Pd tenors in pentlandite are found in the Deep Platreef and the lowest in the near-surface Platreef. The results of this study extend the known range of concentrations of Pd in solid solution in pentlandite as previously analysed for this location (see Figure 10.2A).

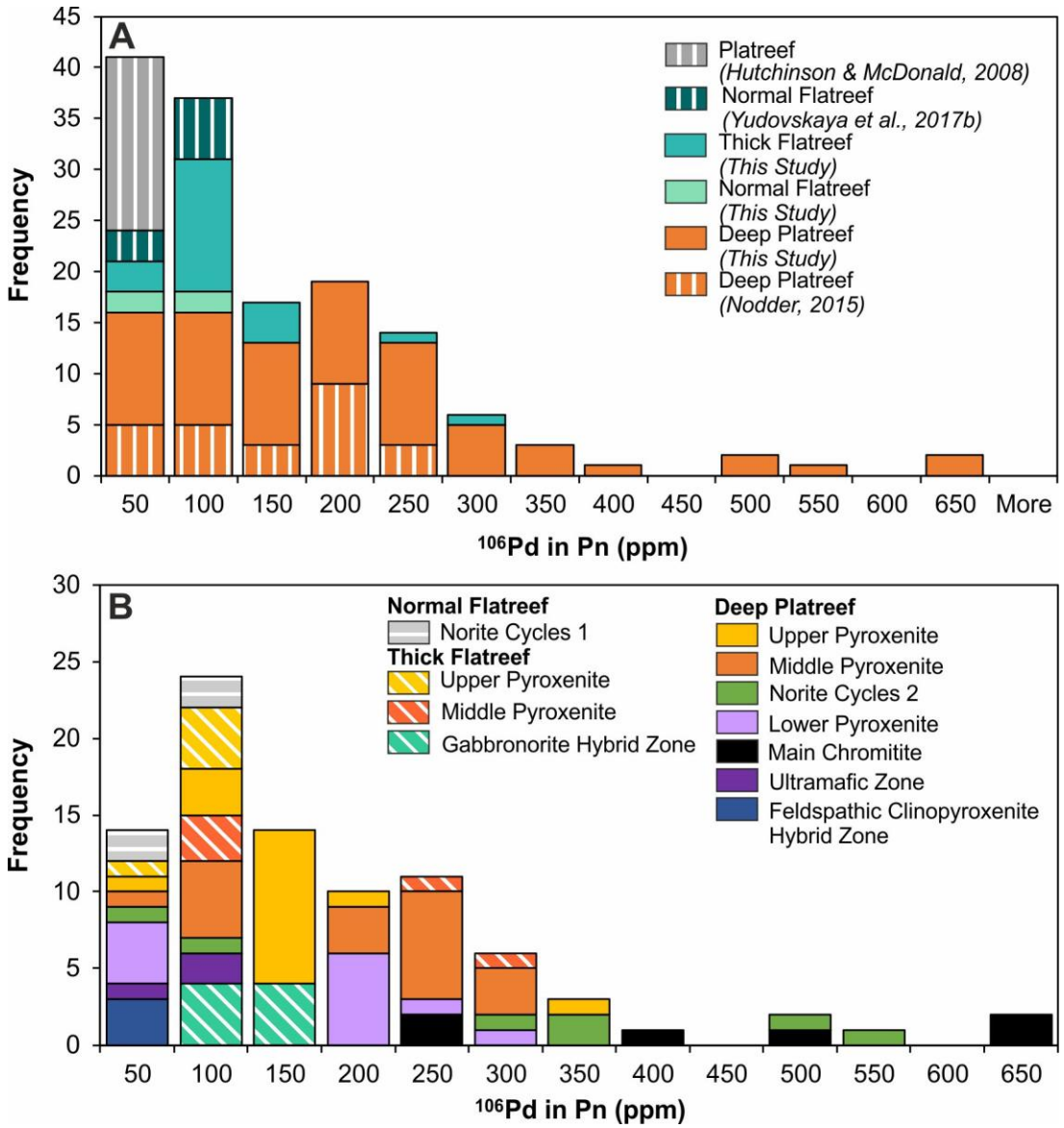

Figure 10.2: Histograms of the concentration of ^{106}Pd in solid solution in pentlandite. (A) The distribution of ^{106}Pd within Platreef rocks from across the Turfspruit project area incorporating data from other studies as referenced in the plot. (B) Showing the variability in the ^{106}Pd concentrations between different stratigraphic units. Note: Flatreef sulphides have a stripe pattern fill and Deep Platreef sulphides have a solid fill.

In addition to the change in the range of Pd concentration observed between the different down-dip sectors on Turfspruit there is also observed a control with stratigraphic height. The distribution of the Pd tenor between the different stratigraphic units of the Flatreef and Deep Platreef are shown in Figure 10.2B.

The highest Pd concentrations (between 231 to 637 ppm) are obtained from the Main Chromitite (MCHR) unit of the Deep Platreef; this stratigraphic unit is only intersected in the deepest holes drilled on Turfspruit. The time-resolved analysis (TRA) plots for the highest grade pentlandite grains analysed from the MCHR unit are shown in Figure 10.3A. The lowest Pd concentrations are observed in the immediate footwall stratigraphic units to the MCHR including the Ultramafic Zone (UMZ) and the Feldspathic Clinopyroxenite Hybrid Zone (HZ_{FCPX}) units at the base of the drill hole (see Table 10.1 and Figure 10.2B). The Norite Cycles 2 (NC2) unit contains two populations of sulphides based on their Pd concentrations >300 ppm and <100 ppm Pd. These populations are found in different samples both of which sample the base of a norite cycle; the highest values correspond to a significant accumulation of base-metal sulphides in a thick pyroxenite unit (1.71 m) compared to a relatively sulphide-poor and thin pyroxenite (0.4 m). The pentlandites of the Upper Pyroxenite (UP) and Middle Pyroxenite (MP) units of the Deep Platreef contain systematically more Pd in pentlandite than equivalent sulphides in the Flatreef.

The majority of the pentlandites analysed are enriched in Pd, many grains also contain elevated concentrations in the other PGEs particularly in the chromite-bearing samples of the MP and MCHR units, as shown in Figure 10.3B and 10.3C. The highest Rh concentration, up to 391 ppm, were recorded in the MCHR sample also containing the highest Pd concentrations (shown in Figure 10.3A). In Table 10.1 it is shown that the PPGE are elevated over IPGE in all pentlandite grains analysed; the maximum concentrations of the IPGE and Pt are: 17.1 ppm Os, 25.7 ppm Ir, Ru 105 ppm and 10.3 ppm Pt. In the 4^{th} chromite-stringer, Pt and Ir were observed to form discrete peaks with As and Bi suggesting the presence of a PGM, as shown in Figure 10.3C.

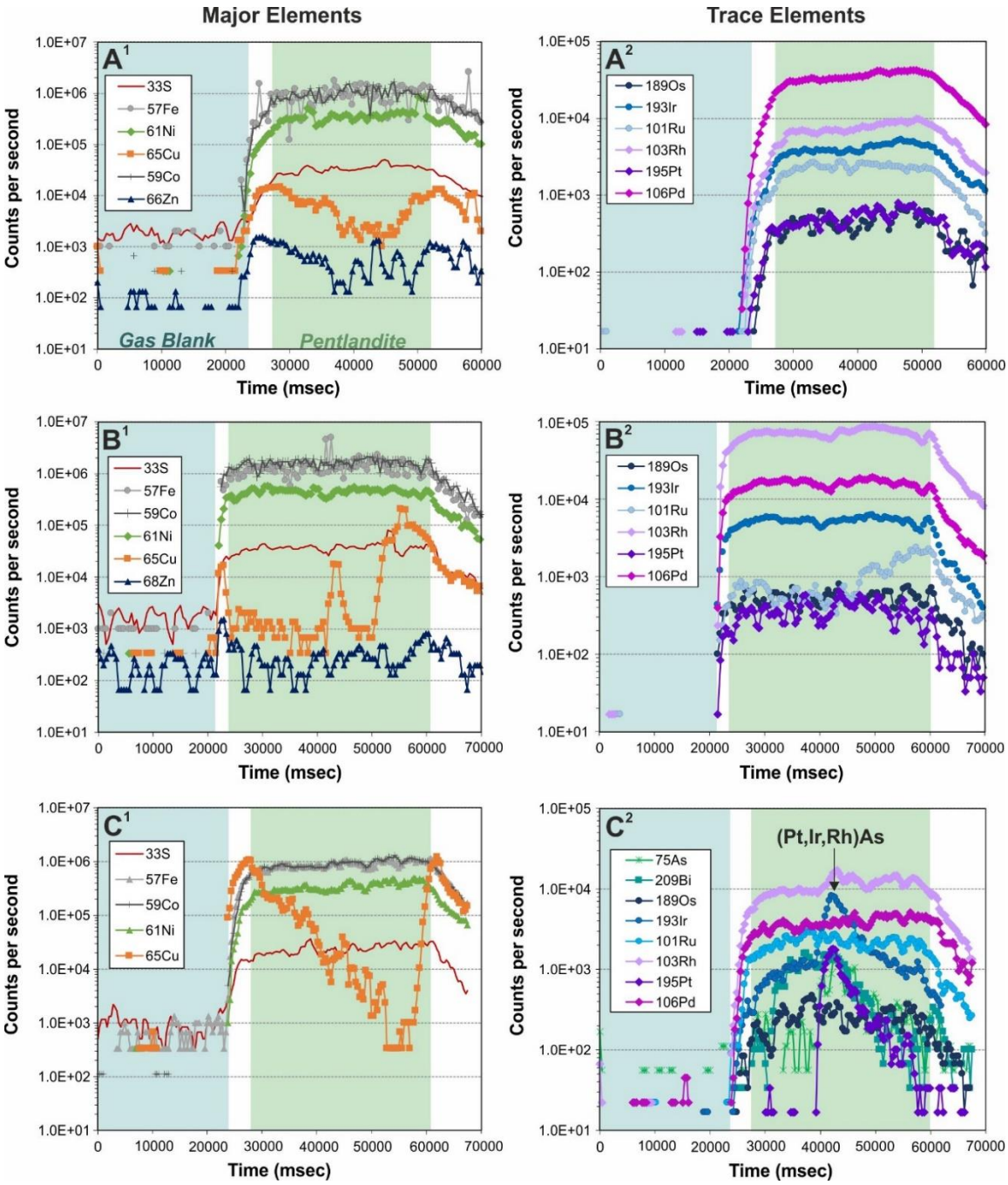

Figure 10.3: Selected time-resolved laser spectra for pentlandite grains analysed in chromite-bearing lithologies from: (A and B) the Main Chromitite unit, as sampled in D1_14; and (C) the 4th chromite stringer on the contact between the Upper and Middle Pyroxenite, as sampled in GS20B.

Pentlandite grains hosted in the silicate-dominated lithologies are dominated by Pd with only minor concentrations of the other PGE (see Figure 10.4). In the Upper Pyroxenite (UP) unit, elevated semi-metal concentrations including As, Sb and Te are observed in the TRA plot for the pentlandite as shown in Figure 10.4A, however the Pd (68.4 ppm) and Ru (3.7 ppm) appear to behave independently of these elements.

The precious metal concentrations of Au are typically below detection limits (0.01 ppm) in all stratigraphic units; whereas the Ag concentration is more variable with values up to 38 ppm. Argentian pentlandite was frequently identified (see Figure 10.4B) in all stratigraphic units, it can be present as inclusions in pentlandite or on the edges of pentlandite typically in contact with chalcopyrite.

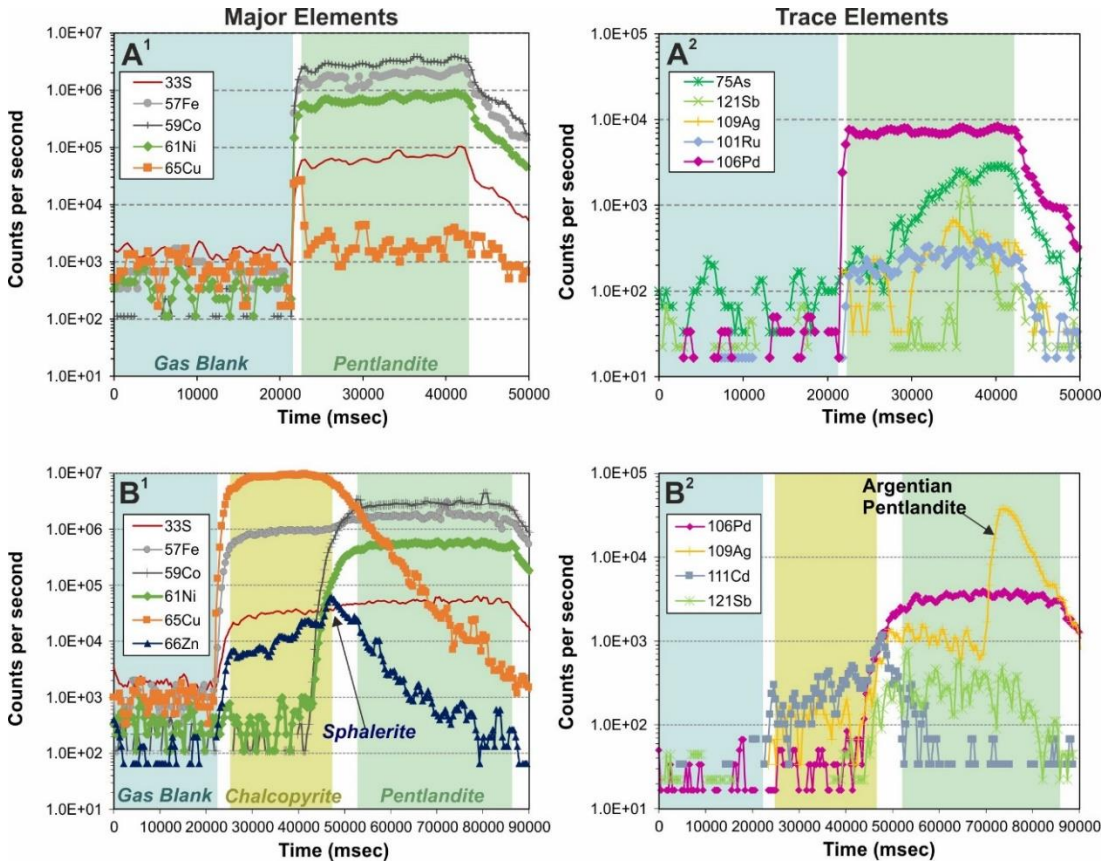

Figure 10.4: Selected time-resolved laser spectra for pentlandite in silicate-dominated lithologies from: (A) the Upper Pyroxenite unit as sampled in 345_03B; and (B) the Feldspathic Clinopyroxenite Hybrid Zone, as sampled in 345_16.

10.1.2 Trace Elements in Pyrrhotite

The trace element composition of pyrrhotite was analysed in samples from the Platreef, Flatreef (Normal and Thick reef facies) and the Deep Platreef. A summary of the trace element data is provided in Table 10.2. The pyrrhotite data is characterised by lower PPGE/IPGE ratios, compared to the pentlandite data, indicating enrichment in the IPGE. Elevated As and Sb semi-metal concentrations (up to 103 ppm) are recorded in the Main Chromitite (MCHR) and Ultramafic Zone (UMZ) of the Deep Platreef indicating possible role of PGMs in the PGE distribution. The lowest overall PGE contents are recorded in pyrrhotites from the Platreef with the Upper Pyroxenite (UP) sample from the top contact with the Mottled Anorthosite unit (MAN) containing the only detectable PGE at 0.08 and 0.46 ppm accompanied by significantly elevated

S/Se ratios from 14156 to 20275. In contrast, the pyrrhotite from the base of the logged interval in the Hornfels Hybrid Zone (HZ_{HF}) hosts no detectable PGE and the Se content is below the detection limit (12 ppm).

Table 10.2: A summary of the trace element data collected on pyrrhotite sulphides analysed from the different stratigraphic units in the Deep Platreef, Platreef, Normal and Thick Flatreef. Note: stratigraphic codes can be found in the text and the data shown are average values calculated for each stratigraphic unit.

	Count	ΣPGE_{AV}	$\Sigma PPGE_{AV}$	$\Sigma IPGE_{AV}$	PPGE/ IPGE	$\Sigma AsSb_{AV}$	$\Sigma TeBi_{AV}$	S/Se_{Av}
		ppm				ppm	ppm	
Deep Platreef								
UP	24	8.42	4.65	3.77	1.24	0.08	0.23	3102
MP	6	20.7	3.23	17.5	0.18	0.04	0.41	3248
NC2	8	11.1	1.52	9.60	0.16	0.03	0.70	3221
LP	12	7.86	2.05	5.82	0.35	0.10	0.22	3164
MCHR	6	39.5	28.4	11.2	2.55	8.99	1.35	3520
UMZ	9	1.29	0.54	0.75	0.71	11.4	0.36	3570
HZ_{FCPX}	2	0.75	0.45	0.29	1.54	0.23	0.00	3273
Normal Flatreef								
NC1	4	6.29	1.39	4.90	0.28	0.10	0.38	3077
Thick Flatreef								
UP	7	11.3	6.66	4.60	1.45	0.00	0.10	3849
MP	5	25.8	11.2	14.7	0.76	0.10	0.99	2996
HZ_{GBRN}	6	5.46	0.71	4.74	0.15	0.00	0.21	3983
$HZ_{GBRNwCHR}$	6	5.77	4.37	1.40	3.12	0.09	1.68	3641
Platreef								
UP	9	0.23	0.23	0.00	-	0.64	0.33	16615
HZ_{HF}	3	0.00	0.00	0.00	-	0.15	0.16	b.d.l

A histogram showing the distribution of the IPGE concentration within the pyrrhotite grains as analysed from across the different downhole sectors within the Turfspruit project area is shown in Figure 10.5A. The greatest range in concentrations are observed in the Deep Platreef samples; corresponding with observations on pentlandite (see Figure 10.2). Pyrrhotite from the Flatreef samples analysed in this study have lower IPGE concentrations than those measured from the Normal Flatreef by Yudovskaya et al., (2017b). The data from the Platreef samples as analysed in the current study and in Hutchinson & McDonald (2008) have the lowest IPGE concentrations.

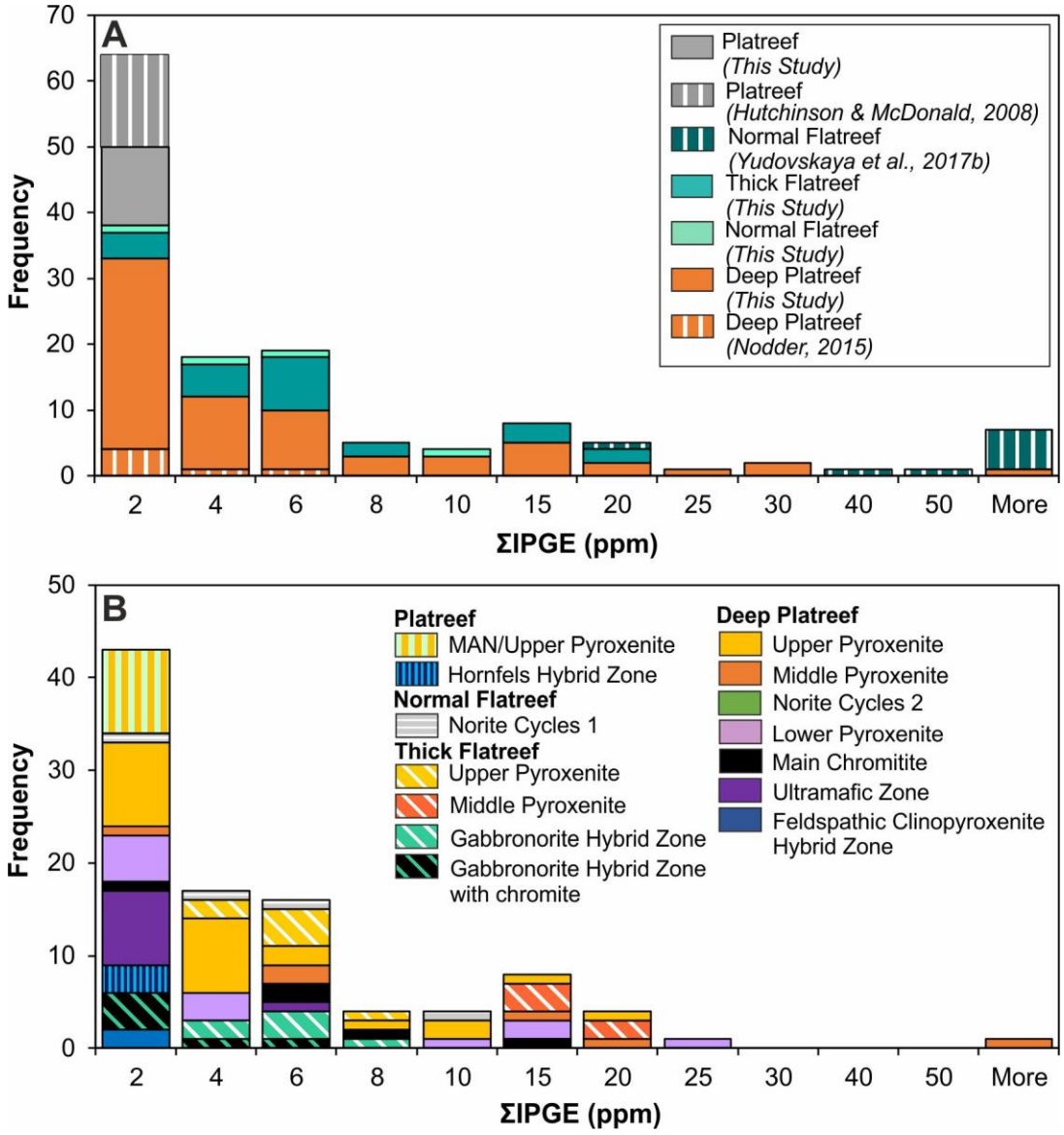

Figure 10.5: Histograms showing the variation in the total IPGE content of pyrrhotite. (A) Comparing the IPGE concentrations across the different down-dip sectors of the Platreef on Turfspruit. (B) The distribution of the IPGE concentration in pyrrhotite between the different stratigraphic units. Note: Platreef samples have a vertical stripe pattern fill, Flatreef samples have a diagonal stripe pattern fill and Deep Platreef samples have a solid fill.

The data is further subdivided in Figure 10.5B to illustrate the variability in the IPGE content of pyrrhotite between the different stratigraphic units within each drill hole studied. The pyrrhotites with the highest ΣIPGE concentrations are identified in samples containing chromite-stringers in the Middle Pyroxenite (MP) unit. The Main Chromitite (MCHR) unit doesn't contain the highest IPGE contents; this is unusual considering that chromite grains are known to concentrate the IPGE (e.g. Pagé & Barnes, 2016).

In the time-resolved analysis (TRA) plots the IPGE form as discrete micro-inclusions PGM nuggets (without any accompanying semi-metals) as shown in Figure 10.6A

based on the presence of multiple narrow peaks. In contrast, the IPGE in pyrrhotite from the 4th chromite stringer (see Figure 10.6B) are more uniformly distributed in the sulphide. The presence of Pt, Ir and Rh arsenide phases, containing up to 53 ppm As, are identified in the MCHR unit (see Figure 10.6C).

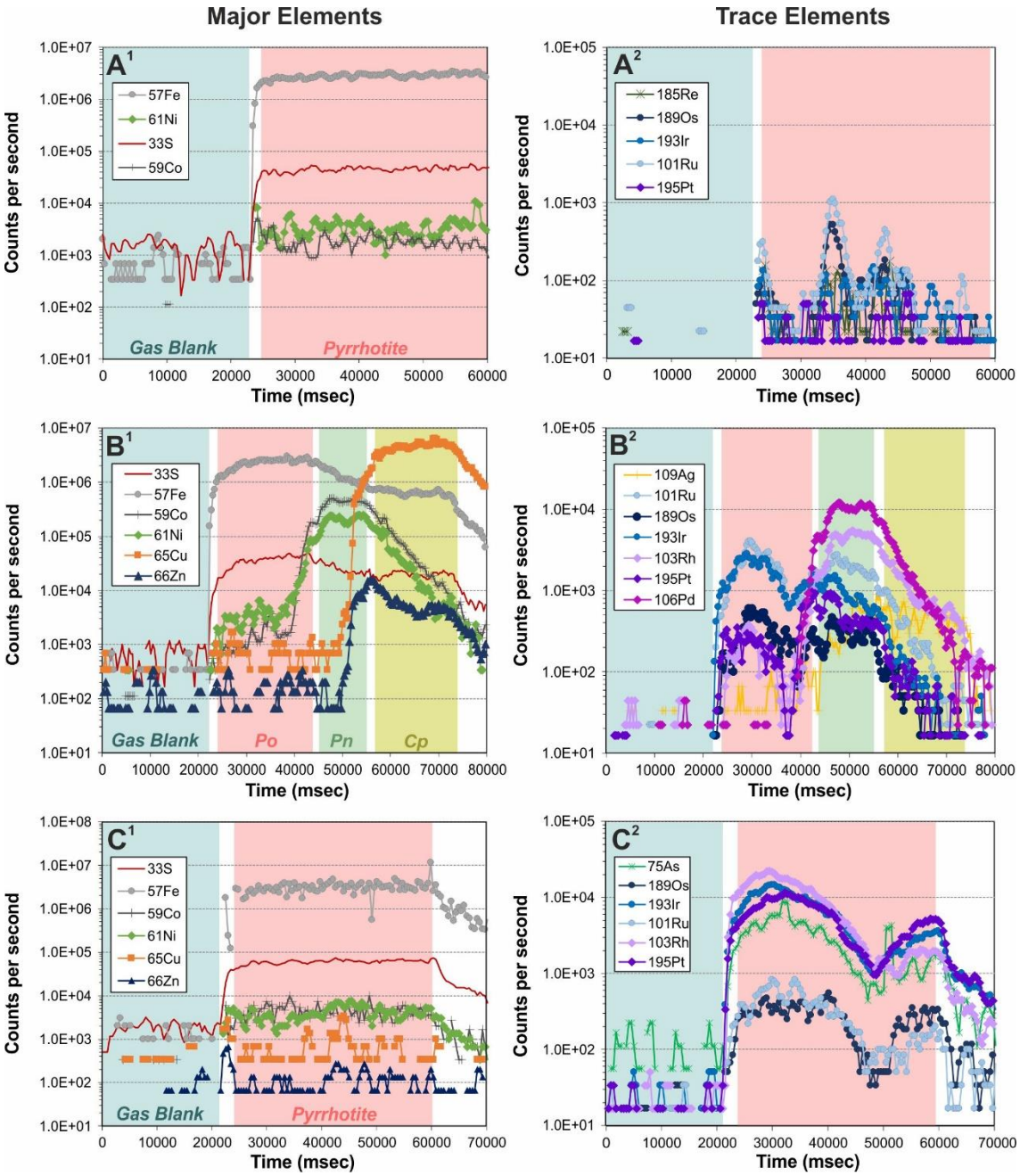

Figure 10.6: Selected time-resolved laser spectra for pyrrhotite from: (A) the Upper Pyroxenite unit as sampled in GS5A; (B) the 4th chromite stringer on the Upper/Middle Pyroxenite contact as sampled in GS20B; and (C) the Main Chromitite unit as sampled in D1_14.

10.1.3 Trace Elements in Cu-Rich Minerals

The trace elements in the Cu-rich sulphides, chalcopyrite and cubanite, are present in very low concentrations typically <10 ppm in pure chalcopyrite (see Table 10.3). The

only systematic difference observed between the Deep Platreef chalcopyrite analyses and those from the Flatreef samples is that in the former most stratigraphic units have elevated zinc concentrations that are typically 10x higher than those recorded in the Flatreef samples (see Table 10.3). These elevated zinc concentrations are identified as sphalerite inclusions in chalcopyrite as identified in microscope studies.

Elevated PGE concentrations typically correspond to analyses where there is trace pentlandite; an example time resolved analysis (TRA) plot showing this effect is provided in Figure 10.7A from the chalcopyrite grain containing the highest ΣPGE concentrations. In Figure 10.7A, Pd and Rh are present in solid solution (62.1 ppm and 8.84 ppm, respectively) and they appear to behave sympathetically with the slightly elevated Ni and Co contents indicating that the latter may be controlling the PGE concentrations as opposed to Cu. Also shown in Figure 10.7A, is a Pt micro inclusion on the edge of the chalcopyrite grain in contact with pentlandite with the approximate formula $Pt(As,Sb,Bi)_2$. In contrast, a sample from the Upper Pyroxenite (UP; see Figure 10.7B) unit shows trace pentlandite on the edge of the chalcopyrite grain but maintains elevated Pd and Rh in solid solution throughout the rest of the analysis despite the loss of elevated Ni and Co.

Cubanite was analysed in two samples from the Lower Pyroxenite (LP) and Ultramafic Zone (UMZ) of the Deep Platreef. All PGE concentrations were below detection limits in cubanite from the UMZ sample which recorded elevated S/Se ratios of 13296 significantly above the mantle range of 2850 to 4350 (Queffurus & Barnes, 2015). Two chalcopyrite grains analysed in the same sample (345_14) from the UMZ also contain significantly elevated S/Se ratios of between 9394 to 13173 and values of >5000 were also identified in chalcopyrite from the Upper Pyroxenite, Middle Pyroxenite and Norite Cycle 2 units. The cubanite analysed from the LP unit contains slightly elevated Pd (4.66 ppm), Rh (9.50 ppm) and Ag concentrations (57.7 ppm). The morphology of the cubanite between these two occurrences is different; in the LP unit the cubanite is present as exsolution lamellae in chalcopyrite whereas in the UMZ it is massive and appears to form from the breakdown of pyrrhotite as demonstrated by the patchy distribution of relict pyrrhotite in the cubanite.

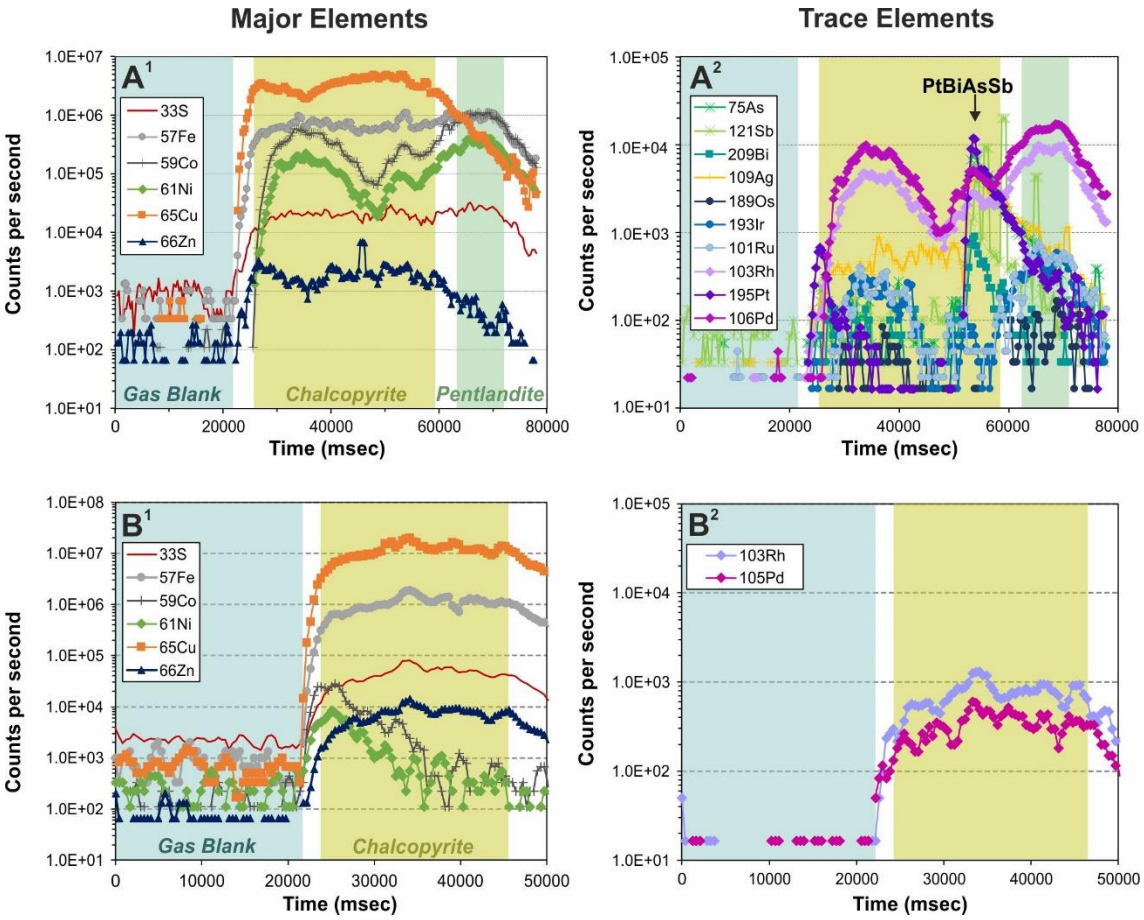

Figure 10.7: Selected time-resolved laser spectra for chalcopyrite from: (A) the 4th chromite stringer on the contact between the Upper/Middle Pyroxenite units as sampled in GS20B; (B) the Upper Pyroxenite unit as sampled in 345_03B.

Table 10.3: Summary of the trace element data collected on chalcopyrite and cubanite. Note: Cp = chalcopyrite, Cb = cubanite. Trace Pn corresponds to < 5% Ni concentration, Pn mix corresponds to > 5% Ni. Stratigraphic codes can be found in the text and the data shown are average values calculated for each stratigraphic unit.

		Mineral	Count	ΣPGE_{AV}	$\Sigma PPGE_{AV}$	$\Sigma IPGE_{AV}$	PPGE/ IPGE	$\Sigma AsSb_{AV}$	$\Sigma TeBi_{AV}$	S/Se_{Av}	Zn_{Av}	Cd_{Av}
				ppm				*ppm*			*ppm*	
Deep Platreef		*Cp*	5	0.99	0.93	0.05	17.3	0.14	0.07	3673	3544	5.52
	UP	*Cp (Pn mix)*	1	53.0	48.0	5.02	9.55	0.64	0.00	1424	2901	2.61
		Cp	6	0.14	0.10	0.05	2.10	0.03	0.37	5239	2084	7.19
		Cp (Pn trace)	3	13.4	10.7	2.67	3.99	0.18	0.24	3144	2287	7.04
	MP	*Cp (Pn mix)*	1	130	129	0.88	146	120	6.17	2564	1225	6.96
		Cp	5	0.88	0.62	0.26	2.38	0.89	1.72	3575	814	6.53
	NC2	*Cp (Pn trace)*	1	19.1	18.9	0.18	106	0.00	4.08	2647	982	6.53
		Cp	4	0.93	0.71	0.22	3.28	1.49	0.27	2766	2335	13.7
		Cp (Pn trace)	2	11.4	10.9	0.43	25.4	0.00	0.02	3783	9635	18.1
		Cp (Pn mix)	1	88.7	84.7	4.04	21.0	0.00	11.8	3711	409	b.d.l
		Cp (Cb mix)	1	8.72	8.64	0.07	116	46.1	0.49	3870	4210	8.54
	LP	*Cb*	2	7.1	4.5	2.5	1.8	0.00	0.00	3406	189	6.39
	MCHR	*Cp*	3	1.19	0.61	0.58	1.04	1.61	0.13	3291	167	13.2
		Cp	3	0.00	0.00	0.00	0.00	12.9	0.44	8863	7191	8.63
		Cp (Pn trace)	2	5.6	4.44	1.15	3.86	0.00	0.20	3382	2300	3.25
	UMZ	*Cb*	2	0.01	0.00	0.01	0.00	140	0.53	13296	3328	7.87
		Cp	2	0.41	0.41	0.00	-	0.08	0.24	2845	3832	9.69
		Cp (Pn trace)	1	2.07	1.85	0.23	8.19	186	0.62	4993	4930	13.84
	HZ_{FCPX}	*Cp (Pn mix)*	1	7.98	7.98	0.00	-	74.3	0.71	2420	1971	5.70
Normal Flatreef, NC1		*Cp*	3	0.95	0.88	0.07	12.9	0.00	4.2	2452	344	8.34
Thick Flatreef		*Cp*	2	0.20	0.16	0.04	4.25	0.00	0.41	3505	736	14.7
	UP	*Cp (trace Pn)*	1	2.30	6.74	3.98	1.69	0.00	0.06	3195	200	7.25
	MP	*Cp*	1	0.00	0.00	0.00	0.00	0.00	0.00	3667	315	10.4
		Cp	3	1.90	0.56	1.34	0.42	0.98	0.22	2640	480	8.04
	HZ_{GBRN}	*Cp (trace Pn)*	1	15.7	15.5	0.17	94.0	0.00	0.31	3599	229	7.11
	$HZ_{GBRNwCHR}$	*Cp*	3	1.48	1.48	0.00	-	1.06	9.63	3135	145	19.1

10.2 Platinum-Group Mineral Study

The results of a platinum-group mineral (PGM) study on polished thin sections (PTS) from selected samples of the Deep Platreef are presented here; in addition to some preliminary data from the Normal and Thick Flatreef. A detailed methodology is provided in Chapter 4 (section 4.6). The focus of this study is on establishing the Deep Platreef PGM assemblage following recent PGM studies on the Flatreef (normal-reef facies) by Yudovskaya et al., (2017b) in addition to two studies on the shallow Platreef at Turfspruit including a PGM study by Hutchinson & Kinnaird (2005) and a combined PGM and LA-ICP-MS study by Hutchinson & McDonald (2008).

Issues of sample representivity have been raised concerning the use of PTS to evaluate precious metal deportment in samples (Cabri, 2015). This primarily concerns the reporting of PGM occurrences as frequencies whereby a large number of very-fine grained PGM are assigned statistical significance despite contributing little to the overall PGM mass balance. To mitigate this all PGM assemblages reported for samples from hereon in are reported as relative proportions i.e. based on the calculated area of each PGM, unless stated otherwise.

In total, >1500 individual PGM were identified and categorised according to their: composition, size, mineralogical associations and textural features. The primary division of the PGM is into compositional groupings including: (1) Pt/Pd sulphides; (2) laurite; (3) Pt/Pd telluride; (4) Pt/Pd bismuthides; (5) Pt/Pd bismuthotellurides; (6) Pt/Pd arsenides; (7) Pt/Pd antimonides; (8) Pt/Pd arsenoantimonides; (9) PGE sulfarsenides; (10) Pd Mercurides; (11) Pd germanides; (12) Pt-Fe alloy; (13) Pt/Pd Sn alloy (14) Pt/Pd Pb-alloy and (15) Electrum. The size of each PGM was calculated using the short- and long-axes, measured on the SEM, and assuming an elliptical shape (see Chapter 4 section 4.6).

10.2.1 Deep Platreef PGM Assemblage

The PGM assemblage of the Deep Platreef has been characterised in 24 polished thin sections, an overview of the results are shown in Figure 10.8. The samples analysed cover all stratigraphic units with particular focus on mineralised intervals as delineated in the grade profiles also shown in Figure 10.8. The PGMs with assigned mineral names are listed in Table 10.4; for details on the determination of mineral formula and stoichiometry see Chapter 4 (section 4.6).

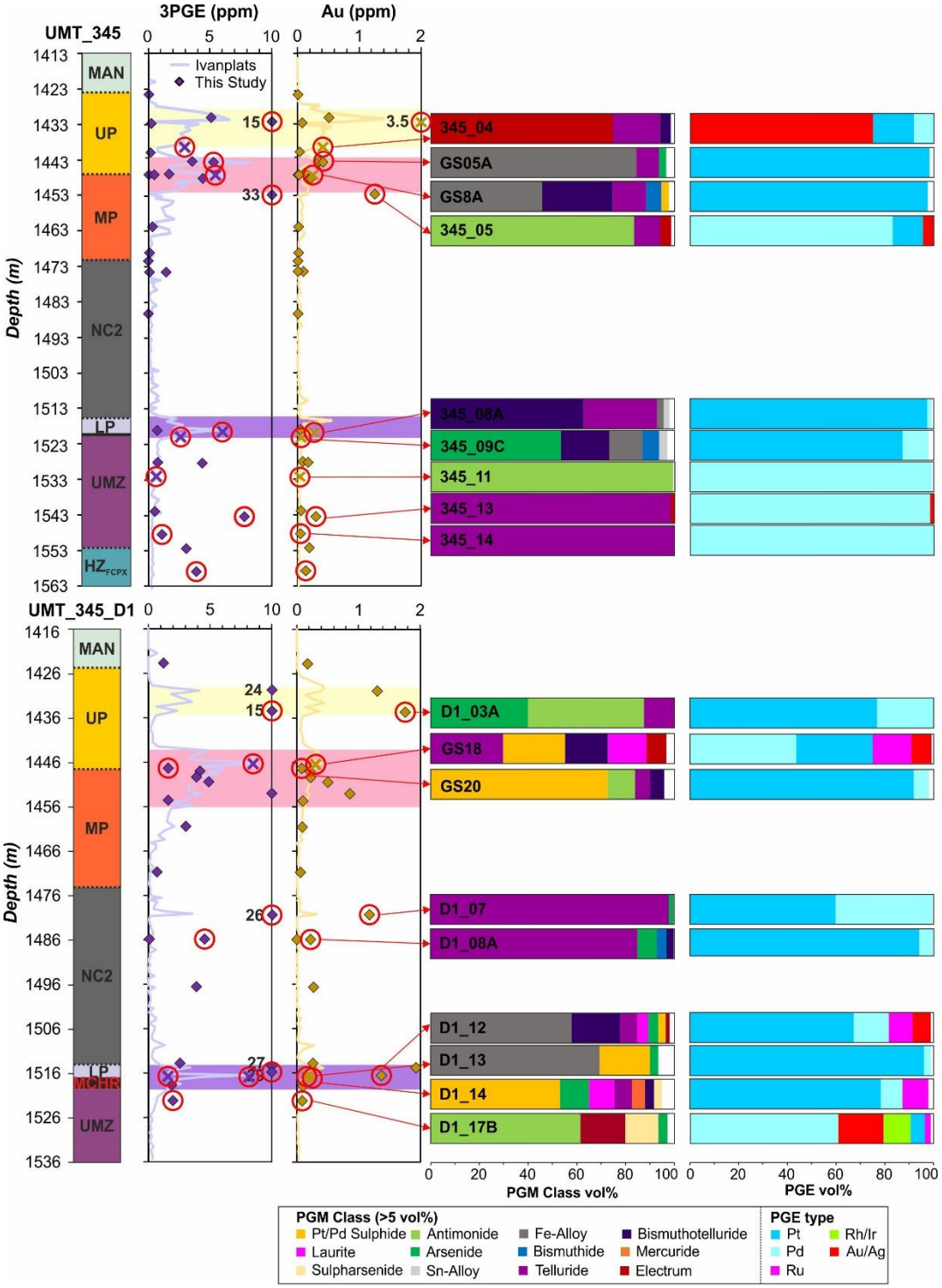

Figure 10.8: Downhole stratigraphic logs and grade profiles highlighting the location of samples analysed for their PGM assemblage (right) and a summary of the results with the distribution of each PGM class and precious metal distribution (as relative proportions, left). Note: shaded areas on grade profiles denote mineralised intervals as follows: yellow = Upper Reef; red = Middle Reef; purple = Lower Reef.

Table 10.4: Mineral names and ideal formulas for all occurrences of PGM and Au-Ag minerals identified in the different stratigraphic units as sampled in the Deep Platreef on Turfspruit. Note: n values relate to the number of samples analysed and all mineral names assigned based on PGM stoichiometry (as outlined in Cabri, 2002) determined using semi-quantitiative (non-standardised) Energy-Dispersive spectra.

		UP Upper Reef		UP Middle Reef		MP Middle Reef		NC2		LP Lower Reef		MCHR Lower Reef		UMZ	
		n=3		n=2		n=5		n=2		n=5		n=5		n=4	
Ideal Formula	Mineral Name	Area %	Grain #	Area %	Grain #	Area %	Grain #	Area %	Grain #	Area %	Grain #	Area %	Grain #	Area %	Grain #
Gold and Silver Phases															
AuAg	Electrum	75.2	7	1.15	2	4.71	3	0.05	3	1.09	43	2.67	8	5.21	5
Ag_2S	Acanthite	-	-	-	-	-	-	-	-	0.04	2	-	-	-	-
Ag_2Te	Hessite	0.0	1	-	-	1.20	5	-	-	0.02	2	0.03	2	0.27	2
AgTe	Empressite	-	-	-	-	0.02	1	-	-	-	-	-	-	-	-
$(Ni,Fe,Ag)_9S_8$	Argentian Pentlandite	-	-	-	-	-	-	5.73	5	2.51	12	-	-	19.39	4
PGE Sulphides															
PtS	Cooperite	-	-	1.37	4	41.15	18	0.06	2	1.41	29	36.28	61	-	-
(Pt,Pd)S	Braggerite	-	-	-	-	0.07	1	-	-	0.32	10	5.25	14	-	-
$(Cu,Fe)_4(Pt,Pb)_4NiS_8$	Kharaelakhite	-	-	-	-	-	-	-	-	0.11	5	0.32	2	-	-
RuS_2	Laurite	-	-	0.61	2	13.61	14	-	-	19.43	43	6.94	7	-	-
		-	-	-	-	-	-	-	-	-	-	0.19	1	-	-
PGE Tellurides, Bismuthides and Bismuthotelurides															
PdBiTe	Michenerite	1.6	1	-	-	1.22	6	1.34	12	0.58	4	-	-	25.47	18
Pd(Bi,Te)	Sobolevskite	-	-	-	-	0.00	0	1.50	4	0.36	25	2.14	15	4.97	17
Pd(Te,Bi)	Kotulskite	4.8	10	-	-	0.89	4	0.87	3	5.14	16	0.87	3	-	-
$Pt(Te,Bi)_2$	Moncheite	13.8	3	10.21	6	4.06	11	65.66	89	13.56	84	5.57	29	-	-
$PtBi_2$	Insizwaite	-	-	2.00	3	0.43	4	0.12	2	0.29	5	1.97	21	-	-
PtBiTe	Maslovite	-	-	3.93	3	-	-	-	-	7.64	27	2.84	10	0.00	2
$PdBi_2$	Froodite	0.3	1	-	-	-	-	-	-	-	-	0.05	3	0.07	9
Pd_3HgTe_3	Temagamite	-	-	-	-	0.06	1	-	-	-	-	-	-	-	-
$Pd(Te,Bi)_2$	Merenskyite	1.9	2	-	-	24.25	11	20.13	25	-	-	-	-	-	-
PdSbTe	Testbiopalladinite	-	-	-	-	-	-	-	-	-	-	-	-	0.02	1
	Unknown	0.3	1	0.13	2	-	-	0.01	1	0.00	2	0.13	4	0.05	2
PGE Arsenide, Antimonides															
$PtSb_2$	Geversite	0.6	3	-	-	4.64	46	0.12	4	-	-	1.02	3	0.62	3
Pd_2Sb	Naldrettite	0.7	1	-	-	1.17	13	-	-	0.00	1	-	-	0.00	1
$PtAs_2$	Sperrylite	0.6	7	2.46	5	0.63	39	4.30	22	2.80	16	15.55	29	0.93	9
$Pd_{5+x}Sb_{2-x}$	Stibiopalladinite	-	-	-	-	0.13	3	-	-	-	-	0.10	2	0.04	3
Pt(Sb,Bi)	Stumpflite	-	-	-	-	0.10	1	-	-	-	-	0.07	5	-	-
PdSb	Sudburyite	-	-	-	-	-	-	-	-	-	-	-	-	20.11	52
$Pd_{11}Sb_2As_2$	Isomertieite	0.2	1	-	-	-	-	-	-	0.01	1	-	-	-	-

	Unknown	-	-	-	-	1.61	12	0.04	2	-	-	0.02	1	19.40	6
PGE Sulpharsenides															
PtAsS	Platarsite	-	-	-	-	-	-	0.03	1	0.02	2	1.82	16	-	-
RhAsS	Hollingworthite	-	-	-	-	0.03	1	0.03	1	0.00	1	0.24	4	3.36	21
RuAsS	Ruarsite	-	-	-	-	-	-	-	-	0.01	1	0.05	1	0.05	2
IrAsS	Irarsite	-	-	-	-	-	-	-	-	0.00	2	-	-	-	-
PGE Metal Alloys															
Pt-Fe	Undifferentiated	-	-	77.64	7	-	-	-	-	43.79	157	11.33	15	-	-
$(Pt,Pd)_3Sn$	Rustenburgite	-	-	0.50	2	-	-	-	-	0.49	61	0.72	10	-	-
Pd_2Sn	Paolovite	-	-	-	-	-	-	-	-	0.01	2	-	-	0.04	5
Pd_3Sn	Atokite	-	-	-	-	-	-	-	-	0.03	4	0.08	4	0.00	1
Pd_2Sn_2	Stannopalladinite	-	-	-	-	-	-	-	-	0.00	1	-	-	-	-
	Sn-alloy Unknown	-	-	-	-	-	-	0.01	1	0.00	2	-	-	-	-
Pd_3Pb	Zvyagintsevite	-	-	-	-	-	-	-	-	0.09	9	-	-	-	-
Pd_3Pb_2	Plumbopalladinite	-	-	-	-	-	-	-	-	0.05	1	-	-	-	-
PGE Other															
$(Pd,Pt)_2Ge$	Palladogermanide	-	-	-	-	-	-	-	-	0.03	7	-	-	-	-
PdHg	Potarite	-	-	-	-	-	-	-	-	0.16	3	3.74	2	-	-
	Total	100	38	100	36	100	194	100	177	100	580	100	272	100	163

The overview of the PGM assemblage of the Deep Platreef, as shown in Figure 10.8, illustrates the zonal distribution of certain PGM classes. This is evident in the restricted distribution of Pt/Pd sulphides and laurite to stratigraphic contacts with chromite stringers i.e. on the contact between the Upper Pyroxenite (UP) and Middle Pyroxenite (MP) units and within the Main Chromitite (MCHR) unit. In contrast, telluride and bismuthide PGMs are found ubiquitously regardless of the host rock lithology. The principal control on the PGM composition appears to be lithological although secondary hydrothermal alteration may also play a role with altered lithologies containing elevated arsenide and antimonide populations. As shown in Table 10.4, the majority of PGM phases are carriers of Pt and Pd, the only significant concentrations of Ru are found in laurite (up to 14 and 20% in the MP and LP units, respectively) and negligible Rh and Ir in sulpharsenide phases.

The presence of PGE sulphides in the Platreef orebody were originally thought to be geographically restricted to sections where the underlying footwall rocks are composed of the anhydrous basement rocks such as on Drenthe, Overysel and Zwartfontein north (Gain & Mostert, 1982; Kinloch, 1982; Holwell & McDonald, 2007). Sulphide PGM phases are notably absent and/or rare in studies on the shallow Platreef where the underlying footwall is composed of dolomites e.g. on Sandsloot (Armitage et al., 2002; Holwell et al., 2006). The identification of PGE sulphides including cooperite, braggerite and laurite (see Table 10.4) has only recently been noted on Turfspruit in a study on the Flatreef by Yudovskaya et al., (2017b) and in the current study on the Deep Platreef.

The textural settings of the PGMs identified in the Deep Platreef are presented in Table 10.5 and a summary for each stratigraphic unit is shown in Figure 10.9. In all stratigraphic units a significant proportion of the PGM are hosted either in or adjacent to base metal sulphides. In Figure 10.9B it can be seen that pentlandite hosts the majority of PGM in all stratigraphic units; this matches the observed elevated PGE tenors in pentlandites from the Deep Platreef, as presented above in section 10.1.1 above. Alteration silicates are also identified to host a significant number of PGM suggestive of remobilisation of either the PGM or of sulphur; significant S-loss of former sulphide minerals leaving satellite PGM in secondary silicates has been identified in the shallow Platreef on Turfspruit by Hutchinson & Kinnaird (2005).

Table 10.5: An overview of the textual setting of PGM between the different stratigraphic units of the Deep Platreef on Turfspruit.

	UP Upper Reef	UP Middle Reef	MP Middle Reef	NC2	LP Lower Reef	MCHR Lower Reef	UMZ
	n=2	n=2	n=5	n=2	n=5	n=5	n=4
Enclosed in Sulphide	27	22	18	16	20	20	40
Po	11	6	6	2	2	1	6
Pn	11	8	9	9	11	15	19
Cp	0	3	3	1	3	1	12
Py	0	0	0	1	0	1	0
Po/Pn	0	6	0	1	2	1	1
Po/Cp	5	0	1	0	1	0	0
Cp/Pn	0	0	0	1	1	0	2
Py/Pn	0	0	0	1	0	0	0
Sulphide/Silicate	16	36	24	34	23	16	9
Po/Sil	6	11	1	8	3	3	0
Pn/Sil	5	17	15	22	11	9	6
Cp/Sil	5	8	8	4	9	3	3
Sulphide/Magnetite	0	0	0	0	0	0	3
Po/Mgn	0	0	0	0	0	0	1
Pn/Mgn	0	0	0	0	0	0	1
Cp/Mgn	0	0	0	0	0	0	1
Sulphide/Chromite	0	6	5	1	3	14	1
Po/Chr	0	6	2	1	1	3	1
Pn/Chr	0	0	2	0	1	7	0
Cp/Chr	0	0	1	0	2	3	0
Py/Chr	0	0	0	0	0	0	0
Cp/Rt	0	0	1	1	0	0	0
Po/Ilm	0	0	0	0	0	0	0
Enclosed in Chromite	0	0	0	0	0	8	0
Chr	0	0	0	0	0	2	0
Chr/Chr	0	0	0	0	0	6	0
Chromite/Silicate	0	3	4	0	3	15	0
Chr/Sil	0	3	4	0	3	13	0
Rt/Sil	0	0	1	0	0	0	0
Enclosed in Magnetite	8	0	0	0	0	0	5
Magnetite/Silicate	3	0	0	0	0	0	0
Enclosed in Ilmenite	0	0	0	0	0	1	0

Enclosed in Niccolite	0	0	0	0	0	0	1
Primary Silicate	8	11	6	7	18	5	7
Interstitial	0	0	5	3	10	5	0
Cumulate	5	6	0	4	5	0	6
Primary/Primary	0	0	1	0	2	0	0
Oikocryst	3	6	0	0	2	0	0
Primary/Alteration	0	3	5	0	3	0	1
Alteration Silicates	38	19	38	43	29	21	34
w BMS	24	19	21	40	18	17	26
No BMS	14	0	8	2	11	4	9
Sum Total	100	100	100	100	100	100	100

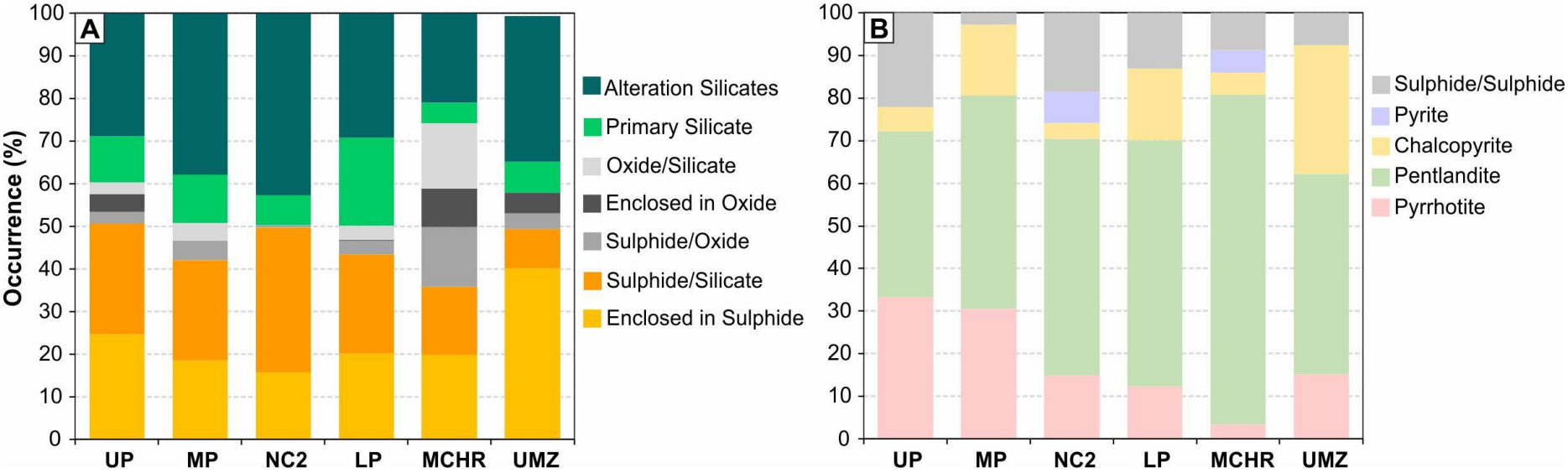

Figure 10.9: Stacked bar charts for each stratigraphic unit summarising the textural setting of the PGMs identified. (A) A summary of the distribution of PGM between all textural settings observed. (B) A closer look at the distribution of the PGM between the various sulphide phases present.

The range in the size of the longest axis measured for all PGMs identified within the Deep Platreef are shown in Figure 10.10. No systematic change in the size of the PGM between the different stratigraphic units was observed. In all stratigraphic units the size (longest axis) of the majority of PGMs analysed varies between 1 to 8 µm (see Figure 10.10). The maximum long axis measured is 102 µm in length (with an area of 8172 µm^2) in a pegmatoidal gabbronorite sample from the Ultramafic Zone (UMZ). The smallest range in PGM sizes is observed within the Main Chromitite (MCHR) unit.

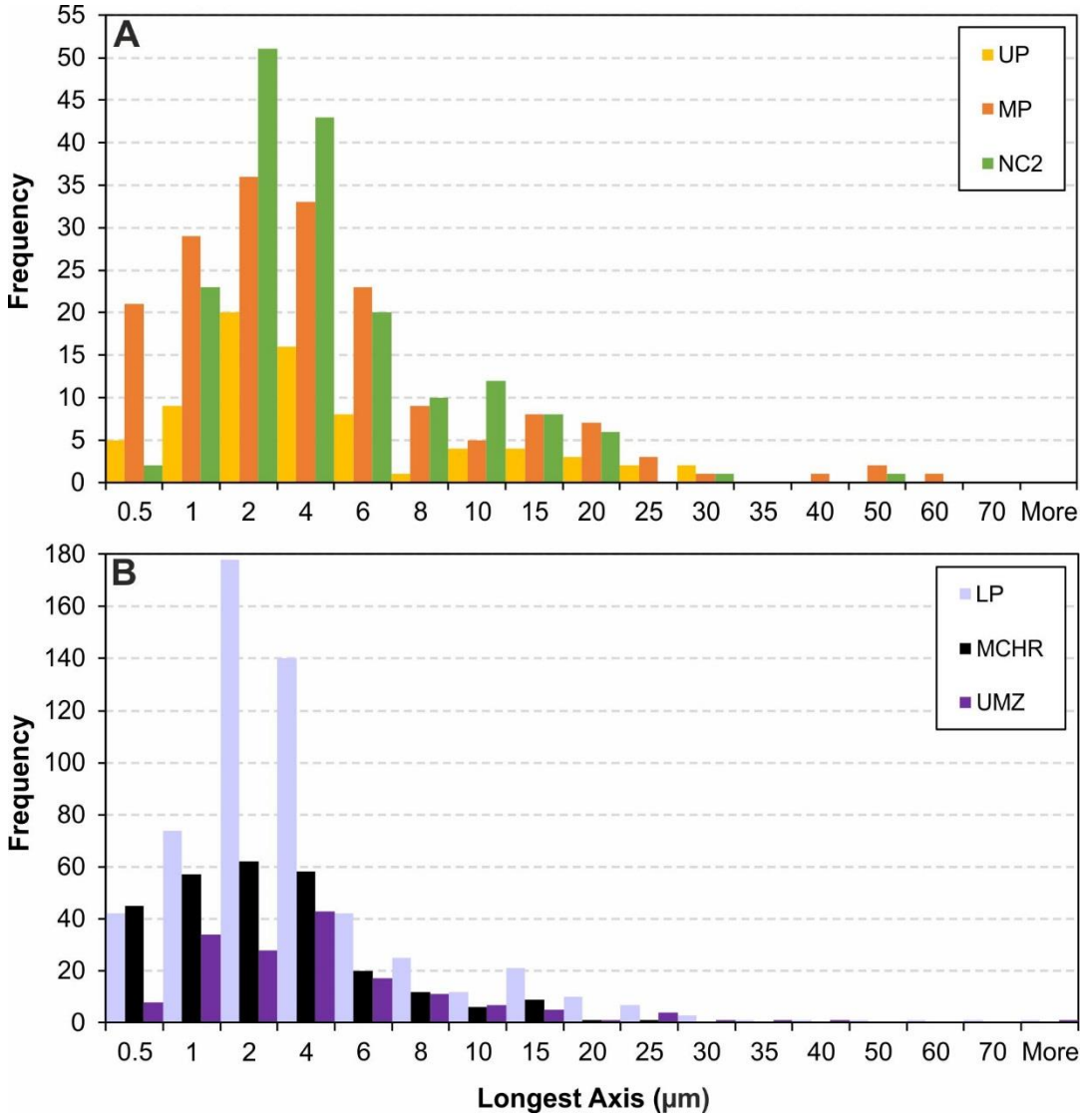

Figure 10.10: The range of PGM size (longest axis) for the various stratigraphic units in the Deep Platreef on Turfspruit. (A) Upper Pyroxenite (UP), Middle Pyroxenite (MP) and Norite Cycles 2 (NC2) and; (B) Lower Pyroxenite (LP), Main Chromitite (MCHR) and Ultramafic Zone (UMZ).

The PGM assemblage of the Upper Pyroxenite (UP) was identified in samples covering the two mineralised intervals, as shown in Figure 10.8 namely the Upper Reef and Middle Reef. The PGM assemblages between these two mineralisation events varies significantly with the Upper Reef dominated by electrum (75 %, see Figure

10.11A) compared to Pt-Fe alloys (77 %, see Figure 10.11D) in the Middle Reef. Other PGM phases identified in the Upper Reef interval include tellurides (23 %, predominantly moncheite), antimonides (1.4%, naldrettite and geversite) and arsenides (0.6%, sperrylite). The majority of the PGM are identified either in alteration silicates (38 %) with nearby BMS phases (see Figure 10.11A and 10.11B) or enclosed in sulphide minerals (27%). In the Middle Reef interval (see examples in Figure 10.11C and 10.11D), the other PGM phases identified include Pt-tellurides (10%, moncheite), Pt-bismuthotellurides (4 %, maslovite), Pt-arsenide (2.5 %, sperrylite) and minor (< 2 %) electrum, cooperite and laurite. The majority of the PGMs are found spatially associated with sulphides either on sulphide-silicate contacts (36 %, see Figure 10.11D), enclosed in sulphide (22 %) or in alteration silicates with nearby sulphide (19 %, see Figure 10.11C).

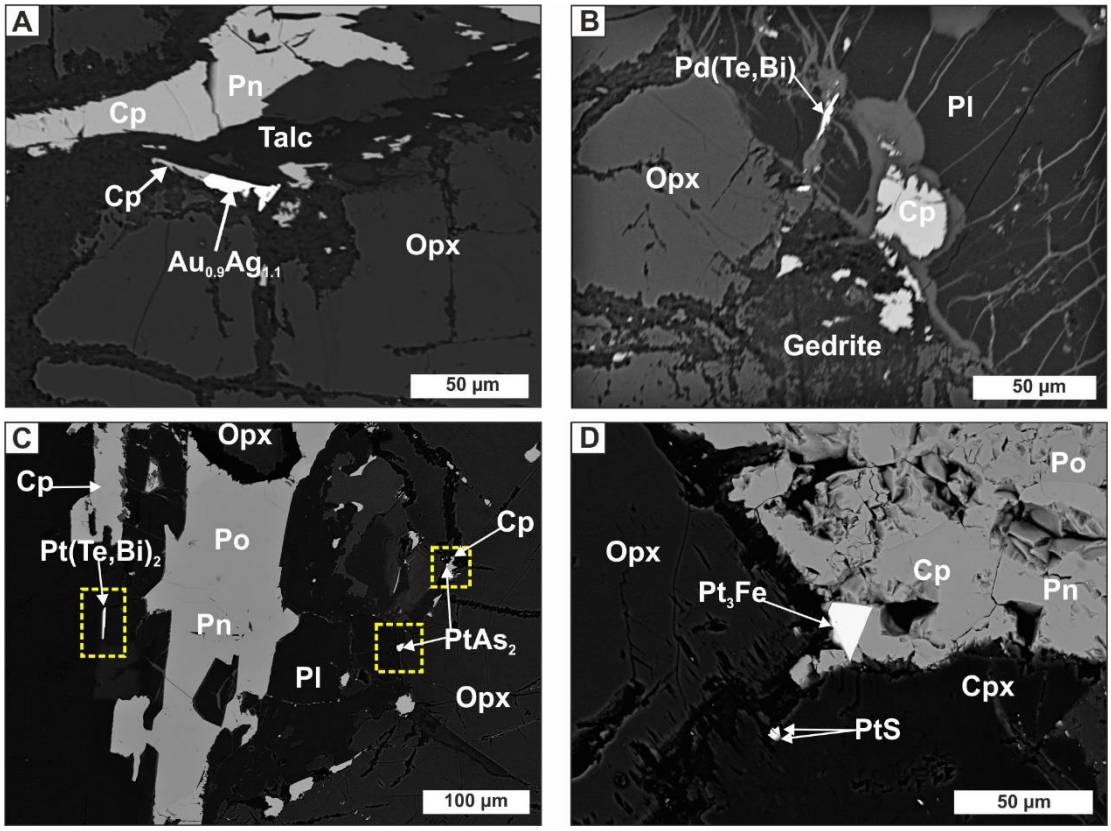

Figure 10.11: Backscattered electron images of the PGM assemblage within the Upper and Middle Reef mineralisation within the UP unit. (A) Electrum attached to fragmentary chalcopyrite on edge of polyphase BMS (345_04). (B) Kotulskite isolated in alteration silicates (345_04). (C) Three PGMs, one moncheite and two sperrylites, spatially associated with BMS (GS05A). (D) Euhedral Pt-Fe alloy on the edge of chalcopyrite and cooperite in silicates (GS05A). Note: Po, pyrrhotite; Pn, pentlandite; Cp, chalcopyrite; Opx, orthopyroxene; Cpx, clinopyroxene; Pl, plagioclase.

In addition to PGM phases a number of other accessory minerals were identified in the UP unit including: zircon, uraninite (UO_2), cobaltite (CoAsS), native bismuth,

monazite ((Ce,La,Nd,Th)PO_4) and galena (see Figure 10.12). These trace minerals are typically found in alteration pathways including in talc/tremolite alteration of orthopyroxene (see Figure 10.12A), and clinopyroxene (see Figure 10.12B); the only exception to this is galena found as anhedral inclusions in sulphides (mainly chalcopyrite, see Figure 10.12D). Monazite is found in interstitial areas associated with quartz and phlogopite (see Figure 10.12C).

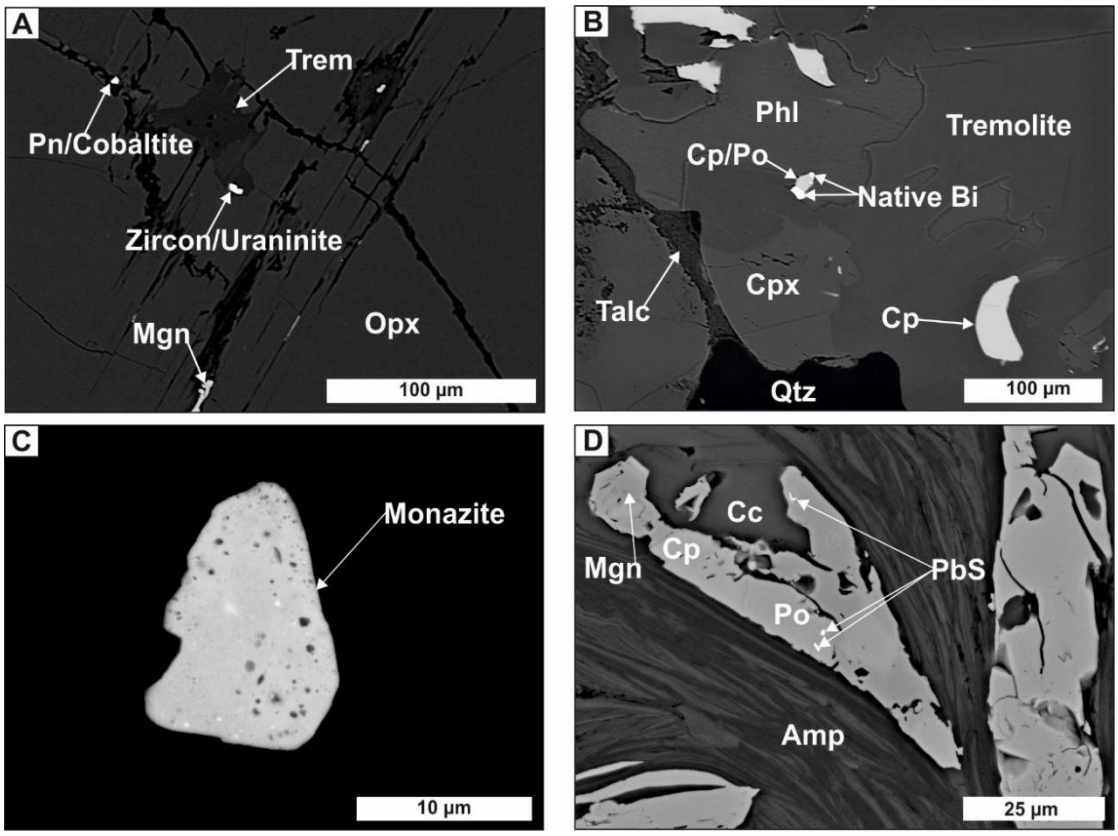

Figure 10.12: Backscattered electron images of accessory minerals identified within the Upper Pyroxenite unit. (A) Cobaltite, zircon and uraninite in alteration pockets in orthopyroxene (Opx, 345_04); (B) Native bismuth attached to polyphase sulphides in alteration silicates (345_04); (C) A pitted monazite grain (345_04). (D) Galena hosted as fine-grained inclusions in pyrrhotite (GS5A). Note: Po, pyrrhotite; Pn, pentlandite; Cp, chalcopyrite; Mgn, magnetite; Phl, phlogopite; Opx, orthopyroxene; Cpx, clinopyroxene; Amp, amphibole; Cc, calcite.

The dominant PGM composition of the 3rd and 4th chromite stringers (as analysed in samples GS18A/B and GS20A/B, respectively) varies with height; the top of the chromite stringers are dominated by Pt-sulphide phases and the base by antimonide and telluride phases.

The feldspathic orthopyroxenite hanging wall to the 3rd chromite stringer is dominated by cooperite (61 %, see Figure 10.13A and 10.13B), laurite (26 %) and Pt-Pd tellurides (12%, dominated by moncheite; see Figure 10.13C and 10.13D) with minor (< 1%) stibiopalladinite and hessite (Ag_2Te). The majority of the PGM are located in alteration silicates (59 %) spatially associated with fragments of BMS (see Figure 10.13A,

10.13B and 10.13D) and on sulphide-silicate contacts (24 %, see Figure 10.13C). No association with chromite grains is observed and no PGM are observed enclosed in sulphides. The PGM grains are typically sub- to euhedral and the average size is coarse-grained at 74 μm^2.

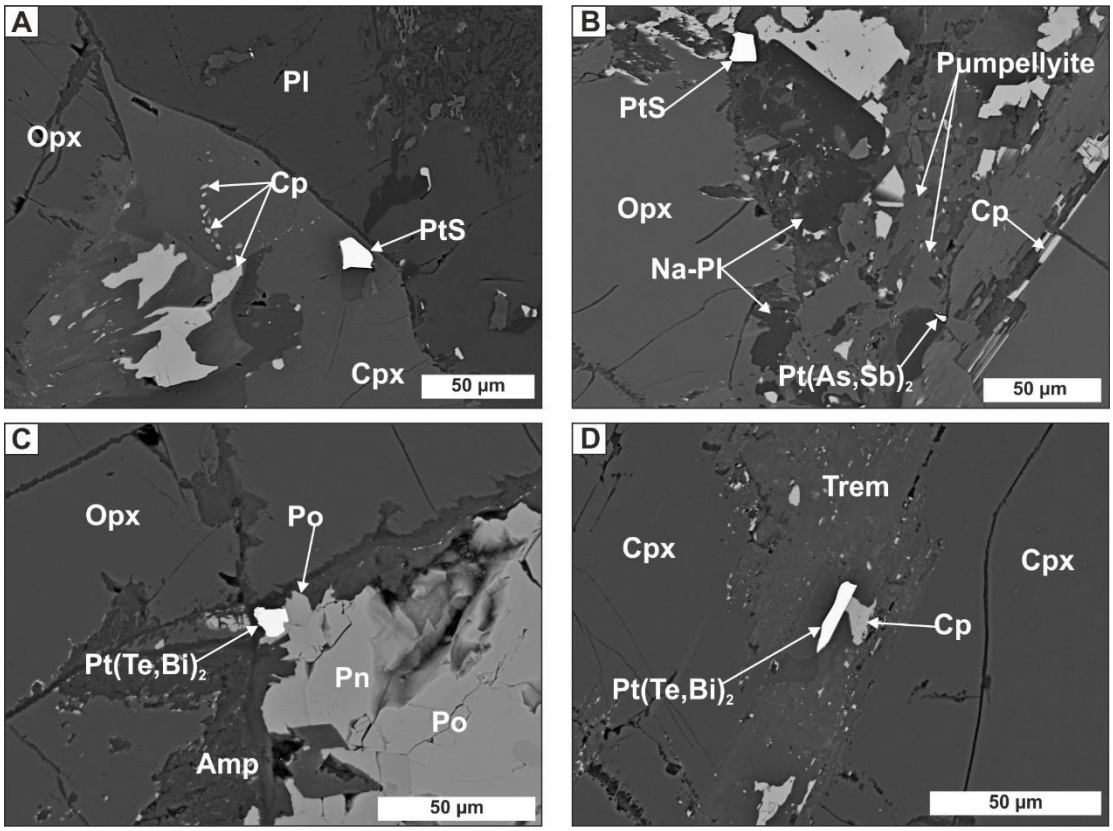

Figure 10.13: Backscattered electron images of the PGM assemblage from the top of the 3rd chromite-stringer in the UP unit as sampled in GS18A. (A) Cooperite hosted on the contact between clinopyroxene and plagioclase. (B) Cooperite associated with fragmentary sulphides on edge of orthopyroxene in contact with Na-plagioclase. (C) Moncheite on the edge of a polyphase sulphide in contact with an amphibole alteration rim formed on the contact between the sulphide and orthopyroxene. (D) Moncheite in tremolite alteration in clinopyroxene. Note: Po, pyrrhotite; Pn, pentlandite; Cp, chalcopyrite; Na-Pl, sodic plagioclase; Pl, plagioclase; Opx, orthopyroxene; Cpx, clinopyroxene; Amp, amphibole.

The 3rd chromite stringer and the pegmatoidal footwall was sampled in GS18B. In this locality, the PGM assemblage is more varied than in the hanging wall consisting of: Pd-tellurides (60 %, merenskyite), laurite (17 %, see Figure 10.14B), electrum (11 %), cooperite (4 %, see Figure 10.14A) and minor arsenide-antimonide phases (see Figure 10.14C and 10.14D). The arsenide and antimonide phases identified include geversite, sperrylite and stibiopalladinite (in addition to some unknown minerals); these account for 6% relative proportion but were the most frequently counted grains (61 %). In contrast, only one grain each of laurite and electrum were identified as large euhedral grain (see Figure 10.14B) with areas of 257 μm^2 and 273 μm^2, respectively. The arsenide and antimonide phases demonstrate a characteristic morphologically;

they form as anhedral films on the edge of sulphides interpreted as an exsolution texture as shown in Figure 10.14C and 10.14D. The majority of the PGM are located in alteration silicates (30 %), on sulphide- silicate contacts (26 %) and enclosed in sulphide (20%, mostly pentlandite).

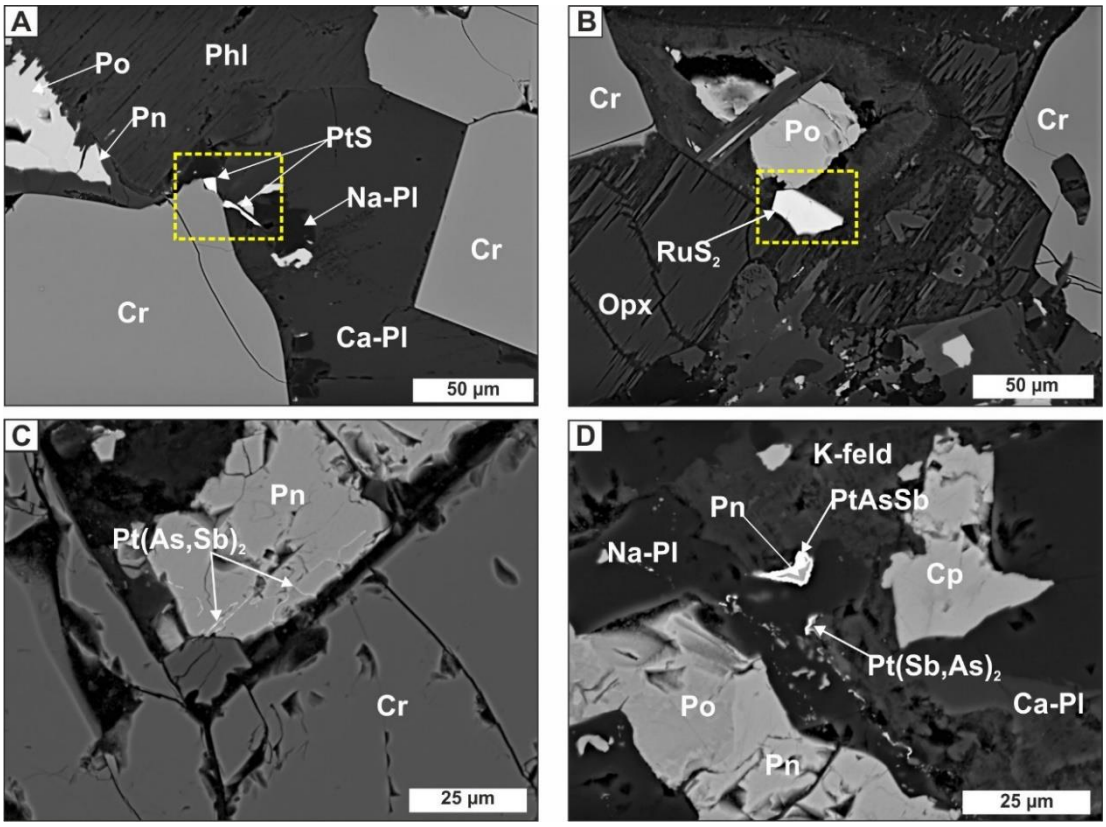

Figure 10.14: Backscattered electron images of selected PGM from the 3rd chromite-stringer as sampled in GS18B. (A) Two cooperite grains on the outside edge of chromite in contact with interstitial plagioclase. (B) A large laurite grain in altered orthopyroxene associated with pyrrhotite. (C) A geversite rim on the grain boundary between pentlandite and pyrrhotite. (D) A geversite rim around pentlandite in interstitial altered plagioclase. Note: Cr, chromite; Po, pyrrhotite; Pn, pentlandite; Cp, chalcopyrite; Na-Pl, sodic plagioclase; K-feld, K-feldspar; Opx, orthopyroxene.

The pegmatoidal feldspathic orthopyroxenite in the footwall of the 3rd chromite stringer, is sulphide-rich and a pegmatoidal base metal sulphide (BMS) was observed to host numerous PGMs in a variety of textural settings. In the pyrrhotite and pentlandite core of the BMS cooperite grains were identified as inclusions (see Figure 10.15D), electrum was identified in the chalcopyrite portion on the edge of the BMS (see Figure 10.15C) and michenerite and hessite in amphibole alteration on the edge of the BMS (see Figure 10.15A and 10.15B). Amphibole laths penetrate into the BMS perpendicular to the grain margin and are accompanied by quartz on the contact between the BMS and silicates indicating the percolation of felsic later-stage hydrothermal fluids. These textures are described for the Merensky Reef in Li et al.,

(2005) and in the shallow Platreef by Hutchinson & Kinnaird (2005) and Junge et al., (2018).

The PGM identification away from sulphides in the silicate areas within this unit was made more difficult because of the formation of clusters of galena in interstitial areas dominated by plagioclase (as shown in Figure 10.15E). In addition, accessory minerals including clusters of zircon and rutile were observed (see Figure 10.15F).

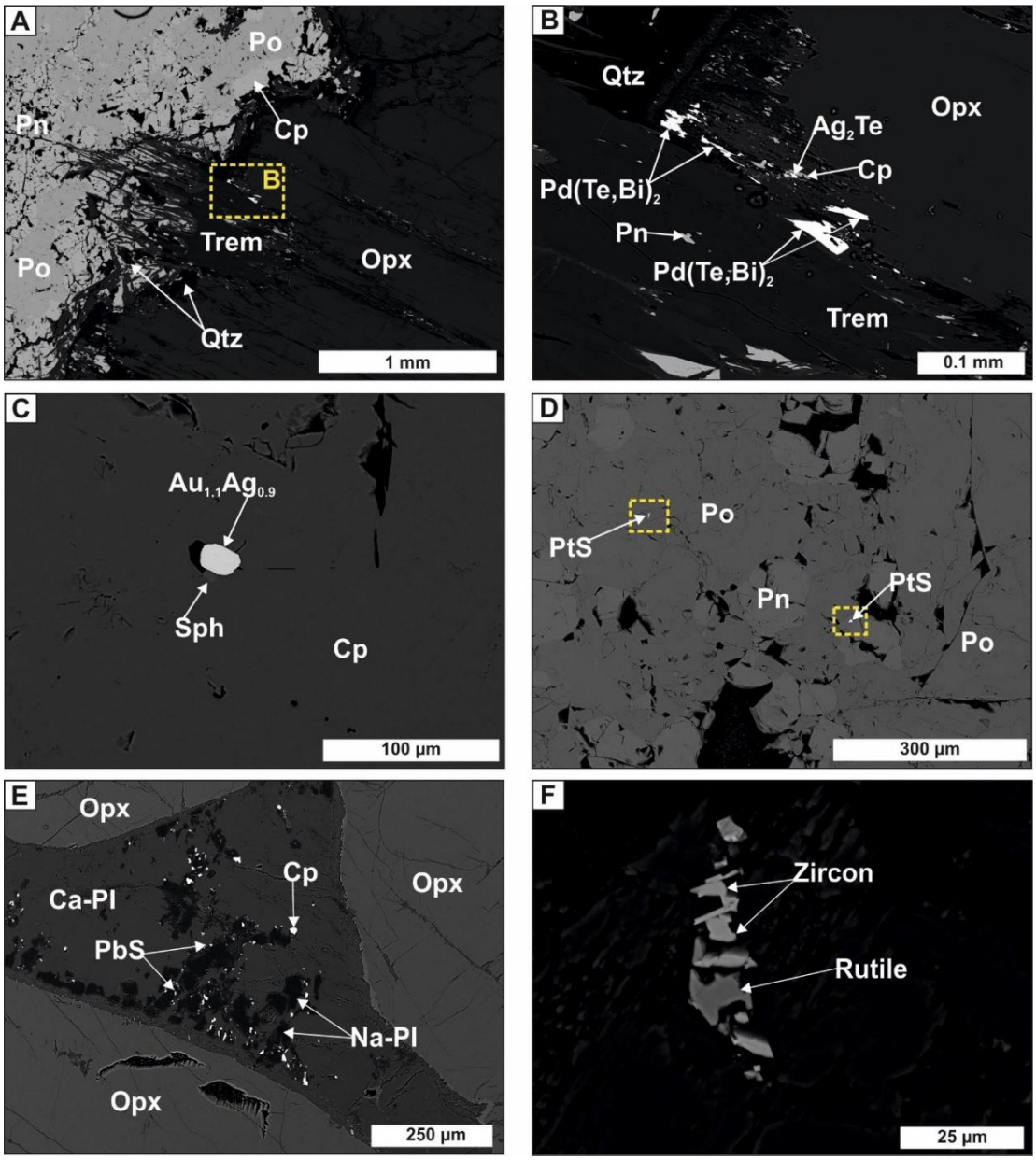

Figure 10.15: Backscattered electron images of the PGM assemblage in the pegmatoidal BMS mineralised unit below the 3rd chromite stringer as sampled in GS18B. (A) On the edge of a very coarse, polyphase BMS talc-tremolite alteration detaches a cluster of PGM as shown in B. (B) A cluster of Pd- and Ag-telluride phases hosted in alteration silicates. (C) Euhedral electrum hosted in chalcopyrite accompanied by minor sphalerite. (D) Multiple cooperite inclusions in the middle of the pegmatoidal BMS. (E) Plagioclase-dominated interstitial areas contain numerous galena grains associated with Na-plag. (F) A cluster of the accessory phases

zircon and rutile. Note: Cr, chromite; Po, pyrrhotite; Pn, pentlandite; Cp, chalcopyrite; Sph, sphalerite; Trem, tremolite; Opx, orthopyroxene; Qtz, quartz.

The 4th chromite stringer demonstrates similar characteristics to that of the 3rd chromite stringer with a change in the dominant PGM type with height. The top of the 4th chromite stringer is dominated by Pt-sulphides (90 %); based on the frequency of analysed grains this accounts for 6 % of the total grain count reflecting the coarse-grained size of the PGM identified (up to 1504 µm^2, see Figure 10.16A). In comparison, laurite grains were identified at the same frequency however, as a relative proportion they account for only 2 %. This chromite stringer records the first appearance of a sulpharsenide phase with the identification of hollingworthite as part of a polyphase assemblage accompanied by sperrylite and michenerite on the edge of a chromite grain (see Figure 10.16B). Pt/Pd arsenide and antimonide phases including the minerals geversite, naldrettite, stibiopalladinite and sperrylite are frequently recorded but all have areas < 5 µm^2.

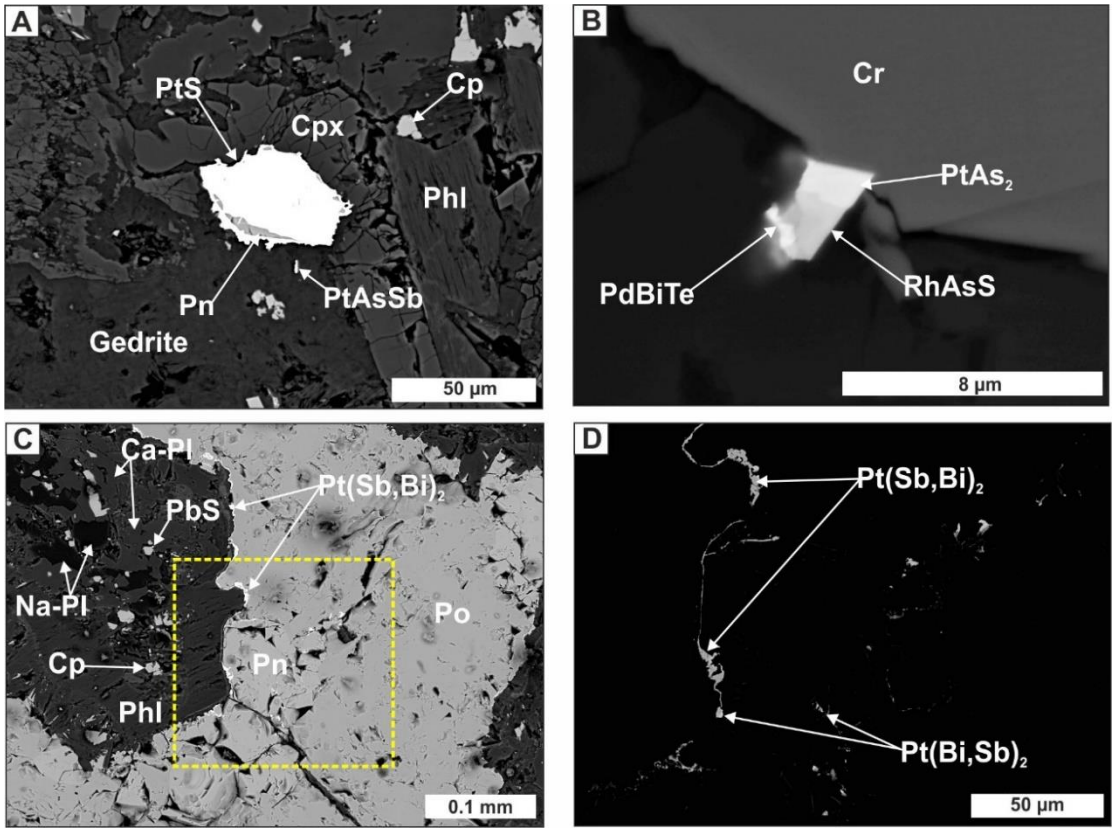

Figure 10.16: Backscattered electron images of the PGM assemblage in the 4th chromite-stringer. (A) Coarse-grained, subhedral cooperite enclosed in alteration silicates (GS20A). (B) A polyphase PGM consisting of sperrylite, hollingworthite and michenerite on the edge of a chromite grain (GS20A). (C and D) A mixture of geversite and insizwaite form on the edge of a polyphase pyrrhotite and pentlandite BMS (GS20B). Note: Cr, chromite; Po, pyrrhotite; Pn, pentlandite; Cp, chalcopyrite; Na-Pl, sodic plagioclase; Ca-Pl, calcic plagioclase.

The base of the 4th chromite stringer is dominated by Pt-antimonide phases (56 %, geversite), an exceptional example of the morphology of this PGM is shown in Figure 10.16C and 10.16D. The complex geversite PGM as shown in Figure 10.16C and 10.16D is accompanied by lesser amounts of insizwaite containing appreciable amounts of antimony.

The PGM assemblage of the Norite Cycles 2 unit (NC2) was analysed in samples of sulphide-bearing pyroxenite from the base of a norite cycle. The dominant PGM, as shown in Figure 10.17, are moncheite (66 %), merenskyite (20 %) and sperrylite (4 %); other minor phases identified include argentian pentlandite, Pd-bismuthides, hollingworthite and platarsite. The largest proportion of PGM phases are identified in alteration silicates associated with sulphides (40 %, see Figure 10.17E and 10.17F), on sulphide-silicate contacts (34 %, see Figure 10.17A), enclosed in sulphide (16 %, see Figure 10.17B and 10.17D) and enclosed in primary silicate minerals (see Figure 10.17C).

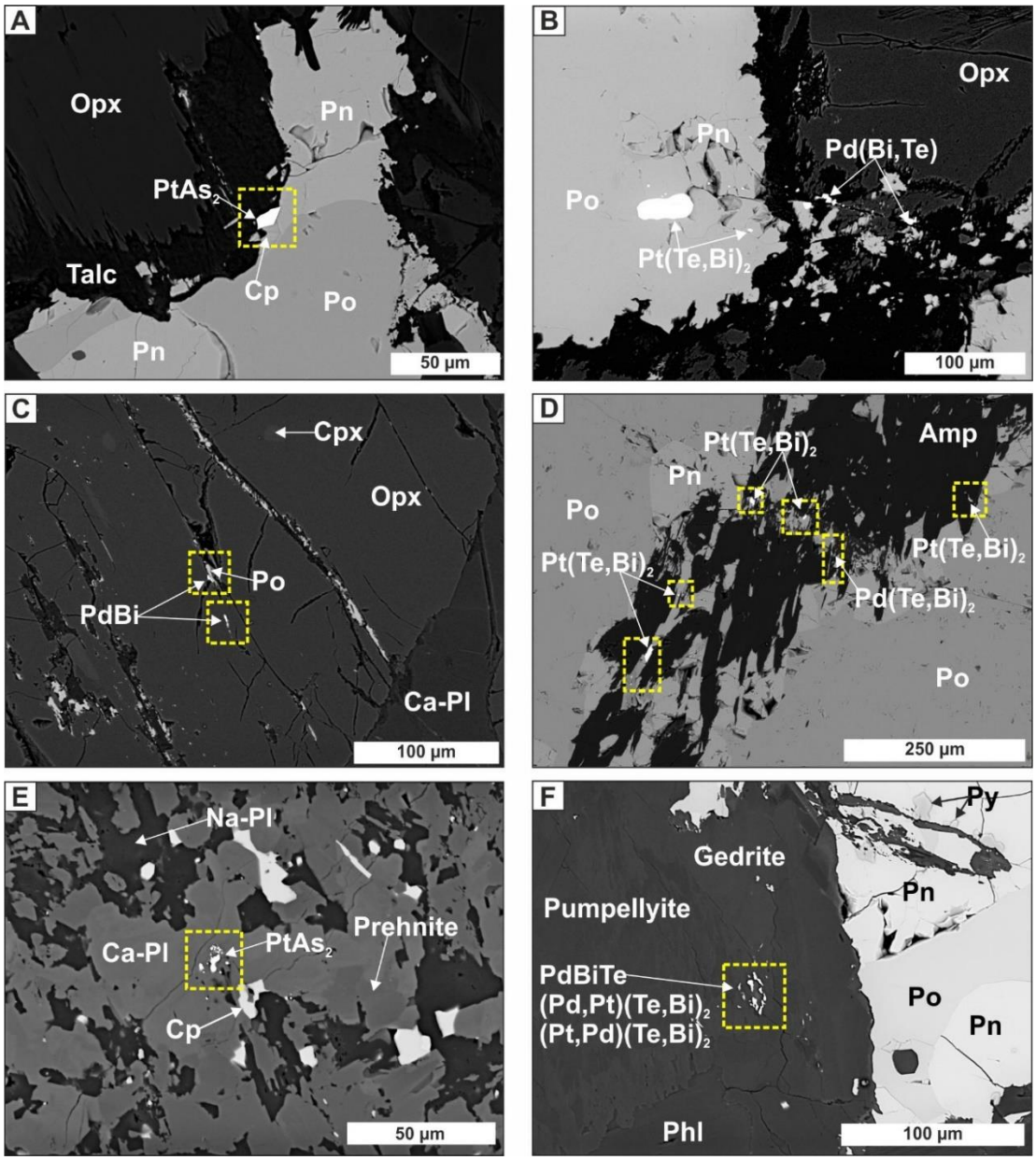

Figure 10.17: Backscattered electron images of the PGM assemblage within the NC2 unit. *Images A to C from sample D1_08A and D to F from D1_07.* (A) Euhedral sperrylite on the edge of pentlandite (D1_08A). (B) A cluster of moncheite and sobolevskite associated with sulphide. (C) Kotuluskite grains enclosed in orthopyroxene. (D) Numerous moncheite grains associated with pentlandite being altered by tremolite. (E) A cluster of sperrylite in plagioclase undergoing alteration. (F) A cluster of merenskyite and moncheite in alteration silicates in proximity to a polyphase BMS. Note: Cr, chromite; Po, pyrrhotite; Pn, pentlandite; Cp, chalcopyrite; Amp, amphibole; Opx, orthopyroxene; Na-Pl, sodic plagioclase; Ca-Pl, calcic plagioclase.

The Lower Pyroxenite (LP) unit hosts the beginning of the Lower Reef mineralisation event (see Figure 10.8). The greatest variability in the PGM compositions are identified in the LP unit (as shown in Table 10.4); PGMs identified only in this stratigraphic unit include: potarite, palladogermanide, plumbopalladinite, zvagintsevite and stannopalladinite. These phases are typically small and do not significantly contribute

to the overall PGM budget (<0.5 %). Pd-germanide phases were first identified in the Platreef by Armitage et al., (2002) and have subsequently been identified by Holwell et al., (2006) and Junge et al., (2018). In addition, a number of precious metal phases were identified including electrum, hessite, acanthite and argentian pentlandite. Texturally, the PGM are principally found on sulphide-silicate contacts (23 %), enclosed in sulphides (20 %, predominantly pentlandite), in alteration silicates associated with sulphides (18 %) and in primary silicates (18 %).

The dominant PGM phases in the LP unit are Pt-Fe alloys (44 %), laurite (19 %) and Pt/Pd tellurides (19%, mostly moncheite). The morphology of the Pt-Fe alloy is distinctive, they are most commonly found as: (A) idiomorphic grains (see Figure 10.18D); (B) in clusters of euhedral to subhedral grains or; (C) intergrown with pyrrhotite (see Figure 10.18C), pentlandite (see Figure 10.18A and 10.18B) or chromite (see Figure 10.18E) forming a symplectite texture. Pt-Fe alloy symplectites are described in Yudovskaya et al., (2011) along strike (northwards) at an equivalent depth on the Akanani project. The presence, as shown in Figure 10.18C, of an exsolution within the confines of a cube suggests that the Pt-Fe alloy was originally idiomorphic but under changing chemical conditions upon cooling it became unstable and exsolved. The dominance of Pt-Fe alloys in this stratigraphic unit may result from the presence of disseminated chromite producing a local oxidising environment leading to S removal from a PGM of original sulphide composition adjacent to chromite grains, as shown in progress in Figure 10.18F.

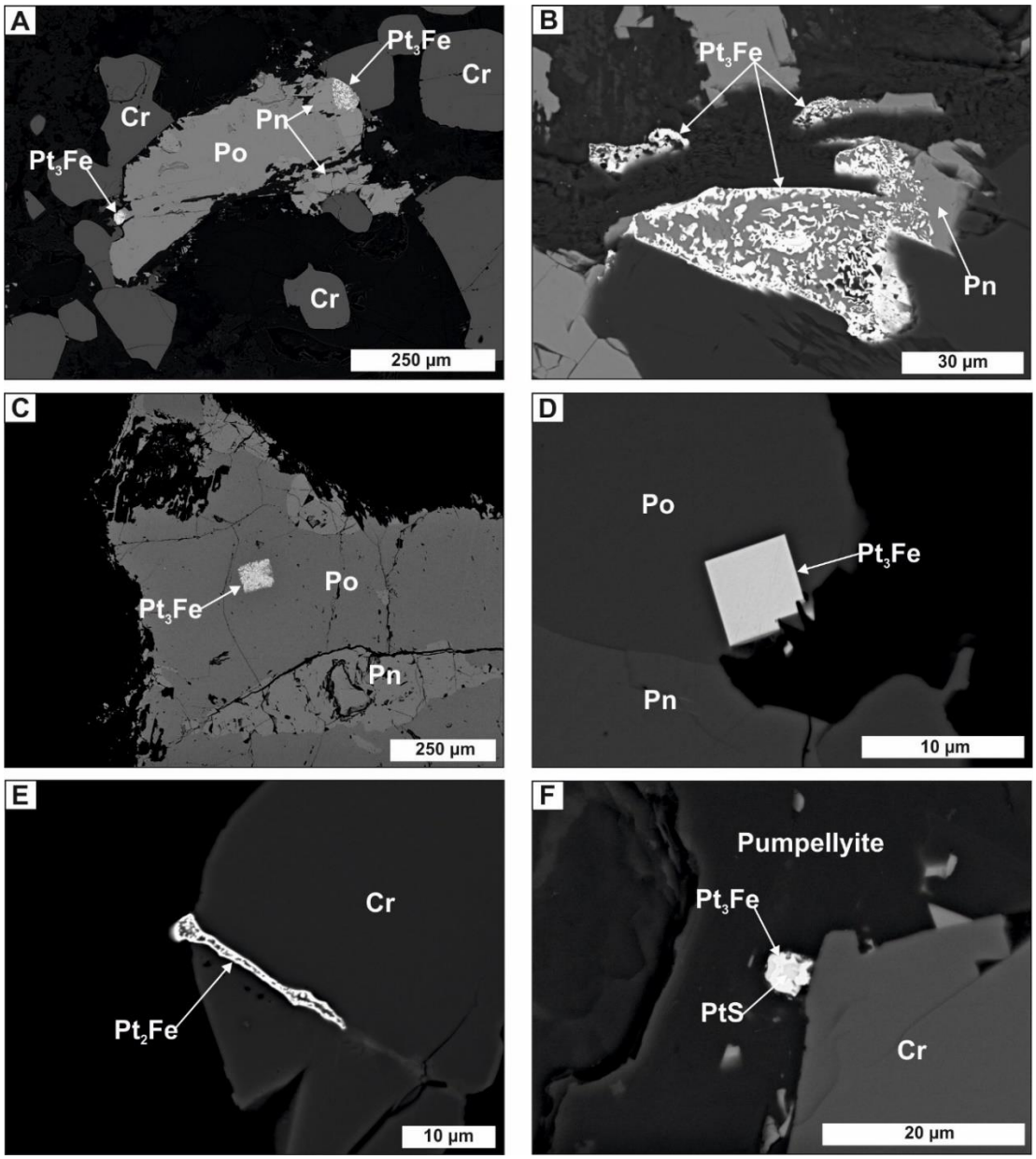

Figure 10.18: Backscattered images showing characteristics of Pt-Fe alloys in the Lower Pyroxenite unit. (A) Two occurrences of large isoferroplatinum symplectite intergrowths with pyrrhotite and pentlandite sulphides (D1_12C). (B) A close-up of the graphic intergrowth between isoferroplatinum and pentlandite (D1_13). (C) A large cubic symplectite isoferroplatinum in pyrrhotite (D1_12A). (D) Euhedral isoferroplatinum on the edge of pyrrhotite (345_08A). (E) Tetraferroplatinum with a graphic texture along a fracture in a chromite grain (345_09C). (F) Intergrowth of cooperite and isoferroplatinum on the outside edge of a chromite grain surrounded by pumpellyite (D1_12F). Note: Cr, chromite; Po, pyrrhotite; Pn, pentlandite.

Laurite is heterogeneously distributed in the LP unit; and is absent in three of the five samples analysed but contributed between 5 and 10 % of the overall PGM budget within the other two samples. The laurite grains are predominantly found on sulphide/silicate contacts, frequently chalcopyrite (see Figure 10.19A and 10.19B). Laurite is also found on chromite-silicate (see Figure 10.19C) and chromite-sulphide (see Figure 10.19D) contacts. No laurite was observed as inclusions in chromite grains

in this stratigraphic unit. Finally, laurite was also observed in interstitial silicates including plagioclase (see Figure 10.19E) and amphibole in alteration pocket in clinopyroxene (see Figure 10.19F).

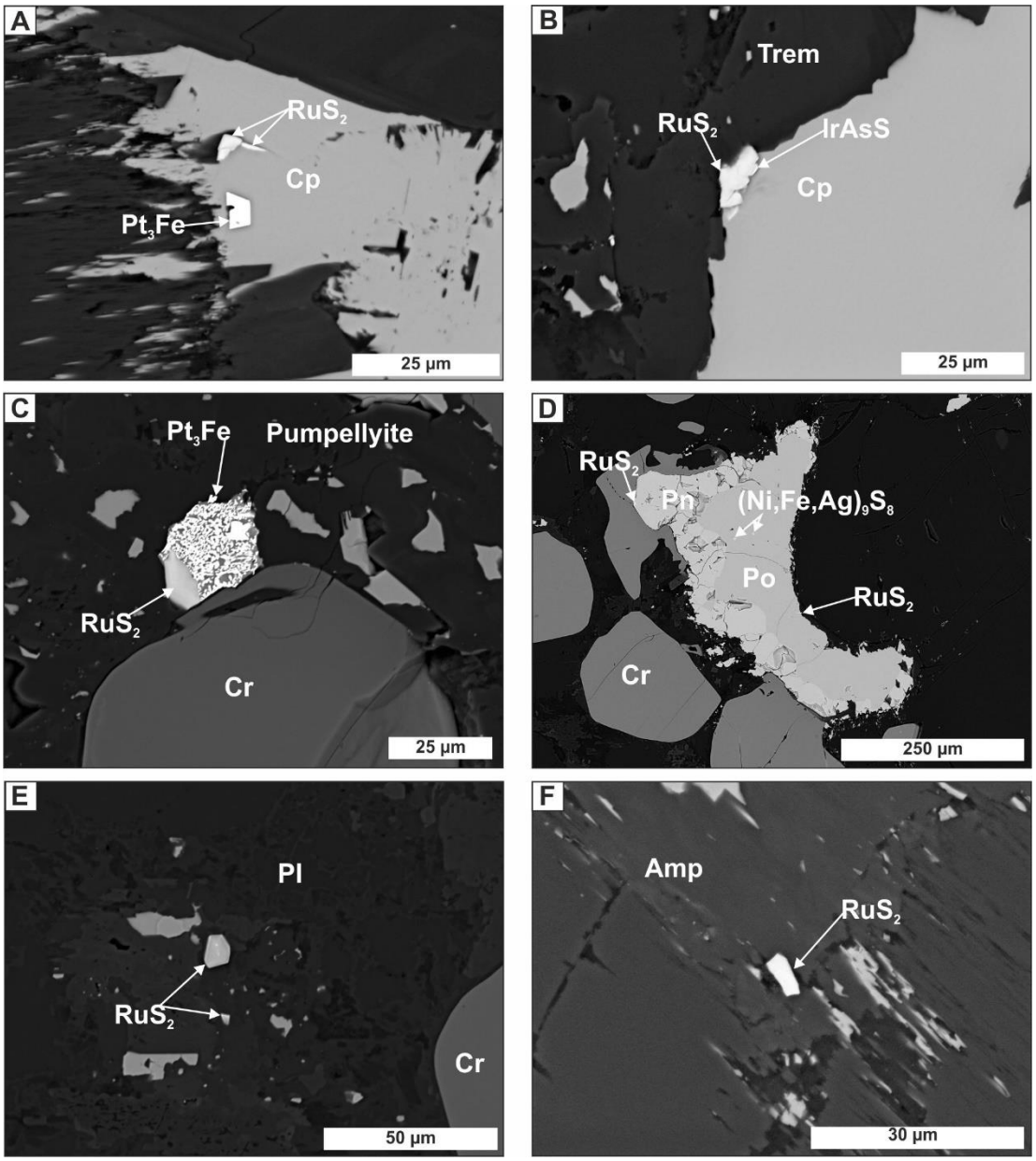

Figure 10.19: Backscattered electron images of showing the various host phases of laurite found in the Lower Pyroxenite unit. (A) Laurite and euhedral isoferroplatinum in chalcopyrite (D1_12C). (B) Laurite (with minor irarsite) on the outside edge of chalcopyrite surrounded by tremolite (D1_12C). (C) Laurite with adjacent isoferroplatinum on the outside edge of a chromite grain (D1_12C). (D) A polyphase base metal sulphide (pyrrhotite and pentlandite) hosting two laurite grains and argentian pentlandite as inclusions in pyrrhotite (D1_12C). (E) Euhedral, zoned laurite isolated in altered plagioclase (D1_12C). (F) Isolated subhedral laurite hosted in amphibole alteration of an orthopyroxene (D1_12F). Note: Cr, chromite; Po, pyrrhotite; Pn, pentlandite; Cp, chalcopyrite; Pl, plagioclase; Amp, amphibole; Trem, tremolite.

The PGE mineralogy of the Lower Reef mineralisation as hosted in the Main Chromitite (MCHR) unit consists of: cooperite (36 %), sperrylite (15 %), Pt-Fe alloy (11%), laurite

(7 %), moncheite (6 %) and braggerite (5 %) with all other phases contributing to < 5 %. The majority of the PGM phases identified are carriers of Pt (80 %) and Pd (11 %) with minor Ru (3 %) and Rh (2 %). For example, only seven laurite grains were identified in the chromitite, compared to 43 grains in the hanging wall LP unit. One laurite grain was found as a euhedral inclusion in chromite (see Figure 10.21D); this textural association is indicative of early, high-temperature formation of laurite as demonstrated experimentally by Finnigan et al., (2008). Laurite was more frequently found as part of polyphase PGMs with sperrylite (see Figure 10.22B) and in one example with rustenburgite. The presence of polyphase PGM in the MCHR unit, typically hosting a sulpharsenide phases, was observed to be greater than in any other stratigraphic unit. The PGMs were identified in a variety of locations in proximity to chromite grains including: (1) enclosed in chromite (8 %); (2) on sulphide-chromite boundaries (14%) and; (3) on chromite-silicate boundaries (15%). Some examples are shown in Figure 10.20 including PGM found: on chromite grain boundaries (Figure 10.20A), at triple junctions between compacting chromite grains (Figure 10.20B), along internal fractures (Figure 10.20C) and as inclusions (Figure 10.20D).

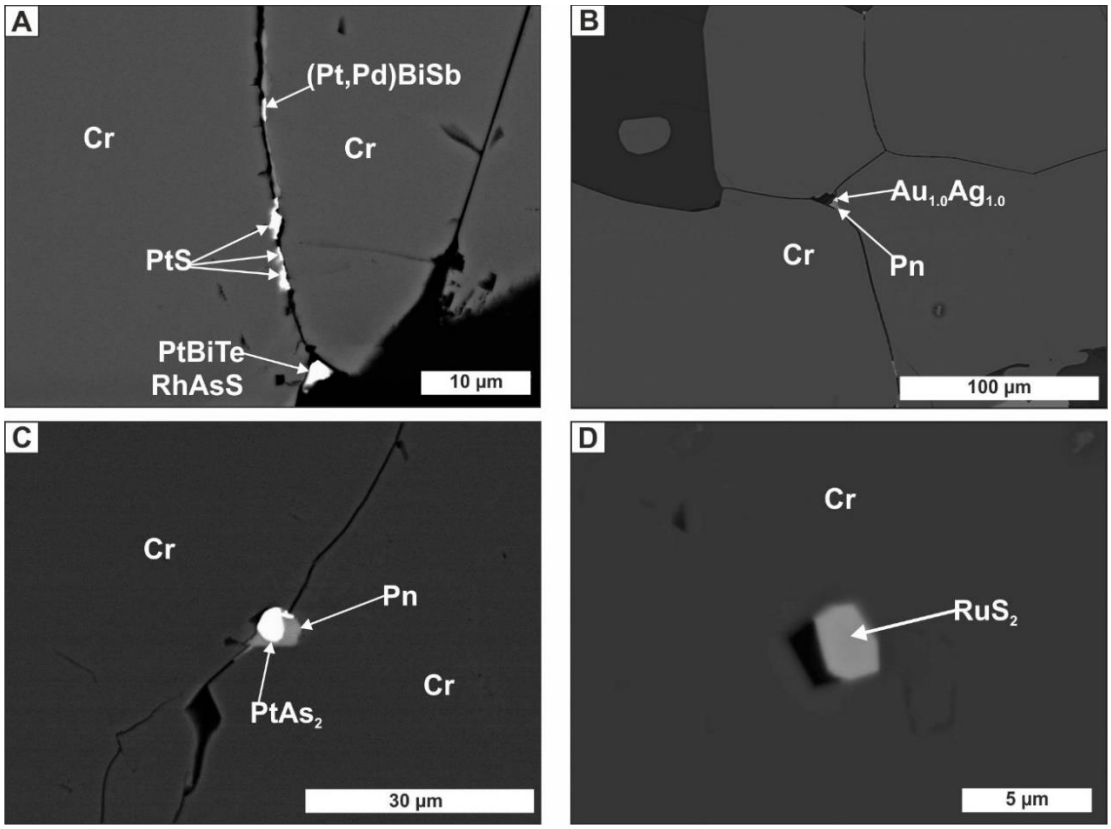

Figure 10.20: Backscattered electron images of PGM hosted in association with chromite grains from the Main Chromitite unit. (A) A broad range of PGM on the boundary between two chromite grains (D1_14B). (B) Electrum and pentlandite at a triple junction between chromite grains (D1_13C). (C) Sperrylite and pentlandite on fracture in centre of chromite grain (D1_14A). (D) Euhedral laurite inclusion in a chromite crystal (D1_13C). Note: Cr, chromite; Po, pyrrhotite; Pn, pentlandite.

The second most common textural association of the PGM are with base metal sulphides: enclosed in sulphide (mostly pentlandite, 20 %) and on sulphide-silicate contacts (16 %), some examples are shown in Figure 10.21 below. In Figure 10.21A, a pyrrhotite and pentlandite sulphide inclusion in a chromite grain hosts multiple PGM including two Pt-Fe alloys and maslovite. This sulphide also hosts an ilmenite grain with two electrum grains crystallised on the edge. The replacement of pyrrhotite by pyrite was observed occasionally in the MCHR unit some examples are shown in Figure 10.21C and 10.21D; the pyrite typically appears euhedral and retains the PGM species present in the pyrrhotite.

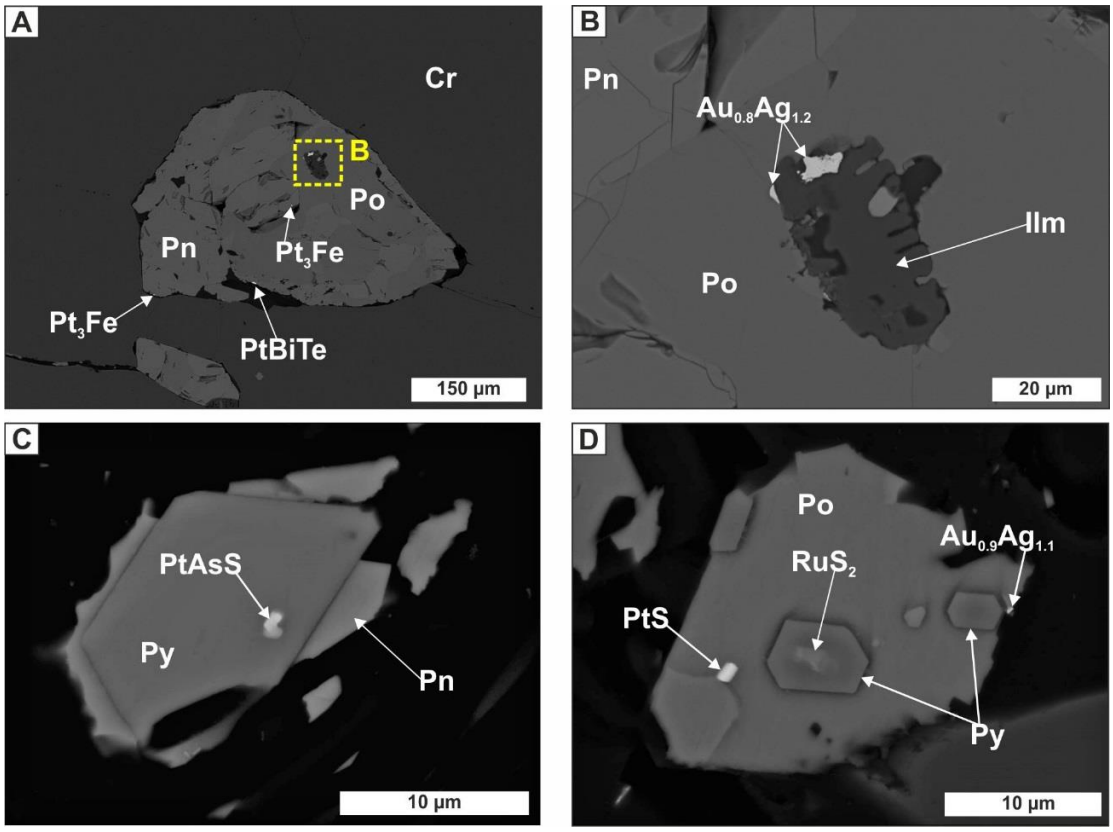

Figure 10.21: Backscattered electron images of the PGM assemblage found in association with sulphides in the Main Chromitite unit. (A) A polyphase sulphide inclusion in chromite hosting three PGM comprising two isoferroplatinum and one masloyite. Highlighted in the yellow box is the location of image B (D1_13); (B) Ilmenite grain hosted in pyrrhotite with two electrum grains on the edge (D1_13); (C) Euhedral pyrite with a rim of pentlandite hosts a subhedral platarsite PGM (D1_13C); (D) Pyrrhotite sulphide with euhedral pyrite overprint, hosting electrum and cooperite (D1_13C). Note: Cr, chromite; Po, pyrrhotite; Pn, pentlandite; Py, pyrite; Ilm, ilmenite.

The last stratigraphic unit analysed for its PGM assemblage in the Deep Platreef was the Ultramafic Zone (UMZ); the PGM in all samples are Pd-dominated (ranging from 65 to 100%). There is a distinct difference between the PGM composition based on the lithological variability of the samples with serpentinised samples dominated by Pd-

antimonides (sudburyite) compared to Pd-bismuthotellurides (michenerite) within unaltered samples; the best examples of each of these sub-types are covered here.

The PGM assemblage of the unaltered pegmatoidal gabbronorite, as sampled in 345_13, is dominated by bismuthotelluride PGMs (98 %). The base metal sulphides present in this sample are coarse-grained and compositionally comple with abundant massive cubanite. The PGM are hosted mainly in alteration silicates in close proximity to sulphides (42%, see Figure 10.22A) and enclosed in sulphide (38% mostly in chalcopyrite, see Figure 10.22D). The largest PGM analysed, a michenerite grains, has an area of 8172 μm^2 as shown in Figure 10.22A and 10.22B; the total area of all PGMs identified in this sample is 9982 μm^2 making the other PGM phases identified statistically insignificant. This large grain is part of a cluster of five grains all dominated by michenerite-compositions but with some variability with electrum (see Figure 10.22B) and sperrylite (see Figure 10.22C) also identified.

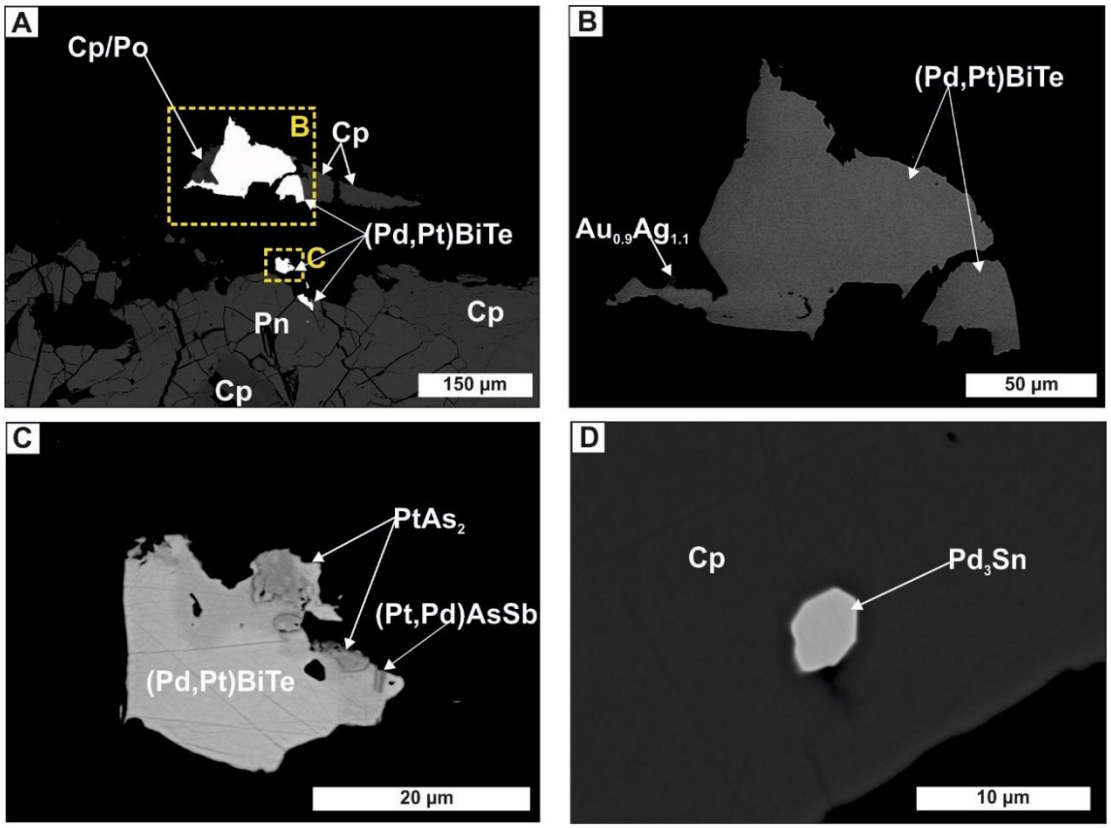

Figure 10.22: Backscattered electron images of selected PGM from the pegmatoidal gabbronorite of the Ultramafic Zone as sampled in 345_13. (A) Location of a very large cluster of michenerite PGMs detached from the edge of a pegmatoidal polyphase base metal sulphide; (B) The largest PGM grain analysed, composed predominantly of michenerite with minor electrum attached on the edge; (C) A polyphase PGM dominated by michenerite with exsolution of sperrylite and an unknown arseno- antimonide phase; (D) Euhedral paolovite hosted in chalcopyrite. Note: Cp, chalcopyrite; Po, pyrrhotite; Pn, pentlandite.

The strongly-serpentinised feldspathic harzburgite sample (D1_17B) has a PGM assemblage dominated by Pd-antimonide (62 %, mainly sudburyite) with significant electrum (18 % represented by one grain, see Figure 10.23A) and Rh-bearing sulpharsenide (14 %). The sulpharsenide phases identified are mostly hollingworthite, showing variable solid solution with irarsite and more rarely ruarsite (see Figure 10.23B and 10.23C). The majority of the PGM phases are enclosed within sulphides (47 %, mostly in pentlandite); examples are shown in Figure 10.23A to 10.23D. The sulphide assemblage shows significant evidence of oxidation with pyrrhotite replaced by magnetite (see Figure 7.23D).

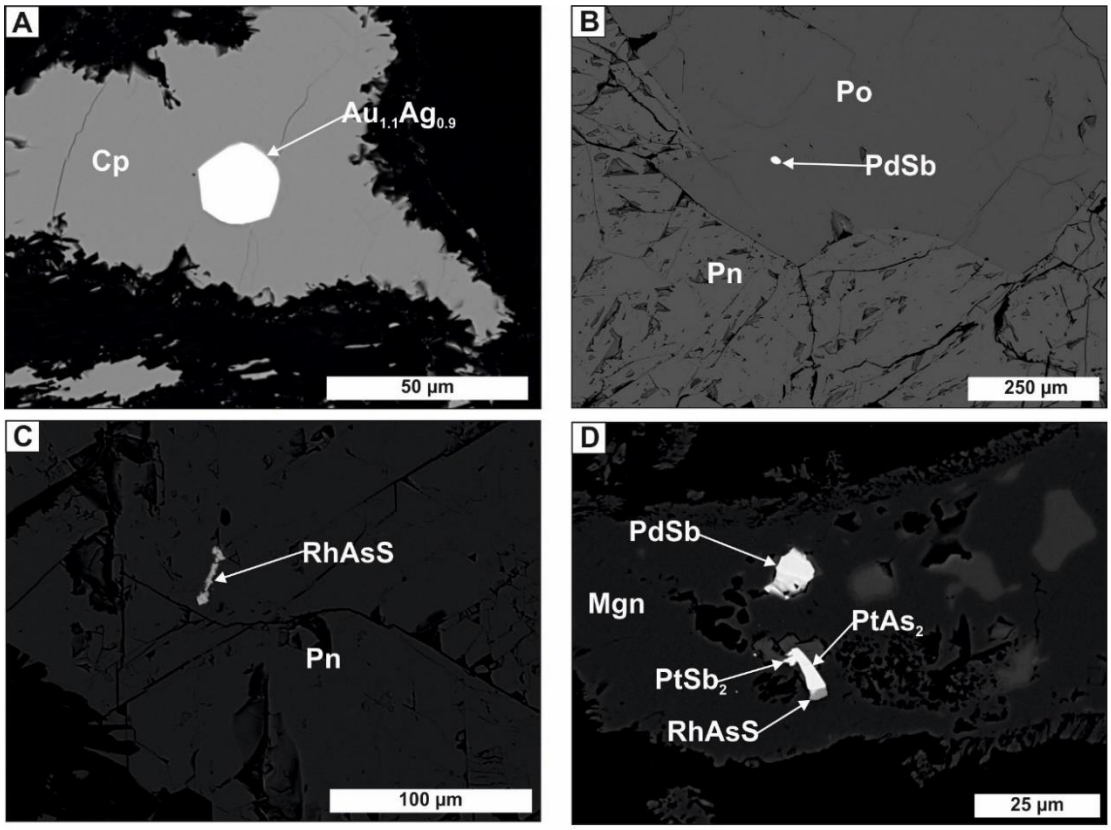

Figure 10.23: Backscattered electron images of selected PGM from a strongly serpentinised sample of the Ultramafic Zone in D1_17B. (A) A large euhedral electrum sitting in chalcopyrite with altered edges; (B) Euhedral, sudburyite hosted in pyrrhotite; (C) Anhedral hollingworthite hosted in pentlandite; (D) A oxidised sulphide converting to magnetite hosting two PGMs including a monomineralic sudburyite and a polyphase mixture of sperrylite with minor hollingworthite and geversite. Note: Cp, chalcopyrite; Po, pyrrhotite; Pn, pentlandite; Mgn, magnetite; Trem, tremolite.

The UMZ unit in sample D1_17B also contains abundant niccolite (NiAs) with 15 grains identified in addition to breithauptite (NiSb, see Figure 10.24B) and altaite (PbTe, see Figure 10.24A). The range in size of niccolite varies from < 1 µm^2 to 1382 µm^2 and it was observed in a range of settings including: as inclusions in sulphides (typically pentlandite, see Figure 10.24C), on sulphide-silicate contacts (see Figure 10.24A and

10.24B) and within alteration silicates (see Figure 10.24D). Niccolite was identified as a host for sudburyite PGMs as shown in Figures 10.24A and 10.24B.

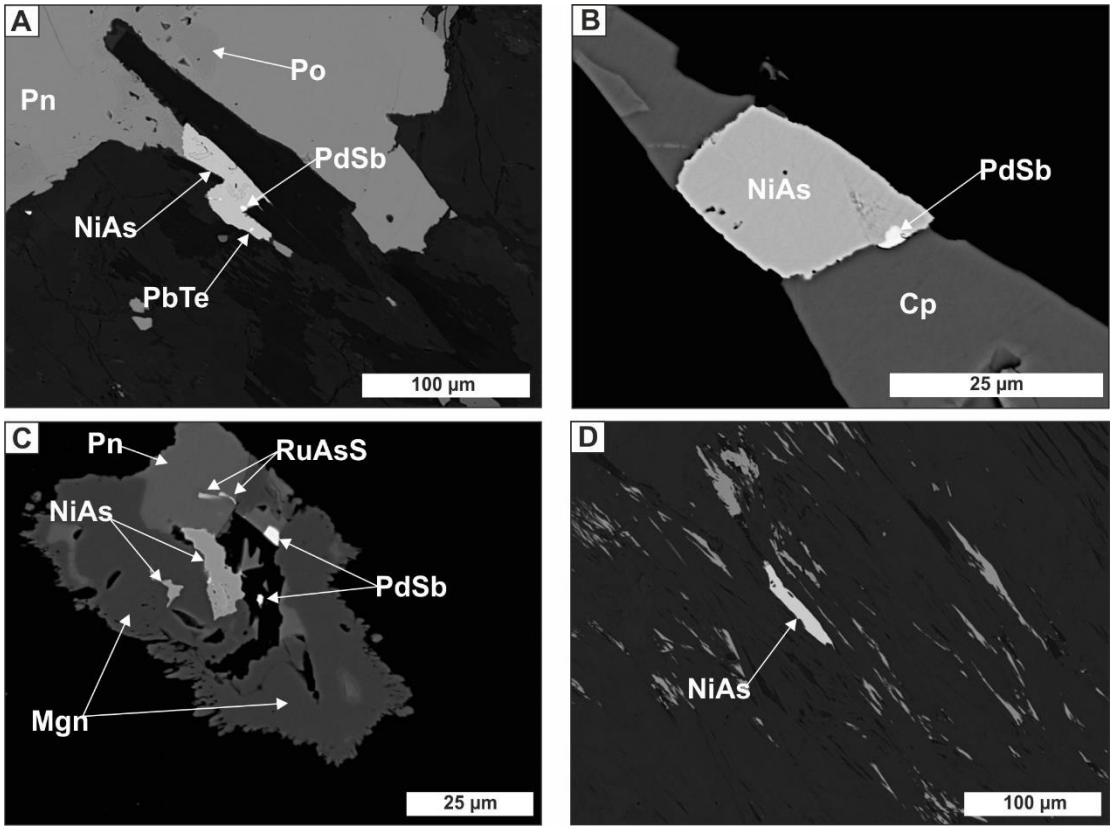

Figure 10.24: Backscattered electron images of selected heavy minerals identified within the strongly serpentinised sample of the Ultramafic Zone in D1_17B. (A) Niccolite on the edge of pentlandite hosting sudburyite and altaite; (B) Niccolite within chalcopyrite hosting breithauptite; (C) Niccolite in a strongly oxidised pentlandite, which also hosts ruarsite and sudburyite PGMs; (D) Niccolite in amphibole alteration silicates with minor sulphides (mostly Cp) no PGMs identified. Note: Cp, chalcopyrite; Po, pyrrhotite; Pn, pentlandite; Mgn, magnetite.

The increased presence of niccolite towards the base of the drill hole corresponds with observations by Hutchinson & Kinnaird (2005) in the shallow Platreef on Turfspruit. In the Platreef rocks Hutchinson & Kinnaird (2005) observe niccolite as inclusions in sulphides leading them to suggest that significant amounts of As were introduced into the system before sulphide formation and this accounts for the abundance of semi-metal-bearing PGM phases observed in that study. The LA-ICP-MS data on the PGE tenor of sulphides in this unit, as presented in section 10.1, confirm that this stratigraphic unit contain low concentrations of PGE (typically < 50 ppm) similar to those analysed in the shallow Platreef by Hutchinson & McDonald (2008, see Figure 10.2).

10.2.2 Flatreef PGM Assemblage

A preliminary study of the Flatreef PGM assemblage was conducted on two samples; one each from the Thick and Normal Flatreef drill holes. The samples chosen are from

stratigraphic units not present in the Deep Platreef including: (1) the Gabbronorite Hybrid Zone (HZ_{GBRN}) at the base of drill hole TMT_006_D2 hosting the Hybrid Reef mineralisation and; (2) the Norite Cycle 1 (NC1) unit at the top of UMT_233 hosting the Upper Reef mineralisation. A summary of the results are presented in Figure 10.25; the most remarkable observation is the similarity in the PGM assemblage between the two samples despite being hosted in different lithologies from different stratigraphic units in separate drill holes.

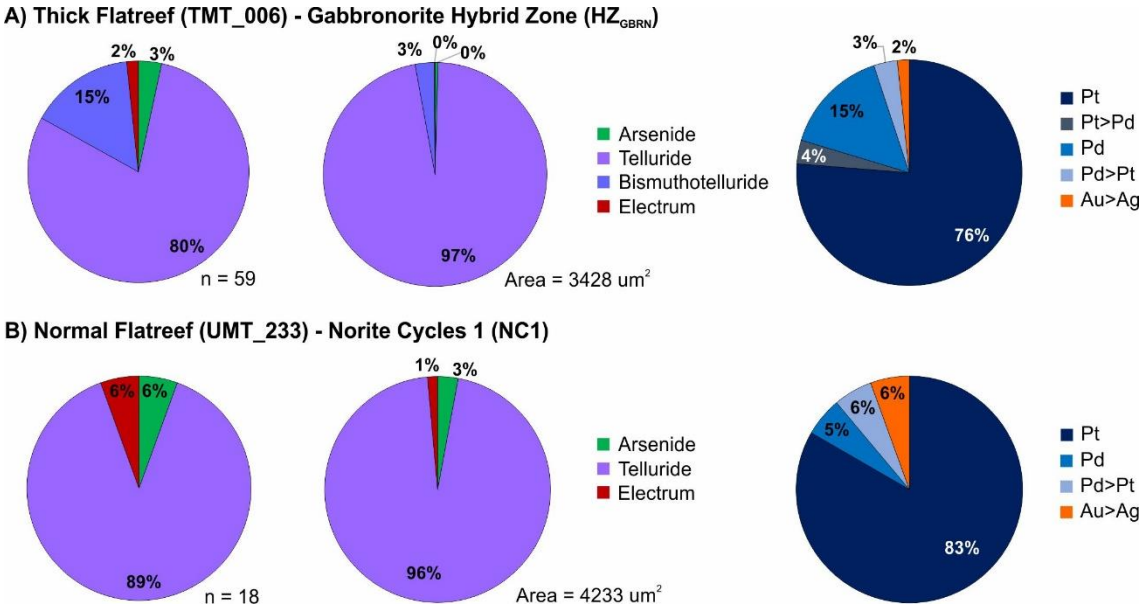

Figure 10.25: A summary of the PGM population in the Flatreef samples; from left to right the pie charts represent the frequency of each PGM class, the relative proportion of each PGM class and the number of precious metal phases.

A total of 59 PGMs were identified in the Thick Flatreef and 18 in the Normal Flatreef sample; the PGM population of each is dominated by Pt-tellurides (moncheite) and no carriers of Rh, Ru, Os or Ir were identified. The mineral identification for each PGM occurence is shown in Table 10.6.

The textural settings of the PGM phases varies between the drill holes; for a summary see Figure 10.26. In the Normal Flatreef the majority of the PGMs are located in interstitial plagioclase (50 %), enclosed in sulphide (17 %, mostly chalcopyrite), on sulphide-silicate contacts and in alteration silicates associated with sulphides (11 %). Whereas, in the Thick Flatreef the greatest number of PGM are enclosed in sulphide (63 %, mostly pyrrhotite), on the contact between primary silicate minerals and alteration silicates (22 %), on sulphide-silicate contacts (7 %) and in alteration silicates (7 %).

Table 10.6: Mineral names and ideal formula for all occurrences of PGM and Au-Ag phases identified in the Thick and Normal Flatreef.

		Thick Flatreef		Normal Flatreef	
		HZ_{GBRN}		NC1	
		n=1		n=1	
Ideal Formula	**Mineral Name**	**Area (%)**	**Grain #**	**Area (%)**	**Grain#**
Gold and Silver Phases					
AuAg	Electrum	0.11	1	1.43	1
PGE Tellurides, Bismuthides					
PdBiTe	Michenerite	0.94	7	-	-
Pd(Te,Bi)	Kotulskite	0.05	1	10.39	1
$Pt(Te,Bi)_2$	Moncheite	98.26	45	84.82	14
$Pd(Te,Bi)_2$	Merenskyite	0.03	1	-	-
	Unknown	0.18	1	0.43	1
PGE Arsenide, Antimonides					
$PtAs_2$	Sperrylite	0.43	2	2.93	1
	Total	100	58	100	18

	Normal	*Thick*
	NC1	HZ_{GBRN}
	n=1	n=1
Enclosed in Sulphide	16.7	62.7
Po	0.0	40.7
Pn	0.0	10.2
Cp	11.1	0.0
Py	0.0	0.0
Po/Pn	0.0	11.9
Cp/Pn	5.6	0.0
Py/Pn	0.0	0.0
Sulphide/Silicate	16.7	6.8
Pn/Sil	0.0	3.4
Cp/Sil	0.0	3.4
Primary Silicate	50.0	1.7
Interstitial	50.0	0.0
Cumulate	0.0	1.7
Primary/Alteration	5.6	22.0
Alteration Silicates	11.1	6.8
with BMS	11.1	3.4
No BMS	0.0	3.4
Sum Total	100	100

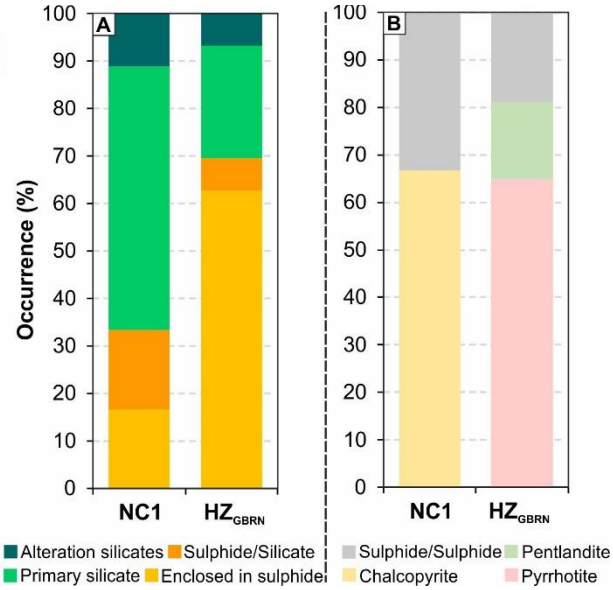

Figure 10.26: Textural analysis of the mineralogical siting of PGM phases from the Normal and Thick Flatreef drill holes.

The average grain size is larger in the Flatreef samples compared to the Deep Platreef with all the PGMs identified >1 µm in size with the largest long axis measuring 99 µm (see Figure 10.27). This may partially be affected by the PGM composition, the dominant PGM phase identified in both Flatreef samples is lath-shaped moncheite.

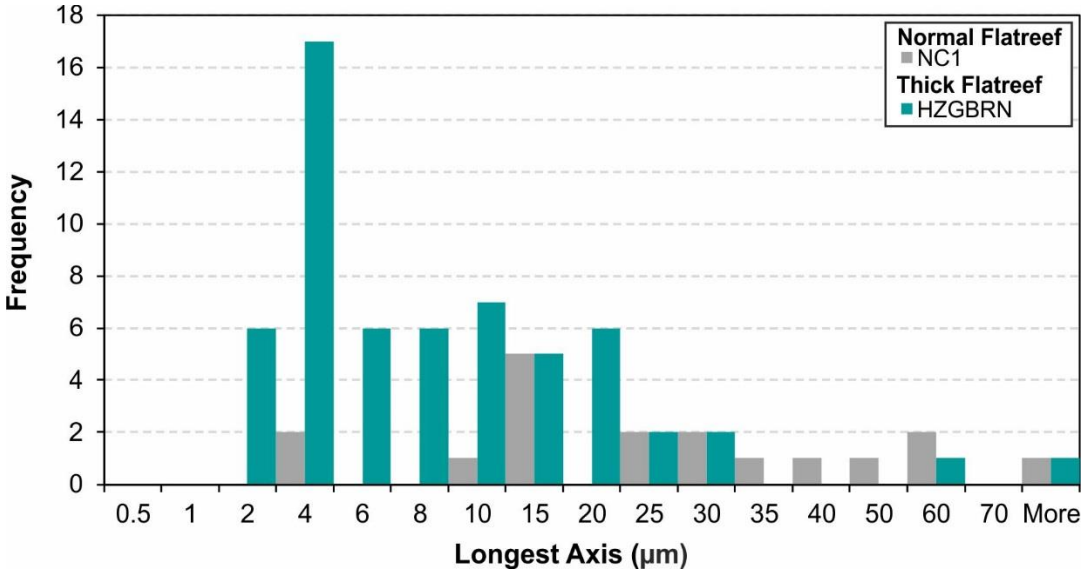

Figure 10.27: Histogram showing the size distribution of the longest axis (µm) for the PGM in the Flatreef samples.

A summary of the mineralogical settings of the moncheite in the NC1 unit of the Normal Flatreef are shown in Figure 10.28; despite the range of host minerals shown the PGM composition remains unchanged. In all images, with the exception of Figure 10.28D, the PGM are associated with sulphides present either as an interstitial phase (see Figure 10.28A and 10.28B) or fragmentary in alteration (see Figure 10.28C).

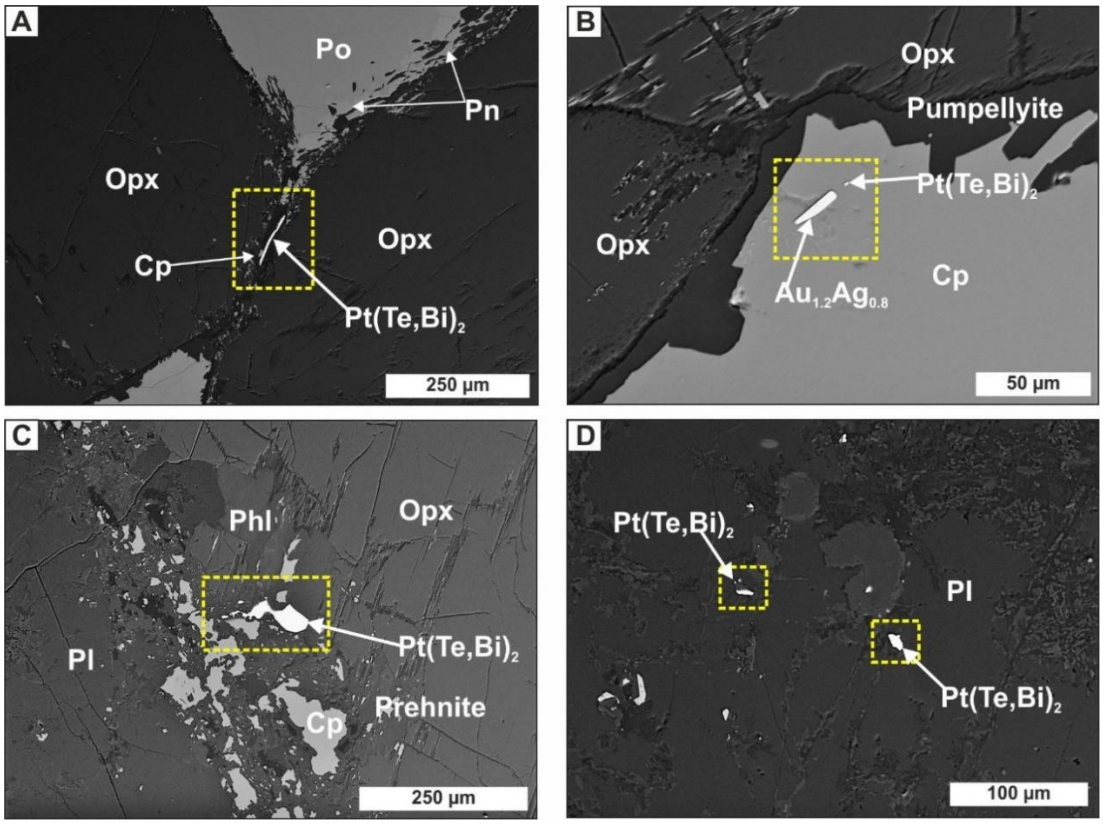

Figure 10.28: Backscattered electron images of the PGM assemblage from the NC1 unit as sampled in the Normal Flatreef in 233_04. (A) Moncheite associated with interstitial sulphide

between two orthopyroxene grains. (B) Moncheite and electrum on the edge of chalcopyrite. (C) Moncheite associated with fragmentary chalcopyrite on the contact between orthopyroxene and plagioclase. (D) Two moncheite grains isolated in altered plagioclase. Note: Cp, chalcopyrite; Po, pyrrhotite; Pn, pentlandite; Opx, orthopyroxene; Phl, phlogopite; Pl, plagioclase.

In the Thick Flatreef, most of the dominant Pt-telluride phases were identified at locations closely associated with a pegmatoidal base metal sulphide (BMS); with the PGM typically enclosed on the edges of either pyrrhotite or pentlandite (see Figure 10.29A to 10.29B). In this setting the PGM are found as clusters of two or more grains; the majority of the PGMs identified in this sample are present in one cluster of 34 individual PGMs, as shown in Figure 10.29A. Hydrothermal alteration on the edges of the BMS initially results in tremolite needles penetrating into the sulphide (see Figure 10.29B) and can ultimately lead to the detachment of the PGM from the sulphide as shown in Figure 10.29C. The sperrylite PGMs identified were found in a recrystallisation pathway in between two pegmatoidal clinopyroxene grains with associated tremolite (see Figure 10.29D).

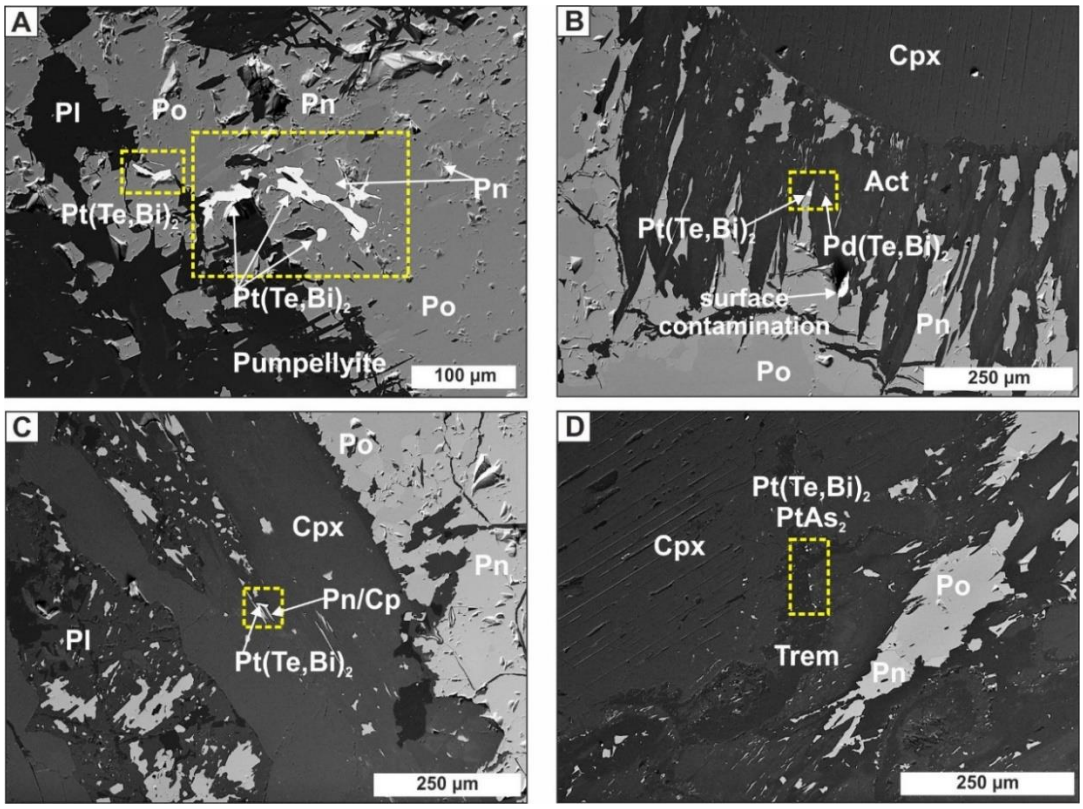

Figure 10.29: Backscattered electron images of the PGM assemblage identified in the Gabbronorite Hybrid Zone as sampled in the Thick Flatreef in TMT_34. (A) A cluster of moncheite on the edge of a pegmatoidal pyrrhotite and pentlandite sulphide. (B) Moncheite on the pentlandite-rich rim of the pegmatoidal sulphide being altered by tremolite. (C) Moncheite isolated in secondary silicates from the edge of the pegmatoidal sulphide. (D) Fine-grained sperrylite and moncheite in an alteration pathway between sulphides and clinopyroxene. Note: Cp, chalcopyrite; Po, pyrrhotite; Pn, pentlandite; Cpx, clinopyroxene; Trem, tremolite; Act, actinolite; Pl, plagioclase.

Chapter 11

Discussion & Conclusions

11.0 Overview

The primary results of this study are presented in Chapters 5 to 10, the following final chapter aims to bring together the results into five discussion topics as listed and briefly summarised below:

1. **The Role of Magmatic Processes:** an overview of the evidence provided in this study for the dominant role of orthomagmatic processes in the formation of the stratigraphy and associated Ni-Cu-PGE mineralisation across the Turfspruit deposit. Key petrogenetic processes considered include: (1) the timing of sulphur saturation; (2) estimations of the R factors involved based on the measured PGE tenors in sulphides and; (3) whether the mineralisation and crystallisation processes occurred in situ or formed deeper in the magmatic plumbing system.
2. **The Role of Contamination:** a summary of the potential sources of contamination of the Platreef on Turfspruit and characterisation of their major and trace element geochemistry. This is followed by a summary of the geochemical, petrological and sulphur isotopic evidence for crustal contamination of the Platreef magma across the Turfspruit deposit.
3. **The Role of Hydrothermal Fluids:** a look at the potential sources of hydrothermal fluids in the Platreef on Turfspruit and any evidence for their role in the mobilisation and redistribution of metals and alteration of the host silicate assemblage.
4. **Correlations across the Bushveld Complex:** a review of the proposed stratigraphic correlations between the northern limb PGE ore deposits as hosted in the Deep Platreef and Grasvally Norite-Pyroxenite-Anorthosite member with the Upper Critical Zone (UCZ) on eastern and western limbs.
5. **Emplacement model:** combining all the results as outlined in sections 11.1 to 11.4 to evaluate the validity of two petrogenetic models for the development of the Platreef Ni-Cu-PGE orebody. An emplacement model is presented with a time evolved series of events for the intrusion of the Platreef on Turfspruit.

Finally, conclusions from the study are outlined in section 11.6 and recommendations for future work are listed in section 11.7.

In order to provided context to the following discussions an overview of the drill hole logging is provided on the next page in Figure 11.1. The drill holes are positioned relative to a reference stratigraphic horizon identified across the deposit, this is the contact between the Upper Pyroxenite (UP) and Middle Pyroxenite (MP) units. Any deposit-wide stratigraphic correlations below this level are difficult (see Figure 11.1) a function of the varying composition of the footwall and degree of the magma-sediment interaction.

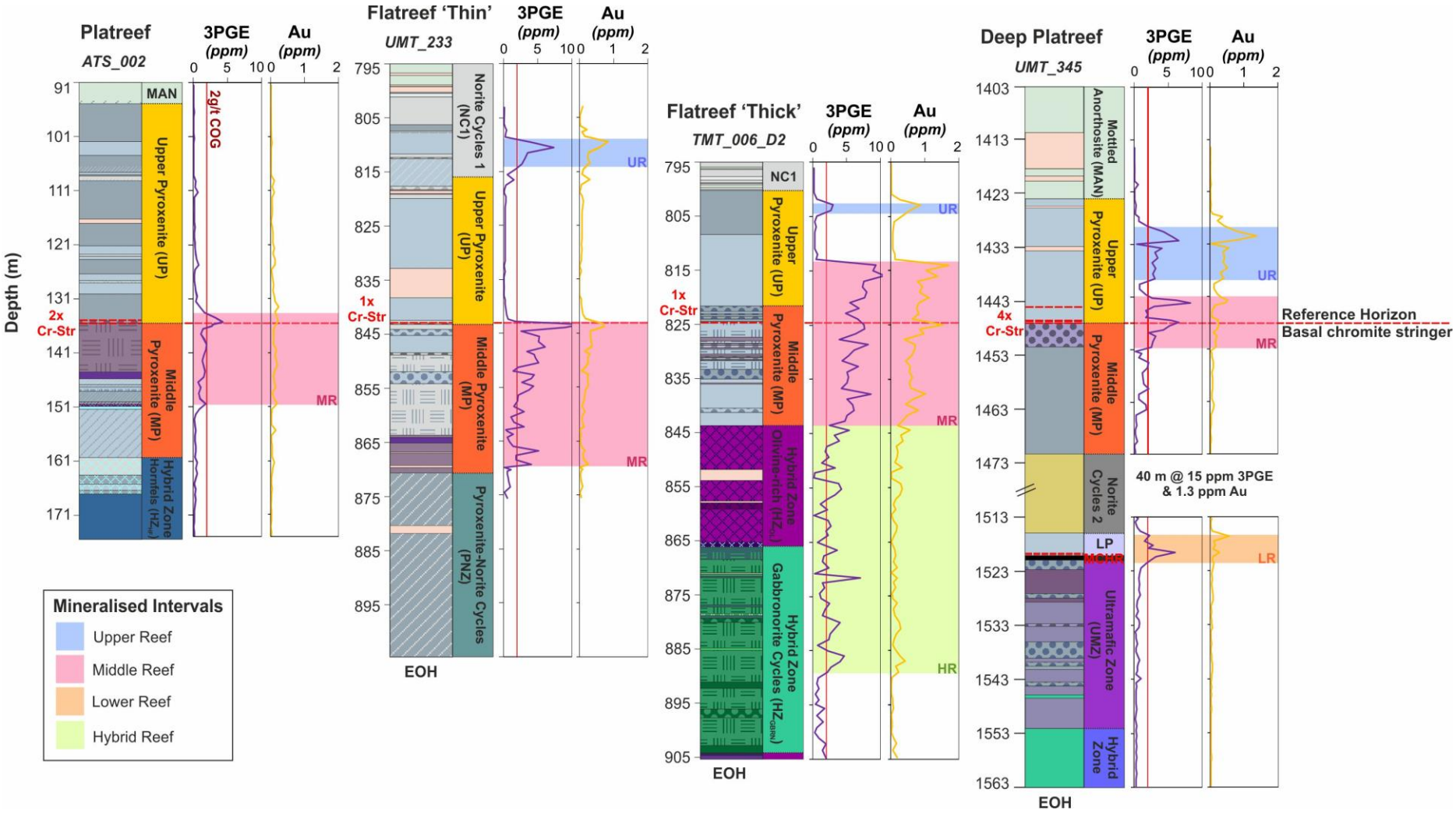

Figure 11.1: The results of the lithological logging and stratigraphic units used in the current study along with the down hole grade profiles for 3PGE and Au. Note: for a geological legend please refer to Chapter 5. Abbreviations: UR – Upper Reef, MR - Middle Reef; LR – Lower Reef; HR – Hybrid Reef.

11.1 The Role of Magmatic Processes

In order to assess the role of magmatic processes in the formation of the Ni-Cu-PGE orebody on Turfspruit it is important to revisit the fundamental petrogenetic processes established in the literature (as outlined in Chapter 2). In Chapter 2, three key processes are highlighted as being fundamental to Ni-Cu-PGE ore genesis in the upper crust these are: (1) the timing and trigger mechanism of sulphide saturation in the silicate magma (see section 2.2.3); (2) an effective process enabling the interaction of the immiscible sulphide liquid with high volumes of ultramafic magma to upgrade the metal tenor of the sulphide (see section 2.2.4) and; (3) the physical accumulation of the sulphide liquid into significant concentrations amenable to mining (see section 2.2.5). The following sub-sections outline the evidence collected in this study which place constraints on these three factors for the development of the Turfspruit deposit. Finally, this section ends on a discussion on whether the magmatic processes operated either at the site of emplacement (in situ) or at an earlier stage with pre-formed PGE-rich sulphides transported to the site of their deposition.

11.1.1 Establishing the Timing and Trigger for Sulphide Saturation

The literature on Ni-Cu-PGE deposits associated with mafic/ultramafic intrusions identifies two principal mechanisms triggering initial sulphur saturation in the parental magma, which typically vary depending on the location of the mineralisation:

A. Marginal ‘contact-style’ deposits form through complex physical and chemical interactions between the magma and surrounding country rocks. Sulphur saturation is achieved either through the addition of crustal S or via devolatisation/assimilation of wall rocks altering the geochemical conditions of the magma;
B. In the interior of the intrusion orthomagmatic processes, such as fractional crystallisation and magma mixing, are dominant in causing sulphur saturation and forming ‘reef-style’ deposits.

The Platreef intruded into sedimentary rocks of the Transvaal Supergroup; as such it has been characterised as a ‘contact-style’ deposit in numerous review papers on magmatic sulphide deposits (e.g. Naldrett, 2004; Maier, 2005; Barnes & Ripley, 2016). There is abundant evidence for two-way material transfer between the sediments and the injecting magma adjacent to autoliths/xenoliths and on the footwall/hangingwall contact. In addition to its marginal location the Platreef mineralised interval is thicker (between 10 to 400 m), contains elevated sulphide concentrations (5 to 20 vol%) and records a highly variable range in sulphur isotope values along the strike length (as summarised in Figure 11.4, below). However, the whole-rock PGE grades (e.g. 30 m at

7 g/t, Thick Flatreef this study) and elevated metal tenors of base metal sulphides (up to 600 ppm; Deep Platreef this study) are an order of magnitude greater than other 'contact-style' deposits. Consequently, the Platreef doesn't conform with the two classic categories of Ni-Cu-PGE deposits as outlined above. This has resulted in a variety of hypotheses being proposed in the literature for the Platreef ore petrogenesis that can be broadly classified into contamination, magmatic and hybrid models as follows:

Hypothesis 1 (contamination) – sulphide saturation occurred upon emplacement due to crustal contamination and the assimilation of sulphide-bearing sediments from the immediate wall rocks (e.g. Buchanan et al., 1981; Buchanan & Rouse, 1984; Cawthorn et al., 1981; Barton et al., 1986; Manyeruke et al., 2005; Sharman-Harris et al., 2005). The strongest evidence cited in support of the incorporation of sedimentary sulphur into the Platreef comes from measurements of non-magmatic $\delta^{34}S$ values in ore sulphides that broadly reflect the range of values recorded in the surrounding country rocks. Along the strike of the Platreef the floor rocks of the Transvaal Supergroup contain two main stratigraphic horizons with reservoirs of crustal sulphur: (1) anhydrite ($CaSO_4$) in evaporitic deposits of the Malmani Subgroup and; (2) pyrite in shales (FeS_2) from the lower section (0 to 600 m) of the Duitschland Formation (DF) and from sulphate-bearing minerals hosted in impure limestones and dolomites from the upper section (600 to 1000 m) of the DF.

This hypothesis has been widely rejected as the principal trigger of sulphide saturation in the majority of recent studies on the northern limb (including the current study). The reasons for this include measurements of magmatic sulphur isotope values in unaltered base metal sulphide (BMS) assemblages from ore-bearing horizons along strike (e.g Holwell et al., 2007; Sharman et al., 2013; this study) and the high sulphide PGE tenors (100's ppm) measured in the BMS. The non-magmatic $\delta^{34}S$ values are interpreted to result from localised, in situ contamination acting as an ore-modifying process that potentially dilutes the BMS metal tenors.

Hypothesis 2 (magmatic) – sulphide saturation is achieved through orthomagmatic processes operating either at the site of deposition (e.g. via lateral flow, Yudovskaya et al., 2017b) or at depth with the current exposure representing magma forced up the side walls of the magma chamber due to over-filling (e.g. Naldrett et al., 2008). These models consider the northern limb PGE mineralisation to be directly related and contemporaneous to that of the eastern and western limbs. The suggestion is that with increasing depth a transformation occurs from Platreef to a full Upper Critical Zone (UCZ) stratigraphic sequence hosting the stratiform reefs of the Merensky Reef and UG2 chromitite. The role of magmatic processes is supported by the identification of

magmatic $\delta^{34}S$ values (0 ± 2 ‰) in primary magmatic BMS assemblages consisting of pyrrhotite-pentlandite-chalcopyrite and in the high PGE tenors measured in sulphides. The role of crustal contamination is restricted to a late-stage upon emplacement of the magma causing lithological heterogeneity and diluting/modifying the PGE distribution; the degree to which this occurs depends on the nature or 'reactivity' of the floor rocks.

Hypothesis 3 (hybrid) – early sulphide saturation is initially achieved via crustal contamination at depth in a staging chamber (Holwell et al. 2007; McDonald & Holwell 2007; Penniston-Dorland et al., 2008; Ihlenfeld & Keays, 2011). Subsequent interaction between this immiscible sulphide liquid with multiple new batches of primitive sulphur-undersaturated magma imparts a magmatic signature by: (I) diffusion of magmatic sulphur into the contaminated sulphides eliminating the evidence of contamination (e.g. Ihlenfeld & Keays, 2011; Sharman et al., 2013) and; (II) upgrading the PGE tenor of the sulphides via a process known as multi-stage dissolution-upgrading (Kerr & Leitch, 2005). These original PGE-rich sulphides having formed and accumulated in the plumbing system require subsequent upward transport in a pulse of magma to their final site of deposition whereupon a heterogenous contamination signature is imparted by the country rocks into which they intruded (McDonald & Holwell, 2011). This represents a 'hybrid' model with key parts of both the 'magmatic' and 'contamination' models involved in the Ni-Cu-PGE ore genesis.

The following discussions will present data as collected in the current study that can test the feasibility of Hypotheses 2 and 3. The main distinction between the two is that in Hypothesis 2 only magmatic processes are involved in the formation of the Ni-Cu-PGE mineralisation whereas in Hypothesis 3 an initial pre-emplacement contamination event is required in order to trigger initial sulphur saturation but the PGE-tenor of the sulphide is the product of orthomagmatic processes. The relative role of the orthomagmatic vs. contamination processes can be evidenced in the ore mineralogy and the lithogeochemistry of the host rocks; these are explored in the following sections.

On Turfspruit the most significant ore-bearing lithologies are sulphide-rich pyroxenites namely the Upper, Middle and Lower Pyroxenites (see Figure 11.1). The BMS assemblage occupies the interstitial areas typically shared with other minerals including: plagioclase ± quartz ± phlogopite ± chromite. In this setting the BMS have variably sharp edges with the surrounding silicate phases. Where alteration is prevalent the BMS edges appear ragged with actinolite-tremolite needles replacing the sulphide orientated perpendicular to the silicate contact; this texture is commonly described in this deposit type (e.g. Li et al., 2004 and Junge et al., 2018). The BMS assemblage within these mineralised pyroxenites is dominated by pyrrhotite, pentlandite and chalcopyrite

(approximate quantities of 50:30:20). These different sulphide minerals are typically arranged with a core of pyrrhotite surrounded by a rim of granular pentlandite and chalcopyrite on the margins; these may be preferentially arranged in the paleovertical direction. This texture is interpreted to reflect their successive crystallisation as the magma cools as outlined in Chapter 2 (section 2.3). The sulphide mineralogy is typical of magmatic sulphides that have crystallised from high-temperatures (Naldrett, 2004; Fleet, 2006; see Chapter 2 section 2.3). Pyrrhotite and pentlandite are the exsolution products from monosulphide solid solution (mss) which begins to crystallise at 1000 °C; whereas chalcopyrite forms from the residual intermediate solid solution (iss) which crystallises at ≈ 900 °C (Holwell & McDonald, 2010). Furthermore, this study found evidence for early sulphur saturation on Turfspruit in the form of small (µm-scale), multiphase sulphide melt inclusions with negative crystal shapes in the mineral chromite. The solidus temperature of chromite is between 1200 to 1400 °C meaning that an immiscible sulphide liquid was present and isolated at these temperatures. Fractionated sulphide inclusions in chromite were identified in two mineralised stratigraphic locations: (1) in the chromite stringers on the contact between the Upper and Middle Pyroxenite units in the Deep Platreef and Flatreef (see Figure 8.7F in Chapter 8) also picked up in the Flatreef by Yudovskaya et al., (2017b) and; (2) in the Main Chromitite unit (see Figure 8.18B in Chapter 8). Sulphide inclusions in chromite appear omnipresent along the strike of the Platreef (see Yudovskaya & Kinnaird, 2010; Holwell et al., 2011; and Jones, 2013). A laser-ablation mass spectrometry (LA-ICP-MS) study on the trace element composition of homogenised sulphide inclusions in chromite from Overysel by Holwell et al., (2011) revealed enrichment in PGE (15 analyses with an average ΣPGE concentration of 442 ppm). This PGE-enrichment is interpreted as a primary feature of the sulphide melt because the chromite grain effectively protects it from later-stage processes including: contamination, hydrothermal upgrading, sulphur loss or dilution of precious metal content.

An exception to this ‘typical’ BMS assemblage of the Turfspruit orebody was observed in the shallow Platreef drill hole with significantly more pyrrhotite (> 90%) identified compared to chalcopyrite and pentlandite (< 10%). This mineralogy corresponds to lower average whole-rock Ni (1516 ppm) and Cu (970 ppm) concentrations in the Middle Pyroxenite (MP) unit, compared to the equivalent unit of the Deep Platreef with average values of Ni (2387 ppm) and Cu (1600 ppm). The sulphide textures observed in the shallow Platreef drill hole were also observed to be more variable ranging from: (1) massive with magnetite rims; (2) net-textured and; (3) medium to coarse-grained interstitial to blebby.

Cubanite was observed as an important constituent of the sulphide assemblage over localised intervals in the Deep Platreef. A high proportion of cubanite (up to 25 vol%) was also noted in the Flatreef by Yudovskaya et al., (2017b) in addition to troilite (not seen in this study). Two morphologies of cubanite were identified in this study and in Yudovskaya et al., (2017b): (Type 1) as exsolution lamellae in chalcopyrite, typically in chromite-bearing lithologies (example in Figure 8.15A and Figure 8.18A); (Type 2) as irregular masses (described as granular Yudovskaya et al., 2017b), only identified in the stratigraphic units below the Main Chromitite unit in the Deep Platreef. Experimental studies in the Cu-Fe-S system have shown that lamellar cubanite (type 1) forms via solid-state exsolution at low temperatures (<210 °C) from Fe-rich chalcopyrite (Cabri, 1973). The type 2 cubanite appears to form via the breakdown of chalcopyrite and pyrrhotite based on textural observations (see Figure 8.20D and Figure 9.11C). The pegmatoidal, polyphase sulphides (original pyrrhotite-pentlandite-chalcopyrite) showing this cubanite texture frequently have a magnetite rim on the outside edge in contact with the silicates indicating potentially oxidising fluids which may result in sulphur loss and/or Fe-exchange. Trace-element and sulphur isotope analysis on the type 2 cubanite revealed non-magmatic signatures in S/Se ratios at 13296 (mantle range 2850 to 4350; Queffurus & Barnes, 2015) and $\delta^{34}S$ values of +5.0 ‰ (magmatic range $\delta^{34}S$ 0 ± 2 ‰). The reasons for the heterogenous distribution of cubanite with height are speculated on in Yudovskaya et al., (2017b) who present two options: (A) a separate sulphide melt composition with high Fe/S ratios (possibly due to increasing Duitschland shale contamination down hole) or; (B) low temperature Fe readjustment of sulphides. The concentration of the cubanite in chromite-bearing lithologies supports option B, whereas the non-magmatic trace-element and sulphur isotope values recorded in the type 2 suggest some degree of contamination affecting the sulphide melt composition (option A).

The most common accessory sulphide phases identified include pyrite, galena, sphalerite and argentian (Ag-rich) pentlandite. Pyrite was found as euhedral grains surrounded by relict pyrrhotite typically in chromite-bearing lithologies. The textural relationship between pyrrhotite and pyrite suggests that the latter formed through Fe-exchange with the chromite. Although the trace element concentration of pyrite was not tested in this study a back-scattered electron (BSE) study showed that the reactionary pyrite can inherit the platinum-group minerals (PGM) from the pyrrhotite it replaces (see Chapter 10 Figure 10.21C and 10.21D). The inheritance of PGE from an original pyrrhotite by replacement pyrite has been observed in Dare et al., (2011). Galena was identified as micron-scale clusters of grains in altered interstitial silicate areas (typically plagioclase) associated with fragments of chalcopyrite accompanied by Na-plagioclase

and K-feldspar alteration; similar to descriptions of the shallow Platreef on Turfspruit in Hutchinson & Kinnaird (2005). Electron dispersive spectra (EDS) measured significant concentrations of Se in the galena (up to 17 At% Se); a feature also noted in the Volspruit deposit by Tanner et al., (2018). Sphalerite was typically found as anhedral inclusions and/or in solid solution in chalcopyrite (see Figure 10.7 in Chapter 10, section 10.1.3). The highest Zn concentrations identified in chalcopyrite were found in the Deep Platreef (average >1000 ppm) compared to the Flatreef (<500 ppm) in equivalent stratigraphic units (see Table 10.3, Chapter 10, section 10.1.3). This heterogeneity in the distribution of zinc concentrations in sulphides between the sectors is unexpected considering that their whole-rock zinc concentrations are similar (10's to 100's ppm). This suggests that the elevated zinc concentrations result from different silicate:sulphide ratios (R-factor) in the Deep Platreef possibly due to contamination. Argentian pentlandite ($Ag(Fe,Ni)_8S_8$) was identified in the Deep Platreef drill hole in specific stratigraphic units including the: Norite Cycles 2, Lower Pyroxenite and Ultramafic Zone. Argentian pentlandite is not reported for other localities on the Platreef however it is identified in sulphide deposits elsewhere including Outokumpu (Vuorelainen, Häkli & Papunen, 1972), Noril'sk (Sluzhenikin & Mokhov, 2015) and Sudbury (Cabri & Laflamme, 1976; Dare et al., 2010). In this study argentian pentlandite was identified as inclusions in pyrrhotite (see Figure 10.19D), chalcopyrite and pentlandite (see Figure 10.4B), as well as on sulphide/silicate contacts. Experimental studies show that it is stable at temperatures < 455 °C (Mandziuk & Scott, 1977), exsolved from late-crystallising massive chalcopyrite.

11.1.2 Sulphide PGE Tenor Upgrading

Once an immiscible sulphide liquid forms it must be able to process large volumes of ultramafic magma in order to elevate the sulphides metal tenors to the 000's ppm level. This is based on the R-factor model theory as developed by Campbell & Naldrett (1979) which expresses the silicate:sulphide mass ratio (see Chapter 2, section 2.2.4). The transfer of metals from the silicate melt to the sulphide liquid is promoted by the extreme sulphide-silicate partition coefficients of the PGE (Mungall & Brenan, 2014). Petrogenetic models often struggle to achieve the high R factors (> 10^5) required, especially for stratiform reef-style deposits, and this has always been an issue for models of the Bushveld Complex; put simply the PGE grade is too high for the volume of magma observed known as the 'mass-balance paradox'. The various petrogenetic models which have been suggested for the formation of stratifrom PGE- and chromite-mineralisation are presented in Figure 2.9 (Chapter 2, section 2.4.1.1).

The trace element concentrations of sulphide minerals from the different stratigraphic units of the Deep Platreef, were analysed using the technique of laser ablation

inductively-coupled plasma mass spectrometry (LA-ICP-MS); the results of which are presented in Chapter 10 (section 10.1). This high-resolution analytical technique has been applied to sulphides from the surface Platreef along strike (e.g. Holwell & McDonald, 2007; Hutchinson & McDonald, 2008; Junge et al., 2018) and one study has been conducted on the Flatreef (Yudovskaya et al., 2017b); the data collected here represents the first study on the Deep Platreef extension.

The PGE were identified to be unevenly distributed between the coexisting sulphide phases with: (a) pyrrhotite hosting elevated IPGE concentrations (Os, Ir, Ru up to 60 ppm); (b) pentlandite carrying significant concentrations of Pd (up to 601 ppm) and Rh (up to 391 ppm); (c) no significant carriers of Pt and Au and; (d) chalcopyrite was generally poor in all PGE but contained appreciable Ag, Cd and Zn concentrations. The observed distribution pattern of the PGE between the co-existing sulphide minerals matches that predicted based on their differing partition coefficients firstly between mss and iss and then between the final exsolution products (as outlined in section 2.3 in Chapter 2). For example, IPGE and Rh are highly compatible with mss, hence their concentration in the exsolution products of mss pyrrhotite and pentlandite (Barnes et al., 2006). The exception to this is the Pd enrichment in pentlandite as Pd is incompatible with both mss and iss; significant concentrations of Pd in pentlandite are a feature of many Ni-Cu-PGE deposits (e.g. Godel et al. 2007; Holwell & McDonald 2007; Godel et al., 2008; Junge et al., 2018). This is proposed to occur due to the preferential diffusion of Pd into pentlandite over pyrrhotite during the crystallisation of iss (Barnes et al., 2006; Dare et al., 2010). The absence of platinum in the sulphide analyses indicates it's preferentially concentration into a late-stage immiscible semimetal (Te, Bi, As) rich melt (Fleet et al., 1993; Helmy et al., 2007; Helmy et al., 2010).

This study identified that pentlandite is the principal sulphide host of PGE containing significant amounts of both Pd and Rh with the highest concentrations identified in chromite-bearing lithologies (see Figure 10.2B and 10.3 in Chapter 10, section 10.1.1). An overview of the measured Pd concentrations in pentlandites from all sectors of the Turfspuit deposit are shown in Figure 11.2B. The results show a systematic increase in the Pd tenor moving westwards and down-dip from the surface Platreef to the Deep Platreef (see Figure 11.2B). The range of Pd concentrations in pentlandite for the Turfspruit deposit varies from < 50 ppm in the shallow Platreef (Hutchinson & McDonald, 2008), up to 312 ppm in the Flatreef (this study and Yudovskaya et al., 2017b) and >600 ppm in the Deep Platreef (this study). The highest PGE tenors Pd concentrations in pentlandite were analysed in the Main Chromitite unit accompanied by elevated Os (6 –

11 ppm), Ir (10 – 26 ppm), Ru (9 – 94 ppm), Rh (31- 391 ppm) and Pt (4 – 7 ppm) concentrations.

The Pd concentration of comparable Ni-Cu-PGE deposits in the Bushveld Complex are also shown in Figure 11.2. The reef pyroxenites in the shallow Platreef in the northern (Overysel) and central (Sandsloot) sectors have sulphides with a range in Pd concentrations between 50 to 200 ppm with slightly higher concentrations recorded in the northern sector (see Figure 11.2A). These values are higher than those obtained in the lateral equivalent shallow Platreef on Turfspruit in the southern sector (see Figure 11.2B), which has variably been attributed to: (1) the different geochemistry of the floor rocks i.e. anhydrous granites vs volatile-rich carbonates; (2) the central sector is in proximity to the feeder staging chamber (Yudovskaya et al., 2011; McDonald et al., 2009); (3) local variations in the R-factors attained (Ihlenfeld & Keays, 2001; Sharman et al., 2013). The Pd content of pentlandite analysed in the Flatreef and Deep Platreef portions of the Turfspruit orebody (see Figure 11.2B) are on the same order of magnitude as those measured in stratiform reefs of the Merensky and UG2 chromitite i.e. 100's ppm ΣPGE (see Figure 11.2D). To achieve the measured PGE tenors of sulphides in the Deep Platreef, particularly Pd and Rh in pentlandite, that are comparable to 'reef-style' deposits the petrogenetic model needs to account for the extremely high R values required (10^5 to 10^6 ; Naldrett, 2011). The results from a study by Smith et al., (2014) on the Grasvally Norite-Pyroxenite-Anorthosite (GNPA) member (see Figure 11.2C), separated from the Platreef by the Ysterberg-Planknek fault, adds an extra level of complexity. Smith et al., (2014) recognised a primary and secondary BMS mineral assemblage with systematically lower Pd concentrations (< 50 ppm) in pentlandite recorded in the primary sulphide assemblage compared to the secondary sulphides (150 to 400 ppm). The syn- to post-magmatic hydrothermal processes responsible for the low-temperature alteration of sulphides is not accounted for in R-factor models.

An attempt to model the R-factors involved in the formation of the Platreef is presented in Ihlenfeld & Keays (2011) using equations as outlined in Lesher & Burnham (2001). They calculated a range of R-factors from ≈100 to ≈ 7000 that varied between sulphides in the different sectors; for example, higher and less variable R-factors were calculated for Overysel compared to Sandsloot. The PGE grade in sulphides from the Deep Platreef measured in this study are higher than those used in the Ihlenfeld & Keays (2011) so it can be expected that the R-factors will exceed 7000. In Figure 11.2B there is significant variability between the different sectors of the orebody on Turfspruit; this either implies a highly variable R factors or dilution from crustal contamination.

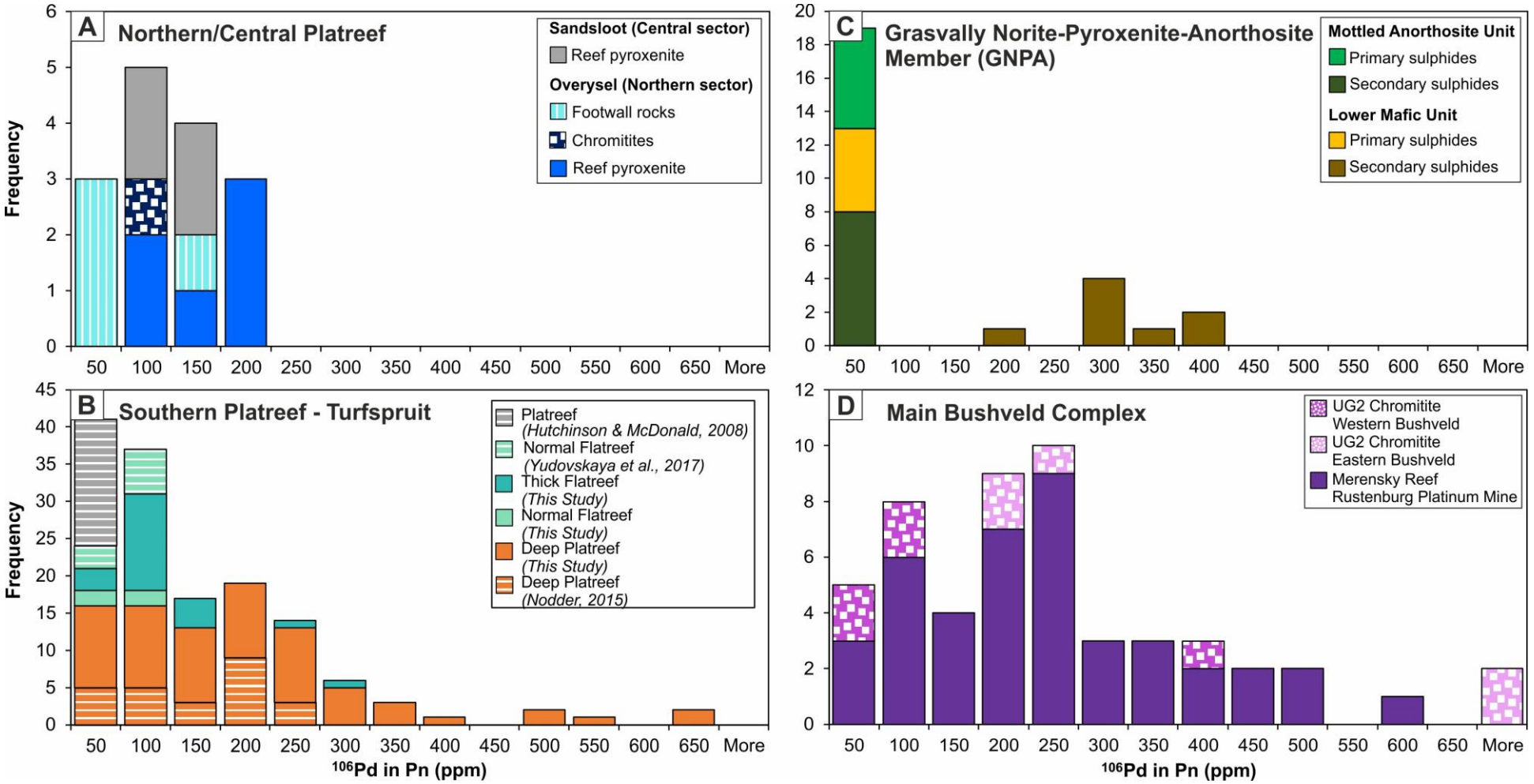

Figure 11.2: The variability of ^{106}Pd in pentlandite measured using LA-ICP-MS from across the Bushveld Complex. (A) The northern sector of the Platreef (Holwell & McDonald, 2006). (B) On Turfspruit in the southern sector of the Platreef (references in figure); (C) the GNPA-member, located on the northern limb south of the Ysterberg-Planknek fault (Smith et al., 2014) and; (D) The range of data from the Merensky Reef on the Western limb at the Rustenburg platinum mine (Godel et al., 2007) and for the UG2 chromitite (Osbahr et al., 2014).

The LA-ICP-MS results presented above show that a significant proportion of the PGE deportment of mineralised rocks is hosted in solid-solution in sulphides. The primary base-metal sulphides (BMS) can also host PGE as discrete platinum-group minerals (PGM), which represent the final phases to exsolve at low temperatures from the BMS. The incompatible PGE (Pt, Pd and Au) and a semi-metal melt (e.g. Bi, Te, As) are typically expelled to the margins of the sulphides during the crystallisation of iss. This is why PGMs are frequently found on either sulphide-sulphide or sulphide-silicate contacts. This peripheral location makes them vulnerable to late-stage sulphide replacement by actinolite-tremolite-chlorite assemblages, which can result in the isolation of PGM in secondary silicates (Li et al., 2004). This texture is described as 'satellite grains' frequently accompanied with fine-grained, monomineralic sulphides detached from the larger remnant BMS.

Lateral variations in the PGM assemblage of the Platreef orebody related to the composition of the local footwall have been recognised since the earliest studies by Kinloch (1982). Initially, the occurrence of PGE sulphides was thought to be limited to the northern sector on the farms Drenthe, Overysel and Zwartfontein North where the footwall rocks are composed of anhydrous La Pucella granites (Gain & Mostert, 1982; Kinloch, 1982; Holwell & McDonald, 2007). In locations where the footwall to the Platreef is composed of dolomites e.g. on Sandsloot and Turfspruit, PGM sulphide phases are notably absent and/or rare (see Armitage et al., 2002; Holwell et al., 2006; Hutchinson & Kinnaird, 2005). This contrasts with the PGM assemblage of the Merensky Reef and the UG2 Chromitite which shows remarkable consistency across the eastern and western limbs with the PGM assemblage dominated by either Pt/Pd sulphides or Pt-Fe alloys (Kinloch, 1982).

Previous PGM studies on the shallow Platreef at Turfspruit by Hutchinson & Kinnaird (2005) and Hutchinson & McDonald (2008) record a PGM assemblage dominated by Pd arsenide- and antimonides phase accompanied by significant decoupling of PGM from the sulphides into interstitial and alteration silicates. This semi-metal rich PGM assemblage has been interpreted to be result from the introduction of As- and Sb- into the magmatic system through the assimilation/devolatisation of the Duitschland sedimentary footwall rocks and xenoliths (Hutchinson & Kinnaird, 2005). Moving down-dip to the Flatreef, a more recent study by Yudovskaya et al., (2017b), covering the Upper Reef and Main Reef (equivalent to the Upper and Middle Reef of this study) interval revealed a zonal distribution in the PGM phases around chromite-stringers. In the Main Reef, this zonal distribution is represented by a change from a PGM

assemblage dominated by Pt sulphides (90 %, mostly cooperite) in and above the chromitite to one dominated by Pt-Fe alloys below the chromitite.

The absence of Pt and Au identified in the LA-ICP-MS study on sulphides indicates that these elements are present as PGMs. A complimentary PGM study focused on samples covering the various stratigraphic units and lithologies of the Deep Platreef is presented in Chapter 10 (section 10.2). The PGM assemblage of the Deep Platreef shows a strong lithological control on the distribution of certain PGM types. The identification of Pt-sulphides, laurite, and Pt-Fe alloys was restricted to the chromite-bearing lithologies: (I) on the Upper Pyroxenite/Middle Pyroxenite contact, hosting the Middle Reef (also identified at this locality by Yudovskaya et al., 2017b) and; (II) in the Lower Pyroxenite and Main Chromitite units hosting the Lower Reef. The preservation of PGM sulphides in the Flatreef and Deep Platreef is considered to be indicative of low degrees of contamination and their collection in sulphide results from primary magmatic processes (Lee 1996; Godel et al. 2007; Hutchinson & McDonald 2008; Dare et al. 2010; references therein). These PGM are spatially associated with magmatic sulphides that are believed to have formed from an initial homogenous, high-temperature mono-sulphide solution (mss) (Lee 1996; Ballhaus & Sylvester 2000; Godel et al. 2007; Holwell & McDonald, 2007). In all stratigraphic units > 40% of all PGM were identified to be spatially and texturally associated with sulphides (see Figure 10.9) as follows: (1) enclosed in sulphides; (2) on sulphide/silicate contacts and; (3) on sulphide/oxide mineral contact.

The Middle Reef mineralised interval in the Deep Platreef, associated with four chromite-stringers, demonstrates a zonal distribution in the PGM similar to that identified in the Flatreef by Yudovskaya et al., (2017b). The third and fourth chromite-stringers were sampled for their PGM assemblage; they both show variations in their PGM distribution with height across the chromitite. In the 3rd chromite-stringer the top is dominated by Pt-sulphide (65 %), laurite (22 %) and Pt/Pd-tellurides (13 %, merenskyite and moncheite). Three grains of cooperite and one of laurite identified had very large areas >100 μm^2; the majority of the other grains have sizes < 5 μm^2. The base of the chromite-stringer is dominated by Pd-bismuthotellurides (68 %, merenskyite), laurite (13 %) and electrum (13%). At the base the mineral assemblage is dominated by a few very coarse grain sizes (i.e. >100 μm^2). For example, laurite and electrum are both represented by one very coarse grain with an area of 257 μm^2 and 257 μm^2, respectively. Similarly four out of the seven merenskyite grains analysed were >200 μm^2. In contrast, the Pt was identified as geversite ($PtSb_2$) and sperrylite ($PtAs_2$) with all grains typically <2 μm^2. These coarse-grain sizes at the base

of the chromite reflect an increase in the silicate grain size to pegamtoidal feldspathic orthopyroxenite. This zonal distribution observed should be considered speculative because of this strong nugget effect with the PGM assemblage dominated by the presence of one or two very coarse PGMs. In the 4th chromite-stringer the top of the chromite PGM assemblage is dominated by Pt-sulphides (cooperite, 90%), this is entirely represented by one grain with an area of 1504 μm^2 (see Figure 8.16A). At the base of the 4th chromite-stringer the PGM assemblage is compositionally very different to the top; it is dominated by Pt-antimonide (57 %, geversite), Pt-telluride (19 %, moncheite) Pd-bismuthotelluride (17 %, michenerite) and Pt-bismuthide (6 %, insizwaite). The geversite and inisizwaite appear in solid solution and were identified in a rim around a coarse-grained base-metal sulphide (see Figure 10.16C and 10.16D). This 4th chromite-stringer is more disseminated than the other three, and the base marks the first appearance of olivine in a pegmatoidal olivine orthopyroxenite; this location represents a lithostratigraphic contact between the Upper and Middle Pyroxenite. This mineralogy of Sb-bearing PGMs is not normal of magmatic PGM assemblages and Sb is often interpreted as being introduced into the magmatic system via hydrothermal fluid activity derived from the assimilation of sediments (see Hutchinson & Kinnaird, 2005 and Holwell et al., 2006).

The greatest variability in the composition of the PGM minerals was observed in the Lower Reef mineralised interval (see Figure 11.1), which is hosted across two stratigraphic units: (1) the silicate-dominated Lower Pyroxenite (LP) and; (2) the chromite-dominated Main Chromitite (MCHR) unit. The PGM assemblage varies significantly between these two units reflecting the different mineralogical compositions of the host rock lithologies. Chromite is known to be a carrier of PGE, in particular the IPGE and Pt, consequently chromitites typically show distinct trends in their PGE geochemistry including: (1) arched chondrite-normalised PGE profiles peaking on Rh and Pt; (2) Pt:Pd ratios >1 and; (3) an PGM assemblage dominated by sulphides and sulpharsenides (Kinloch, 1982; Kinloch & Peyerl 1990; Barnes & Maier 2002; Wilson & Chunnett, 2006).

The highly mineralised LP unit (8 ppm 3PGE) was found to contain > 500 discrete PGMs mainly hosting Pt (70 %) as Pt-Fe alloys (55 %, isoferroplatinum) and Pt/Pd bismuthotellurides (34 %; moncheite, michenerite, maslovite, kotulskite and sobolevskite). The dominant Pt-Fe alloys were principally found in a symplectite intergrowth with base metal sulphides (pyrrhotite pentlandite and chalcopyrite), as shown in Figure 10.18. This texture has been interpreted to result from the exsolution of Pt during mss decomposition (Mostert et al., 1982; Majzlan et al., 2002). In certain

textural settings, adjacent to chromite grains, Pt-Fe alloys appear to be developed through desulphurisation of an original cooperite (see Figure 10.19C; Li & Ripley, 2006). Although Pt-Fe alloys are identified in unaltered PGE reefs in the Union section on the western limb, in general the dominance of Pt-Fe alloys in the Bushveld Complex have been attributed to hydrothermal activity based on their dominance in pothole reefs (Kinloch, 1982). In addition, a wide-selection of exotic compositions which constitute <0.5 % were identified unique to this stratigraphic unit including: potarite (PdHg), palladogermanide ($(Pd,Pt)_2Ge$), plumbopalladinite (Pd_3Pb_2), zvagintsevite (Pd_3Pb) and stannopalladinite (Pd_2Sn_2). Although unusual the majority of these PGM species have been identified elsewhere in the Platreef, principally on Sandsloot by Armitage et al., (2002), Holwell et al., (2006) and Junge et al., (2018). In Kinloch (1982) these elements are considered residual and may be concentrated in late volatile-rich fluids derived from the sediments; they alloy with Pd to form a low-temperatures (< 400°C; Malevskii et al., 1976) PGM assemblage. The IPGEs are hosted in laurite found concentrated locally contributing between 5 to 10% in two of the five thin sections studied.

The MCHR unit PGM assemblage is also Pt-dominated (83 %) as Pt-sulphide phases (50 %, cooperite), sperrylite (15 %) and Pt-Fe alloys (10 %). The other PGM phases identified include: Pd-bearing PGM (9 %), laurite (5 %) and electrum (3 %). An important textural observation was identified with one laurite grain as an inclusion in a chromite grain (see Figure 10.20D); this textural relationship supports the early saturation of the magma in PGM. Minor IPGE sulpharsenide (1 to 4 %) minerals of the hollingworthite-irarsite-platarsite series were identified typically in polyphase PGMs. In comparison to the Middle Reef all PGM in the MCHR were identified to range in size from <1 μm^2 to 100 μm^2 (average 4.5 μm^2) significantly lower than Middle Reef average of 42 μm^2.

If the Lower Reef mineralisation event is considered as a whole it shows the inverse of the zonal distribution in PGM species as recorded in the Main Reef by Yudovskaya et al., (2017b). The hanging wall of the is dominated by Pt-Fe alloys and Pt-sulphides in the chromitite. This change in PGM assemblage may be due to reduced fO_2 conditions in the hangingwall of the chromitite (Kinloch, 1982).

Outside of the mineralised intervals the PGM content of the non-mineralised stratigraphic units is more variable; telluride and bismuthide phases are identified ubiquitously whereas arsenide and antimonide phases are concentrated in serpentinised lithologies the stratigraphic units below the Main Chromitite (MCHR) unit and in serpentinised samples at the base of the Middle Reef mineralisation (as

discussed in section 11.3). The footwall of the MCHR unit, as represented by the Ultramafic Zone (UMZ), shows textural, mineralogical and geochemical evidence of contamination (for details see section 11.2.3). The PGM assemblage from the UMZ was found to be Pd-dominated (61 %) comprising predominantly antimonide phase (62 %, sudburyite, naldrettite). Also found to contain significant sulpharsenide phases (14 %) in the irarsite/hollingworthite solid solution.

A preliminary study (two samples) on the PGM assemblage in the Flatreef sector 'Normal'- and 'Thick'- reef facies found that they contained a near-identical PGM assemblage, dominated by Pt-telluride phase moncheite (at 96% and 97%, respectively). This is despite significant differences in the host lithologies and stratigraphic height with the two samples from: (1) the Gabbronorite Hybrid Zone hosting the 'Hybrid Reef' at the base of the Thick Flatreef drill hole and; (2) the Norite Cycle 1 unit in the Normal Flatreef hosting the Upper Reef mineralisation. A Pt-Pd bismuthotelluride dominated PGM assemblage is considered a characteristic of the Platreef mineralisation, that is found ubiquitously along strike (e.g. Kinloch, 1982; McDonald & Holwell, 2011; van der Merwe et al., 2012).

In addition to identifying PGM the back-scattered electron (BSE) imagery also picked up other micron-scale and dense accessory minerals including: galena (PbS ± Se), altaite (PbTe), niccolite (NiAs), breithauptite (NiSb), monazite ((Ce, La, Nd, Th)(PO_4, SiO_4)), zircon, uraninite (UO_2), cobaltite (CoAsS) and native Bi. Galena and zircon was identified ubiquitously, the distribution of the remaining heavy minerals was restricted to certain stratigraphic units. Niccolite, breithauptite and altaite were only identified in the Ultramafic Zone (UMZ), in the lower stratigraphic portion of the Deep Platreef drill hole, present as inclusions in pentlandite and chalcopyrite on sulphide/silicate contacts and in (for further details see section 11.3). The native Bi (area up to 9 μm^2) and monazite uraninite were identified in the Upper Pyroxenite (Upper Reef interval) and at the base of the drill hole in the Feldspathic Clinopyroxenite Hybrid Zone (HZ_{FCPX}).

11.1.3 Physical Concentration of Sulphides

On a deposit scale, there are observed sectoral discrepancies in the stratigraphy and mineralisation of the Turfspruit orebody moving from east to west and down-dip. The pre-emplacement geometry of the sedimentary floor rocks is believed to be partially responsible; particularly in the development of the Flatreef deposit. In the Platreef and Deep Platreef sectors the orebody was deposited on slopes dipping at a ≈ 40° angle. Conversely, the Flatreef orebody was deposited in a flat-lying graben-like structure; it

is currently unknown whether similar 'Flatreefs' are present along the strike length of the Platreef. The results of extensive drilling across the deposit reveals that the Platreef magmatic event broadly follows the trace of the graben-structure rather than truncating it.

The footwall rocks of the Platreef, the Transvaal Supergroup, experienced ductile deformation prior to the intrusion of the Bushveld magmas resulting in open-folded sedimentary strata (Nex, 2005; McDonald & Holwell, 2011; Brits et al., 2018). The overall regional structure is interpreted as a synformal monocline striking NNW and dipping to the SW (Nex, 2005; Brits et al., 2018) with the small-scale folding creating the Flatreef interpreted as parasitic folds on the major limb (Brits et al., 2018). Brits et al., (2018) recognise two principal folding events as having a substantial impact on the formation of the geometry of the orebody on Turfspruit: (I) a major fold axis orientated NNW-SSE (D^1 event) and; (II) refolding gently with axis trending ENE-WSW (D^2 event). The deformation of the footwall sediments confirms that they were well-consolidated (lithified) prior to the intrusion of the Platreef magma. The Turfpsruit deposit has also been affected by several late- to post-emplacement brittle faulting events centred on the pre-existing fault zones. On the Tweefontein property (directly north of Turfspruit) these brittle faults have been observed to redistribute the PGE mineralisation into faults (Nex, 2005). No such extensive remobilisation of the mineralisation has thus far been evidenced on Turfspruit although thrust-faulting has been proposed to result in duplication of the stratigraphy in certain drill holes (Nodder, 2015).

Thickness variations in the Platreef magmatic package (10 to 400 m) are identified along the strike of the Platreef corresponding to structures in the footwall. For example, observations in the central sector at the Sandsloot pit reveal that the igneous reef thickens (30 to 60 m) in footwall synforms and is thinner (< 20 m) on antiforms (Holwell et al., 2005). Hutchinson & Kinnaird (2005) note that the Platreef on Turfspruit and Macalcaskop is thickest in footwall structural embayments accompanied by greater lithological variability. The Flatreef embayment structure is bounded by two major fault zones; on the eastern edge is the Nkwe shear zone and on the western limit the Tshukudu fault zone (for details see Brits et al., 2018). Brits et al., (2018) record thickness variations in the magmatic rocks in the Flatreef, which they interpret to result from a combination of localised magmatic infill of a graben-structure and a volume increase in the magma chamber due to devolatisation of carbonates. In a study on Ni-Cu-PGE magmatic systems by Barnes et al., (2016) they note that the most favourable depositional environments involve: (1) high volume

flow over a horizontal floor or; (2) a change in flow regime caused e.g. by a transition from vertical to lateral flow or a change in the width of the conduit. The transition from the Deep Platreef to Flatreef could therefore be an ideal depositional environment for the PGE-rich immiscible sulphide-liquid in the Platreef magma as it represents a change from sub-vertical to horizontal flow. The presence of significant xenoliths of hornfelsed calc-silicate and siliclastic rocks are noted in the Flatreef sector (examples shown in Figure 5.1 in Chapter 5) evidence of widening of the conduit by thermochemical melting and/or dissolution or physical erosion of the country rocks (roof and floor).

The local geometry will affect the collection of a sulphide melt, particularly if the magma intrudes along pre-existing anisotropies or structural planes of weakness such as lithological contacts, foliations and faults. The significant geochemical variability with stratigraphic height in the floor rocks of the Duitschland Formation (DF) from carbonates in the Upper DF to shales in the Lower DF is an example of a prominent local anisotropic characteristics. These sediments will have different melting points and rheological properties. The extent to which thermomechanical erosion of the DF occurs is dependent on differing rates of: crystallisation, magma flow and country rock melting/assimilation (Barnes et al., 2016).

11.1.4 Lithostratigraphy of the PGE-Mineralised Intervals

The mineralogy, mineral chemistry and whole-rock geochemistry of the stratigraphic units hosting the PGE mineralised horizons can place constraints on the magmatic (or non-magmatic) processes involved in their formation. An overview of the lithostratigraphy of the mineralised intervals, defined as >2 g/t 3PGE (Pt+Pd+Rh), across the Turfspruit deposit are shown in Figure 11.1. In Figure 11.1 it is obvious that the number, thickness, grades and petrological features of the mineralisation varies between drill holes; a summary of the features are presented in Table 11.1.

The number of PGE mineralised intervals intersected increases systematically moving down-dip between sectors from one in the Platreef, two in the Flatreef and three in the Deep Platreef. The thickness of the mineralised intervals varies from 2 to 60 m with the thickest intersections and highest grades identified in the Thick Flatreef (see Table 1.1), known by geologists working on the project as the ‘super hole’. All mineralised intervals identified on Turfspruit correspond with elevated sulphide concentrations, typically between 5 to 10 vol% sulphides and up to 20 vol% in the Thick Flatreef. In all drill holes the base metals Ni and Cu have a strong correlation (R^2 0.84-0.98) indicating that their distribution is controlled by the presence of

sulphides. The Ni and Cu concentrations also vary sympathetically with grade suggesting that the distribution of PGE is controlled by the presence of sulphide minerals.

Table 11.1: An overview of the petrological and geochemical characteristics of the mineralised intervals within all drill holes studied. Lithological abbreviations: FOPX feldspathic orthopyroxenite; NOR norite; OLOPX olivine orthopyroxenite; HRZ harzburgite; PAPX parapyroxenite; GBRN gabbronorite. Mineral abbreviations: QTZ quartz; PHL phlogopite; CR-STR chromite stringer; CR-DISS chromite disseminated; CHR chromitite; BMS base metal sulphide.

	Platreef	**Normal Flatreef**	**Thick Flatreef**	**Deep Platreef**
	ATS_002	**UMT_233**	**TMT_006**	**UMT_345**
Upper Reef				
Thickness (m)	-	5	2	11
Av. 3PGE (per m)	-	4	3.4	4.2
Grade (overall)	-	20.5	6.9	46
Strat Unit	-	NC1	UP	UP
Lithology	-	FOPX, NOR	FOPX	FOPX
Petrology	-	QTZ, PHL	PHL	QTZ, PHL
Geochemistry	-	Pt/Pd 1.3, Cu/Pd 1007, Ni/Cu 1.9	Pt/Pd 2.0, Cu/Pd 2466, Ni/Cu 2.3	Pt/Pd 1.4, Cu/Pd 1163, Ni/Cu 2.1
Middle Reef				
Thickness (m)	7	20	30	11
3PGE (per m)	3.2	4.6	7	5.3
Grade (overall)	37	93	212	60
Strat Unit	MP	MP	UP/MP	UP/MP
Main Lithology	OLOPX	FOPX, NOR	FOPX, OLFOPX	FOPX, OLOPX
Petrology	2 CR-STR Pegmatoidal 5-10 vol% BMS	1 CR-STR Pegmatoidal 5-10 vol% BMS	CR DISS Pegmatoidal 5 - 20 vol% BMS	4 CR-STR Pegmatoidal 5-10 vol% BMS
Geochemistry	Pt/Pd 1, Cu/Pd 1319, Ni/Cu 2.3	Pt/Pd 1.3, Cu/Pd 1227, Ni/Cu 1.9	Pt/Pd 1, Cu/Pd 989, Ni/Cu 2.0	Pt/Pd 1.1, Cu/Pd 1407, Ni/Cu 2.4
Lower (Deep Platreef) and Hybrid Reef (Normal and Thick Flatreef)				
Thickness (m)	-	3.2	23 (10)	6
Av. 3PGE (per m)	-	3.88	2.4 (2.8)	3.9
Grade (overall)	-	12.4	54 (30)	23
Strat Unit	-	MP/PNZ	HZ_{OLWEBS} (HZ_{GBRN})	LP/MCHR
Main Lithology	-	HRZ	PAPX (GBRN)	FOPX, GBRN, CHR
Petrology	-	>5 vol% BMS	>5 vol % BMS	5 vol % BMS, CHR
Geochemistry	-	Pt/Pd 1.3, Cu/Pd 1227, Ni/Cu 1.9	Pt/Pd 0.9 (0.8), Cu/Pd 1489 (1393), Ni/Cu 1.8 (1.6)	Pt/Pd 1.4, Cu/Pd 746, Ni/Cu 1.8

The dominant host lithology of the PGE mineralisation are sulphide-bearing pyroxenites containing variable amounts of: orthopyroxene, plagioclase, olivine and clinopyroxene. The pyroxenite mineral assemblage follows the crystallisation sequence of orthopyroxene-clinopyroxene-plagioclase; where olivine is present it precedes orthopyroxene. In the downhole geochemical profiles, shown in Chapter 7 (section 7.1), the massive pyroxenites (Upper and Middle Pyroxenite units) are characterised by uniform internal profiles in all drill holes. The pyroxenites contain consistent Cr contents (≈ 2000 - 3500 ppm) which reflects the lack of fractionation

and magmatic cyclicity in the mineralised lithologies as observed in the core which has led to questions on whether they intruded as crystal-free melts or crystal-bearing mushes (a discussion on this is provided below in section 11.1.5).

The first mineralised interval, the Upper Reef, is identified in different stratigraphic and developed to a varying extent across the Turfspruit deposit including: (1) absent in the Platreef; (2) hosted in the Norite Cycle 1 (NC1) unit in the Normal Flatreef and; (3) found in the Upper Pyroxenite (UP) unit in both the Thick Flatreef and Deep Platreef. In Yudovskaya et al (2017b) between one to two chromite-stringers are identified to accompany the Upper Reef mineralisation (as sampled in UMT_314); in contrast, no chromite-stringers were identified at this location in this study. A summary of the mineralogical and geochemical characteristics of the Upper Reef and their implication for the mineralisation processes from the drill holes studied across the deposit are provided below:

Deep Platreef - the base-metal sulphides (BMS) hosting the PGE mineralisation in the feldspathic orthopyroxenite of the UP unit are present interstitially. The BMS share the interstitial space with plagioclase, quartz and phlogopite (see Figure 8.5C); in addition to alteration minerals including talc and tremolite. The BMS assemblage consists of pyrrhotite, pentlandite and chalcopyrite in the approximate proportions 40:25:30 (see Figure 8.5E and 8.5F). The mineralised interval is 11 m thick with an average grade of 4.2 ppm (3PGE) accompanied by elevated Au concentrations at 1.4 ppm. Consequently, the chondrite-normalised Ni-Cu-PGE-Au profile, as shown in Figure 7.26B (Chapter 3, section 7.3.1), peaks on Au. In the downhole geochemical profiles over the Upper Reef interval the Pt/Pd ratio decreases moving downhole from 1.9 at the top to 1.4 at the base. This is accompanied by a reversal in the Cu/Pd ratio from 6009 in the unmineralized hanging wall to 2437 in the Upper Reef interval. At the level of the Upper Reef interval the UP unit is intruded by numerous quartz-feldspar veins which have potentially caused localised PGE redistribution (see section 11.3).

Thick Flatreef - the mineralised interval is much thinner compared to the Deep Platreef at 2 m thick and contains a lower average grade of 3.4 ppm (3PGE) and 0.7 ppm Au. The BMS assemblage is dominated by pyrrhotite and pentlandite in the proportion 70:30; there is a notable absence of the intermediate solid solution (iss) crystallisation product, chalcopyrite (see Figure 8.22 in Chapter 8, section 8.1.2). The BMS are found in the interstitial spaces without any other mineral phase present; contrasting with observations in the Deep Platreef. The peak in 3PGE grade corresponds to elevated Pt/Pd ratios (up to 2.1), a decrease in Cu/Pd ratio (average

2466) and high Ni and Cu concentrations (7075 ppm). There is a sharp increase in the Cu/Pd ratio directly above the mineralised interval to > 20000 indicative of a new impulse of magma.

Normal Flatreef - the BMS are heterogeneously distributed in a vari-textured feldspathic orthopyroxenite at the base of the NC1 unit, as described in Chapter 5 (section 5.3.3). In the host rock the dominant cumulate orthopyroxene grain sizes range from fine-grained to pegmatoidal, examples of these textures are shown in Figure 8.32 (Chapter 8, section 8.1.3). Plagioclase is developed as oikocrysts in pegmatoidal leucocratic pods (see Figure 8.32A and 8.32B) within which euhedral medium- to coarse-grained orthopyroxene grains are developed with exsolved chromite. Coarse-grained phlogopite is spatially associated with medium- to coarse-grained BMS. The variability in the distribution of the BMS is picked out in spiky profiles for 3PGE, Au, Ni + Cu (see Figure 7.11F, 7.11G and 7,11H). The Ni and Cu content of the samples analysed forms two populations whose concentrations varies from 100's ppm to 1000's ppm. This is also reflected in the major element downhole geochemical profiles with significant variability over short distances in the Al_2O_3 (wt %), CaO (wt %), SiO_2/Al_2O_3, CaO/Al_2O_3 and Cr/MgO contents. The Cr/MgO values range from 52 to 95 (average 68), they are generally lower than those observed in the massive pyroxenite lithologies (>80). All CaO/Al_2O_3 values (0.6 to 0.9) are within the magmatic range. The Pt/Pd ratio decreases steadily over the Upper Reef interval from 1.92 at the top to 0.91 at the base (average 1.29) indicative that the mineralisation is related to a new impulse of magma. This higher Pt/Pd ratio is reflected in the shape of the chondrite-normalised Ni-Cu-PGE-Au profile for sulphide-rich (>5 vol %) samples from the NC1 unit which rises steadily from Os to Pt, is flat-lying to Au and increases to Cu. This contrasts to the sulphide-poor NC1 profile which peaks on Pd; and is different to the Upper Reef in the Thick Flatreef and Deep Platreef which both peak on Au.

The principal Ni-Cu-PGE mineralisation event, namely the Middle Reef, can be traced across the entire Turfspruit deposit (see Figure 11.1). This mineralisation event is equivalent to the Main Reef event as described in Yudovskaya et al., (2017b) and Grobler et al., (2018). The Middle Reef mineralisation is located on the contact between the top of the Middle Pyroxenite (MP) unit and the base of the Upper Pyroxenite (UP) unit. This locality marks the first appearance of olivine, the presence of chromite-stringers and pegmatoidal grain sizes. Despite this mineralised contact being broadly recognisable across the Turfspruit deposit there are significant

variations observed between the different drill holes studied, as shown in Figure 11.3 and outlined in Table 11.1.

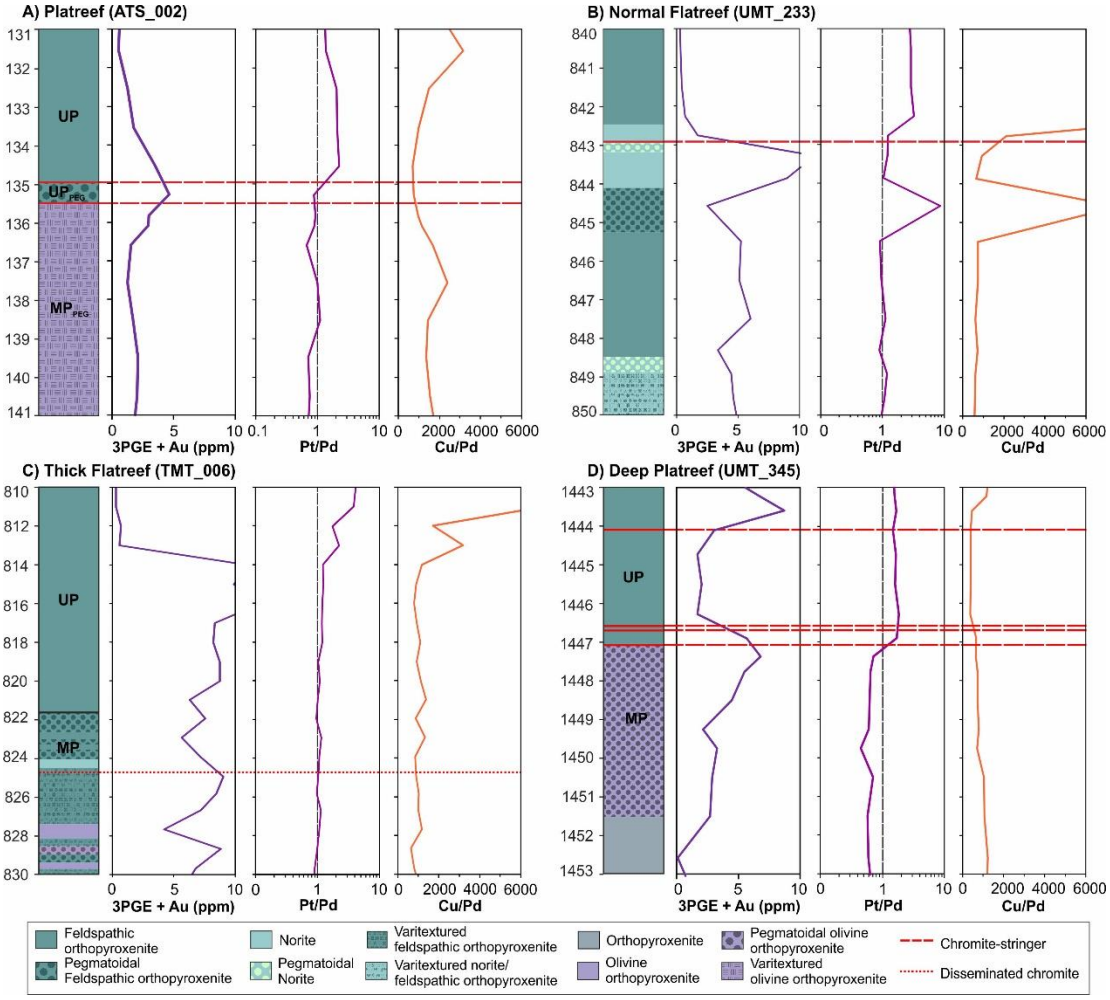

Figure 11.3: Lithological logging, grade (3PGE + Au), Pt/Pd and Cu/Pd downhole geochemical profiles of the Middle Reef mineralisation event as identified across the Turfspruit deposit.

The petrological features of this mineralised interval vary between the drill holes including: (1) the presence of between one and four chromite-stringers; (2) variable thickness and mineralogy of pegmatoidal regions; (3) the presence and/or absence of olivine-bearing lithologies. In the shallow Platreef (Figure 11.3A) two chromite stringers are identified with a footwall of pegmatoidal olivine-bearing rocks (< 10 vol% olivine); the Deep Platreef drill hole closely resembles this (see Figure 11.3D) with the distinction that it contains four chromite stringers. The olivine composition in the Deep Platreef was measured to be Mg-rich with Fo_{80-83} indicating that they are magmatic in origin. In the two Flatreef drill holes the Middle Reef has a varied appearance; olivine is notably absent in the Normal Flatreef and is present only as relict grains in the Thick Flatreef (see Figure 11.3B and 11.3C). In the Normal Flatreef, one well-developed chromite stringer is found on the contact between norites at the

base of the UP unit and the pegmatoidal norite marking the beginning of the MP unit. In the Thick Flatreef the presence of chromite is discontinuous and disseminated (accompanied by perovskite) and doesn't correspond with the largest peak in grade (see Figure 11.3C). On a deposit-wide scale the presence of olivine-bearing rocks in the Middle Reef has been correlated with calc-silicate xenoliths and footwall compositions (Grobler et al., 2018; as evidenced in the heavy S isotope ratios for both of these drill holes, see section 11.2).

The downhole geochemical profiles across the Middle Reef interval are shown in Figure 11.3. In most drill holes, with the exception of the Thick Flatreef (see Figure 11.3C), the presence of chromite-stringers correspond to the highest peak in grade (3PGE + Au) accompanied by low Cu/Pd ratios (typically < 1000) and elevated Pt/Pd ratios (> 1) in the immediate hanging wall. Combined these factors suggest that the chromite-stringers formed at the base of a new intrusive magmatic episode as interpreted from similar geochemical profiles for the Merensky Reef by Naldrett et al., (2009). This interpretation supports the dominant role of orthomagmatic processes in the formation of the Middle Reef mineralisation. The UP and MP units are interpreted to have formed in two separate intrusive episodes, with the chromite-stringers on the contact between them deposited at the base of the new pulse of magma.

In contrast, the downhole profiles for the Thick Flatreef over the Middle Reef interval are distinct (see Figure 11.3C). The 3PGE grade (up to 12 ppm), Pt/Pd (up to 1.2) and Cu/Pd (up to 3190) peak significantly (≈ 8 m) above the first occurrence of chromite. The Pt/Pd (average 1.0) and Cu/Pd (< 1000) ratio of the Middle Reef mineralisation event in the Thick Flatreef are uniform over a significant interval (30 m). In contrast, the Ni/Cu ratio shows an overall decrease with depth from 2.3 at the top to 1.6 at the base of the MP unit potentially indicative of cumulative fractionation of an original sulphide melt migrating downwards. These pattern in Pt/Pd and Ni/Cu are maintained to the end of the drill hole accompanied by elevated grade known as the Hybrid Reef. The PGE mineralisation cross cuts lithological contacts although there is a drop in the grade moving from an average of 7 ppm in the Middle Pyroxenite to 3 ppm in the Olivine Websterite (HZ_{OLWEBS}) and Gabbronorite (HZ_{GBRN}) stratigraphic units. The grade shows considerably more local heterogeneity which corresponds to the more irregular distribution of sulphides.

Similar patterns in the Pt/Pd and Ni/Cu profiles acting independently of lithological complexity was observed in the shallow Platreef on Turfspruit by Hutchinson & Kinnaird (2005) and Hutchinson & McDonald (2008). They interpret this to suggest

significant vertical redistribution of Ni, Cu, Pt and Pd. On Sandsloot footwall mineralisation is proposed to occur via hydrothermal fluid fluxing, which results in decoupling of the PGE from sulphides. In contrast, the Thick Flatreef profiles the Ni and Cu concentrations have a sympathetic relationship with PGE mineralisation consistent of transport within a sulphide liquid. This bears closer resemblance to the footwall sulphide mineralisation into the Archean gneiss footwall observed on Overysel by Holwell et al., (2006) where a sulphide liquid penetrates into the footwall rocks. To achieve this requires the development of a permeable interconnected sulphide network which is proposed to occur via partial melting of the floor rocks. The problem with this model when applied to the Flatreef is the absence of increasing fractionation in the Pt/Pd (or Pd/Ir) ratio moving down hole.

The Lower Reef mineralisation event, only identified in the Deep Platreef, is hosted in the Lower Pyroxenite (LP) and Main Chromitite (MCHR) stratigraphic units (see Figure 11.1). The Lower Reef is 6 m thick and carries 4 ppm (3PGE) although the downhole grade profile varies across the mineralised interval, as shown in Figure 7.3 (Chapter 7, section 7.1.1). The highest grades are attained in the LP unit (6 ppm) which forms the hanging wall of the MCHR (up to 3 ppm) and the grade drops off sharply in the footwall of the Ultramafic Zone (UMZ).

The LP unit is relatively thin (4.09 m) compared to the other pyroxenite-units (> 10 m thick), is lithologically diverse (olivine gabbronorite to feldspathic orthopyroxenite) and vari-textured (pegmatoidal, poikilitic); examples are shown in Figure 8.12 (Chapter 8, section 8.1.1). The LP unit contains fine-grained disseminated chromite found in the following textural settings: (a) in embayments on the edges of orthopyroxene grains (see Figure 8.13B); (b) as inclusions in clinopyroxene (see Figure 8.13C) and; (c) in recrystallisation pathways (see Figure 8.13A). The recrystallisation pathway, as shown in Figure 8.13A, is composed of fine-grained minerals including orthopyroxene, clinopyroxene, chromite and plagioclase. They appear to form via the breakdown of strongly corroded orthopyroxene grains either by solid state deformation or via an infiltrating melt (indicated by the presence of plagioclase). These reactionary textures are indicative that the chromite formed after the orthopyroxene through reaction with a plagioclase-clinopyroxene melt at high temperatures. Occasional aggregates of chromite grains form annealed masses with negative crystal habit to the co-existing orthopyroxene cumulate mineral (see Figure 8.13E). The BMS assemblage consists of medium- to coarse-grained pyrrhotite, pentlandite and chalcopyrite in the proportions 50:40:10 found interstitially (see Figure 8.13C and 8.13D); visible PGMs are identifiable in the sulphides (typically

pyrrhotite) with a symplectite texture (see Figure 8.13F). The top of the chromitite in contact with the LP unit is characterised by annealed chromite grains and equilibrium texture (120° triple junctions) in the monomineralic orthopyroxneite directly above. This possibly indicates high melt/fluid fluxes across the contact which ties in with Pt-Fe alloy dominated PGM assemblage and the higher grades found in this hanging wall (see Figure 8.15). The chondrite-normalised Ni-Cu-PGE-Au profile for the LP unit samples suggest that the sulphides are the dominate host of the PGE mineralisation. Two profiles were identified which varied depending on whether disseminated chromite is present or not: (a) sulphide-rich gabbro increases gradually from Os to Pt then is flat-lying to Cu; (b) a chromite-bearing gabbronorite gradually increases to Pd, with lesser Au and Cu.

The MCHR unit, a 1 m thick chromitite, contains between 60 to 80 vol% chromite, interstitial plagioclase and coarse-grained orthopyroxene oikocrysts and hosts elevated BMS concentrations up to 5 vol%. The BMS assemblage is similar to the LP unit but with minor cubanite present. The BMS are found in a range of textural settings (as shown in Figure 8.18) including as disseminated blebs, coarse-grained aggregates in altered silicates, mobilised in cross-cutting alteration veins and as polyphase inclusions. The chondrite-normalised Ni-Cu-PGE-Au profile for the MCHR unit as analysed in the Deep Platreef by Nodder (2015) are less fractionated than the LP unit and also have a pattern typical of a sulphide liquid which steadily rises from Os to Pt, is flat lying to Rh and the increase to peak on Pd. This is opposed to a normal chromite-arch shaped profile as typifies the UG2 chromitite of the eastern and western limbs. This supports a model for the in situ crystallisation of chromite with the PGE mineralisation controlled by early-formed sulphides.

Grobler et al., (2018) question whether the sporadic chromite-occurrences beneath the MP unit in the Flatreef can be correlated to the MCHR unit. The chromite-bearing intervals identified in the Pyroxenite-Norite Zone (PNZ) of the Normal Flatreef (see Figure 5.27) and in both the HZ_{OLWEBS} and HZ_{GBRN} (see Figure 5.22E) in the Thick Flatreef vary significantly from the MCHR unit in the Deep Platreef. In the Flatreef the chromite-occurrence typically contain lower Cr concentrations (up to 30,000 ppm, compared to 169,872 ppm in the Deep Platreef), elevated clinopyroxene contents and are finer-grained. Importantly, the chromite-occurrences in the Flatreef don't correspond to any peak in PGE grade.

11.1.5 Transported vs In Situ Crystallisation

A key question in any petrogenetic model for the Platreef is whether the magmatic processes responsible for the Ni-Cu-PGE mineralisation operated: (1) in situ at the

site of deposition or; (2) at depth in the magma conduit with the PGE-rich sulphides transported upwards to their final site of deposition. This ambiguity can also be applied to the formation of the high-temperature minerals chromite and orthopyroxene i.e. whether the intrusion was emplaced as crystal-sulphide liquid mush or a crystal-free melt.

In a typical magma column there is a cumulate pile with the resident magma above (as outlined in Chapter 2, section 2.2.5); in a closed-system progressive cooling results in fractional crystallisation and increased solidification of the magma column (for a schematic representation see Figure 2.4). In a sulphide-crystal mush, pre-existing grains and the immiscible sulphide liquid are transported in the magma. The transport model requires the mobilisation of a sulphide liquid from the initial site of accumulation at a deeper level in the system and transport upwards to shallower levels. The exact mechanisms of how a dense sulphide liquid is remobilised in the upper crust are poorly understood but it represents a multi-stage process involving initial entrainment, upward transport and mechanical deposition of suspended sulphide droplets (Barnes et al., 2016). The mechanical sedimentation of sulphide droplets is enhanced by sulphide coalescence during transport which emphasises the aforementioned density contest between the sulphide melt and silicate magma. The separation of a sulphide liquid from the cumulate silicate phases is impeded by two factors: (1) magma viscosity and; (2) falling temperature increasing crystallisation rates. A silicate framework of crystals will affect the downward migration and concentration of a sulphide liquid. In the sulphide-rich pyroxenites hosting the PGE mineralisation of the Platreef the medium- to coarse-grained orthopyroxene crystals have medium-grained interstitial areas potentially producing a permeable network for the downward migration of sulphides.

The Platreef is envisaged to have resulted from multiple intrusive episodes, with three most commonly proposed, forming a sill-like complex (Kinnarid, 2005; Manyeruke et al., 2005; McDonald & Holwell, 2007; McDonald & Holwell, 2011). The intrusion of the Platreef sills as a liquid-crystal mush has been proposed by Manyeruke et al., (2005) from studies on Townlands and for elsewhere on the northern limb by McDonald & Holwell (2007). The lithological logging, geochemical and mineral chemistry data acquired in this study supports this interpretation for the principal ore-bearing mineralised pyroxenites. This is based on their lithological homogeneity and the observed lack of vertical fractionation recorded both in the down hole mineral chemistry (see Figure 8.45 and 8.46 in Chapter 8, section 8.2.2) and bulk rock geochemical profiles (see Figure 7.1 in Chapter 7, section 7.1). Furthermore, the

presence of metasedimentary xenoliths/autoliths identified on the top contact of the Platreef indicates that there was no overlying magma column.

The Norite Cyclic units (NC1 and NC2) represent an interesting counterpoint to the massive pyroxenites as they demonstrate typical in situ fractionation trends. In particular, the 40 m thick NC2 unit (only found in the Deep Platreef), contains repetitive magmatic cycles of chromite-pyroxenite-norite-leuconorite-anorthosite. These cycles are very small (< 30 cm) and record variably complete or incomplete mineral sequences, as outlined above. Evidence for non-sequential deposition in the NC2 unit was identified in the form of ball and flame structures produced by a sulphide-rich pyroxenite slumping into anorthosite (see Figure 5.14B in Chapter 5, section 5.3.1). This indicates that both liquid and mush processes contributed to the observed layering and that there was instability in the crystal pile that mobilised the mushes. The chromite and pyroxenite at the base of each cycle typically host sulphides (up to 10 vol%), which contain elevated PGE grade. The base of each cycle effectively represents a miniature (cm-scale) versions of the Merensky Reef. This suggests that they formed via periodic magma replenishment albeit in low volumes. The Pd content of pentlandites analysed from this stratigraphic unit range from 34 to 525 ppm, equivalent to values obtained in the Middle Reef, indicative that the parental magma to this unit is the same as that of the main mineralised massive pyroxenites. The platinum-group mineral (PGM) assemblage is Pt-dominated (94 %) as tellurides (85 %, moncheite) and arsenides (8 %, sperrylite); this can be interpreted as a primary magmatic assemblage for the Platreef.

Yudovskaya et al., (2017b) argue for an in situ petrogenetic model for the development of the Middle Reef mineralisation within the Flatreef. They propose the mixing of a new and residual fractionated hybrid magma via lateral flow during a voluminous phase of magmatism. The constant magma flow across the top of the cumulate pile enables the sulphides to achieve the high R factors as indicated in the PGE tenors. A key line of evidence for this is the zonal variation in the PGM assemblage of the Main Reef (Middle Reef equivalent) in the Flatreef on Turfspruit (as described in section 11.1.2 above). In section 11.1.4, reversals in the Pt/Pd and Cu/Pd ratios at the level of mineralisation indicates that the mineralised intervals formed from new injections of magma with distinct PGE budgets. The problem with this model is that it requires a volume of mafic magma to have passed over the rocks for which there is no longer preserved any evidence of on the surface (McDonald & Holwell, 2007).

11.2 The Role of Contamination

Crustal contamination is envisaged as a key ore-forming process in the literature on 'contact-style' Ni-Cu-PGE deposits found on the margins of mafic/ultramafic intrusions. In section 11.1, magmatic processes are advocated as being dominant in the petrogenesis of the PGE-rich sulphides in the Platreef. The number and timing of contamination events affecting the Platreef in the literature varies from one (Hyporthesis 2) to two (Hypothesis 3); the results of this study support the latter. The two stages of crustal contamination are proposed to have influenced the development of the Platreef orebody on Turfspruit as follows: (a) initial sulphur saturation is triggered by the assimilation of crustal sulphur from wall rocks in a staging chamber at depthand; (b) upon emplacement via the in situ interaction between the Platreef magma and the floor rocks of the Duitschland Formation sediments. The majority of the evidence is preserved for the second event (b) which variably affects the host-rock lithogeochemistry and dilutes the PGE-grade of the sulphides, this is the one universal recognised contamination event.

Contamination processes operating on a regional and local scale have been identified along the strike length as observed in studies on the near-surface Platreef. Local contamination, resulting from in situ sediment-magma interaction, leads to the development of para-igneous lithologies. The chemistry of which has been observed to vary as a function of the lithological variability in the footwall sediments (Harris & Chaumba, 2001). The footwall Transvaal Supergroup sediments includes: quartzites, banded iron formations, shales, dolomites and limestones. These compositions can variably add excess SiO_2, Al_2O_3, CaO, MgO and FeO to the magma though processes relating to contact metamorphism ranging from volatile loss to partial melting. The majority of para-lithologies contain either elevated clinopyroxene or olivine contents (e.g. Sandsloot); their metamorphic origin is confirmed by low whole-rock Cr contents and high CaO contents (Harris & Chaumba, 2001). In contrast, a regional contamination event for the Platreef is recognised by Ihlenfeld & Keays (2011) based on a homogenous contamination signature including: (I) elevated REE concentrations; (II) Nb- and Ta-anomalies in primitive-mantle normalised spidergrams and; (III) consistent contaminated incompatible element ratios (low $(Nb/Th)_{PM}$ and high $(Th/Yb)_{PM}$).

Two sources of crustal contamination of the Platreef on Turfspruit have been recognised and geochemically characterised in the current study with the results presented in Chapter 6. These are the immediate floor rocks composed of the Duitschland Formation (DF) and the basement rocks of the Pietersburg Greenstone

Belt (PGB). This study represents the first time that a full suite of major and trace elements (including PGE), in addition to sulphur isotopes have been analysed on the same samples from the DF and PGB. Extensive drilling across the Turfpsruit licence area has provided abundant evidence for the interaction between the Platreef intrusion and the country rocks of the DF in the presence of: (a) metasedimentary xenoliths/autoliths, examples shown in Figure 5.1 (Chapter 5, section 5.0); (b) contact-metamorphosed country rocks intersected at the base of the drill holes (e.g. the Hornfels Hybrid Zone in the Platreef, drill hole ATS_002) and; (c) in the development of para-igneous lithologies (e.g. the Olivine Websterite Hybrid Zone as developed in the Thick Flatreef, drill hole TMT_006_D2). The complex and highly-variable contact-skarn mineralogy observed in drill holes across the Turfspruit deposit (see Figure 5.1 in Chapter 5) highlights the lithological variability of the DF.

The basement rocks of the Platreef are typically assumed to be Archean granites and gneisses, which form the floor rocks to the Platreef in the northern sector on Overysel (McDonald & Holwell, 2011). However, on a regional geological map (see Figure 6.1 in Chapter 6) in the southern sector of the Platreef (Townlands and Turfspruit) the PGB outcrops and from observed field relationships appears to dip beneath the Transvaal Supergroup sediments. The PGB outcrops mostly on the southern side of the Ysterberg-Planknek fault, that marks the most southerly extent of the Platreef, however, there is also a slither on the northern side. This study, therefore considers the PGB to represent a possible indirect source of crustal contamination, affecting the southern sector of the Platreef. Any interaction between the PGB and the parental magmas of the Platreef on Turfspruit would occur at depth below the base of the Transvaal Supergroup.

11.2.1 Geochemical Characteristics of the Hinterland

The results of a multi-element geochemical study on the Duitschland Formation (DF) and the Pietersburg Greenstone Belt (PGB) are presented in Chapter 6. The results are interpreted to represent near-primary compositions as both sample sets were collected at locations > 10 km away from the Bushveld intrusion i.e. beyond the high temperature contact metamorphic aureole. This addresses one of the problems with the current dataset on the country rocks as presented in the literature on the Platreef, which is that all the data has been obtained from either autoliths/xenoliths or the direct wall rocks which have undergone significant modification from high-temperature contact metamorphism.

Fieldwork on farm Duitschland highlighted the very distinct litho- and chemostratigraphy of the DF sediments, which are frequently divided into: (1) an upper sequence, ≈ 400 m thick, dominated by carbonate rocks with interbedded siliclastic units and; (2) a lower sequence, ≈ 600 m thick, dominated by shales, mudstones and sandstones interbedded with carbonate lithologies. This stratigraphic variability is significant because the Platreef magma on Turfspruit interacts with the DF in situ. This means that depending on the level of intrusion the magma will either be interacting with shale-rich (lower) or carbonate-rich (upper) country rocks that will impart a distinct geochemical signature. This lithological change also represents a significant change in the mineralogy of sulphur present as sulphates in the upper DF and in sulphides in the lower DF. This mineralogical difference of the sulphur reservoir will affect the degree to which the sulphur can be effectively transferred from the sediments to the magma and will impact the inherited isotopic composition.

The major element geochemical data collected on the DF was used to characterise the sediments primary composition. The results of this study confirm that there are distinct geochemical variations between the two dominant lithological-types i.e. silicates and carbonates. The highest SiO_2 (>40 wt%), Al_2O_3 (>5 wt%) and ΣREE (>100 ppm) are identified in the silicate rocks; whereas, the highest CaO (>25 wt%) and MgO (> 35 wt%) are found in limestones and dolomites, respectively. The present lithologies have characteristic CaO/Al_2O_3 ratio defining two significant populations: (1) CaO/Al_2O_3 >10 in carbonates (ranging from 17 to 570) and; (2) CaO/Al_2O_3 <0.5 in siliclastics (ranging from 0.01 to 0.51). This study confirms that the sedimentary rocks of the footwall plot outside of the magmatic range of CaO/Al_2O_3 values (0.6 to 1.0) for the Platreef feldspathic orthopyroxenites as defined in Kinnaird (2005).

All sediments of the DF have fractionated chondrite-normalised rare-earth element (REE) patterns with average La_N/Yb_N values of the shales and carbonates at 9.1 and 9.3, respectively. The fine-grained silicate lithologies from the Lower DF contain REE concentrations an order of magnitude higher (ΣREE < 100 ppm) than the carbonate-dominated lithologies of the Upper DF (ΣREE < 55 ppm). A pronounced negative Eu anomaly is recorded in the Malmani dolomites (McDonald et al., 2005) and this is reflected in the pyroxenite lithologies observed on Sandsloot where Malmani dolomites form the footwall rocks (0.48-0.80; Holwell & McDonald, 2006). In comparison, the dolomites of the DF have a heterogenous Eu-anomaly with both positive and negative Eu/Eu* values ranging from 0.8 to 1.2 and the shales of the DF have a similar range from 0.6 to 0.9. Consequently, no distinct Eu-anomaly is observed in the magmatic rocks in the Platreef orebody on Turfspruit.

The lithological units of PGB can also be stratigraphically divided into a lower metaigneous sequence and an upper metasedimentary sequence (de Wit, 1991). The metavolcanic rocks of the Eersteling Formation have flat-lying chondrite-normalised REE profiles (average La_N/Yb_N 0.85) and do not have a Nb and Ta anomaly on primitive-mantle normalised trace element spidergrams. This REE and incompatible element pattern is typical of uncontaminated mantle-derived melts from mid-ocean ridge basalts (MORB). In contrast, the metasedimentary Uitkyk Formation have fractionated patterns with the finer-grained silicates showing greater fractionation (average La_N/Yb_N 15.14) compared to the metaconglomerates (average La_N/Yb_N 4.09). This observed pattern reflects the sedimentary origin of the rocks with the coarser-grained proximal deposits more likely to retain heavy REE-bearing minerals.

The PGE metal basket of the Platreef on the northern limb is noticeably different to that of the eastern and western limbs. The Platreef is consistently more Pd and Au rich with a Pt/Pd ratio of 1:1 compared to the average of the wider Bushveld Complex at 2:1 (McDonald et al., 2005). This difference can be explained by either the Platreef forming from: (A) a more fractionated parental magma or; (B) the parental magma assimilating Pd-rich country rocks in the marginal location of the Platreef. The validity of the second hypothesis (B) can be examined by testing the PGE composition of the country rocks contaminating the magma. The results of a whole-rock PGE geochemical study are presented in Chapter 6 (section 6.3.4). The DF contains significantly elevated PGE concentrations above the background upper continental crust (1.2 ppb) with average ΣPGE concentration of 27 ppb in shales and 11 ppb in dolomites. These values are comparable to those in the modelled parental magmas of the Bushveld Complex (see Table 6.1, Chapter 6). The Pt:Pd ratio of the DF sediments varies from 0.5 to 2.3 (average 1.4) with no systematic variation observed between the shales and carbonate lithologies. Although the DF sediments are enriched in PGE relative to the background continental crust it is difficult to envisage a mechanism whereby this additional PGE content can be effectively introduced and homogenised into the Platreef magma in situ on Turfspruit. In addition, the DF aren't preferentially enriched in Pd over Pt so will their assimilation will not significantly shift the Pt:Pd ratio from 2:1 to 1:1. The PGE content (average ΣPGE 14.8 ppb) of the PGB was observed to be comparable to those of the Baberton Greenstone Belt (average ΣPGE 14.8 ppb) on the southern side of the Thabazimbi Murchison Lineament. The Pt:Pd ratio of the PGB rocks was also observed to vary from 1.0 to 3.3 (average 2.2) with no systematic variability between the metasedimentary and metaigneous rock types. The pyrite-mineralised metaconglomerate analysed was

found to contain significant gold concentrations at 3.9 ppm; if this mineralisation is effectively homogeneised at depth in the magma it may account for the slightly elevated Au concentrations in the Platreef compared to the eastern and western limbs.

The sulphur isotope composition of the DF sediments was tested in the current study (see Chapter 9, section 9.1.1) on relatively fresh rocks a significant distance (> 10 km) from the Bushveld Complex intrusion. Previous studies on the Platreef have measured the DF sulphur isotopic composition on samples of xenoliths/autoliths from the immediate footwall of the intrusion. For example, graphite layers on Turfspruit analysed by Buchanan & Rouse (1984) recorded $\delta^{34}S$ values of -2.4 ‰ to +2.0 ‰ and a study by Sharman et al., (2005) identified +9.7 ‰ for hornfels (shales) and +27.69 ‰ to +28.17 ‰ for calc-silicates. The measured isotopic compositions of xenoliths may or may not reflect true 'end-member' compositions, given devolatilization and alteration effects imposed by the high grade contact metamorphism from the intruding magmas. This study extracted chromium reducible sulphur (CRS) from the DF samples; no carbonate-associated sulphur (CAS) was recovered. The limitations of the method restricted the data to sulphides not sulphates; to overcome this the results of this study are combined with the results of Guo et al., (2009; for details see Chapter 4, section 4.5).

The sulphur content in the DF sediments was not observed to be significant with visible estimations of <0.5 wt% in the pyrite-bearing shales and a maximum value of 0.158 wt% obtained on a hand-held XRF. The sulphur isotope values of the DF vary with stratigraphic height. The pyritic shales in the Lower DF have $\delta^{34}S$ values ranging from +2.7 to +4.6 ‰. No sulphur-bearing evaporite horizons were identified in the field in the Upper DF however anhydrite xenoliths were identified in the drill core (see Figure 5.1, Chapter 5). One sample from the Upper DF hosting secondary Cu-mineralisation recorded a $\delta^{34}S$ value of +11.9 ‰. The CAS data on the Upper DF collected in Guo et al., (2009) shows that they contain extremely heavy $\delta^{34}S$ values of the Upper DF up to + 44 ‰ (average +22 ‰). Consequently, the DF sediments have two reservoirs of sulphur that are characterised by distinct ranges in $\delta^{34}S$ values that do not overlap as follows: (1) the Upper DF contains $\delta^{34}S$ values > + 10‰ dominated by CAS and; (2) the Lower DF contains $\delta^{34}S$ values < + 10‰ dominated by CRS (see Figure 9.5, Chapter 9 section 9.1.1)

A limited sulphur isotope study was also conducted on samples from the PGB. The PGB has been identified in this study as a potential source of crustal sulphur that the

Platreef magma in the southern sector may have interacted with at depth before ascending through the Transvaal Supergroup. All samples of the PGB analysed for their $\delta^{34}S$ composition come from the Uitkyk Formation in the upper part of the stratigraphy; they record positive values ranging from +1.5 to +6.3 ‰. In the PGB the sulphide content of the gold-mineralised metaconglomerate was more considerable at around 20 modal% pyrite as shown in Figure 6.6E (Chapter 6, section 6.2). This range of $\delta^{34}S$ values overlaps with those recorded in the Lower DF and as such cannot be used to uniquely distinguish a PGB input into the sulphur budget of the magma.

11.2.2 Crustal Contamination of the Platreef Magma on Turfspruit

It has been proposed that the degree of in situ crustal contamination decreases moving down-dip and westwards across the Turfspruit deposit (Yudovskaya et al., 2017b; Grobler et al., 2018). The drill holes chosen for this study cover this transition with depth and sample each sector of the orebody from the highly contaminated shallow Platreef, the transitional Flatreef, and finally the proposed primary magmatic stratigraphy of the Deep Platreef.

Crustal contamination of mafic/ultramafic magma will modify the geochemistry and consequently affect the observed mineralogy and petrology of the crystallised rocks. An overview of the results of detailed logging performed in this study are shown in Figure 11.1 (based on the results as presented in Chapter 5). A new stratigraphic framework was developed in this study, the stratigraphic subdivisions are shown in Figure 11.1. The top stratigraphic units of each drill hole (namely the Upper and Middle Pyroxenite units) can be correlated with relative ease across the deposit however, moving downhole towards the footwall contact the stratigraphic sequence becomes increasingly more contaminated. Stratigraphic units demonstrating petrological features not considered consistent with a typical of ‘magmatic’ mineral assemblage and textures in geochemical equilibrium are labelled as ‘Hybrid Zones’ in the nomenclature applied in this study. A summary of the lithological (Chapter 5) and mineralogical (Chapter 8) observations interpreted as indicative of contamination are provided below:

Deep Platreef (section 5.3.1, section 8.1.1): evidence of progressively increasing levels of contamination are identified from the Main Chromitite (MCHR) unit downhole. The effects of contamination were principally observed in the silicate mineralogy but also in the presence of increasing amounts of cubanite (type 2) in the sulphide assemblage. In the MCHR unit calc-silicate xenoliths and cross-cutting veins were identified in the drill core (see Figure 5.15). The sulphide assemblage of the

MCHR unit was observed to contain coarse-grained, compositionally complex aggregates of sulphide (pyrrhotite-pentlandite-chalcopyrite-cubanite) surrounded by tremolite in alteration pockets in oikocrystic orthopyroxene (see Figure 8.17D and 8.17E). The footwall of the MCHR unit consists of vari-textured harzburgite and pegmatoidal orthopyroxenite of the Ultramafic Zone (UMZ). The lithologies show varying degrees of alteration, both serpentinite-magnetite and amphibole-chlorite assemblages (see Figure 8.20). In the UMZ unit the sulphides are irregularly distributed and are found in a range of textural settings as: (1) pegmatoidal aggregates (cubanite-dominated) in leucocratic melt pods (see Figure 8.20D); (2) mobilised in serpentinite veins (see Figure 5.16A); (3) disseminated (Figure 5.16C) and; (4) net-textured (see Figure 5.16). The olivine-content is hosted in interstitial troctolite to coarse-grained orthopyroxene; this textural setting is similar to that shown in Figure 5.2B above a recognisable calc-silicate xenolith. The olivine compositions are Mg-rich (Fo_{80-82}), which are traditionally considered to be magmatic but could also be derived from the assimilation of dolomite. The olivine-gabbronorite at the base of the UMZ unit appears to bifurcate the underlying finer-grained Feldspathic Clinopyroxenite Hybrid Zone (HZ_{FCPX}), which potentially represents a marginal unit. The HZ_{FCPX} is finer grained (1 to 2 mm orthopyroxene; see Figure 8.21 and 5.17D) than the overlying medium-grained to pegmatoidal ultramafic units indicative that it cooled quicker. Microxenocrysts (mm-scale) of calcite were also identified in the HZ_{FCPX}.

Thick Flatreef (section 5.3.2, section 8.1.2): evidence of contamination increases towards the base of the Middle Pyroxenite (MP) unit with the presence of thin (< 10 cm) xenoliths/autoliths composed of fine-grained, black olivine interpreted as dolomitic skarn (see Figures 5.19C, 5.20 and 5.21). In proximity to the dolomitic skarn the overlying orthopyroxenite typically shows fine-grained olivine chadacrysts enclosed in medium-grained orthopyroxene oikocrysts; this texture is only developed on the cm-scale but implies that the olivine crystallised first. On the top contact of the MP unit the disseminated chromite is found associated with the accessory mineral perovskite ($CaTiO_3$; see Figure 8.25A)) which can be found in metamorphosed impure limestone (Deer, Howie & Zussman, 1992). The Olivine Websterite Hybrid Zone (HZ_{OLWEBS}) contains more abundant and thicker (up to 87 cm) intervals of dolomitic skarn (see Figures 5.20 and 5.21). The pyroxenites directly above the contaminant are strongly altered by variable talc-serpentinite-tremolite; sulphides contained are pyrrhotite-dominated and show a spatial association with apatite (see Figure 8.26). The mineralogy of the skarn are composed of densely-packed,

equigranular, fine-grained olivine with interstitial base-metal sulphides (pyrrhotite-pentlandite-chalcopyrite) showing variable alteration by magnetite. The olivine appears variably fresh or extensively altered by either serpentinite minerals (see Figure 8.27C) or talc (see Figure 8.27A). The Gabbronorite Hybrid Zone (HZ_{GBRN}) is vari-textured and inequigranular with evidence of the mixing between two magmas as described above in section 11.1.4.

Normal Flatreef (section 5.3.3, section 8.1.3): no direct evidence of contamination was observed in the mineralogy of the Normal Flatreef. The last logged unit the Pyroxenite-Norite Zone (PNZ) is suggested in Grobler et al., (2018) to result from variable shale-assimilation. The PNZ compositionally ranges between norite and pyroxenites and display weak layering developed on the cm-scale; this non-systematic, small-scale compositional variability accompanied by inequigranular textures is considered indicative of crustal contamination.

Platreef (section 5.3.4 and section 8.1.4): the entire logged sequence of the Platreef shows textural and mineralogical differences to that of the other drill holes. One of the biggest differences is in the base metal sulphide (BMS) mineral assemblage which in each stratigraphic unit is dominated by pyrrhotite (90 vol%) with only minor pentlandite and chalcopyrite. At the top of the drill hole, on the contact between the Mottled Anorthosite (MAN) unit and the Upper Pyroxenite, a calc-silicate xenolith was identified (see Figure 5.29C). The UP unit is noticeably finer-grained (< 2 mm) below the xenolith compared to the equivalent unit in the other drill holes studied (2 to 5 mm); indicative that the UP unit crystallised faster against the cold surface of the xenolith. The average grain size increases moving downhole away from this top contact but shows more variability than recognised in this unit from elsewhere in the deposit. A locally developed fabric was identified in the UP unit directly overlying the Middle Pyroxenite (MP) unit created by the preferential alignment of orthopyroxene grains at 90° to the core axis. The BMS content of the UP unit is heterogeneously distributed and only locally present (over a metre) in quantities up to 5 vol%; they are unmineralized and found spatially associated with interstitial quartz and apatite. A calc-silicate xenolith was also identified towards the base of the Middle Pyroxenite (15 m below the chromite-stringer on the PGE mineralised UP/MP contact) as shown in Figure 5.32; the xenolith is overlain by a feldspathic harzburgite representative of a para-igneous lithology. The logged interval ends in a fine-grained hornfels xenolith (see Figure 5.32C and 5.33) which retains a foliated texture, attesting to its metasedimentary origin. The fine-grained hornfels matrix contains clusters of calcite, amphibole, chlorite and quartz (see Figure 8.42). In both the Platreef and Thick

Flatreef drill holes the contacts between the magmatic rocks with xenoliths were observed to be irregular either convex or concave in contrast to the sharp-planar magmatic contacts.

The geochemistry of cumulate rocks is primarily controlled by the modal mineralogy (Harris & Chaumba, 2001), therefore comparing the whole-rock geochemical data with end-member mineral compositions should give an indication on the degree of contamination. The whole-rock data was modelled in the orthopyroxene-clinopyroxene-plagioclase-olivine end-member compositional field for the major element ratios Al_2O_3/MgO and CaO/MgO in Chapter 7 (section 7.1). The whole-rock data for the Deep Platreef (Figure 7.2) and Normal Flatreef (Figure 7.10) drill holes show little evidence of crustal contamination with most samples plotting within the mineral fields. In the Thick Flatreef (Figure 7.6), samples from the Olivine Websterite Hybrid Zone (HZ_{OLWEBS}) span a large range of concentrations in MgO, CaO and Al_2O_3. Three samples consistently plot outside the olivine-clinopyroxene tie line towards very high MgO concentrations (> 40 wt%), which is indicative of dolomite assimilation. In the Platreef (Figure 7.14), two samples consistently plot outside the mineral fields at low MgO concentrations (< 10 wt% MgO). These samples represent a highly altered leucogabbronorite from the Upper Pyroxenite unit and a fine-grained hornfels from the Hornfels Hybrid Zone (HZ_{HF}). The average MgO (wt%) concentration of the DF shales analysed in this study was around 4.3 wt% (range between 1.7 to 7.7 wt%) so shale-assimilation could account for this observation.

In order to better understand the observed geochemical variability with depth, selected major and trace element data are plotted in downhole profiles for each drill hole in Chapter 7 (section 7.1). Three general trends are observed in the geochemical profiles: (1) abrupt changes on lithostratigraphic contacts associated with norite-pyroxenite and pyroxenite-chromitite; (2) the two main, thick (>10 m), PGE-mineralised pyroxenites (Upper and Middle Pyroxenite) in all drill holes have a uniform internal geochemical signature; (3) spiky geochemical variability. The third type of profile is interpreted to result from contamination processes as magmatic processes typically impart either a sharp reversals on lithological contacts and/or systematic changes with increasing height (i.e. fractionation trends). A summary of the geochemical contamination signature as identified in each drill hole are provided below:

Deep Platreef (see Figure 7.1 and 7.3, section 7.1.1): the greatest variability in the geochemical profile is recorded in the Ultramafic Zone (UMZ) corresponding to the observed lithological and textural heterogeneity as described above. The lithologies

of the UMZ have a mineral assemblage, dominated by olivine and orthopyroxene, but have low Cr contents, consistent with a non-magmatic origin (from 51 to 1934 ppm, average 440 ppm). In comparison, the pyroxenite lithologies higher up in the stratigraphy contain typically > 2000 ppm Cr. The UMZ contains a number of CaO/Al_2O_3 values above the magmatic range (0.6 to 1.0) with a maximum of 1.8 indicative of carbonate-material assimilation. In contrast, the highest CaO/Al_2O_3 values (1.45 to 2.50) are recorded on the contact between the Upper Pyroxenite (UP) and Middle Pyroxenite (MP) unit. This corresponds with the development of pegmatoidal textures and a antimonide-dominated PGM assemblage (see section 11.2) evidence of fluid alteration over this interval (for more details see section 11.3).

Thick Flatreef (see Figure 7.5 and 7.7, section 7.1.2): a spiky geochemical profile is observed in the Olivine Websterite Hybrid Zone (HZ_{OLWEBS}) unit and the Gabbronorite Hybrid Zone (HZ_{GBRN}). The V and Cr concentrations drop significantly moving downhole from the Middle Pyroxenite (MP) unit to the HZ_{OLWEBS}. The Cr/MgO ratio decreases significantly moving downhole from the MP unit from 85 to 498 (average excluding visible chromite 155) to the HZ_{OLWEBS} from 2036 to 0.03 (average excluding visible chromite 33). The highest Cr/MgO values in the HZ_{OLWEBS} correspond to intervals of visible chromite and the lowest a sample of dolomitic skarn, which also has the highest $Mg\#_{91}$ recorded. The CaO/Al_2O_3 ratio in the HZ_{OLWEBS} fluctuates between 0.09 to 3.3 with most samples plotting outside the magmatic range indicating the interaction with both carbonate (>1.0) and shale (<0.6) lithologies. In the HZ_{GBRN} unit the geochemical variability can be accounted for by the varying abundances of the major mineral plagioclase, clinopyroxene and orthopyroxene. They contain a moderate range Cr/MgO ratios 42 to 2132 (average excluding visible chromite 68). The majority of the data plots < 80 and within the Main Zone range (see Figure 7.5H); this potentially supports the magma mixing of a compositionally distinct magma to that of the overlying pyroxenites. The highest Cr/MgO value of 2132 corresponds the presence of disseminated chromite in a clinopyroxenite which also records the highest CaO/Al_2O_3 value within this unit of 2.06.

Normal Flatreef (Figure 7.9 and 7.11, section 7.1.3): due to the sparsity of data it is difficult to draw too many conclusions from the downhole geochemical profiles. Towards the base of the Middle Pyroxenite (MP) unit, > 10 m below the chromite-stringer on the top contact, the pyroxenites composition deviates from the typical MP unit range. The Cr/MgO ratio decreases from an average of 108 over the Middle Reef interval to 72 at the base of the MP unit.

Platreef (Figure 7.13 and 7.15, section 7.1.4): again despite the limited data collected on this drill hole a few overall trends can be established. The majority of samples have CaO/Al_2O_3 ratios either on or just below the magmatic range; the exception to this is the hornfels sample at the base of the logged interval at 1.51. The greatest geochemical variability is observed in the Cr/MgO (16 to 102) and SiO_2/Al_2O_3 (2 to 22) ratios. Three samples have Cr/MgO ratios >80, two from the Upper Pyroxenite unit and one from the Middle Pyroxenite units; in most other drill holes the majority of data from these stratigraphic units are characterised by Cr/MgO ratios > 80. The para-harzburgite above the has a Cr/MgO value of 16 confirming its contact-metamorphic origin.

In section 11.2.1 above, it is recognised that the rare earth element (REE) concentration of the Duitschland Formation sediments varies significantly between the two dominant lithologies, shales (ΣREE > 100 ppm) and carbonates (ΣREE < 50 ppm). The chondrite-normalised REE plots for the various stratigraphic units within all drill holes are presented in Chapter 7 (section 7.2). In general, in all drill holes the uncontaminated pyroxenites are characterised by a restricted range in normalised REE concentrations around 10 and have a characteristic U-shaped profile defined by LREE fractionation to a minor negative Eu-anomaly and gently positive gradient for the HREE concentrations. In comparison, the contaminated stratigraphic units show a broader range in compositions, which depending on the nature of the contaminant are typically skewed towards higher (> 10) or lower (< 10) REE concentrations.

Primitive-mantle normalised incompatible trace element ratios have been shown to be useful for identifying crustal contamination of a mantle-derived magma (Lightfoot & Hawkesworth, 1988; Lightfoot et al., 1990; Ihlenfeld & Keays, 2011). In Chapter 7 (section 7.2.6), the incompatible trace element ratios $(Nb/Th)_{PM}$ and $(Th/Yb)_{PM}$ are plotted for each drill hole (see Figure 7.23). The majority of data points in all drill holes plot within the contaminated magma field defined by low $(Nb/Th)_{PM}$ ratios (< 1.0) and elevated $(Th/Yb)_{PM}$ ratios (> 5.0). The drill hole data overlaps with the data for the Duitschland Formation sediments, which also contain very low $(Nb/Th)_{PM}$ ratios (0.04 to 0.2) and high $(Th/Yb)_{PM}$ ratios (10.4 to 56.8). This represents a sharp contrast to the lines of evidence of contamination presented thus far, it indicates a homogenous contamination event that affected all drill holes equally. This matches observations on the primitive-mantle normalised spidergrams, which show a consistent Nb-Ta anomaly and enrichment in LILE elements (see Appendix C). This contamination signature has also been identified along the strike of the Platreef on Overysel, Sandsloot and Townlands (Ihlenfeld & Keays, 2011) and the Grasvally Norite-

Pyroxenite-Anorthosite (GNPA) member (Smith, 2014); it therefore, represents a regional contamination event which fully equilibrated with the parental magma of the northern limb.

11.2.3 Sulphur Isotope Evidence of Crustal Contamination

A review of the literature on the application of sulphur isotopes to our understanding of Ni-Cu-PGE deposits can be found in Chapter 2 (section 2.4.2) and specific studies on the northern limb are presented in Chapter 3 (section 3.3.3). The sulphur isotope composition of sulphide minerals is a key tool in identifying crustal sulphur in magmatic systems; furthermore, if the country rocks have a distinct isotopic signature they can be used to pinpoint the exact source of the contamination. A summary of the sulphur isotope data available in the literature on Ni-Cu-PGE and 'reef-style' PGE deposits is presented in Figure 11.4; in addition, the results of the current study are shown in the regional context of the northern limb of the Bushveld Complex.

The range of $\delta^{34}S$ values in sulphide-rich Ni-Cu-PGE deposits such as Uitkomst and Noril'sk found in magma conduits are characterised by a large range in $\delta^{34}S$ values, both positive and negative excursions, outside of the magmatic range (see Figure 11.4). In contrast, the sulphide-poor Merensky Reef and UG2 chromitite have a narrow range in $\delta^{34}S$ values with averages on or just outside of the magmatic range e.g. + 1.65 ‰ and +2.66 ‰, respectively (Penniston-Dorland et al., 2012). The range of $\delta^{34}S$ values recorded in the igneous rocks of the Platreef demonstrate considerable variability along the strike of the northern limb (see Figure 11.4). For example, in the Northern sector (Overysel to Nonnenwerth), where the footwall rocks are composed of the La Pucella granite (average of - 0.07 ‰; McDonald et al., 2017), a dominant magmatic signature is preserved in the Platreef rocks (e.g. Oversel reef pyroxenites average +1.7 ‰). Further south, where the footwall rocks are composed of the Transvaal Supergroup sediments of the geochemically diverse Chuniespoort group, a very large range in $\delta^{34}S$ values are measured in sulphides from the Platreef (skewed towards heavy signatures). The heaviest values in the footwall rocks are recorded in the carbonate-associated sulphur in the Upper Duitschland Formation (DF) up to + 42 ‰ (Guo et al., 2009) and the lightest values in the footwall are -14.5 ‰ on Tweefontein (Sharman et al., 2013). In Figure 11.4 and in the accompanying literature it is established that the Platreef sulphide budget represents a two-component system, the end-members of which are: (1) a primary magmatic sulphides with $\delta^{34}S$ values ranging from 0 to + 2 ‰ (Holwell et al., 2007) and; (2) sedimentary sulphur derived from the Transvaal Supergroup.

The results of a sulphur isotope ($\delta^{34}S$ values) study on the variably contaminated magmatic stratigraphy across the Turfspruit deposit and on country rocks in the hinterland are presented in Chapter 9. A zonal distribution in the range of $\delta^{34}S$ values was observed between the different sectors of the Platreef orebody on Turfspruit and in the downhole $\delta^{34}S$ profiles within each drill hole, which can be characterised as follow: (1) in the Platreef, contaminated $\delta^{34}S$ values are recorded at the top and base of the drill hole; (2) in the Flatreef (both 'Normal'- and 'Thick'-reef facies) a consistent downhole sulphur isotope profile is recorded centred on the edge of the magmatic range and; (3) in the Deep Platreef drill hole the $\delta^{34}S$ values progressively increase with depth.

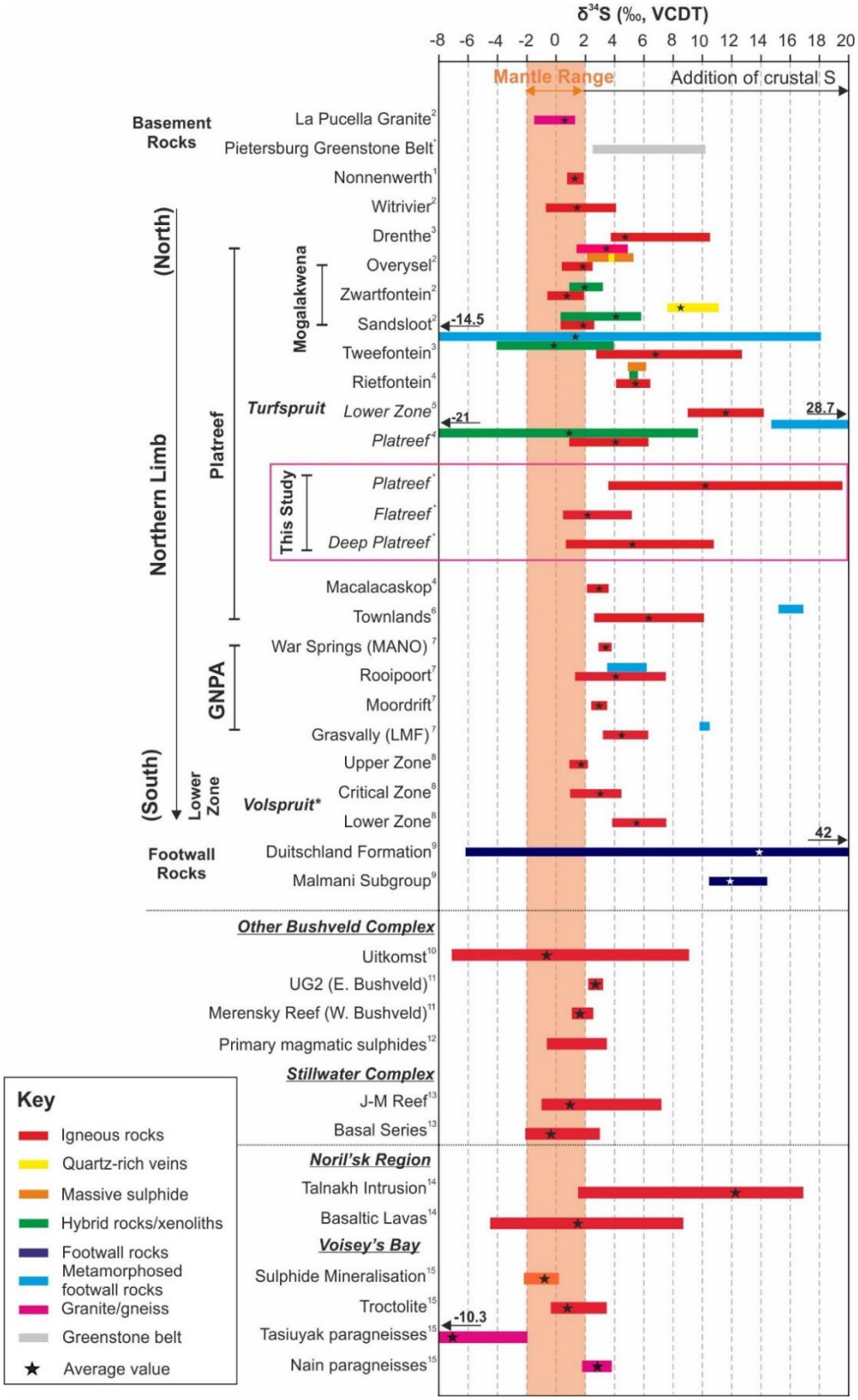

Figure 11.4: A summary of the available S isotope literature on the northern limb and wider Bushveld Complex in addition to selected reef-style and contact-style PGE deposit locations. The results from the current study are highlighted in a pink box. References: (1) Manyeruke (2015); (2) Holwell et al., (2007); (3) Sharman-Harris et al., (2013); (4) Sharman-Harris et al., (2005); (5) Yudovskaya et al., (2017); (6) Manyeruke et al., (2005).; (7) Smith et al., (2016); (8) Hulbert, . (9) Guo et al., (2009); (10) Sarkar et al., (2008). (11) Penniston-Dorland et al., (2012). (12) Liebenberg (1968). (13) Ripley et al., (2017); (14) Malitch et al., (2014); (15) Ripley et al., (1999).

In the shallow Platreef all sulphides analysed record non-magmatic $\delta^{34}S$ values (from + 3.6 to + 19.6 ‰) indicating that the entire magmatic stratigraphy is contaminated. This matches observations on the sulphide mineralogy (pyrrhotite-dominated) and the accompanying interstitial silicate mineral assemblage (see section 11.2.2 above). The $\delta^{34}S$ downhole pattern for the Platreef matches previous observations on the shallow Platreef with increasing $\delta^{34}S$ towards the footwall contact (e.g. Sharman-Harris et al., 2005). This profile was expected for the Platreef drill hole where the magmatic package contains numerous xenoliths and has a hornfels footwall, a sample of which records a very heavy $\delta^{34}S$ value of +19.6 ‰. One of the most significant results was the identification of heavy $\delta^{34}S$ values at the top (+14.4 ‰) of the shallow Platreef drill hole. This sample was taken from the top contact between the Mottled Anorthosite (MAN) unit and the Upper Pyroxenite (UP) unit located above a calc-silicate xenolith. The pyrrhotite analysed in this sample also contains elevated S/Se ratios (up to 16615). These very heavy $\delta^{34}S$ values indicates that the magmatic rocks originally intruded with a roof and floor of Upper DF sediments, as both $\delta^{34}S$ values are > +10 ‰ above the range of the Lower DF.

In the Deep Platreef, the upper part of the stratigraphy (< 1460 m) is dominated by magmatic $\delta^{34}S$ values and in the lower part of the stratigraphy (> 1520 m) the $\delta^{34}S$ values become increasing more contaminated moving downhole. The primary magmatic sulphide assemblage of pyrrhotite-pentlandite-chalcopyrite as identified in the Upper Pyroxenite (UP) unit, hosting the Upper Reef mineralised interval is dominated by magmatic $\delta^{34}S$ values +0.7 to + 2.4 ‰ (average +1.7 ‰). These magmatic $\delta^{34}S$ values correspond with the sharp contacts observed between the BMS and silicates in the UP unit (see Figure 9.10A, Chapter 9 section 9.1.5). The Middle Reef mineralised interval at the base of the UP unit, in contact with the Middle Pyroxenite (MP) unit, is characterised by a larger range in $\delta^{34}S$ values from +1.1 to +6.0 (average +3.3 ‰). This corresponds to the development of a pegmatoidal silicate assemblage in the host rock and more ragged edges on the sulphides (see Figure 9.10B) caused by secondary alteration silicates actinolite-tremolite. The Lower Reef mineralisation event hosted in the Lower Pyroxenite (LP) and the Main Chromitite (MCHR) units, marks the beginning of a steady positive shift to elevated $\delta^{34}S$ values downhole. This is unexpected because the Deep Platreef is underlain by a thick (> 10 m) homogenous unit known as the Feldspathic Clinopyroxenite Hybrid Zone (HZ_{FCPX}) as opposed to metasedimentary floor rocks. The sulphur isotope composition in the LP unit varies between +3.7 ‰ to +6.3 ‰ (average +4.9 ‰) and in the MCHR unit from +2.5 ‰ to +9.5 ‰ (average +5.4 ‰). The Ultramafic Zone,

which forms the footwall to the MCHR, is outlined in section 11.2.2 above to be variably contaminated and correspondingly has $\delta^{34}S$ values between +2.2 to + 9.2 ‰ (average +6.2 ‰). At the base of the drill hole the HZ_{FCPX} contains the most contaminated values from +8.5 to +10.8 ‰ (average +9.6 ‰). Previous studies on the material transfer on the igneous/footwall contact suggest only limited exchange during emplacement i.e. over a few metres with the advection of sulphur from the Platreef to the wall rocks envisaged to occur via hydrothermal fluids (Sharman-Harris et al., 2005; Holwell et al., 2007; Penniston-Dorland et al., 2008). This sulphur isotope data records contaminated $\delta^{34}S$ values maintained over a distance >30 m away from the marginal HZ_{FCPX} unit at the base of the drill hole.

The Flatreef drill holes have a narrow range of $\delta^{34}S$ values from +0.5 to +5.2, compared to the other sectors of the deposit. In the 'Normal' Flatreef the Upper and Middle Reef mineralisation events have average $\delta^{34}S$ values of +2.0 ‰ and + 1.9 ‰, respectively. Towards the base of the drill hole the chromite-bearing Pyroxenite-Norite Zone records only a slightly elevated $\delta^{34}S$ values of +3.4 ‰. Similarly, in the 'Thick' Flatreef the Upper and Middle Reef mineralisation events have an average $\delta^{34}S$ value of +1.9 ‰. The underlying contaminated Olivine Websterite (HZ_{OLWEBS}) and Gabbronorite (HZ_{GBRN}) Hybrid Zones record a similar range in $\delta^{34}S$ values +0.7 to +5.2 ‰ (average +2.4 ‰). In addition, one sample of a olivine skarn (with fine-grained net-textured sulphides) also gave a magmatic value +1.0 ‰. This contrasts with the observed contaminated mineralogy and geochemistry of the host lithologies in the and suggest that either: (1) the contaminant material (impure limestone/dolomite) contained no or low sulphur concentrations or; (2) the sulphide melt postdates the devolatisation of the assimilated dolomites.

In order to constrain the origin of the crustal sulphur added to the Platreef magma on Turfspruit a complimentary study on the sulphur isotope composition of the Duitschland Formation (DF) footwall rocks was conducted (see section 11.2.1). The sulphur isotopic composition of the DF is vertically stratified with the Upper DF characterised by $\delta^{34}S$ values > +10 ‰ and the Lower DF $\delta^{34}S$ values < +10 ‰. This stratification of the $\delta^{34}S$ values reflects variations in the lithogeochemistry of the DF with height from the carbonate-dominated Upper DF and the shale-dominated Lower DF (for more details see section 11.2.1). Therefore, the sulphur isotopic composition of the DF rocks cannot be accounted for by one end-member value; there are two reservoirs of sulphur with very different compositions. This result places constraints on the height of intrusion of the magmatic rocks with respect of the DF stratigraphy.

The results of this sulphur isotope study, in combination with the geochemical and mineralogical evidence as provided in section 11.2.2, requires contributions of crustal sulphur from both the potential contaminants of the Lower DF and Upper DF in varying proportions. A simple two-end member mixing model of Ripley & Li, (2003) was used to estimate the degree of contamination required in order to obtain the non-magmatic heavy $\delta^{34}S$ values measured across the Turfspruit deposit (see Chapter 9, section 9.3). The models of assimilation are very sensitive to the estimated whole-rock sulphur concentrations (Chapter 9, section 9.3). A range of whole-rock sulphur concentrations were modelled ranging from 0.05 wt% to 1.0 wt%; these values were based on variety of observations, XRF data and from whole-rock sulphur data measure in the Transvaal Supergroup by Klein & Beukes (1989). The results show that the elevated $\delta^{34}S$ values (> +10 ‰) in the magmatic rocks can only be achieved through the assimilation of sulphate from the Upper DF. The best fit models for the Platreef and Deep Platreef data require mixing of between <1 to 5 % of Upper DF contaminant (containing 0.5 wt% sulphur and a $\delta^{34}S$ value of + 20 ‰). This excludes the two heaviest results for the Platreef which would require up to 17% assimilation to account for the +19.6 ‰ recorded in the hornfels metasedimentary floor rock. The lighter values recorded in the Flatreef were modelled for the Lower DF sediments, in order to satisfy all the recorded values the maximum measured $\delta^{34}S$ value of +8.9 ‰ which estimated assimilation ranging from <1 % to 6.5 %. The results of the modelling show that the range of $\delta^{34}S$ values observed can be satisfied by variable amounts of assimilation of the DF, no other reservoir of crustal S is needed. These values are comparable to those calculated by Holwell et al., (2007) of 6 % assimilation of Malmani sedimentary rocks to produce the mean calc-silicate xenolith $\delta^{34}S$ values of +4.4 ‰.

The material exchange between coeval silicate and sulphide melts (R-factors) are not only recorded in the trace element concentration of the sulphide (e.g. Pd concentrations as covered in section 11.1.2) but can also be recorded by sulphur isotopes (Ripley & Li, 2003). An R-factor model by Sharman et al., (2013) using $\Delta^{33}S$ and $\delta^{34}S$ values calculated R factors ranging from 0 to ≈5000 (50% with R = 500). These values are slightly lower than those estimated in Ihlenfeld & Keays (2011) based on the Cu and Pd concentrations. Local variations in the R factors can be used to explain the significant range of PGE tenors (see Figure 11.2) and sulphur contamination along the strike of the Platreef and moving down-dip. The opposing effects of the R factor on the Pd concentration and $\delta^{34}S$ values in sulphides are shown in Figure 11.5 based on the modelled results from a komatiite Ni-Cu (PGE) deposit

from Lesher & Burnham (2011). An additional factor to consider here is that these R-factor models don't take into consideration the transfer of wall-rock sulphur into the Platreef sulphides via post-emplacement hydrothermal activity which will result in artificially low R factor estimations (see Figure 11.5).

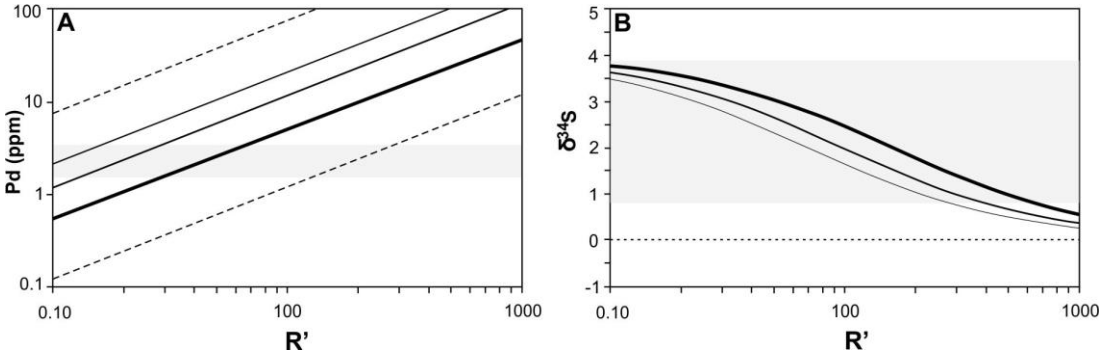

Figure 11.5: Two mass balance models from Kambalda Ni-Cu (PGE) sulphide ores depending on the mass fraction of silicate magma (R') models for: (A) Pd concentration and; (B) $\delta^{34}S$ values. Modified after Lesher & Burnham (2011).

11.3 The Role of Hydrothermal Fluids

The varying roles of magmatic vs hydrothermal processes in Ni-Cu-PGE ore genesis are still debated in the literature; for a summary see Chapter 2 (section 2.2.6). The results of this study, as outlined so far in section 11.1, indicate that the primary sulphide-hosted PGE mineralisation can be attributed to magmatic processes. Hydrothermal fluids in the Platreef magmatic system may be derived from a number of sources/processes including: (a) exsolving from the magma itself; (b) devolatilisation of the surrounding sedimentary rocks; (c) metamorphic dehydration processes and; (d) meteoric waters. On Turfspruit the Platreef intrusions variably interact with Duitschland Formation (DF) sediments. The DF stratigraphy includes a wide compositional range of sedimentary rocks including dolomites, impure limestones and silicate rocks (for details see section 11.2). The assimilation of the carbonate component, which dominates the upper part of the DF stratigraphy, would release CO_2, H_2O and potentially NaCl if evaporitic horizons are present (anhydrite is evidenced in the core, see Figure 5.1F). Experimental studies have shown that NaCl brines are very effective at dissolving certain PGE (Pt + Pd) from sulphides and transporting these as chloride complexes under oxidising conditions (Hanley et al., 2005). It is therefore possible that syn- or post-magmatic hydrothermal fluids can cause significant redistribution of the PGEs, in addition to modifying the host-rock mineral assemblage and introducing hydrous mineral phases.

The general opinion in the literature on the Platreef is that hydrothermal fluids acted as a secondary remobilisation process resulting in the physiochemical decoupling of

PGE from sulphides. Evidence for hydrothermal material transfer across the intrusion/wall contacts, limited to within a few meters, have been noted in studies by Kinnaird et al. (2005), Hutchinson & McDonald (2008) and Penniston-Dorland et al., (2008). The importance of the composition of the footwall rocks on the degree and nature of hydrothermal fluids is highlighted in Holwell et al., (2006) – this can be used to explain the varying geochemical complexities observed along the strike of the Platreef. The current study has so far outlined evidence for material transfer occurring between the magma and country rock as evidenced in: (1) Pd arsenide- and antimonide platinum-group minerals; (2) the geochemistry of Hybrid Zone lithologies (see section 11.2.3); (2) mineralogical textures and exotic accessory phases and; (3) non-magmatic $\delta^{34}S$ values (see section 11.2.3).

11.3.1 Granitic Veins and Hydrothermal Alteration

Two types of granitic intrusives were identified in the logging (see Chapter 5) and described as: (1) a sub-solvus granite hosting red and white feldspar (see Figure 5.6A); (2) quartz-feldspar veins (QFV) often with a characteristic granophyric texture (see Figure 5.8B). The sub-solvus granite, type 1, was only identified in the Main Zone in the Deep Platreef. The QFVs were found more widely across the deposit in a range of stratigraphic units. The QFVs variably host a range of accessory phases including massive base-metal sulphides (BMS; an example is shown in Figure 5.27A), coarse-grained phlogopite, apatite, monazite, zircon and rare hydrocarbons (McDonald & Holwell, 2011). These observations correspond to those as outlined in Brits et al., (2018) who recognised two sets of granitic dykes that form an anastomosing swarm across the deposit. Two origins for these granite intrusions are outlined in the literature on the northern limb including: (1) they form part of the Lebowa Granite Suite (syn-Bushveld; Nex, 2005; Brits et al., 2018); (2) are derived from local partial melting of footwall Transvaal Supergroup sediments and/or Archean granite-gneiss basement (Nex, 2005) and; (3) they represent partial melt channels of metapelitic xenoliths contaminating the Platreef in situ (Johnson et al., 2010).

The QFVs have sharp contacts with the mafic/ultramafic host rocks, are orientated between 40 to 90° to the core axis and show extensive hydrothermal alteration of the adjacent lithologies. They are typically < 1m thick, however in the Deep Platreef a 6.67 m thick sheet (see Figure 5.8 in Chapter 5, section 5.3.1) is identified within the Mottled Anorthosite unit near the contact with the Main Zone. An example of the contact between a QFV and the feldspathic orthopyroxenite of the Upper Pyroxenite (UP) unit in the Deep Platreef was imaged using a multi-element energy-dispersive spectra (EDS) map as shown in Appendix D (see Figure D.2). This EDS image

effectively shows that orthopyroxene is replaced by amphibole-group minerals with the interstitial feldspar showing patchy sericite and quartz alteration. The trace minerals phlogopite and apatite were also found spatially associated with the QFV. The feldspar-component of the QFV is Na-rich but shows significant modification by sericite alteration; this accounts for the sanidine and oligoclase feldspar compositions of the QFV, reported in Chapter 8 (section 8.2.1, Figure 8.44A). The chondrite-normalised REE profiles for three samples of the QFV from the Deep Platreef (see Figure 7.18B), Thick Flatreef (see Figure 7.19C) and Normal Flatreef (see Figure 7.20C) all contain REE concentrations above those of the ultramafic rocks and have REE fractionation patterns typical of the mineral apatite with a strong Eu-anomaly (up to Eu/Eu* 0.17) although they show varying degrees of fractionation (up to $La_{N/}Yb_N$ 35) and.

A high density of QFV intrusions (up to four) are identified over the interval from the Upper Reef to the base of the Middle Reef in the Deep Platreef and the interstitial mineralogy is more complex than in the equivalent unit in the Flatreef drill holes sampled. The principal differences are the presence of Na-rich plagioclase (pure-albite An_0; see Table 8.2 in Chapter 8) and significant quartz (up to 5 vol%) accompanied by exotic accessory minerals identified using electron microscopy (see Chapter 10, Figure 10.12) such as (La-Ce) monazite (hosting inclusions of Pb-minerals), uraninite, sphalerite and cobaltite. The presence of the REE-rich mineral monazite has a profound effect on the whole-rock chondrite-normalised REE plots for a subset of samples from the Upper Reef and Middle Reef interval in the Deep Platreef (see Figure 7.18B and 7.18C in Chapter 7, section 7.2,). Where monazite has crystallised in the interstitial assemblage a positive curve in the LREE from La to Nd is observed before dropping to a moderate negative Eu-anomaly (Eu/Eu* 0.8). Monazite is found as a rare accessory phase in granitic rocks, however a metasomatic origin from marble is also known (Deer, Howie & Zussman, 1992). The interstitial mineral assemblage of Na-rich plagioclase, monazite and hydrous phlogopite is similar to that identified in the Volspruit subzone by Tanner et al., (2019) and explained via contamination of the primitive magmas via dolomites of the Malmani Subgroup.

The presence of both apatite and Na-plagioclase in the QFV potentially indicates the presence of a Cl-rich fluid or NaCl-brine capable of altering the PGE distribution. The highest grade samples analysed from the Upper Reef interval in the Deep Platreef was identified in the highly altered feldspathic pyroxenite at 15 ppm 3PGE and 3.5 ppm Au directly overlying the QFV; compared to the average over this interval of 4.2

ppm 3PGE and 0.5 ppm Au. Similarly in the Normal Flatreef, a sample of feldspathic harzburgite above a QFV (see Figure 5.26) contains elevated 4.5 ppm (3PGE) compared to the background values of < 1 ppm (3PGE). The localised development of olivine (in interstitial troctolite) in the pyroxenite adjacent to this QFV may also be caused by via fluid flux melting of orthopyroxene driven by devolatisation of the QFV.

11.3.2 Lithologies showing Evidence for Hydrothermal Alteration

Hydrothermal activity in rocks can be expressed both in mineralogical transformations and in mineral textures. Hydrothermal alteration was observed at varying degrees of intensity in most stratigraphic units and appeared to be concentrated on certain lithological contacts. A number of mineralogical and textural features identified in Chapter 8 indicate a certain degree of hydrothermal fluid activity variably affected all drill holes studied across the Turfspruit deposit. The most commonly observed evidence for hydrothermal alteration in the silicate host rocks include: alteration of primary silicate minerals by hydrous phases, pegmatoidal lenses/pods/veins, fine to coarse grained hydrous minerals and late-stage cross-cutting mm-scale amphibole/calcite veining.

The most common alteration assemblage observed in the sulphide-bearing PGE mineralised pyroxenite units in all drill holes consists of quartz-chlorite-actinolite-tremolite; where olivine is present serpentinite-magnetite alteration is dominant. The degrees to which these alteration assemblages are developed is highly variable between the stratigraphic units however there is observed an overall trend of increasing alteration moving downhole in the Deep Platreef and Platreef drill holes. The hydrous mineral phlogopite is identified in the Upper Pyroxenite (UP) unit in all drill holes studied; it is typically spatially associated with interstitial quartz and base-metal sulphides. This assemblage could be indicative that the UP unit crystallised from the most evolved melt; however evidence to the contrary is shown with a return of quartz and phlogopite in the interstitial assemblage in the Ultramafic Zone (UMZ) (see Figure 8.20C). Another hydrous mineral apatite was identified at specific localities in the UP unit in the shallow Platreef and in the Olivine Websterite Hybrid Zone (HZ_{OLWEBS}) in the Thick Flatreef drill holes. The apatite is typically medium-grained and spatially associated with pyrrhotite-dominated sulphides and may be accompanied by ilmenite and/or quartz.

The least altered lithologies, in all drill holes, were observed to be those in the Norite Cycles (NC1 and NC2) units. These very thin (cm-scale) cycles are the only stratigraphic units that record a lithological sequence typical of in situ magmatic

fractionation of a melt. The interstitial spaces are smaller in this unit and restricted to the thin basal pyroxenite; in the anorthosite layers the tight packing of preferentially orientated feldspar laths could create an impermeable barrier to fluids. In contrast, evidence for fluid alteration was most prominent on the stratigraphic and lithological contacts between: (1) the Mottled Anorthosite (MAN) and the Upper Pyroxenite (UP) in the Platreef and Deep Platreef; (2) on the Upper/Middle Pyroxenite (MP) contact in all drill holes and; (3) in the stratigraphic units below the MP unit in all drill holes. The top contact between the UP and the MAN units in both the Deep Platreef and the Platreef drill holes studied is characterised by a front of hydrothermal alteration. The expression of this hydrothermal front is slightly different between the two drill holes. In the shallow Platreef the UP and MAN units are separated from one another by a thin (6 mm), fine-grained hydrothermal alteration front. In this alteration front chlorite is the dominant matrix mineral however fine-grained orthopyroxene and magnetite are also identified and they frequently form orthopyroxene-magnetite symplectites (see Chapter 8, section 8.1.4, Figure 8.37). In the Deep Platreef, the orthopyroxenes in the UP on the same contact have also been extensively altered by chlorite and amphibole. Chlorite is a common hydrothermal alteration product of orthopyroxene at low temperatures < 400 °C (Deer, Howie & Zussman, 1992). This low-temperature silicate alteration assemblage identified on the top contact of the UP where a thick MAN is developed potentially supports the interpretation that the MAN represents a chilled horizon of Main Zone-type magma (McDonald et al., 2005). A combination of mineralogical, geochemical and isotopic observations on the contact between the UP and MP unit hosting the Middle Reef mineralisation event in the Deep Platreef could be interpreted as resulting from hydrothermal fluids. The following features including: pegmatoidal textures, elevated $\delta^{34}S$ values (up to +4.4 ‰) above the magmatic range, slightly elevated CaO/Al_2O_3 ratios (1.5 to 2.5) and elevated whole-rock LREE concentrations.

11.3.3 Evidence of Hydrothermal Activity Affecting PGE Mineralisation

In section 11.1 it was established that an immiscible sulphide liquid, formed at magmatic temperatures (≈ 1200 °C), acted as the primary collector of PGE from the silicate magma. As this sulphide liquid cooled the PGE distributed between the different phases of the base metal sulphide (BMS) assemblage and into a semi-metal rich melt, as outlined in section 11.1.2. This effectively restricts the role of hydrothermal fluids to redistributing the PGE either syn- or post-emplacement. It is important to note that despite not being a fundamental ore genetic process the effects of hydrothermal activity may still be significant, particularly in redistributing the PGE.

Previous studies characterising the ore mineralogy of the Platreef along strike have reported that the interaction of the magma with the metasedimentary footwall rocks has released fluids that have caused localised (scale of microns to centimetres) decoupling of the PGE from BMS (Hutchinson & Kinnaird, 2005; Kinnaird, 2005; Kinnaird et al., 2005; Holwell et al., 2006). In order to gain an understanding of the effects of hydrothermal processes on the distribution of PGE on a variety of scales in the Turfspruit deposit this study has assessed the whole-rock PGE data and the mineralogical distribution both as discrete micron-scale PGM and as found in sulphides.

To assess the relationship between sulphides and PGE in bulk-rock geochemical analyses a series of correlation matrices are produced. A strong correlation of PGE with sulphides is a notable feature of the primary mineralisation of the Platreef on Turfspruit (see section 11.1.2); therefore, any weak or moderate correlation is indicative of secondary modification via hydrothermal processes. The sulphur concentration of the rocks was not measured, instead Ni and Cu are used as a proxy for sulphide. This proxy is appropriate because in bivariate plots, as presented in Chapter 7 (section 7.1), Ni and Cu have a strong positive relationship ($R^2 > 0.84$) in the mineralised pyroxenite units in all drill holes.

The correlation matrices for the bulk-rock Ni-Cu-PGE-Au data of the stratigraphic units of the Deep Platreef are shown in Figure 11.6. In all stratigraphic units the individual PGE show a strong correlation with one another, suggesting that they are all behaving similarly. The strongest correlations between the PGE and base metals are observed in the Upper Pyroxenite (UP; see Figure 11.6A) and in the combined data for the Lower Pyroxenite (LP) and Main Chromitite (MCHR) units (see Figure 11.6C). In the Middle Pyroxenite unit (see Figure 11.6B) Ni only shows a moderate correlation with the PGE, this result probably reflects the presence of olivine in this unit. In most stratigraphic units Cu and PGE show a strong correlation; with the exception of Rh and Pt which may be formed as PGMs. The weakest correlation (small negative) of the base metals (Ni and Cu) with PGE is observed in the Ultramafic Zone (UMZ) and Feldspathic Clinopyroxenite Hybrid Zone (HZ_{FCPX}) as shown in Figure 11.6D. This matches the measured low PGE tenors and high $\delta^{34}S$ values of the sulphides from these stratigraphic units and suggests that the PGE may have preferentially formed as PGM (see section 11.1.2).

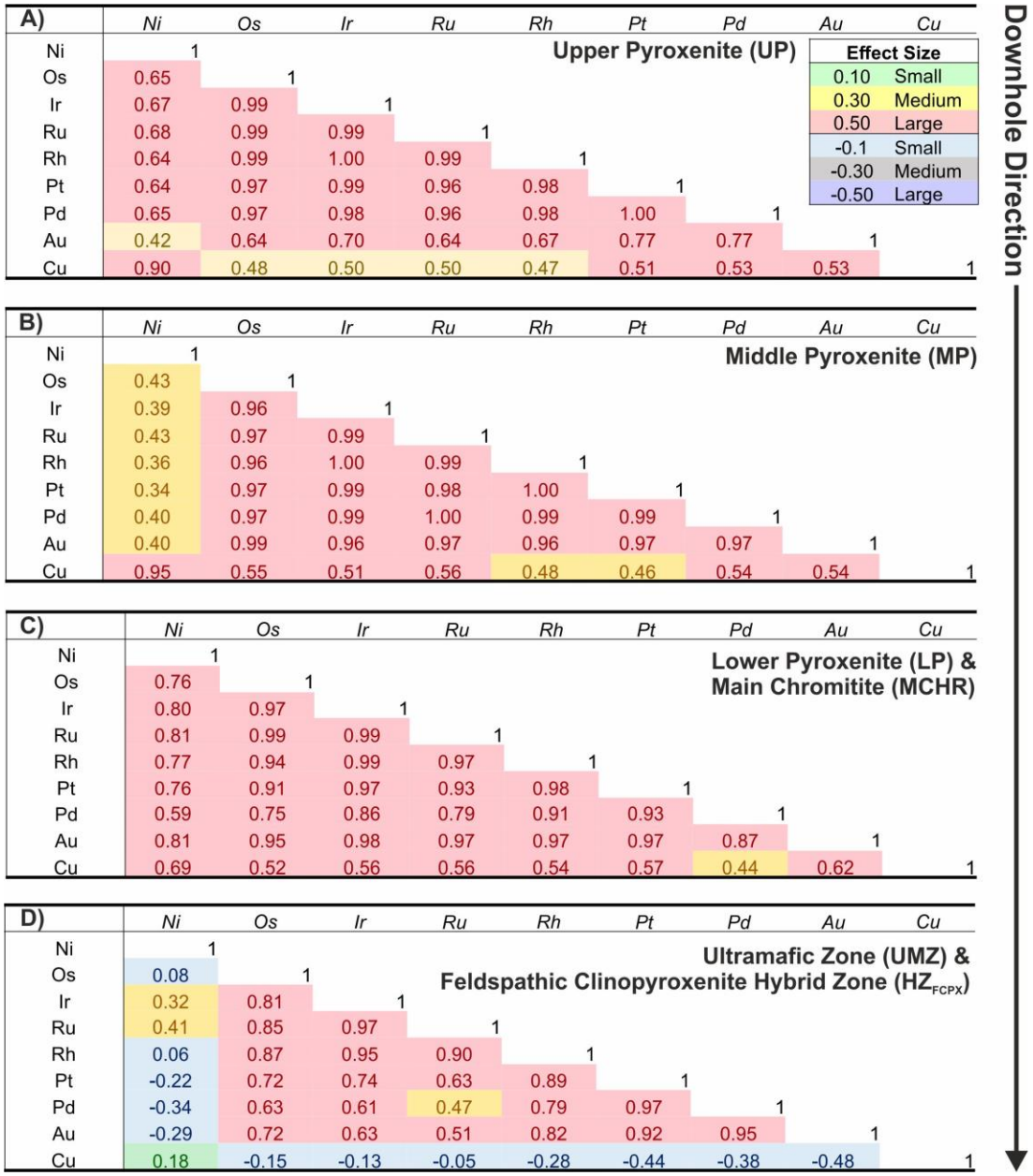

A)	Ni	Os	Ir	Ru	Rh	Pt	Pd	Au	Cu
Ni	1								
Os	0.65	1							
Ir	0.67	0.99	1						
Ru	0.68	0.99	0.99	1					
Rh	0.64	0.99	1.00	0.99	1				
Pt	0.64	0.97	0.99	0.96	0.98	1			
Pd	0.65	0.97	0.98	0.96	0.98	1.00	1		
Au	0.42	0.64	0.70	0.64	0.67	0.77	0.77	1	
Cu	0.90	0.48	0.50	0.50	0.47	0.51	0.53	0.53	1

B)	Ni	Os	Ir	Ru	Rh	Pt	Pd	Au	Cu
Ni	1								
Os	0.43	1							
Ir	0.39	0.96	1						
Ru	0.43	0.97	0.99	1					
Rh	0.36	0.96	1.00	0.99	1				
Pt	0.34	0.97	0.99	0.98	1.00	1			
Pd	0.40	0.97	0.99	1.00	0.99	0.99	1		
Au	0.40	0.99	0.96	0.97	0.96	0.97	0.97	1	
Cu	0.95	0.55	0.51	0.56	0.48	0.46	0.54	0.54	1

C)	Ni	Os	Ir	Ru	Rh	Pt	Pd	Au	Cu
Ni	1								
Os	0.76	1							
Ir	0.80	0.97	1						
Ru	0.81	0.99	0.99	1					
Rh	0.77	0.94	0.99	0.97	1				
Pt	0.76	0.91	0.97	0.93	0.98	1			
Pd	0.59	0.75	0.86	0.79	0.91	0.93	1		
Au	0.81	0.95	0.98	0.97	0.97	0.97	0.87	1	
Cu	0.69	0.52	0.56	0.56	0.54	0.57	0.44	0.62	1

D)	Ni	Os	Ir	Ru	Rh	Pt	Pd	Au	Cu
Ni	1								
Os	0.08	1							
Ir	0.32	0.81	1						
Ru	0.41	0.85	0.97	1					
Rh	0.06	0.87	0.95	0.90	1				
Pt	-0.22	0.72	0.74	0.63	0.89	1			
Pd	-0.34	0.63	0.61	0.47	0.79	0.97	1		
Au	-0.29	0.72	0.63	0.51	0.82	0.92	0.95	1	
Cu	0.18	-0.15	-0.13	-0.05	-0.28	-0.44	-0.38	-0.48	1

Figure 11.6: A series of correlation matrices for the different stratigraphic units in the Deep Platreef (UMT_345 and UMT_345_D1 combined) using bulk geochemical data Ni, Cu, PGE and Au.

For comparison, correlation matrices of the whole-rock Ni-Cu-PGE data in the various stratigraphic units of the more contaminated Thick Flatreef (TMT_006_D2), are presented in Figure 11.7. The Upper Pyroxenite unit (see Figure 11.7A), shows strong correlation between all elements, with the exception of Ni and Pd with a moderate correlation. The Middle Pyroxenite (MP) unit (see Figure 11.7B) displays much more variation in the observed correlation coefficients than in the equivalent unit in the Deep Platreef. In the MP unit Ni has a small to medium correlation coefficient with all PGE and Au has a small negative correlation with the IPGE (Ir, Os, Ru) and Rh. In the Olivine Websterite Hybrid Zone (HZ_{OLWEBS}), as shown in Figure 11.7C, most PGE

have a small positive to small negative correlation with Ni; with the exception of a medium correlation with Pd. All PGE in the HZ_{OLWEBS} have a strong correlation with Cu; Ni and Cu show a small negative correlation. The opposite trend to the HZ_{OLWEBS} unit is seen in the Gabbronorite Hybrid Zone (HZ_{GBRN}), as shown in Figure 11.7D, with all the PGE have a small positive and negative correlation with Cu and a strong correlation to Ni.

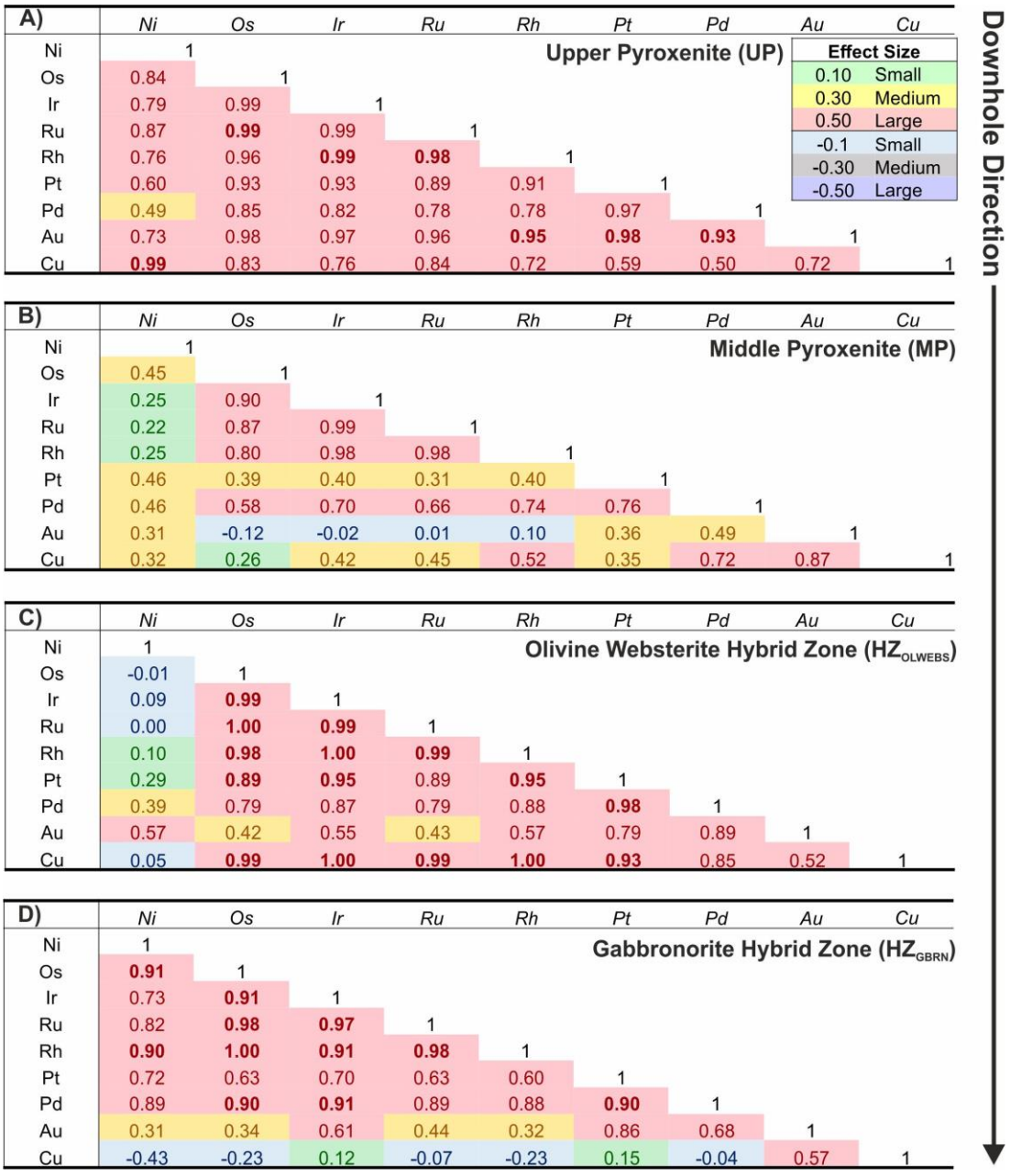

A) Upper Pyroxenite (UP)

	Ni	Os	Ir	Ru	Rh	Pt	Pd	Au	Cu
Ni	1								
Os	0.84	1							
Ir	0.79	0.99	1						
Ru	0.87	**0.99**	0.99	1					
Rh	0.76	0.96	**0.99**	**0.98**	1				
Pt	0.60	0.93	0.93	0.89	0.91	1			
Pd	0.49	0.85	0.82	0.78	0.78	0.97	1		
Au	0.73	0.98	0.97	0.96	**0.95**	**0.98**	**0.93**	1	
Cu	**0.99**	0.83	0.76	0.84	0.72	0.59	0.50	0.72	1

Effect Size	
0.10	Small
0.30	Medium
0.50	Large
-0.1	Small
-0.30	Medium
-0.50	Large

B) Middle Pyroxenite (MP)

	Ni	Os	Ir	Ru	Rh	Pt	Pd	Au	Cu
Ni	1								
Os	0.45	1							
Ir	0.25	0.90	1						
Ru	0.22	0.87	0.99	1					
Rh	0.25	0.80	0.98	0.98	1				
Pt	0.46	0.39	0.40	0.31	0.40	1			
Pd	0.46	0.58	0.70	0.66	0.74	0.76	1		
Au	0.31	-0.12	-0.02	0.01	0.10	0.36	0.49	1	
Cu	0.32	0.26	0.42	0.45	0.52	0.35	0.72	0.87	1

C) Olivine Websterite Hybrid Zone (HZ_{OLWEBS})

	Ni	Os	Ir	Ru	Rh	Pt	Pd	Au	Cu
Ni	1								
Os	-0.01	1							
Ir	0.09	**0.99**	1						
Ru	0.00	**1.00**	**0.99**	1					
Rh	0.10	**0.98**	**1.00**	**0.99**	1				
Pt	0.29	**0.89**	**0.95**	0.89	**0.95**	1			
Pd	0.39	0.79	0.87	0.79	0.88	**0.98**	1		
Au	0.57	0.42	0.55	0.43	0.57	0.79	0.89	1	
Cu	0.05	**0.99**	**1.00**	**0.99**	**1.00**	**0.93**	0.85	0.52	1

D) Gabbronorite Hybrid Zone (HZ_{GBRN})

	Ni	Os	Ir	Ru	Rh	Pt	Pd	Au	Cu
Ni	1								
Os	**0.91**	1							
Ir	0.73	**0.91**	1						
Ru	0.82	**0.98**	**0.97**	1					
Rh	**0.90**	**1.00**	**0.91**	**0.98**	1				
Pt	0.72	0.63	0.70	0.63	0.60	1			
Pd	0.89	**0.90**	**0.91**	0.89	0.88	**0.90**	1		
Au	0.31	0.34	0.61	0.44	0.32	0.86	0.68	1	
Cu	-0.43	-0.23	0.12	-0.07	-0.23	0.15	-0.04	0.57	1

Figure 11.7: A series of correlation matrices for the different stratigraphic units in the Thick Flatreef using bulk geochemical data Ni, Cu, PGE and Au.

To summarise, the whole-rock Ni-Cu-PGE data show some complicated relationships between the base metals (as proxies for sulphides) and PGE which varies between the different stratigraphic units and between drill holes. Generally, more decoupling

of the datasets is observed moving downhole where the lithologies show significant evidence of contamination (see Figure 11.6D). The cause of this decoupling downhole may relate to increased levels of hydrothermal activity moving towards the footwall contact which may be expressed as: (a) the mechanical detachment of PGM on the edge of the sulphide into the surrounding silicates and; (b) the development of a semi-metal rich platinum-group mineral assemblage. This study identified PGM assemblages dominated by antimonide phases in two locations; (1) associated with the 4th chromite stringer on the contact between the Upper and Middle Pyroxenite hosting the Middle Reef mineralisation event; (2) in a serpentinised sample from the Ultramafic Zone (UMZ) in the footwall of the Main Chromitite (for more details see section 11.1.2). PGM studies on the northern limb have interpreted Pd- antimonide and arsenide PGMs as hydrothermally derived (Hutchinson & Kinnaird, 2005; Holwell et al., 2006; Smith, 2014).

The relationship between the sulphur isotope composition of sulphides and the Pd tenor in pentlandite as measured in sulphides from the Deep Platreef and Flatreef drill holes are shown in Figure 11.8. In the Deep Platreef, it can be seen that there is a negative trend between elevated Pd tenors in pentlandite and heavy δ^{34}S values; this reflects the opposing R factors required to produce these values. The highest Pd tenors do not correspond with the most magmatic range of δ^{34}S values. Rather a moderately heavy range of δ^{34}S values between +4 to +6 ‰ are recorded in the sulphides with the maximum Pd concentrations. In addition, the samples this is identified in also contain the greatest difference in the isotopic ratios between coexisting sulphide minerals; potentially indicative of low temperature fluid-driven processes fractionating the sulphide removing light sulphur and potentially increasing the PGE tenor. This requires further investigation, but it is envisaged that the alteration processes in operation may be similar to those as described in Holwell et al., (2017) in the GNPA member Ni-Cu-PGE deposit.

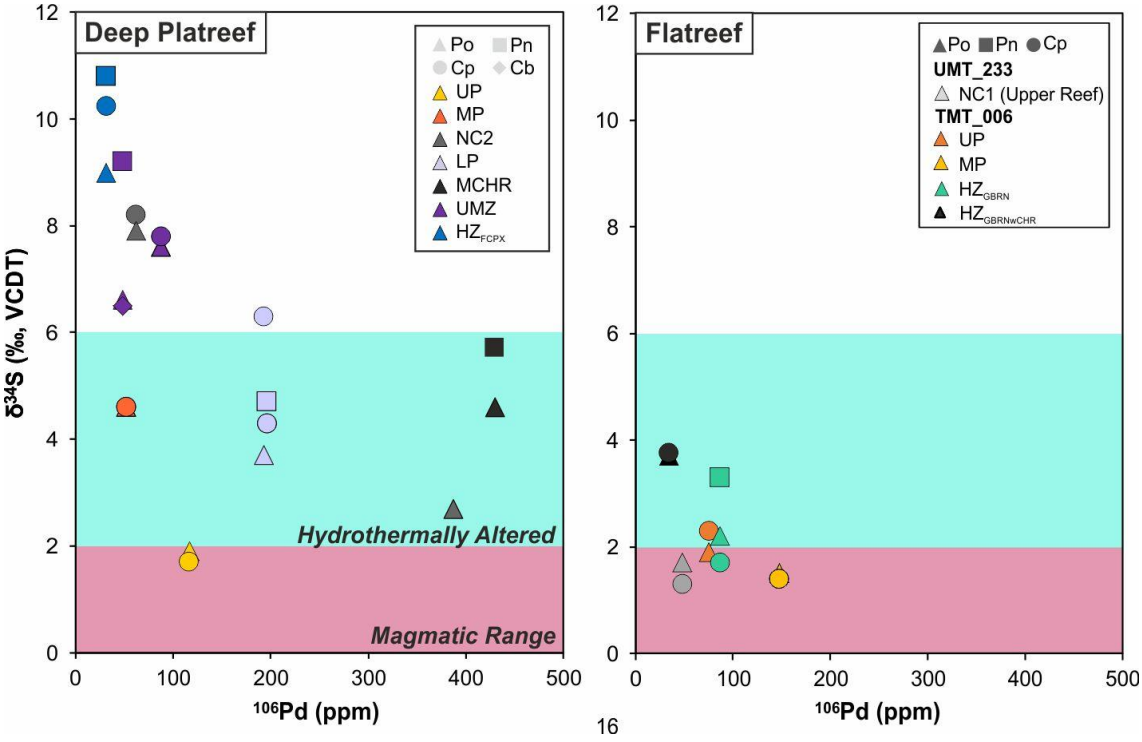

Figure 11.8: Bivariate plots of $\delta^{34}S$ vs ^{106}Pd (ppm). (A) Deep Platreef. (B) Flatreef.

11.4 Correlations across the Bushveld Complex

The northern limb is separated from the other limbs of the Bushveld Complex by a translithospheric fault known as the Thabazimbi-Murchison Lineament (TML). Geophysical evidence supports that the eastern and western limbs of the Bushveld Complex are joined at depth forming a saucer-shaped intrusion (Cawthorn & Webb, 2001; Webb et al., 2011); for more details see Chapter 3 (section 3.1.2). The relationship between the eastern and western limbs and the northern limb remains speculative with little consensus of opinion on the nature and extent of interaction between the magmas intruding either side of the TML. The TML formed during the tectonic amalgamation of the Pietersburg Block and Kaapvaal Shield located on the north and south side of the fault, respectively; for more details see Chapter 3 (section 3.1.1). The Pietersburg Block represents a former back-arc whereas the Kaapvaal Shield a more evolved continental terrane with granitoids (Zeh et al., 2013). This means that the mantle-derived parental melts of the Bushveld Complex likely interacted with different sub-continental lithospheric mantle (SCLM) and continental crust when intruding either side of the TML. The deep-seated magmatic plumping system of the Bushveld Complex is poorly understood with uncertainty surrounding: (a) the total size of the Rustenburg Layered Suite (RLS) intrusion; (b) the location and nature of the primary magma feeder zone and; (c) whether the magmatic events were

sourced from one large magma reservoir or multiple sub-chambers on the different limbs.

The stratigraphic framework of the RLS, as shown in Figure 11.9C, can only be partially applied to the magmatic package of rocks on the northern side of the TML. In the literature it is generally accepted that the Upper Zone and Main Zone are present on all limbs (see van der Merwe, 1978; Ashwal et al., 2005; Roelofse & Ashwal, 2012); despite some significant differences in the northern limb as highlighted in Chapter 3 (section 3.3.1). One of the most important differences is the observed magmatic unconformity at the base of the Main Zone in contact with top of the ultramafic rocks of the Platreef (Holwell & Jordaan, 2006). This magmatic break on the Main Zone and Upper Critical Zone contact in the eastern and western limbs is not observed or supported by geochemical data. The Lower Zone is also confidently identified on the northern limb as satellite bodies and irregular intrusions separated from the Platreef by country rock interlayers (e.g. Yudovskaya et al., 2013). This leaves the uncertainty centred on the most economically important subdivision of the RLS, the Critical Zone, which includes the sub-groups of the Lower Critical Zone (LCZ) and the Upper Critical Zone (UCZ). No LCZ equivalent units have been identified on the northern limb, however analogues to the UCZ have been proposed (see Figure 11.9B).

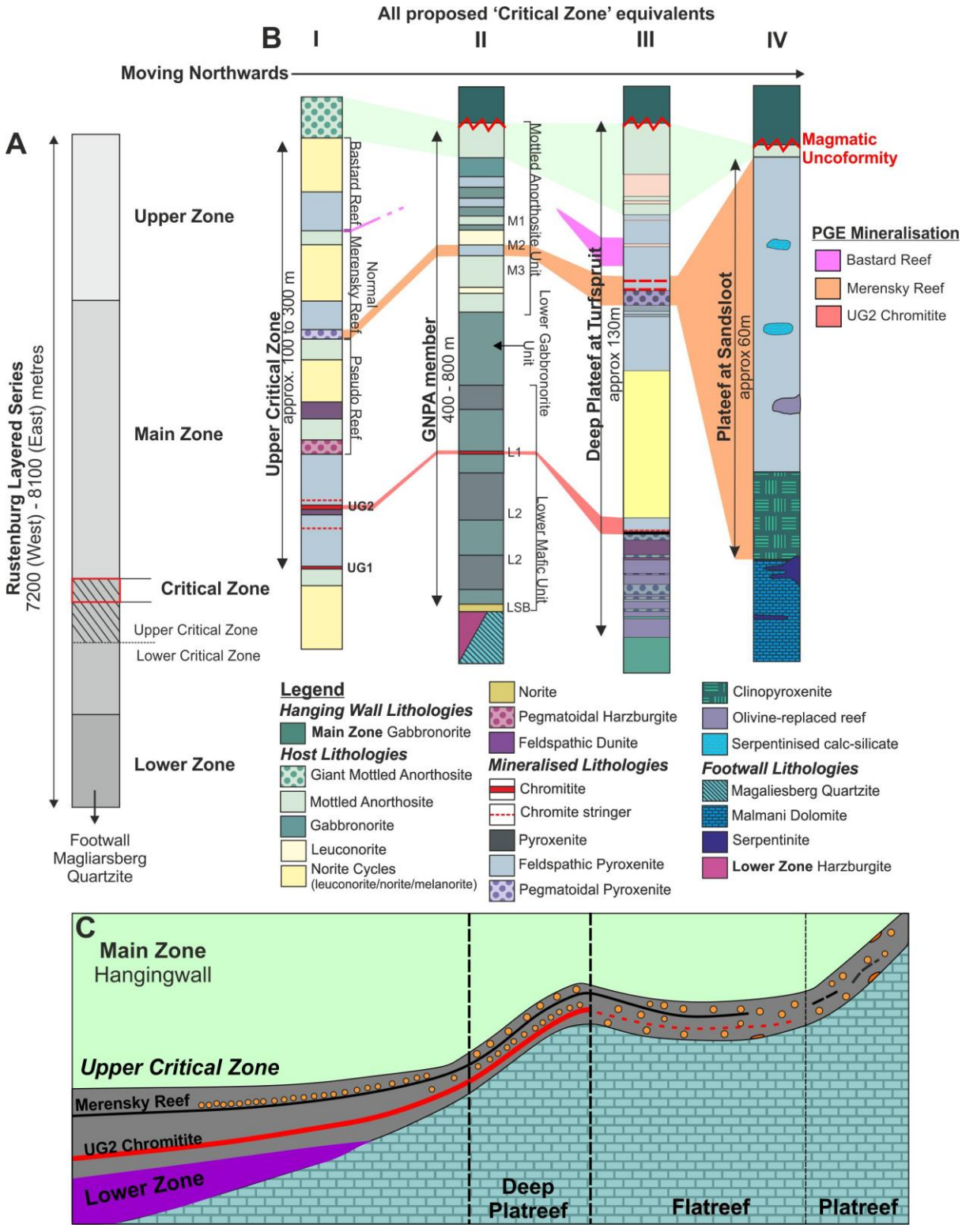

Figure 11.9: A summary of the stratigraphic correlations across the Bushveld Complex as proposed in models proposing that the lateral continuity of the Ni-Cu-PGE deposits on the northern limb with the Upper Critical Zone (UCZ). (A) A stratigraphic column of the Rustenburg Layered Suite; (B) Stratigraphic columns for the (I) the UCZ, (II) the GNPA member; (III) the Deep Platreef; (IV) the Platreef. (C) A schematic diagram of the transition from the Platreef to the UCZ with depth on the Turfspruit locality.

On the northern limb the Platreef and Grasvally Norite-Pyroxenite-Anorthosite) member occupy the same stratigraphic position, i.e. directly below the Main Zone (see Figure 11.9B), in locations north and south of the Ysterberg-Planknek fault, respectively. In terms of the RLS succession this places them in the stratigraphic position of the UCZ hosting the Merensky Reef and UG2 Chromitite. The fact that both the Platreef and GNPA member also host Ni-Cu-PGE mineralisation provides support to this correlation and has led to attempts to identify direct equivalents of the mineralisation events (as shown in Figure 11.9B). Until recently, attempts to apply the UCZ stratigraphy to the northern limb has been unsuccessful because the typical stratiform marker horizons (e.g. chromite-stringers) are either absent or discontinuous and the host rocks don't demonstrate well-developed laterally continuous layering. The discovery of deep intersections of the Platreef westwards of the surface exposure (see Figure 11.9C) contained both chromite-stringers and magmatic cyclicity opens up a new possibility to critically asses the application of the UCZ stratigraphy on the northern limb.

11.4.1 Magmatic Lineage of the Northern Limb

A key question for many authors working on the northern limb is whether the PGE-mineralisation in the Platreef and Grasvally Norite-Pyroxenite-Anorthosite (GNPA) member formed from the same parental magmas as the stratiform reefs hosted in the Upper Critical Zone (UCZ). This is supported by authors who suggest that the Platreef and GNPA member transition with depth into a full UCZ succession (Maier et al., 2008; Naldrett et al., 2008). However, geochemical studies on both the near-surface Platreef and the GNPA member note some significant differences in their geochemistry and mineralogy compared to that of the UCZ (e.g. McDonald et al., 2005, McDonald & Holwell, 2011; Smith, 2014). These differences have variably been attributed to: (1) the northern limb crystallised from a compositionally distinct parental magma from the eastern and western limbs (e.g. McDonald et al., 2005; McDonald & Holwell, 2011; Smith, 2014) or; (2) extensive crustal contamination of the Platreef and GNPA member resulting from their marginal position (Naldrett et al., 2008; Maier et al., 2008). A summary of selected geochemical data used to understand the magmatic lineage of the rocks across the Bushveld Complex including the Platreef, GNPA member and UCZ rocks are presented in Table 11.2.

The parental magma compositions of the Rustenburg Layered Suite (RLS), as identified on the eastern and western limbs of the Bushveld Complex, has been modelled as a high-Mg basalt (B1 magma) and a tholeiitic basalt (B2/B3 magma; Sharpe, 1981, Harmer & Sharpe, 1985). The Lower Zone and Lower Critical Zone crystallised from the B1 magma, the Upper Critical Zone from the B2 magma and the Main Zone the B3

magma (Barnes et al., 2010). The different geochemical composition of these parental magmas imparts some distinct major and trace element ratios on the resulting cumulates. In particular, the Cr/MgO (Seabrook et al., 2005) and Ce/Sm (Maier & Barnes, 1998) ratios have proved highly effective at distinguishing between Critical Zone and Main Zone rocks on a number of localities on the eastern and western limbs. When these same geochemical parameters have been applied to samples from the Platreef and GNPA member a more ambiguous result is given (McDonald & Holwell, 2011).

Table 11.2: Whole-rock multi-element data used to determine the magmatic lineage of selected Ni-Cu-PGE deposits in the Bushveld Complex, combined with the results from the Deep Platreef in the current study. Source: [1] this study; [2] Holwell (2006); [3] Barnes & Maier (2002); [4] Smith (2014); [6] Maier & Barnes, 1998. For other references see McDonald & Holwell, 2011.

	Cr/MgO	Ce/Sm	Pt/Pd
Main Zone			
Deep Platreef[1]	71	7	1
Platreef (Sandsloot)[2]	55-76	5.3-8.9	0.97
Eastern and Western limbs[3]	40-60	4-10[6]	2
Deep Platreef[1]			
Upper Pyroxenite	51-1124	5-11	0.7-1.3
Middle Pyroxenite	96-3451	4.8-11.3	0.4-2.3
Norite Cycle 2	96-422	8.5-12	0.8-1.5
Lower Pyroxenite	119-418	5.6-8.6	1.0-2.0
Main Chromitite	4588-13340	4.6-6.0	1.3-1.8
Ultramafic Zone	11-276	4.8-11.6	0.2-0.8
Feldspathic Clinopyroxenite Hybrid Zone	140-147	4.2-5.9	0.2-0.5
Footwall Rocks[1]			
Duitschland Formation (carbonates)	0-112	6.9-14.6	0.8-1.7
Duitschland Formation (silicates)	0-1372	6.7-15.6	0.5-2.3
Upper Critical Zone Equivalents			
Platreef (Sandsloot)[2]	76-148	5.3-9.6	
GNPA member (MANO)[4]	3-558	6-13	<1
GNPA member (LMF)[4]	20-19310	5-15	>1
GNPA member (LGN)[4]	47-89	9-11	
Upper Critical Zone	>100	9-17 [6]	2
Merensky Reef	100-129	5.3-10.1	
UG2 Chromitite		12.3 [6]	2.2[3]

The Cr/MgO ratios can distinguish between Main Zone rocks (<80) and Critical Zone (>100; Seabrook et al., 2005). The one sample of the Main Zone analysed in this study from the Deep Platreef has a Cr/MgO value of 71 and Ce/Sm of 7; these results fall within the range as identified elsewhere on the northern limb but are slightly elevated above the range of the eastern and western limbs (see Table 11.3). In the mafic/ultramafic lithologies of the stratigraphic units in the Deep Platreef the majority of samples have Cr/MgO ratios >90. Exceptions to this with lower ratios were identified in altered rocks from the Upper Pyroxenite unit and the Ultramafic Zone both of which show

evidence of modification of magmatic compositions by contamination and hydrothermal processes (see Table 11.3). The Deep Platreef has higher Cr/MgO ratios than those observed in the Platreef corresponding to the presence of chromitites.

A distinct range in the Ce/Sm ratios is also observed within cumulates of the Main Zone (4-10) and for the UCZ (9 to 17; Maier & Barnes, 1998; see Figure 7.22A). However, on the northern limb data from the Platreef and GNPA member consistently plot in the Main Zone field (Maier et al., 2008; McDonald & Holwell, 2011; Smith 2014). The results of this study match those of previous studies on the northern limb with the majority of the Ce/Sm ratios in all stratigraphic units of the Deep Platreef plotting within the Main Zone range of Ce/Sm values; this matches the results on the shallow Platreef and GNPA member (see Table 11.3). In the Union section of the western limb a systematic increase in the Ce/Sm ratio with depth was observed (Maier & Barnes, 1998); this trend is not observed in the Ce/Sm ratios of the Deep Platreef as shown in Table 11.3. This observed relationship with the marginal deposits of the Platreef and GNPA member plotting within the Main Zone range of Ce/Sm ratios has been proposed to result from in situ crustal contamination (Maier et al., 2008; Smith, 2014). The Ce/Sm ratios of the two sources of contamination for the Platreef on Turfspruit represented by the Duitchland Formation (DF) and Pietersburg Greenstone Belt (PGB) were analysed in this study (see Figure 7.22B). The results on the DF sediments show that they contain a range of Ce/Sm ratios from 7.7 to 15.6 (average 10.9), which covers both the Critical Zone and Main Zone fields and the average falling in between the two. However, there is a significant contrast in the range of concentrations with the fine-grained siliciclastic rocks of the Lower DF containing anomalously high Ce (> 20 ppm) and Sm (> 3 ppm) concentrations. The carbonate lithologies (dolomite and limestone) in the Upper DF have Ce and Sm concentrations comparable to the magmatic rocks. This means that the Ce/Sm ratio is of limited use in determining an in situ contamination signature because the sedimentary and magmatic ranges overlap – and it certainly wouldn't drive a Critical Zone to Main Zone signature. It is to be noted that the PGB samples show a similar distribution pattern to the DF samples (see Figure 7.22B).

The chondrite-normalised REE profile of the silicate rocks of the Upper Critical Zone (UCZ), as shown in Figure 7.17A (Chapter 7, section 7.2), have a pronounced positive Eu-anomaly (Eu/Eu* 3.68), resulting from the fractionation of cumulate plagioclase (Maier & Barnes, 1998). In comparison, the Platreef pyroxenites (see Figure 7.17B and 7.17C) typically have a small negative Eu-anomaly reflecting the crystallisation of plagioclase from in interstitial trapped liquids. The Platreef pyroxenites, particularly in the southern sector, have higher overall concentrations of the REE than the UCZ

silicates. This can be explained by the assimilation of shales containing elevated REE concentrations (see section 11.2.).

The contrasting results for the Cr/MgO and Ce/Sm ratios implies that the Platreef and GNPA member cumulates formed from the mixing of two compositionally different magmas including a tholeiitic (Main Zone) and a more ultramafic (potentially Critical Zone) magmas. The timing of this mixing for the Platreef and GNPA-member is constrained by the observed field relationships of a magmatic unconformity on the contact between the Main Zone and the Platreef (Holwell & Jordaan, 2006); this means that they can't have mixed in situ (see Chapter 3, section 3.31). To overcome this limitation McDonald & Holwell (2011) propose an early phase of Main Zone magma migrating into the established network of Lower zone magma chambers and mixing with any residual Lower Zone magma producing a compositionally hybrid magma. This 'hybrid' magma represents the parental magma to the Platreef which transports pre-formed orthopyroxene-olivine crystals and an immiscible sulphide liquid out of the staging chamber upwards to form the Platreef. Similarly, the Merensky Reef is proposed to have formed from mixing of two magmas: a residual B1 with a new influx of B2 (Critical Zone) magmas (e.g., Eales et al. 1990; Barnes & Maier, 2002).

The Platreef and GNPA-members are notably more Pd-rich (Pt/Pd ≈1 or <1) compared to the PGE mineralisation on the eastern and western limbs; this has been recognized since the earliest investigations by Wagner (1929). The results of this study match those elsewhere along the strike of the Platreef which identifies localised deviations ranging from <0.1 to >10. In the Deep Platreef the reversals from low (<1) to high (>2) Pt/Pd ratios are observed to occur on lithostratigraphic contacts hosting PGE mineralisation (see section 11.1.4). This matches the interpretation of the Platreef emplacement as a multi-stage series of sills with different PGE budgets (e.g. Kinnaird, 2005; Hutchinson & McDonald, 2008). Authors who propose the lateral continuity of the Platreef and GNPA member with the Merensky Reef and UG2 Chromitite suggest that high Pt/Pd cumulates will be identified westwards and down-dip from the current exposure of the Platreef (e.g. Maier et al., 2008). Maier et al., (2008) suggests that the low Pt/Pd ratios in the Platreef are controlled by the greater mobility of Pd in hydrothermal fluids and its partitioning into sulphide melt which migrate towards the margin of the intrusion. In the current study, which samples this transition from deep to shallow Platreef, a comparison of the average Pt/Pd values for all rocks types over the logged interval in all drill holes on Turfspruit showed remarkably little variation in the Pt/Pd ratio (average 1.0). There was no observed systematic change to more Pt-rich compositions with depth.

11.4.2 Correlating the Stratigraphy of the Deep Platreef with the Upper Critical Zone

The continuity of horizons of distinct petrological characteristics was not traditionally considered to be a characteristic of the Platreef mineralisation; the lack of marker horizons (e.g. chromite stringers) initially hampered efforts to define and trace the apparently erratic mineralisation (Cawthorn, 2010). On Turfspruit, the discovery of high grade PGE mineralised layers at depth (>700 m) demonstrating reasonable continuity and conformity to a layered package of mafic/ultramafic rocks and with the development of persistent chromite layers, opens up new possibilities to reinvestigate the relationship between the Platreef and the Upper Critical Zone (UCZ). The Deep Platreef drill hole (UMT_345) used in this study potentially represents the most uncontaminated and complete stratigraphic sequence of the Platreef identified to date on the northern limb with which to compare to the UCZ stratigraphy.

Moving down-dip and westwards on Turfspruit the near-surface contaminated Platreef transitions into a more magmatic sequence of rocks originally known as the Turfspuit Cyclic unit (TCU). The TCU nomenclature was introduced by Grobler & Nielsen (2012) for a sector of the orebody known as the Flatreef where direct correlations to the Bastard Reef and Merensky Reef of the UCZ stratigraphy are identified. This model is supported in a study on the Flatreef by Yudovskaya et al., (2017b) who identified two PGE mineralised intervals the 'Upper Reef' and 'Main Reef' and presented geochemical and mineralogical evidence for the correlation of the latter with the Merensky Reef. The TCU stratigraphic framework was later modified in Nodder (2015), Grobler & Dunnett (2016) and Grobler et al., (2018) considering the Deep Platreef extension which incorporates a proposed UG2 Chromitite. Grobler et al., (2018) also infer that the rocks beneath the UG2 chromitite represent the first Lower Critical Zone (LCZ) cumulates identified on the northern limb. This transformation to a full Critical Zone stratigraphy with depth has been proposed in models for the Platreef by Naldrett et al., (2008) and Maier et al., (2008).

The logged lithologies and stratigraphic divisions used in this study across the deposit are shown in Figure 11.1 and a close up of the Deep Platreef stratigraphy is shown in Figure 11.10. The proposed stratigraphic correlations to the UCZ are shown in Figure 11.1, following the work of Nodder (2015) and Grobler et al., (2018) and include: (1) the interval from the base of the Main Zone to the base of the Upper Reef mineralisation event are correlated to the Bastard Cyclic Unit; (2) the interval between the Upper and Middle Reef to the Merensky Cyclic Unit; (3) the interval from the Lower Pyroxenite to the ultramafic rocks below the Main Chromitite are correlated with the UG2 chromitite. In Grobler et al., (2018) the Upper, Middle and Lower Reef are proposed to be equivalent

to the Bastard Reef, Merensky Reef and the UG2 Chromitite of the UCZ, respectively. These correlations are primarily based on the stratigraphic position and lithogeochemistry; a more thorough investigation is conducted here on the Deep Platreef drill hole (UMT_345).

11.4.2.1 Upper Reef – Bastard Reef Correlations

The proposed correlation of the Upper Reef to the Bastard Reef is based on the following similarities identified on a deposit-wide scale by Grobler et al., (2018): (a) its stratigraphic position directly below the Main Zone; (b) a peak in PGE grade and; (c) it is hosted in a pyroxenite at the base of the Norite Cycle 1 (NC1) unit ± a chromite-stringer. Grobler et al., (2018) noted an inverse relationship between the thickness of the Upper Reef and the composition of the hanging wall so that where cyclical layers of the Norite Cycle 1 (NC1) unit (e.g. in the Normal Flatreef drill hole) are developed the reef is thinner than where there is a thick Mottled Anorthosite (MAN) unit (e.g. in the Deep Platreef drill hole). In the current study, the Upper Reef was variably developed between the drill holes as outlined in Table 11.1. No chromite-stringers were observed in association with the Upper Reef mineralisation in this study.

The Bastard Reef in the eastern and western limbs is found at the base of the Bastard Cyclic Unit (BCU); it bears lithological resemblance to the Merensky Reef but carries significantly lower grade average 1 ppm (3PGE + Au; Maier & Barnes, 2008). The Bastard Reef PGE mineralisation is identified over a width of a few decimetres associated with the presence of base-metal sulphides (Maier & Barnes, 2008). The lithologies present within the BCU include (from the base upwards): (I) chromite-stringer (1 to 5 mm); (II) pyroxenite (3 to 5 m); (II) melanorite (5 to 10 m); (III) leuconorite (2 to 3 m), (IV) Giant Mottled Anorthosite (0 to 50 m) (de Klerk, 2005). The chromite-stringer is typically present on the base of the pyroxenite, overlying the top of the Merensky Cyclic Unit (MCU) as defined by a mottled anorthosite. In comparison, the Upper Reef in the Deep Platreef is hosted within a feldspathic orthopyroxenite with the PGE closely associated with base-metal sulphides (BMS) hosted in the interstitial areas with quartz and phlogopite. The PGE mineralisation is much thicker, up to 11 m and contains an average grade of 4.2 ppm (3PGE) accompanied by elevated Au concentrations (up to 3.5 ppm). The chondrite-normalised Ni-Cu-PGE-Au profile for the Upper Reef is compared to the Bastard Reef in Figure 7.26B (Chapter 7, section 7.3.1). The Upper Reef profile shows higher overall concentrations of PGE, elevated Ni and Cu contents, a greater degree of fractionation and peaks on Au. The Bastard Reef profile also contains elevated Ni and Cu contents and increases from Os to peak on Au (Barnes &

Maier, 2002). The average Pt/Pd ratios of the Bastard Reef pyroxenite is 3.0 (Barnes & Maier, 200) compared to an average of 1.4 for the Upper Reef interval.

11.4.2.2 Middle Reef – Merensky Reef Correlations

The Merensky Reef is found at the base of the Merensky Cyclic Unit (MCU) on the eastern and western limbs. The Merensky Reef is traditionally described as laterally continuous carrying persistent grade (Cawthorn, 2002), however there are significant variations between the different limbs (eastern and western) and sectors (e.g. north-western, south-eastern). These differences include: (a) variable footwall lithologies (anorthosite to pyroxenite); (b) mineralogy (± olivine) and mineral textures (e.g. pegmatoidal); (c) thickness of the mineralised interval (a few centimeters to 12 m); (d) grade; (e) the development of between one to five chromite-stringers and; (e) stratigraphic height i.e. 'normal' vs 'pothole' (see Chapter 3, section 3.2.2.1). Consequently, the stratigraphy and petrography of the Merensky Reef are unreliable characteristics on which to base a comparison as these are observed to vary significantly along strike on the eastern and western limbs.

The visual similarity between the Middle Reef and the Merensky Reef is striking. They are both characterised by the presence of chromite stringers, pegmatoidal regions and hosted in feldspathic orthopyroxenite ± olivine; as summarised in Figure 11.3. The observed mineralogy of the Middle Reef in the Deep Platreef most closely resembles the Merensky Reef as present in the Union mine on the north-western limb. At this locality the mineralised interval consists of an orthopyroxenite with underlying pegmatoidal harzburgite and chromite-stringers on base and upper contacts (as described in Viljoen et al., 1986; de Klerk, 1992).The MCU on the western limb is between 20 to 25 m in thickness and includes a sequence of (from base to top; Naldrett et al., 2009): (I) footwall anorthosite, norite or pyroxenite; (II) lower chromite-stringer (0.02 to 0.4 m) (III) feldspathic pyroxenite (3 to 15 m); (IV) upper chromitite-stringer (0.2 to 0.1 m); (V) melanorite (5 to 15 m); (VI) leuconorite (5 m); (VII) mottled anorthosite (2 to 5 m). At the base of the pyroxenite is the Merensky Reef (0.6 to 4 m) with an average grade of 6 ppm (3PGE; Vermaak, 1995); in comparison, the Middle Reef is significantly thicker at 11 m and but contains a similar average grade of 5.3 ppm (3PGE). The main difference between the MCU and the Middle Reef mineralisation on Turfspruit is the lack of magmatic cyclicity developed in the host rocks in the latter.

In both the Merensky Reef and Middle Reef the PGE mineralisation is found associated with base metal sulphides (BMS) and chromite. The BMS content varies between 0.5 to 8 vol % in the Merensky Reef (Godel et al., 2007) and the consists of pyrrhotite,

pentlandite and chalcopyrite. The BMS assemblage in the Middle Reef is comparable, however the major element composition of pentlandites analysed in the Deep Platreef were found to contain lower Co concentrations (typically < 1 wt %) than those analysed from the Merensky Reef (typically > 1 wt%; Godel et al., 2017) and no positive linear relationship between the concentrations of Co and Pd was observed (see Figure 10.1A, Chapter 10, section 10.1.1). The Ni content of the pentlandites analysed ranges from 30 to 40 (wt %); higher than those analysed in the Merensky Reef (Godel et al., 2007). The mineral chemistry of the chromite grains from the Middle Reef were analysed and found to contain elevated TiO_2 contents (between 0.7 to 3.9%); this corresponds to the presence of exsolutions of ilmenite identified in section 8.1.1 (see Figure 8.7). The TiO_2 concentration of the Merensky Reef chromitites as presented in Li et al., (2005) varies from 0.55 to 0.74 wt% significantly lower and with a narrower range of values than the Middle Reef chromite grains indicative that the latter formed from a more evolved magma. This is further supported by the Fe^{3+} contents (6.43 to 8.77) which are significantly elevated above those recorded in the Merensky Reef (1.49 to 1.71) by Li et al., (2005). The chromite-stringers in the Middle Reef are characterised by abundant sulphide-bearing inclusions, typically either monomineralic chalcopyrite or polyphase BMS (see Figure 8.6C, 8.6D, 8.7E and 8.7F in Chapter 8 section 8.1.1). In contrast, the inclusions in chromite grains from the Merensky Reef have been found to host a wide range of silicate minerals including orthopyroxene, plagioclase, Na-/K- phlogopite, hornblende, quartz and apatite (Li et al., 2005). The presence of abundant hydrous phases in inclusions in the chromites of the Merensky Reef supports the involvement of fluids in the formation of the mineralisation as suggested by Mathez et al., (1994), Mathez (1995) and Ballhaus & Stumpfl (1986). The absence of hydrous phase inclusions but the presence of fractionated BMS with inverse crystal shapes in chromite in the Middle Reef supports the key role of sulphides in the formation of the PGE mineralisation.

The Merensky Reef chondrite-normalised Ni-Cu-PGE-Au pattern has a characteristic arch-shaped profile with enrichment in PGE over Ni and Cu and a peak at Pt reflecting the high Pt/Pd ratios (Barnes & Maier, 2002, see Figure 7.26C). In comparison, the same profiles for the Middle Reef mineralisation increase steadily from Os to Rh are flat-lying to Pt and then peaks on Pd (see Figure 7.26C). The average Pt/Pd ratios varies between the Merensky Reef at 1.9 (western limb; Barnes & Maier, 2002) and the Middle Reef at 1.1. The observed sympathetic relationship between elevated Pt/Pd ratios and depleted Cu/Pd ratios on depth profiles across the Middle Reef mineralised intervals (see Figure 11.3) matches those observed in the Merensky Reef by Naldrett et al.,

(2009). In the Middle Reef the mineralised feldspathic orthopyroxenite (Pt/Pd 1.6) with chromite stringers above the pegmatoidal olivine orthopyroxenite (Pt/Pd 0.6); the PGM assemblage indicates hydrothermal alteration and mobilisation of Pd by fluids into the footwall as antimonide PGMs. In the Merensky Reef the majority (between 65 to 85%) of the PGE are hosted as PGM especially as Pt-Fe alloy, Pt/Pd sulphides and Pt/Pd bismuthides (Kinloch, 1982; Godel et al., 2007) and show considerable lateral continuity across the eastern and western limbs (see Figure 11.10C to 11.1F). The distribution of PGM phases across the Merensky Reef are zoned with Ir-group PGMs preferentially hosted in the chromitites, a feature also observed in the chromitites from the Deep Platreef (Prichard et al., 2004; Godel et al., 2007). Yudovskaya et al., (2017b) identified a similar zoning pattern in the Middle Reef in the Flatreef sector of the Turfspruit deposit which they interpret as indicating a similar mechanism of reef formation. This distribution is less well-developed in the PGM assemblage of the Middle Reef interval as analysed in the current study and there is more variability in the composition of the PGMs (see Figure 11.10B). The main sulphide phase hosting PGE in the Merensky Reef is pentlandite containing up to 600 ppm (Godel et al., 2007); similarly in the Middle Reef pentlandite contains significant Pd concentrations up to 310 ppm.

11.4.2.3 Lower Reef – UG2 Chromitite Correlations

The UG2 Chromitite is hosted in the UG2 Cyclic Unit (UG2CU) consisting of (from base to top): (1) a pegmatoidal pyroxenite/harzburgite (0.4 m); (2) the UG2 chromitite seam (0.6 to 1.1 m thick; Mathez & Mey, 2005); (3) medium-grained feldspathic orthopyroxenite with chromite blebs (11 m). Two to four lead-stringers seams ranging from 0.1 to 14 cm thick are identified in the hangingwall (Cawthorn, 2002); these are recorded in the Deep Platreef in Nodder (2015) but chromite was found as disseminations in the current study. This lithological sequence closely resembles the uphole transition across the Lower Reef from: (1) a pegmatoidal orthopyroxenite (0.3 m) in the Ultramafic Zone (UMZ); (2) a chromitite (1 m) seam, Main Chromitite (MCHR) and; (3) medium-grained gabbronorites ± olivine and feldspathic orthopyroxenite of the Lower Pyroxenite (LP) unit (4 m). In Nodder (2015) and Grobler et al., (2018) the MCHR unit is directly correlated to the UG2 Chromitite. The separation between the Merensky Reef and the UG2 Chromitite varies between the western (40 – 140 m; Cawthorn 1999) and eastern limbs (up to 360 m; Barnes & Maier, 2002). The Main Chromitite unit is separated from the last chromite-stringer of the Middle Reef by 73 m within the range of the western limb.

The mineralogy of the UG2 Chromitite and MCHR unit are similar with both consisting of between chromite (60-90 modal%), with interstitial plagioclase (5-15 modal %) and

orthopyroxene (5-25 modal%; McClaren & de Villiers, 1982). The chromite compositions from the MCHR unit, as reported in Chapter 8 (section 8.2.3) plot at elevated Fe^{3+} and lower Cr_2O_3 contents relative to the UG2 Chromitite (McClaren & DeVilliers, 1982). The MCHR unit has an average TiO_2 values of 1.0 wt%, this is similar but still elevated above the 0.78 wt% TiO_2 recorded for the UG2 chromitite (McClaren & DeVilliers, 1982). This suggests that they crystallised from a more fractionated magma than the chromitites of the UCZ; an observation also made for the chromitites in the Middle Reef (section 11.4.2.2). The orthopyroxene and plagioclase compositions in the UG2 were determined by McClaren & de Villiers (1982) to be bronzite (En_{80}) and bytownite (An_{75}), respectively; similar average compositions are recorded in the MCHR unit with En_{83} and An_{70}.

The average PGE content of the UG2 Chromitite varies between the limbs from ≈ 9.0 g/t in the western limb and ≈ 7.0 g/t in the eastern part (Kinnaird et al. 2002). The Lower Reef unit is significantly lower grade with 3.9 ppm but is distributed over a thicker interval (6 m). The downhole grade profiles across the UG2CU peaks within the chromitite itself with a PGE depleted hangingwall (Gain, 1985; Osbahr et al., 2014). In contrast, the downhole grade profile for the Lower Reef interval peaks in the hanging wall LP unit. The chondrite-normalised Ni-Cu-PGE-Au profiles for the UG2 Chromite show the typical arch-shaped profiles of chromite-bearing lithologies; in contrast, the MCHR unit profile shows that the distribution of the PGE are controlled by a sulphide liquid. This matches the elevated base metal sulphide (BMS) concentrations in the MCHR unit (up to 5 vol %) compared to the low varying between <0.1 to 0.2 modal% (Gain, 1985). The BMS assemblage in the UG2 chromite seam is dominated by pentlandite and chalcopyrite with rare pyrrhotite and pyrite (Osbahr et al., 2014; Junge et al., 2014); in contrast a more even distribution of pyrrhotite, pentlandite and chalcopyrite with minor cubanite and pyrite are identified in the Deep Platreef. The PGE deportment of the UG2 Chromitite is hosted within sulphides and PGMs with the latter typically dominant. Pentlandite is the principal host of Pd (up to 1000 ppm) and Rh (200 ppm), but also carries significant Ru, Os and Ir (Osbahr et al., 2014). This corresponds to similar analyses on with the maximum Pd- and Rh- concentrations in pentlandite up to 638 ppm and 391 ppm, respectively in the MCHR unit. The dominant PGMs in the UG2 Chromitite are Pt-sulphides (cooperite), Pt-Fe alloys and laurite (see Figure 11.10C to 11.10F; Kinloch, 1982; McClaren & de Villiers, 1982). The PGM assemblage of the MCHR unit is also dominated Pt-sulphides but in general shows more compositional variability (see Figure 11.10B). The Lower Reef interval as a whole shows a zonal distribution in the dominant PGM-type from Pt-sulphides in the chromite to Pt-Fe alloys in the hanging wall.

In summary, all three mineralisation events in the Deep Platreef on Turfspruit are characteristically thicker (> 6 m), more sulphide-rich (between 5 to 10 vol %) and dominated by a PGE fractionation pattern typical of a sulphide liquid when compared to the proposed equivalent units of the UCZ. The Upper, Middle and Lower Reefs show many similarities in terms of their mineralogy, stratigraphic position and major element geochemistry (e.g. Cr/MgO ratios) when compared to their equivalent units. In addition, the Middle and Lower Reef mineralisation events, associated with the presence of chromitites, were found to preferentially host a PGM assemblage dominated by; Pt sulphides, Pt-Fe alloys and laurite (see Figure 11.10B) similar to those of the Merensky Reef and UG2 Chromitite (see Figure 11.10C to 11.10F). The trace element data (elevated REE concentrations of the host pyroxenites) and trace mineral compositions (e.g. chromite chemistry) highlight the differences between the proposed equivalent units; this reflects the observations above on the magmatic lineage of the rocks (section 11.4.1) concerning the Ce/Sm ratios which indicates that the Platreef formed from compositionally different magmas to those of the UCZ. The Upper Reef comparison is complicated by the presence of numerous late-stage granitic intrusives affecting this interval in the drill hole studied; the main similarity is that they both peak on Au but the Upper Reef is significantly altered and in general doesn't make a good test study. The large range of $\delta^{34}S$ values for sulphides from both the Middle Reef +1.1 to + 6.0‰ and the Main Chromitite + 2.2 to + 9.5 ‰ indicates some role of hydrothermal fluids probably derived from calc-silicates affecting the sulphide mineralisation. This contrasts with the very limited range of $\delta^{34}S$ values identified for the Merensky Reef +1.1 to +2.5 and UG2 Chromitite +2.2 to +3.2 ‰ (Penniston-Dorland et al., 2012). In the Middle Reef, a zonation in the PGM assemblage was observed across the 4th chromite-stringer from being dominated by Pt-sulphides at the top of the chromite-stringer to Pt-antimonides at the base with a Pd-antimonide assemblage in the high grade footwall. This provides further evidence of transport of PGE (particularly Pd) into the footwall via hydrothermal fluids. In the Lower Reef a significant difference to the UG2 Chromitite mineralisation is that the grade in the former parks in the hanging wall as opposed to within the chromite seam (Gain, 1982; Osbahr et al., 2014. The PGM assemblage is also zoned with Pt-sulphides in the chromitite and Pt-Fe alloys in the silicate hanging wall possibly; the cause of this is either due to upwards transport by magmatic/metasomatic fluids and variable fS_2 and fO_2 conditions in the host rocks. Evidence of these late-stage hydrothermal processes causing redistribution of PGEs, typically thought to be restricted to the shallow Platreeef, in operation in the Deep Platreef provides a warning for models comparing it to the uncontaminated stratiform reefs.

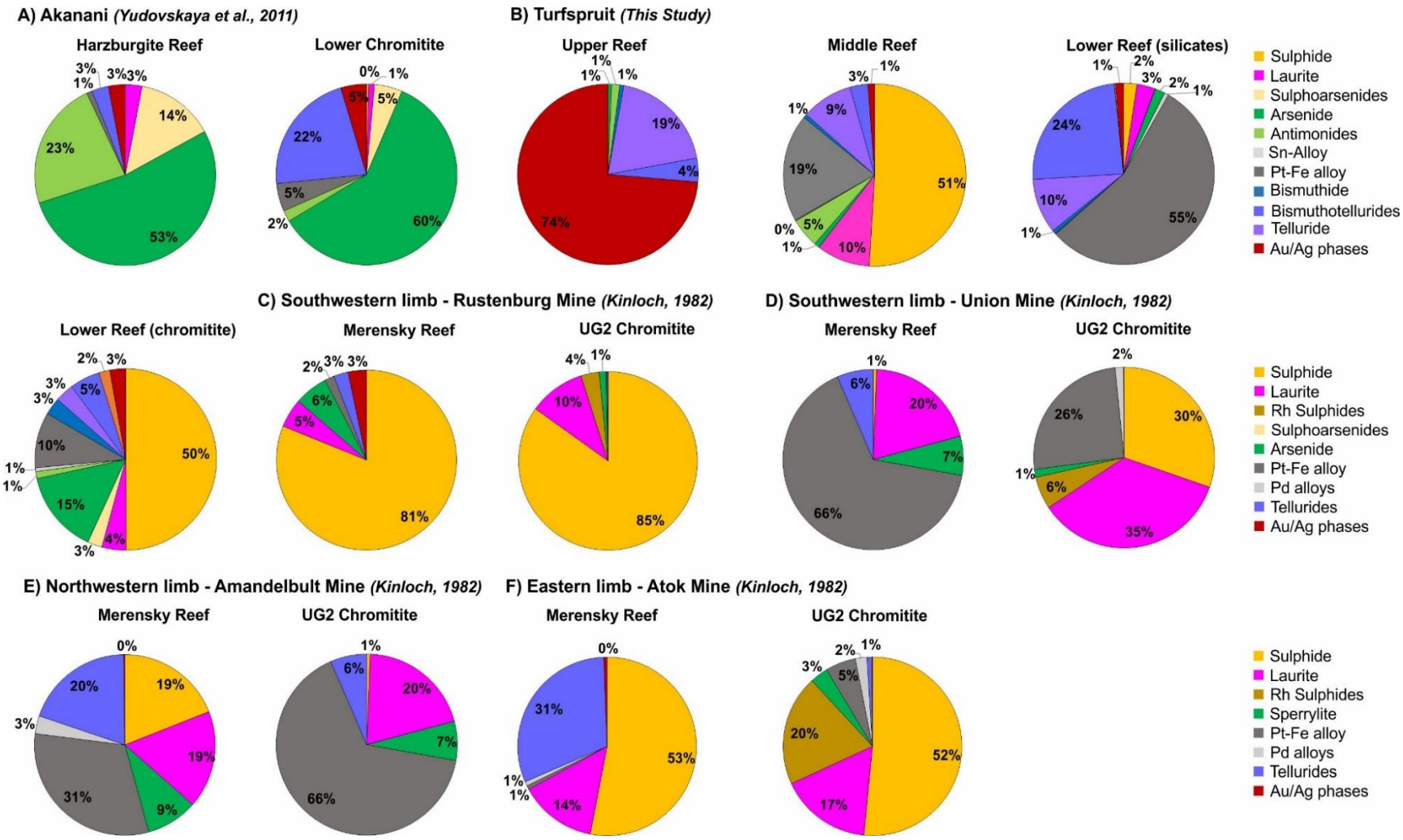

Figure 11.10: A comparison of the PGM compositions of the Deep Platreef with the PGM assemblages of the Merensky Reef and UG2 chromitite All PGM data represent relative proportions.

11.4.3 Correlating to the Grasvally Norite-Pyroxenite-Anorthosite member

The Grasvally Norite-Pyroxenite Norite Anorthosite (GNPA) member, is located south of the Ysterberg-Planknek fault on the northern limb; a summary of the geological features are outlined in Chapter 3 (section 3.3.1). The Ysterberg-Planknek (Y-P) fault, which divides the Platreef (north) from the Grasvally Norite-Pyroxenite-Anorthosite (GNPA) member (south), forms part of the Thabazimbi-Murchison lineament relay system. Questions have been raised on whether the Y-P fault represents a dyke-like feeder zone to the sill-like intrusions of the Platreef or whether this fault zone acted as a barrier to the interaction of magmas along the northern limb (Friese, 2004; Kinnaird et al., 2005; McDonald et al., 2005; Maier et al., 2008). Many authors have suggested that the GNPA member is equivalent to the Upper Critical Zone (UCZ) including van der Merwe (1976; 1978; 2008), Hulbert (1983) and Maier et al., (2008). This analogy is questioned in McDonald et al. (2005) on mineralogical, geochemical and textural differences; as discussed above in section 11.4.1. On the northern limb, the Platreef and GNPA member are considered lateral equivalents by some authors (e.g. Wagner, 1929; von Gruenewaldt et al., 1989; McDonald et al., 2005; Maier et al., 2008; van der Merwe, 2008; Naldrett, 2008; and Smith, 2014). The Platreef and GNPA member are both located at the base of the Main Zone and host base-metal sulphide (BMS) and PGE mineralisation. A model for this relationship is presented in Smith (2014), and reproduced in Figure 3.9 (Chapter 3, section 3.3.1), where the GNPA member is depicted as a down-dip extension of the Platreef.

The BMS and PGE mineralisation of the GNPA member has been studied on Rooipoort by Maier et al., (2008) and on Grasvally by Smith (2014) and Smith et al., (2014). Two significant BMS- and PGE-mineralised horizons are identified in the GNPA member hosted in the Lower Mafic Formation (LMF) unit and Mottled Anorthosite (MANO) unit (see Figure 11.1). Maier et al., (2008) interpret these two PGE mineralised zones as direct equivalents of the UG2 Chromitite and Merensky Reef, respectively. In the MANO unit the BMS- and PGE-mineralisation are found in intergranular areas closely associated with the minerals quartz and phlogopite; a similar mineral assemblage and textural setting to that observed in the Upper Reef in the Upper Pyroxenite unit of the Deep Platreef. In contrast, the LMF unit hosts two laterally continuous PGE- and BMS-bearing chromitites which host the highest grades (> 4 ppm, Smith, 2014). The chondrite-normalised whole-rock Ni-Cu-PGE profiles of the chromitites have two patterns match which vary depending on the sulphur content: (1) contain elevated Ir and peak on Pt/Rh producing an arch-shaped

profile similar to the mineralised chromitites found in the eastern and western limbs and; (2) sulphide-rich chromitites peak on Pd. Similarly the sulphide-rich (5 vol%) chromities in the Deep Platreef also have a fractionated chondrite-normalised whole-rock Ni-Cu-PGE profile which peaks on Pd. In contrast, to the UCZ but in line with the Platreef the GNPA member is Pd-dominated with Pt/Pd ratios typically <1 in non-chromitiferous rocks (Smith, 2014).

The primary BMS assemblage of the GNPA member, consisting of pyrrhotite, pentlandite and chalcopyrite, has been affected to varying degrees by low temperature (< 200 °C) alteration the end product of which is a secondary assemblage of pyrite and millerite (Smith, 2014). This sulphide mineralogical transformation is not observed in the Platreef or anywhere else in the Bushveld Complex; rather low temperature alteration is typically expressed in the replacement of BMS by secondary silicates actinolite-talc-tremolite-chlorite (Armitage et al., 2002; Li et al., 2005; Holwell et al., 2006; Holwell & McDonald, 2007; Yudovskaya et al., 2011; Junge et al., 2018; this study). The secondary sulphides host higher concentrations of PGE in sulphide than the primary assemblage (see Figure 11.2C), indicating that secondary processes are significantly affecting the trace element deportment (for details see Holwell et al., 2017).

The platinum-group mineral (PGM) assemblage of the GNPA member was studied by Smith (2014) who found no lithological control on the PGM speciation. The GNPA member PGM assemblage was observed to be dominated by Pt arsenides (50 %), Pd bismuthotellurides (15 %), Pt-Pd tellurides (14 %), Pd antimonides (10%) and Au/Ag minerals (8 %) with a noticeable lack of PGE sulphides and alloys (see Figure 11.11F). This contrasts with findings of this study on the Deep Platreef which showed considerable variation in the dominant PGMs between the different lithological units (see Figure 11.11B) – a feature also identified in PGM studies on the shallow Platreef as summarised in Figure 11.11A, 11.11B and 11.11C (e.g. Holwell et al., 2006; McDonald & Holwell, 2007; Yudovskaya et al., 2011). Furthermore, there is a large difference in the measured PGE tenor in sulphides between the Deep Platreef and the GNPA member. A LA-ICP-MS study by Smith et al., (2014) on sulphides from the GNPA member measured significantly lower PGE concentrations, up to 35 ppm Pd in pentlandite, in unaltered ‘primary’ sulphides (see Figure 11.2B) compared to the typically >100 ppm measured in the Deep Platreef (see Figure 11.2C). The PGE tenor of the sulphides are interpreted to be inherited prior to emplacement in both this study and in Smith et al., (2014), therefore in order to explain the significant differences in the concentrations measured involves understanding the magmatic processes

operating at depth. The differences in the PGE tenor measured in sulphides from the Platreef and GNPA member can be explained by: (1) they formed from parental magmas with different initial concentrations of PGE; (2) the sulphides experienced variable R factors in the two localities due to different volumes of magma flux and/or; (3) the sulphides underwent variable degrees of dissolution-upgrading prior to emplacement. Considering that the overall bulk Pt/Pd ratios of the Platreef and GNPA member are the same proposal (1) is discounted. This leaves options (2) and (3) both of which require that the GNPA member and the Platreef formed in discrete chambers part of a larger interconnected network. Fundamentally, the magmatic processes upgrading the PGE tenors of sulphides in the GNPA member staging chamber were less efficient than those operating in the Platreef.

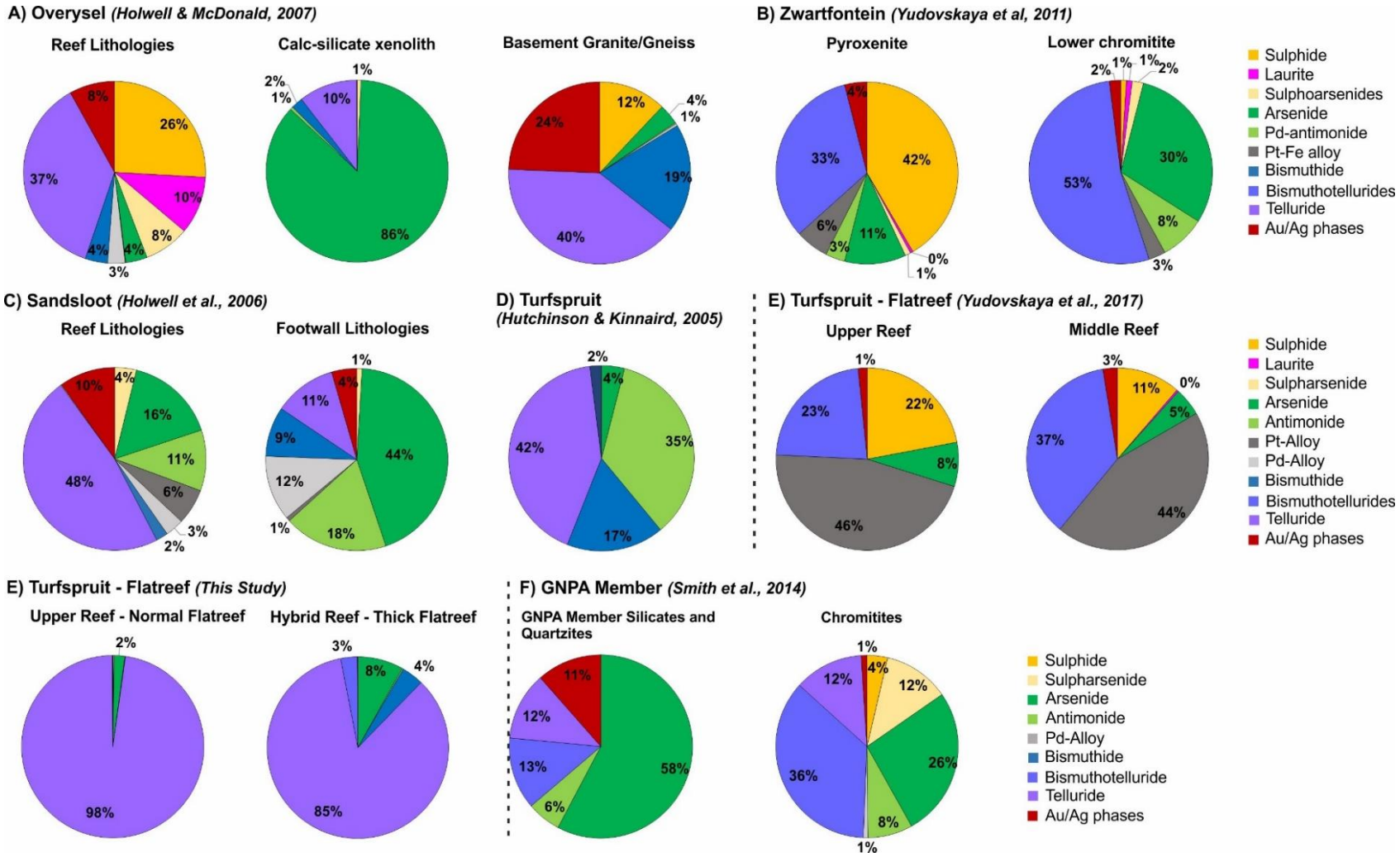

Figure 11.11: A comparison of the PGM compositions on the northern limb moving from top left to bottom right represents movement along strike from north to south. All PGM data represent relative proportions with the exception of the Turfspruit data from Hutchinson & Kinnaird (2005), which represents modal %.

11.5 Platreef on Turfspruit Emplacement Models

The Platreef orebody on Turfspruit, displays characteristics of both 'contact-style' and 'reef-style' Ni-Cu-PGE deposits. The 'contact-style' features identified in the Platreef orebody include: (1) it's marginal position with evidence for magma-sediment interaction both on the contacts between the intrusion and the metasedimentary wall rocks and in the form of xenoliths/metasedimentary interlayers; (2) elevated sulphide concentrations (typically between 5 to 20 vol% in mineralised rocks) carrying significant Ni and Cu as by-products; (3) increased thicknesses of the mineralised interval (> 10 m) and; (4) the identification of a semi-metal rich PGM assemblage. The 'reef-style' features identified include: (1) elevated Pd tenors in pentlandite (>100 ppm); (2) a PGM assemblage including Pt-sulphides, laurite and Pt-Fe alloys associated with chromite-stringers; (3) the presence of laterally continuous chromite-stringers and; (4) magmatic $\delta^{34}S$ values recorded in sulphides from unaltered host rock. The degree to which the features of both 'contact-style' and 'reef-style' are identified varies across the deposit systematically with depth. This may reflect lower degrees of contamination or moving closer to the magmatic source with increasing depth.

The Platreef Ni-Cu-PGE orebody contains an excess of sulphide and chalcophile elements. They are present in quantities considerably above the concentrations that could be dissolved in the parental magma as represented in the current thickness of the host intrusion. In the literature review on the Bushveld Complex, as presented in Chapter 3, two petrogenetic models for the Platreef Ni-Cu-PGE mineralisation are outlined in some detail (section 3.3.3), a brief summary of each model is provided below:

Model 1 – the Platreef represents a marginal extension of the Upper Critical Zone (UCZ) as identified on the eastern and western limbs of the Bushveld Complex (Cawthorn et al., 2002; Naldrett et al., 2008; Maier et al., 2008; Grobler et al., 2018).

Model 2 – the Platreef magma was emplaced with pre-formed sulphides containing high PGE tenors formed in a staging chamber (Kinnaird, 2008; McDonald et al., 2009; McDonald & Holwell, 2011).

The feasibility of these emplacement models will be assessed using the results of the current study as outlined in sections 11.1 to 11.4 above.

11.5.1 Model 1 – A Marginal Extension of the Upper Critical Zone

Model 1 suggests that the Platreef represents a marginal facies of the Upper Critical Zone (UCZ) with the PGE mineralisation equivalent to that of the Merensky Reef. The

development of Model 1 is based on long-standing observations on the lithological, geochemical and stratigraphic similarities of the Platreef to the Merensky Reef and UCZ stratigraphy. The main principles of Model 1 are that the northern limb and the rest of the Bushveld Complex are petrogenetically related as follows: (1) crystallised from the same parental magmas namely the B1, B2 and B3 magmas of Sharpe (1981) and; (2) the PGE mineralisation formed contemporaneously. There are two interpretations on the nature of this relationship, these can be subdivided into: (1a) the PGE mineralised rocks of the Platreef are transported and are laterally continuous with the Merensky Reef and UG2 chromitite (Naldrett et al., 2008; Maier et al., 2008; Grobler et al., 2018); (1b) the Platreef crystallised from the same parental magmas but formed in a separate discrete system (not-laterally continuous) with mineralisation processes occurring in situ (Yudovskaya et al., 2017b).

One of the most advanced and explicit models correlating the Platreef to the UCZ is the nested 'pudding basin' model as developed by Naldrett et al., (2008); a representation of this model is shown in Figure 3.11 (Chapter 3 section 3.3.3) and an interpretation for the Turfspruit locality is shown in Figure 11.9C above. In summary, the 'pudding basin' model suggests that the Platreef crystallised from residual UCZ magma expelled to the shallow periphery of the magma chamber due to overpressurisation in the centre caused by a new influx of magma. The Bushveld Complex is envisaged to be compartmentalised into a series of three interconnected magma chambers one supplying the northern limb and the largest feeding the eastern and western limbs. The current exposure of the northern limb as a marginal facies is the result of the degree of erosion, which is less than that experienced on the eastern and western limbs where deeper parts of the magma chamber are exposed. The fundamental principal of this model (1a) is that moving down-dip a more magmatic stratigraphy is developed that will eventually (at an unspecified depth) transform into a full Rustenburg Layered Suite (RLS) stratigraphic sequence as identified elsewhere in the Bushveld Complex. This transformation with depth should be recorded in: (1) improved continuity of marker horizons e.g. chromite stringers; (2) narrower intervals of mineralisation at higher grades; (3) higher Pt/Pd ratios (> 1) and; (4) the preservation of magmatic cyclicity.

The discovery of westward extensions of the Platreef mineralisation including the Deep Platreef on Turfspruit and the Akanani project on Zwartfontein on a superficial level provide evidence for this model. On Akanani Mitchell & Scoon (2012) identified analogues of the Merensky Reef and Pseudo Reef and on Turfspruit direct comparisons to the UCZ stratigraphy covering the sequence from the Bastard Reef

to the UG2 Chromitite are proposed in Grobler et al., (2018). The focus of the current study has been on the Deep Platreef as recognised on Turfspruit, which represents the ideal location to test this model. According to model 1a of Naldrett et al., (2008) and Maier et al., (2008) the Platreef stratigraphic sequence should become increasingly more magmatic with depth. The data collected in this study samples the transition from highly contaminated shallow Platreef (0 to 300 m), the transitional Flatreef (700-100 m) and the more magmatic Deep Platreef (> 1000 m). A cross-section of the Platreef orebody on Turfspruit is shown in Figure 11.12 along with a summary of key mineralogical and geochemical data considered suitable for establishing the relative influence of contamination vs magmatic processes on the development of the stratigraphic sequence and associated mineralisation. A key tool for identifying contamination of the sulphides in the Platreef on Turfspruit are the $\delta^{34}S$ values. A magmatic signature of sulphides are found in both the Flatreef and Deep Platreef sectors however all sulphides analysed from the Platreef have contaminated $\delta^{34}S$ values. The range of $\delta^{34}S$ values varies significantly between the Flatreef (+ 0.5 to +5.2 ‰) and Deep Platreef (+ 0.7 to +10.8 ‰) sectors. An important prediction by Maier et al., (2008) is that moving down-dip the Pt/Pd ratio should become more Pt-rich; no systematic increase in Pt/Pd ratio moving down-dip is observed in Figure 11.12. The average Pt/Pd ratios for the Upper and Middle Pyroxenite units, as identified in all drill holes across the deposit, initially increases from the Platreef (0.7) to the Normal Flatreef (1.3) but both the Thick Flatreef and Deep Platreef contain average Pt/Pd ratios of 1.0. The variables that increase systematically with depth are: (1) the metal tenors in sulphide, this is expressed as the IPGE tenor in pyrrhotite, Pd concentration in pentlandite and the Zn concentration in chalcopyrite; (2) the average Mg# in orthopyroxene of the Middle Pyroxenite unit which increases from $Mg\#_{78}$ in the Platreef to $Mg\#_{81}$ in the Deep Platreef. The highest average whole-rock Cr, Ni and Cu contents are all hosted in the Flatreef sector of the orebody, in particular in the Thick Flatreef. The lowest whole-rock concentrations of Cr, Ni and Cu are identified in the Platreef and this is believed to result from the accumulation of sulphides in the Flatreef leaving the up-dip Platreef relatively depleted.

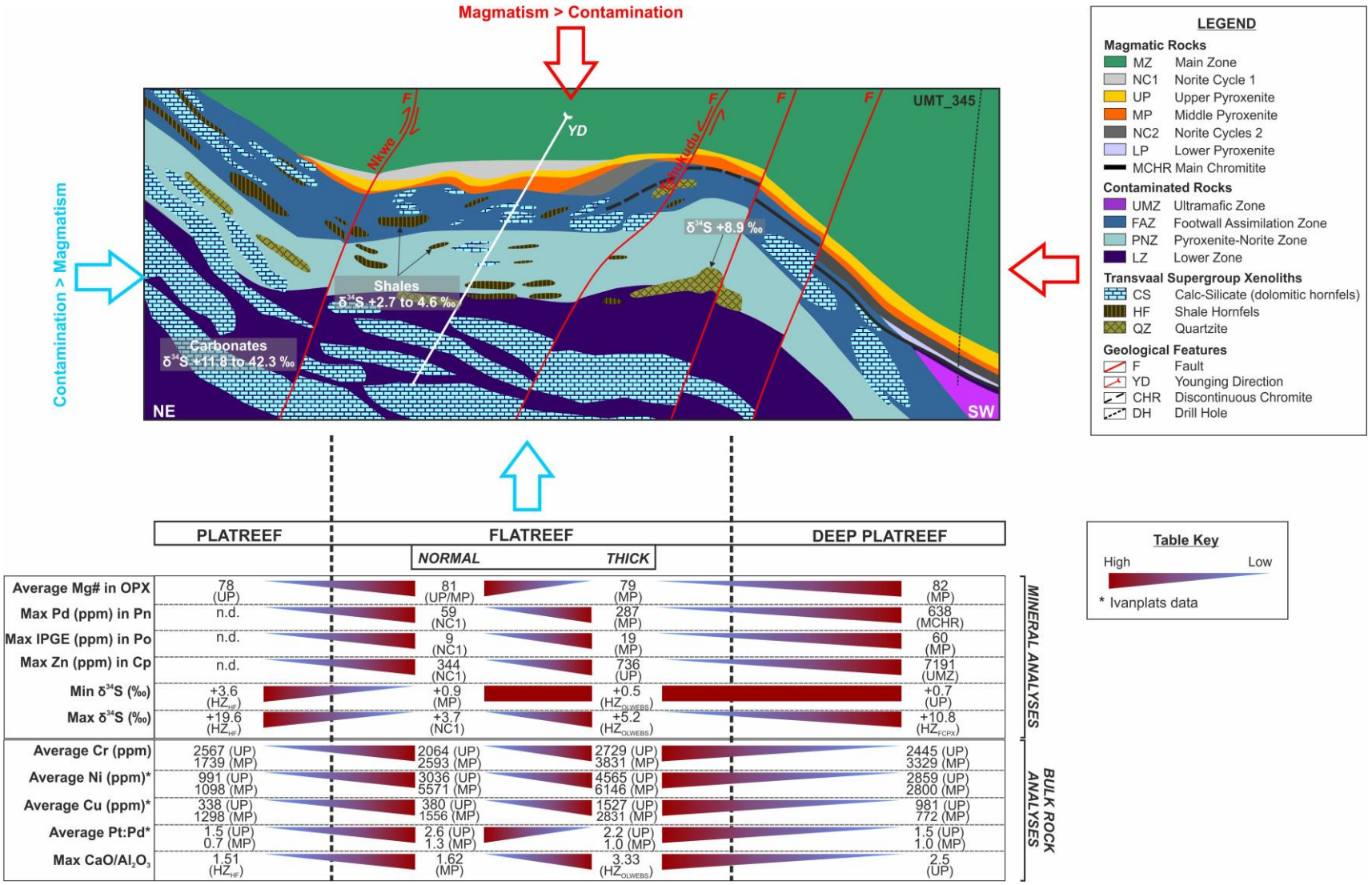

Figure 11.12: A summary of the geochemical and mineralogical variability observed between the different sectors of the Turfspruit deposit moving down-dip from east to west. Note: stratigraphic units the data is from are in brackets. Cross-section modified from Ivanplats drilling data. Abbreviations: Po – pyrrhotite, Pn – pentlandite and Cp – chalcopyrite.

In summary, the initial geological logging results of this study appear to support model 1a; all four of the key observations to test the model, as outlined above, are observed and they become more persistent moving down-dip from the Platreef to the Deep Platreef. However, the quantitative geochemical and mineralogical data highlights the localised variability and additional complexity between the 'zones' of the orebody. The geometry of the deposit has a strong control on the relative influence of contamination vs magmatic processes with magmatic processes appearing to dominant in the Flatreef portion of the orebody. In addition, the varying geochemistry and reactivity of the floor rocks with lithostratigraphic height forming the compositionally distinct Upper and Lower Duitschland Formation impart a strong signature on the magma which will change depending on the level of intrusion.

The correlation of the Turfspruit stratigraphy in the Deep Platreef to that of the UCZ is examined in section 11.4 and several important differences are recorded. Principally, the magmatic lineage of the Ni-Cu-PGE deposits on the northern limb, both the Platreef and GNPA member, doesn't match that of the Merensky Reef in the UCZ. The Ce/Sm ratios of the cumulate rocks in the Platreef, Flatreef and Deep Platreef consistently plot within the Main Zone field. This cannot be explained by in situ crustal contamination because studies on the Ce/Sm ratios of the country rocks reveal that they contain an average Ce/Sm ratios in between the Main Zone and Critical Zone values. This homogenous signature must mean that it represents an original feature of the parental magma. The Main Zone intrudes a significant time after the Platreef is solidified meaning that this took place at depth as opposed to in situ mixing of a new and residual magma. Neither of the models for the Platreef proposed by Naldrett et al., (2008) and Maier et al., (2008) can explain the break in magmatism observed between the deposition of the Main Zone and the Platreef. Isotope studies across this same contact in the Bushveld Complex (Seabrook et al., 2005) suggests continuous interaction between the Main Zone and Critical Zone magmas during the formation of the Merensky Reef.

11.5.2 Model 2 – A Platreef Staging Chamber

A staging chamber (Model 2) was first suggested for the formation of the Platreef in Lee (1996) and further developed by Holwell et al., (2007) and McDonald & Holwell (2007). A representation of this model as applied to the surface Platreef is shown in Figure 3.12 (Chapter 3, section 3.3.3). Model 2 is based on two fundamental principles: (1) sulphide saturation occurred at an early-stage at depth in the magmatic plumbing system due to the assimilation of crustal sulphur and; (2) pre-formed, high PGE-tenor sulphide droplets are transported upwards in the magma flow to the depositional site. The deep magmatic processes are most commonly cited as taking place in a staging chamber, however

equally these processes could operate in any favourable depositional point in a magma conduit (e.g. in a dilatational jog). Model 2 has been modified based on the lines of evidence as presented in this study and discussed in sections 11.1, 11.2 and 11.3 for the emplacement of the Platreef on Turfspruit. The proposed emplacement model for the Platreef on Turfspruit is shown in Figure 11.13**;** it is divided into a surface system (left-hand side) and a deep system (right-hand side). The surface system is more constrained by evidence collected in the current study than the deep system with the magmatic processes operating at depth more speculative. The following stages are proposed to occur sequentially in the emplacement of the Platreef on Turfspruit:

1. **Development of the footwall geometry (Figure 11.13A[1])** during pre-emplacement folding and faulting of the Transvaal Supergroup, on a regional and local scale. The overall structure has been interpreted as a regional synformal monocline dipping to the SW. On Turfspruit, localised faulting and folding results in the development of a graben-like structure, which provides an ideal depositional environment for Ni-Cu-PGE sulphides and results in the formation of the Flatreef deposit hosting mineralised intervals up to 60 m thick. The unique crustal architecture results in the division of the Turfspruit ore deposit into the Platreef, Flatreef and the Deep Platreef based on similar characteristics.
2. **Early-stage contamination (1st event, Figure 11.13A[2])** involves the assimilation of crustal sulphur and LILE elements from the Pietersburg Greenstone Belt (PGB) or Transvaal Supergroup in a staging chamber through the interaction of the ascending magma with the wall rocks. Homogenisation of the contaminant material with the magma triggers initial sulphide-saturation and an immiscible sulphide liquid accumulates in a favourable depositional site. The original crustal $\delta^{34}S$ (+3.4 to +6.3 ‰ in PGB rocks) and S/Se ratios (> 4000) are eliminated through interaction with high volumes of sulphur-undepleted magma. Evidence of this event is maintained in the LILE-enrichment, incompatible element ratios (low $(Nb/Th)_{PM}$ ratios and high $(Th/Yb)_{PM}$) and Nb/Ta anomalies.
3. **Sulphide liquid is progressively enriched in PGE, Ni and Cu (Figure 11.13B[2])** in the staging chamber through interaction with multiple batches of pre-Platreef silicate magma. The enrichment is enhanced via 'multi-stage dissolution upgrading' as described in Kerr & Leitch (2005) and initially proposed for the Platreef staging chamber by McDonald et al., (2012). These processes result in high Pd tenors in sulphides that are comparable to those of the Merensky Reef (Godel et al., 2007; see Figure 11.2) at relatively low R factors and impart low S/Se ratios (<2500). The semi-metals, Te and Bi which form a primary magmatic

PGM assemblage as found ubiquitously across the Platreef, are also scavenged by the sulphide liquid at this stage. Evidence of Ni-Cu-PGE depleted pre-Platreef magma is identified in Lower Zone cumulates as identified on the northern limb by McDonald & Holwell (2007) and McDonald et al., (2009).

4. **Early Bushveld intrusions of Lower Zone magma (Figure 11.13B[1])** form ultramafic cumulates comprising dunite, harzburgite and pyroxenite compositions that are Ni-depleted having achieved sulphide saturation at depth (McDonald et al., 2009). The Lower Zone intrudes unconformably into the footwall sediments as numerous sill-like bodies up to 700 m thick multi-stage intrusive episode (van der Merwe, 1976; Yudovskaya et al., 2013). The Lower Zone intrusions are typically separated from the Platreef mafic/ultramafic sequence by interlayers of country rocks (Yudovskaya et al., 2013). The degree of sulphide mineralisation in the Lower Zone intrusions has been observed to correlate with the sulphur content of the footwall rocks (Yudovskaya et al., 2013).
5. **A new magma enters the staging chamber (Figure 11.13C[2])** (compositionally between B2 and B3) and mixes with any residual Lower Zone magma (B1 composition) remaining to produce a hybrid magma which forms the parental magma of the Platreef. Evidence of this hybridisation event is shown in contrasting Cr/MgO and Ce/Sm ratios indicative of interaction between both Lower and Main Zone magmas. When exiting the staging chamber the hybrid magma entrains and transports the PGE-rich sulphides upwards to their site of deposition at the level of the Duitschland Formation of the Transvaal Supergroup (McDonald & Holwell 2011; McDonald et al. 2012).
6. **Intrusion of Platreef hybrid magmas (Figure 11.13C[1])** took place as multiple influxes of both a liquid-crystal bearing mush and crystal-free magmas intruding as composite sill-like bodies. The initial pulses become significantly contaminated by a roof and floor of the Duitschland Formation and cooled quicker creating the Hybrid Zone lithologies such as the fine-grained Feldspathic Clinopyroxenite in the Deep Platreef and the Pyroxenite-Norite Zone in the Normal Flatreef. The Main Chromitite (MCHR), as identified in the Deep Platreef, forms in situ on top of the strongly contaminated Ultramafic Zone. The MCHR unit pinches out moving up-dip and eastwards because of the distal location to the main feeder and/or through increasing dilution by crustal contamination. The pyroxenites hosting the Upper and Middle Reef mineralisation are intruded as liquid-crystal mushes during a very voluminous magma which enters the Flatreef and Platreef sectors. The geometry of the intrusion broadly follows that of the

faulted and folded footwall leading to localised thickening in the Flatreef structure with the PGE-bearing sulphides preferentially deposited along the horizontal floor, leading the Platreef relatively depleted.

7. **Late-stage contamination (2nd event, Figure 11.13C[1])** during emplacement occurs in situ with the Platreef hybrid magma interacting with a roof and floor of Duitschland Formation (DF) sediments. This imparts a heterogenous contamination signature across the Turfspruit deposit which varies depending on whether the level of intrusion coincided with the carbonate-dominated Upper DF or the shale-rich Lower DF. Crustal sulphur from the DF is introduced into the magma via hydrothermal fluids leaching sulphate from the Upper DF sediments and partial melting of sedimentary pyrite from the Lower DF (McDonald & Holwell, 2011). The zonation in the $\delta^{34}S$ values with stratigraphic height and between the down-dip sectors of the orebody suggest local interaction with both the Upper and Lower DF sediments. Hydrothermal fluids derived from the floor rocks also introduce varying amounts of the semi-metals As- and Sb- into the magmatic system which leads to decoupling of the PGE from the base metal sulphides. Where contamination levels are high the base metal sulphide mineral assemblage can be altered from a primary pyrrhotite-pentlandite-chalcopyrite assemblage to: (1) a pyrrhotite-dominated assemblage as identified throughout the Platreef and adjacent to xenoliths in the Thick Flatreef which shows a spatial association with magnetite and/or apatite; (2) increasing cubanite levels as identified in the Main Chromitite and Ultramafic Zone in the Deep Platreef.
8. **Solidification of the Platreef (Figure 11.13D[1])** occurs during a break in the magmatism as evidenced in field contact relationships in the open-pits of the Mogalakwena mine complex (Holwell & Jordaan, 2006).
9. **Intrusion of Main Zone (Figure 11.13D[1] and 11.13D[2])** magma (B3 composition) as a voluminous magmatic episode which deposits > 1 km of gabbronorite cumulates. The Main Zone exploits the top contact of the Platreef which represents a magmatic unconformity. In the Platreef sector, a remnant of calc-silicate at the top of the drill hole attests to a former roof of Upper DF.
10. **Late-stage granitic intrusives** represented by quartz-feldspar veins (QFV) form after either partial or complete crystallisation of the Platreef. Localised hydrothermal alteration of the adjacent host rocks introduces the accessory minerals monazite and apatite into the altered interstitial areas, dominated by plagioclase. This causes elevated LREE concentrations in the pyroxenite units hosting the QFVs. The composition of the QFV containing Na-plagioclase and

Cl-bearing apatite releases Na-Cl fluids into the host pyroxenites that can cause significant redistribution of the PGE especially the more mobile Pd- and Au.

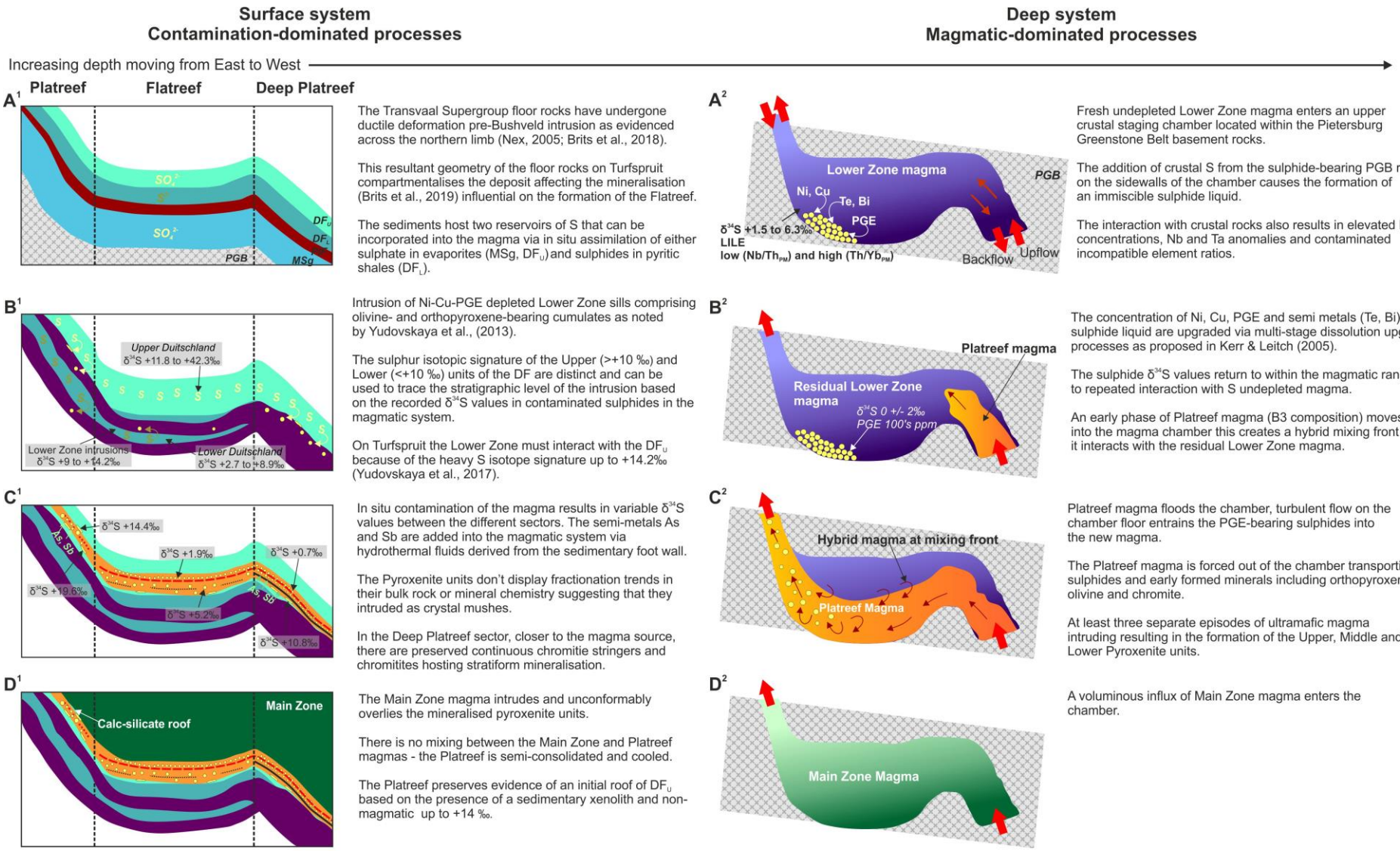

Figure 11.13: A schematic model for the intrusion of the Platreef on Turfspruit, for details see the text in the figure.

11.6 Conclusions

The discussions topics covered above are based on the results of a multi-disciplinary study on the nature and origin of the Ni-Cu-PGE mineralisation and stratigraphy of the Platreef on Turfspruit and the cause of the variability observed across the deposit. In summary, the preceding chapters detail a role for a combination of magmatic, contamination and hydrothermal processes in the petrogenetic history of the Platreef on Turfspruit. A summary of the main conclusions from each of the sections above are presented below.

Section 11.1 – the principal ore hosting minerals are magmatic base metal sulphides comprising pyrrhotite-pentlandite-chalcopyrite and discrete platinum-group minerals (PGMs). The dominant host rock for the PGE mineralisation are sulphide-rich (5 to 20 vol%) pyroxenites which show enrichment in Pd over Pt. The whole-rock Ni and Cu contents have a strong correlation with the PGE grade. The identification of sulphide inclusions in chromite grains confirms that an immiscible sulphide liquid was present at high-temperatures early in the crystallisation history. Pentlandite is the principal host of both Pd and Rh; whereas Pt, Ru and Au are found as PGMs (especially moncheite, Pt-Fe alloys, cooperite, laurite and electrum). The chromite-bearing mineralised intervals have PGM assemblages dominated by Pt-sulphides and Pt-Fe alloys; they also host Ir-group PGMs. In unaltered silicate-dominated lithologies Pt tellurides are the principal PGMs representative of a primary magmatic Platreef assemblage as identified elsewhere along strike. In contrast, strongly serpentinised lithologies in contaminated lithologies host Pd-antimonides dominated PGM assemblages indicative of hydrothermal redistribution by fluids derived from sediment devolatisation.

The observed thicknesses of the PGE mineralised interval is related to the pre-emplacement crustal architecture, the geochemistry of the floor rocks and redistribution by hydrothermal fluids. This matches observations along the strike of the Platreef structural highs and embayments are observed to have a significant control on the thickness of the PGE mineralised interval. This is expressed on Turfspruit in the development of the graben-style geometry of the Flatreef which acted as a favourable depositional environment for the thick-mineralised intervals and left the up-dip Platreef relatively depleted in Ni- Cu- and PGE.

The stratigraphy of the Platreef formed from multiple influxes of new magma hosting pre-formed sulphide liquid and crystals. Sympathetic reversals in Pt/Pd and Cu/Pd ratios on the lithostratigraphic contacts in most drill holes indicates that they represent new intrusions of magma with a different PGE budget and may correspond with the presence of chromitites. The exception to this is observed in the Thick Flatreef drill hole which

maintains a consistent Pt/Pd (1.0) ratio over > 60m; the development of the stratigraphic units is affected by significant contamination of dolomitic compositions.

Section 11.2 - the Platreef magma on Turfspruit was affected by two-stages of crustal contamination. The geochemical evidence for crustal contamination of the Platreef magma as observed in this study can be grouped into those which are: (a) homogenous, recorded in all drill holes across the deposit and identified on a regional scale and; (b) heterogenous signatures, that vary between the different sectors of the orebody. The first contamination, affecting the entire deposit equally (a), is identified in the incompatible element ratios (e.g. low $(Nb/Th)_{PM}$ and high $(Th/Yb)_{PM}$ ratios), enrichment in LILE elements and pronounced negative Nb and Ta anomalies. The contamination must have occurred at an early-stage in order to be homogenised in the parental magma, this probably took place in the main or subsidiary magma reservoir in the upper crust. The Pietersburg Greenstone Belt (PGB) or lower units of the Transvaal Supergroup at depth represent the potential sources of this contamination. Evidence that the Platreef parental magma was contaminated prior to intrusion is also recorded on the farms Overysel, Sandsloot and Tweefontein by Ihlenfeld & Keays (2011) and in the GNPA member by Smith (2014).
In contrast, the second contamination event occurred upon-emplacement of the Platreef through interaction of the magma with the immediate wall rock sediments. On Turfspruit, the immediate floor and roof of the intrusion are composed of the carbonates and siliciclastic rocks of the Duitschland Formation (DF). The lithostratigraphic heterogeneity of the DF between the Upper and Lower sediments is recorded in the sulphur isotope composition, the whole-rock major element ratios and the REE concentrations. Platreef magmas contaminated by shales of the Lower DF have elevated REE concentrations, $\delta^{34}S$ values < +10 ‰ and CaO/Al_2O_3 ratios <0.6. In contrast, contamination from the carbonates of the Upper DF results in low REE concentrations, $\delta^{34}S$ values > +10 ‰ and CaO/Al_2O_3 ratios >1.0.

Section 11.3 – hydrothermal activity is concentrated on lithostratigraphic contacts and generally increases moving downhole closer to the footwall contact. The late-stage intrusion of granitic veins significantly affects the interstitial silicate mineral assemblage of the host rocks adding REE-bearing minerals such as apatite and monazite resulting in anomalously high overall REE concentrations in the Upper and Middle Pyroxenites in the Deep Platreef. The QFVs also possibly release Na-Cl brines capable of locally redistributing the PGE content and causing elevated Pd and Au concentrations. Evidence for hydrothermal activity is greatest where the floor rocks are composed of

calc-silicates (as evidenced in the Deep Platreef by elevated $\delta^{34}S$ values +10.8 ‰) where post-emplacement fluid interaction results in the decoupling of the PGE from base metal sulphides and the development of Sb-bearing PGM.

Section 11.4 – a critical assessment of the proposed correlations between the Platreef and Grasvally Norite-Pyroxenite-Anorthosite (GNPA) member with the Upper Critical Zone (UCZ) of the eastern and western limbs of the Bushveld Complex. This section highlights the potential problems with this correlation which should still be held with caution. The parental magma of the Platreef on Turfspruit represents a 'hybrid' composition, as supported by contrasting Cr/MgO and Ce/Sm ratios, which consistently plot within the Critical Zone and Main Zone ranges, respectively. The Main Zone range of Ce/Sm values identified in the Platreef rocks on Turfspruit cannot be accounted for via in situ contamination of the Duitschland Formation sediments which have an average value between the Main and Critical Zone. Therefore, this Main Zone signature must have been homogenised in the parental magma prior to emplacement based on the observed magmatic unconformity between the Platreef and Main Zone. The magmatic lineage of the rocks of the Deep Platreef indicates a similar petrogenesis as the GNPA member. The observed differences in the BMS assemblage and PGE tenors of sulphides can be explained considering the Platreef and GNPA member chambers as discrete but connected as part of a larger magmatic system. The PGE upgrading processes in the Platreef chamber operated more efficiently than those in the GNPA member chamber. The Upper, Middle and Lower Reef mineralisation events as preserved in the Deep Platreef are compared to the proposed equivalent units in the UCZ including the Bastard Reef, Merensky Reef and UG2 Chromitite. The mineralisation events of the Deep Platreef are consistently thicker, more sulphide-rich and Pd-dominated compared to the proposed UCZ equivalents; this matches the sulphur isotope evidence indicating significant contamination and hydrothermal activity over the mineralised intervals at this location.

Section 11.5 – the proposed lateral continuity of the Platreef to the Merenksy Reef is rejected based on the evidence outlined in the current study; most critically is the lack of a systematic increase in the Pt/Pd ratio moving down-dip across the Turfspruit deposit (consistent average 1.0). The preferred model for the development of the Platreef Ni-Cu-PGE orebody on Turfspruit involves initial sulphide saturation at depth in a staging chamber triggered by crustal contamination via digestion of sulphide-bearing wall rocks potentially sourced from the Pietersburg Greenstone Belt (PGB). The Ni, Cu, PGE and semi-metals (Te and Bi) are scavenged by the sulphide liquid via orthomagmatic

processes operating in the chamber; this is envisaged to be dominant in ore genesis. Subsequent upgrading occurs in a magmatic system via processes of 'multistage dissolution upgrading' (Kerr & Leitch, 2005). Upon emplacement, in situ contamination by Duitschland Formation sediments introduces lithological and mineralogical heterogeneity and leads to hydrothermal redistribution of the PGE via decoupling from sulphides and the formation of Sb-bearing platinum-group minerals.

11.7 Recommendations for Future Work

- To conclusively establish whether the Middle Reef is contemporaneous with the Merensky Reef, as inferred in models proposing their lateral continuity (e.g. Model 1 in section 11.5.1 above), a high-precision U-Pb dating study on zircon should be conducted. This would complement the recent dating studies on the Merensky Reef such as those by Scoates & Freidman (2008) and Mungall et al., (2016). The magmatic zircons should be selected with care as the intrusion of late-stage quartz-feldspar veins into the Middle Reef interval unit of the Deep Platreef appear to have altered the interstitial assemblage and may affect the crystallisation age.
- One of the best ways to test for the presence of hydrothermal fluids, their composition and the timing of their introduction is using fluid inclusions. If these are identified in high temperature minerals such as orthopyroxene or chromite this would indicate their early introduction and a feature of the primary magma. A recent fluid inclusion study by McFall et a., (2018) on the Aurora Cu-Ni-Au-PGE deposit, hosted in the Main Zone of the northern limb, identified polyphase liquid-vapour-solid inclusions (solid phase identified as halite inclusions) in primary magmatic minerals. Although Aurora is located at a completely different stratigraphic level to the Platreef it attests to the presence of chlorine-rich fluids in the Bushveld magmatic system. A fluid inclusion study on the Hybrid Zones (e.g. the fine-grained Feldspathic Clinopyroxenite at the base of the Deep Platreef and Olivine Websterite of the Thick Flatreef) where assimilated dolomite is inferred. Dolomites should release water, CO_2 and potentially contain NaCl that may be trapped in crystallising minerals. In addition, a combination of observations on the Middle Pyroxenite unit of the Deep Platreef hosting the Middle Reef mineralisation could be interpreted as a role of fluids including: pegmatoidal textures, elevated $\delta^{34}S$ values (up to +4.4 ‰) above the magmatic range, slightly elevated CaO/Al_2O_3 ratios (1.5 to 2.5) and elevated whole-rock LREE concentrations.

- The sulphur isotope data reported in this study was not able to distinguish any input from the Pietersburg Greenstone Belt (PGB) because the range of $\delta^{34}S$ values overlapped with those of the Duitschland Formation. The $\delta^{34}S$ dataset on the PGB rocks should be coupled with a mass independent fractionation (MIF) study performed on the same samples. This may be able to constrain any interaction between the PGB and Platreef magmatic rocks which would likely occur at depth and result in probably homogenous contaminated signature (i.e. non-zero $\Delta^{33}S$). The Duitschland Formation and Pietersburg Greenstone belt should have distinct MIF signatures.
- The Platreef represents a multicomponent system (as defined in Lesher & Burnham, 2001) as such mass balance modelling of the elemental and isotopic compositions can provide information on their relative roles as a function of R. For example: R factor modelling to calculate the elevated Pd concentrations (> 600 ppm) in the Main Chromitite unit in sulphides containing elevated $\delta^{34}S$ values (up to +9.5 to +5.5 ‰).

Reference List

Altermann, W., and Nelson, D. R. 1998. Sedimentation rates, basin analysis and regional correlations of three Neoarchean and Palaeoproterozoic sub-basins of the Kaapvaal craton as inferred from precise U-Pb zircon ages from volcaniclastic sediments. *Sedimentary Geology*. **120**: 225-256.

Armitage, P.E.B., McDonald, I., Edwards, S.J., and Manby, G.M. 2002. Platinum-group element mineralisation in the Platreef and calc-silicate footwall at Sandsloot, Potgietersrus District, South Africa. *Appl. Earth Sci. (Trans. Inst. Min. Metall. B).* **111**, B36 – 45.

Armitage, P.E.B. 2011. *Development of the Platreef in the Northern Limb of the Bushveld Complex at Sandsloot, Mokopane District, South Africa.* PhD Thesis, University of Greenwich.

Arndt N. T., Lesher C. M., and Czamanske G. K. 2005. Mantle-Derived Magmas and Magmatic Ni- Cu-(PGE) Deposits. *Economic Geology*. **100**th Anniversary Volume: 5–23.

Ashwal, L. D., Webb, S. J., and Knoper, M. W. 2005. Magmatic stratigraphy in the Bushveld Northern Lobe: continuous geophysical and mineralogical data from the 2950 m Bellevue drillcore. *South African Journal of Geology.* **108**: 199-270.

Ballhaus, C. G., and Stumpfl, E. F. 1986. Sulfide and platinum mineralization in the Merensky Reef: evidence from hydrous silicates and fluid inclusions. *Contributions to Mineralogy and Petrology.* **94** (2): 193-204.

Ballhaus, C., and Sylvester, P. 2000. Noble metal enrichment processes in the Merensky Reef, Bushveld Complex. *Journal of Petrology*. **41:** 545-561.

Barnes, S. J. 1986. The effect of trapped liquid crystallization on cumulus mineral compositions in layered intrusions. *Contributions to Mineralogy and Petrology*. **93** (4): 524-531.

Barnes, S. J., Cruden, A. R., Arndt, N., and Saumur, B. M. 2016. The mineral system approach applied to magmatic Ni-Cu-PGE sulphide deposits. *Ore Geology Reviews*. **76**: 296-316.

Barnes, S. J., and Roeder, P. L. 2001. The Range of Spinel Compositions in Terrestrial Mafic and Ultramafic Rocks. *Journal of Petrology*. **42** (12): 2279-2302.

Barnes, S-J, Cox, R. A., Zientek, M. L. 2006. Platinum-group element, gold, silver and base metal distribution in compositionally zoned sulphide droplets from the Medvezky Creek Mine, Norilsk, Russia. *Contribution Mineralogy and Petrology.* **152**:187–200

Barnes, S-J., and Lightfoot, P. 2005. Formation of Magmatic Nickel Sulphide Ore Deposits and Processes Affecting Their Copper and Platinum Group Element Contents.

In: Hedenquist J. W, Thompson, J. F. H, Goldfarb R. J, Richards J. P (eds.). *Economic Geology*. **100**th Anniversary Volume: 179-213.

Barnes, S-J., and Maier, W. D. 2002. Platinum-Group Element Distributions in the Rustenburg Layered Suite of the Bushveld Complex, South Africa. *In:* The Geology, Geochemistry, Mineralogy and Mineral Beneficiation of Platinum-Group Elements. Edited by L.J. Cabri, *Canadian Institute of Mining, Metallurgy and Petroleum*. Special Volume **54:** 431-458.

Barnes, S-J., Maier, W. D., and Curl, E. A. 2010. Composition of the Marginal Rocks and Sills of the Rustenburg Layered Suite, Bushveld Complex, South Africa: Implications for the Formation of the Platinum-Group Element Deposits. *Economic Geology*. **105** (8): 1491 – 1511.

Barnes, S-J., Makovicky, E., Makovicky, M., Rose-Hansen, J., and Karup-Moller, S. 1997. Partition coefficients for Ni, Cu, Pd, Pt, Rh, and Ir between monosulphide solid solution and sulphide liquid and the formation of compositionally zoned Ni-Cu sulphide bodies by fractional crystallisation of sulphide liquid. *Canadian Journal of Earth Sciences.* **34**: 366-374.

Barnes, S-J., and Naldrett, A. J. 1985. Geochemistry of the J-M (Howland) Reef of the Stillwater Complex, Minneapolis Adit area; I, Sulfide chemistry and sulphide-olivine equilibrium. *Economic Geology*. **80** (3): 627-645.

Barnes, S-J., Naldrett, A. J., and Gorton, M. P. 1985. The Origin of the Fractionation of Platinum-Group Elements in Terrestrial Magmas. *Chemical Geology.* **53:** 303-323

Barnes, S-J., Prichard, H. M., Cox, R. A., Fisher, P. C., and Godel, B. 2008. The location of the chalcophile and siderophile elements in platinum-group element ore deposits (a textural, microbeam and whole rock geochemical study): Implication for the formation of the deposits. *Chemical Geology*. **248**: 295-317.

Barnes, S-J., and Ripley, E. M. 2016. Highly siderophile and strongly chalcophile elements in magmatic ore deposits. *Reviews in Mineralogy and Geochemistry*. **81** (1): 725-774.

Barton, J. M., Cawthorn, R. G., and White, J. 1986. The Role of Contamination in the Evolution of the Platreef of the Bushveld Complex. *Economic Geology*. **81**:1096-1104.

Begg, G. C., Hronsky, J. A. M., Arndt, N. T., Griffin, W.L., O'Reilly, S. Y., and Hayward, N. 2010. Lithospheric, Cratonic, and Geodynamic Setting of Ni-Cu-PGE Sulphide Deposits. *Economic Geology.* **105:** 1057-1070.

Bekker, A., Holland, H. D., Wang, P.-L., Rumble, III, D., Stein, H.J., Hannah, J.L., Coetzee, L.L., and Beukes, N.J., 2004. Dating the rise of atmospheric oxygen. *Nature*. **427:** 117-120.

Bekker, A., Kaufman, A.J., Karhu, J.A., Beukes, N.J., Swart, Q.D., Coetzee, L.L., and Eriksson, K. A., 2001. Chemostratigraphy of the Paleoproterozoic Duitschland Formation, South Africa: Implications for coupled climate change and carbon cycling. *American Journal of Science.* **301:** 261-285.

Beukes, N. J., and Gutzmer, J. 2008. Origin and paleoenvironmental significance of major iron formations at the Archean-Paleoproterozoic boundary. *Society of Economic Geology Review.* **15**: 5-47.

Beukes, J. J., Roelofse, F., Gauert, C. D. K., and Grobler, D. F. 2018. Geochemical and sulphur isotope study on the origin of PGE mineralisation at Turfspruit, Northern Limb, Bushveld Complex. 13th International Platinum Symposium, 30th June – 6th July 2018. Abstract.

Bond, G.C. 1968. Periodic Variations in the Catalystic Properties of Metals: The Influence of Solid State Parameters on Adsorption and Catalysis. *Platinum Metals Review.* **12** (3): 100 – 105.

Borisov, A., and Palme, H. 1997. Experimental determination of the solubility of platinum in silicate melts. *Geochimica et Cosmochimica Acta*. **61**: 4349-4357.

Boudreau, A. E., and McCallum, I.S. 1992. Concentration of Platinum-Group Elements by Magmatic Fluids in Layered Intrusions. *Economic Geology.* **87**:1830–1848.

Boudreau, A. E., and Meurer, W. P. 1999. Chromatographic separation of the platinum-group elements, gold, base metals and sulphur during degassing of a compacting and solidifying igneous crystal pile. *Contributions to Mineralogy and Petrology*. **134**: 174-185.

Buick, I. S., Maas, R., and Gibson, R. 2001. Precise U–Pb titanite age constraints on the emplacement of the Bushveld Complex, South Africa. *Journal of the Geological Society*. **158**: 3–6.

Brenan, J. M., and Rose, L. A. 2002. Experimental constraints on the wetting of chromite by sulphide liquid. *The Canadian Mineralogist*. **40**: 1113-1126.

Brits, J. A. N., Grobler, D. F., Bumby, A. J., and Crossingham, A. 2018. The Structure of the Flatreef Deposit, Northern Limb, Bushveld Complex [Abs]. 13th International Platinum Symposium 30th June to 6th July 2018. Abstract.

Brooks, C. K., Keays, R. R., Lambert, D. D., Frick, L. R., and Nielsen, T. F. D. 1999. Re-Os isotope geochemistry of Tertiary picritic and basaltic magmatism of East Greenland: constraints on plume-lithosphere interactions and the genesis of the Platinova reef, Skaergaard intrusion. *Lithos.* **47** (1-2): 107-126.

Buchanan, D. L. 1988. Platinum-Group Element Exploration. Developments in Economic Geology 26. Elsevier Science B.V. Amsterdam, The Netherlands.

Buchanan, D. L., Nolan, J., Suddaby, P., Rouse, J. E., Viljoen, M. J., and Davenport, J. W. J. 1981. The Genesis of Sulphide Mineralisation in a Portion of the Potgietersrus Limb of the Bushveld Complex. *Economic Geology*. **76**: 568-579.

Buchanan, D. L., and Rouse, J. E. 1984. Role of Contamination in the Precipitation of Sulphides in the Platreef of the Bushveld Complex. Sulphide deposits in mafic and ultramafic rocks, pp. 141-146.

Cabri, L. J. 1973. New Data on Phase Relations in the Cu-Fe-S System. *Economic Geology*. **68**: 443-454.

Cabri, L. J. 2002. The Geology, Geochemistry, Mineralogy and Mineral Beneficiation of Platinum-group Elements. *CIM Special Volume.* **54**: 852.

Cabri, L. J. 2015. Importance of sample preparation, representivity, and reporting methodologies for quantitative evaluation of precious metal mineralogy. Poster presented at the American Geophysical Union conference.

Cabri, L. J., and Laflamme, J. H. G. 1976. The mineralogy of the platinum group elements from some copper-nickel deposits of the Sudbury area, Ontario. *Economic Geology*. **71**: 1159-1195.

Cabri, L. J., and Laflamme, J. H. G. 1981. Analyses on minerals containing platinum-group elements. In: Platinum-Group Elements: Mineralogy, Geology, Recovery (L. J. Cabri Ed). *Canadian Institute Mining and Metallurgy.* Special Volume **23**: 151-173.

Cameron, E. N. 1982. The upper critical zone of the eastern Bushveld Complex; precursor of the Merensky Reef. *Economic Geology.* **77** (6): 1307-1327.

Campbell, I. H., and Barnes, S. J. 1984. A Model for the Geochemistry of the Platinum-Group Elements in Magmatic Sulphide Deposits. *Canadian Mineralogist*. **22**: 151-160

Campbell, I. H., and Naldrett, A. J. 1979. The influence of silicate:sulphide ratios on the geochemistry of magmatic sulphides. *Economic Geology.* **74**: 2248-2253.

Campbell, I. H., Naldrett, A. J., and Barnes, S. J. 1983. A model for the origin of the platinum-rich sulphide horizons in the Bushveld and Stillwater Complexes. *Journal of Petrology*. **24**: 133-165.

Canfield, D. E., Raiswell, R., Westrich, J. T., Reaves, C. M., and Berner, R. A. 1986. The use of chromium reduction in the analysis of reduced inorganic sulfur in sediments and shales. *Chemical Geology*. **54** (1-2): 149-155.

Cawthorn, R. G. 2003. Genesis of magmatic oxide deposit—a view from the Bushveld Complex. *Norges Geologsike Undersokelse*. Special Publication **9**: 11–20.

Cawthorn, R. G. 2005. Chapter 3: Stratiform Platinum-Group Element Deposits in Layered Intrusions. In: Mungall, J. E ed. Exploration for Platinum-Group Element Deposits. *Mineralogical Association of Canada Short Course Series.* **35**: 57 - 73.

Cawthorn, R.G. 2010. The Platinum Group Element Deposits of the Bushveld Complex in South Africa. *Platinum Metals Review.* **54** (4): 205-215.

Cawthorn, R. G. 2011. Geological interpretations from the PGE distribution in the Bushveld Merensky and UG2 chromitite reefs. *Journal of the South African Institute of Mining and Metallurgy*. **111**: 67–79.

Cawthorn, R. G., Barnes, S. J., Ballhaus, C., and Malitch, K. N. 2005. Platinum Group Element, Chromium and Vanadium Deposits in Mafic and Ultramafic Rocks. *Economic Geology*. 100th anniversary volume, pp. 215-249

Cawthorn, R. G., Barton, J.M., and Vilijoen, M.J. 1985. Interaction of Floor Rocks with the Platreef on Overysel, Potgietersrus, Northern Transvaal. *Economic Geology*. **80**: 988-1006.

Cawthorn, R. G., Lee, C. A., Schouwstra, R. P., and Mellowship, P. 2002. Relationship between PGE and PGM in the Bushveld Complex. *The Canadian Mineralogist*. **40**: 311-328.

Cawthorn, R. G., and Walraven, F. 1998. Emplacement and Crystallisation Time for the Bushveld Complex. *Journal of Petrology*. **39** (9): 1669 – 1687.

Cawthorn, R. G., and Webb, S. J. 2001. Connectivity between the western and eastern limbs of the Bushveld Complex. *Tectonophysics*. **330:** 195 – 209.

Chamber of Mines of South Africa. 2014. Facts and Figures 2013-2014. Accessed from http://www.chamberofmines.org.za/media-room/facts-and-figures on the 10/10/2015.

Cheney, E. S., and Twist, D. 1991. The conformable emplacement of the Bushveld mafic rocks along a regional unconformity in the Transvaal succession of South Africa. *Precambrian Research.* **52**: 115-132.

Chetty, D., Gryffenberg, L., Lekgetho, T.B., and Molebale, I. J. 2009. Automated SEM study of PGM distribution across a UG2 flotation concentration bank: implications for understanding PGM floatability. *The Journal of the Southern African Institute of Mining and Metallurgy*. **109**: 587-593.

Chung, H-Y., and Mungall, J. E. 2009. Physical constraints on the migration of immiscible fluids through partially molten silicates, with special reference to magmatic sulphide ores. *Earth and Planetary Science Letters*. **286**: 14-22.

Clarke, B., Uken, R., and Reinhardt, J. 2009. Structural and compositional constraints on the emplacement of the Bushveld Complex, South Africa. *Lithos*. **111**: 21-36.

Cole, J., Webb, S. J., Finn, C. A. 2014. Gravity models of the Bushveld Complex – Have we come full circle? *Journal of African Earth Sciences.* **92**: 97-118.

Cornell, D. H., Schütte, S. S., and Eglington, B. L. 1996. The Ongeluk basaltic andesite formation in Griqualand West, South Africa: submarine alteration in a 2222 Ma Proterozoic sea. *Precambrian Research*. **79**: 101-123.

Dare, S. A. S., Barnes, S-J., and Prichard, H. M. 2010. The distribution of platinum-group elements (PGE) and other chalcophile elements among sulphides from the Creighton Ni-Cu-PGE sulphide deposit, Sudbury, Canada, and the origin of palladium in pentlandite. *Mineralium Deposita*. **45** (8): 765-793.

Dare, S. A. S., Barnes, S-J., Prichard, H. M., and Fisher, P. C. 2011. Chalcophile and platinum-group element (PGE) concentrations in the sulphide minerals from the McCreedy East deposit, Sudbury, Canada, and the origin of PGE in pyrite. *Mineralium Deposita*. **46**: 381- 407.

Dare, S. A. S., Barnes, S-J., Prichard H. M., and Fisher, P. C. 2014. Mineralogy and Geochemistry of Cu-Rich Ores from the McCreedy East Ni-Cu-PGE Deposit (Sudbury, Canada): Implications for the Behaviour of Platinum Group and Chalcophile Elements at the End of Crystallization of a Sulphide Liquid. *Economic Geology.* **109**:343–366.

Deer, W. A., Howie, R. A., and Zussman, J. 1992. An introduction to the rock forming minerals. Pearson Prentice Hall, China (2nd edition). p 12-13.

Department of Mines. 1978. 2428 Nylstroom. Geological Survey South Africa. Printed in Pretoria, South Africa.

Department of Mineral and Energy Affairs. 1985. 2328 Pietersburg. Geological Survey South Africa. Printed in Pretoria, South Africa.

Dorland, H. C. 2004. *Provenance Ages and Timing of Sedimentation of Selected Neoarchean and Paleoproterozoic Successions in the Kaapvaal Craton*. PhD Thesis at Rand Afrikaans University, Johannesburg. 326 pp.

Droop, G. T. R. 1987. A general equation for estimating Fe^{3+} concentrations in ferromagnesian silicates and oxides from microprobe analyses, using stoichiometric criteria. *Mineralogical Magazine.* **51**: 431-5.

Duan, J., Li, C., Qian, Z., Jiao, J., Ripley, E. M., Feng, Y. 2016. Multiple S isotopes, zircon Hf isotopes, whole-rock Sr-Nd isotopes, and spatial variations of PGE tenors in the Jinchaun Ni-Cu-PGE deposit, NW China. *Miner Deposita*. **51**: 557-574.

Eales, H. V., and Cawthorn, R.G. 1996. The Bushveld Complex. In *Developments in Petrology 15* Layered Intrusions Ed. Cawthorn, R.G. Elsevier Science B.V. Amsterdam, The Netherlands.

Eales, H. V., and Costin, G. 2012. Crustally Contaminated Komatiite: Primary Source of the Chromitites and Marginal, Lower and Critical Zone Magmas in a Staging Chamber Beneath the Bushveld Complex. *Economic Geology*. **107**: 645 – 665.

Eales, H. V., De Klerk, W. J. and Teigler, B., 1990. Evidence for magma mixing processes within the Critical and Lower Zones of the northwestern Bushveld Complex, South Africa. *Chemical Geology*. **88** (3-4): 261-278.

Eales, H. V., and Reynolds, I. M. 1986. Cryptic variations within chromitites of the upper critical zone, northwestern Bushveld Complex. *Economic Geology*. **81** (5): 1056-1066.

Eckstrand, O.R., and Hulbert, L.J. 2007. Magmatic nickel-copper-platinum group element deposits, in Goodfellow, W.D., ed., Mineral Deposits of Canada: A Synthesis of Major Deposit Types, District Metallogeny, the Evolution of Geological Provinces, and Exploration Methods: Geological Association of Canada, Mineral Deposits Division, Special Publication. **5**: 205-222.

European Commission. 2014. Enterprise and Industry. Defining 'critical' raw materials. Accessed from http://ec.europa.eu/enterprise/policies/raw-materials/critical/index_en.htm on the 23/01/2015.

European Commission. 2017. Study on the review of the list of Critical Raw Materials – Final Report. Accessed from http://ec.europa.eu/growth/sectors/raw-materials/specific-interest/critical_en on the 20/10/2018.

Farquhar, J., Bao, H., and Thiemens, M. 2000. Atmospheric Influence of Earth's Earliest Sulfur Cycle. *Science*. **289**: 756-758.

Farquhar, J., and Wing, B. A. 2003. Multiple sulfur isotopes and the evolution of the atmosphere. *Earth and Planetary Science Letters*. **213**: 1-13.

Farquhar, J., Wing, B. A., McKeegan, K. D., Harris, J. W., Cartigny, P., and Thiemens, M. H. 2002. Mass Independent Sulphur Inclusions in Diamond and Sulphur Recycling on Early Earth. *Science*. **298**: 2369-2372.

Farquhar, J., Wu, N., Canfield, D. E., and Oduro, H. 2010. Connections between Sulfur Cycle Evolution, Sulfur Isotopes, Sediments, and Base Metal Sulfide Deposits. *Economic Geology*. **105**: 509-533.

Finnigan, C. S., Brenan, J. M., Mungall, J. E., and McDonough, W. F. 2008. Experiments and Models Bearing on the Role of Chromite as a Collector of Platinum Group Minerals by Local Reduction. *Journal of Petrology.* **49** (9): 1647 – 1665.

Fleet, M. E. 2006. Phase equilibria at high temperatures. *Reviews in Mineralogy and Geochemistry*. **61**: 365-420.

Fleet, M. E., Chryssoulis, S. L., Stone, W. E., and Weisener, C. G. 1993. Partitioning of platinum-group elements and Au in the Fe-Ni-Cu-S system: experiments on the

fractional crystallisation of sulphide melt. *Contributions to Mineralogy and Petrology*. **115**: 36-44

Fleet, M. E., Crocket, J. H., Liu, M., and Stone, W. E. 1999. Laboratory partitioning of platinum-group elements (PGE) and gold with application to magmatic sulphide – PGE deposits. *Lithos*. **47**: 127-142.

Fleet, M. E., Liu, M., and Crocket, J. H. 1999. Partitioning of trace amounts of highly siderophile elements in the Fe-Ni-S system and their fractionation in nature. *Geochimica et Cosmochimica Acta.* **63** (17): 2611 – 2622.

Fleet, M. E., and Stone, W. E. 1991. Partitioning of platinum-group elements in the Fe-Ni-S system and their fractionation in nature. *Geochimica et Cosmochimica Acta.* **55**: 245 – 253.

Frauenstein, F., Veizer, J., Beukes, N., van Niekerk, H. S., Coetzee, L. L. 2009. Transvaal Supergroup carbonates: Implications for Paleoproterozoic $\delta^{18}O$ and $\delta^{13}C$ records. *Precambrian Research*. **175**: 149-160.

Gain, S. B. 1985. The geologic setting of the platiniferous UG-2 chromitite layer on the farm Maandagshoek, eastern Bushveld Complex. *Economic Geology*. **80** (4): 925-943.

Gain, S. B., and Mostert, A. B. 1982. The geological setting of the platinoid and base metal sulphide mineralisation in the Platreef of the Bushveld Complex on Drenthe, north Potgietersrus. *Economic Geology*. **77**: 1395-1404.

Gauert, C. 2001. Sulphide and oxide mineralisation in the Uitkomst Complex, South Africa: origin in a magma conduit. *Journal of African Earth Sciences*. **32** (2): 149-161.

Gilbert, S. E., Danyushevsky, L., Robinson, P., Wohlgemuth-Ueberwasser, C., Pearson, N., Savard, D., Norman, M., and Hanley, J. 2013. A Comparative Study of Five Reference Materials and the Lombard Meteorite for the Determination of the Platinum-Group Elements and Gold by LA-ICP-MS. *Geostandards and Geoanalytical Research.* **37** (1): 51-64.

Godel, B., Barnes, S-J., and Maier, W. D. 2006. 3-D Distribution of Sulphide Minerals in the Merensky Reef (Bushveld Complex, South Africa) and the J-M Reef (Stillwater Complex, USA) and their Relationship to Microstructures Using X-Ray Computed Tomography. *Journal of Petrology*. **47** (9): 1853-1872.

Godel, B., Barnes, S-J., and Maier, W. D. 2007. Platinum-Group Elements in Sulphide Minerals, Platinum-Group Minerals, and Whole-Rocks of the Merensky Reef (Bushveld Complex, South Africa): Implications for the Formation of the Reef. *Journal of Petrology*. **48** (8):1569-1604.

Good, N., and de Wit, M.J. 1997. The Thabazimbi-Murchison Lineament of Kaapvaal Craton, South Africa: 2700 Ma of Episodic Deformation. *Journal of the Geological Society of London.* **154**: 93-97.

Grobler, D. F., Brits, J. A. N., Maier, W. D., and Crossingham, A. 2018. Litho- and chemostratigraphy of the Flatreef PGE deposit, northern Bushveld Complex. *Mineralium Deposita*. **54** (1): 3-28.

Grobler, D. F., and Dunnett, T. 2016. New Stratigraphic Framework for the Platreef Project, Northern Limb, Bushveld Complex. Internal Document.

Grobler, D. F., and Nielsen, S. A. 2012. Upper Critical Zone (Merensky Reef – UG2) Correlates within the Platreef, Turfspruit 241KR, Northern Limb, Bushveld Igneous Complex: Internal Report, Platreef Resources Pty Ltd., 27 February 2012, 31 p.

Groves, D. I., Ho, S. E. Rock, N. M. S., Barley, M. E., Muggeridge, M. T. 1987. Archean cratons, diamond and platinum: Evidence for coupled long-lived crust-mantle systems. *Geology*. **15**: 801-805.

von Gruenewaldt, G. 1979. A Review of Some Recent Concepts of the Bushveld Complex, with Particular Reference to Sulphide Mineralisation. *Canadian Mineralogist.* **17**: 233-256.

von Gruenewaldt, G., and Harmer R.E. 1992. Tectonic setting of Proterozoic layered intrusions with reference to the Bushveld Complex. In: Proterozoic Crustal Evolution, Ed: Condie, K. C. Developments in Precambrian Geology 10. Elsevier, Amsterdam.

von Gruenewaldt, G., Hulbert, L. J., and Naldrett, A. J. 1989. Contrasting platinum-group element concentration patterns in cumulates of the Bushveld Complex. *Mineralium deposita.* **24** (3):219-229.

Gunn, G. 2014. *Critical Metals Handbook*. John Wiley & Sons.

Gunn, G., Benham, A., and Minks, A. 2009. Platinum commodity profile. British Geological Society. Accessed from https://www.bgs.ac.uk/downloads/start.cfm?id=1401 on the 15/02/2015.

Guo, Q., Strauss, H., Kaufman, A. J., Schröder, S., Gutzmer, J., Wing, B., Baker, M. A., Bekker, A., Jin, Q., Kim, S-T., and Farquhar, J. 2009. Reconstructing Earth's surface oxidation across the Archean-Proterozoic transition. *Geology*. **37** (5): 399-402.

Gutzmer, J., and Beukes, N. J. 1998. High grade manganese ores in the Kalahari manganese field: Characterisation and dating of ore forming events. Unpublished report. Rand Afrikaans University, Johannesburg. 221 pp.

Hall, A.L. 1932. The Bushveld Igneous Complex in the central Transvaal. Geological Society, South Africa Memoir. **28**: 554p.

Hall, G. E. M., Pelchat, J. -C. and Loop, J. 1988. Separation and recovery of various sulphur species in sedimentary rocks for stable sulphur isotopic determination. *Chemical Geology.* **67:** 35-45.

Hanley, J. J., Mungall, J. E., Spooner, E. T. C. and Pettke, T. 2005. Fluid and melt inclusion evidence for platinum-group element transport by high salinity fluids and halide melts below the JM Reef, Stillwater Complex. In Montana, USA: 10th International Platinum Symposium "Platinum-Group Elements-from Genesis to Beneficiation and Environmental Impact", Oulu, Finland (pp. 94-97).

Hannah, J. L., Bekker, A., Stein, H. J., Markey, R. J., and Holland, H. D. 2004. Primitive Os and 2316 Ma age for marine shale: implications for Paleoproterozoic glacial events and the rise of atmospheric oxygen. *Earth and Planetary Science Letters*. **225**: 43-52.

Harmer, R. E., and Armstrong, R. A. 2000. Duration of Bushveld (sensu lato) magmatism: constraints from new SHRIMP zircon chronology. Abstract, Workshop on the Bushveld Complex, Gethlane Lodge, Burgersfort.

Harmer, R. E., and Sharpe, M. R. 1985. Field relation and strontium isotope systematics of the marginal rocks of the eastern Bushveld Complex. *Economic Geology*. **80**: 813-837.

Harney, D. M. W., and Von Gruenewaldt, G. V. 1995. Ore-forming processes in the upper part of the Bushveld Complex, South Africa. *Journal of African Earth Sciences*. **20** (2): 77 – 89.

Harris, C., and Chaumba, J. B. 2001. Crustal Contamination and Fluid-Rock Interaction during the Formation of the Platreef, Northern Limb of the Bushveld Complex, South Africa. *Journal of Petrology*. **42** (7): 1321 – 1347.

Hatton, C. J. 1995. Mantle plume origin for the Bushveld and Ventersdorp magmatic provinces. *Journal of African Earth Sciences.* **21** (4): 571-577.

Helmy, H. M., Ballhaus, C., Berndt, J., Bockrath, C., and Wohlgemuth-Ueberwasser, C. 2007. Formation of Pt, Pd and Ni tellurides: experiments in sulfide-telluride systems. *Contrib Mineral Petrol.* **153**:577-591.

Helmy, H. M., Ballhaus, C., Wohlgemuth-Ueberwasser, C., Fonseca, R. O. and Laurenz, V. 2010. Partitioning of Se, As, Sb, Te and Bi between monosulfide solid solution and sulfide melt–application to magmatic sulfide deposits. *Geochimica et Cosmochimica Acta*. **74** (21): 6174-6179.

Hiebert, R. S., Bekker, A., Wing, B. A., and Rouxel, O. J. 2013. The Role of Paragneiss Assimiliation in the Origin of the Voisey's Bay Ni-Cu Sulfide Deposit, Labrador: Multiple S and Fe Isotope Evidence. *Economic Geology*. **108**: 1459-1469.

Hiemstra, S. A. 1985. The distribution of some platinum-group elements in the UG-2 chromitite layer of the Bushveld Complex. *Economic Geology.* **80** (4): 944-957.

Hoatson, D. M. 1998. Platinum-group element mineralisation in Australian Precambrian layered mafic-ultramafic intrusions. *AGSO Journal of Australian Geology and Geophysics.* **17**: 139-152.

Holness, M. B., Nielsen, T. F. D., Tegner, C. 2017. The Skaergaard Intrusion of East Greenland: Paradigms, Problems and New Perspectives. *Elements*. **13**: 391-396.

Holwell., D. A., Adeyemi, Z., Ward, L. A., Smith, D. J., Graham, S. D., McDonald, I., Smith, J. W. 2017. Low temperature alteration of magmatic Ni-Cu-PGE sulphides as a source for hydrothermal Ni and PGE ores: A quantitative approach using automated mineralogy. *Ore Geology Reviews.* **91:** 718-740.

Holwell, D. A., Armitage, P.E.B., and McDonald, I. 2005. Observations on the relationship between the Platreef and its hangingwall. *Applied Earth Science (Trans. Inst. Min. Metall. B*). **114**: B199 – 207.

Holwell, D. A., Boyce, A. J., and McDonald, I. 2007. Sulphur Isotope Variations within the Platreef Ni-Cu-PGE Deposit: Genetic Implications for the Origin of Sulphide Mineralisation. *Economic Geology*. **102**: 1091-1110.

Holwell D. A., and Jordaan, A. 2006. Three-dimensional mapping of the Platreef at the Zwartfontein South mine: implications for the timing of magmatic events in the northern limb of the Bushveld Complex, South Africa. *Applied Earth Science (Trans. Inst. Min. Metall. B*). **115** (2): 41-48.

Holwell D. A., and McDonald, I. 2007. Distribution of platinum-group elements in the Platreef at Overysel, northern Bushveld Complex: a combined PGM and LA-ICP-MS study. *Contrib Mineral Petrol.* **154**: 171 – 190.

Holwell, D. A., and McDonald, I. 2010. A Review of the Behaviour of Platinum Group Elements within Natural Magmatic Sulphide Ore Systems. *Platinum Metals Review.* **54** (1): 26-36.

Holwell, D. A., McDonald, I., and Armitage, P.E.B. 2006. Platinum-group mineral assemblages in the Platreef at the Sandsloot Mine, northern Bushveld Complex, South Africa. *Mineralogical Magazine.* **70** (1): 83 – 101.

Holwell, D. A., McDonald, I., and Butler, I.B. 2011. Precious metal enrichment in the Platreef, Bushveld Complex, South Africa: evidence from homogenised magmatic sulphide melt inclusions. *Contributions Mineral Petrology*. **161**: 1011-1026.

Huber, H., Koeberl, C., McDonald, I., and Reimold, U. W. 2001. Geochemistry and petrology of Witwatersrand and Dwyka diamictites from South Africa: Search for an extraterrestrial component. *Geochimica et Cosmochimica Acta*. **65** (12): 2007-2016.

Hughes, H. S. R. 2015. *Temporal, Lithospheric and Magmatic Process Controls on Ni, Cu and Platinum-Group Element (PGE) Mineralisation: A Case Study from Scotland*. PhD Thesis, Cardiff University.

Hulbert, L. J. 1983. A petrographical investigation of the Rustenburg Layered Suite and associated mineralization south of Potgietersrus. D.Sc. dissertation, Pretoria, South Africa, The University of Pretoria.

Hulbert, L. J., and von Gruenewaldt, G. 1982. Nickel, Copper and Platinum Mineralisation in the Lower Zone of the Bushveld Complex, South of Potgietersrus. *Economic Geology.* **77**: 1296-1306.

Hulbert, L. J., and von Gruenewaldt, G. 1985. Textural and Compositional Features of Chromite in the Lower and Critical Zones of the Bushveld Complex South of Potgietersrus. *Economic Geology*. **80**: 872-895

Hutchinson, D., Foster, J., Prichard, H., and Gilbert, S. 2015. Concentration of Particulate Platinum-Group Minerals during Magma Emplacement; a Case Study from the Merensky Reef, Bushveld Complex. *Journal of Petrology.* **56** (1): 113 – 159.

Hutchinson, D., and Kinnaird, J. 2005. Complex multistage genesis for the Ni-Cu-PGE mineralisation in the southern region of the Platreef, Bushveld Complex, South Africa. *Applied Earth Science (Trans. Inst. Min. Metall. B).* **114**: 208-224.

Hutchinson, D., Kinnaird J. A., and Schurmann, L. 2004. Complex multi-stage mineralisation history in the southern sector of the Platreef, Bushveld Complex, South Africa. Abstract Volume Geoscience Africa, University of the Witwatersrand, South Africa.

Hutchinson, D., and McDonald, I. 2008. Laser ablation ICP-MS study of platinum-group elements in sulphides from the Platreef at Turfspruit, northern limb of the Bushveld Complex, South Africa. *Mineralium Deposita*. **43**:695-711.

Huthmann, F. M., Yudovskaya, M. A., Frei, D., and Kinnaird, J. A. 2016. Geochronological evidence for an extension of the Northern Limb of the Bushveld Complex, Limpopo Province, South Africa. Precambrian Research. **280**: 61-75.

Huthmann, F. H., Yudovskaya, M. A., Kinnaird, J., McCreesh, M., and McDonald, I. 2018. Geochemistry and PGE of the lower mineralised Zone of the Waterberg Project, South Africa. *Ore Geology Reviews*. **92**: 161-185.

Ihlenfeld, C., and Keays, R. R. 2011. Crustal contamination and PGE mineralisation in the Platreef, Bushveld Complex, South Africa: evidence for multiple contamination events and transport of magmatic sulphides. *Mineralium Deposita*. **46**: 813-832.

Irvine, T. N. 1975. Crystallization sequences in the Muskox intrusion and other layered intrusions—II. Origin of chromitite layers and similar deposits of other magmatic ores. *Geochimica et Cosmochimica Acta.* **39:** 991-1020.

Irvine, T. N. 1977. Origin of chromitite layers in the Muskox intrusions and other stratiform intrusions: a new interpretation. *Geology.* **5:** 273-277.

Ivanhoe Mines. 2015. Platreef Project. Accessed from http://www.ivanhoemines.com/s/platreef.asp, on the 23/01/2015.

Johnson, T. E., Brown, M., Gibson, R., and Wing, B. 2004. Spinel-cordierite synplectite replacing andalusite: evidence for melt-assisted diapirism in the Bushveld Complex, South Africa. *Journal of Metamorphic Geology.* **22:** 529-545.

Johnson, T. E., Brown, M., and White, R. W. 2010. Petrogenetic modelling of strongly residual metapelitic xenoliths within the southern Platreef, Bushveld Complex, South Africa. *Journal of Metamorphic Geology.* **28**: 269-291.

Johnson, T. E., Gibson, R. L., Brown, M., Buick, I. S., and Cartwright, I. 2003. Partial Melting of Metapelitic Rocks Beneath the Bushveld Complex, South Africa. *Journal of Petrology.* **44** (5): 789-813.

Johnson Matthey. 2013. Platinum 2013 Interim Review. Accessed from http://www.platinum.matthey.com/documents/market-review/2013-interim/presentation-to-analysts/platinum-2013-interim-review-slide-presentation-.pdf, on the 05/02/2015.

Johnson Matthey. 2015. Production. South Africa. Accessed from http://www.platinum.matthey.com/about-pgm/production/south-africa, on the 15/02/2015.

Johnson Matthey. 2018a. PGM Market Report. Accessed from http://www.platinum.matthey.com/services/market-research/pgm-market-reports on the 01/12/2018.

Johnson Matthey. 2018b. Price Charts. Accessed from http://www.platinum.matthey.com/prices/price-charts on the 22/10/2018

Jones, R. E. 2013. *Petrological and geochemical study of Platreef chromitites, northern Bushveld, South Africa.* PhD thesis. Cardiff University.

Jugo, P.J., and Lesher, C.M., 2005. Redox changes caused by evaporate and carbon assimilation at Noril'sk and their role in sulfide precipitation [abs.]. Geological Society of America Abstracts with Programs 39, 360.

Junge, M., Oberthür, T., Kraemer, D., Melcher, F., Piña, R., Derrey, I. T., Manyeruke, T., and Strauss, H. 2018. Distribution of platinum-group elements in pristin and near-surface oxidised Platreef ore and the variation along strike, northern Bushveld Complex, South Africa. *Mineralium Deposita*, pp. 1-28.

Junge, M., Oberthür, T., and Melcher, F. 2014. Cryptic variation of chromite chemistry, platinum group element and platinum group mineral distribution in the UG2 chromitite:

an example from the Karee mine, western Bushveld Complex, South Africa. *Economic Geology.* **109**: 795-810.

Junge, M., Wirth, R., Oberthür, T., Melcher, F., and Schreiber, A. 2015. Mineralogical siting of platinum-group elements in pentlandite from the Bushveld Complex, South Africa. *Mineralium Deposita*. **50**: 41-54.

Katz, A. 2015. Investopedia. A Beginner's Guide to Precious Metals. Accessed from http://www.investopedia.com/articles/basics/09/precious-metals-gold-silver-platinum.asp, on the 15/02/2015.

Keays, R. R. 1995. The role of komatiitic and picritic magmatism and S-saturation in the formation of ore deposits. *Lithos*. **34**: 1-18.

Kelley, S. P and Fallick, A. E. 1990. High precision spatially resolved analysis of $\delta^{34}S$ in sulphides using a laser extraction system. *Geochimica et Cosmochimica Acta*. **54**: 883–888.

Kerr, A., and Leitch, A. M. 2005. Self-Destructive Sulphide Segregation Systems and the Formation of High-Grade Magmatic Ore Deposits. *Economic Geology*. **100**: 311-332.

Kinloch, E. D. 1982. Regional Trends in the Platinum-Group Mineralogy of the Critical Zone of the Bushveld Complex, South Africa. *Economic Geology*. **77:** 1328-1347.

Kinloch, E. D., and Peyerl, W. 1990. Platinum-group minerals in various rock types of the Merensky Reef: Genetic implications. *Economic Geology*. **85**: 537-555.

Kinnaird, J. A. 2005. Geochemical evidence for multiphase emplacement in the southern Platreef. *Applied Earth Science (Trans. Inst. Min. Metall. B).* **114**: 225-242.

Kinnaird, J. A. 2008. An Overview of the Platreef [abs]. Platreef Workshop, 3rd, Mokopane, 11th – 13th July 2008, Abstracts.

Kinnaird, J.A., and McDonald, I. 2005. An introduction to the mineralisation in the northern limb of the Bushveld Complex. *Transactions of the Institute of Mining and Metallurgy*. **114**: 194 – 198.

Kinnaird, J.A., and McDonald, I. 2018. The Northern Limb of the Bushveld Complex: A New Economic Frontier. SEG Special Publication. **21**: 157-177.

Kinnaird, J. A., Yudovskaya, M., McCreesh, M., Huthmann, F., Botha, T. J. 2017. The Waterberg Platinum Group Element Deposit: Atypical Mineralisation in Mafic-Ultramafic Rocks of the Bushveld Complex, South Africa. *Economic Geology*. **112** (6): 1367-1394.

Klein, C., and Beukes, N. J. 1989. Geochemistry and Sedimentology of a Facies Transition from Limestone to Iron-Formation Deposition in the Early-Proterozoic Transvaal Supergroup, South Africa. *Economic Geology*. **84** (7): 1733-1774.

Klemd, R., Junge, T., Oberthür, T., Herderich, R., Schouwstra, R., and Roberts, J. 2016. Platinum-group element concentration in base-metal sulphides from the Platreef, Mogalakwena Platinum Mine, Bushveld Complex, South Africa. *South African Journal of Geology*. **119** (4): 623-638.

Klemm, D. D., Henckel, J., Dehm, R., and von Gruenewaldt, G. 1985. The Geochemistry of Titanomagnetite in Magnetite Layers and Their Host Rocks of the Eastern Bushveld Complex. *Economic Geology.* **80**: 1075-1088.

de Klerk, W. J. 1992. *Petrogenesis of the Upper Critical Zone of the Western Bushveld Complex with emphasis on the UG1 footwall and Bastard units*. Ph.D. thesis, Rhodes University, Grahamstown, pp. 294.

de Klerk, L. 2005. Bushveld Stratigraphy on Rooipoort, Potgietersrus Limb [abs.]. Platreef Workshop, 2nd, Mokopane, South Africa, 28th – 30th October 2005. Abstracts.

Kruger, F., J. 1994. The Sr-isotopic stratigraphy of the western Bushveld Complex. *South African Journal of Geology*. **97** (4):393-398.

Kruger, F., J. 2005. Filling the Bushveld Complex magma chamber: lateral expansion, roof and floor interaction, magmatic unconfrmities, and the formation of giant chromitite, PGE and Ti-V magnetite deposits. *Mineralium Deposita.* **40**: 451-472.

Kruger, F. J. 2010. The Merensky and Bastard cyclic units and the Platreef of the Bushveld Complex: consequences of Main Zone magma influxes and dynamics. The 4th International Platinum Conference, Platinum in transition 'Boom or Bust', The Southern African Institute of Mining and Metallurgy. 43-46 pp.

Kvadsheim A. 2017. "*Origin and development of sulphide bearing norites in the basal Platreef, Turfspruit, Northern Bushveld*". MESci dissertation, Cardiff University.

Labidi, J., Cartigny, P., Birck, J. L., Assayag, N. & Bourrand, J. J. 2012. Determination of multiple sulphur isotopes in glasses: A reappraisal of the MORB $\delta^{34}S$. *Chemical Geology.* **334:** 189-198.

Latypov, R., Chistyakova, S., and Kramers, J. 2017. Arguments against syn-magmatic sills in the Bushveld Complex, South Africa. *South African Journal of Geology*. **120** (4): 565-574.

Latypov, R., Chistyakova, S., Page, A., and Hornsey, R. 2016. Field Evidence for the In Situ Crystallisation of the Merensky Reef. *Journal of Petrology*. **56** (12): 2341-2372.

Lee, C. A. 1996. A review of mineralisation in the Bushveld Complex and some other Layered Intrusions. In *Developments in Petrology 15* Layered Intrusions Ed. Cawthorn, R.G. Elsevier Science B.V. Amsterdam, The Netherlands.

Lesher, C. M. 1989. Komatiite-associated nickel-sulphide deposits. In Ore Deposition Associated with Magmas (J. A. Whitney & Naldrett, A. J, eds). *Reviews in Economic Geology*. **4**: 45-101.

Lesher, C. M. 2017. Roles of xenomelts, xenoliths, xenocrysts, xenovolatiles, residues and skarns in the genesis, transport, and localisation of magmatic Fe-Ni-Cu-PGE sulphides and chromite. *Ore Geology Reviews*. **90**: 465-484

Lesher, C. M., and Burnham, O. M. 2001. Multicomponent elemental and isotopic mixing in Ni-Cu-(PGE) ores at Kambalda, Western Australia. *The Canadian Mineralogist*. **39**: 421-446.

Li, C., Maier, W. D., and de Waal, S. A., 2001. The role of magma mixing in the genesis of PGE mineralisation in the Bushveld Complex: Thermodynamic calculations and new interpretations. *Economic Geology*. **96**: 653-662.

Li, C. and Ripley, E. M. 2006. Formation of Pt–Fe alloy by desulfurization of Pt–Pd sulfide in the J–M reef of the Stillwater complex, Montana. *The Canadian Mineralogist.* **44** (4): 895-903.

Li, C., Ripley, E. M., Maier, W. D., Gomwe, T. E. S. 2002. Olivine and sulfur isotopic compositions of the Uitkomst Ni-Cu sulphide ore-bearing complex, South Africa: evidence for sulfur contamination and multiple magma emplacements. *Chemical Geology*. **188**: 149-159.

Li, C., Ripley, E. M., and Naldrett, A. J. 2003. Compositional Variations of Olivine and Sulfur Isotopes in the Noril'sk and Talnakh Intrusions, Siberia: Implications for Ore-Forming Processes in Dynamic Magma Conduits. *Economic Geology*. **98**: 69-86.

Li, C., Ripley, E.M., Merino, E and Maier, WD. 2004. Replacement of base metal sulphides by actinolite, epidote, calcite and magnetite in the UG2 and Merensky Reef of the Bushveld Complex. *Economic Geology*. **99**:173-184.

Li, C., Ripley, E. M., Sarkar, A., Shin, D., Maier, W. D. 2005. Origin of phlogopite-orthopyroxene inclusions in chromites from the Merensky Reef of the Bushveld Complex, South Africa. *Contrib Mineral Petrol*. **150**: 119-130.

Li, C., Ripley, E. M., and Naldrett, A. J. 2009. A new genetic model for the giant Ni-Cu-PGE sulfide deposits associated with the Siberian flood basalts. *Economic Geology*. **104**: 291-301.

Liebenberg, L. 1968. *The sulphides in the layered sequence of the Bushveld Igneous Complex.* DSc. Thesis, University of Pretoria, 260 p. Unpublished.

Liebenberg, L. 1979. The sulphides in the layered sequence of the Bushveld igneous complex. *Geological Society of Southern Africa Special Publication*. **1**: 108-208.

Lightfoot, P. C. 2007. Advances in Ni-Cu-PGE Sulphide Deposit Models and Implications for Exploration Targets. In “Proceeding of Exploration 07: Fifth Decennial International Conference on Mineral Exploration” edited by B. Milkereit. 629-646.

Lightfoot, P., and Hawkesworth, C. J. 1988. Origin of Deccan Trap lavas: evidence from combined trace element and Sr-, Nd- and Pb-isotope studies. *Earth and Planetary Science Letters.* **91** (1-2): 89-104.

Lightfoot, P. C., Hawkesworth, C. J., Devey, C. W., Rogers, N. W., Van Calsteren PWC 1990. Source and differentiation of Deccan Trap Lavas: implications of geochemical and mineral chemical variations. *Journal of Petrology*. **31**:1165–1200.

Lightfoot, P. C., Hawkesworth, C. J., Hergt, J., Naldrett, A. J., Gorbachev, N. S., Fedorenko, V. A., and Doherty, W. 1993. Remobilisation of the continental lithosphere by a mantle plume: major- and trace-element, and Sr-, Nd- and Pb-isotope evidence from picritic and tholeiitic lavas of the Noril’sk District, Siberian Trap, Russia. *Contributions to Mineralogy and Petrology*. **114** (2): 171-188.

Liu, Y., and Brenan, J. 2015. Partitioning of platinum-group elements (PGE) and chalcogens (Se, Te, As, Sb, Bi) between monosulfide-solid solution (MSS), intermediate solid solution and sulphide liquid at controlled fO^2-fS^2 conditions. *Geochimica et Cosmochimica Acta.* **159**: 139-161.

Lodders, K. 2003. Solar System Abundance and Condensation Temperatures of the Elements. *The Astrophysical Journal.* **591:** 1220-1247.

Lorand, J-P., Luguet, A., and Alard, O. 2013. Platinum-group element systematics and petrogenetic processing of the continental upper mantle: A review. *Lithos*. **164-167**: 2-21.

Lorand., J-P., and Luguet, A. 2016. Chalcophile and Siderophile Elements in Mantle Rocks: Trace Elements Controlled by Trace Minerals. *Reviews in Mineralogy & Geochemistry*. **81**: 441-488.

Maier, W. D. 2005. Platinum-group element (PGE) deposits and occurrences: Mineralisation styles, genetic concepts and exploration criteria. *Journal of African Earth Sciences.* **41**: 165 – 191.

Maier, W. D., and Barnes, S-J. 1998. Concentrations of rare earth elements in silicate rocks of the Lower, Critical and Main Zones of the Bushveld Complex. *Chemical Geology*. **150**: 85-103.

Maier, W. D., and Barnes., S-J. 1999. Platinum-Group Elements in Silicate Rocks of the Lower, Critical and Main Zones at Union Section, Western Bushveld Complex. *Journal of Petrology.* **40** (11): 1646-1671.

Maier, W. D., Barnes, S. J., Campbell, I. H., Fiorentini, M. L., Peltonen, P., Barnes, S-J., and Smithies, R. H. 2009. Progressive mixing of meteoritic veneer into the early Earth's deep mantle. *Nature.* **460**: 620-623.

Maier, W. D., Barnes, S-J., and Groves, D. I. 2013. The Bushveld Complex, South Africa: formation of platinum, chrome- and vanadium-rich layers via hydrodynamic sorting of a mobilized cumulate slurry in a large, relatively slowly cooling, subsiding magma chamber. *Mineralium Deposita*. **48**: 1-56.

Maier, W. D., Barnes, S-J., de Klerk, W. J., Teigler, B., and Mitchell, A. A. 1996. Cu/Pd and Cu/Pt of silicate rocks in the Bushveld Complex: Implications for platinum-group element exploration. *Economic Geology*. **91**:1151-1158.

Maier, W. D and Groves, D. I. 2011. Temporal and spatial controls on the formation of magmatic PGE and Ni-Cu deposits. *Mineralium Deposita.* **46**: 841 – 851.

Maier, W. D., de Klerk, L., Blaine, J., Manyeruke, T., Barnes, S-J., Stevens, M. V. A., Mavrogenes, J. A. 2008. Petrogenesis of contact-style PGE mineraliszation in the northern lobe of the Bushveld Complex: comparison of data from the farms Rooipoort, Townlands, Drenthe and Nonnenwerth. *Mineralium Deposita*. **43**: 255-280.

Maier, W. D., Peltonen, P., McDonald, I., Barnes, S. J., Barnes, S.-J., Hatton, C., and Viljoen, F. 2012. The concentration of platinum-group elements and gold in southern Africa and Karelian kimberlite-hosted mantle xenoliths: Implications for the noble metal content of Earth's mantle. *Chemical Geology.* **302-303**: 119-135.

Majzlan, J., Makovicky, M., Makovicky, E. and Rose-Hansen, J. 2002. The system Fe–Pt–S at 1100 C. *The Canadian Mineralogist*. **40**(2): 509-517

Malevskii,A . Y., et al., 1976, Minerals of the Pt_3Sn-Pd_3Sn series: Vsesoyuznoy Geog. *Obshchestvo Zapiski*. **105**: 9-17.

Malitch, K. N., Latypov, R. M., Badanina, I. Y., Sluzhenikin, S. F. 2014. Insights into ore genesis of Ni-Cu-PGE sulphide deposits of the Noril'sk Province (Russia): Evidence from copper and sulfur isotopes. *Lithos*. **204**: 172-187

Mandzuik, Z. L., and Scott, S. D. 1977. Synthesis, Stability and Phase Relations of Argenital Pentlandite in the System Ag-Fe-Ni-S. *Canadian Mineralogist.* **15**: 349-364.

Manyeruke, T. D., and Maier, W. D. 2004. The petrography and geochemistry of the Platreef on the farm Townlands, near Potgietersrus, northern Bushveld Complex. Platreef Workshop, Mokopane, 16th – 19th July, 2004, Abstracts.

Manyeruke, T. D., Maier, W. D., and Barnes, S-J. 2005. Major and trace element geochemistry of the Platreef on the farm Townlands, northern Bushveld Complex. *South African Journal of Geology*. **108**: 381-396.

Marquis, E. 2015. *Petrogenesis of the harzburgitic to troctolitic units in the Turfspruit Cyclic Unit, Northern Bushveld Complex, South Africa.* MESci Geology thesis. Cardiff University.

Martini., J. E. J. 1979. A copper-bearing bed in the Pretoria Group in northeastern Transvaal. *Geological Society of South Africa, Special Publication*. **6**: 65-72.

Mathez, E. A. 1989. Interactions Involving Fluids in the Stillwater and Bushveld Complexes: Observations from the Rocks. *Reviews in Economic Geology*. **4**: 167 – 177.

Mathez, E. A. 1995. Magmatic metasomatism and formation of the Merensky Reef, Bushveld Complex. *Contributions Mineralogy and Petrology*. **119**: 277-286.

Mathez, E. A., Agrinier, P., and Hutchinson, R. 1994. Hydrogen isotope composition of the Merensky Reef and related rocks, Atok section, Bushveld Complex. *Economic Geology*. **89**(4): 791-802.

Mathez, E. A., Hunter, R. H., and Kinzler, R. 1997. Petrologic evolution of partially molten cumulate: the Atok section of the Bushveld Complex. *Contributions Mineralogy and Petrology.* **129**: 20-34.

Mathez, E. A., and Mey, J. L. 2005. Character of the UG2 Chromitite and Host Rocks and Petrogenesis of its Pegmatoidal Footwall, Northeastern Bushveld Complex. *Economic Geology*. **100** (8): 1617-1630.

Mathez E.A. and Peach C.L. 1989. Geochemistry of Platinum-Group Elements in Mafic and Ultramafic Rocks. *Reviews in Economic Geology*. **4**: 33 – 41.

Matich, T. 2014. Platinum Outlook 2015: A Brighter New Year. Accessed from: http://platinuminvestingnews.com/9658-platinum-outlook-2015-brighter-year-aal-imp-lmi-south-africa-strike-russia-price.html, on the 15/02/2015.

Mavrogenes, J. A., and O'Neill, H. St. C. 1999. The relative effects of pressure, temperature and oxygen fugacity on the solubility of sulphide in mafic magmas. *Geochimica et Cosmochimica Acta.* **63** (7/8): 1173-1180.

McBirney, A. R. 1996. The Skaergaard Intrusion. In *Developments in Petrology 15* Layered Intrusions Ed. Cawthorn, R.G. Elsevier Science B.V. Amsterdam, The Netherlands.

McCallum, I. S. 1996. The Stillwater Complex. In: Cawthorn RG, (ed) Layered Intrusions. Elsevier Science, pp. 441–484.

McClaren, C. H. and de Villiers, J. P. 1982. The platinum-group chemistry and mineralogy of the UG-2 chromitite layer of the Bushveld Complex. *Economic Geology*. **77**(6): 1348-1366.

McDonald, I., Harmer, R. J, Holwell, D. A, Hughes, H. S. R, and Boyce, A. J. 2017. Cu-Ni-PGE mineralisation at the Aurora Project and potential for a new PGE province in the Northern Bushveld Main Zone. *Ore Geology Reviews*. **80**: 1135-1159.

McDonald, I., and Holwell, D. A. 2007. Did Lower zone magma conduits store PGE-rich sulphides that were later supplied to the Platreef? *South African Journal of Geology*. **110**: 611−616.

McDonald, I., and Holwell, D. A. 2011. Geology of the Northern Bushveld Complex and the Setting and Genesis of the Platreef Ni-Cu-PGE deposit. *Economic Geology*. **17**: 297 – 327.

McDonald, I., Holwell, D. A., and Armitage, P. E. B. 2005. Geochemistry and mineralogy of the Platreef and "Critical Zone" cumulates of the Northern limb of the Bushveld Complex, South Africa: implications for Bushveld Stratigraphy and the development of PGE mineralisation. *Mineralium Deposita.* **40**: 526 – 549.

McDonald, I., Holwell, D. A., and Wesley, B. 2009. Assessing the potential involvement of an early magma staging chamber in the generation of the Platreef Ni-Cu-PGE deposit in the northern limb of the Bushveld Complex: a pilot study of the Lower Zone Complex at Zwartfontein. *Applied Earth Science (Trans. Inst. Min. Metall. B).* **118** (1): 5-20.

McDonald, I., Jones, R. E., Holwell, D. A., and Butler, I. B. 2012. Platinum-group element tenors and S/Se ratios of Platreef sulphide melt inclusions [abs.]. Platreef Workshop, 5th, Mokopane, South Africa, 9th-12th January 2012. Abstracts.

McDonald, I., and Tredoux, M. 2005. The history of the Waterberg deposit: why South Africa's first platinum mine failed. *Applied Earth Sciences (Trans. Inst. Min. Metall. B)*. **114**: B264-B272.

McDonald, I., and Viljoen, K. S. 2006. Platinum-group element geochemistry of mantle eclogites: a reconnaissance study of xenoliths from the Orapa kimberlite, Botswana. *Applied Earth Science*. **115** (3): 81-93.

McDonough, W.F. 1998. Earth's core. In: Encyclopedia of geochemistry. Marshall, C.P. and Fairbridge, R.W. (Editors), Kluwer Academic Publishers, Dordrecht. 151-156

McDonough, W. F., and Sun, S.-s. 1995. The composition of the Earth. *Chemical Geology*. **120**: 223-253.

McFall, K., McDonald, I., and Tanner, D. 2018. Evidence for hydrothermal modification in the Aurora Cu-Ni-PGE prospect, Northern Bushveld Compled, South Africa. 13th International Platinum Symposium, 30th June – 6th July 2018. Abstract.

McLaren, C. H., and De Villiers, J. P. R. 1982. The platinum-group chemistry and mineralogy of the UG2 chromitite layer of the Bushveld Complex. *Economic Geology*. **77**: 1348-1366.

Meisel, T., and Horan, M. F. 2016. Analytical Methods for the Highly Siderophile Elements. *Reviews in Mineralogy & Geochemistry*. **81**: 89-106.

Merensky, H. 1925. Report on the platinum occurrence on the properties of Potgietersrust Platinums Limited. Report to Shareholders, London and Rhodesia Mining and Land Company Ltd., Johannesburg, South Africa, 6 pp.

van der Merwe, M. J. 1976. The Layered sequence of the Potgietersrus Limb of the Bushveld Complex. *Economic Geology*. **71** (7):1337-1351.

van der Merwe, M. J. 1978. *The geology of the basic and ultramafic rocks of the Potgietersrus limb of the Bushveld Complex*. Ph.D. thesis, South Africa, University of the Witwatersrand.

van der Merwe, M. J. 2008. The geology and structure of the Rustenburg Layered Suite in the Potgietersrus/Mokopane area of the Bushveld Complex. *Mineralium Deposita.* **43** (4): 405-419.

van der Merwe, F., Viljoen, F., and Knoper, M. 2012. The mineralogy and mineral associations of platinum group elements and gold in the Platreef at Zwartfontein, Akanani Project, Northern Bushveld Complex, South Africa. *Miner Petrol*. **106**: 25-38.

Meurer, W. P., Willmore, C. C., and Boudreau, A. E. 1999. Metal redistribution during fluid exsolution and migration in the Middle Banded series of the Stillwater Complex, Montana. *Lithos*. **47** (1-2): 143-156.

Meyer, R., and de Beer, J. H. 1987. Structure of the Bushveld Complex from resistivity measurements. *Nature.* **325**: 610-612.

Mills Davies J. E. 1925. The geology of the Transvaal platinum deposits. *S. Afr. Min. Eng.* **36:** 63-66.

Mitchell, A.A., 1990. The stratigraphy, petrography and mineralogy of the Main Zone of the northwestern Bushveld Complex. *South African Journal of Geology.* **93** (5-6): 818-831.

Mitchell, A. A., and Scoon, R. N. 2007. The Merensky Reef at Winnaarshoek, eastern Bushveld Complex: a primary magmatic hypothesis based on a wide reef facies. *Economic Geology*. **102**: 971-1009.

Mitchell, A. A., and Scoon, R. N. 2012. The Platreef of the Bushveld Complex, South Africa: A New Hypothesis of Multiple, Non-Sequential Magma Replenishment based on Observations at the Akanai Project, North-West of Mokopane. *South African Journal of Geology*. **115** (4): 535-550.

Molyneux, T.G. 1970a. The geology of the area in the vicinity of Magnet Heights, eastern Transvaal, with special reference to the magnetic iron ore. *Special Publication Geological Society South Africa.* **1**: 228-241.

Molyneux, T. G. 1970b. A geological investigation of the Bushveld Complex in the Sekhukhuneland and part of the Steelpoort Valley. *Transactions of the Geological Society of South Africa*. **77**: 329-338.

Mondal, S. K. and Mathez, E. A. 2006. Origin of the UG2 chromitite layer, Bushveld Complex. *Journal of Petrology*. **48** (3): 495-510.

Mostert, A.B., Hofmeyr, P.K. and Potgieter, G.A., 1982. The platinum-group mineralogy of the Merensky Reef at the Impala platinum mines, Bophuthatswana. *Economic Geology*. **77**(6): 1385-1394.

Mudd, G.M. 2012. Key trends in the resource sustainability of platinum group elements. *Ore Geology Reviews*. **46**: 106-117.

Mungall, J. E., Andrews, D. R. A., Cabri, L. J., Sylvester, P. J., and Tubrett, M. 2005. Partitioning of Cu, Ni, Au, and platinum group elements between monosulphide solid solution and sulphide melt under controlled oxygen and sulphur fugacities. *Geochimica et Cosmochimica Acta.* **69** (17): 4349 – 4360.

Mungall, J. E., and Brenan, J. M. 2014. Partitioning of platinum-group elements and Au between sulphide liquid and basalt and the origins of mantle-crust fractionation of the chalcophile elements. *Geochimica et Cosmochimica Acta.* **125**: 265-289.

Mungall, J. E., Kamo, S. L., and McQuade, S. 2016. U-Pb geochronology documents out-of-sequence emplacement of ultramafic layers in the Bushveld Igneous Complex of South Africa. *Nature Communications*. **7**: 13385.

Mungall, J. E., and Su, S. 2005. Interfacial tension between magmatic sulphide and silicate liquid: Constraints on kinetics of sulphide liquation and sulphide migration through silicate rocks. *Earth and Planetary Science Letters*. **234**: 135-149.

Muzundo, T. 2015. Mogalakwena Mine: Whose Mine is it – the Miner, the Metallurgist, and the Mine-Planner? 6th Platreef Workshop, Mokopane 8th-10th May 2015. Abstract.

Naldrett, A. J. 1966. Tale–Carbonate Alteration of some Serpentinized Ultramafic Rocks south of Timmins, Ontario. *Journal of Petrology*. **7** (3): 489-499.

Naldrett, A. J. 1999. World-class Ni-Cu-PGE deposits: key factors in their genesis. *Mineralium Deposita*. **34**: 227-240.

Naldrett, A. J. 2004. Magmatic Sulphide Deposits: Geology, Geochemistry and Exploration. Berlin, Germany, Springer Verlag. p 727.

Naldrett, A. J. 2010. Secular Variation of Magmatic Sulphide Deposits and Their Source Magmas. *Economic Geology.* **105**: 669-688.

Naldrett, A.J. 2011. Fundamentals of Magmatic Sulphide Deposits. Reviews in *Economic Geology*. **17**: 1-50.

Naldrett, A. J., Cameron, G., von Gruenewaldt, G., and Sharpe, M. R. 1987. The Formation of Stratiform PGE Deposits in Layered Intrusions. Origins of Igneous Layering. Parson, I. (eds). D. Reidel Publishing Company. 313-397 pp.

Naldrett, A. J., and Duke, J. M. 1980. Platinum metals magmatic sulphide ores. *Science*. **208** (4451): 1417-1424.

Naldrett, A. J., and von Gruenewaldt, G. 1989. Association of Platinum-Group Elements with Chromitite in Layered Intrusions and Ophiolite Complexes. *Economic Geology*. **84**: 180-187.

Naldrett, A. J, Hoffman, E. L., Green, A. H., Chen-Lin Chou, and Naldrett, S. R. 1979. The Composition of Ni-Sulphide Ores, with particular reference to their content of PGE and Au. *Canadian Mineralogist*. **17**: 403-415.

Naldrett, A. J., Kinnaird, J., Wilson, A., and Chunnett, G. 2008. Concentration of PGE in the Earth's Crust with Special Reference to the Bushveld Complex. *Earth Science Frontiers.* **15** (5): 264 – 297.

Naldrett, A. J., Kinnaird, J. A., Wilson, A., Yudovskaya, M. and Chunnett, G. 2011. Genesis of the PGE-enriched Merensky Reef and chromitite seams of the Bushveld Complex. *Reviews in Economic Geology.* **17:** 235-296.

Naldrett, A. J., and Lehmann, J. 1988. Spinel non-stoichiometry as the explanation for Ni-, Cu-and PGE-enriched sulphides in chromitites. *Geo-Platinum*. **87**:93-109.

Naldrett, A.J., Wilson, A., Kinnaird, J., and Chunnett, G. 2009. PGE Tenor and Metal Ratios within and below the Merensky Reef, Bushveld Complex: Implications for its Genesis. *Journal of Petrology.* **50**: 625-659.

Naldrett A. J, Wilson A, Kinnaird J, Yudovskaya M, Chunnett G. 2012. The origin of chromitites and related PGE mineralization in the Bushveld Complex: new mineralogical and petrological constraints. *Mineralium Deposita* **47**: 209–232.

Naslund, H. R., and McBirney, A. R. 1996. Mechanism of formation of igneous layering. In Cawthorn, R. G. (Ed.), Layered Intrusions, Elsevier, pp. 1-43.

Nell, J. 1985. The Bushveld Metamorphic Aureole in the Potgietersrus Area: Evidence for a 2-Stage Metamorphic Event. *Economic Geology*. **80**: 1129-1152.

Newton, R. J., Bottrell, S. H., Dean, S. P., Hatfield, D. and Raiswell, R. 1995. An evaluation of the use of the chromous chloride reduction method for isotopic analyses of pyrite in rocks and sediment. *Chemical Geology.* **125:** 317-320.

Nex, P. A. 2005. The structural setting of mineralisation on Tweefontein Hill, northern limb of the Bushveld Complex, South Africa. *Applied Earth Science*. **114** (4): 243-251.

Nielsen, S., and Grobler, D. 2012. The Turfspruit Cyclic Unit. Platreef Resources Ivanplats. Internal company document.

Nielsen, J. K. and Hanken, N. -M. 2002. Description of the chromium reduction method for extraction of pyrite sulphur. University of Tromsø.

Nodder, S., M. 2015. *Correlating the Bushveld's northern limb with the western and eastern limbs: a geochemical and petrological study.* Exploration and Resource Geology MESci Thesis, Cardiff University.

Oberthür, T., Cabri, L. J., Weiser, T. W., McMahon, G., and Müller, P. 1997. Pt, Pd and other trace elements in sulphides of the main sulphide zone, Great Dyke, Zimbabwe: a reconnaissance study. *Canadian Mineralogist*. **35**: 597-609.

O'Driscoll, B., and González-Jiménez, J. M. 2016. Petrogenesis of the Platinum-Group Minerals. *Reviews in Mineralogy and Geochemistry*. **81**: 489-578.

Ohmoto, H. and Rye, R. O. 1979. Isotopes of sulphur and carbon. *In: Geochemistry of Hydrothermal deposits.* (ed. Barnes, H. L.), John Wiley & Sons, 509-567.

Okrugin, A. V. 2011. Origin of Platinum-Group Minerals in Mafic and Ultramafic Rocks: From Dispersed Elements to Nuggets. *The Canadian Mineralogist*. **49**: 1397-1412.

Olszak-Humienik, M. and Jablonski, M. 2014. Thermal behaviour of natural dolomite. *Journal of Thermal Analysis and Calorimetry*. **119** (3): 2239-2248.

O'Neill, H., St. C. Dingwell, D. B., Borisov, A., Spettel, B., and Palme, H. 1995. Experimental petrochemistry of some highly siderophile elements at high temperatures, and some implications for core formation at the mantle's early history. *Chemical Geology*. **120**: 255-273.

Osbahr, I., Klemd, R., Oberthür, T., and Brätz, H. 2013. Platinum-group element distribution in base-metal sulphides of the Merensky Reef from the eastern and western Bushveld Complex, South Africa. *Mineralium Deposita.* **48**: 211-232.

Osbahr, I., Oberthür, T., and Klemd, R. 2014. Platinum-group element distribution in base-metal sulphides of the UG2 chromitite, Bushveld Complex, South Africa – a reconnaissance study. *Mineralium Deposita.* **49**: 655 – 665.

Pagé, P., and Barnes, S-J. 2016. The influence of chromite on osmium, iridium, ruthenium and rhodium distribution during early magmatic processes. *Chemical Geology*. **420**: 51-68.

Park, J-W., Hu, Z., Gau, S., Campbell, I. H., and Gong, H. 2012. Platinum group element abundances in the upper continental crust revisited – New constraints from analyses of Chinese loess. *Geochimica et Cosmochimica Acta*. **93**: 63-76.

Parker, H. M., Khul, T., Valenta, M. 2012. NI 43-101 Technical Report on Updated Mineral Resource Estimate, Platreef Project, Limpopo Province, Republic of South Africa: Report prepared by AMEC for Ivanplats Ltd.

Patten, C., Barnes, S-J., Mathez, E. A., and Jenner, F. E. 2013. Partition coefficients of chalcophile elements between sulphide and silicate melts and the early crystallisation history of sulphide liquid: LA-ICP-MS analysis of MORB sulphide droplets. *Chemical Geology*. **358**: 170-188.

Peach C. L., Mathez E. A., and Keays, R. R. 1990. Sulfide melt-silicate melt distribution coefficients for the noble metals and other chalcophile metals as deduced from MORB: Implications for partial melting. *Geochemica et Cosmochimica Acta.* **54**: 3379–3389.

Peach, C. L., Mathez, E. A., Keays, R. R., and Reeves, S. J. 1994. Experimentally determined sulphide melt-silicate melt partition coefficients for iridium and palladium. *Chemical Geology*. **117**: 361-377.

Penberthy, C. J., Oosthuyzen, E. J., and Merkle, R. K. W. 2000. The recovery of platinum-group elements from the UG-2 chromitite, Bushveld Complex – a mineralogical perspective. *Mineralogy and Petrology*. **68**: 213-222.

Penniston-Dorland, S. C., Mathez, E. A., Wing, B. A., Farquhar, J and Kinnaird, J. A. 2012. Multiple Sulphur Isotope Evidence for Surface-Derived Sulphur in the Bushveld Complex. *Earth and Planetary Science Letters.* **337-338:** 236-242.

Penniston-Dorland, S. C., Wing, B. A., Nex, P. A. M., Kinnaird, J. A., Farquhar, J., Brown, M., and Sharman, E. R. 2008. Multiple sulphur isotopes reveal a magmatic origin for the Platreef platinum group element deposit, Bushveld Complex, South Africa. *Geology*. **36** (12): 979-982.

Peregoedova, A., Barnes, S-J., and Baker, D. R. 2004. The formation of Pt-Ir alloys and Cu-Pd rich sulphide melts by partial desulphurisation of Fe-Ni-Cu sulphides: Results of experiments and implications for natural systems. *Chemical Geology*. **208**: 247-264.

Pickard, A. L. 2003. SHRIMP U-Pb zircon ages for the Palaeoproterozoic Kuruman Iron Formation, Northern Cape Province, South Africa: evidence for simultaneous BIF deposition on Kaapvaal and Pilbara Cratons. *Precambrian Research*. **125**: 275-315.

Prichard, H. M., Barnes, S-J., Maier, W. D. and Fisher, P. C. 2004. Variations in the nature of the platinum-group minerals in a cross-section through the Merensky Reef at Impala Platinum: Implications for the mode of formation of the reef. *The Canadian Mineralogist*. **42** (2): 423-437.

Prichard, H. M., Knight, R. D., Fisher, P. C., McDonald, I., Zhu, M. -F. & Wang, C. Y. 2013. Distribution of platinum-group elements in magmatic and altered ores in the Jinchuan intrusion, China: an example of selenium remobilization by postmagmatic fluids. *Mineralium Deposita.* **48:** 767-786.

Pronost, J., Harris, C., and Pin, C. 2008. Relationship between footwall composition, crustal contamination, and fluid-rock interaction in the Platreef, Bushveld Complex, South Africa. *Miner Deposita*. **43**: 825-848.

Queffurus, M., and Barnes, S-J. 2015. A review of sulfur to selenium ratios in magmatic nickel – copper and platinum-group element deposits. *Ore Geology Reviews*. **69**: 301-324.

Rasmussen, B., Bekker, A., and Fletcher, I. R. 2013. Correlation of Paleoproterozoic glaciations based on U-Pb zircon ages for tuff beds in the Transvaal and Huronian Supergroups. *Earth and Planetary Science Letters*. **382**: 173-180.

Ripley, E. M. 1991. Platinum-group element geochemistry of the Cu-Ni mineralization in the basal zone of the Babbitt Deposit, Duluth Complex, Minnesota; reply. *Economic Geology*. **86** (6): 1358-1362.

Ripley, E. M., and Li, C. 2003. Sulfur isotope exchange and metal enrichment in the formation of magmatic Cu-Ni-(PGE) deposits. *Economic Geology*. **98**: 635-641.

Ripley, E. M., and Li, C. 2013. Sulfide Saturation in Mafic Magmas: Is External Sulfur Required for Magmatic Ni-Cu-(PGE) Ore Genesis? *Economic Geology.* **108**: 45-58.

Ripley, E. M., and Li, C. 2017. A review of the application of multiple S isotopes to magmatic Ni-Cu-PGE deposits and the significance of spatially variable $\Delta^{33}S$ values. *Economic Geology*. **112**: 983-991.

Ripley, E. M., Li, C., Moore, C. H., and Schmitt, A. K. 2010. Micro-scale S isotope studies of the Kharaelakh intrusion, Noril'sk region, Siberia: Constraints on the genesis of coexisting anhydrite and sulphide minerals. *Geochimica et Cosmochimica Acta.* **74**: 634-644.

Ripley, E. M., Lightfoot, P. C., Li, C., and Elswick, E. R. 2003. Sulfur isotopic studies of continental flood basalts in the Noril'sk region: Implication for the association between lavas and ore-bearing intrusions. *Geochimica et Cosmochimica Acta.* **67** (15): 2805-2817.

Ripley, E. M., Park, Y-R., Li, C., Naldrett, A, J. 1999. Sulfur and oxygen isotopic evidence of country rock contamination in the Voisey's Bay Ni-Cu-Co deposit, Labrador, Canada. *Lithos.* **47**: 53-68.

Ripley, E. M., Sarkar, A., and Li, C. 2005. Mineralogic and Stable Isotope Studies of Hydrothermal Alteration at the Jinchuan Ni-Cu Deposit, China. *Economic Geology*. **100**: 1349-1361.

Robb, L. 2005. Introduction to Ore-Forming Processes. Oxford: Blackwell Publishing.

Roberts, K. 2004. Technical report on the Platreef project, northern limb, Bushveld Complex, Limpopo province, Republic of South Africa: Technical Report for Anooraq Resources Corporation, March 19th, 2004 (available at www.sedar.com).

Robinson BW, Kusakabe M (1975) Quantitative preparation of sulfur dioxide for 34S/32S analyses from sulfides by combustion with cuprous oxide. *Analytical Chemistry*. **47**:1179–1181.

Roelofse, F., and Ashwal, L. D. 2012. The Lower Main Zone in the Northern Limb of the Bushveld Complex – a > 1.3 km Thick Sequence of Intruded and Variably Contaminated Crystal Mushes. *Journal of Petrology*. **53** (7): 1449-1476.

Rollinson, H. 1993. Using geochemical data: evaluation, presentation, interpretation. Longman Scientific & Technical.

Rose, L. A., and Brenan, J. M. 2001. Wetting properties of Fe-Ni-Co-Cu-OS melts against olivine: Implications for sulphide melt mobility. *Economic Geology*. **96** (1): 145-157.

Royal Society of Chemists (RSC). 2015. Periodic Table > Platinum. Accessed from, http://www.rsc.org/periodic-table/element/78/platinum, on the 15/02/2015.

Rudnick, R.L., and Gao, S. 2004. Composition of the Continental Crust. In: *Treatise on Geochemistry.* Holland, H.D. and Turekian, K.K. (Editors), Elsevier, Amsterdam. **3**: 1-64.

Salters, V. J. M., and Stracke, A. 2004. Composition of the depleted mantle. *Geochemistry, Geophysics, Geosystems (G^3)*. **5** (5): 1-27.

Sarkar, A., Ripley, E. M., Li, C., Maier, W. D. 2008. Stable isotope, fluid inclusion, and mineral chemistry constraints on contamination and hydrothermal alteration in the Uitkomst Complex, South Africa. *Chemical Geology.* **257**: 129-138.

Schiffries, C. M. 1982. The Petrogenesis of a Platiniferous Dunite Pipe in the Bushveld Complex: Infiltration Metasomatism by a Chloride Solution. *Economic Geology.* **77:** 1439-1455.

Schouwstra. R. P., Kinloch, E. D., and Lee, C. A. 2000. A short Geological Review of the Bushveld Complex. *Platinum Metals Review*. **44** (1): 33-39.

Schröeder, S., Beukes, N. J., and Armstrong, R. A. 2016. Detrital zircon constraints on the tectonostratigraphy of the Paleoproterozoic Pretoria Group, South Africa. *Precambrian Research*. **278**: 362-393.

Scoates, J. S., and Friedman, R. M. 2008. Precise age of the Platiniferous Merensky Reef, Bushveld Complex, South Africa, by the U-Pb zircon chemical abrasion ID-TIMS technique. *Economic Geology.* **103** (3): 465 – 471.

Scoon, R. N., and Teigler, B. 1994. Platinum-Group Element Mineralisation in the Critical Zone of the Western Bushveld Complex: I. Sulfide Poor-Chromitites below the UG-2. *Economic Geology*. **89**: 1094-1121.

Seabrook, C. L., Cawthorn, R. G., and Kruger, F. J. 2005. The Merensky Reef, Bushveld Complex: Mixing of Minerals not Mixing of Magmas. *Economic Geology*. **100**: 1191-1206.

Sharman-Harris, E. R., Kinnaird, J. A., Harris, C., and Horstmann, U. E. 2005. A new look at sulphide mineralisation of the northern limb, Bushveld Complex: a stable isotope study. *Applied Earth Science (Trans. Inst. Min. Metall. B*). **114**: 252-263.

Sharman, E. R., Penniston-Dorland, S. C., Kinnaird, J., Nex, P. A. M., Brown, M., and Wing, B.A. 2013. Primary Origin of Marginal Ni-Cu-(PGE) Mineralisation in Layered Intrusions: $\Delta^{33}S$ Evidence from the Platreef, Bushveld, South Africa. *Economic Geology*. **108**: 365-377.

Sharpe, M. R. 1981. The chronology of magma influxes to the eastern compartment of the Bushveld Complex as exemplified by its marginal border groups. *Journal of the Geological Society of London.* **138**: 307-326.

Sharpe, M. R., and Irvine, T. N. 1983. Melting relations of two Bushveld chilled margin rocks and implications for the origin of chromitite. *Carnegie Institute Washington Year Book.* **82**: 295-300.

Shima, H., and Naldrett, A. J. 1975. Solubility of sulfur in an ultramafic melt and the relevance of the system Fe-S-O. *Economic Geology*. **70** (5): 960-967.

Siebert, C., Kramer, J. D., Meisel, T., Morel, P., and Nägler, T. F. 2005. PGE, Re-Os, and Mo isotope systematics in Archean and early Proterozoic sedimentary systems as proxies for redox conditions of the early Earth. *Geochimica et Cosmochimica Acta.* **69** (7): 1787-1801.

Silver, P.G., Fouch, M. J., Gao, S. S., and Schmitz, M. 2004. Seismic anisotropy and mantle fabric, and the magmatic evolution of Precambrian southern Africa. *South African Journal of Geology.* **107**: 45-58.

Sluzhenikin, S. F. and Mokhov, A. V. 2015. Gold and silver in PGE–Cu–Ni and PGE ores of the Noril'sk deposits, Russia. *Mineralium Deposita*. **50** (4): 465-492.

Sluzhenikin, S. F., Yodovskaya, M., Grobler, D. F., Brits, J. A. N., Costin, G. 2015. Contact Metamorphic and Contact Metasomatic Rocks in the Platreef Foorwall on Turfspruit (Preliminary Data). 6th Platreef Workshop, Mokopane 8th-10th May 2015. Abstract.

Smart, G. D. 2013. *PGE in the Platreef: a petrological and geochemical study of the Turfspruit Cyclic Unit on the Turfspruit Farm Prospect.* Exploration and Resource Geology MESci Thesis, Cardiff University.

Smith, D. S., Basson, I. J., and Reid, D. L. 2003. Normal Reef Subfacies of the Merensky Reef at Northam Platinum Mine, Zwartklip Facies, Western Bushveld Complex, South Africa. *The Canadian Mineralogist.* **42**: 243 – 260.

Smith, J. W. 2014. *The nature and origin of PGE mineralisation in the Rooipoort area, northern Bushveld Complex, South Africa.* PhD Thesis, University of Leicester.

Smith, J. W., Holwell, D. A., and McDonald, I. 2014. Precious and base metal geochemistry and mineralogy of the Grasvally Norite-Pyroxenite-Anorthosite (GNPA) member, northern Bushveld Complex, South Africa: implications for a multistage emplacement. *Mineralium Deposita.* **49**: 667-692.

Smith, J. W., Holwell, D. A., McDonald, I., and Boyce, A. 2016. The application of S isotopes and S/Se ratios in determining ore-forming processes of magmatic Ni-Cu-PGE sulphide deposits: A cautionary case study from the northern Bushveld Complex. *Ore Geology Reviews*. **73**: 148-174.

South African Committee for Stratigraphy (SACS). 1980. Stratigraphy of South Africa, Part 1, Kent, L.E., comp., Geological Survey of South Africa Handbook 8: Pretoria, Geological Survey of South Africa, pp. 690.

Streckeisen, A. 1976. To each plutonic rock its proper name. *Earth Science Reviews*. **12**: 1-33.

Stumpfl, E. F., and Rucklidge, J. C. 1982. The Platiniferous Dunite Pipes of the Eastern Bushveld. *Economic Geology.* **77:** 1419-1431.

Summer, D.Y., and Bowring, S. A. 1996. U-Pb geochronologic constraints on deposition of the Campbellrand Subgroup, Transvaal Supergroup, South Africa. *Precambrian Research.* **79**: 25-35.

Tanner, D., Mavrogenes, J. A., Arculus, R. J., and Jenner, F. E. 2014. Trace Element Stratigraphy of the Bellevue Core, Northern Bushveld: Multiple Magma Injections Obscured by Diffusive Processes. *Journal of Petrology*. **55** (5): 859-882.

Tanner, D., McDonald, I., Harmer, R. E., Muir, D., and Hughes, H. S. R. 2019. A record of assimilation preserved by exotic minerals in the lowermost platinum-group element deposit of the Bushveld Complex: the Volspruit Sulphide Zone. *Lithos*. **324-325**: 584-608.

Thode, H. G. 1970. Sulphur Isotope Geochemistry and Fractionation between Coexisting Sulphide Minerals. *Mineralogical Society of America Special Publication.* **3**: 133-144.

Tredoux, M., Lindsay, N. M., Davies, G., and McDonald, I. 1995. The fractionation of platinum-group elements in magmatic systems, with the suggestion of a novel causal mechanism. *South African Journal of Geology.* **98** (2): 157 167.

Tredoux, M., and McDonald, I. 1996. Komatiite WITS-1, low-concentration noble metal standard for the analysis of non-mineralised samples. *Geostandards and Geoanalytical Research*. **20** (2): 267-276.

Tredoux, M., Sellschop, J. P. F., Davies, G., de Wit M. J. 1985. The behaviour of the PGE and Au during partial melting and fractional crystallization: evidence from magmas on the Kaapvaal Craton. *Canadian Mineralogist*. **23**: 317–318.

Tredoux, M., de Wit M. J., Hart, R. J., Armstrong, R. A., Lindsay, N. M., and Sellschop, J. P. F. 1989. Platinum Group Elements in a 3.5 Ga Nickel-Iron Occurrence: Possible Evidence of a Deep Mantle Origin. *Journal of Geophysical Research*. 94 (B1):795–813.

Tuttle, M. L., Goldhaber, M. B. & Williamson, D. L. 1986. An analytical scheme for determining forms of sulphur in oil shales and associated rocks. *Talanta.* **33**: 953-961.

Vermaak, C. F. 1995. The Platinum-Group Metals — A Global Perspective. Mintek, Randburg, South Africa, 247 p.

Vernon, R. H. 2004. A Practical Guide to Rock Microstructure. Cambridge, UK. Cambridge University Press.

Viljoen, M. J. 2016. The Bushveld Complex: Host to the World's Largest Platinum, Chromium and Vanadium Resources. *Episodes*. **39** (2): 239-268.

Viljoen, M. J., De Klerk, W. J., Coetzer, P. M., Hatch, N. P., Kinloch, E. and Peyerl, W. 1986. The union section of rustenburg platinum mines limited with reference to the Merensky Reef. *Mineral deposits of southern Africa*. **2**: 1061-1090.

Viljoen, M. J., and Schurmann, L. W. 1998. Platinum group metals. In: Wilson, M. G. C, Anhaeusser, C. R., (eds) The mineral resources of South Africa. Council for Geosciences, Pretoria, pp 532-568.

Voordouw, R., Gutzmer, J., and Beukes, N. J. 2009a. Intrusive origin for upper group (UG1, UG2) stratiform chromitite seams in the Dwars River area, Bushveld Complex, South Africa. *Mineral Petrol*. **97**: 75-94.

Voordouw, R., Gutzmer, J., and Beukes, N. J. 2009b. Zoning of platinum-group mineral assemblages in the UG2 chromitite determined through in situ SEM-EDS based image analysis. *Mineralium Deposita*. **45**:147-159.

Vuorelainen, Y., Häkli, T. A., and Papunen, H., 1972. Argentian pentlandite from some Finnish sulfide deposits. *American Mineralogist: Journal of Earth and Planetary Materials*. **57**(1-2): 137-145.

Wagner, P. A. 1929. The Platinum Deposits and Mines of South Africa: Edinburgh, Oliver and Boyd, 326 p.

Wagner, T, Boyce, A. J, Fallick, A. E. 2002. Laser combustion analysis of $\delta^{34}S$ of sulfosalt minerals: Determination of the fractionation systematics and some crystal-chemical considerations. *Geochimica et Cosmochimica Acta*. **66**: 2855–2863.

Walraven, F. 1997. Geochronology of the Rooiberg Group, Transvaal Supergroup, South Africa. Economic Geology Research Unit Information Circular, University of the Witwatersrand, Johannesburg 316, p. 21.

Walraven, F., and Hattingh, E. 1993. Geochronology of the Nebo Granite, Bushveld Complex. *South African Journal of Geology.* **96**: 31-41.

Walraven, F., and Martini, J. 1995. Zircon Pb-evaporation age determinations of the Oak Tree Formation, Chuniesport Group, Transvaal Sequence: Implications for Transvaal-Griqualand West basin correlations. *South African Journal of Geology*. **98**: 58-67.

Webb, S.J., Ashwal, L.D., and Cawthorn, R.G. 2011. Continuity between eastern and western Bushveld Complex, South Africa, confirmed by xenoliths from kimberlite. *Contributions to Mineral Petrology.* **162:** 101-107.

Weise, S., Yudovskaya, M., and Kinnaird, J. 2008. Geological Observations on the Main Zone – Platreef Contact on the Farms Turfspruit, Tweefontein, Vaalkop, Zwartfontein and Overysel [abs]. Platreef Workshop, 3rd, Mokopane, 11th – 13th July 2008, Abstracts.

White, J.A. 1994. The Potgietersus Prospect – Geology and Exploration History. XVth CMMI Congress Johannesburg SAIMM. **3**: 173-181.

Wilson, A., and Chunnett, G. 2006. Trace Element and Platinum Group Element Distributions and the Genesis of the Merensky Reef, Western Bushveld Complex, South Africa. *Journal of Petrology*. **47** (12): 2369-2403.

Wilson, A., and Zeh, A. 2015. Emplacement and Magma Compositions of the Lowest Successions of the Bushveld Complex. Abstract from: 6th Platreef Workshop, Mokopane 8th – 10th May 2015.

de Wit, M. J. 1991. Archean greenstone belt tectonism and basin development: some insights from the Baberton and Pietersburg greenstone belts, Kaapvaal Craton, South Africa. *Journal of African Earth Sciences*. **13** (1): 45-63.

de Wit, M. J., Armstrong, R. A., Kamo, S. L., Erlank, A. J. 1993. Gold-bearing sediments in the Pietersburg Greenstone Belt: Age Equivalents of the Witwatersrand Supergroup Sediment, South Africa. *Economic Geology*. **88**:1242 – 1252.

de Wit, M. J., Jones, M. G., and Buchanan, D. L. 1992. The geology and tectonic evolution of the Pietersburg Greenstone Belt, South Africa. *Precambrian Research*. **55**: 123-153.

World Platinum Investment Council Ltd (WPIC). 2014. Investment Research. Accessed from, http://www.platinuminvestment.com/investment-research, on the 15/02/2015.

Wronkiewic, D. J., and Condie, K.C. 1989. Geochemistry and mineralogy of sediment from the Ventersdorp and Transvaal Supergroups, South Africa: Cratonic evolution during the early Proterozoic. *Geochimica et Cosmochimica Acta*. **5:** 343-354.

Yamamoto, M. 1976. Relationship between Se/S and sulphur isotope ratios of hydrothermal sulphide minerals. *Mineralium Deposita*. **11**: 197-209.

Yudovskaya, M., Belousova, E., Kinnaird, J., Dubinina, E., Grobler, D. F., and Pearson, N. 2017a. Re-Os and S isotope evidence for the origin of Platreef mineralisation (Bushveld Complex). *Geochimica et Cosmochimica Acta*. **214**: 282-307.

Yudovskaya, M., A., and Kinnaird, J., A. 2010. Chromite in the Platreef (Bushveld Complex, South Africa): occurrence and evolution of its chemical composition. *Miner Deposita*. **45**:369-391.

Yudovskaya, M. A., Kinnaird, J.A., Grobler, D. F., Costin, G., Abramova, V. D., Dunnett, T., and Barnes, S-J. 2017b. Zonation of Merensky style platinum mineralisation in Turfspruit thick reef facies (northern limb of the Bushveld Complex). *Economic Geology*. **112** (6): 1333-1365.

Yudovskaya, M. A., Kinnaird, J. A., Naldrett, A. J., Rodionov, N., Antonov, A., Simakin, S., and Kuzmin, D. 2013a. Trace-element study and age dating of zircon from chromitites of the Bushveld Complex (South Africa). *Mineralogy and Petrology*. **107** (6): 915-942.

Yudovskaya, M. A., Kinnaird, J.A., Naldrett, A. J., Mokhov, A. V., McDonald, I., and Reinke, C. 2011. Facies variation in PGE mineralisation in the central Platreef of the Bushveld Complex, South Africa. *The Canadian Mineralogist.* **49:** 1349 – 1384.

Yudovskaya, M. A., Kinnaird, J.A., Sobolev, A. V., Kuzmin, D. V., McDonald, I., and Wilson, A. H. 2013b. Petrogenesis of the Lower Zone Olivine-Rich Cumulates Beneath the Platreef and Their Correlation with Recognized Occurrences in the Bushveld Complex. *Economic Geology.* **108:** 1923 -1952.

Yudovskaya, M. A., Kinnaird, J. A., Udachina, L. V., Distler, V. V., and Kuz'min, D. V. 2014. Role of Magmatic and Fluid Concentrating in Formation of Platinum Mineralisation in the Lower Zone and Platreef as follows from Composition of Phlogopite, Cumulus Silicates and Sulphide Melt, the Northern Limb of Bushveld Complex. *Geology of Ore Deposits*. **56** (6): 451-478.

Yudovskaya, M. A., Naldrett, A. J., Woolfe, J.A.S., Costin, G., and Kinnaird, J. A. 2015. Reverse Compositional Zoning in the Uitkomst Chromitites as an Indication of Crystallisation in a Magmatic Conduit. *Journal of Petrology*. 1-21.

Zeh, A., Jaguin, J., Poujol, M., Boulvais, P., Block, S., and Paquette, J-L. 2013. Juvenile crust formation in the northeastern Kaapvaal Craton at 2.97 Ga – Implications for Archean terrane accretion, and the source of Pietersburg gold. *Precambrian Research.* **233**: 20-43.

Zeh, A., Ovtcharova, M., Wilson, A., and Schaltegger, U. 2015. The Bushveld Complex was emplaced and cooled in less than one million years – results of zirconology, and geotectonic implications. *Earth and Planetary Science Letters.* **418**: 103-114.

Zhabina, N., and Volkov, I. 1978. A method of determination of various sulphur compounds in sea sediments and rocks. 3rd International Symposium on Environmental Biogeochemistry. Ann Arbor Science Publications, 735-746.

Zientek, M. L. 2012. Magmatic Ore Deposits in Layered Intrusions – Descriptive Model for Reef-Type PGE and Contact-Type Cu-Ni-PGE Deposits. U.S. Geological Survey Open-File Report 2012 – 1010, 48 p.

Zientek, M. L., and Loferski, P. J. 2010. Platinum-Group Elements – So Many Excellent Properties. U.S. Geological Survey Mineral Resource Program.

Zientek, L. M., and Ripley, E. M. 1990. Sulfur Isotope Studies of the Stillwater Complex and Associated Rocks, Montana. *Economic Geology*. **85**: 376-391.

Appendix A

For Chapter 5: Core Logging and Sampling

A1 (drill hole collar locations) to A2 (cross-sections) removed because of copyright ownership.

A3 Summary tables of the sampling data

Table A3.1: Core samples taken from the deep Platreef for the current study (prefix HS) and those made available to the current study from Smart (2013) (prefix GS). Note: CR STR = chromite stringer.

Sample_ID	From (m)	To (m)	Interval (m)	This Study	Reason
HS_345_01	1380.97	1381.07	0.10	MZ	Representative
HS_345_02	1408.42	1408.52	0.10	MAN	Representative
GS1B	1424.52	1424.68	0.16	UP	Representative
GS2B	1431.00	1431.15	0.15	UP	Representative
HS_345_03	1432.45	1432.60	0.15	UP/QFV	Contact
HS_345_04	1439.37	1439.47	0.10	UP	High Grade
GS3B	1440.60	1440.82	0.22	UP	Representative
GS4B	1443.30	1443.46	0.16	UP	CR-STR
GS5B	1443.46	1443.67	0.21	UP	CR-STR
GS6B	1446.80	1446.93	0.13	UP	High Grade
GS7B	1447.08	1447.18	0.10	UP	CR-STR
GS7C	1447.18	1447.22	0.04	UP	CR-STR
GS8B	1447.22	1447.26	0.04	UP/MP	CR-STR
GS8C	1447.26	1447.40	0.14	UP/MP	CR-STR
GS9B	1448.08	1448.26	0.18	MP_U	High Grade
GS10B	1449.60	1449.75	0.15	MP_U	High Grade
HS_345_05	1452.67	1452.77	0.10	MP_U	Alteration
GS11B	1455.54	1455.79	0.25	MP_L	Representative
GS12B	1460.28	1460.43	0.15	MP_L	Representative
GS13B	1461.71	1461.87	0.16	MP_L	Representative
GS14B	1469.02	1469.19	0.17	MP_L	Representative
GS15B	1471.37	1471.42	0.05	NC2	Representative
GS16B	1472.50	1472.68	0.18	NC2	Representative
GS17B	1474.36	1474.55	0.19	NC2	Representative
HS_345_06	1486.17	1486.27	0.10	NC2	Contact
HS_345_07	1518.95	1519.135	0.185	LP	CR-STR
HS_345_08	1519.60	1519.73	0.13	LP	CR-bearing
HS_345_09	1521.04	1521.14	0.10	MCHR	Grade
HS_345_10	1528.07	1528.22	0.15	UMZ	Type
HS_345_11	1532.12	1532.24	0.12	UMZ	Alteration
HS_345_12	1541.83	1541.93	0.10	UMZ	Type
HS_345_13	1543.34	1543.44	0.10	UMZ	Grade
HS_345_14	1548.22	1548.32	0.10	UMZ	Type
HS_345_15	1552.18	1552.325	0.145	HZ_{FCPX}	Type
HS_345_16	1558.82	1558.94	0.12	HZ_{FCPX}	Min
HS_D1_01	1423.69	1423.745	0.055	UP	Contact
HS_D1_02	1429.84	1429.94	0.10	UP	Grade
HS_D1_03	1434.55	1434.70	0.15	UP	Type
GS18C	1446.40	1446.54	0.14	UP	CR-STR/Grade
GS19C	1446.68	1446.93	0.25	UP	CR-STR

GS19D	1446.93	1447.08	0.15	UP	CR-STR
GS20C	1447.28	1447.46	0.18	MP_U	CR/PEG
GS21B	1448.00	1448.15	0.15	MP_U	PEG
GS22B	1449.19	1449.69	0.50	MP_U	PEG
GS23B	1450.39	1450.56	0.17	MP_U	PEG
HS_D1_04	1452.96	1453.09	0.13	MP_U	Grade
GS24B	1454.57	1454.72	0.15	MP_L	Type
HS_D1_05	1460.41	1460.565	0.155	MP_L	Type
HS_D1_06	1470.69	1470.83	0.14	MP_L	Contact
HS_D1_07	1480.24	1480.39	0.15	NC2	Grade
HS_D1_08	1485.81	1485.99	0.18	NC2	Cycle
HS_D1_09A	1496.57	1496.72	0.15	NC2	Cr-content
HS_D1_09B	1496.72	1496.87	0.15	NC2	Cr-content
HS_D1_09C	1496.87	1496.98	0.11	NC2	^Cr-contet
HS_D1_10	1513.76	1513.89	0.13	LP HW	Cr-Stringer
HS_D1_11	1514.495	1514.645	0.15	LP HW	Grade
HS_D1_12	1516.34	1516.67	0.33	LP HW	^ Cr-Content
HS_D1_13	1516.68	1516.78	0.1	LP CHR	Contact
HS_D1_14	1516.78	1516.94	0.16	CHR	Type
HS_D1_15	1518.69	1518.81	0.12	CHR	Texture
HS_D1_16	1519.88	1520.03	0.15	CHR FW	^ Cr-Content
HS_D1_17	1522.19	1522.34	0.15	CHR FW	Type
HS_D1_18	1534.67	1534.84	0.17	CHR FW	Type

Table A3.2: Core samples collected during the current study from the Flatreef and Platreef. The prefix of the samples distinguishes between the different drill holes studied.

Sample_ID	From (m)	To (m)	Interval (m)	Ivanplats Strat	Strat	Reason
TMT_01	800.12	800.24	0.12	HW1/MD1	NC1/UP	Contact
TMT_02	801.6	801.71	0.11	MD1	UP	Grade
TMT_03	803.06	803.21	0.15	MD1	UP	Grade
TMT_04	805.31	805.48	0.17	MD1	UP	Type
TMT_05	808.79	808.89	0.1	MD1	UP	Type
TMT_06	811.33	811.53	0.2	MD1	UP	Type
TMT_07	813.48	813.68	0.2	MD1	UP	Grade
TMT_08	816.02	816.22	0.2	MD1	UP	Grade
TMT_09	819.03	819.19	0.16	MD1	UP	Grade
TMT_10	821.45	821.54	0.09	MD1/M1U	UP/MP	CR-STR
TMT_11	821.54	821.74	0.2	M1U	MP	Type
TMT_12	823.96	824.13	0.17	M1U	MP	CR-bearing
TMT_13	824.6	824.75	0.15	M1U	MP	CR-STR
TMT_14	827.54	827.70	0.16	M1U	MP	Type
TMT_15	830.23	830.43	0.2	M1U	MP	Type
TMT_16	832.16	832.29	0.13	M1U	MP	Type
TMT_17	836.55	836.75	0.2	M1U	MP	Assimilation
TMT_18	838.3	838.6	0.3	M1U	MP	High Grade
TMT_19	840.64	840.92	0.28	M1U	MP	Type
TMT_20	843.36	843.54	0.18	M1U/FAZ	MP/HZ (OL)	PAPX
TMT_21	843.9	844.1	0.2	FAZ	HZ_{OLWEBS}	PAPX
TMT_22	845.58	845.75	0.17	FAZ	HZ_{OLWEBS}	CR-bearing
TMT_23	845.75	845.85	0.1	FAZ	HZ_{OLWEBS}	CR-bearing
TMT_24	849.62	849.84	0.22	FAZ	HZ_{OLWEBS}	Type
TMT_25	851.73	851.93	0.2	QFV	HZ_{OLWEBS}	Type
TMT_26	854.73	854.9	0.17	FAZ	HZ_{OLWEBS}	PX
TMT_27	858.24	858.39	0.15	FAZ	HZ_{OLWEBS}	PHA
TMT_28	860.58	860.74	0.16	FAZ	HZ_{OLWEBS}	OLOPX/PAPX

TMT_29	865.74	865.94	0.2	FAZ	HZ_{OLWEBS}	Assimilation
TMT_30	870.03	870.18	0.15	FAZ	HZ_{GBRN}	MPV/POPX
TMT_31	871.70	871.97	0.27	FAZ	HZ_{GBRN}	Type
TMT_32	873.35	873.60	0.25	FAZ	HZ_{GBRN}	Type
TMT_33	878.56	878.76	0.2	FAZ	HZ_{GBRN}	Type
TMT_34	881.29	881.40	0.11	FAZ	HZ_{GBRN}	High grade
TMT_35	885.93	886.13	0.2	FAZ	HZ_{GBRN}	High grade
TMT_36	875.59	875.75	0.16	FAZ	HZ (OL)	CR-bearing
TMT_D1_01	862.47	862.67	0.2	M1U	MP	Grade/Texture
TMT_D1_02	869.79	869.89	0.1	FAZ	HZ_{GBRN}	CR-bearing
233_01	807.62	807.92	0.3	BAR	NC1	TEXTURE
233_02	808.56	808.66	0.1	BAR	NC1	TYPE
233_03	809.57	809.82	0.25	BAR	NC1	GRADE
233_04	810.06	810.21	0.15	BAR	NC1	Grade
233_05	810.50	810.70	0.2	BAR	NC1	Grade
233_06	811.72	811.87	0.15	BAR	NC1	Grade
233_07	812.39	812.54	0.15	BAR	NC1	Grade
233_08	813.24	813.39	0.15	BAR	NC1	Grade
233_09	816.58	816.73	0.15	MD1	UP	>PHL + S
233_10	842.87	842.99	0.12	MD1	UP	HW CR-STR
233_11	843.00	843.24	0.24	M1U	MP	High Grade
233_12	843.27	843.45	0.18	M1U	MP	High Grade
233_13	845.10	845.30	0.2	M1U	MP	High Grade
233_14	847.18	847.32	0.14	M1U	MP	Granophyre veins
233_15	862.10	862.31	0.21	PNZ	PNZ	Grade
233_16	866.70	866.85	0.15	PNZ	PNZ	Grade
233_17	867.16	867.30	0.14	PNZ	PNZ	Reference
233_18	902.30	902.45	0.15	PNZ	PNZ	Cr-bearing
ATS_01	94.30	94.54	0.24	HW2/MD3	MAN/UP	Contact
ATS_02	98.375	98.485	0.11	MD3	UP	Type
ATS_03	108.72	108.81	0.09	MD3	UP	Sheared
ATS_04	131.28	131.41	0.13	MD3	UP	Texture
ATS_05	143.95	144.10	0.15	M1L	MP	Type
ATS_06	150.87	151.13	0.26	M1L/FAZ	MP/HZ	Alteration
ATS_07	161.60	161.76	0.16	FAZ	HZ	Sulphide texture
ATS_08	171.63	171.84	0.21	FAZ	HZ	Texture
ATS_09	147.6	147.78	0.18	M1L	MP	Texture

A4 Core Sample Photographs

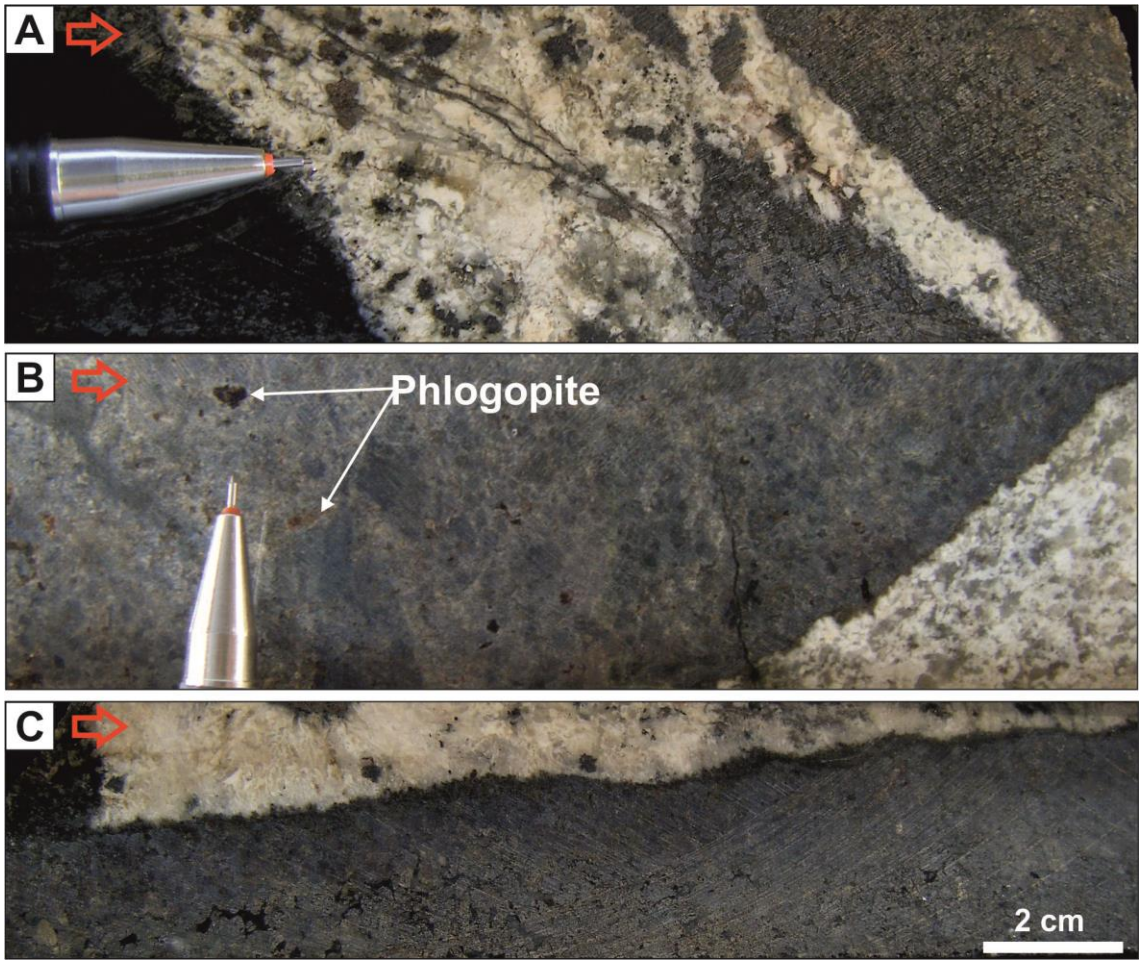

Figure A4.1: Lithological characteristics of the contacts between the QFV and the UP unit in the deep Platreef. (A) A QFV in the UP which shows sharp irregular contact and even shows evidence for entrainment of brecciated fragments of the host rock (UMT_345). (B) A close up of the top contact of the QFV present in core box 217 (UMT_345), the contact is sharp planar and there is an alteration halo where pyroxenes are extensively amphibolised and medium-grained phlogopite is present. (C) A QFV in UMT_345_D1 where the contact with the UP is at a low angle to the core axis, sharp and undulating.

Appendix B

For Chapter 6: Country Rock Geochemistry

For whole-rock geochemical data see Electronic Appendix B

B1 Country Rock Samples

Table B1.1: Samples collected from the Duitschland and De Hoop localities. The sample prefixes denote with location they are from with DTH (Duitschland) and DHP (De Hoop). Coordinate system Hartebeesthoek94_Lo29.

Sample #	S	E	Lithology	DF Section
DTH 1	-013869	2688103	Marl	Lower
DTH 2	-013995	2688241	Shale	Lower
DTH 3	-013995	2688241	Shale	Lower
DTH 4	-013995	2688241	Shale	Lower
DTH 5	-013995	2688241	Shale	Lower
DTH 6	-013985	2688281	Shale	Lower
DTH 7	-013757	2688002	Shaly mudstone	Lower
DTH 8	-013612	2687992	Arkose	Lower
DTH 9	-013247	2687561	Dolomite	Upper
DTH 10	-013086	2687306	Oolitic limestone diamictite	Upper
DTH 11	-012832	2687629	Hornfels	Upper
DTH 12	-012921	2687581	Marl	Upper
DTH 13	-012919	2687587	Marly Shale	Upper
DTH 14	-012909	2687566	Cu-Dolomite	Upper
DTH 15	-012909	2687566	Cu-Dolomite	Upper
DTH 16	-012909	2687566	Cu-Dolomite	Upper
DTH 17	-014975	2685288	Marl	Upper
DTH 18	-013115	2687395	Dolerite	Upper
DTH 19	-013104	2687383	Dolomite	Upper
TB 1	-012425	2687650	Shale	Timeball Hill
TB 2	-012254	2687823	Shale	Timeball Hill
DHP 2	-017202	2673899	Marl	Upper
DHP 3	-017302	2673912	Dolomite	Upper
DHP 4	-017427	2673924	Marl	Upper
DHP 5	-017722	2673959	Shaly mudstone	Lower
DHP 6	-015221	2673674	Marly mudstone	Lower
DHP 7	-015220	2673656	Marl	Upper
DHP 8	-015044	2673648	Gossan	Upper
DHP 9	-015036	2673644	Gossan vuggy	Upper
DHP 10	-015009	2673642	Dolomite	Upper
DHP 11	-016345	2673402	Shale	Upper
DHP 12	-013151	2672052	Dolomite	Upper

Table B1.2: The coordinate system for the PGB samples X and Y positions in UTM WGS 1984.

Sample #	X	Y	Lithology	Formation
PGB1	730574	7330168	Sheared greenstone	Eersteling
PGB2	730574	7330168	Blocky metabasalt	Eersteling
PGB3	726031	7335835	BIF	Uitkyk
PGB4	726031	7335835	Green sandstone/quartzite	Uitkyk
PGB5	726031	7335835	Meta conglomerate	Uitkyk
PGB6	726031	7335835	Metasandstone (red)	Uitkyk
PGB7	726277	7335474	Marl	Uitkyk
PGB8	726310	7335437	Green quartz-pebble conglomerate	Uitkyk
PGB9	726277	7335474	Finely laminated BIF	Uitkyk
PGB10	722758	7333200	Sheared metabasalt?	Uitkyk
PGB11	722758	7333200	Marl	Uitkyk
PGB12	722758	7333200	Meta-sandstone	Uitkyk
PGB13	722816	7332811	Meta-basite/amphibolite?	Ysterberg

PGB14	723234	7332563	BIF	Ysterberg
PGB15	723234	7332563	BIF	Ysterberg
PGB16	723542	7332140	BIF	Ysterberg
HH1	714486	7329066	Mineralised conglomerate	Uitkyk
HH2	714486	7329066	Mineralised conglomerate	Uitkyk

Table B1.3: Structural information from the sedimentary bedding planes collected from the Duitschland Formation.

Farm	S	E	Dip	Dip Direction	Rock Type
Duitschland	-013869	2688103	32	258	Marl
Duitschland	-013618	2687829	22	306	Arkosic sandstone
Duitschland	-012910	2687602	41	267	Dolomite
Duitschland	-012919	2687587	32	278	Shale
Duitschland	-014975	2685288	31	284	Marl
Duitschland	-014469	2688306	48	286	Shale
		Average	*34*	*280*	
De Hoop	24.16599˚	029.15198	30	290	Mudstone
De Hoop	-017171	2673886	42	264	Stromatolite
De Hoop	-018096	2674001	12	292	Chert
		Average	*28*	*282*	

B2 Fieldwork Site Access

Duitschland Farm is accessed from the R518; a game fence prevents general access to the public and any visitation must be prior arranged with the farm owners. A satellite image of the study location is shown in Figure B2.1 and B2.2. It is accessed from Mokopane using the R518 towards Zebiedela; as this is a private property arrangements for visiting were made prior to arriving.

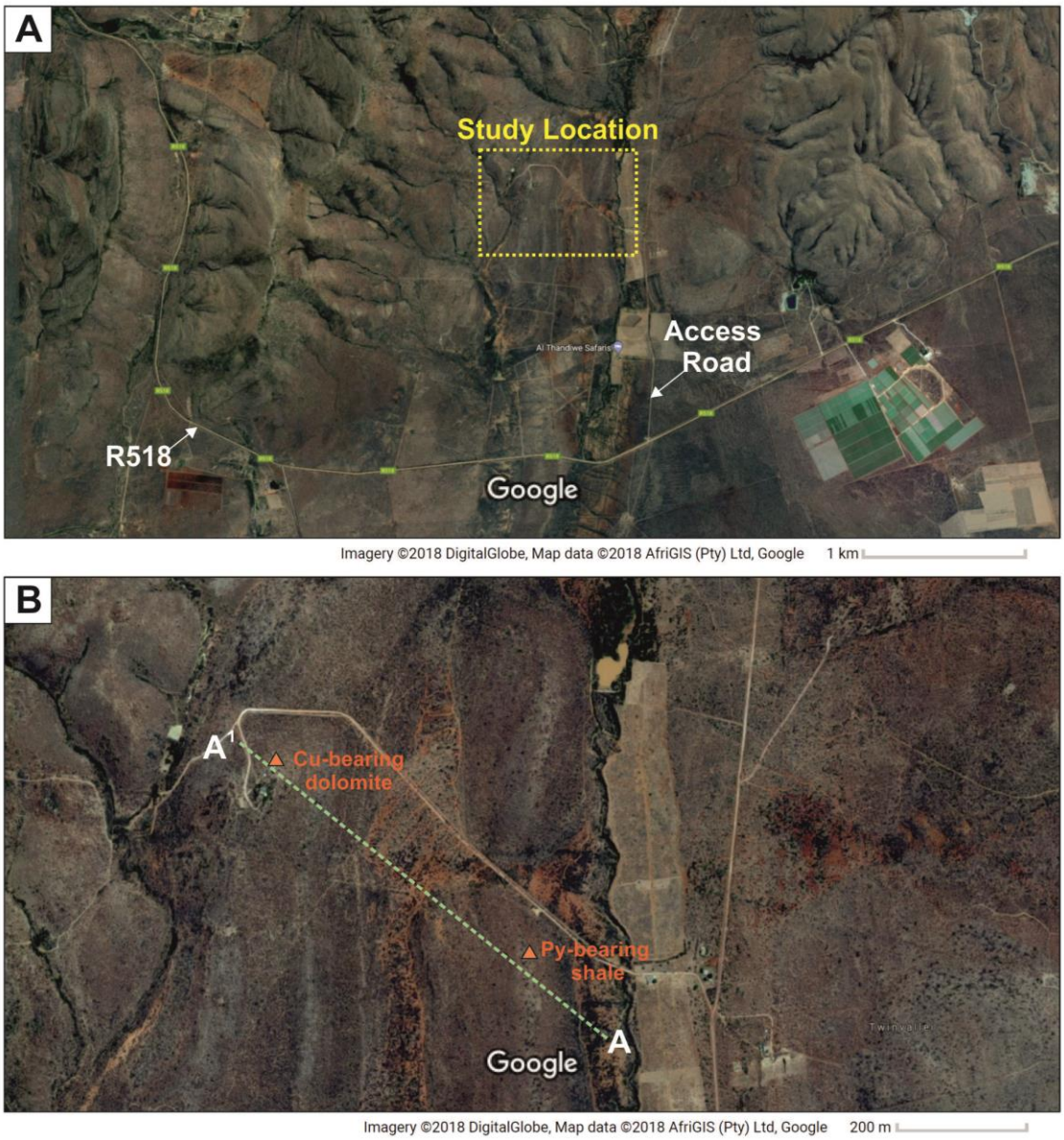

Figure B2.1: Google Earth satellite images showing the access and terrain of the Farm Duitschland. (A) Yellow box denotes the area visited for this study and is shown in B. The farm was accessed from Mokopane along the R518. (B) The two way markers (orange triangles) denote the location of two samples collected by Libby Sharman-Harris at this location.

The farm De Hoop was accessed by following the R101 North from Mokopane before turning off at the Mokopans World Heritage site (see Figure B2.2). The site is a private game farm owned by Ivanplats Pty Ltd.

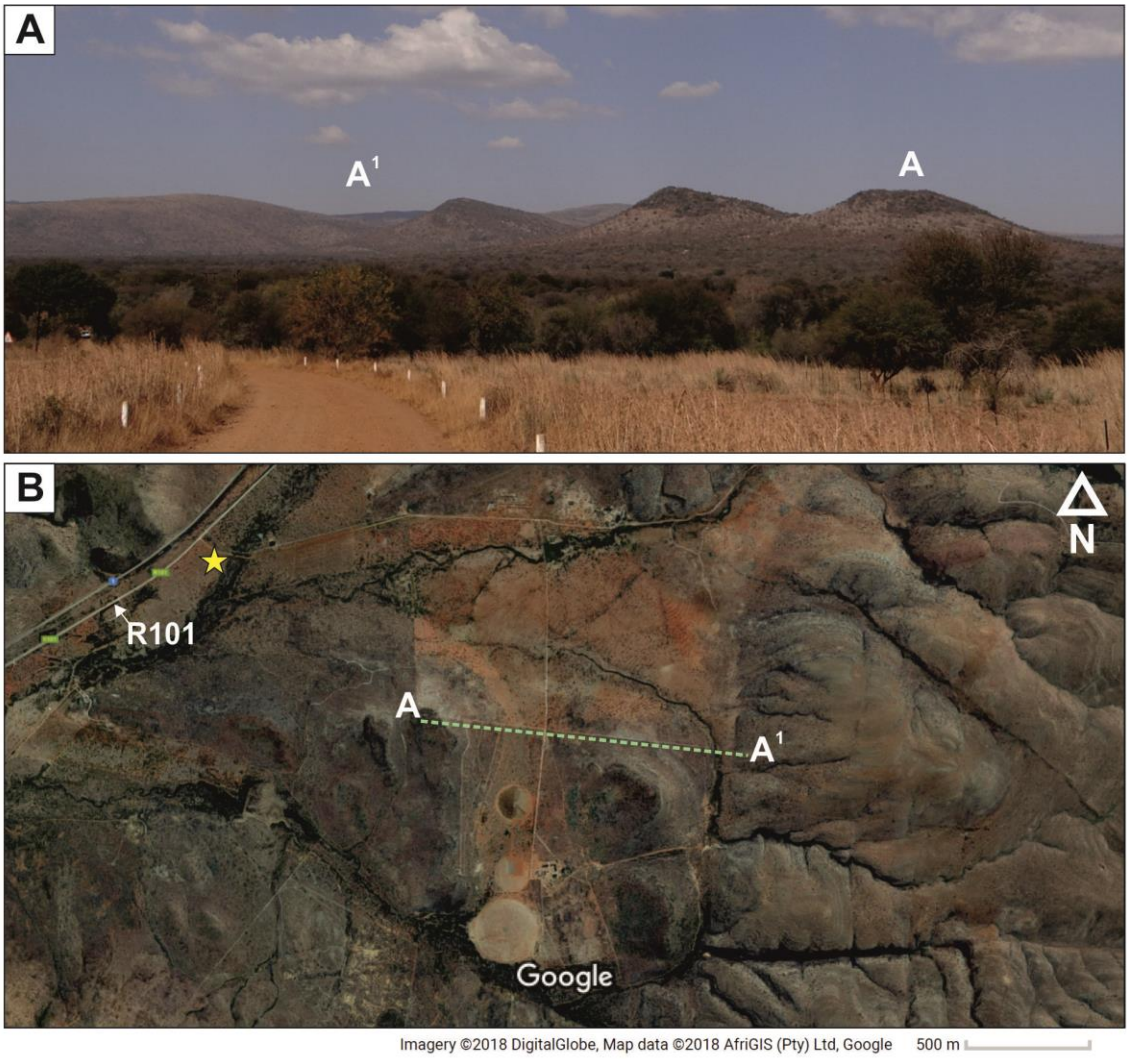

Figure B2.2: A) A photo looking ESE towards the characteristic hills that are formed from rocks of the Duitschland formation. A and A^1 are the start and end points respectively for the sampling transect. (B) A Google Earth satellite image showing a plan view of the De Hoop farm. The farm is accessed via the R101 from Mokopane and there is a small access road to the farm off this soon after the junction with the N1. The transect walked is illustrated using A to A^1. Note: yellow star denotes the location of the photo shown in A.

Appendix C

For Chapter 7: Whole-Rock Geochemistry (Core Samples)

For whole-rock raw data see Electronic Appendix C lithological and stratigraphic abbreviations used are presented below.

Common Lithological Abbreviations: MAN mottled anorthosite, OPX orthopyroxenite, FOPX feldspathic orthopyroxenite, NOR norite, GBRN gabbronorite (M – mela and L – leuco), CHR chromitite, OLOPX olivine orthopyroxenite, HRZ harzburgite, PX pyroxenite, TROC troctolite, FCPX feldspathic clinopyroxenite. OLGBRN olivine-bearing gabbronorite, CPX clinopyroxenite, ASSIM assimilation, QFV quartz-feldspar vein, GRN granite, PAPX parapyroxenite, PLHZ para-lherzolite, OLWEBS olivine websterite

Subscripts: PEG pegmatoidal, CHR chromite-bearing, SERP serpentinised, ALT altered

Stratigraphic Abbreviations: MZ Main Zone, MAN Mottled Anorthosite, UP Upper Pyroxenite, MP Middle Pyroxenite (MP_U Upper and MP_L Lower), NC1 Norite Cycles 1, NC2 Norite Cycles 2, LP Lower Pyroxenite, MCHR Main Chromitite, UMZ Ultramafic Zone, HZ_{FCPX} Feldspathic Clinopyroxenite Hybrid Zone, PNZ Pyroxenite-Norite Zone, HZ_{OLWEBS} Olivine Websterite Hybrid Zone, HZ_{GBRN} Gabbronorite Hybrid Zone.

C1 UMT_345_D1 Downhole Geochemical Profiles

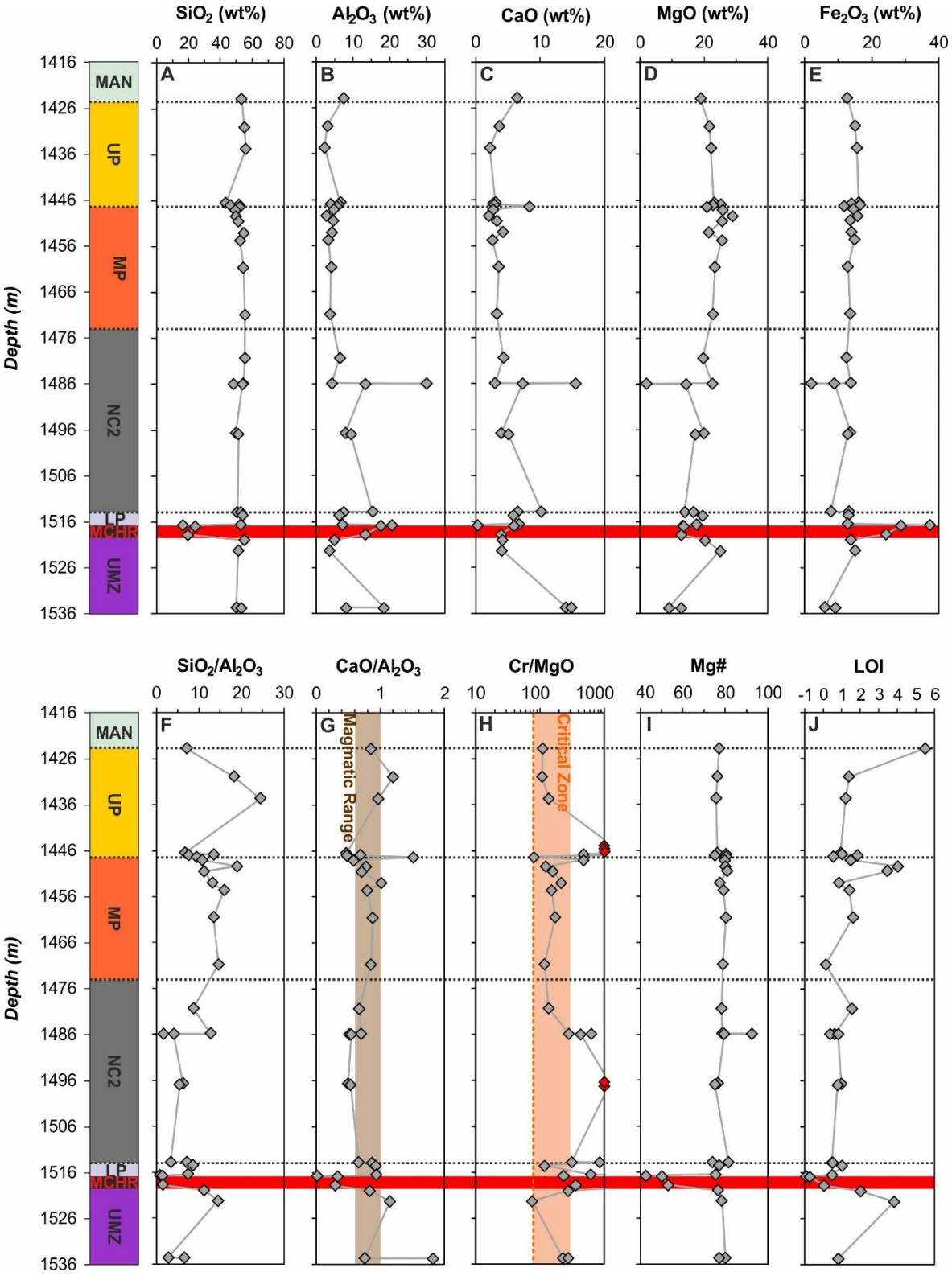

Figure C1.1: Major element geochemical profiles with depth for drill hole UMT_345_D1. (A) SiO_2 wt%; (B) Al_2O_3 wt%; (C) CaO wt%; (D) MgO wt%; (E) Fe_2O_3 wt%; (F) SiO_2/Al_2O_3; (G) CaO/Al_2O_3; (H) Cr/MgO; (I) Mg#; and (J) LOI wt%.

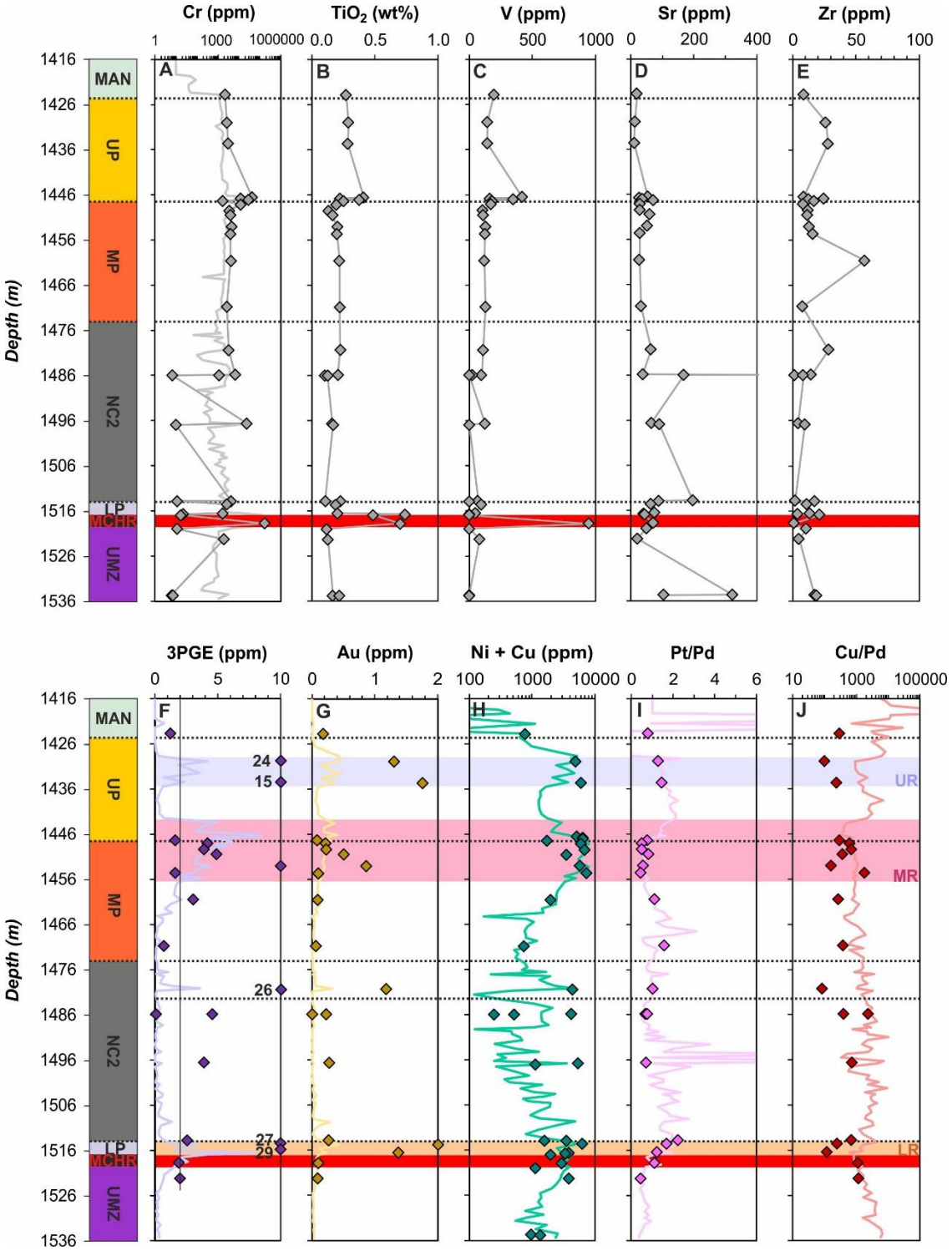

Figure C1.2: Trace element geochemical profiles with depth in drill hole UMT_345_D1. (A) Cr (ppm); (B) TiO_2 (wt%); (C) V (ppm); (D) Sr (ppm); (E) Zr (ppm); (F) 3PGE (ppm); (G) Au (ppm); (H) Ni + Cu (ppm); (I) Pt/Pd; (J) Cu/Pd. Note: lines without points represent data provided by Ivanplats Pty Ltd., and points are data collected in the current study.

C2 Trace Element Spidergrams

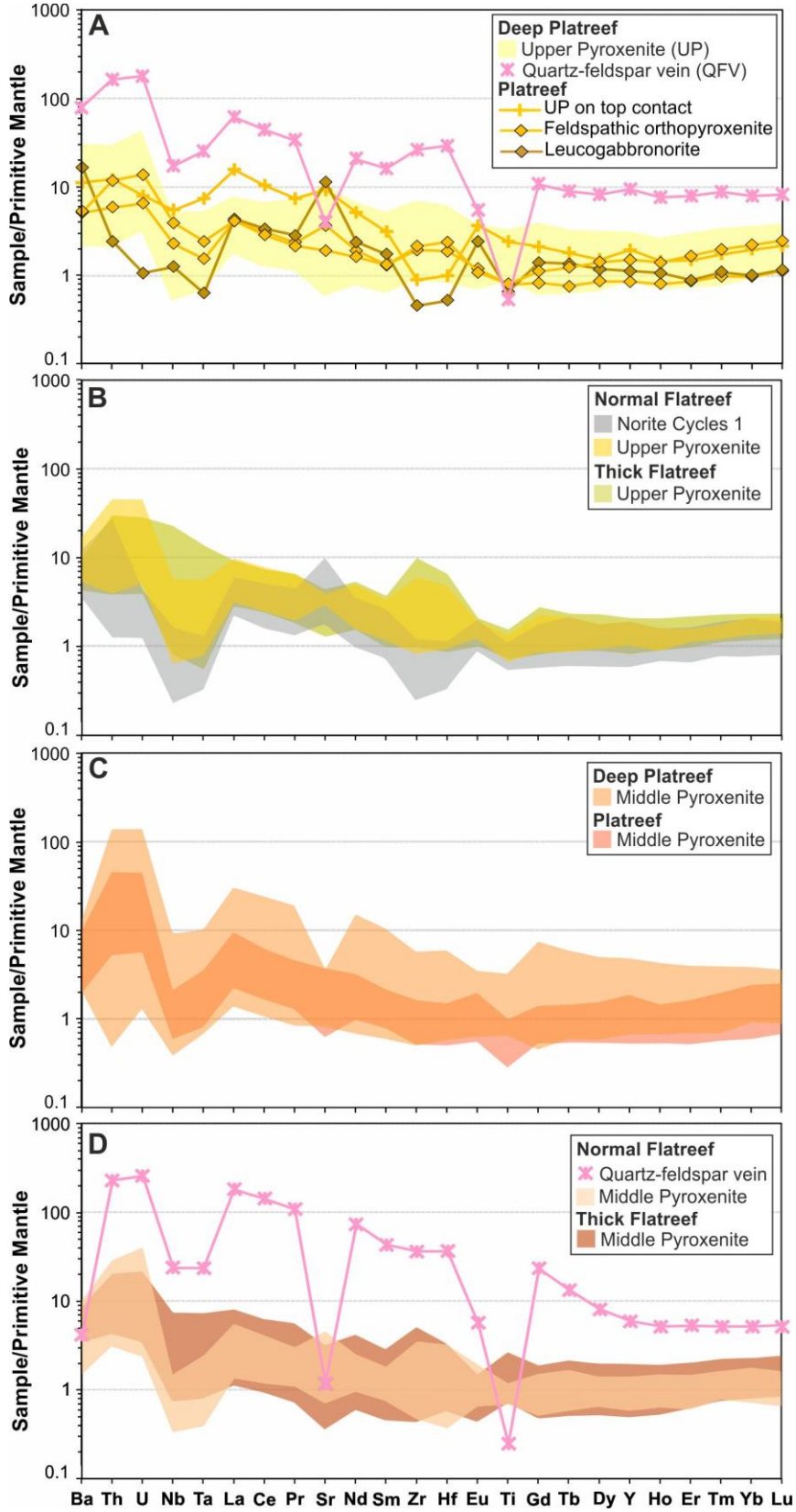

Figure C2.1: Primitive mantle-normalised spidergrams for the pyroxenite-dominated stratigraphic units in all drill holes studied. Normalisation factors from McDonough & Sun (1995).

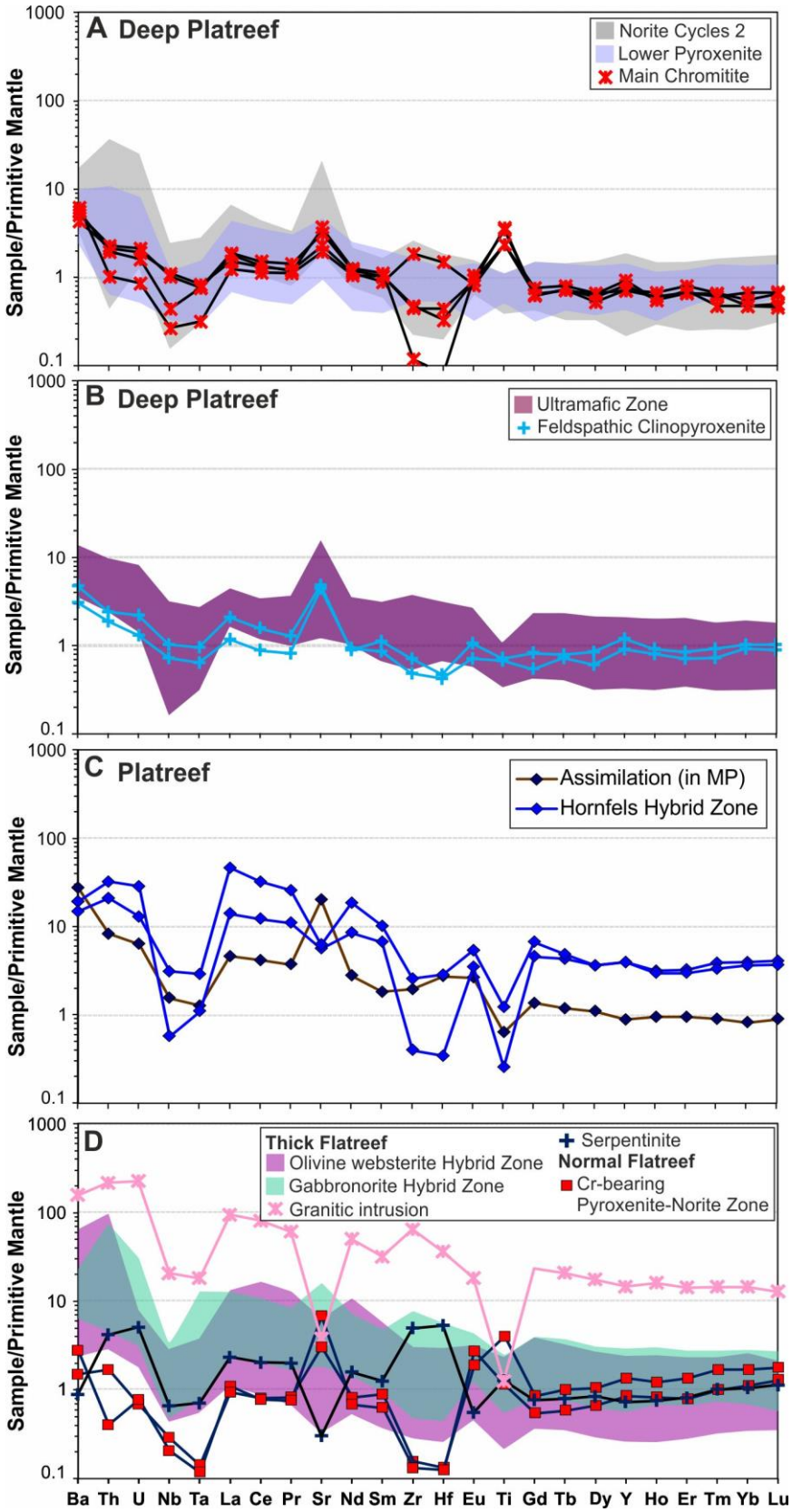

Figure C2.2: Primitive mantle-normalised spidergrams for the stratigraphic units below the level of the Middle Pyroxenite in all drill holes studied. Normalisation factors from McDonough & Sun (1995).

Appendix D

For Chapter 8: Mineralogy and Mineral Chemistry

For mineral chemistry data see Electronic Appendix D.

D.1 Deep Platreef Thin Section Photos

The texture of the adcumulate anorthosite is shown in Figure D.1A; this is dominated by plagioclase exhibiting well developed polysynthetic twining forming sub- euhedral laths that are fine to medium grained (long axis from <1 mm to ≈ 4 mm). Minor interstitial plagioclase is also present (see Figure D.1A). The edges of the cumulate plagioclase are frequently jagged and may be corroded or embayed with adjacent crystals. Minor zoning of cumulate plagioclase crystals was identified in those adjacent to interstitial plagioclase (see Figure D.1A). The smallest plagioclase crystals (< 2 mm) are found contained in pyroxene oikocrysts (see Figure D.1B and D.1C). The pyroxene is found interstitially and typically as oikocrysts creating an ophitic to subophitic texture. The orthopyroxene oikocrysts are typically smaller (up to 3 mm in size) whereas the clinopyroxene oikocrysts can be coarse to very coarse grained (5 to >10 mm). The orthopyroxene oikocrysts contain only plagioclase chadacrysts, whereas the clinopyroxene oikocrysts contain chadacrysts of both orthopyroxene and plagioclase. No mineral alignments were identified in the rock.

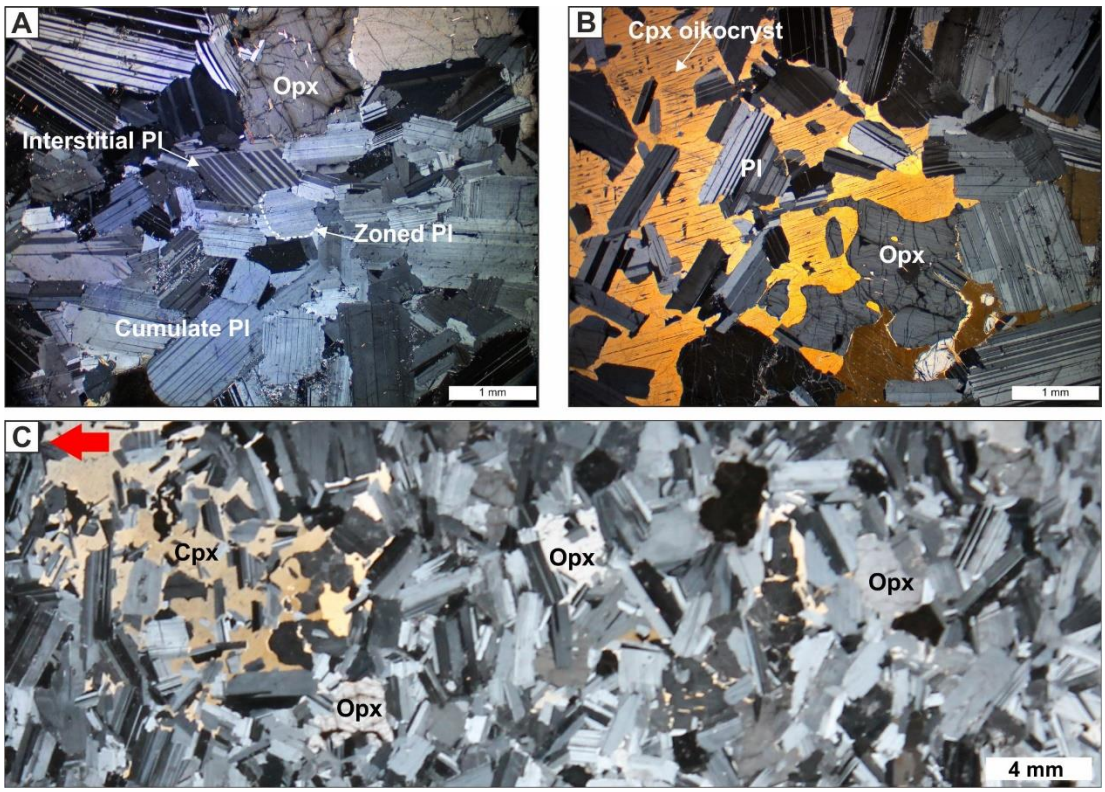

Figure D.1: Photomicrographs of the Main Zone directly above the deep Platreef as sampled in thin section HS_345_01. (A) An example of the typical texture of the anorthosite with plagioclase present interstitially and as a cumulate phase. (B) A clinopyroxene oikocryst

enclosing both plagioclase and embayed orthopyroxene. (C) Overview of the textures and distribution of minerals in the sample.

An example of the contact between the UP and the intrusive quartz-feldspar vein (QFV) is shown in Figure D.2A accompanied by an EDS multi-element map in Figure D.2B. Over the 16 mm distance shown in Figure D.2A the majority of the feldspathic orthopyroxenite has been altered to amphiboles; the relict shape of the orthopyroxenes can be seen in dark green in Figure D.2B. The QFV is compositionally formed of 60 % Na-rich feldspar (with patchy sericite alteration, purple colour in Figure D.2B) and 40 % quartz. The size of the quartz grains increases moving away from the contact with the UP.

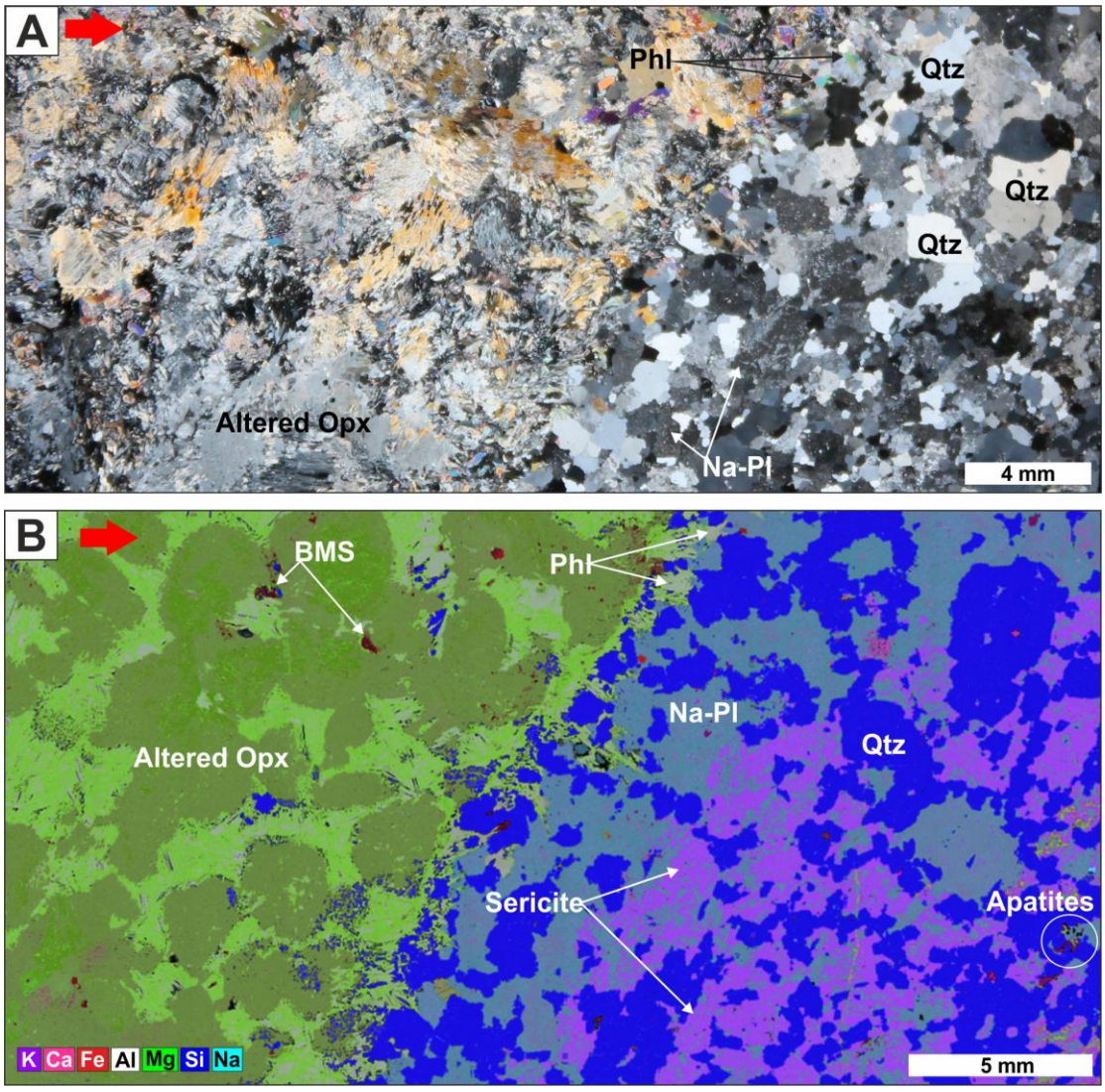

Figure D.2: The contact between a QFV and the UP unit as sampled in 345_03B. (A) Photomicrograph taken in crossed polars. (B) A multi-element EDS map. Note: red arrow points in the downhole direction.

D.2 Mineral Chemistry Calculations

The Mg# and the proportion of orthopyroxene end-member components of enstatite (En), ferrosilite (Fs), wollastonite (Wo); plagioclase anorthosite (An) and olivine forsterite (Fo) using the following equations:

Mg# = 100* (Mg / (Mg + Ca + Mn + Fe))

En = 100*(Mg/(Mg+Ca+Fe))

Fs = 100*(Fe/(Mg+Fe+Ca))

Wo = 100 * (Ca/(Mg+Fe+Ca))

An = 100* (Ca/(Ca+Na))

Fo = 100*(Mg/(Mg+Fe))

Appendix E

For Chapter 9: Sulphur Isotope Geochemistry

E1 XRF Sulphur Screen Methodology

The sulphur contents of homogenous milled powder from whole rock samples was analysed using an Olympus hand-held X-ray fluorescence (XRF) system. An unspecified amount of the sample powder was placed into a sample holder and pressed with a piece of glass to form a flat surface. Over the top was placed a thin-film of mylar, a plastic sheet product made from the resin Polyethylene Terephthalate (PET), and the XRF gun rested on this surface during analysis. The analyses ran for a total of 30 seconds and two analyses were performed on each sample unless sulphur was detected in which case three analyses were taken. A selection of calibration powders with ranging trace metal concentrations were tested prior to unknown samples and a steel plate used as the internal calibration of the XRF system.

Table E1.1: The sulphur concentration of Duitschland Formation sediments on samples that were above detection limits.

Sample	Lithology	S (%)	S (ppm)	S +/-
F_02.1A		0.0286	286	0.0031
F_02.2A		0.0288	288	0.003
F_02.3A	Volcanic?	0.0233	233	0.0031
F_08.1A		0.0333	333	0.0032
F_08.2A		0.0242	242	0.0031
F_08.3A	Limestone	0.0289	289	0.0031
F_09.1		0.1262	1262	0.0034
F_09.2		0.1019	1019	0.0032
F_09.3		0.1049	1049	0.0033
F10		0.0892	892	0.0034
F10.2		0.1058	1058	0.0035
F10.3	Dolomite	0.0631	631	0.0032
DHP10.1		0.0627	627	0.0028
DHP10.2		0.0549	549	0.0029
DHP10.3	Dolomite	0.0606	606	0.0029
DHP12.2		0.0594	594	0.003
DHP12.3	Mudstone	0.0587	587	0.003
DTH15.1		0.0512	512	0.0029
DTH15.2	Cu-dolomite	0.0417	417	0.0028
DTH15.3		0.0451	451	0.0027
DTH19.1		0.0082	82	0.0027
DTH19.2		<LOD	-	0.0122
DTH19.3	Dolomite	<LOD	-	0.0121

E2 Whole-Rock Sulphur Extraction Methodology

The first step in this process was to make the reagent chromous chloride required in the extraction process to strip the sulphur from sulphide minerals. Chromous chloride is made using chromium (III) hexahydrate (see Figure E2.1B) this is mixed with 10% diluted HCl to form a solution. This is reduced to chromous chloride by drawing through a reduction column; the set up of which is shown in Figure E2.1. The reducing column consists of a zinc-mercury amalgam in a 100 ml long glass burette (note: the zinc amalgam must fill a minimum of 30 cm of the column otherwise when the chromium solution is added it will not turn a bright blue colour). The column is activated by passing through HCl; one can tell if the activation is working because the amalgam changes colour from a dull to bright silver (see Figure E2.1A).

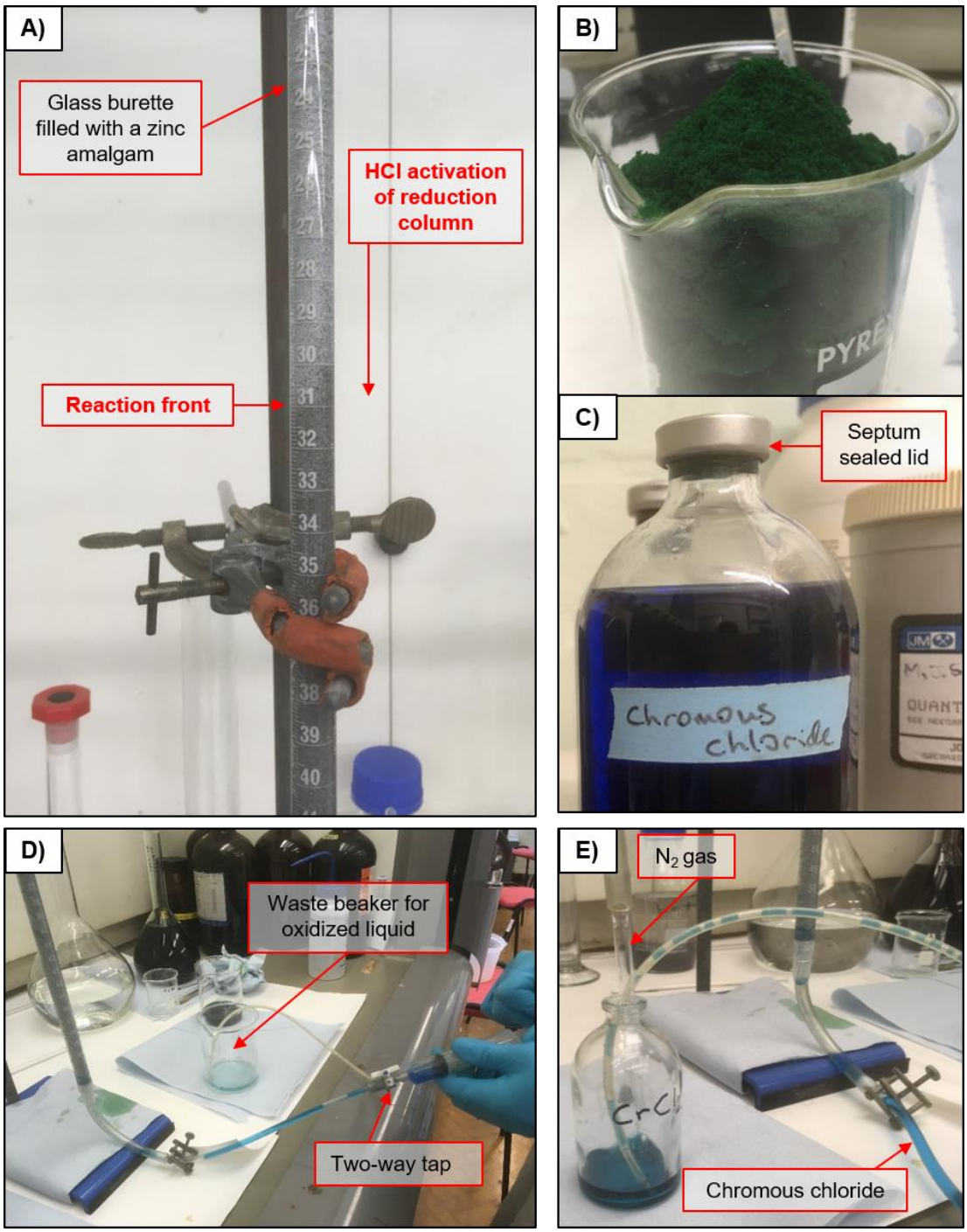

Figure E2.1: A) The zinc amalgam reaction column showing the change from a dull to bright silver as the column is activated by drawing down HCl. B) The main reagent Chromium (III) hexahydrate ($CrCl_3 \cdot 6H_2O$) which is dissolved in hydrochloric acid to form a solution which is passed through the reducing column. C) The end-product of the procedure is a reduced chromous chloride solution. D) The solution is drawn through the column using a syringe, any oxidised liquid (green in colour) or remnant HCl (clear in colour) is discarded into the waste beaker. E) The bright blue reduced solution is pressed into a vacuum sample bottle which has been purged with N_2 gas.

The sulphur-extraction experiment was conducted in a 1L glass, flat-bottomed, reaction vessel sat upon a magnetic hot plate; the equipment setup in a fume

The sulphur-extraction experiment was conducted in a 1L glass, flat-bottomed, reaction vessel sat upon a magnetic hot plate; the equipment setup in a fume cupboard at Cardiff University is shown in Figure E2.2A. Rock powder, weighing between 50-100 g, was loaded into the base of the reaction vessel with a large magnetic stirrer and this was sealed using a five-leg lid fixed on with a wire clamp and silicon grease rubbed on the seal to ensure that it is airtight. The five-legged lid of the reaction vessel was fitted with; (1) two glass stoppers; (2) a septum-sealed stopper (creating an air tight seal and can be penetrated by a needle); (3) a fine-diameter glass rod providing the inlet for the nitrogen gas; (4) the condenser column, linked via a Nalgene tube to a gas bell jar containing 100 ml of 0.1M $AgNO_3$ solution.

Initially, the reaction vessel is purged of air for 20 minutes with nitrogen gas infilling. Once in a reduced state 20 ml concentrated HCl is added before the 60 to 80 ml of chromous chloride. The chromous chloride solution is added to the reaction vessel using a syringe piercing through the septum sealed leg. Chromous chloride is a powerful reducing agent and the reaction proceeds as follows:

$$2Cr^{2+} + S^0 + 2H^+ \rightarrow 2Cr^{3+} + H_2S \quad \text{Equation E.1}$$

This process leads to the complete breakdown of reduced sulphide species into H_2S, including in the presence of Fe^{3+}. During the run of the experiment nitrogen gas is bubbled through the chromous chloride solution in order to transport the released H_2S into the condenser and ultimately through to the gas bell jar. The reaction between H_2S and $AgNO_3$ produces a black precipitate of Ag_2S. The experiment is left to run for ≈ 3 hours or silver nitric solution goes clear there is no more H_2S gas being released and the reaction has ended.

Note: originally ethanol was used as a wetting agent to suppress dust whilst the magnetic stirrer was going during the reaction vessel purge. This was discontinued as it was not deemed necessary after the first couple of samples; when analysed the samples which had been exposed to ethanol gave invalid data due to the presence of organic material and have been discounted from the investigation.

The solution in the gas bell jar is filtered using a titration system passing through a 0.45 μm Millipore filter paper; see Figure E2.2B for equipment setup. This is washed through twice with deionised water. The filter paper with the sulphur precipitate is then placed in a plastic filter paper holder and freeze dried overnight (see Figure E2.2C).

Once completely dehydrated the black Ag_2S precipitate can be removed from the filter paper weighed and placed into glass sample jars ready for S isotope analysis.

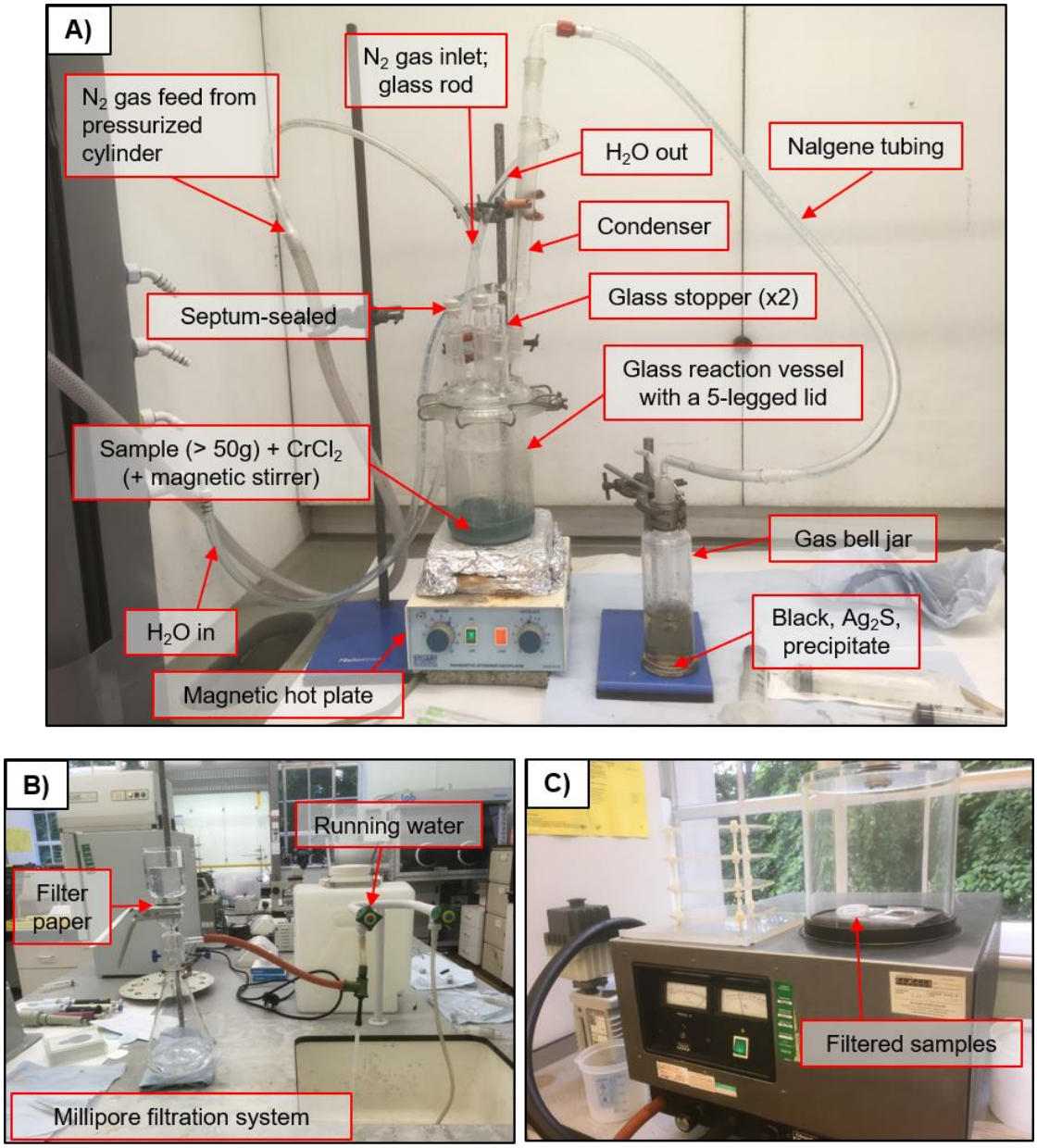

Figure E2.2: A) An example of the equipment set up for sulphur extraction in a fume cupboard. B) The vacuum filtration processes used to separate the Ag2S precipitate. C) Freeze-dryer used to dehydrate the samples.

E3 Results

Table E3.1: The combined results of the S isotope study from both conventional (C) and laser (L) analyses. Abrreviations for sulphide phases: Po – pyrrhotite; Pn – pentlandite; Cp – chalcopyrite; Cb – cubanite; Py – pyrite; Ag_2S – silver sulphide. Note: for polyphase sulphide analyses the dominant sulphide is given first. Note: ++ denotes mineralised samples.

Sample	Strat	Lithology	Mineral	$\delta^{34}S$	Method
Duitschland Fm.					
DTH_2	Lower	Shale (Py-bearing)	Ag_2S	+3.5	C
DTH_3	Lower	Shale (Py-bearing)	Ag_2S	+2.7	C
DTH_4	Lower	Shale (Py-bearing)	Ag_2S	+4.6	C
DTH_7	Lower	Shale (Py-bearing)	Ag_2S	+8.9	C
DTH_15	Upper	Dolomite (Cu-bearing)	Ag_2S	+11.9	C
HS_F_09	Upper	Marble (Cp-bearing)	Cp	+10.39	C
HS_F_10	Upper	Marble	Ag_2S	+5.6	C
Pietersburg Greenstone Belt					
HH_1	Uitkyk Fm	Conglomerate (pyrite-bearing)	Ag_2S	+3.2	C
HH_1	Uitkyk Fm	Conglomerate (pyrite-bearing)	Py	+2.5 (n=3)	L
PGB_4	Uitkyk Fm	Green sandstone/quartzite	Ag_2S	+10.2	C
PGB_7	Uitkyk Fm	Marl	Ag_2S	+36.5	C
PGB_8	Uitkyk Fm	Green quartz-pebble conglomerate	Ag_2S	+47.8	C
PGB_11	Uitkyk Fm	Marl	Ag_2S	+9.9	C
PGB_12	Uitkyk Fm	Meta-sandstone	Ag_2S	+3.5	C
PGB_13	Uitkyk Fm	Meta-basite/amphibolite?	Ag_2S	+6.3	C
Platreef (ATS_002)					
ATS_01A	MAN/UP	Pyroxenite	Po	+14.7 (n=3)	L
ATS_01B	UP	Pyroxenite/leucogabbronorite	Po	+9.9 (n=2)	L
ATS_04	UP	Feldspathic orthopyroxenite	Po	+8.4	L
ATS_04	UP	Feldspathic orthopyroxenite	Po	+9.7	L
ATS_05	MPU	Olivine orthopyroxenite++	PoPn	+6.4	C
ATS_06A	MPL	Harzburgite++	Po	+7.3	C
ATS_07	HZ_{HF}	Hornfels	Po	+3.6	C
ATS_07	HZ_{HF}	Hornfels	Py	+3.8	C
ATS_08	HZ_{HF}	Hornfels	Po	+19.6	C
Flatreef (UMT_233 and TMT_006)					
233_03	NC1	Norite	Cp	+1.3	C
233_03	NC1	Norite	Po	+1.7	C
233_04	NC1	Melanorite/Leuconorite	Cp	+1.3	L
233_04	NC1	Melanorite/Leuconorite	Po	+1.7	L
233_05A	NC1	Norite	Cp	+1.4	L
233_05A	NC1	Norite	Po	+2.3	L
233_07	NC1	Pegmatoidal norite	Pn	+3.7	L
233_07	NC1	Pegmatoidal norite	PoPn	+2.5	L
233_09	UP	FPX	Cp	+1.8	C
233_09	UP	FPX	Po	+2.0	C
233_11A	MP	Chromite-stringer	CpCb	+0.9	L
233_11A	MP	Chromite-stringer	Pn	2.8	L
233_11A	MP	Chromite-stringer	Po	+1.2	L
233_18A	PNZ	$Clinopyroxenite_{CHR}$	Po	+3.4	L
TMT_03	UP	Feldspathic orthopyroxenite++	Pn	+4.9	L
TMT_03	UP	Feldspathic orthopyroxenite++	Po	+2.0	L
TMT_07	UP	Orthopyroxenite++	Cp	+2.0	C
TMT_07	UP	Orthopyroxenite++	Po	+1.3	C
TMT_08	UP	Feldspathic orthopyroxenite++	Cp	+2.3	C
TMT_08	UP	Feldspathic orthopyroxenite++	Po	+1.9	C

TMT_09	UP	Feldspathic orthopyroxenite++	Cp	+1.9	C
TMT_09	UP	Feldspathic orthopyroxenite++	Po	+1.8	C
TMT_12	MP	Orthopyroxenite++$_{PEG/CHR}$	Cp	+1.1	L
TMT_12	MP	Orthopyroxenite++$_{PEG/CHR}$	Po	+1.5	L
TMT_16	MP	Feldspathic orthopyroxenite ++$_{PEG}$	Cp	+1.4	C
TMT_16	MP	Feldspathic orthopyroxenite ++$_{PEG}$	Po	+2.1	C
TMT_17	MP	MNOR++$_{SERP}$	Cp	+1.4	C
TMT_17	MP	*M*NOR++$_{SERP}$	Po	+1.8	C
TMT_18	MP	*M*NOR++$_{SERP/PEG}$	Cp	+1.8	C
TMT_18	MP	*M*NOR++$_{SERP/PEG}$	PoPn	+1.5	C
TMT_24	HZ$_{OLWEBS}$	Olivine Websterite++	Cp	+2.3	L
TMT_24	HZ$_{OLWEBS}$	Olivine Websterite++	Pn	+3.1	L
TMT_24	HZ$_{OLWEBS}$	Olivine Websterite++	Po	+1.1	L
TMT_24	HZ$_{OLWEBS}$	Olivine Websterite++	Po	+1.3	L
TMT_26	HZ$_{OLWEBS}$	*M*GBR++	Cp	+2.3	L
TMT_26	HZ$_{OLWEBS}$	*M*GBR++	Pn	+3.4	L
TMT_26	HZ$_{OLWEBS}$	*M*GBR++	Po	+2.1	L
TMT_27	HZ$_{OLWEBS}$	Olivine Websterite++	Cp	+5.1	L
TMT_27	HZ$_{OLWEBS}$	Olivine Websterite++	Pn	+5.2	L
TMT_29	HZ$_{OLWEBS}$	Serpentinite	Ag_2S	+1.0 (n=2)	C
TMT_32A	HZ$_{GBRN}$	Gabbronorite++	Cp	+1.7	L
TMT_32A	HZ$_{GBRN}$	Gabbronorite++	Pn	+3.3	L
TMT_32A	HZ$_{GBRN}$	Gabbronorite++	Po	+2.2	L
TMT_36	HZ$_{GBRN}$	Gabbronorite++$_{PEG}$	Cp	+2.6	C
TMT_36	HZ$_{GBRN}$	Gabbronorite++$_{PEG}$	Po	+2.2	C
TMT_37A	HZ$_{GBRN}$	Melagabbronorite++$_{CHR}$	Cp	+2.0	L
TMT_37A	HZ$_{GBRN}$	Melagabbronorite++$_{CHR}$	Po	+0.7	L
TMT_37B	HZ$_{GBRN}$	Clinopyroxenite++$_{CHR}$	Cp	+2.8	L
TMT_37B	HZ$_{GBRN}$	Clinopyroxenite++$_{CHR}$	Pn	+4.2	L
TMT_37B	HZ$_{GBRN}$	Clinopyroxenite++$_{CHR}$	Po	+1.7	L
TMT_D1_01	MP	Feldspathic orthopyroxenite ++$_{PEG}$	Cp	+2.1	C
TMT_D1_01	MP	Feldspathic orthopyroxenite ++$_{PEG}$	Cp	+1.4	C
TMT_D1_01	MP	Feldspathic orthopyroxenite ++$_{PEG}$	Po	+1.5	C
TMT_D1_02	HZ$_{GBRN/CHR}$	Clinopyroxenite$_{CHR}$	Cp	+4.0	L
TMT_D1_02	HZ$_{GBRN/CHR}$	Clinopyroxenite$_{CHR}$	Cp	+3.5	L
TMT_D1_02	HZ$_{GBRN/CHR}$	Clinopyroxenite$_{CHR}$	Po	+3.0	L
Deep Platreef (UMT_345 and UMT_345_D1)					
345_04	UP	Feldspathic orthopyroxenite ++	Cp	+1.7	C
345_04	UP	Feldspathic orthopyroxenite ++	Pn	+0.5	L
345_04	UP	Feldspathic orthopyroxenite ++	Po	+1.9	C
345_04	UP	Feldspathic orthopyroxenite ++	Po	+1.6	L
GS5A	UP	Feldspathic orthopyroxenite ++	Po	+0.7	L
GS10A	MP	Altered Pyroxenite**	Po	+1.5	L
345_05	MP	Feldspathic orthopyroxenite ++$_{PEG}$	Cp	+4.6	L
345_05	MP	Feldspathic orthopyroxenite ++$_{PEG}$	Po	+3.3	L
345_05	MP	Feldspathic orthopyroxenite ++$_{PEG}$	Po	+6.0	L
345_08A	LP	Orthopyroxenite$_{CHR}$**	CpCb	+4.3	L
345_08A	LP	Orthopyroxenite$_{CHR}$**	Pn	+4.7	L
345_09A	MCHR	Chromitite**	Cp	+9.5	L
345_09A	MCHR	Chromitite**	PnPo	+5.5	L
345_09B	MCHR	Chromitite**	CpCb	+2.5	L
345_09B	MCHR	Chromitite**	Pn	+4.3	L
345_11	UMZ	FOLOPX$_{PEG/SERP}$	CbCp	+5.0	L
345_11	UMZ	FOLOPX$_{PEG/SERP}$	Pn	+7.0	L
345_11	UMZ	FOLOPX$_{PEG/SERP}$	Po	+6.3	L

345_12	UMZ	Olivine gabbronorite	CpCb	+7.8	L
345_12	UMZ	Olivine gabbronorite	Po	+7.6	C
345_12	UMZ	Olivine gabbronorite	Po	+6.7	L
345_12	UMZ	Olivine gabbronorite	Po	+8.1	L
345_13	UMZ	Gabbro**$_{PEG}$	CbCp	+6.5	L
345_13	UMZ	Gabbro**$_{PEG}$	Pn	+9.2	L
345_13	UMZ	Gabbro**$_{PEG}$	Po	+6.6	L
345_14	UMZ	Olivine Gabbronorite	PoPn	+8.2	C
345_16	HZ$_{FCPX}$	Feldspathic clinopyroxenite	Cp	+10.25 (n=2)	L
345_16	HZ$_{FCPX}$	Feldspathic clinopyroxenite	Pn	+10.8	L
345_16	HZ$_{FCPX}$	Feldspathic clinopyroxenite	Po	+8.5	C
345_16	HZ$_{FCPX}$	Feldspathic clinopyroxenite	Po	+9.1 (n=3)	L
GS18B	UP	FOPX**$_{CHR/PEG}$	Cp	5.1	C
GS18B	UP	FOPX**$_{CHR/PEG}$	Po	1.1	L
GS19A	UP	Feldspathic orthopyroxenite ++$_{CHR}$	Pn	3.3	L
GS19A	UP	Feldspathic orthopyroxenite ++$_{CHR}$	Po	1.7	L
GS20B	UP/MP	GBRN**$_{CHR/PEG}$	Cp	3.4	L
GS20B	UP/MP	GBRN**$_{CHR/PEG}$	Pn	4.2	L
GS20B	UP/MP	GBRN**$_{CHR/PEG}$	Po	4.4	L
GS21A	MP	FOPX**$_{CHR}$	Cp	1.9	L
GS21A	MP	FOPX**$_{CHR}$	Pn	2.5	L
GS23A	MP	Feldspathic orthopyroxenite ++	Cp	1.9	L
GS23A	MP	Feldspathic orthopyroxenite ++	Po	3.6	L
GS23A	MP	Feldspathic orthopyroxenite ++	Pn	2.2	L
D1_07	NC2	Feldspathic orthopyroxenite ++	PoPn	2.7	C
D1_08A	NC2	*M*NOR	Cp	8.2	L
D1_08A	NC2	*M*NOR	Po	7.6	L
D1_08A	NC2	*M*NOR	Po	8.1	L
D1_12E	LP	*M*GBRN**$_{CHR}$	Cp	5.1	L
D1_12E	LP	*M*GBRN**$_{CHR}$	Po	4.8	L
D1_13	LP	OPX**	Cp	6.3	L
D1_13	LP	OPX**	Po	3.7	L
D1_13	LP	OPX**	Po	5.3	L
D1_14	MCHR	CHR**	PnPo	5.7	L
D1_14	MCHR	CHR**	Po	4.6	L
D1_15B	MCHR	*M*GBRN**$_{CHR}$	Cp	2.2	L
D1_15B	MCHR	*M*GBRN**$_{CHR}$	Pn	5.3	L
D1_17B	UMZ	*M*OLWEBS$_{PEG/SERP}$	CpCb	4.4	L
D1_17B	UMZ	*M*OLWEBS$_{PEG/SERP}$	Pn	4.1	L
D1_17B	UMZ	*M*OLWEBS$_{PEG/SERP}$	Po	4.6	L

Table E3.2: Results of duplicate sample analyses. Note: C = conventional and L = laser.

TMT_29/C	**TMT_29/C**	**345_04 Po/C**	**345_04 Po/L**	**HH_1 Ag_2S/C**	**HH_1 Py/L**
+0.9	+1.1	+1.9	+1.9	+3.2	+3.4
± 0.2		± 0.0		± 0.2	

Table E3.3: SUERC conventional S isotope standard analysis results . Note: Cp 1 chalcopyrite, NBS-123 sphalerite and IAEA S-3 Ag_2S.

Cp1 (Cert)	Cp1 (Aug)	Cp1 (Dec)	NBS-123 (Cert)	NBS-123 (Aug)	IAEA S-3 (Cert)	IAEA S-3 (Aug)	IAEA S-3 (Aug)
-4.6	-4.7	-5.2	+17.1	+17.2	-31	-32	-32.1
± 0.5			+0.1		+1.1		

Appendix F

For Chapter 10: PGE Mineralogy and Distribution

For LA-ICP-MS raw data see Electronic Appendix F.

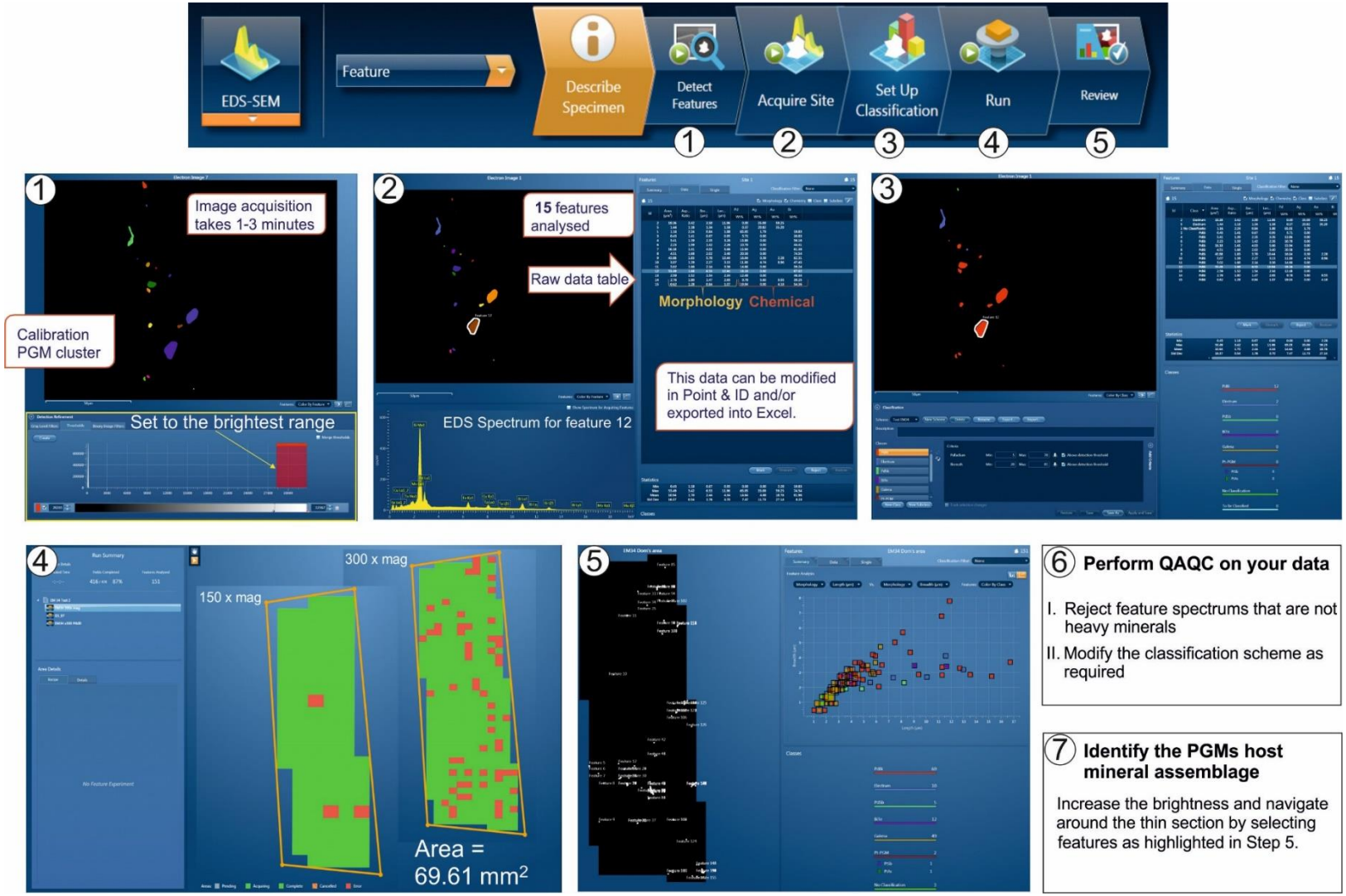

Figure F.1: A step-by-step guide for running an automated search for bright phases using the AZtec Feature Map function.

F2: PGM Distribution Pie Charts for Deep Platreef Samples

Note: from left to right the pie charts represent the count, proportional area (as an estimated volume %), and the number of each precious metal phases.

A) GS18A - 3rd Chromite Stringer (top)

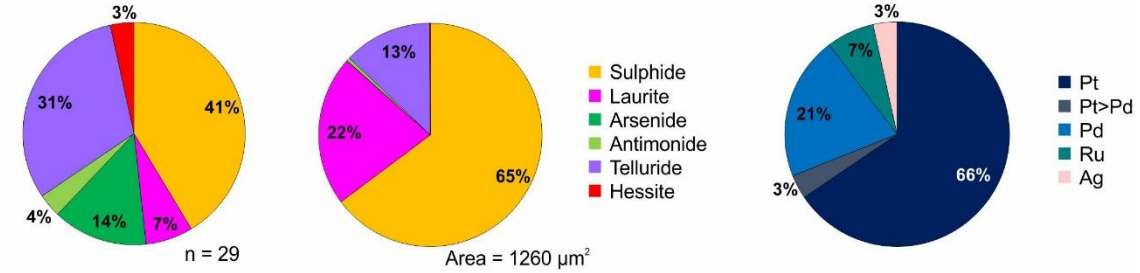

B) GS18B - 3rd Chromite Stringer (base)

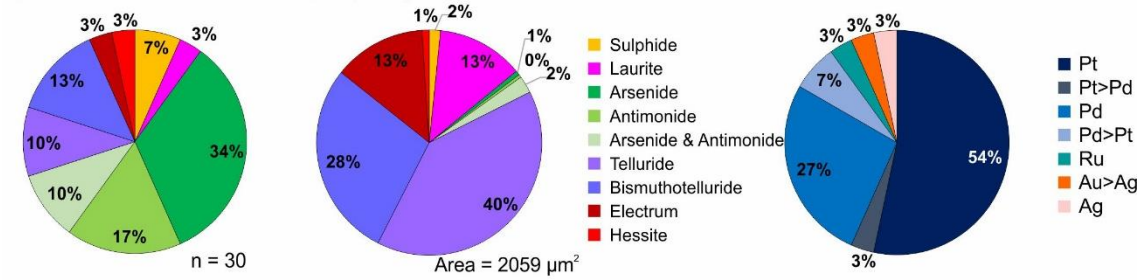

C) GS20A - 4th Chromite Stringer (top)

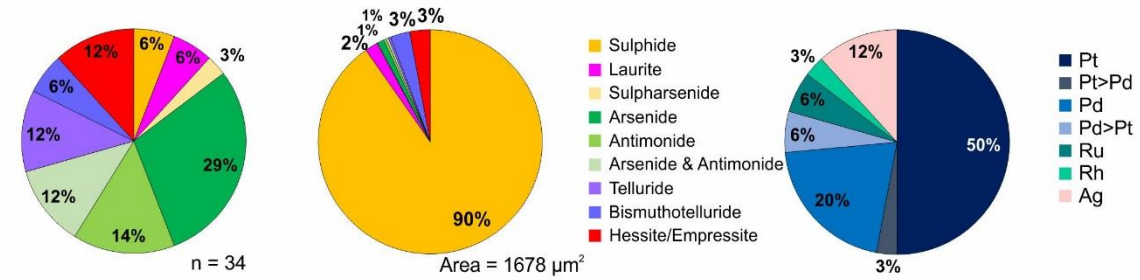

D) GS20B - 4th Chromite Stringer (base)

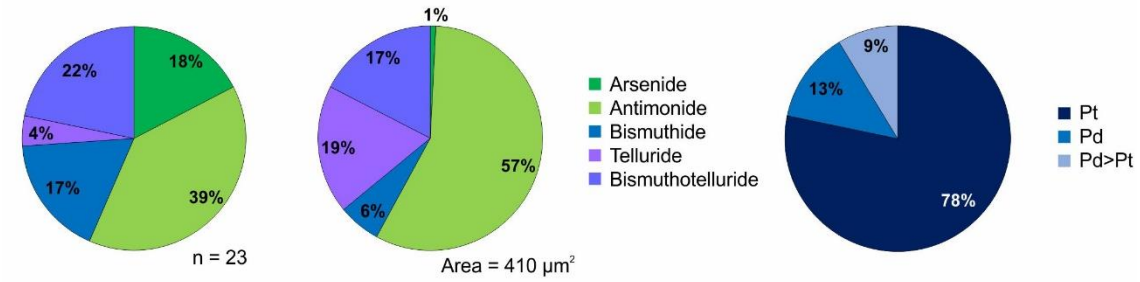

E) 345_05 - Pegmatoidal Orthopyroxenite (serpentinised)

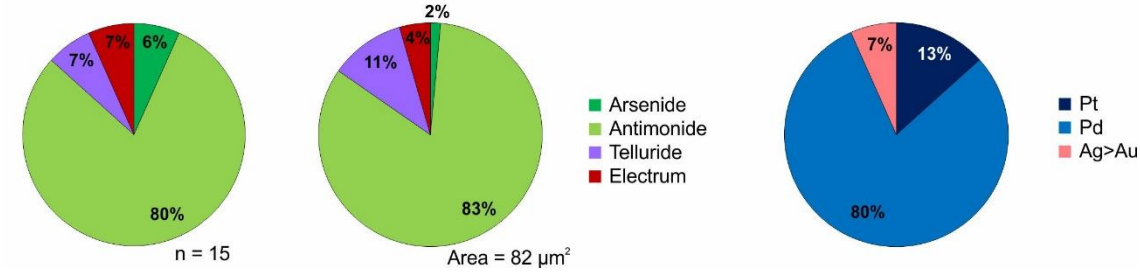

A) Orthopyroxenite (with disseminated chromite) - 345_08A

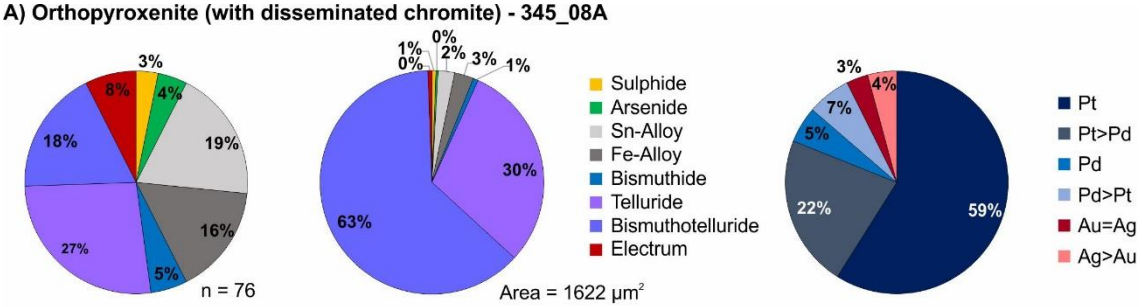

B) Lower Pyroxenite - D1_12A

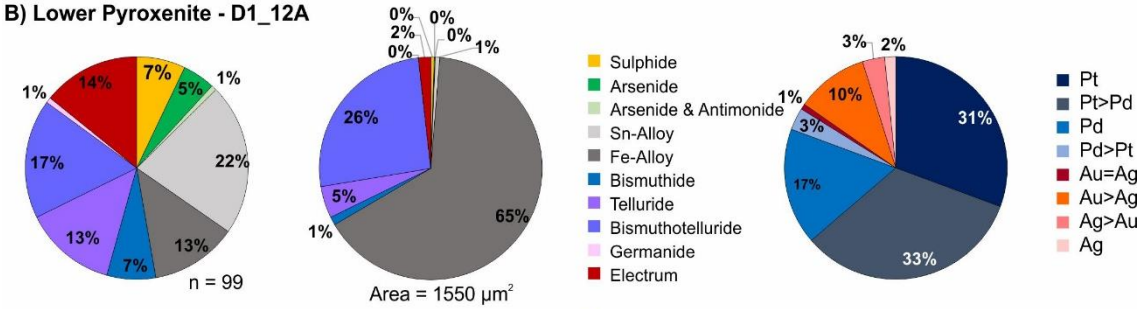

C) Lower Pyroxenite - D1_12C

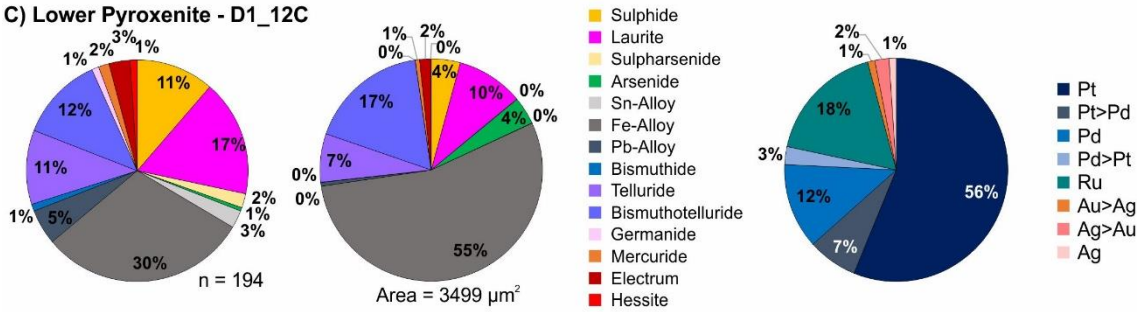

D) Lower Pyroxenite - D1_12F

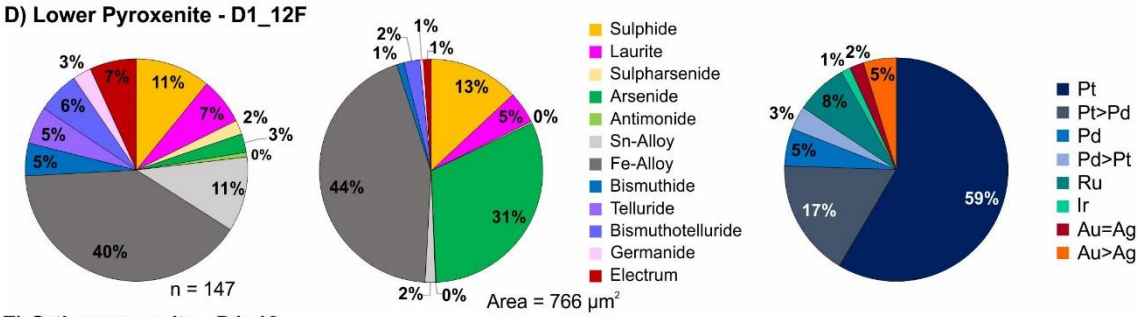

E) Orthopyroxenite - D1_13

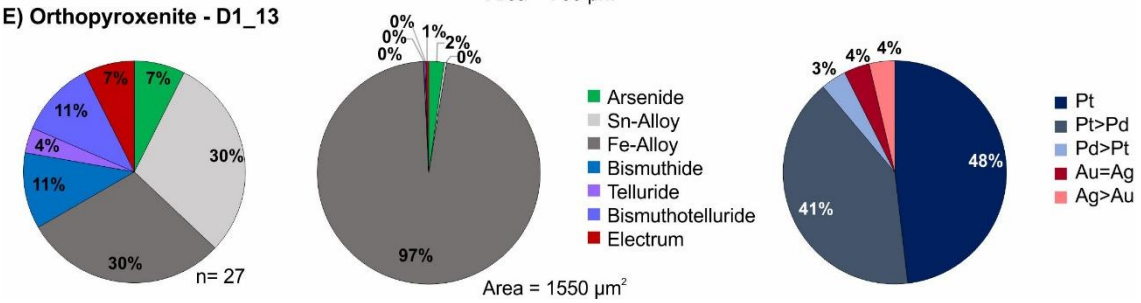

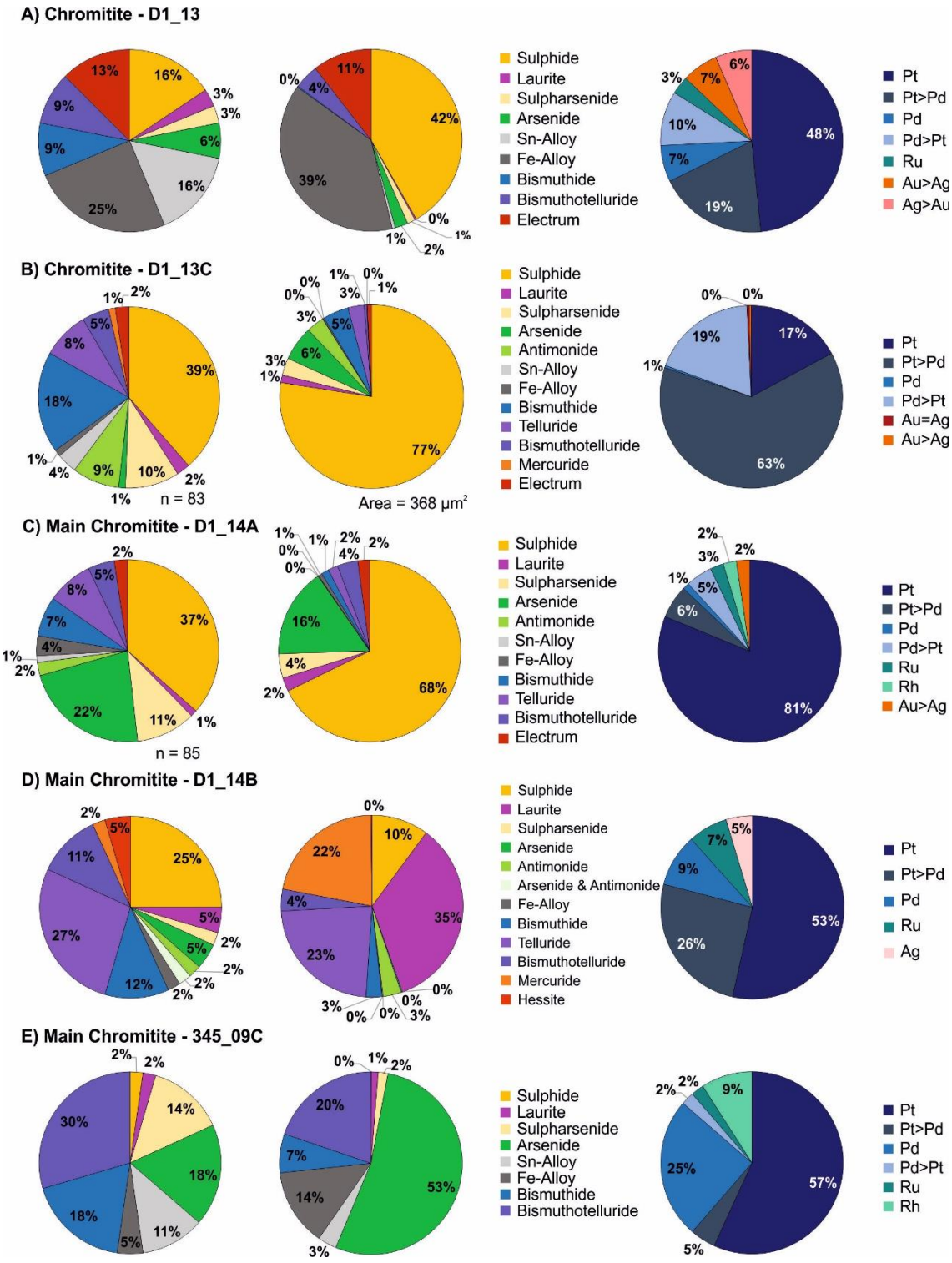
A) Chromitite - D1_13
13%
16%
3%
3%
9%
6%
9%
16%
25%
0%
11%
42%
4%
39%
0%
1%
2%
Sulphide
Laurite
Sulpharsenide
Arsenide
Sn-Alloy
Fe-Alloy
Bismuthide
Bismuthotelluride
Electrum
3%
7%
6%
10%
48%
7%
19%
Pt
Pt>Pd
Pd
Pd>Pt
Ru
Au>Ag
Ag>Au
B) Chromitite - D1_13C
1%
2%
5%
8%
39%
18%
1%
4%
9%
10%
2%
1%
n = 83
0%
0%
1%
0%
3%
1%
3%
5%
3%
6%
1%
77%
Area = 368 µm²
Sulphide
Laurite
Sulpharsenide
Arsenide
Antimonide
Sn-Alloy
Fe-Alloy
Bismuthide
Telluride
Bismuthotelluride
Mercuride
Electrum
0%
0%
19%
17%
1%
63%
Pt
Pt>Pd
Pd
Pd>Pt
Au=Ag
Au>Ag
C) Main Chromitite - D1_14A
2%
5%
8%
37%
7%
4%
1%
2%
22%
11%
1%
n = 85
1%
1%
2%
2%
0%
0%
16%
4%
2%
68%
Sulphide
Laurite
Sulpharsenide
Arsenide
Antimonide
Sn-Alloy
Fe-Alloy
Bismuthide
Telluride
Bismuthotelluride
Electrum
2%
3%
2%
1%
5%
6%
81%
Pt
Pt>Pd
Pd
Pd>Pt
Ru
Rh
Au>Ag
D) Main Chromitite - D1_14B
2%
5%
11%
25%
27%
5%
5%
2%
12%
2%
2%
2%
0%
10%
22%
35%
4%
23%
3%
0%
0%
0%
3%
Sulphide
Laurite
Sulpharsenide
Arsenide
Antimonide
Arsenide & Antimonide
Fe-Alloy
Bismuthide
Telluride
Bismuthotelluride
Mercuride
Hessite
7%
5%
9%
53%
26%
Pt
Pt>Pd
Pd
Ru
Ag
E) Main Chromitite - 345_09C
2%
2%
14%
30%
18%
18%
5%
11%
0%
1%
2%
20%
7%
53%
14%
3%
Sulphide
Laurite
Sulpharsenide
Arsenide
Sn-Alloy
Fe-Alloy
Bismuthide
Bismuthotelluride
2%
2%
9%
25%
57%
5%
Pt
Pt>Pd
Pd
Pd>Pt
Ru
Rh

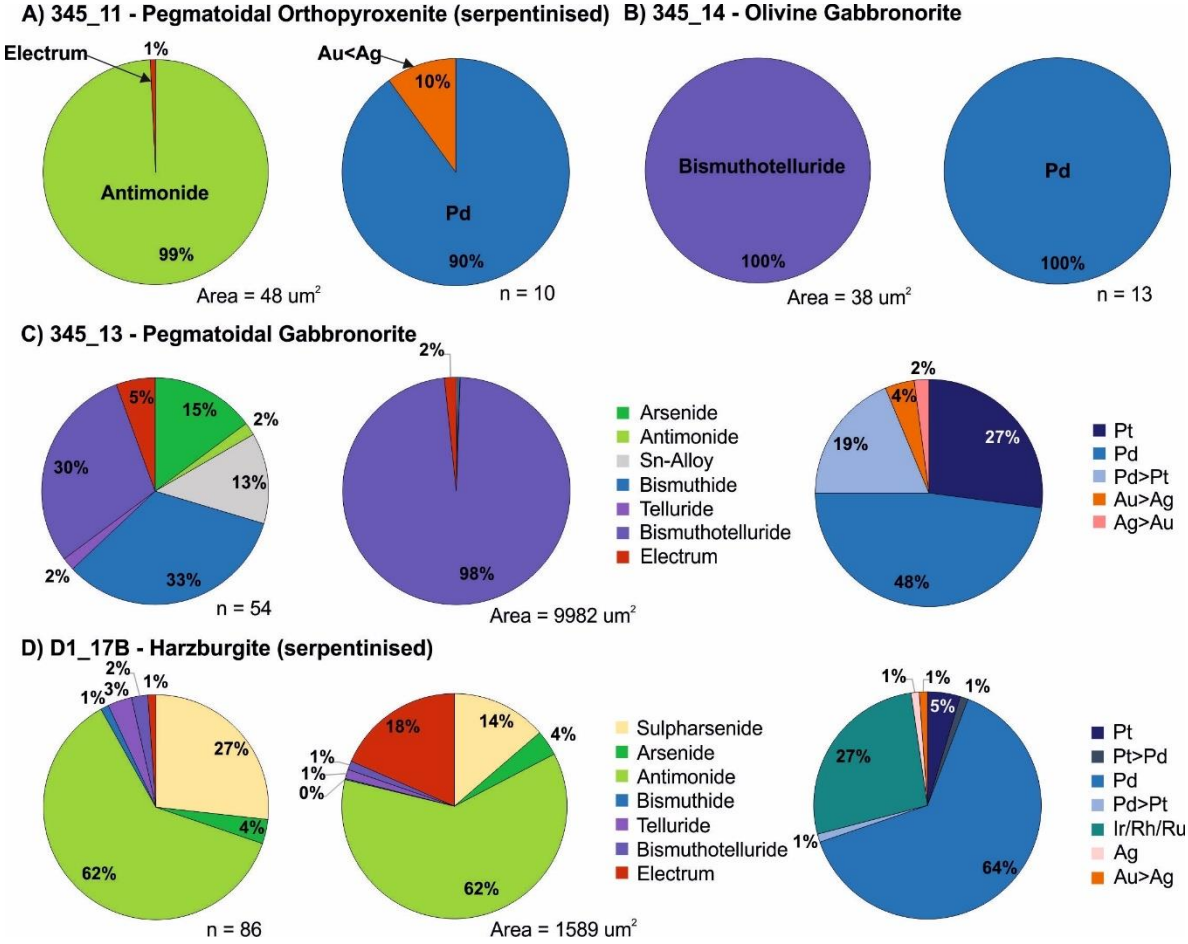
A) 345_11 - Pegmatoidal Orthopyroxenite (serpentinised)
B) 345_14 - Olivine Gabbronorite
Electrum
1%
Antimonide
99%
Area = 48 um²
Au<Ag
10%
Pd
90%
n = 10
Bismuthotelluride
100%
Area = 38 um²
Pd
100%
n = 13
C) 345_13 - Pegmatoidal Gabbronorite
5%
15%
2%
30%
13%
2%
33%
n = 54
2%
98%
Area = 9982 um²
Arsenide
Antimonide
Sn-Alloy
Bismuthide
Telluride
Bismuthotelluride
Electrum
2%
4%
19%
27%
48%
Pt
Pd
Pd>Pt
Au>Ag
Ag>Au
D) D1_17B - Harzburgite (serpentinised)
2%
3%
1%
1%
27%
4%
62%
n = 86
18%
14%
4%
1%
1%
0%
62%
Area = 1589 um²
Sulpharsenide
Arsenide
Antimonide
Bismuthide
Telluride
Bismuthotelluride
Electrum
1%
1%
1%
5%
27%
1%
64%
Pt
Pt>Pd
Pd
Pd>Pt
Ir/Rh/Ru
Ag
Au>Ag

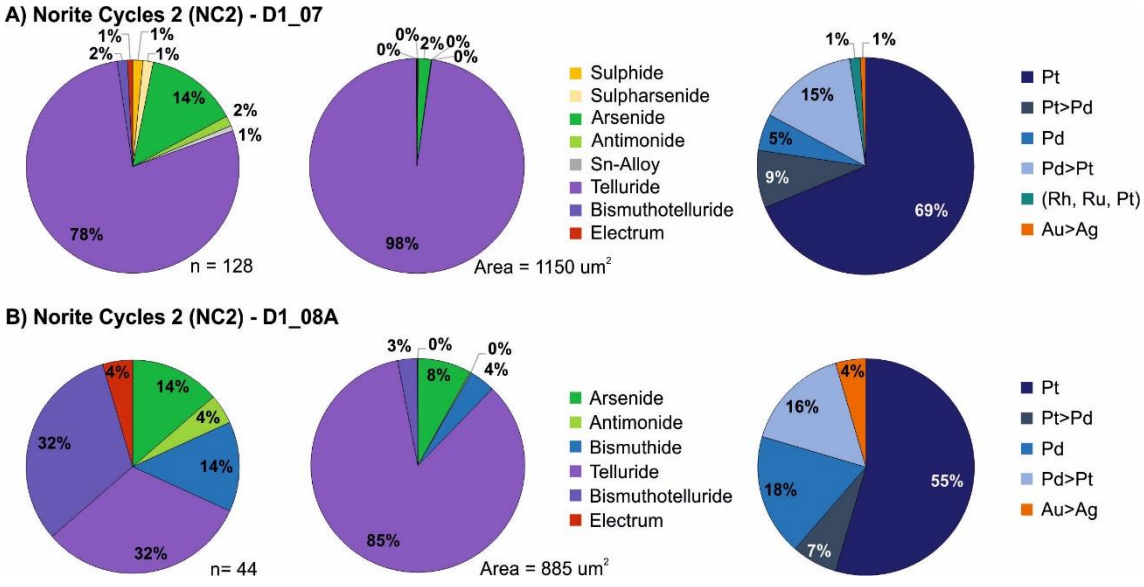
A) Norite Cycles 2 (NC2) - D1_07
1%
1%
2%
1%
14%
2%
1%
78%
n = 128
0%
0%
2%
0%
0%
98%
Area = 1150 um²
Sulphide
Sulpharsenide
Arsenide
Antimonide
Sn-Alloy
Telluride
Bismuthotelluride
Electrum
1%
1%
15%
5%
9%
69%
Pt
Pt>Pd
Pd
Pd>Pt
(Rh, Ru, Pt)
Au>Ag
B) Norite Cycles 2 (NC2) - D1_08A
4%
14%
4%
32%
14%
32%
n= 44
3%
0%
0%
8%
4%
85%
Area = 885 um²
Arsenide
Antimonide
Bismuthide
Telluride
Bismuthotelluride
Electrum
4%
16%
18%
55%
7%
Pt
Pt>Pd
Pd
Pd>Pt
Au>Ag